



# ***Decay Spectroscopy of Neutron-Rich Cadmium Isotopes***

Memoria presentada para la obtención  
del título de doctor

**Jan Taprogge**

Director:  
Andrea Jungclaus (IEM CSIC)

Instituto de Estructura de la Materia  
Consejo Superior de Investigaciones Científicas

Departamento de Física Teórica  
Facultad de Ciencias  
Universidad Autónoma de Madrid

Marzo de 2015



**CSIC**

CONSEJO SUPERIOR DE INVESTIGACIONES CIENTÍFICAS



# Contents

<b>1</b>	<b>Introduction and motivation</b>	<b>1</b>
1.1	Shell structure along N=82	3
1.2	Introduction to the nuclear shell model	4
1.2.1	Previous shell-model calculations in the $^{132}\text{Sn}$ region	5
1.3	r-process	7
1.3.1	Models used to predict nuclear physics input parameters for r-process calculations	9
1.4	$\beta$ decay	12
1.4.1	Fermi decay	13
1.4.2	Total $\beta$ -decay rate	14
1.4.3	Allowed and forbidden decays	14
1.4.4	$\beta$ decays in the $^{132}\text{Sn}$ region	16
<b>2</b>	<b>General setup of an EURICA experiment</b>	<b>19</b>
2.1	Producing the nuclei of interest	19
2.1.1	RIKEN RI Beam factory	20
2.1.2	Fragment separator BigRIPS	21
2.1.3	Production of very neutron-rich nuclei in the RIBF 85 experiment and the particle selection	24
2.2	Active stopper	28
2.2.1	Properties of WAS3ABi	28
2.2.2	Implantation events	30
2.2.3	WAS3ABi calibration	34
2.2.4	Energy shift during the experiments	35
2.2.5	$\beta$ -decay events	36
2.2.6	Ion - $\beta$ correlations	37
2.3	EURICA Ge-Array	41
2.3.1	Addback algorithm	42
2.3.2	Ge-Array: calibration and absolute efficiency	44
2.4	Data processing	48
2.4.1	Data acquisition	48
2.4.2	Raw data preparation	49
2.4.3	Merging and analysis Code	49

<b>3</b>	<b><math>\beta</math>-decay spectroscopy of neutron-rich <math>^{128-133}\text{Cd}</math> and the structure of <math>^{128-132}\text{In}</math></b>	<b>53</b>
3.1	Analysis methods and the $^{128}\text{Cd}$ $\beta$ decay . . . . .	54
3.1.1	$\beta$ -delayed germanium spectrum . . . . .	55
3.1.2	Cleaning of the germanium spectra: multiplicity . . . . .	58
3.1.3	$\gamma$ - $\gamma$ -coincidences . . . . .	58
3.1.4	Relative intensities and conversion coefficient . . . . .	60
3.1.5	$\beta$ -decay feeding and cleaning of $\beta$ -decay spectra . . . . .	61
3.1.6	$\log ft$ values . . . . .	65
3.1.7	Transitions in the $^{128}\text{Cd}$ $\beta$ decay and level scheme . . . . .	65
3.1.8	Conclusions . . . . .	67
3.2	Decay of $^{129}\text{Cd}$ . . . . .	68
3.2.1	Transitions feeding the $11/2^+$ , $13/2^+$ and $17/2^-$ levels . . . . .	73
3.2.2	The 3184-, 3348-, 3888- and 4118-keV levels . . . . .	76
3.2.3	The position of the $1/2^-$ $\beta$ -decaying isomer . . . . .	76
3.2.4	The $^{129}\text{In}$ level scheme, level feeding and $\log ft$ values . . . . .	77
3.2.5	Discussion and conclusions . . . . .	81
3.3	Decay of $^{130}\text{Cd}$ . . . . .	82
3.3.1	Transitions in the $^{130}\text{Cd}$ $\beta$ decay and level scheme of $^{130}\text{In}$ . . . . .	82
3.3.2	Conclusions . . . . .	87
3.4	The $\beta$ decay of $^{131}\text{Cd}$ and $\beta$ -delayed n emission from $^{132}\text{Cd}$ . . . . .	88
3.4.1	Transitions observed in the $\beta$ decay of $^{131}\text{Cd}$ . . . . .	88
3.4.2	Transitions observed after $\beta$ -delayed neutron emissions of $^{132}\text{Cd}$ . . . . .	91
3.4.3	The level scheme of $^{131}\text{In}$ . . . . .	92
3.5	Decay of $^{133}\text{Cd}$ . . . . .	101
3.5.1	Conclusions . . . . .	104
<b>4</b>	<b>Gross properties of <math>^{126-134}\text{Cd}</math> <math>\beta</math> decays</b>	<b>107</b>
4.1	Analysis methods for $\beta$ -decay half-lives . . . . .	107
4.1.1	Lifetime analysis: $\chi^2$ Fit with Bateman equations . . . . .	108
4.1.2	Maximum Likelihood fit . . . . .	110
4.1.3	Error determination in the $\chi^2$ and MLH fits . . . . .	114
4.1.4	$\gamma$ -gated half-lives for $\beta$ -decay . . . . .	116
4.2	$\beta$ -decay half-life results . . . . .	116
4.2.1	The test cases $^{131,132}\text{In}$ for $\gamma$ -gated half-lives . . . . .	117
4.2.2	Comparison of the three methods for $^{130}\text{Cd}$ . . . . .	118
4.2.3	$^{126-134}\text{Cd}$ half-lives . . . . .	127
4.2.4	Discussion and comparison to literature . . . . .	135
4.3	$\beta$ delayed neutron emission probability . . . . .	138
4.3.1	Deducing the $P_n$ value in the current experiment . . . . .	138
4.3.2	$P_n$ values for $^{128-133}\text{Cd}$ . . . . .	140
4.3.3	Comparison to theory and discussion . . . . .	141

<b>5</b>	<b>Isomer spectroscopy of neutron-rich <math>^{128-130}\text{Cd}</math></b>	<b>143</b>
5.1	Analysis methods and isomeric states in $^{128}\text{Cd}$ . . . . .	143
5.1.1	Energy-time-matrix and delayed Ge spectra . . . . .	144
5.1.2	Relative intensities and conversion coefficients . . . . .	147
5.1.3	Half-life analysis of isomeric states . . . . .	149
5.1.4	Centroid shift method . . . . .	153
5.1.5	Conclusions . . . . .	155
5.2	A ms isomeric state in $^{129}\text{Cd}$ . . . . .	155
5.2.1	Triggering of the data acquisition to observe a ms isomeric state	157
5.2.2	Conversion coefficients and multipolarities . . . . .	160
5.2.3	Monte Carlo simulations of the suggested scenarios . . . . .	161
5.2.4	Conclusions . . . . .	163
5.3	A $\mu\text{s}$ isomeric state in $^{129}\text{Cd}$ . . . . .	163
5.3.1	Conclusions . . . . .	165
5.4	The $(8^+)$ isomeric state in $^{130}\text{Cd}$ . . . . .	165
5.4.1	Experimental results . . . . .	166
5.4.2	Conclusions . . . . .	170
5.5	Isomeric ratios . . . . .	170
5.5.1	Calculation of the isomeric ratio . . . . .	171
5.5.2	Isomeric Ratios of long lived states in Ag, Cd, In, Sn populated in fragmentation and relativistic fission. . . . .	172
5.5.3	Comparison to the sharp cut-off model and conclusions . . . . .	175
<b>6</b>	<b>Shell-model comparison</b>	<b>177</b>
6.1	The NA-14 shell-model interaction . . . . .	177
6.2	The ms isomeric state in $^{129}\text{Cd}$ . . . . .	178
6.3	The decay of the $17/2^-$ isomeric state in $^{129}\text{In}$ . . . . .	179
6.4	Shell-model calculations for the N=82 isotones . . . . .	180
6.4.1	The evolution of the N=82 shell gap . . . . .	181
6.4.2	The N=82 shell gap and its impact on r-process calculations . . . . .	183
<b>7</b>	<b>Summary and outlook</b>	<b>185</b>
<b>8</b>	<b>Introducción y resumen en castellano</b>	<b>189</b>
8.1	Introducción . . . . .	189
8.2	Resumen de los resultados y conclusiones . . . . .	190
8.2.1	Espectroscopía de $\beta$ -delayed . . . . .	191
8.2.2	Periodos de semidesintegración $\beta$ . . . . .	206
8.2.3	Probabilidades de emisión de neutrones $P_n$ . . . . .	208
8.2.4	Estados isoméricos . . . . .	210
	<b>Appendices</b>	<b>213</b>
<b>A</b>	<b>Sorting manual</b>	<b>215</b>

A.0.5	Installation of the sorting software . . . . .	215
A.0.6	The important files + setting up the working directories . . . . .	216
A.0.7	The sorting process . . . . .	217
A.1	Latest Germanium calibration file . . . . .	217
<b>B</b>	<b>EURICA angles</b>	<b>221</b>
<b>C</b>	<b>Complementary experimental information</b>	<b>227</b>
C.1	Efficiency calibration coefficients . . . . .	227
C.2	$\gamma$ - $\gamma$ -coincidence information $\beta$ -decay . . . . .	227
C.3	Formulas for the half-life analysis . . . . .	231
C.4	Isomeric ratios . . . . .	232
	List of Figures . . . . .	236
	List of Tables . . . . .	242
	Bibliography . . . . .	245

# Chapter 1

## Introduction and motivation

The shell structure of the atomic nucleus is of particular importance for understanding the properties of the nucleus, with the nucleus being an N-body quantum system for which the basic interaction between constitutive elements is still not well understood. The nucleon-nucleon interaction itself and how it evolves and affects the properties of the nucleus when moving away from the valley of stability is still one of the fundamental questions in nuclear physics. The regions around doubly-magic nuclei, having closed neutron and proton shells, play here a key-role for the investigation. In the vicinity of these, the single-particle energies and the interactions between nucleons (protons or neutrons) can be studied and used to improve models to describe the nuclear structure of nuclei far from the valley of stability.

The present work is focusing on the region around the doubly-magic nucleus  $^{132}\text{Sn}$  (Tin), having 50 protons ( $Z=50$ ) and 82 neutrons ( $N=82$ ). In this region, the properties of nuclei can be studied far away from the valley of stability, with  $^{132}\text{Sn}$  having 8 neutrons more than

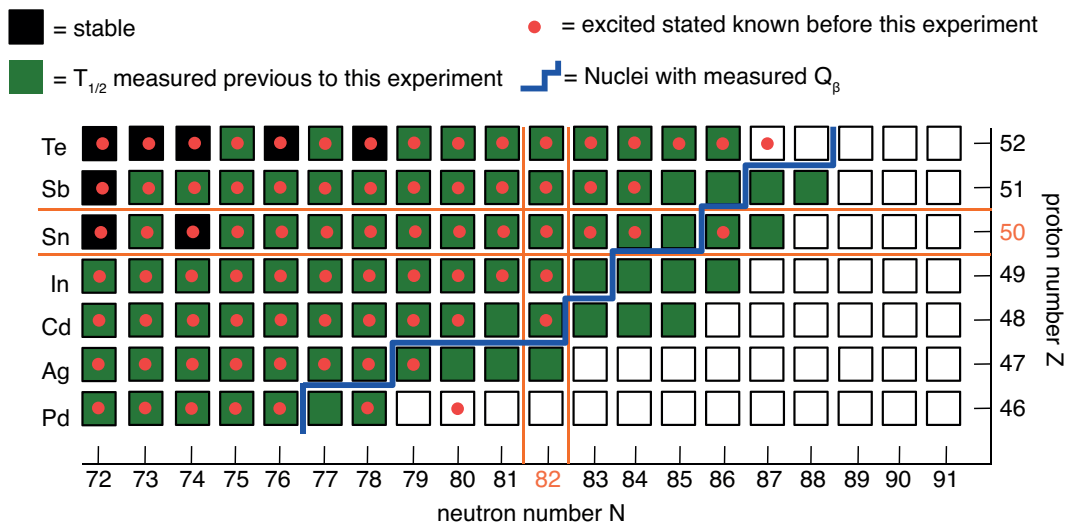


**Figure 1.1:** The region around the doubly magic  $^{132}\text{Sn}$  and an overview what experimental information was available previous to this work as presented in Refs. [1, 2].

the last stable Tin isotope (see Fig. 1.1) and being the heaviest doubly-magic nucleus far off stability which is experimentally accessible. A second motivation to study this region is that it is a crucial region for nuclear astrophysics and in particular the rapid neutron capture process, called r-process in the following. Around  $^{132}\text{Sn}$  experimental information is available for the less exotic isotopes above Tin ( $Z > 50$ ) while below  $^{132}\text{Sn}$  excited states are only known for  $N \leq 82$ . Fig. 1.1 shows the region around the doubly magic  $^{132}\text{Sn}$  and the availability of experimental data previous to the experiments presented in this thesis. Shown in dark green are the nuclei for which  $\beta$ -decay half-lives were measured, while the nuclei with known excited states are marked with a red dot. The  $Q_{\beta}$  value, the energy released in the  $\beta$  decay, was measured for all nuclei on the left side of the blue line. Especially in the region south and even more south-east of  $^{132}\text{Sn}$  an unsatisfactory situation is found with regards to the available experimental data. For several nuclei, still no excited states are known and also  $Q_{\beta}$  values and  $\beta$ -decay half-lives are missing for most of the nuclei.

In the present thesis this problem will be addressed by studying the isomeric and  $\beta$  decays of very neutron-rich Cadmium (Cd) isotopes to obtain information about excited states in those nuclei and in the  $\beta$ -decay daughter nuclei. Furthermore, the gross properties such as  $\beta$ -decay half-lives and  $\beta$ -delayed neutron emission probabilities will be investigated. This work is a natural continuation of the studies presented in Refs. [3–10], where the decay of several isomeric states in  $Z \leq 50$ ,  $N \leq 82$  nuclei were studied. The focus in this thesis is to obtain new experimental information on the  $N \geq 82$  Cadmium and Indium (In) nuclei. The nucleus  $^{131}\text{In}$  is important here because several proton single-hole energies with respect to the  $^{132}\text{Sn}$  core are still missing and as a consequence, no shell model studies have been presented yet for the region  $Z \leq 50$ ,  $N \geq 82$ .

Results from the two experiments presented in this thesis were already published in several works and the knowledge about the region around  $^{132}\text{Sn}$  was extended. In Ref. [11] the observation of yrast ( $6^+$ ) seniority isomers in  $^{136,138}\text{Sn}$  were reported which were used as a benchmark for shell-model calculations far off the valley of stability. To obtain new experimental information on excited states below  $^{132}\text{Sn}$ , the decay of several isomeric states in the Pd isotopes with masses  $A = 126$  and  $128$  was studied in Refs. [12, 13]. In those works the experimental findings were interpreted as an indication for a robust  $N=82$  shell-closure at  $Z=46$ . In an additional work [14] the  $\beta$ -decay half-lives of more than 100 unstable nuclei around  $N=82$  and for  $Z \leq 50$  were measured. The new half-lives were then used to perform r-process calculations and it was concluded that the relative abundances around the neutron shell closures are particularly sensitive to the  $\beta$ -decay half-lives of nuclei on the r-process path.

The following introduction will give a more detailed reason why it is important to gain insight into the properties of the neutron-rich Cadmium and Indium isotopes with  $N \approx 82$  to answer open questions in the region such as the evolution of the  $N=82$  shell-gap below  $^{132}\text{Sn}$ .

## 1.1 Shell structure along N=82

While the evolution of the Z=50 shell gap has been studied over a broad range of nuclei, there is still limited experimental information on the N=82 shell gap below  $^{132}\text{Sn}$ . The evolution of the N=82 shell gap has been the subject of several studies, and a long time ago a quenching of the shell gap was predicted in several of them.

Self-consistent mean-field calculations [15] showed a quenching of the shell gap when coming closer to the neutron drip line as a result of the lowering of low-j orbitals relative to high-j orbitals. As a consequence, the low-j orbitals are becoming more likely the valence states above the shell gap. Neutrons with energies of about 100 keV, as they are typical in the environments related to the r-process, e.g. star explosions, can hardly overcome centrifugal barriers of the high-l orbits. Low-j or low-l neutron valence orbitals at lower excitation energies therefore directly imply the increase of the neutron-capture cross sections. This would have a big impact on the evolution of the r-process at the waiting points due to a reduced neutron-capture time. In Ref. [16] and [17] several models for predicting the nuclear physics input parameters for r-process calculations were compared and it was concluded that models which include a shell quenching below  $^{132}\text{Sn}$  improve the obtained abundance distributions especially in the regions around  $A \approx 120$  and 140. On the contrary, it was shown in later works [18, 19] that a shell quenching is not necessary to explain this behaviour, making it impossible to draw direct conclusions from the abundance distributions obtained with the different models to the N=82 shell gap.

The experimental information available on the N=82 shell gap is still controversial and no direct proof is available of how the shell gap evolves. Dillmann *et al.* [20] concluded from the observations they made in their study of the  $\beta$ -decay of  $^{130}\text{Cd}$ , especially a high  $Q_\beta$ , that shell-quenching can already be observed very closely to the doubly magic  $^{132}\text{Sn}$ . Furthermore, Kautzsch *et al.* [21] tentatively proposed the first excited  $2^+$  state in  $^{130}\text{Cd}$  to have a very low excitation energy of 957 keV and suggested this to be a first proof for the weakening of the shell gap. Though, in a later work by Jungclaus *et al.* [7] no evidence could be found for placing it at 957 keV, and in that work a new level scheme was proposed with the first excited  $2^+$  state being placed at 1325 keV.

One possible approach to answer the question if the shell gap is quenched is to study the properties of the N=82 isotones using the nuclear shell model. The experiment in this thesis could provide crucial input parameters for those shell-model calculations in the region below  $^{132}\text{Sn}$ . As a starting point, a very general introduction is given before the focus is set on the  $^{132}\text{Sn}$  region and shell-model calculations performed in that area. For a more detailed introduction to the nuclear shell model, it is explicitly referred to Refs. [22, 23].

## 1.2 Introduction to the nuclear shell model

The starting point for the nuclear shell model was set in 1949 [24, 25] by assuming a central potential of a harmonic oscillator with mass  $m$ , oscillator frequency  $\omega$  and the distance from the center  $r$ :

$$V_{HO} = m\omega^2 r^2 / 2. \quad (1.1)$$

Furthermore, a spin-orbit coupling term, with  $f$  being a function of the radius  $r$  and  $\vec{l}$ ,  $\vec{s}$  the orbital angular momentum and spin operators of a nucleon, respectively, was added:

$$V_{ls}(r) = f(r)(\vec{l} \cdot \vec{s}) \quad (1.2)$$

The eigenvalues of this harmonic oscillator potential combined with the spin-orbit force accurately described the experimental results known at that time which suggested certain nucleon numbers of either protons or neutrons to be significantly more stable than their direct neighbours. Those numbers of nucleons (2, 8, 20, 28, 50, 82, ...), called magic numbers, were deduced from the experimental observations, and even in 1948 the facts supporting the presence of closed shells in certain nuclei were very convincing. M. G. Mayer summarized some of the experimental results in Ref. [26], including the observation that the isotopic abundance and the number of isotones with 50 or 82 neutrons is significantly higher than for any other neutron number. Furthermore, it is listed that the neutron absorption cross section for nuclei with 50, 82 or 128 neutrons is small in comparison to other nuclei. Also for the number of protons there were several indications known at that time, for example the large number of Tin (Sn,  $Z = 50$ ) isotopes.

While the interpretation of the nucleus in terms of a shell model was proposed in analogy to the atomic shell model, there are several major differences which complicate the situation tremendously. One of them is that in the atomic shell model, the electrons feel the central Coulomb potential created by the nucleus, but in the nucleus the nucleons themselves create a central mean field potential, making the exact description much more complex. To describe the potential, the assumption is made that only two-body interactions are relevant, which in most cases is a good description. The effects of three- and more body interactions are either small in the energy scale of interest, or can be renormalized into effective two-body interactions. The Hamiltonian can then be written as a sum of kinetic (T) and potential energy (V):

$$H = T + V = \sum_{i=1}^A \frac{\vec{p}_i^2}{2m_i} + \sum_{i>k=1}^A V_{ik}(\vec{r}_i - \vec{r}_k) \quad (1.3)$$

Since each nucleon contributes with its one-body nucleon potential  $U_i$  to the mean field potential,  $U_i$  is introduced and formula 1.3 rearranged to:

$$H = \sum_{i=1}^A \left[ \frac{\vec{p}_i^2}{2m_i} + U_i(\vec{r}) \right] + \sum_{i>k=1}^A V_{ik}(\vec{r}_i - \vec{r}_k) - \sum_{i=1}^A U_i(\vec{r}) = H_0 + H_{res} \quad (1.4)$$

Inspecting formula 1.4, one observes that the nuclear Hamiltonian can be sub-divided into two parts and those, if taken individually, have solutions which can be associated directly to experimental information. Solving the Schrödinger equation for  $H_0$  provides the nucleon single particle energies (SPE)  $\epsilon_j$  in a central potential. Those can be compared to the energies of single particle (hole) states in the direct neighbours of doubly-magic nuclei with one proton or neutron more (less) compared to the doubly-closed shell nuclei. The mutual interaction of valence nucleons in the neighbours with two protons or neutrons more (less) on the other hand can be associated with the two-body matrix elements (TBME) of the residual interaction  $H_{res}$ . It is necessary to deduce the SPE and the TBME to perform shell-model calculations and several approaches exist from which some of them are being described here in the following.

The SPE  $\epsilon_j$  can either be directly obtained from experimental data by calculating the difference between the binding energies of the single particle (hole) state  $BE_{p/h}(n, l, j)$  and the ground state  $B_{gs,CS}$  of the corresponding doubly-closed shell (CS) nuclei:

$$\epsilon_j = BE_{p/h}(n, l, j) - B_{gs,CS} \quad (1.5)$$

with  $n$  the radial,  $l$  the orbital angular momentum and  $j$  the total angular momentum quantum number. Alternatively, they are extracted from an empirical globally adjusted central potential like the harmonic oscillator, the Woods-Saxon [27] or the folded Yukawa potential [28]. It has to be mentioned that in the case of a central potential with a certain shape, the results have to be interpreted with caution since they might not carry the full information, e.g. neglecting the actual distributions or interactions of nucleons at the Fermi surface.

One of the problems of the nuclear shell model is that the currently developed potentials are not able to predict the ordering and the spacing of the single particle/hole states for unknown regions, and it is necessary to adjust the models to experimental data. The information on those properties are reasonably well known for the doubly-magic nuclei  $^{16}\text{O}$ ,  $^{40}\text{Ca}$  and  $^{208}\text{Pb}$ , but information is still lacking on the proton single hole energies in the  $^{132}\text{Sn}$  region which makes shell-model calculations more difficult.

### 1.2.1 Previous shell-model calculations in the $^{132}\text{Sn}$ region

Shell-model calculations in the region of the doubly-magic  $^{132}\text{Sn}$  have been performed in several works previous to this thesis. In Refs. [29–31] for example the authors calculated the level schemes of neutron-rich Cadmium and Indium isotopes. In that work, a realistic effective interaction derived from the CD-Bonn nucleon-nucleon (NN) potential was employed. This potential is a charge-dependent NN potential which fits the world proton-proton and proton-neutron data below 350 MeV as available in 2000 with a  $\chi^2/datum \approx 1$  [32].  $^{132}\text{Sn}$  was considered as a closed core and the full major neutron and proton shells, namely the  $0f_{5/2}$ ,  $1p_{3/2}$ ,  $1p_{1/2}$  and  $0g_{9/2}$  orbits for protons and the  $0g_{7/2}$ ,  $1d_{5/2}$ ,  $1d_{3/2}$ ,  $2s_{1/2}$  and  $0h_{11/2}$  orbits for neutrons were taken into account. The neutron single-hole en-

ergies were taken from Ref. [33] and the proton single-hole energies from Ref. [34]. In the latter of those works the position of the  $1p_{3/2}$  and  $0f_{5/2}$  proton single-hole level are stated as 1.65 and 2.75 MeV with respect to the  $0g_{9/2}$  level. However, the position of the  $1p_{3/2}$  orbit has still been an open question and we will see later that the exact position has a significant influence on predictions made by the nuclear shell-model. In the present thesis the  $\beta$  decay of  $^{131}\text{Cd}$  to  $^{131}\text{In}$  is investigated to finally fix the position of the  $1p_{3/2}$  proton single-hole level. The calculations in Refs. [29, 30] show an overall not very good agreement and especially the decay scheme of the  $17/2^-$  isomer in  $^{129}\text{In}$  will be reproduced much better by the shell-model calculations performed for the present work. In Ref. [31] calculations are shown for the decay of isomeric states in  $^{128,130}\text{Cd}$ , two of the nuclei which are also going to be analysed in the present work. In that piece of work an overall not very good agreement is found with the experimental data in Refs. [6, 7]. The calculated positions of most levels deviate by several 100 keV and also the reduced transition probabilities  $B(E2)$  differ significantly. For example the  $B(E2)$  of the  $8^+$  to  $6^+$  transition is predicted to be 0.3 while the experimental values are 1.7(2) or 1.3(2), depending if the 127- or the 137-keV transition is placed between those states.

Additional shell-model calculations in the region south-west of  $^{132}\text{Sn}$  were performed in Refs. [5, 7].  $^{88}\text{Sr}$  was taken as a closed core and the interaction was again based on a G-matrix derived from the CD-Bonn nucleon-nucleon potential [32] as outlined in Ref. [35]. The model space in those calculations did not include core excitations across  $Z=50$  or  $N=82$  and the calculations were done with the code OXBASH [36]. The effective interaction in that case was derived to accurately describe the evolution of experimental single-particle/hole energies for  $^{88}\text{Sr}$  to  $^{100}\text{Sn}$  as taken from Refs. [18, 22]. Additional corrections were then applied to describe the single-hole energies in  $^{132}\text{Sn}$  (Refs. [18, 22]). Those shell-model calculations describe well the experimentally obtained level schemes of  $^{127,130}\text{Cd}$  [5, 7] except for the ordering of the  $(13/2^-)$  and  $(15/2^-)$  levels in  $^{127}\text{Cd}$ . In Refs. [5–7] furthermore large-scale shell-model calculations were performed with the codes ANTOINE and NATHAN [37] using a  $^{78}\text{Ni}$  core and allowing for excitations across the  $Z=50$  proton shell. Also for those calculations the CD-Bonn NN potential was used and the method as described in Ref. [35].

$\beta$ -decay spectroscopy was in most cases the choice to investigate the single particle/hole energies in the  $^{132}\text{Sn}$  region and has provided reliable information on the position of the corresponding levels in the four single particle and hole nuclei around  $^{132}\text{Sn}$ , namely  $^{131}\text{Sn}$  [38–41],  $^{133}\text{Sn}$  [42–44],  $^{133}\text{Sb}$  [45, 46] and  $^{131}\text{In}$  [47]. In the latter, only the position of the  $p_{1/2}$  proton single hole state is firmly established in respect to the  $g_{9/2}$  ground-state (g.s.) from the measurement with the double Penning trap mass spectrometer JYFLTRAP [48]. The results are summarized in Fig. 1.2 where the position of all known single particle and hole states prior to this thesis are shown in respect to the middle of the shell gap  $\lambda_F$  to remove the influence of the Coulomb energy difference  $\Delta E_C$ . As a comparison, also the SPE are stated for the well-studied doubly-magic nucleus  $^{208}\text{Pb}$ , for which all important energies have been reported a long time ago. In this figure, it becomes obvious that for  $^{132}\text{Sn}$  especially values for proton hole states are still missing which displays an



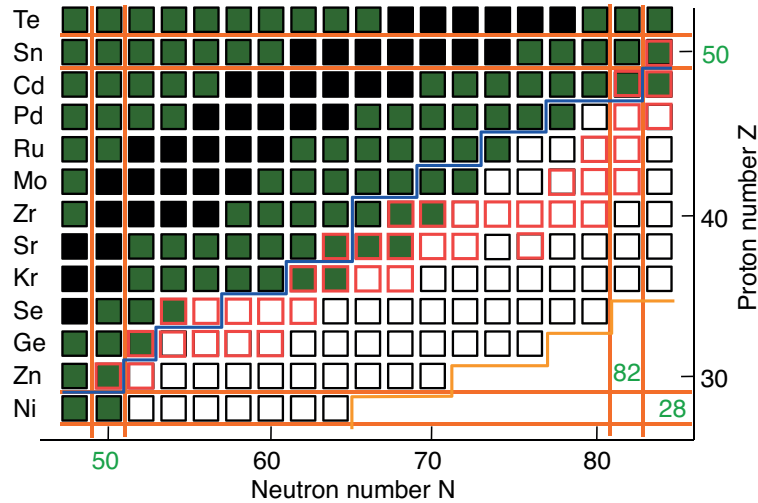


**Figure 1.3:** The Segré Chart in the region below the doubly-magic nuclei  $^{100}\text{Sn}$  and  $^{132}\text{Sn}$ . The stable nuclei are marked in black, the nuclei with known  $\beta$ -decay half-lives in green [51] and the neutron-drip line as calculated with the HFB-24 mass model as a yellow line [52]. The  $Q_\beta$  values of all nuclei of the left side of the blue line have been measured [1] and the orange lines indicate the magic proton and neutron numbers. A schematic r-process path is made visible through the nuclei with red boxes.

Segré chart and also the duration of the r-process, it is inevitable to have precise information about binding energies,  $\beta$ -decay half-lives and neutron-capture cross sections which can be influenced by nuclear structure changes. Especially in experimentally inaccessible regions it is necessary to know about the evolution of the nuclear structure, e.g. the evolution of the  $N=82$  shell closure below  $^{132}\text{Sn}$ , to be able to calculate binding energies, half-lives etc. for the nuclei lying on the path of the r-process.

During the r-process neutron capture processes occur on a very short time scale in a neutron-dense and hot environment creating nuclei with very exotic neutron-to-proton ratios. The neutron capture process is dominant until certain “waiting-points” (WP) are reached. At the WP, the neutron-capture rate comes to an equilibrium with the photo-disintegration rate due to the high photon flux in the very hot scenario and the low neutron capture cross sections  $\sigma_n$  of nuclei with magic neutron numbers. The r-process then has to wait for the  $\beta$ -decay to occur, meaning the r-process path goes along the nuclei with a magic neutron number up to higher  $Z$ . In the case of  $N=82$  (see Fig. 1.3) it climbs up till  $Z \approx 50$ , where the  $\beta$ -decay half-lives and photo-disintegration rates are slower than the neutron-capture process, driving the r-process towards the next neutron-shell closure. Once the r-process ends, the nuclei decay via  $\beta$ -decay and  $\beta$ -delayed neutron emission towards the valley of stability. This process is called “freezing out”. It has to be mentioned here that the abundance distribution of elements as it is observed at the end of the r-process is mainly affected by the waiting points, leading to abundance peaks for elements with  $A \approx 80$ , 130 and 195. The abundance peak at  $A \approx 130$  for example arises from the  $N=82$  shell closure.

To understand the exact shape and height of the abundance peaks and the general abun-

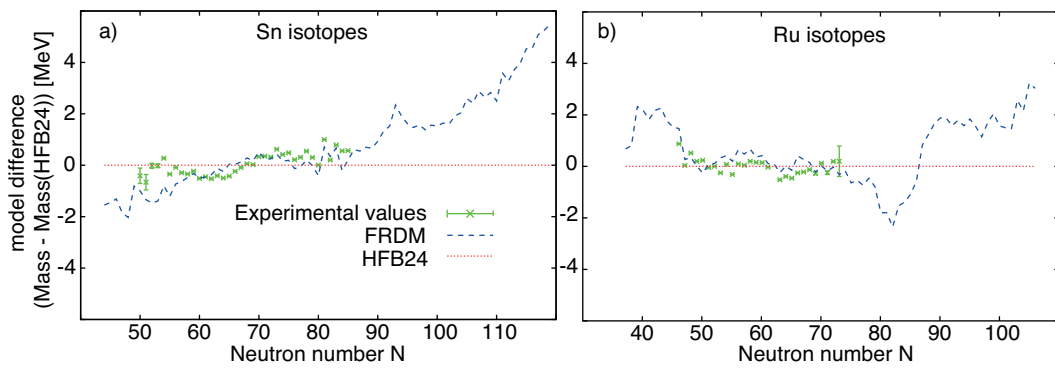


**Figure 1.4:** Difference of mass predictions made by the FRDM [28] model with respect to the mass calculated by the HFB24 [52] model for a) Sn isotopes and b) Ru isotopes. The experimental masses taken from Ref. [1] are shown for comparison.

dance distribution in the universe, it is important to understand the r-process very well. To simulate the r-process, however, several input parameters have to be provided by nuclear physics e.g. the mass, the half-life  $T_{1/2}$ , the  $\beta$ -delayed neutron emission probability  $P_n$ , the neutron separation energy  $S_n$  and the neutron capture cross-section  $\sigma_n$ . Changes or uncertainties in those values can vary on the one hand the path chosen by the r-process, and on the other hand the time scale of the r-process may be affected. This, of course, can change last but not least the whole abundance distribution. In Ref. [53] for example it was shown that the selection of specific sites where the r-process occurs is currently not possible because of the strong dependence on the nuclear physics input parameters which are based partly upon models providing very different results in the unknown areas of the Segré chart. In Ref. [17] the conclusion was drawn that testing models to predict the nuclear input parameters may be possible by comparing the results for abundance distributions, obtained with different models, to the solar-system's isotopic r-process abundance. Sensitivity studies, as for example in Refs. [54–56], have shown that changes in the nuclear masses and half-lives indeed have an influence on the final abundance pattern. It is therefore important to have models which describe those properties as accurately as possible in the experimental regions which are inaccessible until now.

Figure 1.3 shows that most nuclei on the r-process path still have not been experimentally studied and models for those nuclei have to be relied on. It is therefore essential to benchmark those models in regions far away from stability because the predictions made by the models differ significantly in the experimentally for the moment inaccessible regions.

### 1.3.1 Models used to predict nuclear physics input parameters for r-process calculations

One of the nuclear physics input parameters are the nuclear masses. Figure 1.4 shows different predictions for the nuclear masses of a) the Sn and b) the Ru (Ruthenium) iso-

topic chains made by the FRDM [28] and the HFB24 [52] models. The mass predicted by the HFB24 model is subtracted from all of them to emphasize the differences between the models.

FRDM is a macroscopic-microscopic model which takes its name from the used macroscopic model, the finite-range droplet model. In this macroscopic-microscopic model the total nuclear potential energy is calculated from the sum of a macroscopic and a microscopic term:

$$E(Z, N, Shape) = E_{macr}(Z, N, Shape) + E_{micr}(Z, N, Shape) \quad (1.6)$$

FRDM uses the finite-range droplet model for the macroscopic term. In that model  $E_{macr}(Z, N, Shape)$  is calculated from the mass excesses of  $Z$  hydrogen atoms and  $N$  neutrons. Further corrections are then applied to account for: the volume energy, the surface energy, the curvature energy, the  $A^0$  energy, the Coulomb energy, the volume redistribution energy, Coulomb exchange, the surface redistribution energy, the proton form-factor, the charge-asymmetry energy, the Wigner energy, the average pairing energy and the energy of bound electrons. An overview with all terms used for the corrections can be found in Ref [57] and the latest used parameters in those terms are summarized in Refs. [28, 57, 58]. The microscopic model on the other hand corrects for microscopic effects such as: shell effects, pairing effects and deformation. For details it is referred to Ref. [57].

The second model shown in Fig. 1.4 is the HFB24 model. It uses the Hartree-Fock-Bogoliubov method with a Skyrme-type effective interaction and contact-pairing forces together with other correction terms [52]. Similar to FRDM this model has a certain number of parameters which are determined by fitting them to the experimentally available information.

Both mass models show a generally good agreement with the experimental data taken from Ref. [1] as one observes in Fig. 1.4 and they furthermore reproduce the more than 2300 known masses with an average deviation of smaller than 600 keV. However, when going into the experimentally inaccessible regions they show big deviations in their predictions as shown here for the Sn and Ru isotopes. Furthermore, comparing the results in more detail one observes severe differences. For example FRDM predicts the N=82 shell-gap to stay constant until  $Z \approx 40$  [28, 58], while the HFB24 calculations show a quenching [52]. It is therefore essential to know if the N=82 shell gap is quenched below  $Z=50$  or not. Consequently this question is addressed again in the present thesis using shell-model calculations. If the shell gap is quenched then preference could be given to models which predict this shell-quenching, such as for example the HFB-24 model.

Another important input parameter for  $r$ -process calculations are the  $\beta$ -decay half-lives of nuclei on the  $r$ -process path. Fig. 1.5 shows the predictions made by several models for the Cadmium isotopes from N=77 to N=90. The first model is called FRDM+QRPA [63] and is a combination of the finite-range droplet mass model [28, 58] with the quasiparticle

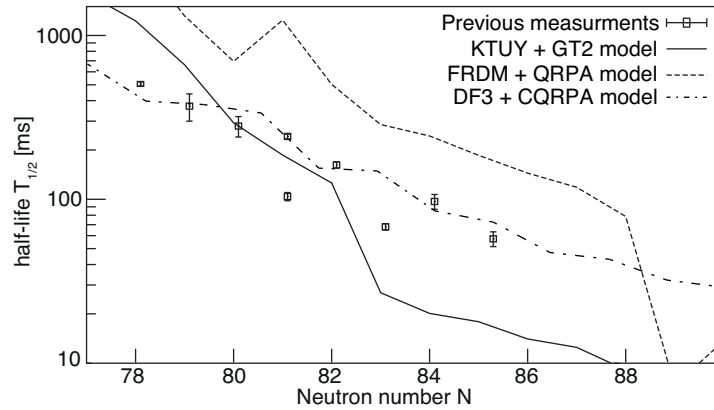


**Figure 1.5:** Experimental Cadmium half-lives for masses 126-132 taken from Refs. [20, 34, 59–62] and theoretical predictions by the FRDM+QRPA (dashed line) [63], KTUY+GT2 (solid line) [64–66] and DF3+QRPA (dashed dotted line) [67, 68] models.

random phase approximation (QRPA) [69] to calculate the Gamow-Teller (GT) strength. The random phase approximation (RPA) is a nuclear theory which starts from a ground-state wavefunction to describe nuclear excitations. This theory is used to describe collective vibrations via particle-hole correlations which are allowed in both the ground-state and excited states [70]. If pairing is included then the theory is called quasiparticle random phase approximation. The first QRPA model was published in 1984 [71] and several improvements have been added over the years. A more detailed discussion can be found in Ref. [69].

In the FRDM+QRPA model first-forbidden transitions are treated within the statistical gross theory framework [72,73].  $\beta$ -decays generally populate multiple states in the daughter nucleus and in the gross theory those decays are treated as a whole rather than individual decays. Therefore, a  $\beta$ -strength function is introduced. The function approximates the real distribution of  $\beta$ -strength by a smooth distribution and is a combination of the final states level density together with an appropriate average of the absolute squares of the nuclear matrix elements [64]. In this sense the Fermi transitions usually show a narrow peak at the isobaric analogue state (IAS), while the GT transitions are represented by a broader peak around the IAS and the forbidden decays by two broader peaks above and below the IAS. In this theory the  $Q_\beta$  value is the crucial input parameter to account for shell effects and deformation.

The second model is KTUY+GT2 which uses the KTUY mass formula [64]. The mass formula includes a gross term to describe the general trend of masses, an odd-even term to include the differences between odd and even nuclei, and a shell term which accounts for general shell effects. Combined with the second generation of gross theory for  $\beta$ -decays (GT2) [65, 66] the KTUY+GT2 model is obtained.

The last nuclear theory to be discussed is the DF3+CQRPA model [67, 68]. This is the first theoretical approach that treats the nuclear  $\beta$  decay in a fully self-consistent microscopic framework. It is based on the energy density-functional theory (DF) [74] and the

continuum QRPA (CQRPA) [75] method to calculate the GT and ff  $\beta$ -strength functions. One of the main limitations of this model is the assumed spherical symmetry. This is a good approximation in the vicinity of the classic shell closures, but limits its application for large-scale r-process calculations. Those calculations need input parameters over a large range of unknown nuclei, most of them not in the vicinity of doubly-magic nuclei.

In Fig. 1.5 the calculated half-lives are compared to the literature values taken from Refs. [20, 34, 59–62] and the observation is made that the predictions made by the different models differ by orders of magnitude and only the DF3+CQRPA model seems to describe the experimental data available previous to this thesis. Nevertheless, the literature half-life values show big jumps which are not expected and therefore the half-lives are going to be remeasured in the present work and then compared again to the three models.

To predict the  $\beta$ -decay half-lives with high accuracy it is essential to know if and how much first forbidden  $\beta$  decays contribute in the region below  $Z=50$  and close to  $N=82$ . This question has been discussed controversially in the past [63, 67, 68]. For example Borzov *et al.* [67] mention a factor of up to two reduction in the half-lives for  $Z<50$  and  $N\approx 82$  when including the ff transitions in their model. The  $\beta$  decays of the neutron-rich Cadmium isotopes observed in the present work are perfect test cases to measure the partial half-lives of first forbidden  $\beta$  decays in the region below  $Z=50$ .

In the following first a general introduction is given to  $\beta$  decays before the most important GT and first-forbidden  $\beta$  decay transitions in the  $^{132}\text{Sn}$  region are being discussed.

## 1.4 $\beta$ decay

In the  $\beta$ -decay process a proton is transformed in a neutron or vice versa with the nucleus either emitting an electron ( $\beta^-$  decay), emitting a positron ( $\beta^+$  decay) or capturing an electron (Electron capture). In the first observations and early studies of  $\beta$ -decays the observation of a continuous energy spectrum caused problems in the explanation of the process which was only resolved in 1933 by W. Pauli [76]. He explained the  $\beta$ -decay as a three-body process involving a new particle, the so called neutrino, which was finally discovered in 1956 by F. Reines [77].

As it was mentioned before, the  $\beta$ -decay can be subdivided into three different processes. A very simple description can be given for all of them when forgetting for the moment about the nuclear properties of the initial and the final states. In the first process ( $\beta^-$  decay) a proton  $p$  is transformed into a neutron  $n$  under the emission of an electron  $e^-$  and an antineutrino  $\bar{\nu}$ . This process happens on the right side of the valley of stability. The transformation of a neutron into a proton under the emission of a positron  $e^+$  and a neutrino  $\nu$  is the second process, called  $\beta^+$  decay, and can be encountered on the left side of the valley of stability. And while there is no competing process for the  $\beta^-$  decay, there is one for the  $\beta^+$  decay. On the left side of the valley of stability it is possible that the nucleus captures an atomic electron under the emission of a neutrino also transforming a

proton into a neutron. The three different types of  $\beta$ -decays are thus for a nucleus  $X$  with mass  $A$ , proton number  $Z$  and neutron number  $N$  :

$$\beta^- : {}^A_Z X_N \rightarrow {}^A_{Z+1} X'_{N-1} + e^- + \bar{\nu}_e \quad (1.7)$$

$$\beta^+ : {}^A_Z X_N \rightarrow {}^A_{Z-1} X'_{N+1} + e^+ + \nu_e \quad (1.8)$$

$$EC : {}^A_Z X_N + e^- \rightarrow {}^A_{Z-1} X'_{N+1} + \nu_e + X_{ray} \quad (1.9)$$

with the parent nucleus  $X$  and the daughter nucleus  $X'$ . An important quantity to describe the process is the energy released in a  $\beta$ -decay which is usually used to define the energy difference between the two ground-states of the parent and the daughter nuclei  $Q_\beta$ :

$$Q_{\beta^-} = \left[ m({}^A_Z X_N) - m({}^A_{Z+1} X'_{N-1}) - m_e \right] c^2 \quad (1.10)$$

$$Q_{\beta^+} = \left[ m({}^A_Z X_N) - m({}^A_{Z-1} X'_{N+1}) - 2m_e \right] c^2 \quad (1.11)$$

$$Q_{EC} = \left[ m({}^A_Z X_N) - m({}^A_{Z-1} X'_{N+1}) \right] c^2 - B_e \quad (1.12)$$

with  $m$  the nuclear mass,  $m_e$  the mass of the electron and  $B_e$  the binding energy of the electron captured in the EC process.

After this very simple consideration of the process a more detailed look will be taken at the influence of the involved states and the description made by Enrico Fermi.

### 1.4.1 Fermi decay

In 1934 E. Fermi [78] proposed the first successful description of the  $\beta$ -decay process based on the neutrino hypothesis. The description starts from his Golden Rule which generally describes the transition rates in quantum system:

$$\lambda = \frac{2\pi}{\hbar} |V_{fi}|^2 \rho(E_f) \quad (1.13)$$

with  $V_{fi}$  being the integral of the interaction and  $\rho(E_f)$  the density of final states.  $V_{fi}$  furthermore can be written as:

$$V_{fi} = \int \Psi_f^* V \Psi_i d\nu \quad (1.14)$$

in which  $\Psi_f^*$  and  $\Psi_i$  are the wave functions of the final and the initial quantum state, respectively, and  $V$  is the interaction.

At that time the underlying interaction was unknown and only later it could be shown that the operator  $O_x$  has a vector and axial vector form (V-A). Nevertheless, Fermi wrote the interaction generally as:

$$V_{fi} = g \int [\Psi_f^* \phi_e^* \phi_\nu^*] O_x \Psi_i d\nu, \quad (1.15)$$

introducing the electron and neutrino wave functions  $\phi_e^*$  and  $\phi_\nu^*$  and  $g$ , a constant factor for the strength of the interaction. The detailed derivation of the partial decay rate for

electrons and neutrons  $d\lambda$ , including the allowed approximation, is not made here, and it is explicitly referred to Refs. [78, 79]. In the allowed approximation the wave functions of the electron and neutrino are expanded in such a way that they do not depend on the orbital angular momentum  $L$ .  $d\lambda$  can then finally be written as:

$$d\lambda = \frac{2\pi}{\hbar} g^2 |M_{fi}|^2 (4\pi)^2 \frac{p^2 dp q^2}{h^6} \frac{dq}{dE_f} \quad (1.16)$$

where  $M_{fi}$  is the nuclear matrix element between the initial and final state and  $p, q$  are the momenta of the electron and the neutrino, respectively.

### 1.4.2 Total $\beta$ -decay rate

Integrating formula 1.16 over all electron and neutrino momenta leads to:

$$\lambda = \frac{g^2 |M_{fi}|^2}{2\pi \hbar^7 c^3} \int_0^{p_{max}} F(Z', p) p^2 (Q - E_{kin})^2 dp \quad (1.17)$$

With the introduction of the Fermi integral  $f(Z', E_0)$ :

$$f(Z', E_0) = \frac{1}{(m_e c)^2 (m_e c^2)^2} \int_0^{p_{max}} F(Z', p) p^2 (E_0 - E_{kin})^2 dp \quad (1.18)$$

where  $E_0$  is the maximum electron energy, formula 1.17 reduces to:

$$ft = \ln(2) \frac{2\pi^3 \hbar^7}{g^2 m_e^5 c^4 |M_{fi}|^2}. \quad (1.19)$$

$t$  in this formula is the half-life  $T_{1/2}$ , related to the decay constant  $\lambda$  in the following way:

$$\lambda = \frac{\ln 2}{T_{1/2}} \quad (1.20)$$

The  $ft$  value, or often its logarithmic value ( $\log ft$ ), is the perfect observable to compare and characterize the strength of  $\beta$ -decays in different nuclei, since they only depend on the nuclear matrix element  $|M_{fi}|^2$  and therefore can be used to identify differences in the nuclear wave functions.

### 1.4.3 Allowed and forbidden decays

The allowed approximation made to obtain formula 1.16 ignores the orbital angular momentum ( $\vec{L} = 0$ ) of the electron and the neutrino and therefore, the only change in the nuclear momentum can come from the spins ( $s_e, s_\nu = 1/2$ ) which can either be parallel or anti-parallel. With the spins being anti-parallel (commonly known as Fermi decay,  $\vec{S} = 0$ ), it can be seen directly that no change in the nuclear spin is possible because of momentum conservation:

$$\vec{l}_i = \vec{l}_f + \vec{L} + \vec{S}. \quad (1.21)$$

Transition	$L$	$\Delta I$	$\Delta\pi$
super allowed	0	0	no
allowed	0	0,1	no
first forbidden	1	0,1	yes
first forbidden unique	1	2	yes
second forbidden	2	1,2	no
second forbidden unique	2	3	no

**Table 1.1:** Classification of  $\beta$ -decays and selection rules in the orbital angular momentum  $L$ , the change in nuclear momentum  $\Delta I$  for Fermi and Gamow-Teller decays, the change in parity and the typical  $\log ft$  values.

In the case of parallel spins ( $\vec{S} = 1$ ), a change of nuclear momentum is possible with:

$$\Delta I = |I_i - I_f| = 0, 1 \quad (1.22)$$

and then we speak of a Gamow-Teller decay. One special case is  $\vec{I}_i = 0$  and  $\vec{I}_f = 0$ , here only Fermi decays are allowed.

Another observation which can be made for allowed decays is that no change in parity is allowed because of the orbital angular momentum of electron and neutrino being  $\vec{L} = 0$  and with the parity for an orbital angular momentum  $L$  being  $(-1)^L$ .

The orbital angular momentum carried away by the electron and the neutrino does not necessarily have to be 0, and one will see later that  $\beta$  decays are observed with a parity change or changes in  $\Delta I$  larger than 1. Those decays are commonly called forbidden decays, which might be a misleading name because they are just less likely in most cases than the allowed decays and have longer half-lives. Nevertheless, they become important in cases where the matrix elements of allowed transitions vanish so that only forbidden decays are possible. Depending on the amount of angular momentum carried away, the forbidden decays are subdivided into e.g. first forbidden ( $L = 1$ ), second forbidden ( $L = 2$ ),... . With the parity of the electron and neutrino wave function being  $(-1)^L$ , a change in parity is observed, for example for first forbidden decays. The selection rules for allowed and forbidden decays, which of course can also be a mixture of Fermi and Gamow-Teller decays, are summarized in Table 1.1. One special case for forbidden transitions is  $\Delta I = L + 1$ , in those cases only GT transitions are possible and they are called forbidden unique.

A classification if a certain decay is allowed or forbidden based on the  $\log ft$  values is unfortunately not always possible, as we can see in Fig. 1.6. The figure shows the distributions of experimental  $\log ft$  values for all transitions summarized in Ref. [80], subdivided into superallowed, allowed and forbidden  $\beta$ -decays. As it can be seen, the distributions, especially the ones of allowed and first forbidden show a big overlap.

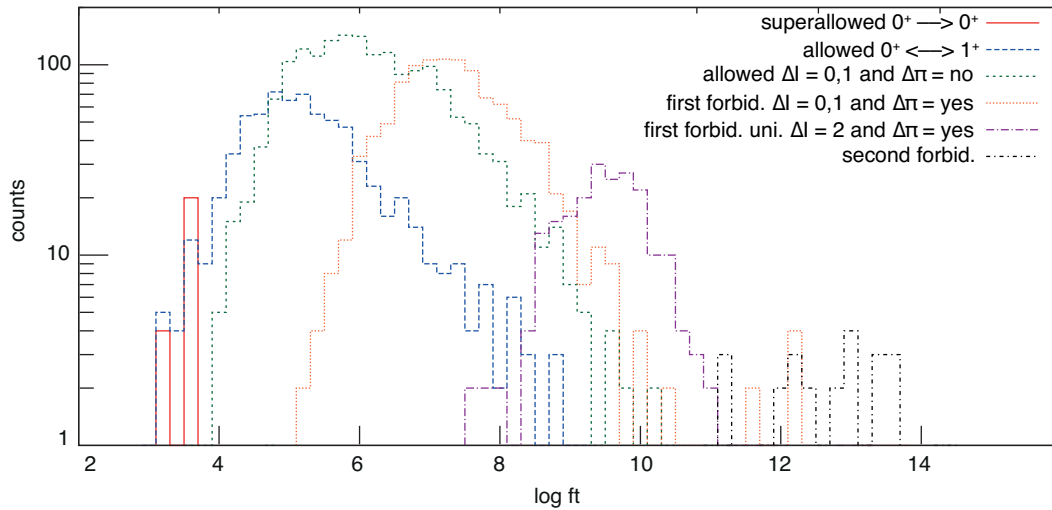


**Figure 1.6:** Overview on known  $\log ft$  values for superallowed, allowed, first and second forbidden transitions in  $\beta$ -decays. The data is taken from Ref. [80].

#### 1.4.4 $\beta$ decays in the $^{132}\text{Sn}$ region

Figure 1.7 shows the proton and neutron orbitals near the  $Z=50$  and  $N=82$  shell gaps. Several Gamow-Teller transitions are possible taking into account all the orbitals, but only two of them show a significant energy release. One of them, the  $\nu g_{7/2} \rightarrow \pi g_{9/2}$  transition, was found in several works to be the main GT transition in the region around  $^{132}\text{Sn}$  [20, 61, 81, 82]. For example, in the decay of  $^{132}\text{In}$  this transition proceeds from the  $\nu f_{7/2} \pi g_{9/2}^{-1}$  g.s. to a  $6^-$  state at 7211 keV in  $^{132}\text{Sn}$  with a  $\log ft$  of 4.6 [82]. We will see later that also in the  $\beta$  decays of the Cadmium isotopes this transition dominates, as it was already shown in Refs. [20, 61] for the decays of  $^{128,130}\text{Cd}$ . In those works  $\log ft$  values of 4.2 and 4.1 were measured for the  $\nu g_{7/2} \rightarrow \pi g_{9/2}$  transition to  $1^-$  states at 1173 and 2120 keV, respectively. The  $\nu f_{7/2} \rightarrow \pi f_{5/2}$  transition, on the contrary, has so far not been experimentally observed and it was found in Ref. [34] that in the decays of  $^{131,132}\text{Cd}$  this transition is most likely hindered due to the high occupancy of the  $\pi f_{5/2}$  orbital.

In the region below  $Z=50$  and  $N=82$  the main contribution is expected from the strong  $\pi g_{9/2}^{-1} \rightarrow \nu g_{7/2}^{-1}$  GT transition, but also first forbidden decays might play a significant role. Especially the question how much ff decays contribute (see Refs. [63, 67, 68]) will be addressed in the present work by investigating the  $\beta$  decays of the Cadmium isotopes with masses  $A=129$  and  $131$ . The dashed arrows in Figure 1.7 illustrate some of the high-energy first forbidden transitions which are of importance in the region. The strongest ff  $\beta$  decay present in most of the decays is of the type  $\nu h_{11/2} \rightarrow \pi g_{9/2}$ . In the  $^{132}\text{In}$  decay this particular one proceeds to the states of the  $\nu f_{7/2} \pi h_{11/2}^{-1}$  multiplet, the lowest positive parity states in  $^{132}\text{Sn}$ . In Ref. [82] a  $\log ft$  of 5.7 was deduced for the corresponding  $8^+$  state, to which the main intensity goes. The second ff transition of importance is  $\nu f_{7/2} \rightarrow \pi g_{7/2}$  and a  $\log ft$  of 5.6 was measured for that one proceeding to a  $(7^+)$  state at 5629 keV. First forbidden transitions of the types  $\nu d_{3/2} \rightarrow \pi p_{1/2}$  and  $\nu s_{1/2} \rightarrow \pi p_{1/2}$  were observed in the decay of  $^{131}\text{In}$  to  $^{131}\text{Sn}$  and in Ref. [39]  $\log ft$  values of 5.1 and 6.4, respectively,

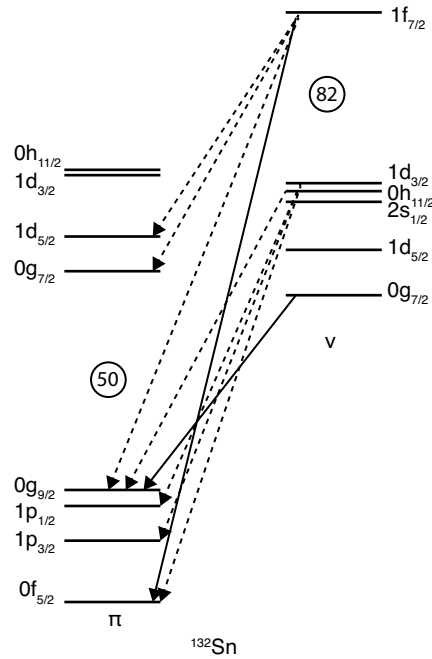


**Figure 1.7:** Schematic presentation of the proton and neutron orbitals near the  $Z=50$  and  $N=82$  shell gaps. The arrows indicate the most important Gamow-Teller (solid) and first forbidden (dashed) decays.

are stated. Unfortunately,  $^{132}\text{In}$  is the only nucleus south-east ( $Z < 50$  and  $N > 82$ ) of  $^{132}\text{Sn}$  which has been studied experimentally. Only for this nucleus the  $\nu f_{7/2}$  orbital comes into play and further studies in that region are therefore necessary to identify the role which this orbital plays in  $\beta$  decays.

For the  $Z=50,51$  nuclei the  $\pi g_{9/2}$  orbital is blocked and low-energy ff transitions ( $\nu f_{7/2} \rightarrow \pi g_{7/2}$  and  $\nu f_{7/2} \rightarrow \pi d_{5/2}$ ) dominate the half-lives. One example where the  $\nu f_{7/2} \rightarrow \pi g_{7/2}$  transition can be found is the g.s. to g.s. decay of  $^{133}\text{Sn}$  to  $^{133}\text{Sb}$  ( $\log ft = 5.44$  [46]). In the decay of  $^{133}\text{Sn}$  to  $^{133}\text{Sb}$  two other first forbidden branches were identified, namely  $\nu f_{7/2} \rightarrow \pi d_{5/2}$  and  $\nu f_{7/2} \rightarrow \pi d_{3/2}$ , and  $\log ft$  values of 6.05 and 7.42, respectively, were measured for transitions of those types.



## Chapter 2

# General setup of an EURICA experiment

EURICA is the acronym for Euroball RIKEN Cluster Array, an array of germanium detectors which is used in conjunction with several ancillary detectors at the RIKEN accelerator facility in Wako-shi (Japan). The array surrounds a passive or active stopper for mainly isomer and  $\beta$ -decay studies of very exotic nuclei. The radioactive beams (RI) are produced by the RIKEN RI Beam factory, identified and separated by the fragment separator BigRIPS and the Zero-Degree spectrometer (ZDS) and then being transported to the focal plane where the stopper, surrounded by the germanium detectors, is placed. In the following sections an introduction is given to the production, separation and identification of the RI beams, followed by a detailed description of the detectors used for the studies of the stopped nuclei.

### 2.1 Producing the nuclei of interest

Extending the knowledge about nuclear structure of nuclei with very exotic proton-to-neutron ratios and to test nuclear theories far away from stability is a challenging task, and it is necessary to built facilities with state-of-the-art accelerators to provide RI beams with high intensities. Commonly there are two approaches used to produce exotic nuclei far away from stability, the so called isotope separation online (ISOL) method [83] or the fragmentation/ fission method.

For the fragmentation/ fission method a stable heavy ion beam impinges on a production target, producing a broad range of nuclei. The nuclei of interest are then selected and identified with a fragment separator and delivered to the experimental set-up. A fragment separator is generally said a magnetic spectrometer with ancillary detectors for the identification.

In the in-flight fission method, as it was used in this experiment, a primary beam of e.g.  $^{238}\text{U}$  at relativistic energies is used and impinges on a lighter target. Two main processes

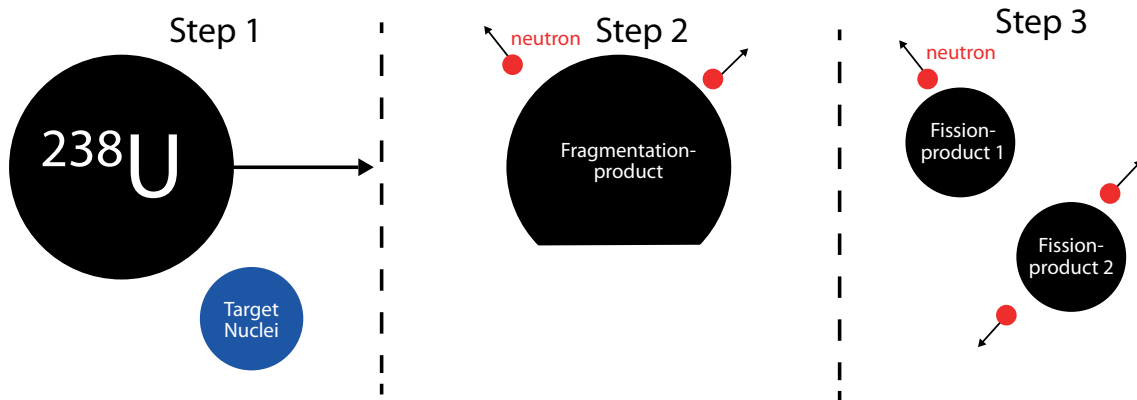


**Figure 2.1:** Schematic of abrasion fission, a method to produce radioactive ion beams. The beam particles are fragmented in the collision with a target nucleus and subsequently undergo fission. In the process neutrons are emitted for further de-excitation of the hot fragmentation and fission products.

contribute then to the induced fission of the  $^{238}\text{U}$  ions for producing fission products over a broad range of elements and masses. In the first method, called coulomb fission, coulomb excitation leads to induced fission of the  $^{238}\text{U}$  ions and in the second method, called abrasion fission, the  $^{238}\text{U}$  ions are fragmented into smaller, still very heavy ions which then undergo fission. The method of abrasion fission is illustrated in Fig. 2.1, where in the first step the fragmentation of  $^{238}\text{U}$  occurs and then in the second step the de-excitation takes place through the emission of neutrons. The still very hot fragmentation product subsequently undergoes fission, resulting in two hot fission products which continue their deexcitation via the emission of mainly neutrons.

Fission products tend to have a neutron-to-proton ratio similar to the initial nucleus. The heavy nuclei used as primary beams tend to have more exotic neutron-to-proton ratios as for example medium mass nuclei, resulting in very neutron-rich fission products [84]. Pioneering work on the in-flight fission method was carried out in 1994 at the Gesellschaft für Schwerionenforschung (Darmstadt, Germany) [85] and by now it is one of the most commonly used methods to produce very neutron-rich nuclei.

### 2.1.1 RIKEN RI Beam factory

The RIKEN RI Beam factory together with the fragment separator became operational in 2007 and consists of four cyclotrons with K-Values of 540, 570, 980 and 2500 MeV with the K 2500-MeV being the world's first super-conducting ring cyclotron (SRC). Ions over a broad band of masses can be accelerated up to 440 MeV/u for light ions and 350 MeV/u for heavy ions (e.g.  $^{238}\text{U}$ ) [86].

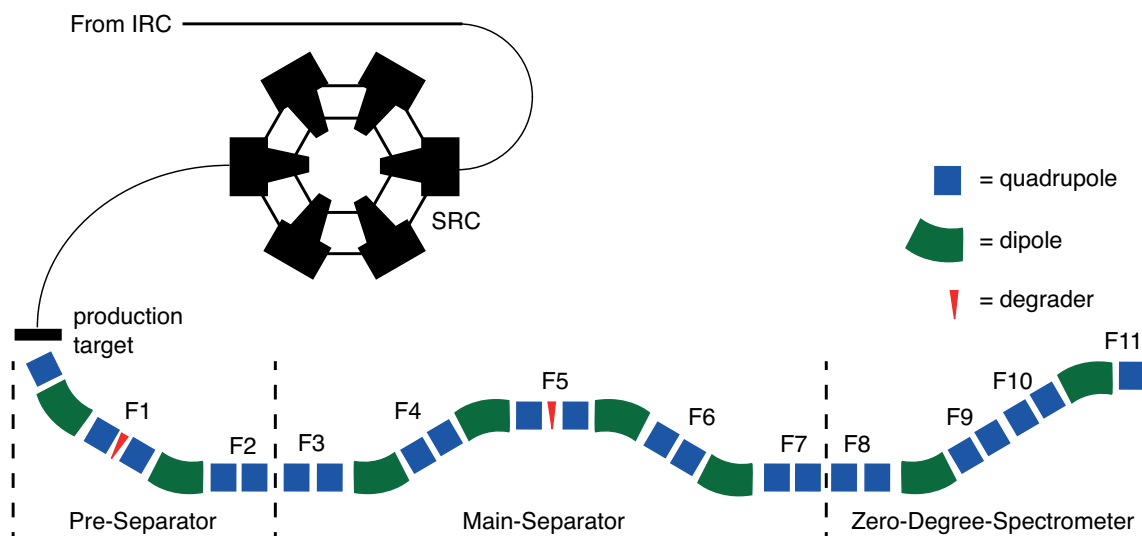


**Figure 2.2:** Schematic of the RI Beam factory at RIKEN with the last step of the acceleration procedure, the super conducting ring cyclotron (SRC), the two-stage fragment separator BigRIPS and the Zero-Degree-Spectrometer. All quadrupoles, dipoles and degraders used in the experiments for the beam separation are indicated together with the abbreviations for the eleven focal planes (F1 to F11).

### 2.1.2 Fragment separator BigRIPS

After the primary beam has been accelerated, it impinges on a production target placed at the entrance to the fragment separator BigRIPS (Big RIKEN projectile-fragment separator), producing a wide range of nuclei which makes it necessary to separate the ions of interest and identify them on an event-by-event basis. Fig. 2.2 shows a schematic layout of the fragment separator with all quadrupole and dipole magnets which are used for beam focussing and bending. The different focal planes are labelled as F1 to F11, to which will be referred later in the text. BigRIPS is subdivided into two parts. The first part is the pre-separator which consists of two room temperature dipoles with a bending angle of  $30^\circ$ , and four super-conducting quadrupole triplets. It is used for the production of the RI beams and a first separation based on the  $B\rho\text{-}\Delta E\text{-}B\rho$  method. By selecting a value for the magnetic field  $B$  in both dipole magnets only the ions with a certain magnetic rigidity  $B\rho$  are being transported to the main separator:

$$B\rho = \frac{\gamma m_0 v}{q} \quad (2.1)$$

with the bending radius  $\rho$  of the ion in the magnetic field, its mass  $m_0$ , charge  $q$ , velocity  $v$  and relativistic factor  $\gamma$ . A further selection is made through the wedge-shaped degrader placed at the first focal plane F1. This focal plane is momentum dispersive and, therefore, ions with different momentum experience different energy losses because of the changing thickness of the degrader based on the ion's position at the focal plane.

In the second half of BigRIPS, the main separator, on the one hand a further selection can be made due to the four dipoles and the degrader placed at the fifth focal plane (F5). On

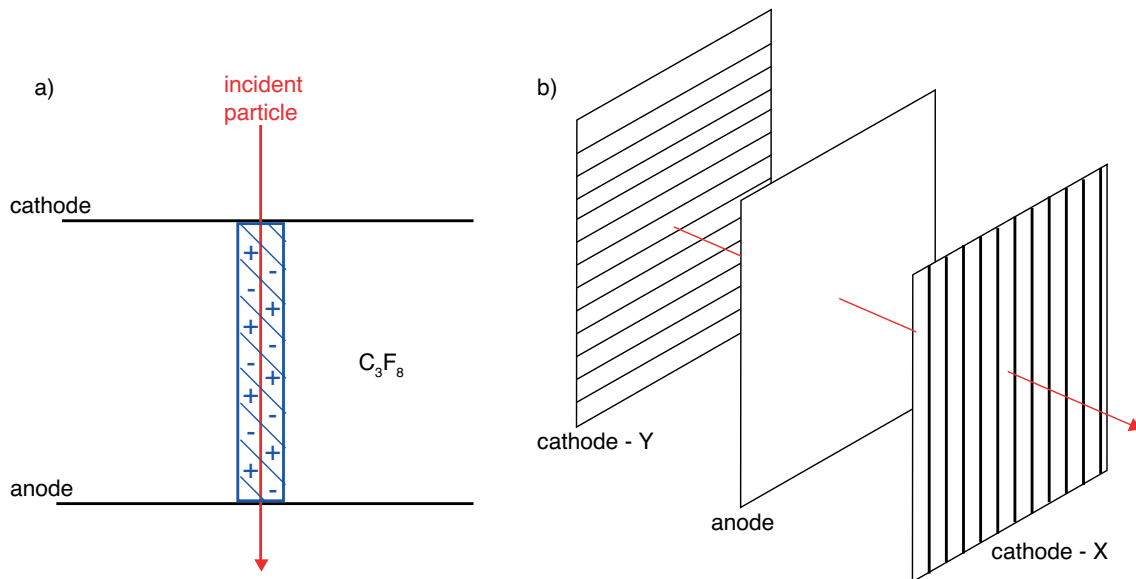


**Figure 2.3:** Schematics of a parallel plate avalanche counter with a) showing the basic principle of an incident particle ionizing the gas in between a cathode and an anode, and b) the basic setup of a PPAC used at the RIKEN RI beam factory with an anode in between two cathodes, which consist of several strips in x- and y-direction for position measurements.

the other hand it is used for the identification of the ions by deducing the nuclear charge and the mass. The detectors and procedures used to identify the ions on an event-by-event basis are explained briefly in the following, for a more detailed description please refer to Refs. [87, 88].

### 2.1.2.1 Position and Time-of-Flight (ToF) measurements

For the position measurement parallel plate avalanche counters (PPAC) are used, which have been developed at RIKEN [89]. Fig. 2.3a) shows the basic principle behind a PPAC, with an incident particle ionizing a gas between a cathode and an anode. The free electrons and the ions are then detected in the anode/cathode because of the applied high voltage. To determine the position of the incident particle, it is necessary to subdivide the cathodes, as shown in Fig. 2.3b). The detectors used at BigRIPS have one anode in between two cathodes with one cathode arranged in such a way to measure the position in x- direction and the other one for the position measurement in y-direction. The PPAC has a total active area of  $240 \times 150 \text{ mm}^2$  and is filled with  $\text{C}_3\text{F}_8$  at a pressure of 30 Torr. The voltage usually applied is below 2000 V and has to be adjusted according to the beam energy and the expected energy loss of the heavy ions.

The cathodes are made of strips which are 2.4 mm thick and have a  $150 \mu\text{m}$  spacing in between them. For the position determination the strips of the x-cathode are arranged vertically and those of the y-cathode horizontally. In both cases the signals are fed into a delay-line with signal readout on both sides. The signals are processed by a Constant-Fraction-Discriminator (CFD) and fed into a Time-to-Digital-Converter (TDC). From the

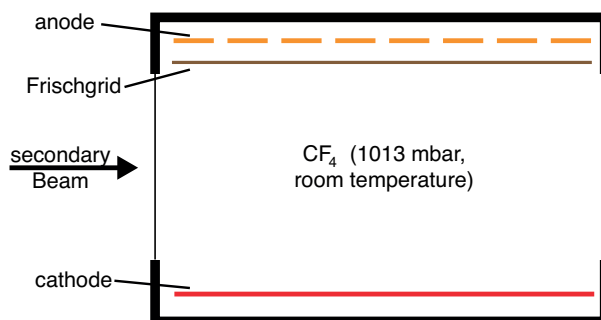


**Figure 2.4:** Schematic figure of one MUSIC, an ionisation chamber filled with CF<sub>4</sub> for the charge identification of the ions via the energy loss measured with 8 individual anodes.

time-difference between the left and the right side of the delay-line the  $x(y)$ -position can be calculated after a time-to-position calibration has been performed. The experimental set-up consists of PPACs at the important focal planes F3, F5 and F7 with each focal plane having at least 2 PPAC for precise beam tracking and the possibility to calculate the angle of the ions at the focal plane with respect to the main beam axis.

The position measurement is needed for a precise calculation of the Time-of-Flight (ToF) of the ions through the different parts of BigRIPS which is used to determine the mass-to-charge ratio (AoQ) and for the velocity correction of the energy loss measurements. The ToF is measured as the time difference of the ion passing through a start- and a stop-scintillator and by the known length of the flight path which is precisely determined by the PPACs. Scintillators are placed at the focal planes F3, F5, F7 and F11 allowing a velocity determination through most parts of BigRIPS.

### 2.1.2.2 Energy loss measurement and deduction of nuclear charge Z

As mentioned before: the nuclear charge  $Z$  is deduced from the energy-loss of the ions. The energy loss in this experiment was measured by two Multiple Sampling Ionisation Chambers, called MUSIC [90]. The chambers are filled with pure CF<sub>4</sub> at room temperature and atmospheric pressure. Each of the detectors has one cathode and 8 anode strips which are used to measure the energy loss. For each MUSIC one obtains eight energy loss measurements and from those the geometrical average is calculated to reduce the statistical error.

Figure 2.4 shows a schematic drawing of one of the MUSIC detectors. Ions passing through the gas create electron-ion pairs and due to the applied electric field the electrons travel to the anodes with the number of electrons created after the ionisation being directly proportional to the energy deposited by the beam particle. The energy-loss of heavy ions in matter is well described by the Bethe-Bloch formula:

$$-\frac{dE}{dx} = \left( \frac{e^2}{4\pi\epsilon_0} \right)^2 \frac{4\pi Z^2 N_A Z_{AP}}{mc^2 \beta^2 A} \left[ \ln \left( \frac{2mc^2 \beta^2}{I} \right) - \ln(1 - \beta^2) - \beta^2 \right] \quad (2.2)$$

In this formula  $e$  is the electronic charge,  $\epsilon_0$  the vacuum permittivity,  $N_A$  the Avogadro constant,  $m$  the rest mass of the electron and  $l$  an experimentally determined parameter describing the average ionisation potential and excitation energy of the absorber material. The absorber material is defined by its atomic number  $Z_A$ , mass  $A$  and density  $\rho$ . The only two parameters entering into the formula of the beam particle are its atomic number  $Z$  and its relativistic factor  $\beta$ . Hence the energy loss of the beam particle in the ionisation chamber can be written as:

$$-\frac{dE}{dx} = Z^2 f(\beta) \quad (2.3)$$

In this expression the dependence of the energy loss on the atomic number  $Z$  can be observed which is multiplied by a function  $f(\beta)$ . The function  $f(\beta)$  is independent of the individual beam particle and, therefore, a calibration with a primary beam and a known atomic number  $Z_P$  can be performed to determine later the atomic number  $Z_F$  of an unknown fragment created in the primary target:

$$-\frac{dE_F}{dx} = \frac{Z_F^2}{Z_P^2} \frac{dE_P}{dx} \quad (2.4)$$

### 2.1.3 Production of very neutron-rich nuclei in the RIBF 85 experiment and the particle selection

In the experiment (RIBF-85) presented in this thesis the nuclei of interest were produced via in-flight fission of a  $^{238}\text{U}$  beam at 350 MeV/u impinging on a 3 mm  $^9\text{Be}$  production target located at the entrance of BigRIPS. The primary beam current was varying in the range 600-900 enA and the implantation rate of selected and identified ions at the last focal plane was in the order of 50-100 particles-per-second (pps). BigRIPS was adjusted for a maximum transmission of  $^{136}\text{Sn}$  while not exceeding a limit of 100 pps at the final focal plane.

Before the experiment started, the event-by-event identification was cross-checked by inserting a passive stopper at the F7 focal plane and checking if for the nuclei  $^{132}\text{Sn}$ ,  $^{134}\text{Sn}$  and  $^{136}\text{Sb}$  the known isomeric states can be observed. After this check was performed, the beam was transported to the F11 focal plane where the nuclei of interest are then implanted in the active stopper WAS3ABi.

To significantly improve the statistics for part of the nuclei, the dataset obtained in the RIBF-85 (Sn-Setting) experiment was combined with the dataset of another experiment. The latter one was carried out using the same set-up, but with the setting of BigRIPS being optimized for the transmission of  $^{128}\text{Pd}$  (Pd-Setting). Fig. 2.5a) and b) show the identification plots of the two settings individually, while the identification plot for all implanted ions in both experiments is shown in Fig. 2.6. To compare the two settings in a more quantitative way, the number of implanted Cadmium ions per isotope and setting are listed in Table 2.1. Especially for  $^{128}\text{Cd}$  to  $^{130}\text{Cd}$  the statistics could be nearly doubled by summing the two datasets, while in the more exotic  $^{131}\text{Cd}$  and  $^{132}\text{Cd}$  still a significant improvement in statistics is being achieved. Table 2.1 furthermore contains the number of

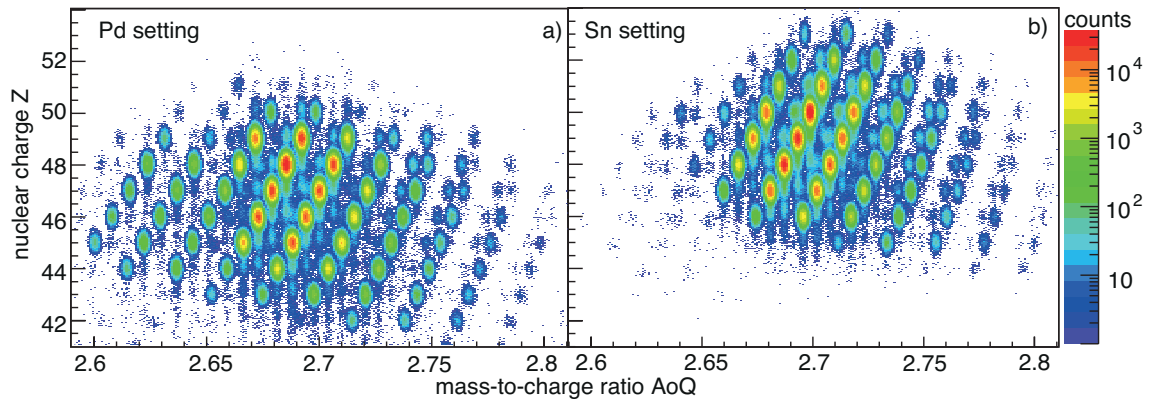


**Figure 2.5:** Identification plot of all implanted ions in a) the Pd Setting (RIBF 60&62 experiment) and in b) the Sn Setting (RIBF-85 experiment) at the RIKEN RIBF facility showing the measured mass-to-charge ratio (AoQ) in BigRIPS using the F3-F5 ToF measurement versus the deduced nuclear charge of the F11 ionization chamber.

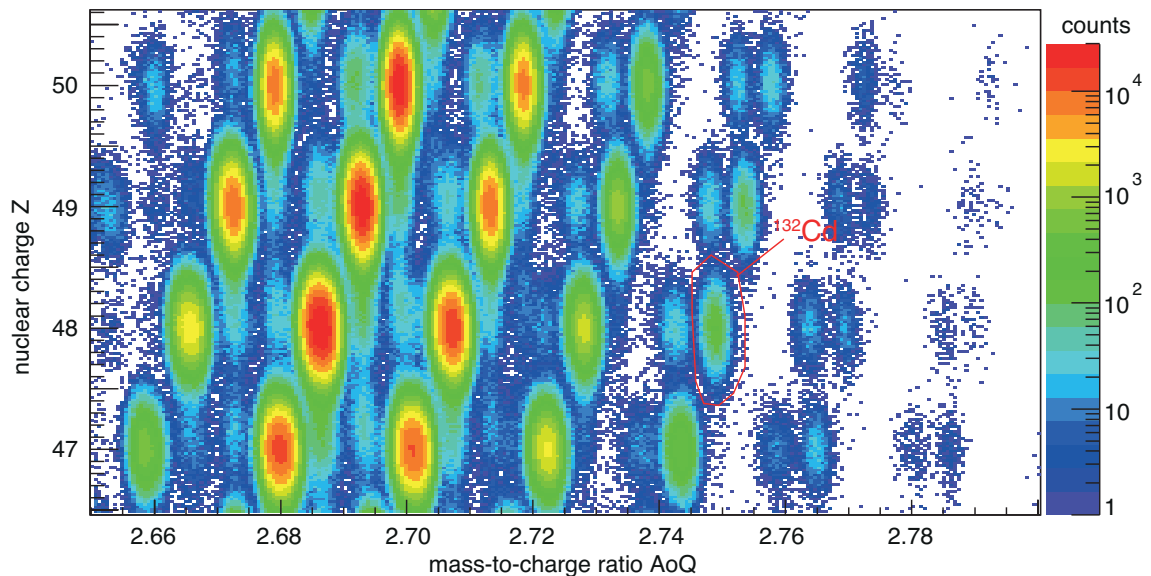


**Figure 2.6:** Identification plot showing the sum of both settings. The mass-to-charge ratio (AoQ) was measured in BigRIPS using the F3-F5 ToF measurement and nuclear charge was determined using the F11 ionization chamber.

ions identified in BigRIPS with the BigRIPS data acquisition being triggered by the plastic scintillator at the focal plane F11.

Comparing the number of ions identified in BigRIPS to the number of ions actually implanted in WAS3ABi, a difference of about 10-15% is observed. This loss can have several reasons. First of all, those ions might not be implanted in the active stopper (WAS3ABi) due to the beam spot being bigger than the active area of the stopper. Investigating the distributions of implanted ions (see later in this chapter in section 2.2.2) in x-, y- and z-direction and assuming a Gaussian distribution of the beam spot, the loss is expected to be in the order of 4-5%. Secondly, some ions do not produce the necessary signals in WAS3ABi to be counted as an implantation event or the events are rejected be-

Isotope	Id BigRIPS Pd Setting	Implantations Pd Setting	Id BigRIPS Sn Setting	Implantations Sn Setting	Implantations Sum
<sup>126</sup> Cd	26987	22431	36	29	22460
<sup>127</sup> Cd	38891	30766	623	543	31309
<sup>128</sup> Cd	210925	191036	235767	204280	395316
<sup>129</sup> Cd	2031428	1854112	2203351	1930588	3784700
<sup>130</sup> Cd	955938	868529	1126387	984643	1853172
<sup>131</sup> Cd	75743	67842	135393	117150	184992
<sup>132</sup> Cd	3816	3025	17234	13246	16271
<sup>133</sup> Cd	79	67	1275	1033	1100
<sup>134</sup> Cd	0	0	73	65	65

**Table 2.1:** Number of identified Cadmium (A=126-133) ions in BigRIPS (Id Bigrips) in both settings, number of implanted Cadmium ions in WAS3ABi (Implantations) and the sum of implanted ions.

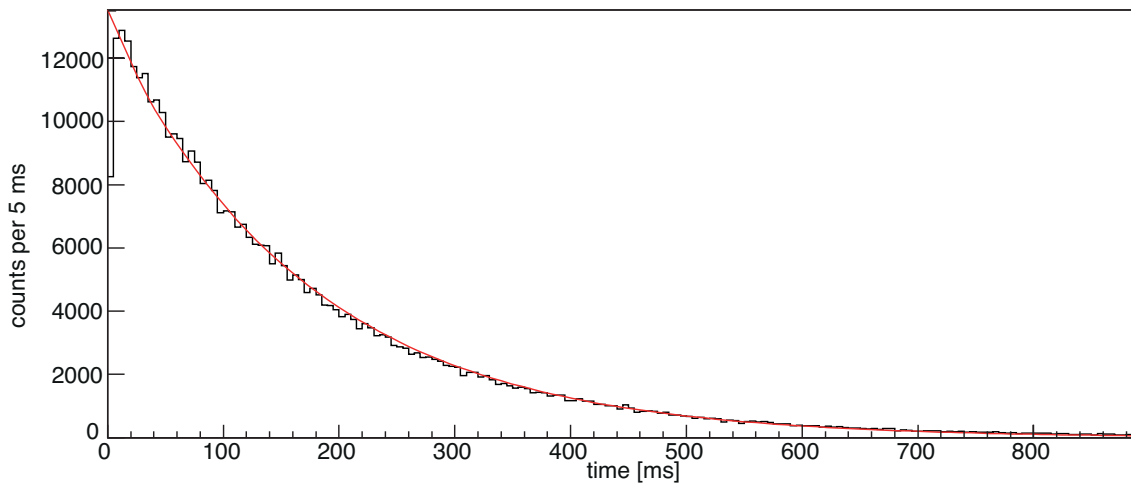


**Figure 2.7:** Time interval distribution of two successive <sup>129</sup>Cd implantations, fitted by an exponential function. The deadtime of WAS3ABi results in a deficit of counts in the first bin.

cause of light ions passing through the eight double-sided silicon strip detectors (DSSSD) at the same time. A light ion creates signals in all DSSSD layers, making it impossible to identify in which layer the ion of interest was stopped. The third reason is the dead time of WAS3ABi which is in the order of about 1 ms after each implantation. Implantation events which occur within that dead time are not registered. Figure 2.7 shows the time difference distribution between two successive <sup>129</sup>Cd implantations. The ion implantation times are Poisson distributions with an average rate  $\lambda$ . The time difference between two successive implantation is then exponentially distributed with a time constant  $\lambda$ . In the figure one observes that in the first time bin counts are missing compared to the fit with an exponential function. Those are implantations which are not registered because of the dead time of WAS3ABi. From the difference of the actually observed number of implantations compared to the fit with the exponential function a loss of 1 % is calculated for the case of <sup>129</sup>Cd. For the other Cadmium isotopes similar results were obtained. An additional reason are reaction losses between the ionization chamber and the DSSSD. Once the

Isotope	Id Beta Pd Setting	Id Beta Sn Setting	Id Beta Sum	Implantations Sum
<sup>126</sup> Cd	20833	20	20853	22460
<sup>127</sup> Cd	27634	412	28046	31309
<sup>128</sup> Cd	169683	181102	350785	395316
<sup>129</sup> Cd	1611362	1668540	3279902	3784700
<sup>130</sup> Cd	739175	811435	1550610	1853172
<sup>131</sup> Cd	57788	91972	149760	184992
<sup>132</sup> Cd	2730	10587	13317	16271
<sup>133</sup> Cd	45	778	823	1100
<sup>134</sup> Cd	0	58	58	65

**Table 2.2:** Number of identified Cadmium ( $A=126-133$ ) ions in both settings with at least one correlated  $\beta$  decay (Id Beta) and sum of implanted Cadmium ions in WAS3ABi (Implantations).

ion passes through the F11 plastic scintillator, it is registered in the BigRIPS data acquisition with its AoQ and Z determined from the different BigRIPS detectors. However, the ion has to pass through additional material before implanting in WAS3ABi: air, degraders and entrance window of the WAS3ABi chamber. Reactions in those materials can be the reason for ion losses, too.

In a second step it is important to know after how much of those ions at least one  $\beta$  decay is observed within a time window of 5 seconds. A summary for that is given in Table 2.2. Compared to the number of implanted ions in WAS3ABi, one observes that to only 85-90% of the ions at least one  $\beta$  decay is being correlated. This difference is related to the limited absolute efficiency of WAS3ABi. However, from this value no direct conclusion can be drawn about the  $\beta$  decay efficiency considering that the observed  $\beta$  decays after an implantation can be also background events. A more detailed analysis of this will be done in chapter 4 in section 4.2.2.4.

To select for the further analysis only the ion of interest, a two-dimensional gate is set on the distribution shown in Fig. 2.6. An example gate is shown in that figure for the selection of <sup>132</sup>Cd. Even for the most exotic cases a clear separation is achieved between the ion of interest and charge-state-contaminations. There is a certain probability that the ions are not fully stripped, for example due to the pick-up of an electron in the detector material or the degraders. The energy loss in the ionization chambers of those ions would still be the same, placing them at the correct Z, but due to the different charge-state the mass-to-charge ratio is changed, leading to contaminations in the plot shown in Fig. 2.6. An example is the accumulation of points on the left side of the illustrated gate of <sup>132</sup>Cd. While for <sup>132</sup>Cd AoQ is expected to be 2.75, a <sup>129</sup>Cd ion with a 47<sup>+</sup> charge state has an AoQ value of 2.745. Only thanks to the high AoQ resolution of BigRIPS a clear separation is possible and the charge-state events can be excluded.

## 2.2 Active stopper

After being separated and identified in BigRIPS, the ions of interest were transported to the last focal plane where an active stopper was placed. The purpose of an active stopper in contrast to a passive stopper is to not only stop the ions but also observe their  $\beta$ -decays. With a cocktail of different nuclei this is a challenging task, especially since the half-lives of the nuclei in the present experiment can be in the order of hundreds of ms. Therefore, opening a gate for the data acquisition after each implanted nuclei long enough to observe the  $\beta$ -decay is not practical and a different approach has to be used. In the present experiment implantations and  $\beta$ -decays are treated as individual events, with the data acquisition being triggered by both of them. The correlation is then done off-line. A typical method is to use highly segmented double-sided silicon strip detectors (DSSSD) in which the ions are stopped in a particular pixel, making it possible to correlate the observed  $\beta$ -decays by means of position and time.

The two types of events can easily be distinguished in the DSSSD because the deposited energy is significantly different. The electrons emitted in the  $\beta$ -decay deposit much smaller energies compared to the several GeV which are observed in the stopping process of an ion in the DSSSD. Before the two types of events and the correlation procedure are discussed in detail, an introduction to the active stopper WAS3ABi is given.

### 2.2.1 Properties of WAS3ABi

In the present experiment WAS3ABi [91–95] consisted of 8 DSSSD placed in an aluminium chamber with a thickness of 2 mm [91]. Each of the DSSSD is divided into 60 strips in x-direction and 40 strips in y-direction with each strip having a width of 1 mm. This results in a total active area of 60x40 mm<sup>2</sup>. To reduce the influence of thermal noise and keep a stable temperature, the DSSSD were cooled with a continuous flow of liquid nitrogen through the chamber. The DSSSD were separated with spacers of 0.5 mm to pack them as closely as possible, as it is shown in Fig. 2.8, without introducing problems due to the voltage applied to each DSSSD. The read-out was performed with an analogue electronics chain consisting of a charge-sensitive pre-amplifier (Clear-Pulse CS-520), a shaping amplifier (CAEN N568B) and an ADC for the energy signals. Behind the shaping amplifier the signals were split and sent also to a timing branch consisting of an inverter, a leading-edge discriminator (LeCroy 3412, 4413) and a TDC. Each of the discriminators has a sum-output which was used for generating the  $\beta$ -decay trigger. The detailed electronics chain is shown in Fig. 2.10.

The challenging task for WAS3ABi is to deal with the two very different kind of events and still being able to give exact position information in both cases and furthermore provide a good energy resolution for the low energy depositions of electrons emitted in the  $\beta$ -decay. In the present experiment linear pre-amplifiers were used which made it possible to obtain energy information only for the  $\beta$ -decay events. The dynamic range was set to



**Figure 2.8:** Picture showing the active stopper WAS3ABi, with its eight closely packed DSSSD, not yet mounted into the chamber. Picture taken from Ref. [96].

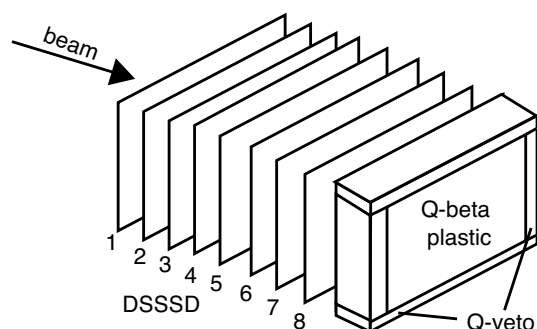


**Figure 2.9:** Schematic of WAS3ABi with its eight DSSSD and the additional Q-beta plastic and Q-veto detectors.

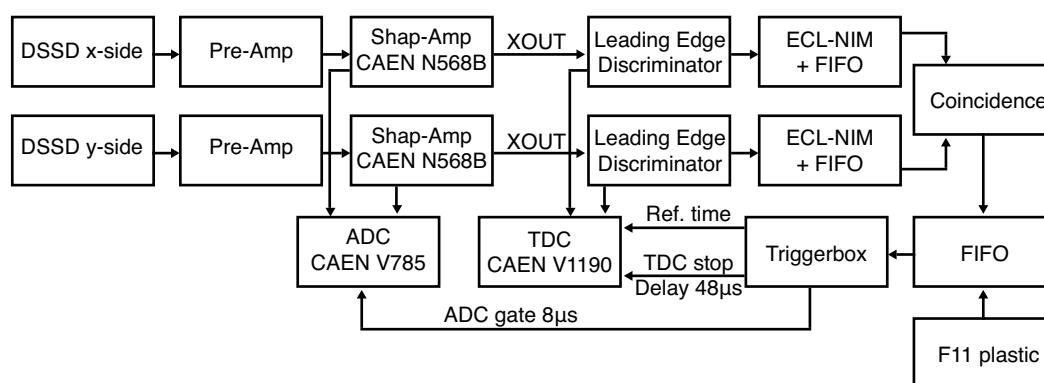


**Figure 2.10:** WAS3ABi electronics scheme.

about 10 MeV, meaning that the position reconstruction for the implantation events could not be performed from the energy information.

Furthermore, a plastic scintillator, called from now on “Q-beta detector”, was placed in the chamber as close as possible to WAS3ABi. This plastic scintillator was used for two different purposes. The Q-beta detector was placed in the center of the beam line and was surrounded by 4 thin layers of plastic which are called “Q-veto detector” from here on. The Q-beta detector could be used to verify that an ion was actually implanted in one of the eight DSSSD by requiring no signal in the Q-beta detector in an implantation event and to discard events where light particles passed through the DSSSD. And second of all, the plastic scintillator measured the energy deposited by electrons emitted in the direction of the Q-beta detector for the purpose of reconstructing the full energy of the electron by adding it to the energies measured in the DSSSD. The Q-veto detector was used to verify that the electrons did not escape the Q-beta plastic. The Q-beta and the Q-veto detectors were read out by a common photomultiplier, and the signal of the two detectors could be separated in the off-line analysis because two different types of scintillators were used with different response times. A schematic of WAS3ABi and the Q-beta/Q-veto detectors is shown in Fig. 2.9 where also the labelling for the eight DSSSD is introduced with

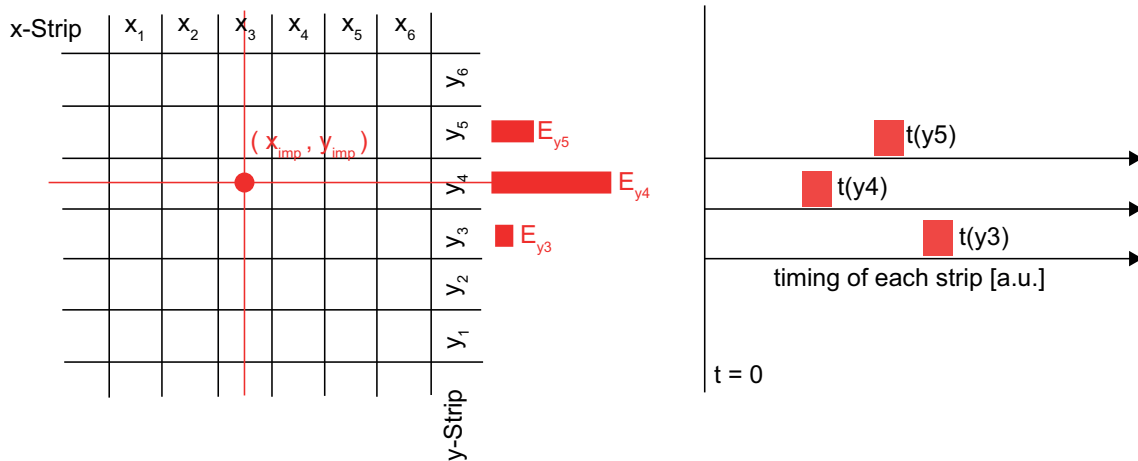


**Figure 2.11:** Illustration of the method used to determine the implantation position in WAS3ABi. The strip where the implantation occurs is expected to have the highest energy deposition and on top has a faster timing compared to the neighbouring strips, making it possible to determine the position from the timing of the different strips.

DSSSD 1 being the first and DSSSD 8 the last in the stack.

### 2.2.2 Implantation events

The implantation events were triggered by the F11 plastic scintillator of BigRIPS with the trigger being sent to all three data acquisition systems (BigRIPS, WAS3ABi, EURICA germanium array). In an implantation event several GeV are deposited in the DSSSD where the ion is stopped (Bragg-Peak). This energy deposition is most likely distributed over several strips in x- and y- direction. All of the signals produce an overflow signal in the ADC and because of that the only available information is the timing of the different strips. The maximum energy deposition is expected in the strip of implantation with the neighbouring strips having relatively lower energies deposited. With the timing signals perfectly aligned a clear difference should be seen, with the highest energy deposition having the fastest timing signal. An illustration of this can be found in Fig. 2.11, where an example is shown for an implantation in y-strip number 4. This strip has clearly the highest energy deposition in the event. The timing distributions shown on the right side of the figure are the expected times measured for the energy depositions due to the implantation in respect to the timing of the trigger ( $t=0$ ) with the implantation strip having a faster timing than the neighbouring strips.

To find the implantation position in the off-line analysis, the eight DSSSD are first checked for their energy signals. Starting with DSSSD 1, placed at the front of the stack, every DSSSD is checked for at least one strip with energy deposition in the overflow of the ADC until a DSSSD is found with no energy deposition. The last DSSSD with an overflow event is then identified as the DSSSD where the nucleus was implanted. This one will be referred to from now on as implantation z-position ( $z_{imp}$ ). The x- and y- strip where the implantation happened is then identified by selecting the strip with the fastest timing.

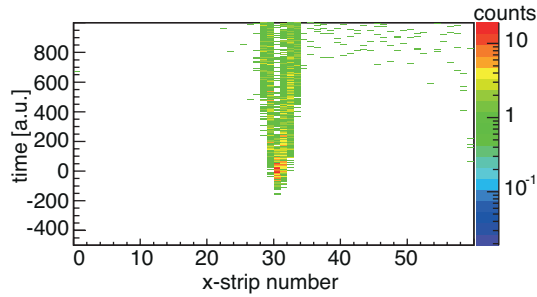


**Figure 2.12:** Time distributions of all x strips in DSSSD 4 with an energy deposition in the overflow gated on events where the ion was implanted in DSSSD 4 and the position determined (maximum energy deposition method) from the low gain DSSSD 1 was x-strip 30.

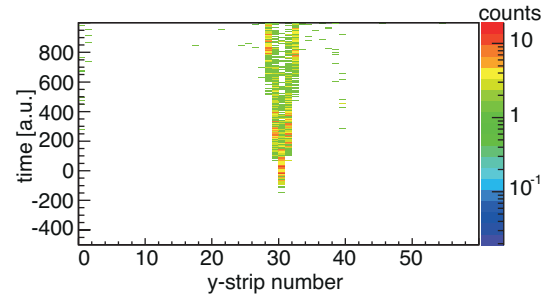


**Figure 2.13:** Time distributions of all y strips in DSSSD 4 with an energy deposition in the overflow gated on events where the ion was implanted in DSSSD 4 and the position determined (maximum energy deposition method) from the low gain DSSSD 1 was y-strip 30.

As a check if this method to identify the x- and y-position actually works as expected, data was taken at the beginning of the experiment where the gain in the first DSSSD was lowered so that the deposited energies in the strips could be measured. The position of an ion passing through the DSSSD 1 and being stopped in a following layer would then unambiguously be determined in the first DSSSD and can be compared to the positions obtained from the timing in the following layers. The large distance of WAS3ABi to the last focal plane compared to the distance of the closely packed DSSSD ensured that the ions should pass perpendicular through the DSSSDs. This makes it possible to correlate the position measured in the first DSSSD to the following DSSSD. Fig. 2.12 (2.13) shows the timing of all x-strips (y-strips) in DSSSD 4 for the events where the ion was stopped in DSSSD 4 and x-strip (y-strip) 30 measured the maximum energy deposition in the first DSSSD. It is then expected that the ion should be stopped in most of the cases in x-strip (y-strip) 30 of DSSSD 4. As can be seen in the two figures, strip number 30 is in both cases faster than the neighbouring strips, proving that the position measurement can be successfully performed via the timing signal. This makes it unnecessary to use logarithmic pre-amplifiers or to even split up the signal in a high and a low energy branch. As a last comment it can be mentioned here that the energy of the implanted ion was not of interest in the present experiment, but the energy of the electrons was.

The implantation positions ( $x_{imp}/y_{imp}$ ) of all Cadmium isotopes with masses  $A=128$  to  $133$  are shown in Fig. 2.14a) and b) for the Pd setting and the Sn setting, respectively. The implantation patterns show as expected a more or less Gaussian distribution, and the number of ions which are not implanted because of the relatively wider beam spot compared to the active area of the DSSSD can be estimated to about 4-5% assuming a Gaussian distribution in x- and y-direction. Fig. 2.15a) and b) show the projection of Fig. 2.14b) on the x- and y-axis for the case of  $^{130}\text{Cd}$ . In these figures the distribution of the implantation position in x- and y-direction is shown together with the fit to a Gaussian distribution. From that fit it is estimated that about 5% of the ions are not implanted in WAS3ABi due to the beam spot being larger than the active area of the stopper.

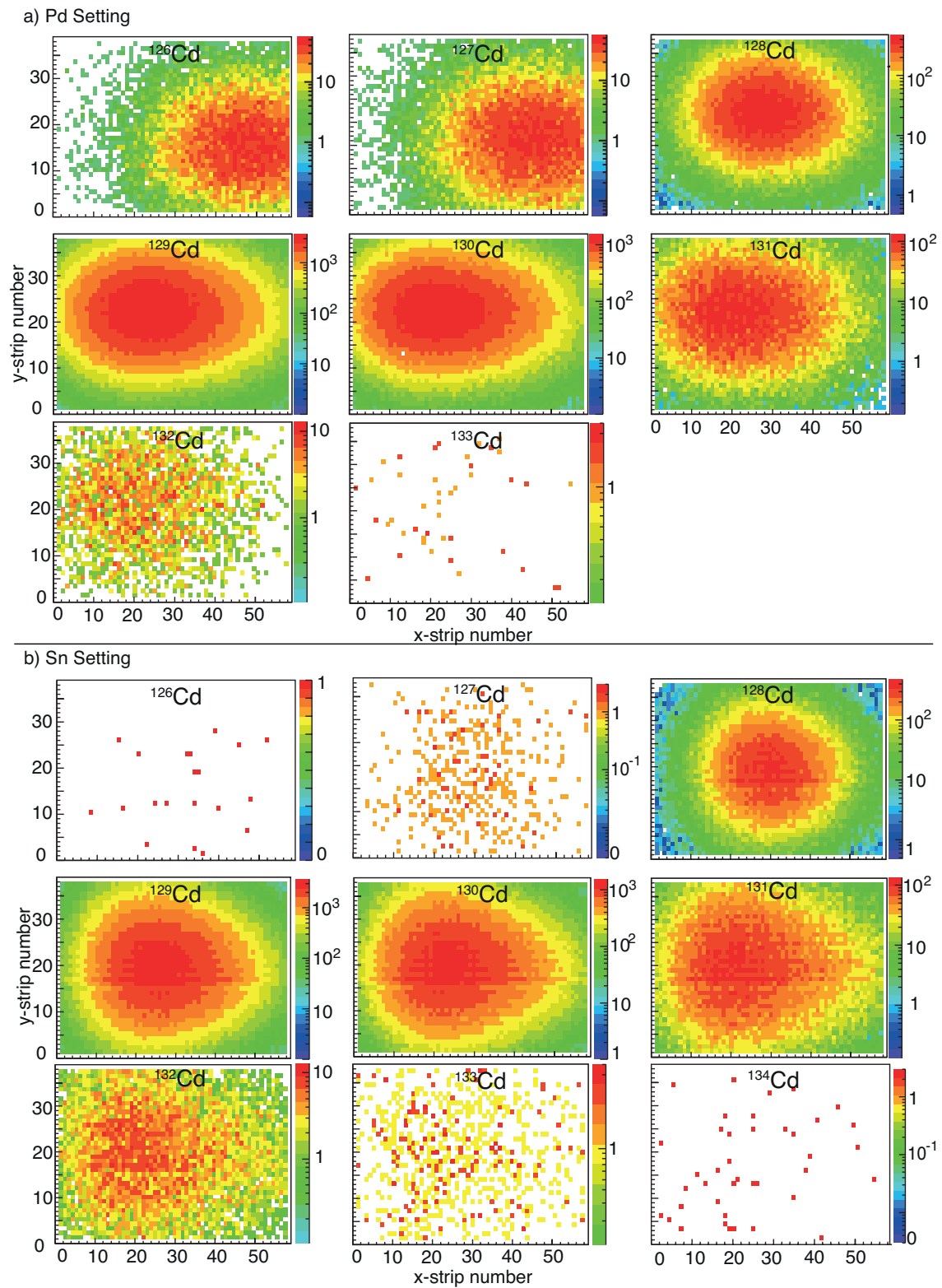


**Figure 2.14:** Implantation pattern showing the positions in x- and y-direction of all implanted Cadmium isotopes with masses  $A=128$  to  $133$  for a) the Pd setting and b) the Sn Setting.

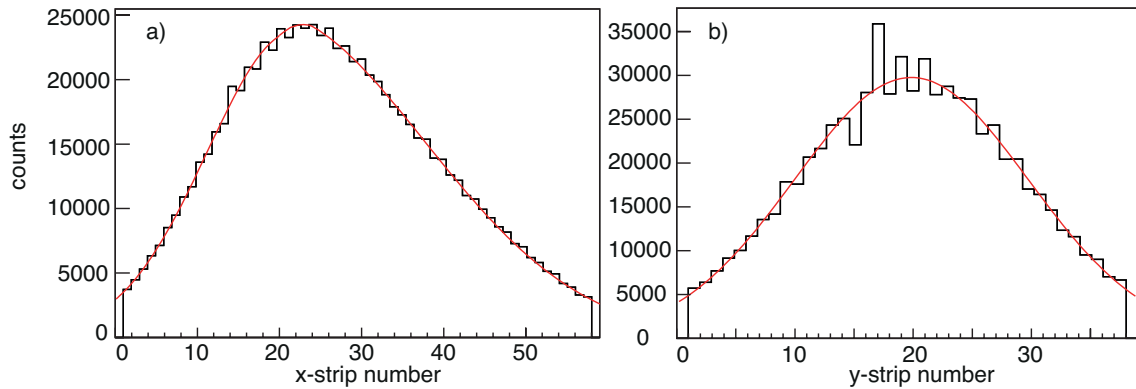


**Figure 2.15:** Projection of Fig. 2.14b) on a) the x- and b) the y-axis for the case of  $^{130}\text{Cd}$  and the fitted Gaussian distribution.

In Fig. 2.16a) and b) the  $z_{imp}$ -distributions are shown for the Pd setting and the Sn setting, respectively, to illustrate in which DSSSD layer the Cadmium isotopes are implanted. Since all ions have a very similar energy, the distribution over the different DSSSD is very narrow and nearly all ions are implanted into one DSSSD layer. In the Pd setting the majority of ions is stopped in DSSSD 3 while in the Sn setting DSSSD 4 is the layer with the most implantations. This information is important for some of the results presented later and, furthermore, it illustrates that in the current experiment two or three layers of DSSSD would have been sufficient to stop all ions of interest. In a similar experiment presented in the thesis of Z. Y. Xu [97] several nuclei in the region around  $^{78}\text{Ni}$  were produced and implanted in WAS3ABi. In that experiment the  $z_{imp}$ -distribution was much wider and nuclei were implanted in nearly all layers. For future experiments this information is important to estimate the maximum implantation rate suitable for an experiment. If the nuclei are distributed over more DSSSD layers, the total implantation rate can be higher without risking loosing correlations between the implantations and the following  $\beta$  decays.

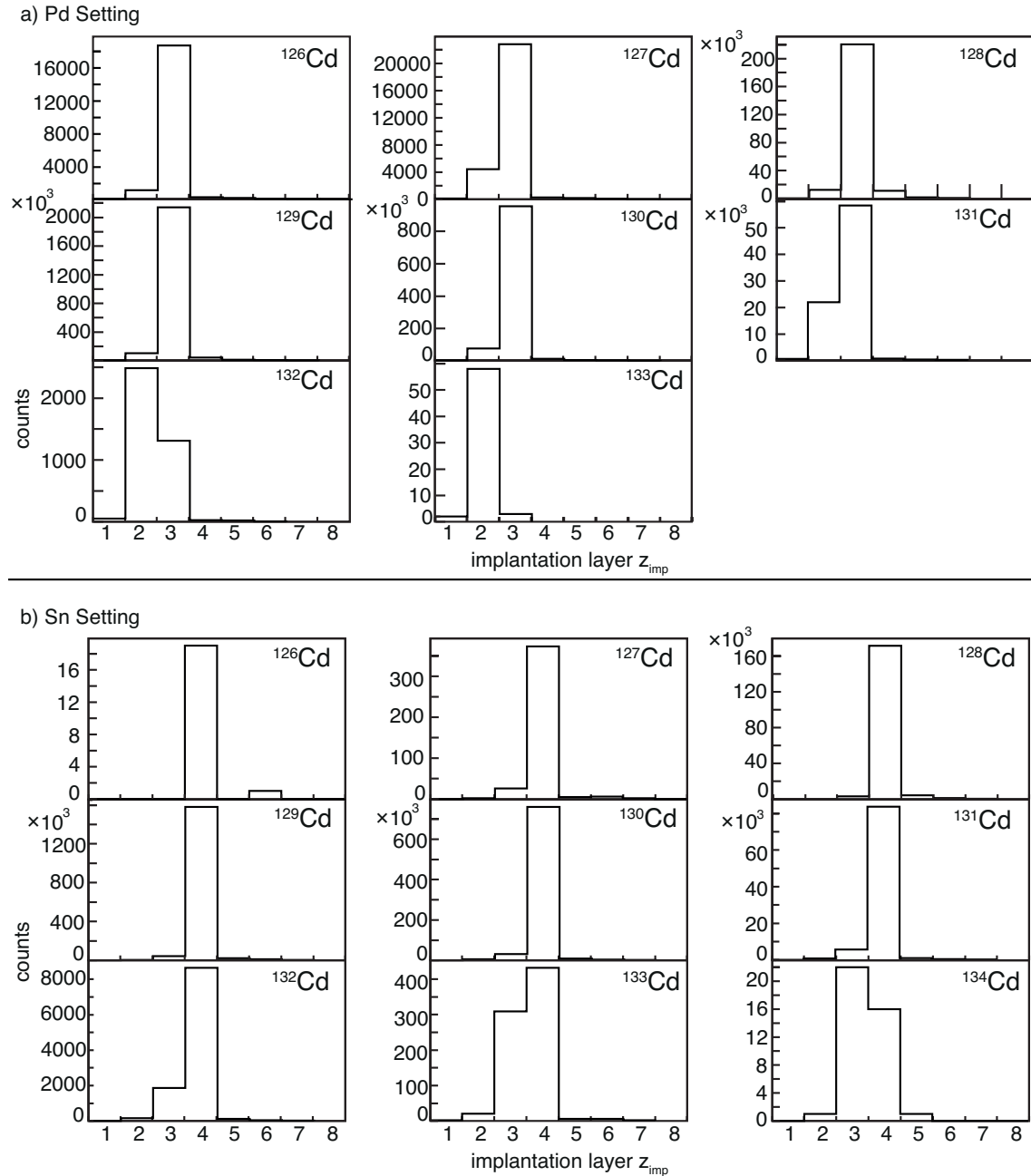


**Figure 2.16:**  $z_{imp}$  distribution, showing in which DSSSD layers the Cadmium isotopes with masses  $A=128$  to  $133$  were implanted in a) the Pd setting and b) the Sn setting.

### 2.2.3 WAS3ABi calibration

Before the discussion about the triggering and measurement of  $\beta$ -decay events with WAS3ABi is done in the following section, it is important to mention the calibration of the eight DSSSD. Without a calibration it is not possible to measure the energy of the electrons. Furthermore, the energies are also essential to determine the position in cases where the electron deposits energy in more than one pixel in the DSSSD.

The eight DSSSD are closely packed and also no vacuum was available inside the chamber which made it impossible to use  $\alpha$  or mono-energetic electron sources for the calibra-

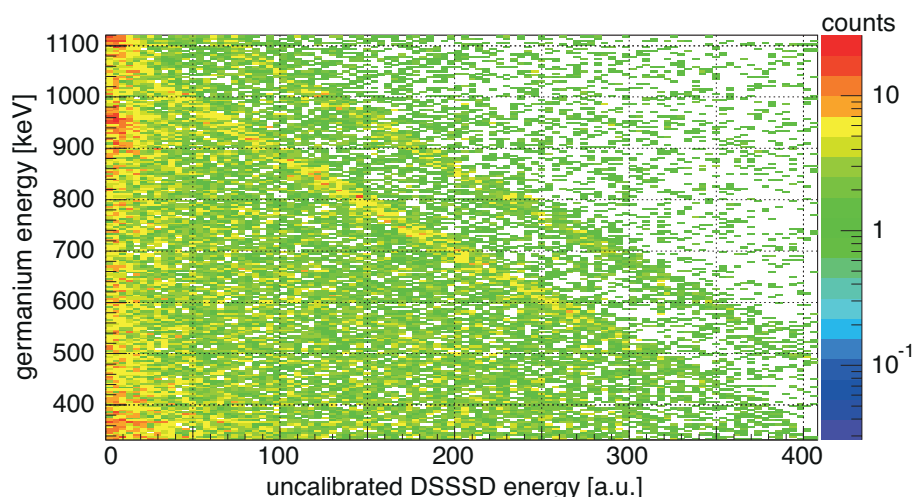


**Figure 2.17:** Matrix for calibrating a single DSSSD strip showing the example of DSSSD 3 x-strip 20. The spectrum is filled with the uncalibrated energy of DSSSD 3 x-strip 20 versus the energy measured in prompt coincidence in the already calibrated germanium detectors. Only events are taken where a single energy deposition was observed in DSSSD 3.

tion procedure. In the present experiment another common method to calibrate DSSSD was used. A  $^{60}\text{Co}$  source was placed inside the WAS3ABi chamber and the data acquisition triggered with WAS3ABi. It had been shown in previous works [98] that the measurement of Compton-scattered events between the DSSSD and the already calibrated germanium crystals can be used to calibrate the DSSSD. For each strip the two anti-correlations in the two dimensional display of uncalibrated DSSSD energy versus germanium energy were fitted with a linear calibration function. An example of this correlation is shown in Fig. 2.17 for a single strip of DSSSD 3. In this plot the anti-correlation is clearly visible for both emitted  $\gamma$ -rays (1173 and 1332 keV) down to about channel 40-50 of the uncalibrated DSSSD energy, which corresponds to about 150-180 keV. The assumed linear calibration function fits perfectly for energies down to this limit, below the limit the calibration may be worse and especially the energy resolution obtained from the sum of all silicon strips could be affected in a negative way by that.

#### 2.2.4 Energy shift during the experiments

One problem which arose concerning the energy calibration of the Si detectors was that an energy shift could be observed in the range of a few keV and while this is only of minor importance for the determination of the  $Q_\beta$  value because of the large  $Q_\beta$  values of about 10 MeV for the neutron-rich Cadmium isotopes, it has a big impact on the low energy calibration. It will be shown later that with the present set-up it was possible to identify ms isomers via the detection of conversion electrons. To be able to compare the energy spectra of the Si detectors to simulated data, it was necessary to correct for the shift in those cases which could be deduced from the expected energy of a conversion electron  $E_c$ , calculated with the conversion coefficient calculator Bricc [99], of a transition with a

known  $\gamma$ -ray energy  $E_\gamma$ . This procedure will be explained in detail when presenting the identified ms isomer.

### 2.2.5 $\beta$ -decay events

The electrons emitted in the  $\beta$ -decays of the implanted ions created a trigger for the data acquisition when they were detected in the Si detectors. To create the  $\beta$ -decay trigger, the sum outputs of the discriminators for each DSSSD were used, and it was required that in at least one x- and one y-strip of one DSSSD an energy deposition above threshold was measured in coincidence. In the off-line analysis as an additional condition it was added that no energy was deposited in the F11 plastic scintillator. This ensured that the energy deposition in the DSSSD did not occur from an implantation or a light particle.

To be able to reconstruct later the  $\beta$ -decay chains via the correlation of implanted ions to the subsequent  $\beta$ -decay events it is inevitable to have a position information for each electron observed in the DSSSD. This requires the application of an add-back algorithm. Due to the very thin DSSSD strips of 1 mm the electrons often deposited energies in several neighbouring strips. Only by adding up the energies deposited in those strips the full energy of the electrons could be reconstructed by adding the add-back energies of the several interaction positions in the same or different DSSSD. To reduce the probability of adding up the energies of different electrons which might have been emitted in random coincidence, only neighbouring strips were summed while non-neighbouring strips were treated as individual energy depositions. This allowed to later discard possible events where in one DSSSD more than one electron was detected.

In the case that no neighbouring strips had an energy deposition, the interaction position of the electron  $(x_\beta, y_\beta)$  was just defined as the center of the strip where it was detected. In the case of several neighbouring strips firing the position was calculated as the energy weighted mean position:

$$x_\beta = \frac{\sum_{i=n}^m E_{xi} \cdot x_i}{\sum_{i=n}^m E_{xi}} \quad (2.5)$$

with  $E_{xi}$  being the energy measured in the  $i$ -th strip and  $i$  counting from strip  $n$  (x-position  $x_n$ ) till strip  $m$  (x-position  $x_m$ ), all strips with an energy deposition over threshold and just neighbouring strips with no intermediate strip having no energy deposition. The y-position calculation is performed in the same way. Fig. 2.18 shows an illustration of the position and energy determination for an event with a single energy deposition in one DSSSD which is distributed over one x- and several y-strips.

While till here it was only mentioned that electrons emitted in the  $\beta$ -decay generate a trigger in WAS3ABi, it has to be added that, of course, WAS3ABi cannot distinguish if a certain energy deposition was the interaction of an electron or an  $\gamma$ -ray with the DSSSD or any other type of particle. The trigger will be called in the following  $\beta$ -decay trigger but that does not exclude that WAS3ABi was maybe triggered by e.g. a Compton electron or an electron emitted in the process of internal conversion. This has to be kept in mind

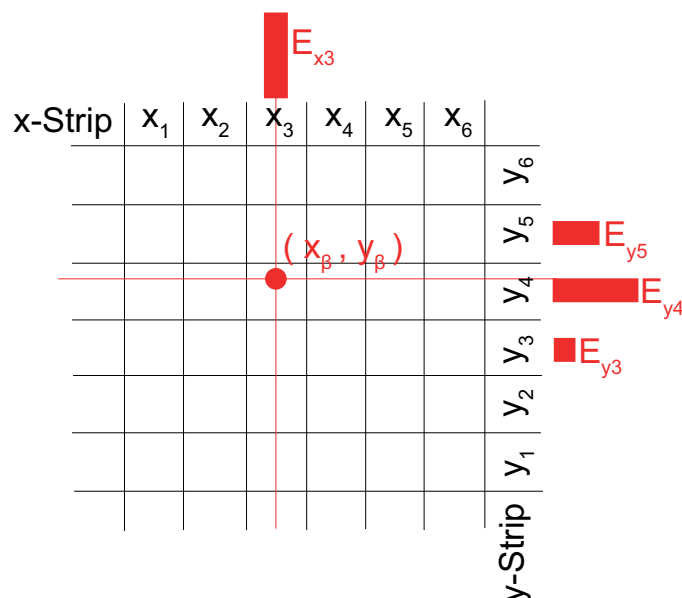


**Figure 2.18:** Illustration of the method to determine the interaction position of  $\beta$ -like particles in WAS3ABi, showing a single interaction position with only one strip with a deposited energy in x-direction and several neighbouring strips with an energy deposition in y-direction.

when later doing the analysis of the  $\beta$ -decay events where the  $\beta$ -decay triggered events are correlated to the implantation events.

### 2.2.6 Ion - $\beta$ correlations

After having now described the methods to obtain the position information for implantation and  $\beta$ -decays (electrons), correlating the implanted ions to the subsequent  $\beta$ -decays can proceed. While it is clear which ion was implanted at what time in which pixel of the DSSSD array, there is no unique information available which  $\beta$ -decay corresponds to which implanted ion. The only way to achieve a reasonable correlation is by means of the decay time and the position difference in x- and y- direction. Depending on the exact implantation position and in which direction the electron is emitted, an energy deposition is expected to happen in the same pixel or the surrounding pixels.

The correlation time was set to five seconds for all nuclei to have also for the ones with the longest half-lives a correlation time which equals about ten half-lives, necessary for the lifetime analysis. For clean  $\beta$ -decay spectra the correlation time was in a subsequent step limited to about three half-lives, as it will be shown later. For each of the  $\beta$ -decays observed in the correlation time after an implantation the position difference in x,y and z direction was calculated as:

$$\Delta x = |x_{imp} - x_{\beta}| \quad \Delta y = |y_{imp} - y_{\beta}| \quad \Delta z = |z_{imp} - z_{\beta}| \quad (2.6)$$

with  $x_{imp}$ ,  $y_{imp}$ ,  $x_{\beta}$  and  $y_{\beta}$  being defined as in the previous sections.  $z_{imp}$  and  $z_{\beta}$  are simply

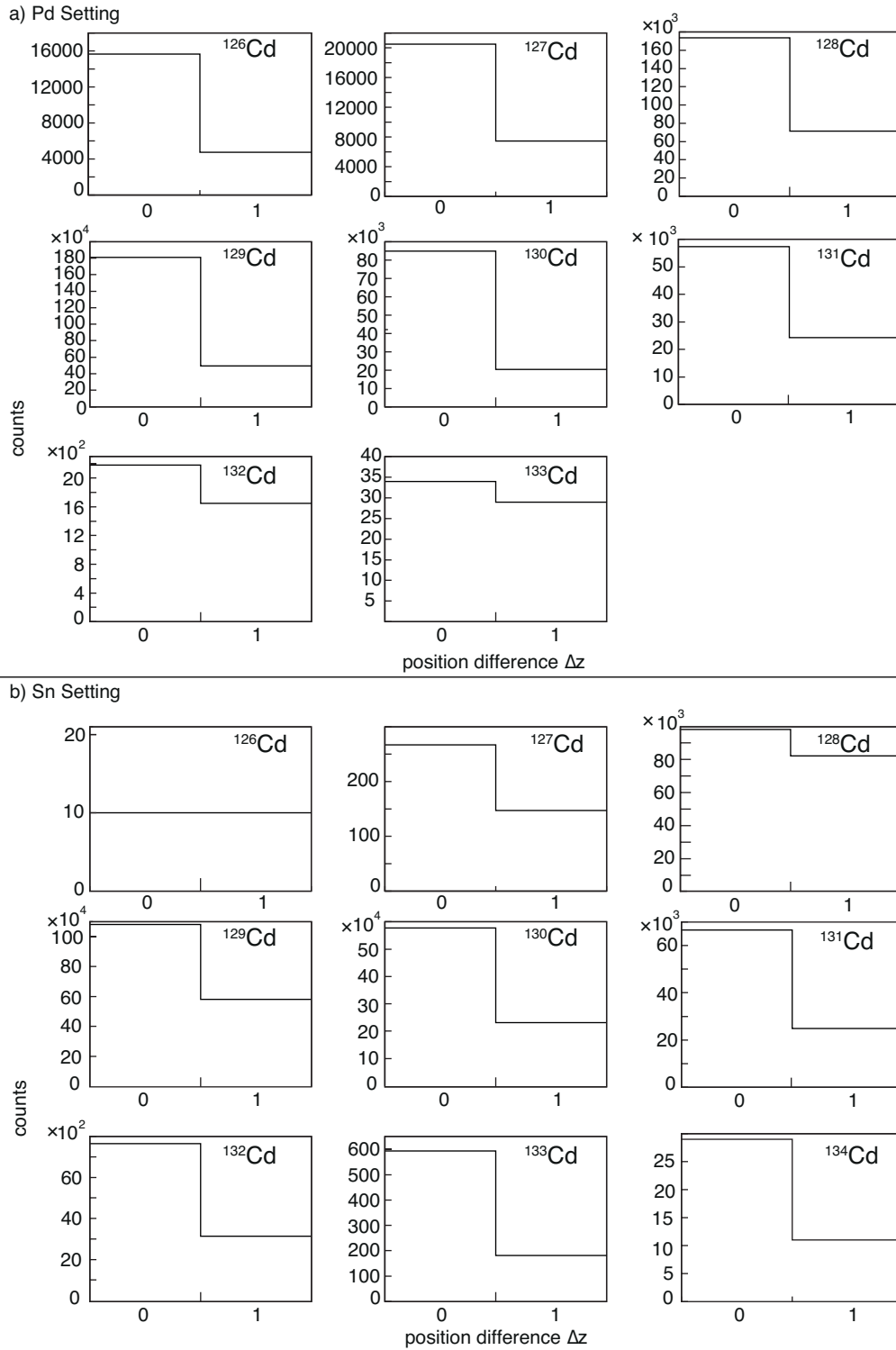


**Figure 2.19:**  $\Delta z$  distribution of all  $\beta$  decays correlated to the implanted Cadmium ions in a) the Pd setting and b) the Sn setting.

the numbers of the DSSSD layers in which the implantation or  $\beta$ -decay was observed, respectively. Only those  $\beta$ -decays were correlated in which the implantation and decay were seen in the same DSSSD or in direct-neighbouring DSSSD ( $\Delta z \leq 1$ ). Figure 2.19 shows  $\Delta z$  for all  $\beta$  decays which were correlated to the implanted Cadmium ions.

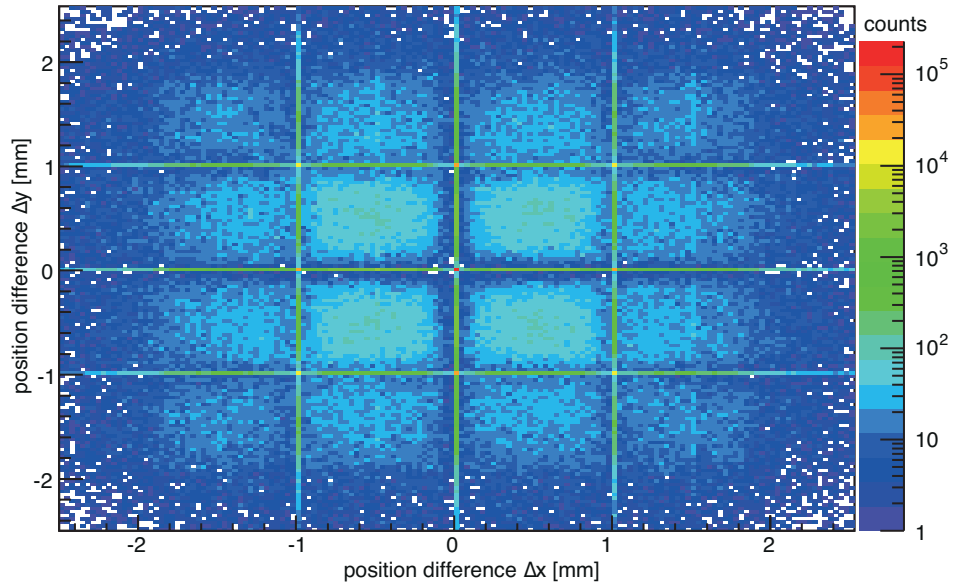


**Figure 2.20:** Zoom on the  $\Delta x$ - $\Delta y$  pattern of all  $\beta$  decays correlated to the implanted  $^{130}\text{Cd}$  ions in the Pd setting.

Furthermore, it was required in a first step that either the same pixel or one of the eight surrounding ones (or the corresponding ones in the neighbouring DSSSD) had an energy deposition above threshold. In a second step the actual measured position of the electron as obtained from the deposited energies in direct-neighbouring pixels was compared to the implantation position and the position difference  $\Delta x$  and  $\Delta y$  was calculated. Fig. 2.20 shows the  $\Delta x$ - $\Delta y$  pattern for all decays correlated to the implanted  $^{130}\text{Cd}$  ions, while in Figure 2.21 the  $\Delta x$ - $\Delta y$  patterns for all other Cadmium isotopes in the Pd setting and the Sn setting, respectively, are presented. In those figures one observes that even though it was required that at least one of the direct neighbouring pixels had an energy deposition above threshold, the position difference is in some cases much bigger. In those cases the electron must have deposited energy in multiple neighbouring pixels and the positions  $x_\beta$  or  $y_\beta$  were calculated with formula 2.5. Limiting the position difference  $\Delta x$  and  $\Delta y$  will be a powerful tool to remove randomly correlated  $\beta$  decays from other nuclei later in this thesis.

The  $\Delta x$ - $\Delta y$  pattern in Fig. 2.20 is essentially the same than the pattern displayed in Fig. 2.21 for the case of  $^{130}\text{Cd}$ . The main difference is the finer binning which allows to observe structures one can not see with the binning of Fig. 2.21. At the integer numbers 0 and 1 in  $\Delta x$  as well as in  $\Delta y$  clearly peaks are visible. Those can be explained by the method how the positions of the implantations and  $\beta$  decays are calculated.  $x_{imp}$  and  $y_{imp}$  are always integers as it was described in section 2.2.2. On the contrary  $x_\beta$  and  $y_\beta$  are either integers or decimal numbers. If only one strip fired than  $x_\beta$  ( $y_\beta$ ) are integers while when more strip fired those positions are calculated based on the energy deposited in each strip.

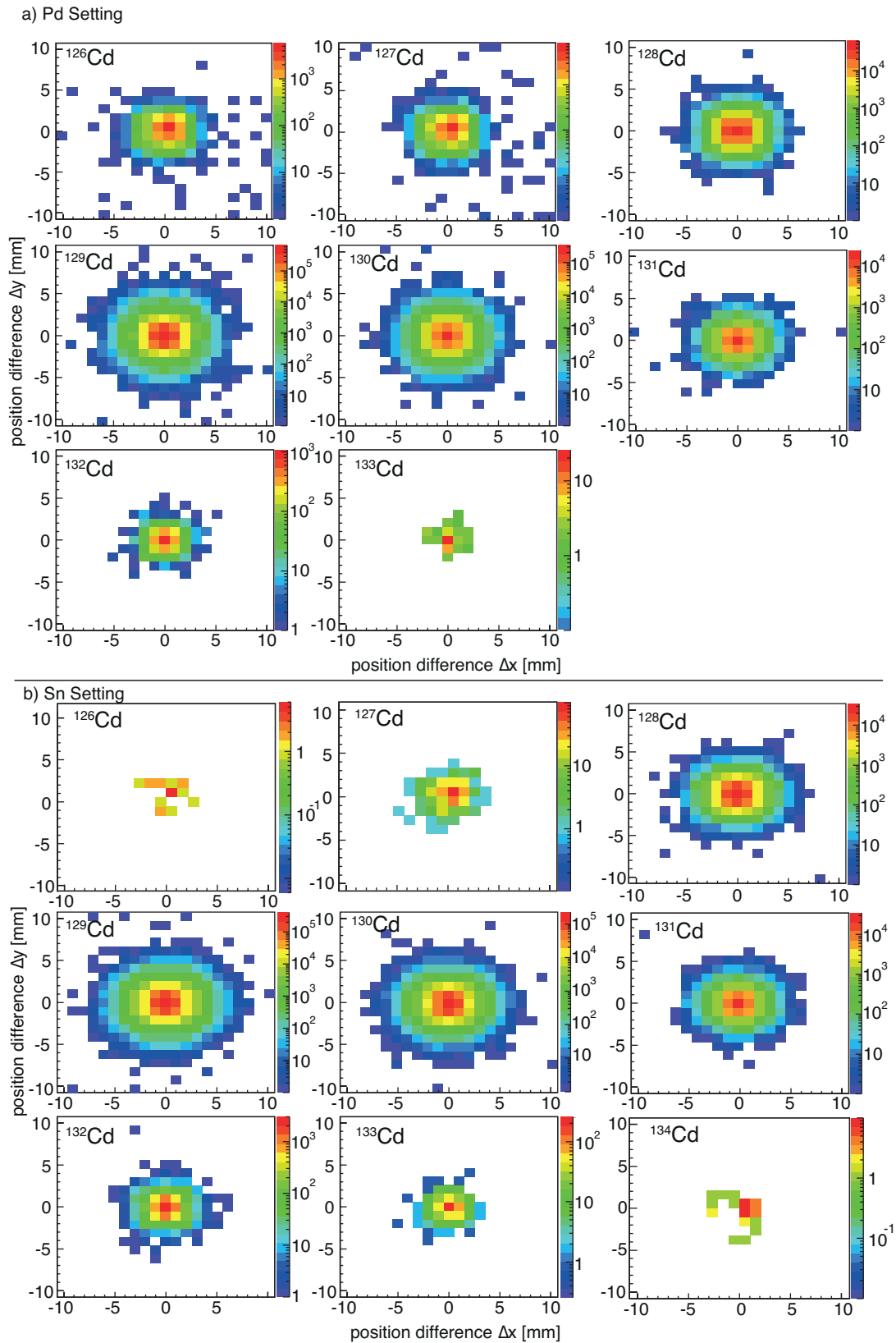


**Figure 2.21:**  $\Delta x$ - $\Delta y$  pattern of all  $\beta$  decays correlated to the implanted Cadmium ions in a) the Pd setting and b) the Sn setting.

## 2.3 EURICA Ge-Array



**Figure 2.22:** Picture of one half of the EURICA Array including the former Euroball cluster detectors and NaI detectors.

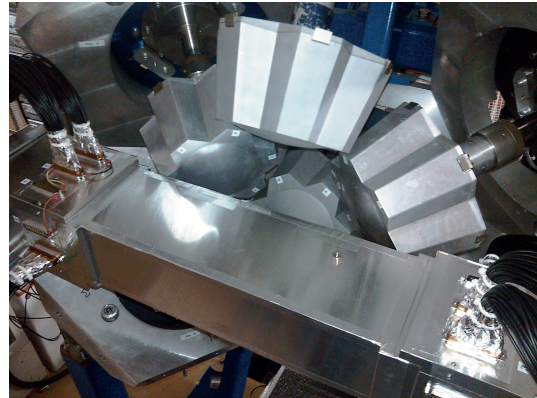


**Figure 2.23:** Picture of the other half of the EURICA Array including the former Euroball cluster detectors and the chamber with the active stopper WAS3ABi.

The nuclei of interest were implanted at the last focal plane in the active stopper WAS3ABi which is surrounded by the EURICA Ge-Array. The Array consists of 12 cluster detectors from the former Euroball array [100] which are placed in close geometry around the passive stopper [101]. One cluster detector is subdivided into 7 encapsulated, tapered, hexagonal shaped Ge crystals in a common cryostat and those crystals are closely packed. Pictures of the array taken during the EURICA campaign in autumn 2012 at RIKEN are shown in Fig. 2.22 and Fig. 2.23. A three-dimensional schematic of the array including the chamber of WAS3ABi is shown in Fig. 2.24 where also the definition of the Cartesian coordinate system is introduced.

Each of the 84 crystals has two parallel outputs, one signal was sent to Digital-Gamma-Finder modules (DGF) while the other signal was further processed by analogue timing electronics. In the digital branch the 84 signals were distributed to 24 DGF modules each having 4 channels and running with a clock frequency of 40 MHz, which corresponds to 25ns time steps. The built-in ADC digitizes the signal and a slow trapezoidal filter is applied afterwards. From this branch one obtains then energy and timing information, while each DGF channel trigger is validated by a GFLT (General First Level Trigger) which corresponds to the main trigger of the whole set-up, thus the signal of the F11 plastic scintillator or WAS3ABi. The main trigger is also fed into one channel of each DGF crate for checking the synchronization of the system and to provide a time-reference signal to calculate the time-difference between the ion passing through the scintillator and the detection of the (delayed)  $\gamma$ -rays. Since the timing resolution (25ns time steps) of the digital branch is not suitable for the measurement of short-lived isomers in the range of a few tenth to hundred ns, the additional analogue timing branch was used to measure the before mentioned time-difference in a more accurate way. The signals from the second pre-amplifier output of the Ge detectors are therefore processed by a standard timing

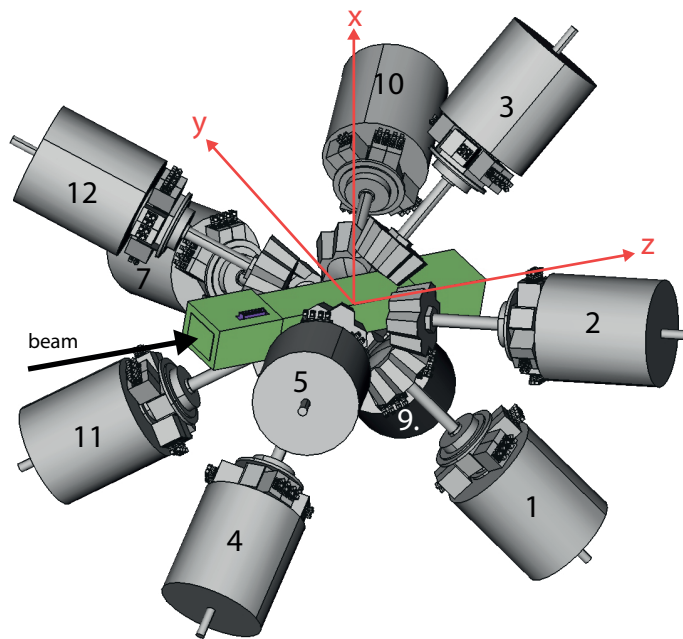


**Figure 2.24:** Schematic of the germanium detector and definition of the coordinate system.

circuit comprising of a Timing-Filter-Amplifier (TFA), a Constant-Fraction-Discriminator (CFD) and a Time-to-Digital-Converter (TDC). The signals from the CFD are fed into two separate TDC modules, one which will be called from now on “short-range-TDC” (TDCs) with a full range of  $1 \mu\text{s}$  and  $0.31 \text{ ns/channel}$  and the other so called “long-range-TDC” (TDCI) with a full range of  $800 \mu\text{s}$  and  $0.73 \text{ ns/channel}$ . More details of the electronics set-up used in this experiment can be found in Fig. 2.25, including the above mentioned parts and the processing of the main trigger for the read-out of the germanium electronics.

### 2.3.1 Addback algorithm

$\gamma$ -rays interact with material in mainly 3 different ways and ionize the material: photoelectric absorption, Compton scattering and pair production. The three different effects are of particular importance for the treatment of the data coming from the germanium detectors in order to improve the efficiency of the detector in the offline analysis. While for the case of photoelectric absorption the full energy of the  $\gamma$ -ray is deposited in one crystal of the array, especially in the case of Compton scattering the energy might be distributed over various crystals. To reconstruct the full energy of the  $\gamma$ -ray, the energies deposited in those crystals have to be added together. For this purpose an add-back algorithm was implemented in the code used for the off-line analysis. The main difficulty is to correctly identify the crystals which belong to the energy deposition of one individual  $\gamma$ -ray. Therefore, within one event the energies of different crystals were only summed up if they fulfilled certain criteria:

1. Direct neighbour and multiplicity condition: The crystals have to be direct neigh-

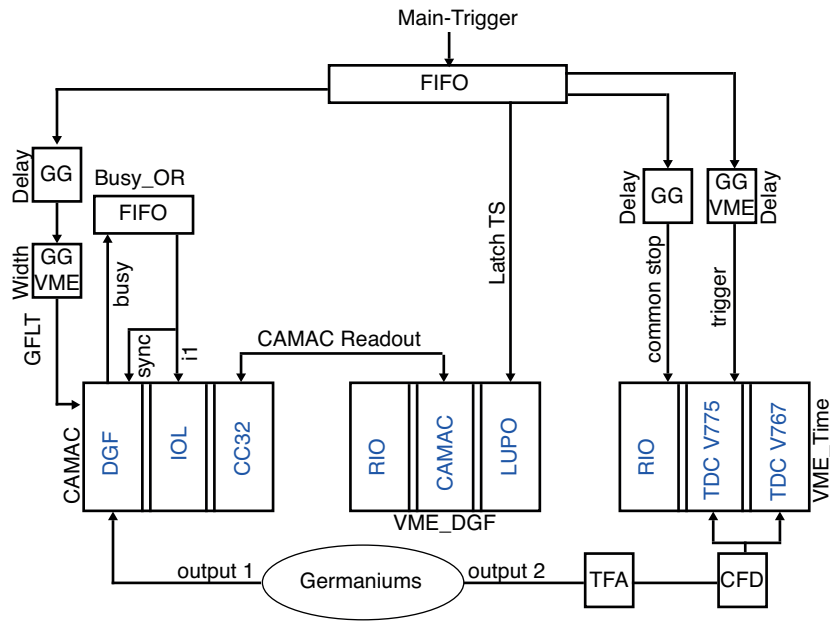


**Figure 2.25:** Scheme of the electronics used for the read-out of the germanium detectors. Words in small letters indicate the used input/output channels of the individual modules, the used abbreviations are as following: Fan-In Fan-Out (FIFO), Gate Generator (GG), General First Level Trigger (GFLT), the abbreviations in blue are names of specific modules which are not explained here in detail.

bours within one cluster and the multiplicity of crystals which recognized an energy deposition within one cluster had to be smaller or equal to 2. Otherwise, the measured energies were treated as independent energy depositions from different  $\gamma$ -rays.

2. Time difference condition: The travel time of the Compton scattered  $\gamma$ -rays to the adjacent crystals is small compared to the timing resolution of the DGF. Therefore, the energies were only summed up if the energy deposition was in prompt coincidence to each other. The time window was selected with a two dimensional cut on the time difference  $\Delta t$  and the energy  $E_{\Delta t}$  which are calculated as following:

$$\Delta t = |t_{DGF,\gamma 1} - t_{DGF,\gamma 2}| \quad (2.7)$$

$$E_{\Delta t} = 1000 \cdot \frac{|E_{\gamma 1} - E_{\gamma 2}|}{|E_{\gamma 1} + E_{\gamma 2}|} + 1 \quad (2.8)$$

An example is shown in Fig. 2.26.

3. Energy condition: The three different ways of interaction of  $\gamma$ -rays with matter have different contributions for different energies. The contribution for low energies of the photoelectric absorption is nearly 100 % while for higher energies the two other effects are dominating. Due to the higher probability of a full energy deposition for low energy  $\gamma$ -rays, a lower energy limit is set within the add-back algorithm to avoid the summation of low energy gamma-rays which are in random-coincidence and fulfil

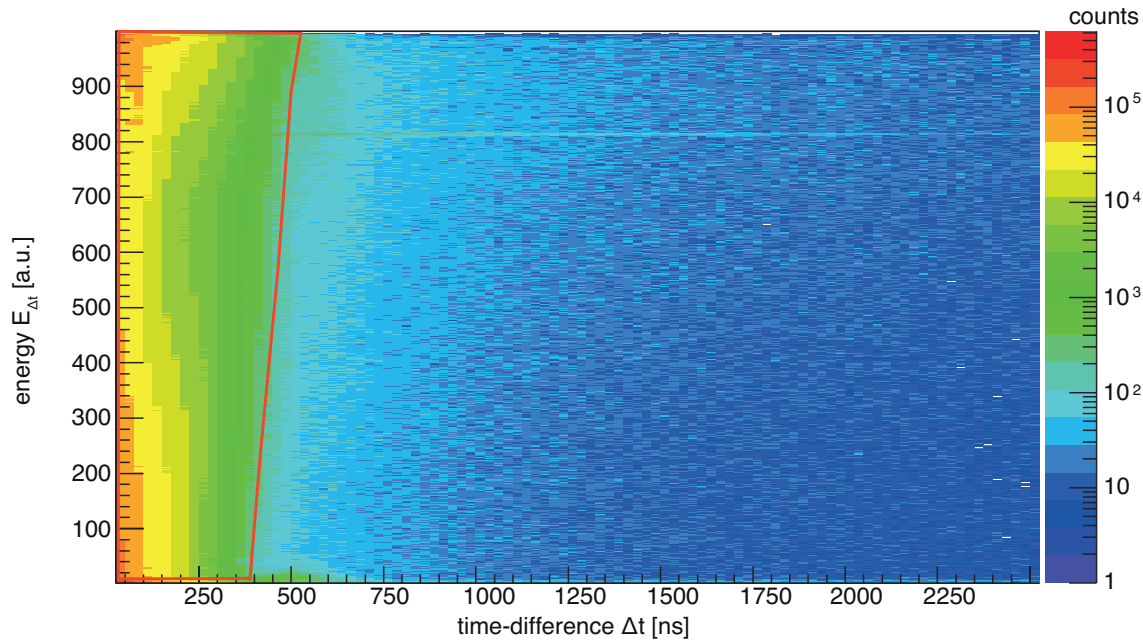


**Figure 2.26:** Time difference between two  $\gamma$ -rays in the same cluster on the x-axis and the energy  $E_{\Delta t}$ , see formula 2.8, on the y-axis. The gate set in the off-line analysis to select prompt coincidences is shown in red.

the above mentioned other criteria. The energy condition has to be chosen carefully, especially if very weak low energy transitions are involved. A typical energy condition is:

$$E_1 + E_2 > 100\text{keV} \quad (2.9)$$

The gain in absolute efficiency of the Ge-Array for higher energetic  $\gamma$ -rays is presented in the following section for calibration data.

### 2.3.2 Ge-Array: calibration and absolute efficiency

Prior to and after the experiment several calibration measurements have been performed with different types of radiation sources. Those measurements are used for two different purposes, first of all the energy calibration of the EURICA Ge-Array and secondly for the determination of the absolute efficiency of the set-up. The calibrations have been performed with various radioactive sources, e.g.  $^{60}\text{Co}$ ,  $^{133}\text{Ba}$  and  $^{152}\text{Eu}$  (see Table 2.3). The energy calibration was performed using the measurement with the latter one using a linear energy calibration function, and the obtained calibration factors and offsets for each crystal are summarized in Appendix A.1. A measurement with a high energy  $\gamma$  source was not performed but the peak position of various known high energy transitions from the actual experimental decay data was compared to the literature values. A good test case are the transitions in  $^{132}\text{Sn}$  which were populated in the  $\beta$ -decay of  $^{132}\text{In}$  in this experiment. The peak positions of the three high energy transitions with the highest relative intensity were fitted with a Gaussian distribution and the obtained peak positions

Isotope	measured activity	measurement date
$^{60}\text{Co}$	unknown	unknown
$^{133}\text{Ba}$	453 kBq	01.01.1998
$^{152}\text{Eu}$	40.9 kBq	01.01.1998

**Table 2.3:** List of the sources used for the determination of the absolute efficiency, including the measured activity and the measurement date.

are 4040.3(2), 4350.9(2) and 4415.3(2) keV. The energies of those transitions have been reported in Ref. [82] to be 4041.1, 4351.9 and 4416.2 keV, respectively. A shift of smaller than 1 keV is observed with respect to the literature value which is sufficient for the further studies in this work.

For the measurement of the absolute efficiency the data acquisition was triggered with a 1 kHz clock to avoid dead time problems. The absolute efficiency of the Ge-Array is the probability that a gamma-ray of a certain energy interacts and the full energy is detected:

$$\epsilon_{abs} = \frac{N_{\gamma, detected}}{N_{\gamma, emitted}} \quad (2.10)$$

The number of detected  $\gamma$ -rays  $N_{\gamma, detected}$  for a certain energy is obtained from fitting the peak area in the energy spectrum and comparing it to the number of emitted  $\gamma$ -rays  $N_{\gamma, emitted}$ . The latter one is calculated from the measurement time and the activity of the source  $A$  (see Table 2.3). The measurement time is calculated from the total number of recorded events  $N_{trigger}$  multiplied by the width of the gate for the DGF  $t_{Gate, DGF}$ , which was 100  $\mu\text{s}$  for all of the source measurements:

$$\epsilon_{abs} = \frac{N_{\gamma, detected}}{N_{trigger} t_{Gate, DGF} A} \quad (2.11)$$

The efficiency is energy dependent and the obtained efficiency values for different energies are therefore fitted with the following function (Ref. [102]):

$$\epsilon_{abs}(e) = \exp \left[ \left( \left( A + B \cdot \left( \log \frac{e}{100} \right) \right)^{-G} + \left( D + E \cdot \left( \log \frac{e}{1000} \right) + F \cdot \log \frac{e}{100} \cdot \log \frac{e}{1000} \right)^{-G} \right)^{\frac{-1}{G}} \right] \quad (2.12)$$

where  $e$  is the energy in keV and A to G are free fit parameters. This function has proven to well describe the energy dependent efficiency of germanium detectors.

One question before starting the experiment was which effect the placement of the Q-beta detectors had on the absolute efficiency of the germanium array. Especially for some of the downstream germanium clusters the plastic detectors had a shadowing effect. To investigate the effect, two measurements were performed, with sources of  $^{133}\text{Ba}$  and  $^{152}\text{Eu}$  placed between the 4th and 5th DSSSD. In the first measurement the Q-beta detector was not installed, while in the second measurement it was placed right behind WAS3ABi,

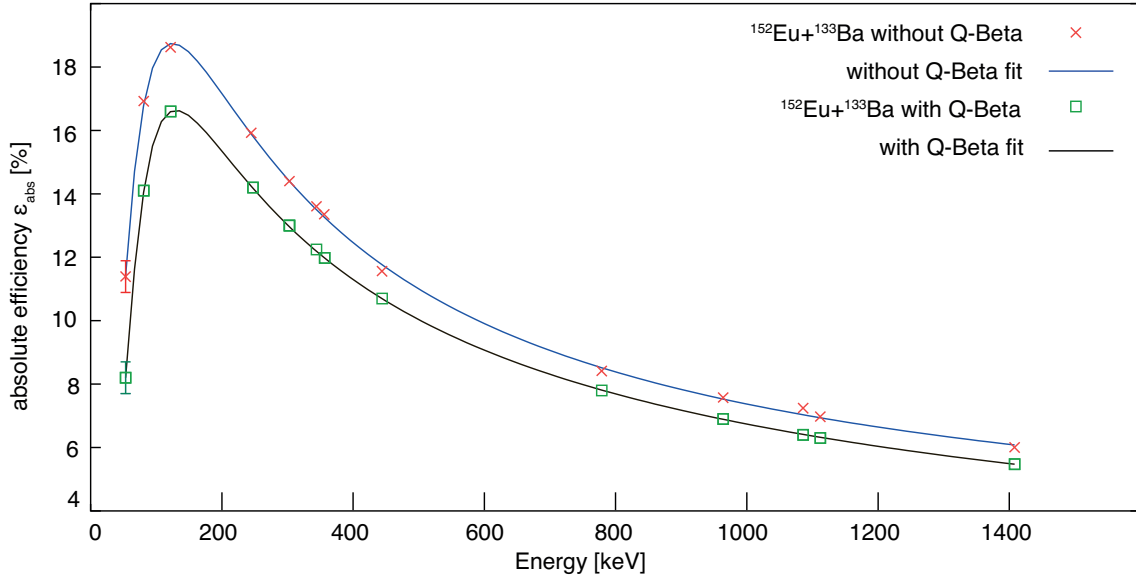


**Figure 2.27:** Absolute Efficiency of the EURICA Ge-Array without and with the Q-beta detector installed.

$i$	$\epsilon_{avg}^{Cr}(i) \text{ (wo } Q_{\beta})$	$\epsilon_{avg}^{Cr}(i) \text{ (w } Q_{\beta})$	$i$	$\epsilon_{avg}^{Cr}(i) \text{ (wo } Q_{\beta})$	$\epsilon_{avg}^{Cr}(i) \text{ (w } Q_{\beta})$
1	0.138(9)	0.146(9)	7	0.141(9)	0.140(9)
2	0.150(10)	0.114(7)	8	-	-
3	0.148(9)	0.097(6)	9	0.141(9)	0.140(9)
4	0.148(8)	0.157(11)	10	0.140(9)	0.097(6)
5	0.148(9)	0.148(9)	11	0.145(9)	0.152(10)
6	0.149(10)	0.141(8)	12	0.143(9)	0.139(8)

**Table 2.4:** Average Efficiency of one crystal for each cluster with and without the Q-beta detector at 500 keV

where it was also during the actual experiment. Figure 2.27 shows the measured absolute efficiencies in both scenarios and the corresponding fits.

The Q-beta detector has a clear influence on the absolute efficiency of the germanium array reducing it by about 5-10% depending on the energy. To further quantify the effect on the individual clusters, the average absolute efficiency for the crystals in one cluster was determined and is shown in Table 2.4. The average efficiency of one crystal in cluster number  $i$  was determined from the following formula:

$$\epsilon_{avg}^{Cr}(i) = \frac{1}{7} \sum_{j=1}^7 \epsilon_{abs}(j) \quad (2.13)$$

with  $j$  the crystal number in the corresponding cluster  $i$  and  $\epsilon_{abs}(j)$  its absolute efficiency. Especially the downstream clusters 2, 3 and 10 show as expected a significant decrease in the average absolute efficiency per crystal.

To improve the absolute efficiency for  $\gamma$ -rays above about 300 keV, the before described add-back algorithm was applied. The results are presented in Fig. 2.28. In this figure

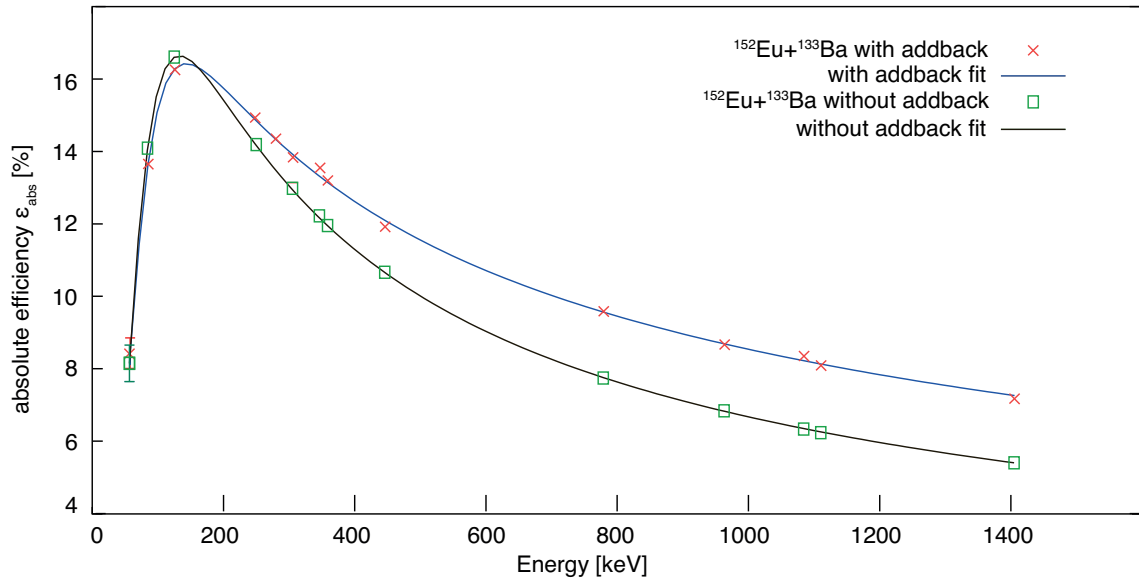


**Figure 2.28:** Absolute Efficiency of the EURICA Ge-Array without and with the addback procedure applied.

$\epsilon_{abs}$  is shown with the Q-beta detector installed for the two cases without and with add-back together with the fitted efficiency curves. A significant improvement of the absolute efficiency for higher energies is achieved when applying the add-back with the add-back conditions set to  $\Delta t < 200\text{ns}$  and  $E_1 + E_2 > 100\text{keV}$ .

As mentioned before, no measurement was performed with a high energy  $\gamma$  source and while the energy calibration can still be performed assuming a totally linear calibration function, the fitted absolute efficiency function is much more complex and an extrapolation from about 1.5 MeV up to the total range of more than 6 MeV is not possible. One possible solution to overcome this problem was to take experimental data and select nuclei which have high energy transitions with as accurate as possible known relative intensities. In the present experiment especially one nucleus was present with known high energy transitions and sufficient statistics, namely  $^{132}\text{Sn}$ . Transitions with energies of 299, 479, 2380 and 4041 keV in  $^{132}\text{Sn}$  were populated through the  $\beta$ -decay of the implanted  $^{132}\text{In}$  ions. The transitions with energies of 299 and 479 keV were used to shift the efficiencies obtained from the transitions observed in  $^{132}\text{Sn}$  in the low energy part onto those extracted from the sources.

The absolute efficiencies of the two transitions were determined using the relative intensities published in Ref. [82] together with the measured  $\beta$ -feeding in that Reference. Via a  $\chi^2$  minimization a shift parameter was determined to adjust the efficiencies to the before determined absolute efficiency curve from the source measurements. Nevertheless, the shift factor was determined to be 0.98 which shows that the efficiencies from source measurements fit well with those obtained from actual in-beam decay data. Finally, the function  $\epsilon_{abs}(e)$  was fitted to the combined data containing the source measurements and the shifted efficiencies determined from the known transitions in  $^{132}\text{Sn}$ . The source and in-beam datasets and the corresponding total fit are shown in Fig. 2.29, with and without

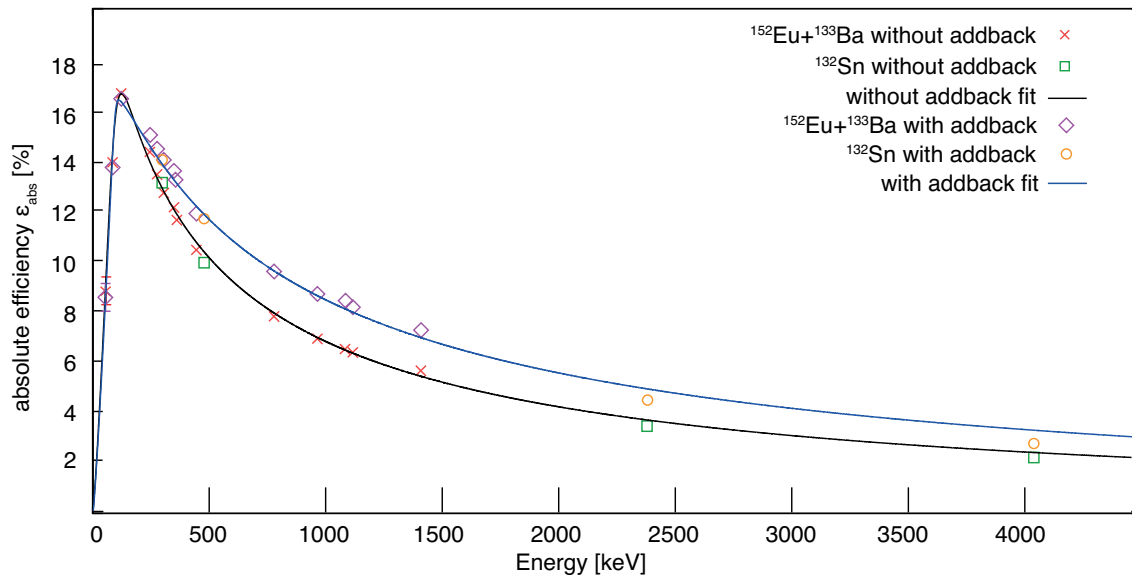


**Figure 2.29:** Absolute Efficiency of the EURICA Ge-Array without and with the add-back procedure applied for up to 4.5 MeV.

the add-back procedure. While the efficiencies determined from transitions in  $^{132}\text{Sn}$  show a very similar behaviour compared to the efficiencies obtained from the source measurements in the case of no add-back, severe differences can be observed when using the add-back algorithm. Additional to that, a relatively lower gain in efficiency was found for the transitions with 2380 and 4041 keV compared to for example the 1408 keV  $\gamma$ -ray emitted from the  $^{152}\text{Eu}$  source. It appears as if the add-back algorithm works less well for higher energies. Even when allowing the add-back algorithm to sum energies of up to three neighbouring crystals, no significant improvement could be found. The problem remains unsolved for the moment. Therefore, it was decided to use the intensities obtained without using the add-back procedure, where the fitted efficiency curve suggests an efficiency of about 2% for 4 MeV  $\gamma$ -rays. All parameters of the fits presented here for the absolute efficiency are stated in Table C.1 in the appendix.

## 2.4 Data processing

After having presented the different detector systems a quick introduction is now given for the data processing and data acquisition systems.

### 2.4.1 Data acquisition

Three independent data taking systems were used during the present experiment, the first one to read out the detectors from BigRIPS, the second for the data taking of the EURICA Ge-array and the last one for the signals of the active stopper WAS3ABi. Some of the BigRIPS signals were also fed into the data taking systems of the Ge detectors and

WAS3ABi for on-line analysis purposes. All three systems included a LUPO (Logic Unit for Programmable Operation) time-stamp module [103] which were synchronized before the experiment, and the synchronization was checked during the whole experiment.

BigRIPS and WAS3ABi used the RIBF DAQ, a data acquisition system developed at RIKEN and a detailed description can be found in Ref. [104]. Both systems used the same data acquisition architecture but were running as completely independent systems, relying on the off-line synchronization via timestamps. The germanium detectors were read out by a different DAQ system, the Multi Branched System (MBS), a data acquisition system developed at GSI and for further information please refer to Refs. [105, 106].

### 2.4.2 Raw data preparation

Before the merging of the data collected with the three independent systems using an off-line merging code, developed by Z. Y. Xu in the framework of his PhD thesis [97], was performed, the raw data had to be prepared. For all detector systems it was necessary to assign the individual electronic channels to the corresponding detector signals and calibrate them. In the case of BigRIPS it was also necessary to further process the data and calculate the needed information, e.g. mass-to-charge ratio and nuclear charge, as it was briefly explained before.

The BigRIPS data processing is not explained here in detail because it was performed by the BigRIPS team. A ROOT-File containing the already calculated AoQ and Z was provided and could be used directly for the merging. The calibration of the raw EURICA germanium data was already explained in detail in this chapter and it can be just noted here that the unpacking, the calibration and the assignment of the individual electronic channels to the corresponding detectors and crystals was made with an analysis code developed for the object-oriented system Go4 (GSI Object Oriented On-line Off-line system) [107] by the EURICA collaboration. The processing of the WAS3ABi raw data was part of the off-line merging software which was based on the Anaroot tool kit developed at RIKEN. The determination of the calibration coefficients for the EURICA and WAS3ABi data was done as part of this thesis and has also already been explained in this chapter.

### 2.4.3 Merging and analysis Code

For all three systems a ROOT-File containing the essential information in an event-by-event structure, including of course the timestamps, was generated and used as a starting point for the merging process. The off-line merging software contains multiple steps which are shown in Fig. 2.30 schematically. In a first step the data of WAS3ABi was merged with the EURICA data, for that the events were correlated based upon the time-stamp information. Due to different cable lengths and delays the timestamps of one system in comparison to another system might have an offset. Therefore, the offset  $TS_{offset}$  was determined and taken into account for the correlation of events within a time window

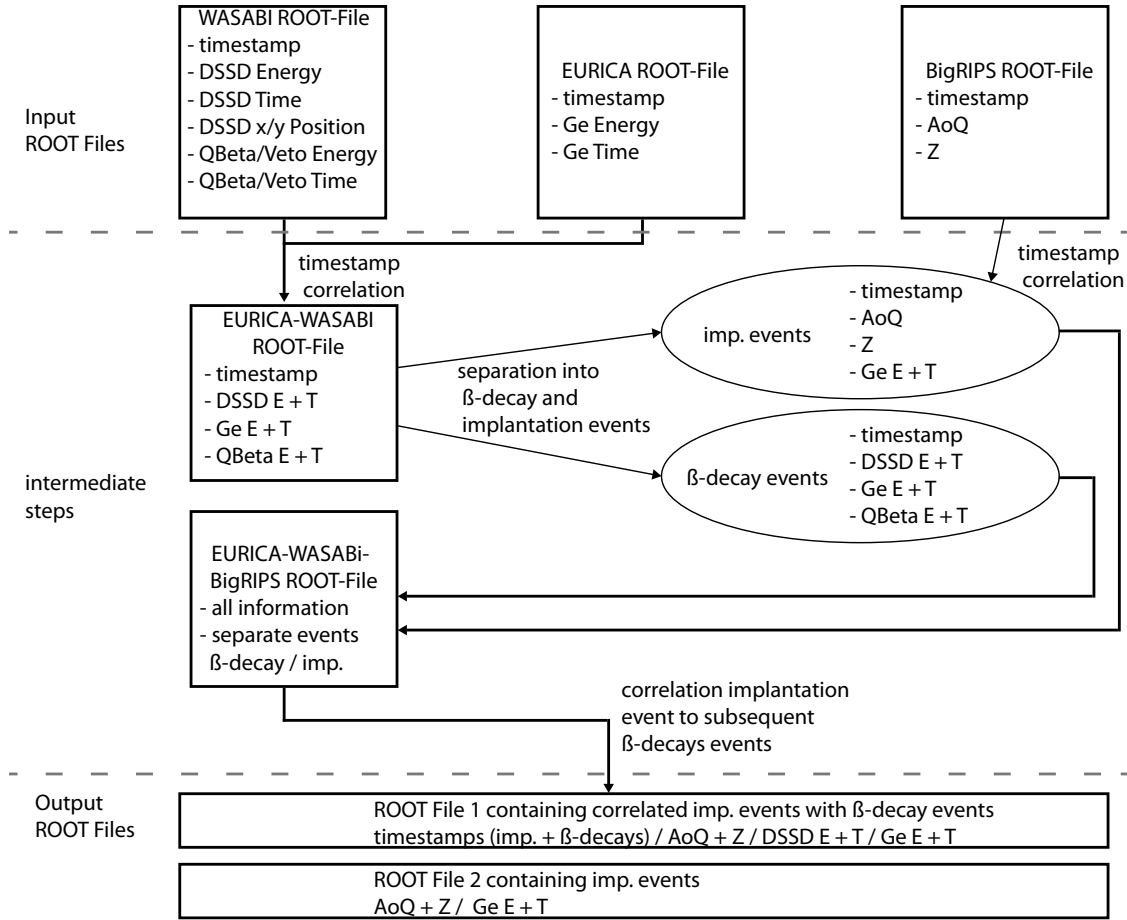


**Figure 2.30:** Schematic of the merging process for the three data acquisition systems based on the timestamp of each system. The essential information of each system contained in each step and the final output ROOT-File are stated.

of  $\pm 75$  ns in the merging process. Events from the different systems were thus only correlated if their timestamps  $TS_{sys1}$  and  $TS_{sys2}$  fulfilled the following requirement:

$$\Delta t = |TS_{sys1} - TS_{sys2} + TS_{offset}| \leq 75ns \quad (2.14)$$

In the second step the events were separated into those associated to the implantation of an ion and those where the  $\beta$ -decay was observed in WAS3ABi. The events in which an implantation was observed were then correlated to the corresponding event in the BigRIPS data using the timestamps, leaving two very different types of events (implantation events and  $\beta$ -decay events). The event-by-event information were stored into one ROOT-File but in two different and independent ROOT-trees. As a final step each implantation event was correlated to the subsequently occurring  $\beta$ -decays ( $\beta$ -ion-correlation) based on the position and time difference. Finally, two output ROOT-Files were created. The first one contained the information for  $\beta$ -decay spectroscopy in an event structure with each event containing one implantation and several  $\beta$ -decays. The second ROOT-File contained the implantation events together with the information from the Ge detectors recorded in a 110  $\mu$ s coincidence window after the implantation.

The  $\beta$ -decay ROOT-File (ROOT File 1) contains then the following variables:

- `ion_x`, `ion_y` and `ion_z` : The implantation position of the ion in x, y and z
- `aoq37` : The mass-to-charge ratio determined in BigRIPS
- `zed` : The nuclear charge measured with the MUSIC
- `t[k]` : The time of the k-th  $\beta$  decay correlated to the implanted ion
- `x[k]`, `y[k]` and `z[k]` : The position x, y and z of the k-th  $\beta$  decay
- `deltaz[k]` : Position difference in z direction between the implantation position and the k-th correlated  $\beta$  decay
- `dssd_ex[k][i]` and `dssd_ey[k][i]` : The energy measured in the x-/y-strips of the i-th DSSSD for the k-th  $\beta$  decay
- `dssd_zmult[k][i]` : The multiplicity of  $\beta$ -like events in the i-th DSSSD of the k-th  $\beta$  decay
- `Qbeta_E[k]` and `Qveto_E[k]` : Energy measured in the Q-beta/Q-veto detector in the k-th  $\beta$  decay
- `Qbeta_T[k]` and `Qveto_T[k]` : Timing information of the Q-beta/Q-veto detector in the k-th  $\beta$  decay
- `gc_hit[k]` : The number of germanium crystals with an energy deposition above threshold in the k-th  $\beta$  decay
- `gc_E[k][l]` : The energy measured in the l-th germanium event in the k-th  $\beta$  decay, l runs from zero to `gc_hit`
- `gc_T[k][l]`, `gc_TDCs[k][l]` and `gc_TDCI[k][l]` : The timing information of the DGF, short-range and long-range TDC in the l-th germanium event of the k-th  $\beta$  decay



## Chapter 3

# $\beta$ -decay spectroscopy of neutron-rich $^{128-133}\text{Cd}$ and the structure of $^{128-132}\text{In}$

In the present experiment the very neutron-rich Cadmium isotopes with masses  $A = 128$  -  $133$  were investigated using the methods of isomer and  $\beta$ -decay spectroscopy. The following chapter contains the information about observed  $\gamma$  rays after populating levels in the neutron-rich Indium isotopes through the  $\beta$ -decay of very neutron-rich  $^{128-133}\text{Cd}$ . In addition to that, the proposed level schemes for those nuclei and the observed  $\beta$ -decay feeding to the levels are presented. The interpretation of the results is concluded in each case with a discussion about the implications for the structure of the very neutron rich Indium isotopes.

Figure 3.1 shows the germanium spectra recorded in coincidence with the observed decays correlated to the implanted Cadmium isotopes with masses  $A=128-131$  within a time window of three half-lives. Furthermore, it was required that  $\Delta x$  and  $\Delta y$  are equal to 0 mm,  $\Delta z = 0$  and only one  $\beta$ -like event in that DSSSD. With the large  $Q_\beta$  values of those isotopes (for example  $Q_\beta = 12.7(3)$  MeV for  $^{131}\text{Cd}$  [1]) high-energetic transitions are expected, but unfortunately, the DGF were set to an energy range of 0 to 6.1 MeV. Looking at figure 3.1 one observes that for the case of  $^{128}\text{Cd}$  this seems to be sufficient, but for example the spectrum recorded in coincidence with the  $\beta$  decays of  $^{131}\text{Cd}$  shows several peaks between five to six MeV and it cannot be dismissed that there are  $\gamma$  rays with energies above 6.1 MeV.

Figure 3.1 shows that especially the spectrum recorded in coincidence with the  $\beta$  decays of the  $^{129}\text{Cd}$  ions shows several hundreds of peaks, and it will become clear later that some of those peaks are contaminations from daughter or granddaughter generation nuclei or even from randomly correlated  $\beta$  decays of other ions. It was therefore necessary to clean the spectra from those contaminations. The chapter begins with an introduction to the different methods used to clean the spectra and construct level schemes from the

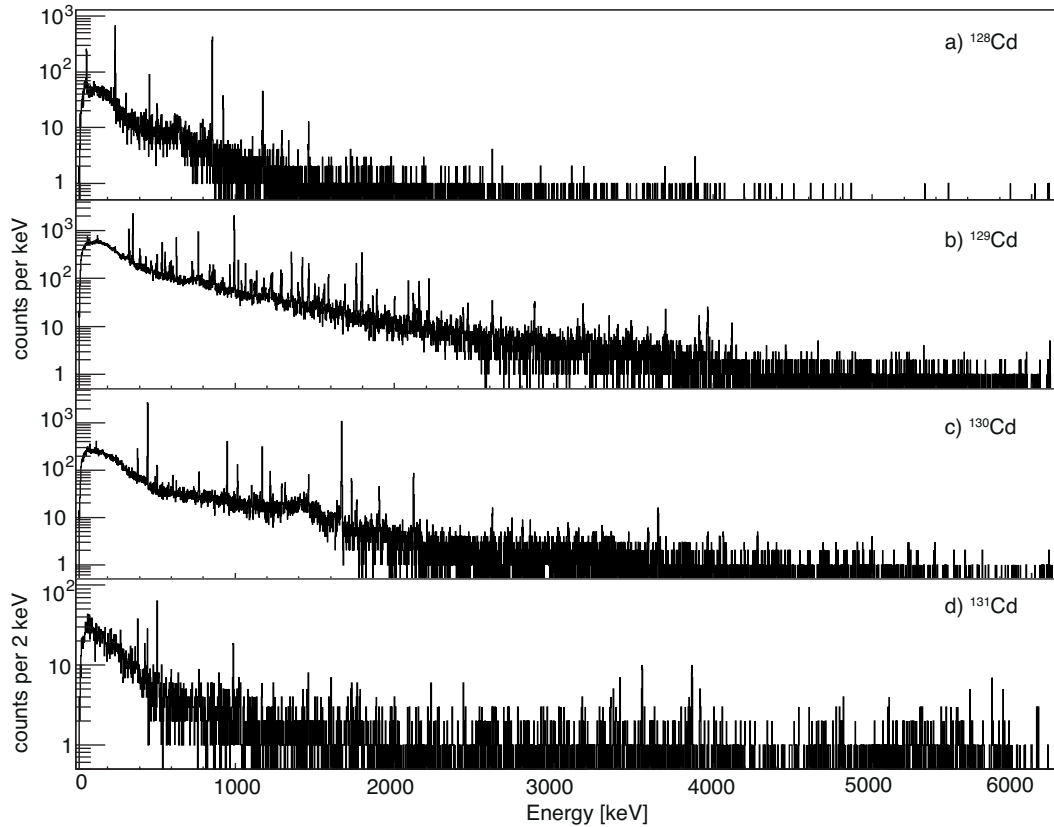


**Figure 3.1:**  $\beta$ -delayed germanium spectra for a)  $^{128}\text{Cd}$ , b)  $^{129}\text{Cd}$ , c)  $^{130}\text{Cd}$  and d)  $^{131}\text{Cd}$ , recorded in coincidence with the observed  $\beta$  decays which were correlated to the implanted ions within a time window of three half-lives. Only decays are correlated which are observed in the same DSSSD than the implantation, with  $\Delta x$  and  $\Delta y = 0$  mm and only one  $\beta$ -like event was allowed in that DSSSD.

experimentally obtained information. All methods are going to be described using the example of the  $^{128}\text{Cd}$   $\beta$  decay, which was already well studied prior to this work. After the introduction of the methods the remaining  $\beta$  decays of  $^{129-133}\text{Cd}$  are shown.

### 3.1 Analysis methods and the $^{128}\text{Cd}$ $\beta$ decay

Results on the  $\beta$  decay from  $^{128}\text{Cd}$  to  $^{128}\text{In}$  were already published in Ref. [61] including the observation of a  $\mu\text{s}$  isomeric state at 248 keV with proposed spin and parity of  $(1^-)$ . The isomeric state was later confirmed in Ref. [30] and a half-life of  $23(2)$   $\mu\text{s}$  measured. In Fig. 3.2 the level of  $^{128}\text{In}$  is presented as it was proposed in Ref. [61].

The tools used in the present work for identifying transitions and building level schemes of excited states, populated in  $\beta$ -decay, are essentially the coincidences of the identified  $\gamma$  rays together with the relative intensities of the individual transitions. All of those tools are now going to be explained in detail, starting with the methods to identify the transitions and clean the germanium spectra.

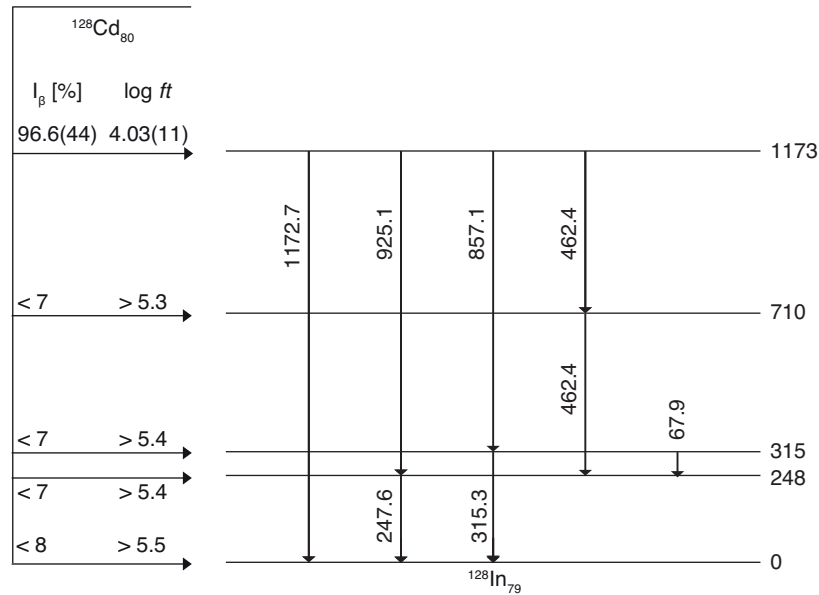


**Figure 3.2:** Proposed level scheme for  $^{128}\text{In}$  taken from Ref. [61] with the  $\beta$ -feeding to each level as obtained in the present experiment and the corresponding  $\log ft$  value. The latter ones were calculated with  $T_{1/2} = 254(2)$  ms, as measured in the present work, and the  $Q_{\beta} = 7070(290)$  keV taken from Ref. [60].

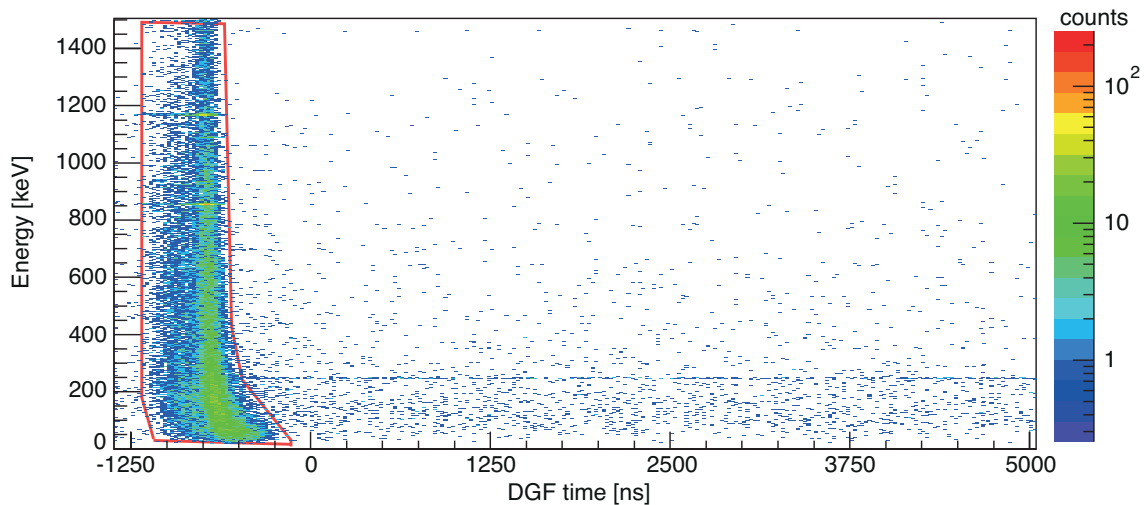


**Figure 3.3:**  $\beta$ -Ge-energy-time matrix for the example of  $^{128}\text{Cd}$ , on the x-axis the DGF timing and on the y-axis the germanium energy. The DGF timing is with respect to the decay trigger. Highlighted with the red gate are the events observed in prompt coincidence with the  $\beta$  decay.

### 3.1.1 $\beta$ -delayed germanium spectrum

After each decay trigger a  $110 \mu\text{s}$  gate is opened for the Ge detectors to measure prompt and delayed  $\gamma$  rays following the  $\beta$  decay, revealing information about the level structure of the daughter nucleus. In Fig. 3.3 the germanium energy is plotted versus the DGF timing, showing which  $\gamma$  rays are observed in prompt and which in delayed coincidence with the  $\beta$ -decays of the implanted  $^{128}\text{Cd}$  ions. The red gate surrounds all  $\gamma$  rays which

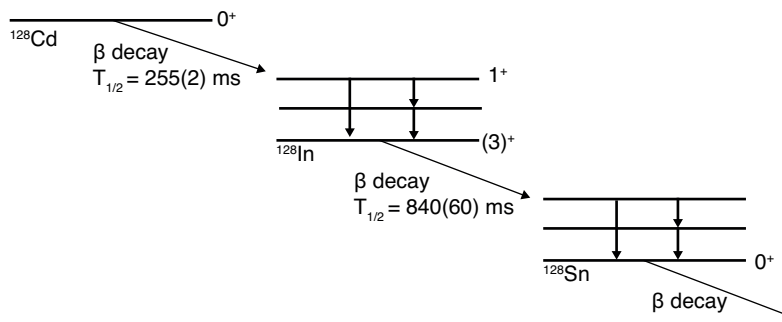


**Figure 3.4:** Basic  $\beta$ -decay scheme of  $^{128}\text{Cd}$  showing the  $\beta$ -decay sequence  $^{128}\text{Cd} \rightarrow ^{128}\text{In} \rightarrow ^{128}\text{Sn} \rightarrow \dots$  as proposed in Refs. [61, 108]. The half-life of the  $0^+$  g.s. of  $^{128}\text{Cd}$  was measured in the present work.

are observed in coincidence, within a time window of  $\pm 250$  ns, with the decays triggering WAS3ABi. The events outside this gate belong to delayed  $\gamma$  rays. One can clearly observe the  $\mu\text{s}$  isomer in  $^{128}\text{In}$  which decays via the 248-keV transition to the g.s.. Projecting the spectrum in Fig. 3.3 on the energy axis one obtains the energy spectrum for transitions observed in prompt and delayed coincidence with the  $\beta$  decays. This spectrum will be called from now on  $\beta$ -delayed germanium spectrum. It can be produced for the full DGF time range or limited to the  $\gamma$  rays observed in prompt coincidence with the  $\beta$  decay. When no isomeric states are present in the daughter nucleus the prompt-gated spectrum provides a much cleaner spectrum compared to the non-gated spectrum.

The main problem involved in investigating these spectra in the present experiment is that there is no possibility of distinguishing directly between parent  $\beta$  decays and  $\beta$  decays of e.g. daughter and granddaughter generation nuclei. One solution to drastically reduce the relative intensities of transitions in e.g. the granddaughter nucleus is to limit the correlation time between implantation and  $\beta$  decay. The daughter nucleus will have in most cases a significantly longer half-life compared to the parent nucleus, giving the possibility to remove parts of the  $\beta$ -decaying successors. As an example the  $\beta$ -decay sequence of  $^{128}\text{Cd}$  is shown in Fig. 3.4. With the half-life of the  $(3)^+$  g.s. of  $^{128}\text{In}$  [108] being more than three times as long as the half-life of the  $0^+$  g.s. of  $^{128}\text{Cd}$  it is possible to remove transitions observed in for example  $^{128}\text{Sn}$  by limiting the correlation time between the implantation and the observed  $\beta$  decays.

Another solution which has a similar impact is to limit the number of decays correlated to one implantation event. Fig. 3.5 shows the  $\beta$ -delayed germanium spectra for a) the first, b) the second, c) the third and d) the fourth decay correlated within 1500 ms after the implantation of a  $^{128}\text{Cd}$  ion. The correlation time here was chosen to approximately six times the half-life, even though later three times will be used, just to show the reduction/disappearance of transitions following the daughter generation  $\beta$  decays when limiting the number of correlated decays. The attention is drawn to the marked peaks, four of them are transitions in  $^{128}\text{In}$ , populated through the  $\beta$ -decay of  $^{128}\text{Cd}$ , and two are transitions in  $^{128}\text{Sn}$ , populated through the  $\beta$ -decay of the daughter nucleus  $^{128}\text{In}$ . While in this case the transitions are well known and can be assigned to the corresponding nuclei,

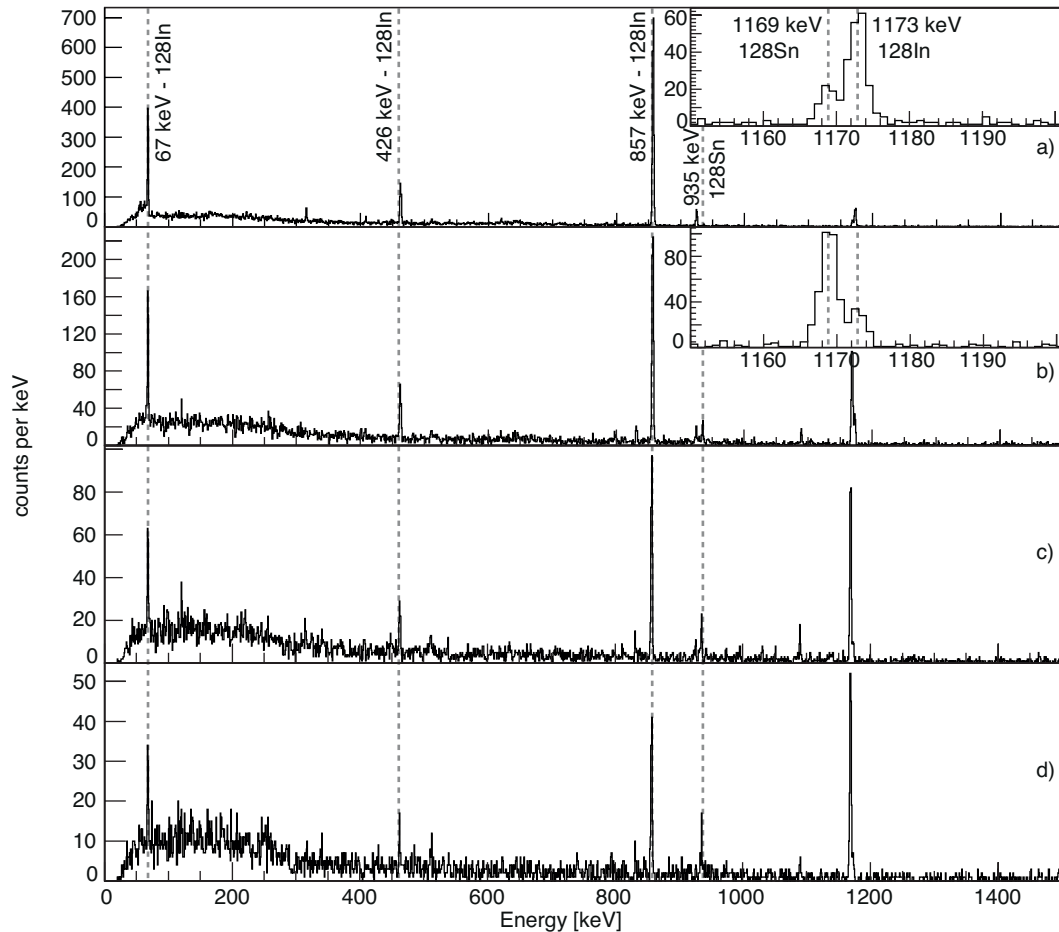


**Figure 3.5:**  $\beta$ -delayed germanium spectra for a) the first, b) the second, c) the third and d) the fourth decay correlated within 1500 ms after the implantation of a  $^{128}\text{Cd}$  ion.

later in this thesis  $\beta$ -delayed germanium spectra are shown for nuclei where the daughter decay is not well studied and it is important to distinguish the origin of the transitions. One can directly observe that in Fig. 3.5a) the transitions known from  $^{128}\text{Sn}$  are barely visible, while the transitions in  $^{128}\text{In}$  are clearly visible. In the spectra for the second, third and fourth observed decay the transitions in  $^{128}\text{Sn}$  appear more clearly and the ratio between intensities of the transitions in  $^{128}\text{In}$  to the ones in  $^{128}\text{Sn}$  change dramatically. The intensity ratio can be best observed in the two small inlay spectra in figs. 3.5a) and b), where the two peaks at 1169 and 1173 keV are shown. In Fig. 3.5a) the 1173-keV transition in  $^{128}\text{In}$  clearly dominates and one obtains an intensity ratio of roughly 4:1, while in Fig. 3.5b) the 1169-keV transition in  $^{128}\text{Sn}$  has about four times more intensity than the 1173-keV transition.

To clean the  $\beta$ -delayed germanium spectra from transitions in the granddaughter or following generation nuclei, it is necessary to limit the spectra to only the first observed decay after an implantation. Nevertheless, it also has to be mentioned that the intensity of transitions populated in the parent decay is reduced. This has to be considered when calculating the absolute transitions intensities in the  $\beta$ -decay.

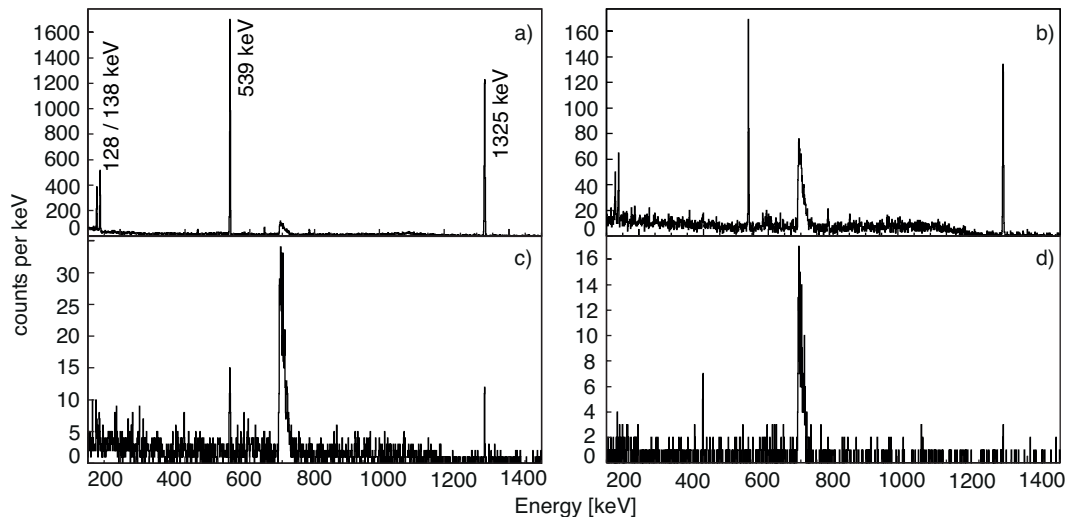


**Figure 3.6:** Delayed Ge spectra recorded in coincidence with the implantation of a  $^{130}\text{Cd}$  ion. a) shows only energies from crystals where no other crystal in the same cluster had an energy deposition between 100 and 6000 keV, while the other spectra show only energies of crystals where exactly b) one, c) two and d) three other crystal in the same cluster had an energy deposition in that range.

### 3.1.2 Cleaning of the germanium spectra: multiplicity

Another method for cleaning the germanium spectrum is to limit the number of crystals and furthermore the number of clusters with one or more crystals with an energy deposition. The example to be shown here is not the  $^{128}\text{Cd}$   $\beta$  decay but the germanium spectrum recorded in delayed coincidence with the implantation of a  $^{130}\text{Cd}$  ion, showing the four transitions de-exciting the  $8^+$  isomer. Those transitions were previously reported in Ref. [7]. Figure 3.6 shows in a) the germanium spectrum recorded in delayed coincidence with the implantation of a  $^{130}\text{Cd}$  ion, with the energy of an individual crystal only being filled in the spectrum if no other crystal in the same cluster measured an energy deposition between 100 to 6000 keV. Figures 3.6b) to d) on the other hand show the same spectrum but requiring that exactly two, three or four crystals, respectively, had an energy deposition in the cluster. One can directly observe that only spectra a) and b) contribute to the intensities of the observed delayed transitions, while c) and d) introduce mainly background. The multiplicity condition has proven to be a powerful tool to clean the delayed germanium spectra after an implantation, but it will be later shown that also in the low statistic  $\beta$  decay cases a significant cleaning can be achieved with it.

### 3.1.3 $\gamma$ - $\gamma$ -coincidences

One of the essential tools for building level schemes in any of the presented cases is the observation and interpretation of  $\gamma$  rays in prompt (delayed) coincidence with other  $\gamma$  rays. If certain  $\gamma$  rays are emitted in a cascade and none of the involved states has a measurable lifetime, then those transitions can be observed in mutual prompt coincidence.

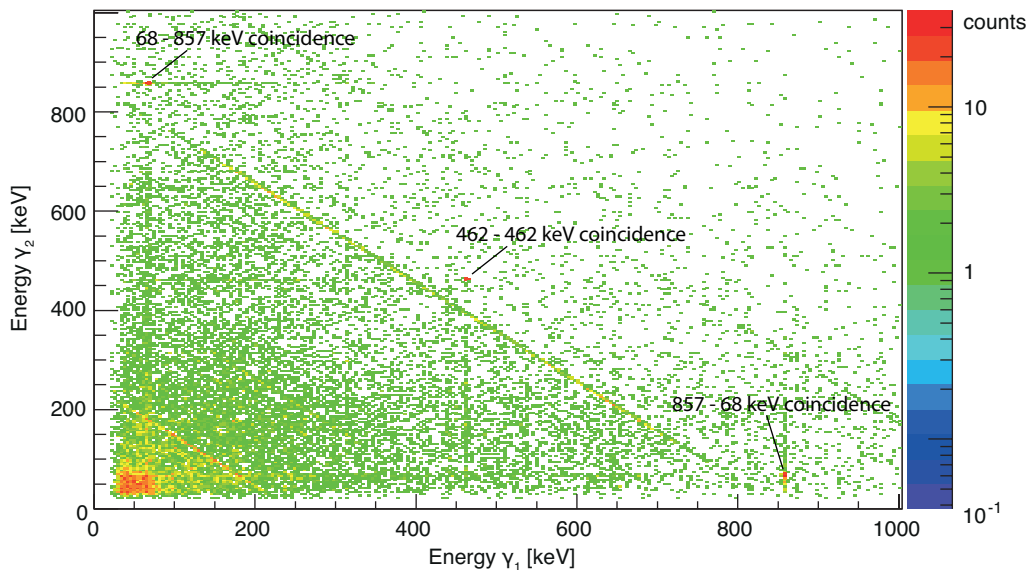


**Figure 3.7:**  $\gamma$ - $\gamma$  matrix (no add-back) for all combinations of  $\gamma$  rays  $\gamma_1$  and  $\gamma_2$  with energies  $E_{\gamma_1}$  and  $E_{\gamma_2}$ , respectively, observed after the first  $\beta$  decay correlated to an implanted  $^{128}\text{Cd}$  ion (correlation time 700 ms). The  $\gamma$  rays have to be observed in prompt coincidence with a maximum time window of  $\pm 250$  ns.

Prompt  $\gamma$ - $\gamma$  matrices were generated for each investigated decay showing all combinations of  $\gamma$  rays (energy  $E_{\gamma_1}$  and  $E_{\gamma_2}$ ) which are observed within a time difference window  $\Delta t$  of  $\pm 250$  ns:

$$\Delta t = |t(\gamma_1) - t(\gamma_2)| < 250\text{ns} \quad (3.1)$$

where  $t(\gamma_1)$  and  $t(\gamma_2)$  are the measured times for the emission of the two  $\gamma$  rays  $\gamma_1$  and  $\gamma_2$ , respectively. Fig. 3.7 shows an example for the  $\beta$  decays correlated to the  $^{128}\text{Cd}$  implantations. The matrix is again limited to the first decay correlated to each implantation within a maximum time range of 700 ms after the implantation and shows the energies without applying the add-back algorithm for prompt coincidences. Clearly visible are the 67.9 keV - 857.1 keV and 462.4 keV - 462.4 keV coincidences and the anti-correlations for the most prominent transitions (e.g. the 857.1-keV transition). Those anti-correlations arise when the energy is not fully deposited in one crystal, but distributed over two crystals because of e.g. Compton-scattering. Parts of those events can later be reconstructed to the full energy when applying add-back. As an additional step the  $\gamma$ - $\gamma$  matrix was also filled in all cases without the prompt time condition, leaving the time window between the two  $\gamma$  rays open, to identify cascades where one or more states have a measurable lifetime.

A gate can then be set on an observed transition in  $E_{\gamma_1}$  and the gated prompt  $\gamma$ - $\gamma$  matrix is projected on the  $E_{\gamma_2}$ -axis. Examples for  $\gamma$ - $\gamma$ -coincidence spectra are shown in Figs. 3.8a) to c) where gates are set on the a) 67.9-, b) 247.6- and c) 857.1-keV transitions observed in coincidence with  $\beta$ -decays of  $^{128}\text{Cd}$ . Spectra a) and c) show the prompt  $\gamma$ - $\gamma$  spectra with the requirement mentioned in formula 3.1 and spectrum b) was produced with no prompt coincidence demanded. One observes the expected coincidences, though

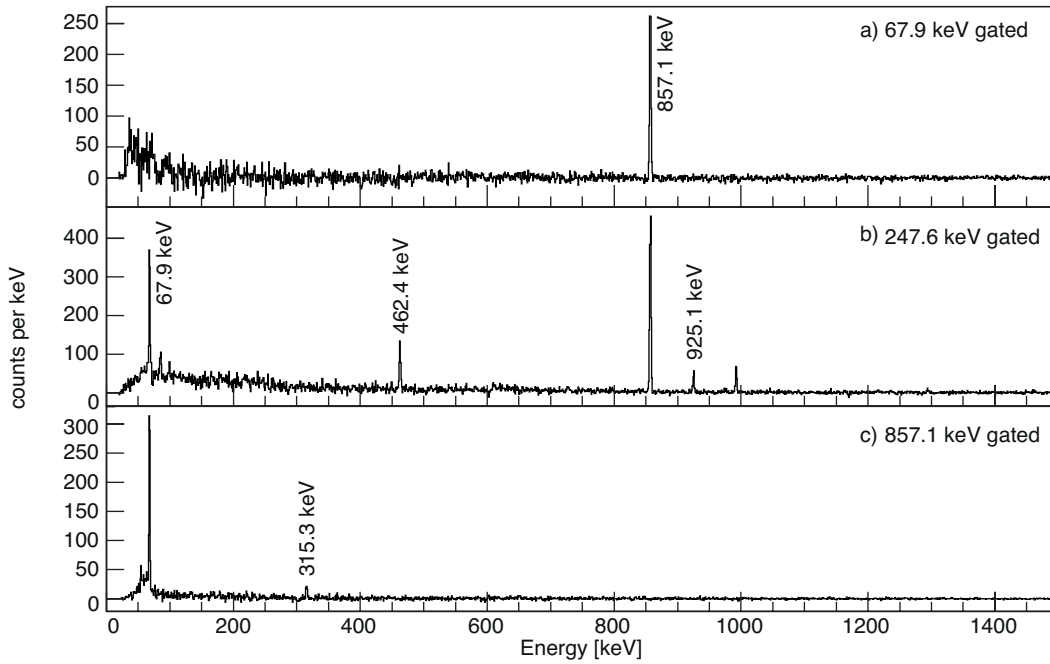


**Figure 3.8:** Germanium spectra observed in prompt coincidence with the a) 67.9-keV, b) 247.6-keV and c) 857.1-keV transitions recorded in coincidence with the decay of the implanted  $^{128}\text{Cd}$  ions. In a) and c) a prompt coincidence window of  $\pm 250$  ns is required, while in b) delayed coincidences between the two  $\gamma$  rays are allowed.

in neither a) nor c) the transition with 247.6 keV is present because of the  $\mu\text{s}$  character of the 248-keV level.

Once a cascade is identified, the  $\gamma$ - $\gamma$ -coincidence spectra can be summed together for this cascade to identify weak coincidences which cannot be identified in the single coincidence spectra.

### 3.1.4 Relative intensities and conversion coefficient

The relative intensity  $I_{\gamma}^{rel}$  of the transitions is in all cases given normalized to one of the transitions, most likely the most intense one. Two methods can be employed to extract the relative intensities of the individual transitions. The first one is to calculate the relative intensities from the peak areas fitted in the  $\beta$ -delayed Ge spectra:

$$I_{\gamma}^{rel} = \frac{N_{\gamma}}{\epsilon_{rel} I_{\gamma, norm}}, \quad (3.2)$$

where  $N_{\gamma}$  is the peak area of the transition in the germanium spectrum,  $\epsilon_{rel}$  is the relative  $\gamma$  ray efficiency for the given energy and  $I_{\gamma, norm}$  the intensity of the transition used for the normalization.

The second method involves the peak areas fitted in the  $\gamma$ - $\gamma$ -coincidence spectra. Those have a lower background and because of that, weak transitions which are only hardly visible in the  $\beta$ -delayed germanium spectra can be fitted with better results. The relative

intensity is then given as:

$$I_{\gamma}^{rel} = \frac{N_{\gamma,coinc}}{\epsilon_{rel}\epsilon_{coinc}I_{\gamma,norm}} \quad (3.3)$$

where  $N_{\gamma,coinc}$  is the fitted peak area of the transition of interest,  $\epsilon_{rel}$  the corresponding relative efficiency and  $\epsilon_{coinc}$  the relative efficiency for the gated transition.

### 3.1.5 $\beta$ -decay feeding and cleaning of $\beta$ -decay spectra

In the case of  $\beta$  decays one is not only interested in the relative intensities, but also in the absolute intensities and the  $\beta$ -decay feeding to a certain state. This feeding can be obtained from the intensity balance of the  $\gamma$  rays feeding and de-exciting this state. For this type of analysis two things have to be taken into account. First of all, the internal conversion coefficient: if the state has a certain probability to de-excite via internal conversion, then this has to be considered for the intensity ratios. And second, care has to be taken in cases where transitions may be unobserved due to low statistics or efficiency limitations. This problem was found a long time ago by Hardy *et al.* [109] and is commonly known as the ‘‘Pandemonium effect’’.

The relative intensities introduced in the last chapter are not sufficient to calculate the absolute  $\beta$ -feeding and one step further has to be taken. Instead of the relative intensities, the absolute intensity per parent decay  $N_{\gamma,Decay}$  is calculated as:

$$I_{\gamma}^{Decay} = \frac{N_{\gamma}}{\epsilon_{abs}N_{decays}} \quad (3.4)$$

with  $N_{decays}$  being the number of observed parent decays and  $\epsilon_{abs}$  the absolute detection efficiency of the germanium array. The determination of  $N_{decays}$  will be explained in the section 4.2.2.4 and  $N_{\gamma}$  is again determined from fitting the peaks in the  $\beta$ -delayed germanium spectrum.

The absolute  $\beta$ -intensity to a particular state is then determined from the intensity balance of all transitions feeding the state ( $\sum_{feeding} I_{\gamma}^{Decay}$ ) and all transitions de-exciting it ( $\sum_{de-exciting} I_{\gamma}^{Decay}$ ) as:

$$I_{\beta} = \sum_{de-exciting} N_{\gamma}^{Decay} - \sum_{feeding} N_{\gamma}^{Decay}. \quad (3.5)$$

The total observed  $\beta$ -feeding  $I_{\beta}^{tot}$  is then given as:

$$I_{\beta}^{tot} = \sum_{levels} I_{\beta}. \quad (3.6)$$

In a first step  $I_{\gamma,Decay}$  and  $I_{\beta}^{tot}$ , as they were obtained in the present experiment for the well-known case of the  $\beta$  decay of  $^{132}\text{In}$  to  $^{132}\text{Sn}$ , were compared to literature values. Table 3.1 shows in the second column  $I_{\gamma,Decay}$  with no additional cuts on the position difference

$E_\gamma$ [keV]	$I_\gamma^{Decay}$ no cuts [%]	$I_{\gamma,lit}^{Decay}$ [%]	$I_\gamma^{Decay}$ $Z_{mult} = 1$ [%]	$I_\gamma^{Decay}$ $\Delta z = 0$ [%]	$I_\gamma^{Decay}$ all & $\Delta x, \Delta y < 1$ [%]	$I_\gamma^{Decay}$ all & $\Delta x, \Delta y = 0$ [%]
299	74.2(13)	44	66.3(15)	61.7(13)	49.7(14)	45.1(17)
479	36.7(7)	24	32.3(8)	31.4(7)	25.4(8)	23.1(9)
2380	35.9(8)	23	31.9(8)	30.3(7)	24.0(7)	21.8(9)
4041	94.7(17)	60	84.2(20)	79.1(17)	63.8(14)	56.2(22)
299	100		68.9(3)	71.0(3)	28.8(1)	20.2(1)

**Table 3.1:** Intensities of selected transitions in  $^{132}\text{Sn}$  populated after the  $\beta$ -decay of  $^{132}\text{In}$  for different cuts (for details see text; all &  $\Delta x, \Delta y < 1$  means here that  $Z_{mult} = 1$  and  $\Delta z = 0$  were also required).  $I_{\gamma,lit}^{Decay}$  is calculated from relative intensities and  $\beta$ -feeding given in Ref. [81]. Errors are not stated in that Reference. The additional line at the end of the table shows the number of counts in the 299-keV line normalized to the number of counts with no cuts applied. This line was added to illustrate how the number of counts in the peak is reduced when the cuts are applied.

or multiplicity of  $\beta$ -like events in the DSSSD. Comparing those values to the literature values of Ref. [81] a disagreement is found with the values of  $I_{\gamma,Decay}$  being in all cases nearly a factor two times larger than in literature. Summing the  $\beta$  feeding to all states in  $^{132}\text{Sn}$  one observed furthermore that  $I_\beta^{tot}$  was larger than 100 %, clearly non-physical. The conclusion was made that, either the deduced number of observed parent decays was too low, or the number of  $\gamma$  rays too high. It has to be noted here that this problem was only observed in nuclei with very high implantation rates, while for low statistic cases, e.g.  $^{128}\text{Cd}$ , the intensities agree well with the literature values.

To search for a solution, the spectra of other nuclei present in this experiment were inspected and all showed additional peaks at e.g. 4041 keV which are not related to the decay of the nuclei of interest. The explanation for that is the high implantation rate of  $^{132}\text{In}$  together with the problem that  $\beta$ -decays have no unique signature. In the present experiment the correlation is performed taking into account position and time information, which of course can lead to a certain amount of false correlations. The  $\beta$  decay of other nuclei, which occur in close proximity to the implantation position of the nuclei of interest and within the selected time window, might be associated to that one. Another possibility is that the  $\beta$  decays happen simultaneously within the opened gate for the data acquisition. Those false correlations depend on a lot of factors, for example the  $\beta$ -decay half-life, but of course, also the implantation rate. Nuclei with a high implantation rate are more likely to be falsely correlated to other ions than nuclei with low implantation rates. Those correlations are random and because of that should not influence the  $\beta$ -decay half-life determinations, but they generate background peaks in the germanium spectra. Those peaks are in most cases clearly separated from the peaks of interest and a problem arises only for nuclei with high implantation rates. Wrongly correlated decays of another  $^{132}\text{In}$  nucleus to the implantation of a certain  $^{132}\text{In}$  ion increase the number of observed  $\gamma$  rays  $N_\gamma$ . As a consequence,  $N_\gamma$  does then not correspond any more to the number of observed  $\beta$ -decays.

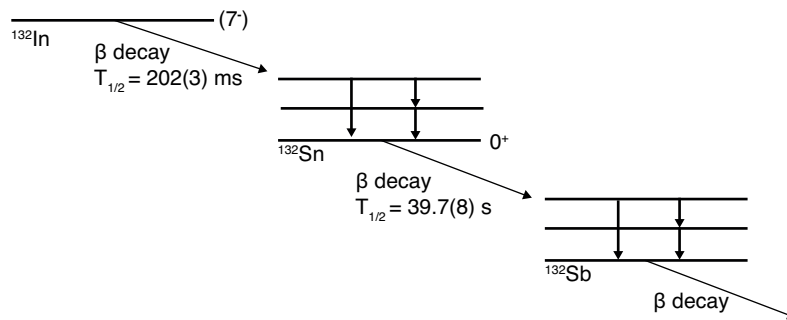


**Figure 3.9:** Basic  $\beta$ -decay scheme of  $^{132}\text{In}$  showing the  $\beta$ -decay sequence  $^{132}\text{In} \rightarrow ^{132}\text{Sn} \rightarrow ^{132}\text{Sb} \rightarrow \dots$  as proposed in Refs. [82, 110]. The half-life of the  $(7^-)$  g.s. of  $^{132}\text{In}$  was measured in the present work.

To address this problem, the number of false correlations has to be reduced as much as possible for the cases with high implantation rates. To achieve that, strict cuts are introduced improving the correlations. Those cuts are:

1. Limiting the position difference between the implantation position and the decay position in x- and y-direction ( $\Delta x, \Delta y < 1$  mm or  $\Delta x, \Delta y = 0$  mm).
2. Correlating only events where decay and implantation were observed in the same DSSSD ( $\Delta z = 0$ ).
3. Excluding events where more than one decay was observed in the DSSSD ( $z_{mult} = 1$ ).

The columns four to six in Table 3.1 show how  $I_{\gamma,Decay}$  changes for different cuts. The limitation on the position difference between implantation position, especially in x- and y-direction, seems to have the biggest impact, but only when applying all cuts at the same time  $I_{\gamma}^{Decay}$  agrees well with the literature values. Because of that, those strict cuts have been used to determine the intensities of all nuclei with high implantation rates. Furthermore, they also clean up the spectra from random correlations improving the quality of the  $\beta$ -delayed germanium spectra.

One disadvantage of requiring those conditions for the correlations is that also the number of good correlations is significantly reduced. The  $\beta$ -decay efficiency, namely the probability to actually observe the  $^{132}\text{In}$   $\beta$  decay after an  $^{132}\text{In}$  ion was implanted, was calculated to 61(2)% without any of those cuts applied. With all cuts ( $z_{mult} = 1$  &  $\Delta z = 0$  &  $\Delta x, \Delta y = 0$ ) applied at the same time the efficiency is reduced to 12(1)% in the present experiment. The last row in Table 3.1 shows the counts in the 299-keV peak, normalized to the counts without any conditions applied. Again those numbers show how drastically the number of counts are reduced by the cuts, leaving only about 20% of the initial counts after applying all cuts.

To further demonstrate the influence of those cuts on the quality of the  $\beta$ -delayed germanium spectra, a closer look is now taken at the spectrum of the  $^{132}\text{In}$  decay. Figure

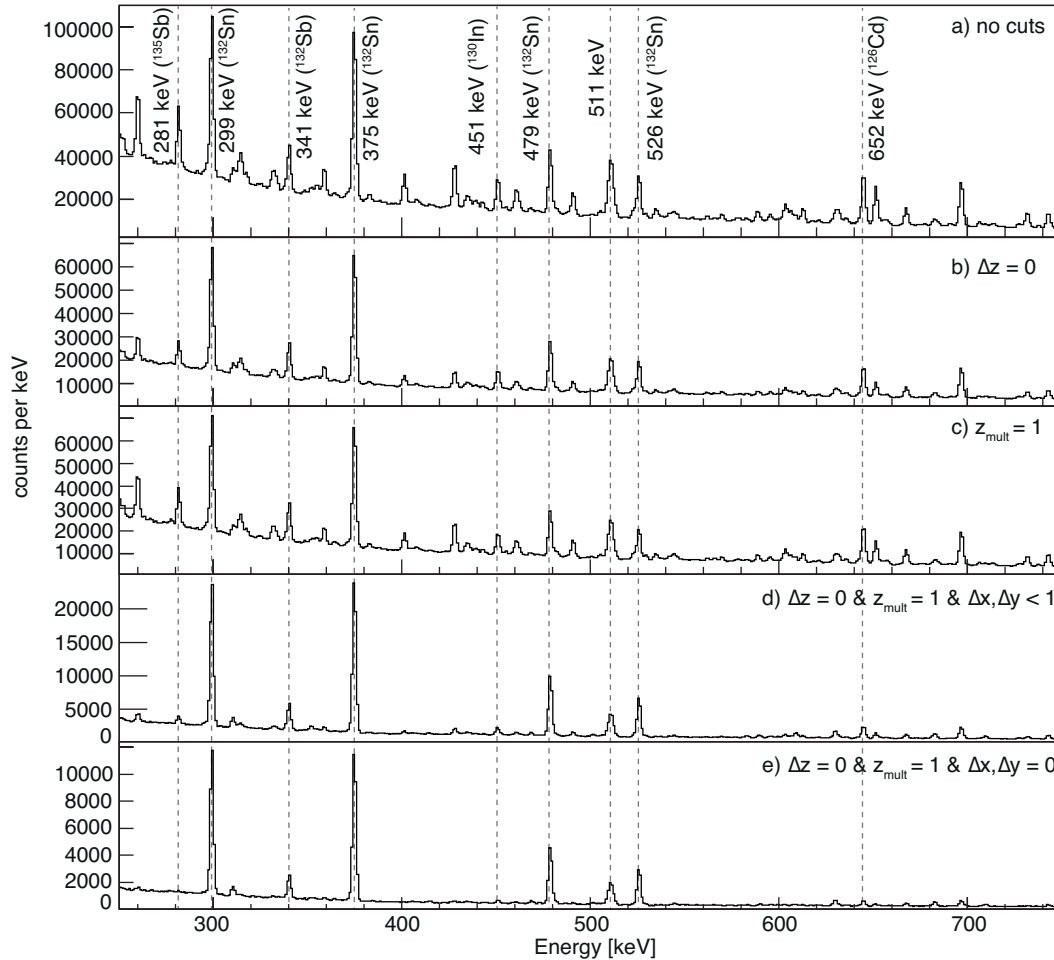


**Figure 3.10:** Germanium spectra of all decays correlated to the implanted  $^{132}\text{In}$  ions. In a) no further limitation on the position difference or the multiplicity of  $\beta$ -like particles in the DSSSD are made, while in b) the decay has to be observed in the same DSSSD layer than the implantation and in c) only one decay event was allowed in the DSSSD. In d) and e) the spectrum is shown for the requirements of b) and c) at the same time together with the additional requirement that the position difference in x- and y-direction is smaller than 1 mm or equal to 0 mm, respectively.

3.10a) shows parts of the spectrum recorded for all observed decays within a maximum time window of 5000 ms after the implantation of a  $^{132}\text{In}$  ion. In that spectrum the most prominent peaks in the daughter nuclei  $^{132}\text{Sn}$  and in the granddaughter nuclei  $^{132}\text{Sb}$  are marked. Figure 3.9 shows an illustration of the  $\beta$  decay sequence of interest starting from  $^{132}\text{In}$ . In that figure one observes that the half-life of the  $0^+$  g.s. in  $^{132}\text{Sn}$  is much longer than the correlation time and therefore, only a small amount of the daughter decays is correlated to the implanted  $^{132}\text{In}$  ions with the correlation time window set to 5000 ms. In addition to this, transitions most likely belonging to the nuclei  $^{126}\text{Cd}$ ,  $^{130}\text{In}$  and  $^{135}\text{Sb}$  are marked. They have been populated in the  $\beta$  decay of  $^{126}\text{Ag}$ ,  $^{130}\text{Cd}$  and  $^{135}\text{Sn}$ , respectively. All those three nuclei had very high implantation rates in the present experiment and the observed  $\beta$  decays are randomly correlated to the implanted  $^{132}\text{In}$  ions.

The spectra shown in Fig. 3.10b) to e) show again the same spectrum as in a) but with additional conditions, which is in b) to correlate only decays which are observed in the

same DSSSD layer than the implantation. In c) it was requested to have only one  $\beta$ -like particle observed in the DSSSD in the same event. For the spectrum shown in d) and e) it was required that the decay and the implantation were in the same DSSSD layer, that only one  $\beta$ -like particle was observed and furthermore, that the position difference in x- and y-direction was smaller than 1 mm or equal to 0 mm, respectively. The spectra clearly demonstrate that the cut on the x- and y-position difference has the biggest influence. In spectrum d) and e) all transitions known from  $^{126}\text{Cd}$ ,  $^{130}\text{In}$  and  $^{135}\text{Sb}$  have nearly disappeared, while the intensities of transitions in  $^{132}\text{In}$  and  $^{132}\text{Sb}$  are only reduced. The cuts on the z-position difference and the multiplicity of  $\beta$ -like particles in the DSSSD also have an influence on the intensity ratio between transitions in the decay chain of interest and random correlations, but nothing like the position difference in x- and y-direction. Spectrum e), where all cuts have been applied with the position difference in x- and y-direction being 0 mm, shows the cleanest spectrum. Nevertheless, the spectrum shown in Fig. 3.10d) is a good compromise between a clean spectrum and a reasonable  $\beta$  efficiency. In the following the  $\beta$  delayed germanium spectra will be shown with the conditions of d) applied.

### 3.1.6 log $ft$ values

From the  $\beta$ -decay feeding to each level the log  $ft$  value (see section 1.4.2) can be calculated using a tabulation of the Fermi integral  $f(Z, E_0)$ . The partial half-life  $t$  is calculated from the  $\beta$ -half-life  $T_{1/2}$  and the direct  $\beta$ -feeding  $I_\beta$  to this level as:

$$t = \frac{T_{1/2}}{I_\beta}. \quad (3.7)$$

The program LOGFT [111], which contains the tabulated Fermi integral, was used to determine the log  $ft$  values in all of the following cases. The  $Q_\beta$  value was in all cases taken from Ref. [1] and the  $T_{1/2}$  as measured in the present work (see chapter 4.2 for the results). It has to be kept in mind here that those values have to be considered as lower limits because of the Pandemonium effect [109], an effect which occurs in all  $\beta$ -decay studies using high-resolution  $\gamma$ -ray spectroscopy.

### 3.1.7 Transitions in the $^{128}\text{Cd}$ $\beta$ decay and level scheme

After all methods have been described now in detail, the results for  $^{128}\text{Cd}$  are presented here. In Fig. 3.11 the  $\beta$ -delayed germanium spectrum, with the add-back algorithm applied, is shown. Only the first decay recorded in a maximum correlation time of 700 ms is filled in the spectrum and furthermore, it is required that implantation and decay were observed in the same DSSSD and with a maximum position difference of 1 mm in x- and y-direction. One observes six transitions, all of them reported in a previous work [61]. To improve the statistics the data sets of the two settings presented in section 2.1.3 were combined with a third data set where BigRIPS was optimized for the transmission of

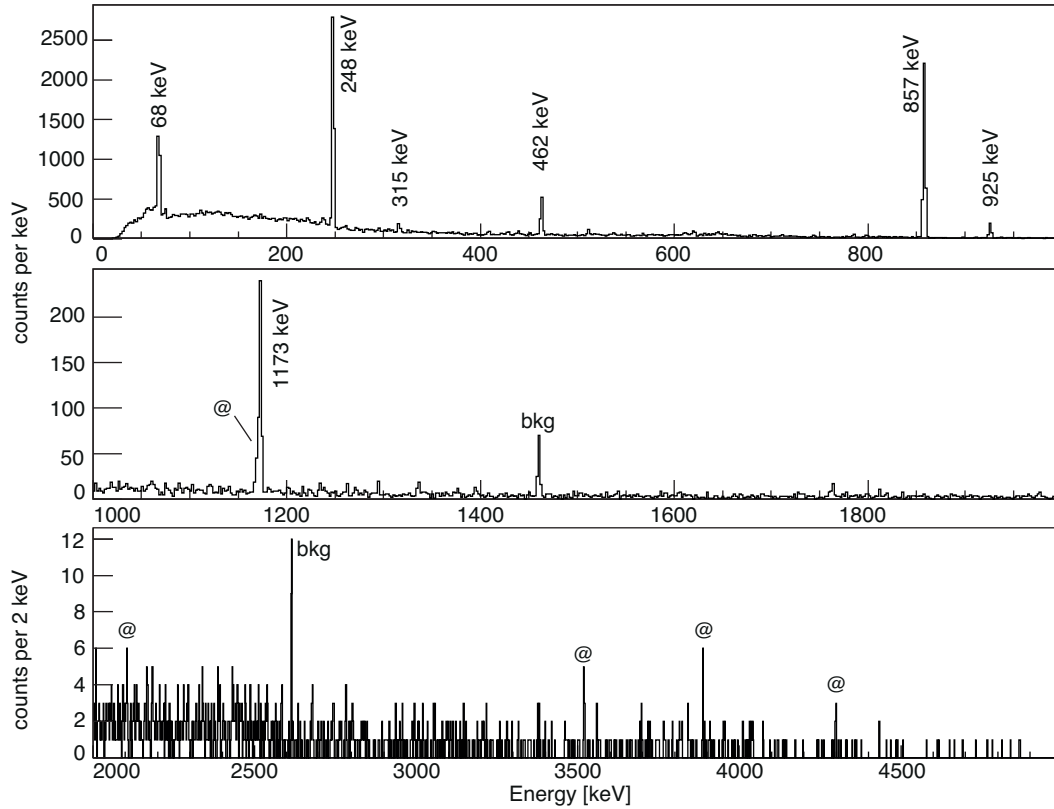


**Figure 3.11:** Ge spectrum in coincidence with the first observed decay of the implanted  $^{128}\text{Cd}$  ions within a maximum time window of 700 ms after the decay. Only events are taken into account where exactly one energy deposition was recorded in the same DSSSD layer where the implantation took place. Furthermore, it is requested that the decay position has a maximum position difference of 1 mm in x and y-direction to the implantation position. The transitions marked with an @ correspond to the decay of the daughter nucleus  $^{128}\text{In}$ . Transitions arising from room background (bkg) are also present in the spectrum.

$E_\gamma$ [keV]	$I_\gamma^{rel}$ [%]	$I_\gamma^{lit}$ [%]	$I_\gamma^{Decay}$ [%]	$E_i$ [keV]	$E_f$ [keV]	$J_i^\pi$	$J_f^\pi$
67.9	36.5(25)	38(4)	26.5(18)	315	248	(1) <sup>-</sup>	(1) <sup>-</sup>
247.6	100(6.6)	100	72.7(49)	248	0	1(-)	3(+)
315.3	3.0(8)	-	2.2(6)	315	0	1(-)	3(+)
462.4	16.0(13)	4.8(10) + 3.9(13)	11.6(20)	-	0	-	-
857.1	98.6(55)	95(10)	71.7(42)	1173	315	1 <sup>+</sup>	(1) <sup>-</sup>
925.1	10.8(10)	12.4(12)	7.8(7)	1173	248	1 <sup>+</sup>	(1) <sup>-</sup>
1172.7	15.5(36)	10.8(11)	11.2(26)	1173	0	1 <sup>+</sup>	(3 <sup>+</sup> )

**Table 3.2:** List of  $\gamma$  rays observed in the  $\beta$ -decay of  $^{128}\text{Cd}$  to  $^{128}\text{In}$  with their energies, relative  $\gamma$  intensities, absolute intensity of  $\gamma$  rays per decays of  $^{128}\text{Cd}$ , energies of the initial and final levels and the spin and parity of the initial and final level proposed in Ref. [61]. The literature values of the relative intensities are taken from reference [61].

$^{126}\text{Rh}$ . In this three data sets in total  $7 \times 10^5$   $^{128}\text{Cd}$  ions were implanted in WAS3ABi. A summary of the energies and relative intensities of the observed transitions is given in Table 3.2 together with the literature values. Most of the values obtained in the present work are in good agreement with the literature values and only for the case of the 462.5-keV

Level [keV]	$I_\beta$ [%]	$I_{\beta,lit}$ [%]	$\log ft$	$\log ft_{lit}$
0		$\sim 5$		$\sim 5.8$
248	$< 7$	$< 17$	$> 5.4$	$> 5.2$
315	$< 7$	$< 12$	$> 5.4$	$> 5.3$
710	$< 7$	$< 2$	$> 5.3$	$> 6.0$
1173	96.6(44)	93(9)	4.03(11)	4.17(12)

**Table 3.3:** Levels in  $^{128}\text{In}$  populated by the  $\beta$ -decay of  $^{128}\text{Cd}$  and the observed  $\beta$ -feeding and corresponding  $\log ft$  value and the corresponding literature values taken from reference [61].

doublet is a severe difference observed.

From the differences in the absolute intensities of the transitions feeding and de-exciting the levels in the  $^{128}\text{In}$   $\beta$ -decay the  $\beta$ -feeding was determined. The results are summarized in Table 3.3. It has to be mentioned here that the splitting of the absolute intensity for the 462.5 keV doublet to the two individual transitions is not possible based on the experimental data. It had to be assumed that the splitting is approximately half/half, as it was reported in Ref. [61], with the errors chosen in such a way that they include the corresponding uncertainties. Nearly 100 % of the  $\beta$ -feeding goes to the state at 1173 keV, which was assigned to have spin and parity  $1^+$  in Ref. [61].

In addition to  $I_\beta$ , Table 3.3 also includes the calculated  $\log ft$  values. Those have been calculated with a  $Q_\beta$  value of 7070 keV taken from [1] and the half-life as it was obtained in the present work. The summary table also contains the literature  $\log ft$  values taken from Ref. [61].

### 3.1.8 Conclusions

The full level scheme obtained from the experimental results in the present work is presented in Fig. 3.2 and is essentially the same as the one suggested by Fogelberg *et al.* [61]. The results are in excellent agreement with the literature values which shows again that the main  $\beta$ -feeding goes to a state at an energy of 1173 keV. From the systematics in the surrounding nuclei with  $Z < 50$  and  $N < 82$  and taking into account the  $\log ft$  of 4.03(11), this state has to be fed by a Gamow-Teller transition, most likely having the character  $\nu g_{7/2} \rightarrow \pi g_{9/2}$ . A slightly larger value of  $\log ft = 4.6$  was reported for a GT transition of the same type in the decay of  $^{132}\text{Sn}$  [82], and in the decay of  $^{131}\text{In}$  a  $\log ft = 4.4$  was measured for a GT transition of that type [41].

No new transitions were identified in the present thesis. However, the  $\beta$  decay of  $^{130}\text{Cd}$  shows a very similar decay pattern compared to the  $\beta$  decay of  $^{128}\text{Cd}$  and in  $^{130}\text{In}$  higher energetic transitions were observed (see section 3.3). Assuming that similar transitions exist in  $^{128}\text{In}$ , an upper limit can be set on the absolute intensity of those transitions per parent  $\beta$  decays of  $^{128}\text{Cd}$ . Inspecting the  $\beta$ -delayed Ge spectra of  $^{128,130}\text{Cd}$  it was decided that a peak with an absolute intensity of  $I_\gamma^{Decay} = 0.6\%$  should be clearly visible. Therefore,

the higher energetic transitions in  $^{128}\text{In}$  have probably absolute intensities per parent  $\beta$  decay of  $^{128}\text{Cd}$  of less than 0.6%.

### 3.2 Decay of $^{129}\text{Cd}$

Already prior to this thesis the decay of  $^{129}\text{Cd}$  was studied in several works and two  $\beta$ -decaying isomeric states were identified by Arndt *et al.* [62, 112–114] with half-lives of 104(6) and 242(8) ms, respectively. In the work of Kratz *et al.* [115] the longer half-life was associated with the proposed  $(11/2^-)$  g.s. and the shorter one with a  $(3/2^+)$   $\beta$ -decaying isomeric state. Yordanov *et al.* [116] observed in a later work two long lived isomeric states in  $^{129}\text{Cd}$  with spins of  $3/2^+$  and  $11/2^-$ . However no direct evidence could be found for the ordering and relative energy of those states.

More experimental information is available on the level scheme of  $^{129}\text{In}$ . De Geer *et al.* [117] reported the  $(9/2^+)$  g.s. and an  $(1/2^-)$   $\beta$ -decaying isomer with the most recent measurement placing the  $(1/2^-)$  state at an excitation energy of 459(5) keV [48]. In addition to this, two long-lived high spin isomeric states have been identified by Fogelberg *et al.* with half-lives of 110 and 700 ms and spin and parity assignments of  $(29/2^+)$  and  $(23/2^-)$ , respectively [118]. In a later work the  $(23/2^-)$  state was placed as an  $\beta$ -decaying isomeric state at an excitation energy of 1630(56) keV [119]. Genevey *et al.* reported in Ref. [29] about a  $17/2^-$   $\mu\text{s}$  isomeric state at 1688 keV and a half-life of 8.5  $\mu\text{s}$  which decays via a cascade to the  $9/2^+$  g.s. Finally, Arndt *et al.* [62] proposed the first more complex level scheme of  $^{129}\text{In}$  populated in the  $\beta$ -decay of  $^{129}\text{Cd}$ . He observed 53 transitions which he associated to this decay and placed part of them in a level scheme.

In the present experiment  $3.8 \times 10^6$   $^{129}\text{Cd}$  ions were implanted in the active stopper WAS3ABi, and their decay will be discussed here to obtain new information about the level scheme of  $^{129}\text{In}$ . The spectrum in Fig. 3.12 shows the germanium spectrum observed in prompt coincidence with the decay of the implanted  $^{129}\text{Cd}$  ions. Only the first correlated decay within a time window of 450 ms between the implantation and the decay is shown. It was furthermore required:  $z_{\text{mult}} = 1$  &  $\Delta z = 0$  &  $\Delta x, \Delta y < 1$  mm. Even after applying all the cuts several contamination lines remain in the spectrum and are now being discussed as an example case. In the corresponding spectra of the other nuclei, which will be discussed later, similar contamination lines are present.

Comparing the spectrum shown in Fig. 3.12 to spectra of the other nuclei produced in this experiment revealed which transitions do not belong to the decay of  $^{129}\text{Cd}$  to  $^{129}\text{In}$  and in most cases their origin can be revealed. In the case of the decay discussed here, known transitions from three other nuclei can be identified. First of all, transitions in  $^{129}\text{Sn}$  (s) are observed, populated through the decay of the daughter nucleus  $^{129}\text{In}$ . As mentioned before,  $\beta$  decays have no unique signature and on top of that, there is a certain chance of not detecting the actual  $\beta$ -decay of  $^{129}\text{Cd}$  because of efficiency limitations. Therefore, the decay of the daughter nucleus  $^{129}\text{In}$  can be detected as the first correlated decay to

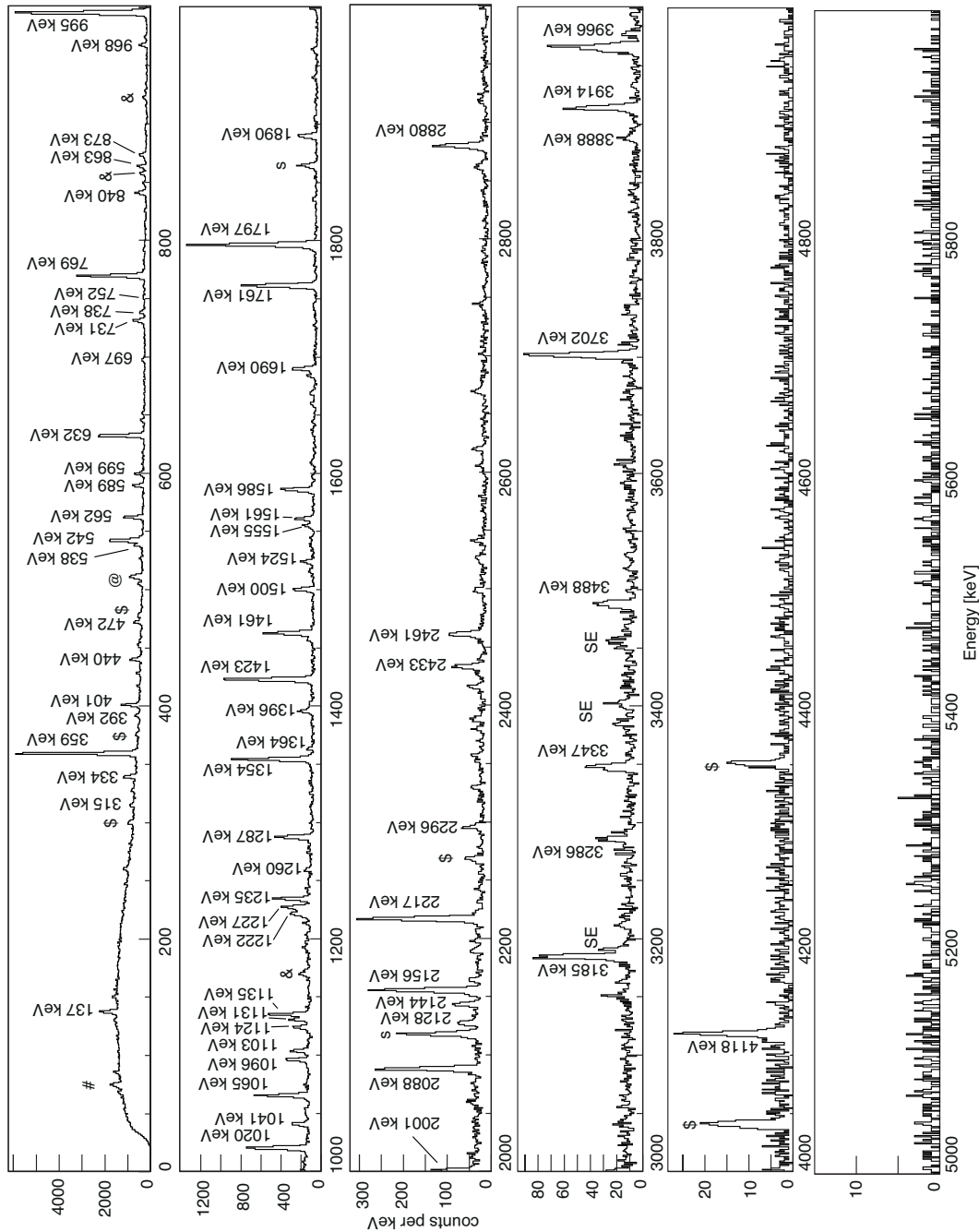


**Figure 3.12:** Ge spectrum in prompt coincidence with the first decay of the implanted  $^{129}\text{Cd}$  ions requiring  $\Delta x$  and  $\Delta y$  to be smaller than 1 mm and the implantation and decay event being detected in the same DSSSD within a maximum time difference of 450 ms. Transitions labelled with symbols correspond to known transitions in  $^{128}\text{In}$  (&), populated after  $\beta$ -delayed neutron emission, in  $^{129}\text{Sn}$  (s), populated after the  $\beta$  decay of the daughter nucleus, in  $^{131}\text{Sn}$  (#) and  $^{132}\text{Sn}$  (\$), due to false correlated  $\beta$  decays. Single escape peaks are marked with (SE) and the peak at 511 keV (@) arises from the annihilation of positrons created in pair production in the germanium detectors.

an implanted  $^{129}\text{Cd}$  ion.

Secondly, known transitions in  $^{128}\text{In}$  (&), populated through  $\beta$ -delayed neutron emission of the  $^{129}\text{Cd}$  ions, are present in the spectrum. It can be noted here that a  $P_n$  value of

3.5(10)% has been measured in the present experiment for  $^{129}\text{Cd}$  (see section 4.3).

The third nucleus from which transitions are present in the spectrum shown in Fig. 3.20 is  $^{132}\text{Sn}$  (§). From a naive point of view there is no logical explanation why those lines should be present in the spectrum and a more detailed analysis was necessary. To start with the explanation, it has to be mentioned that  $^{132}\text{In}$  has one of the highest production rates in this experiment, and the transition with an energy of 4041 keV is present in most of the decay spectra. This leads to the assumption that the line appears through the false assignment of  $^{132}\text{In}$  decays in neighbouring pixels to the nuclei of interest. This assumption is underlined by the fact that for example for  $^{129-131}\text{Cd}$  the observed counts in the 4041-keV peak scales with the number of implantations (counts per  $10^5$  implantations:  $^{129}\text{Cd}$ : 17(4),  $^{130}\text{Cd}$ : 13(4),  $^{131}\text{Cd}$ : 16(4)). For the nuclei with larger statistics it was also possible to look at the decay time of the 4041-keV transition showing a flat distribution. Those  $\gamma$  rays are now either observed because  $\beta$  decays of  $^{132}\text{In}$  occur in random coincidence with the decays of the ion of interest or decays of  $^{132}\text{In}$  are falsely correlated to the other implanted ions. 2513264  $^{132}\text{In}$  ions are implanted in WAS3ABi and the 4041-keV transition has an absolute intensity of 63(3) per 100  $^{132}\text{In}$  decays [82]. Taking into account the absolute efficiency of the germanium array and the  $\beta$  efficiency, it is expected to observe 22500 4041-keV  $\gamma$  rays during the experiment. With a 110  $\mu\text{s}$  gate opened after each implantation one expects less than one count in the 4041-keV peak per  $10^5$  implantations of the Cadmium isotopes. All those observations support the explanation that falsely correlated decay events of  $^{132}\text{In}$  ions in close proximity to the ion of interest are the reason for the appearance of the  $^{132}\text{Sn}$  transitions in all of the decay spectra. For the same reason transitions known from  $^{131}\text{Sn}$  (§) can also be found in the spectrum.

$E_\gamma$ [keV]	$I_\gamma^{rel}$ [%]	$I_\gamma^{lit}$ [%]	$I_\gamma^{Decay}$ [%]	$E_i$ [keV]	$E_f$ [keV]	$J_i^\pi$	$J_f^\pi$
137.2	3.8(6)		1.3(2)	1220	1083	(5/2 <sup>-</sup> )	(3/2 <sup>-</sup> )
334.1	19.9(12)	13.0	6.6(4)	1688	1354	17/2 <sup>-</sup>	13/2 <sup>+</sup>
339.1	6.5(7)	6.0	2.1(2)	1693	1354		13/2 <sup>+</sup>
358.9	57.4(30)	50.0	19.0(10)	1354	995	13/2 <sup>+</sup>	11/2 <sup>+</sup>
391.7	1.4(7)		0.5(2)	2085	1693		
400.8	6.3(6)	7.0	2.1(2)	1621	1220		(5/2 <sup>-</sup> )
439.7	2.7(3)	4.0	0.9(1)	2060	1621		
471.9	1.5(8)		0.5(3)	1555	1083		(3/2 <sup>-</sup> )
504.5*	2.1(2)		0.7(2)				
537.9	2.8(8)	2.0	0.9(3)	1621	1083		(3/2 <sup>-</sup> )
542.0	14.5(10)	11.0	4.8(3)	1762	1220		(5/2 <sup>-</sup> )
561.8	8.5(8)	8.0	2.8(3)	3150	2589	(13/2 <sup>-</sup> )	
589.1	3.2(4)	5.2	1.1(1)	3150	2561	(13/2 <sup>-</sup> )	

Table 3.4 continued on next page

Table 3.4 – continued from previous page

$E_\gamma$ [keV]	$I_\gamma^{rel}$ [%]	$I_\gamma^{lit}$ [%]	$I_\gamma^{Decay}$ [%]	$E_i$ [keV]	$E_f$ [keV]	$J_i^\pi$	$J_f^\pi$
599.2	2.8(4)		0.9(1)	3150	2551	(13/2 <sup>-</sup> )	
631.9	21.0(12)	30.0	7.0(4)	1083	451	(3/2 <sup>-</sup> )	1/2 <sup>-</sup>
731.0	6.2(7)	8.5	2.1(2)	2085	1354		13/2 <sup>+</sup>
752.0	1.4(1.2)		0.5(4)	3184	2433	(5/2 <sup>+</sup> )	
769.2	43.8(40)		14.5(13)	1220	451	(5/2 <sup>-</sup> )	1/2 <sup>-</sup>
840.2	10.8(9)	6.0	3.6(3)	2060	1220		(5/2 <sup>-</sup> )
863.1	3.8(4)	5.5	1.2(1)	2551	1688		17/2 <sup>-</sup>
873.0	3.6(5)		1.2(1)	2561	1688		17/2 <sup>-</sup>
891.0	1.4(1.2)		0.5(4)	2447	1555		
895.0	1.4(1.2)		0.5(4)	2589	1693		
915.0	1.4(1.2)		0.5(4)	3348	2433	(5/2 <sup>+</sup> )	
967.6	6.2(7)		2.0(2)	3184	2217	(5/2 <sup>+</sup> )	
995.1	100.0(51)	100.0	33.1(17)	995	0	11/2 <sup>+</sup>	9/2 <sup>+</sup>
1020.1	10.1(8)	8.5	3.3(3)	2015	995		11/2 <sup>+</sup>
1040.6	2.3(5)		0.7(2)	3184	2143	(5/2 <sup>+</sup> )	
1065.4	8.5(7)	8.0	2.8(2)	3150	2085	(13/2 <sup>-</sup> )	
1096.0	6.7(7)		3.0(2)	3184	2088	(5/2 <sup>+</sup> )	
1103.8*	2.5(13)	5.0	0.8(4)				
1124.1	2.5(13)		0.8(4)	3184	2060	(5/2 <sup>+</sup> )	
1130.6	3.4(9)		1.1(3)	3348	2217	(5/2 <sup>+</sup> )	
1135.2	6.8(7)		2.3(2)	3150	2015	(13/2 <sup>-</sup> )	
1203.5	1.4(1.2)		0.5(4)	3348	2143	(5/2 <sup>+</sup> )	
1221.6	6.3(9)		2.1(3)	2217	995		11/2 <sup>+</sup>
1227.3	3.6(27)		1.2(9)	2447	1220		(5/2 <sup>-</sup> )
1234.6	7.7(11)	5.0	2.5(3)	2589	1354		13/2 <sup>+</sup>
1259.6	1.4(5)		0.5(2)	3348	2088	(5/2 <sup>+</sup> )	
1287.3	7.0(7)		2.3(2)	3348	2060	(5/2 <sup>+</sup> )	
1354.2	20.5(12)	21.0	6.8(4)	1354	0	13/2 <sup>+</sup>	9/2 <sup>+</sup>
1363.6	1.0(5)		0.3(2)	2447	1083		
1395.9*	3.0(15)		1.0(5)				
1422.9	16.9(10)	20.0	5.6(3)	3184	1762	(5/2 <sup>+</sup> )	
1457.0	1.4(1.2)		0.5(4)	3150	1693	(13/2 <sup>-</sup> )	
1462.3	12.2(12)	11.0	4.0(4)	3150	1688	(13/2 <sup>-</sup> )	17/2 <sup>-</sup>
1500.2*	4.4(5)		1.5(2)				
1524.1	2.3(4)		0.7(1)	3971	2447		
1555.2	1.3(4)	5.0	0.4(2)	1555	0		9/2 <sup>+</sup>

Table 3.4 continued on next page

**Table 3.4 – continued from previous page**

$E_\gamma$ [keV]	$I_\gamma^{rel}$ [%]	$I_\gamma^{lit}$ [%]	$I_\gamma^{Decay}$ [%]	$E_i$ [keV]	$E_f$ [keV]	$J_i^\pi$	$J_f^\pi$
1560.9*	2.7(11)	5.0	1.1(4)				
1586.2	8.3(8)	12.0	2.7(3)	3348	1762	(5/2 <sup>+</sup> )	
1689.9*	4.5(5)	6.0	1.5(2)				
1744.4	1.2(6)		0.4(2)	3888	2143		
1761.6	16.4(12)	19.0	5.4(4)	1762	0		9/2 <sup>+</sup>
1796.5	26.4(15)	32.0	8.7(5)	3150	1354	(13/2 <sup>-</sup> )	13/2 <sup>+</sup>
1890.0*	5.0(6)		1.7(2)				
1940.3	0.6(4)		0.2(1)	3702	1762		
2001.1*	5.3(12)		1.8(4)				
2088.0	8.1(9)	5.5	2.7(3)	2088	0		9/2 <sup>+</sup>
2127.6	1.4(7)		0.4(2)	3888	2143		
2143.4	1.4(7)		0.4(2)	2143	0		9/2 <sup>+</sup>
2155.6	6.4(8)		2.1(3)	3150	995	(13/2 <sup>-</sup> )	11/2 <sup>+</sup>
2204.8	0.6(4)		0.2(1)	3966	1762		
2216.8	7.5(9)	8.0	2.5(3)	2217	0		9/2 <sup>+</sup>
2295.6*	1.3(4)		0.4(1)				
2356.0	1.5(7)		0.5(2)	4118	1762		
2433.4	5.3(6)		1.7(2)	2433	0		9/2 <sup>+</sup>
2460.9	2.7(8)	6.0	0.9(2)	4082	1621		
2880.2	4.3(10)	2.5	1.4(3)	4082	1220		(5/2 <sup>-</sup> )
3184.4	4.0(7)	3.0	1.3(2)	3184	0	(5/2 <sup>+</sup> )	9/2 <sup>+</sup>
3286.1	1.3(4)		0.4(1)	3286	0		9/2 <sup>+</sup>
3348.0	3.0(10)	4.0	1.0(3)	3348	0	(5/2 <sup>+</sup> )	9/2 <sup>+</sup>
3487.7	1.4(6)	1.0	0.5(2)	3488	0		9/2 <sup>+</sup>
3701.9	4.7(17)	6.0	1.6(6)	3702	0		9/2 <sup>+</sup>
3888.4	1.1(7)	2.0	0.4(2)	3888	0		9/2 <sup>+</sup>
3913.8	2.7(5)	3.0	0.9(2)	3914	0		9/2 <sup>+</sup>
3966.4	5.0(12)	4.0	1.7(4)	3966	0		9/2 <sup>+</sup>
4118.3	1.7(5)	2.0	0.5(2)	4118	0		9/2 <sup>+</sup>

**Table 3.4:** List of  $\gamma$  rays observed in the  $\beta$ -decay of  $^{129}\text{Cd}$  to  $^{129}\text{In}$  with their energies, relative  $\gamma$  intensities, absolute  $\gamma$  intensities per decays, energies of the initial and final levels and the spin and parity of the initial and final levels proposed in this work. The literature values for the relative intensities are taken from reference [62].

The spectrum shows 75 lines which are associated with the  $\beta$ -decay of  $^{129}\text{Cd}$  and their energies, relative intensities, energies of the initial and final states and spins/parities associated to those states are listed in tables 3.4. The relative intensities from Ref. [62] are

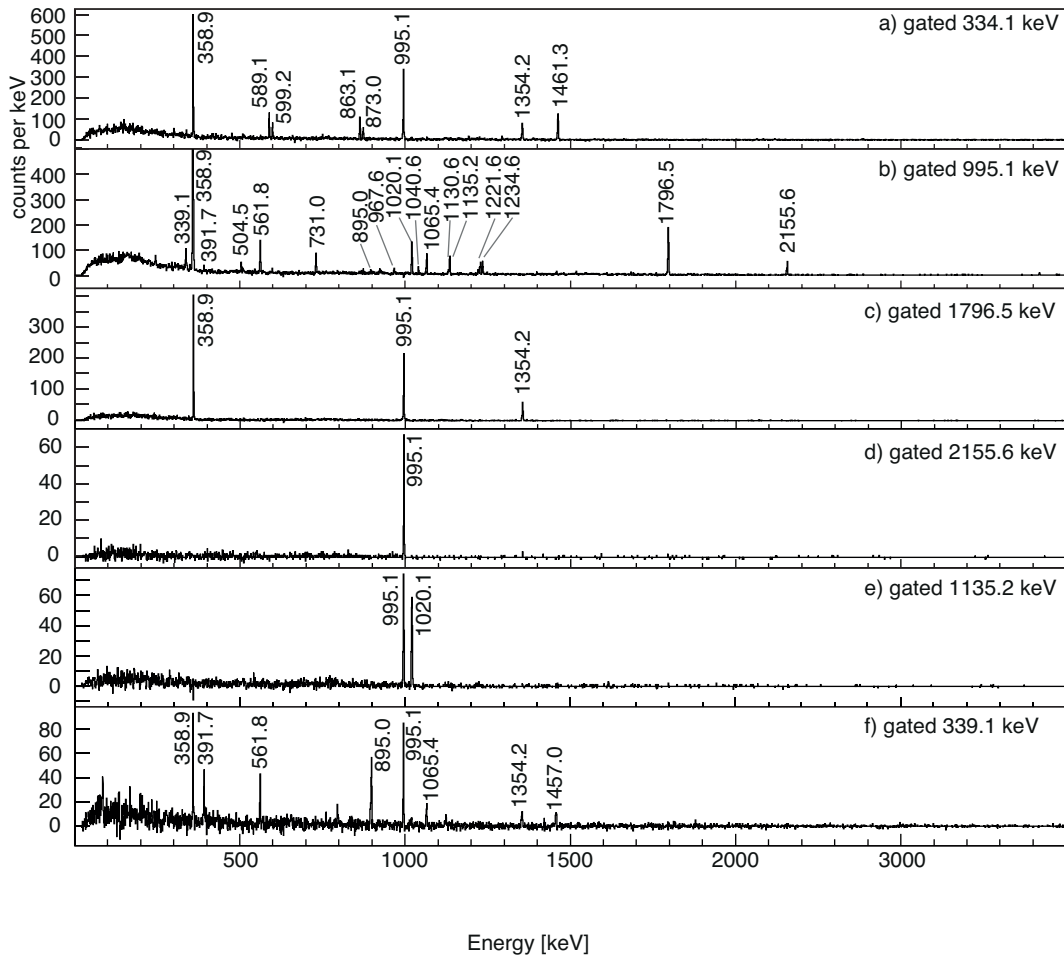


**Figure 3.13:** Germanium spectra observed in a) delayed coincidence with the 334.1-keV transition following the first decay of the implanted  $^{129}\text{Cd}$  ions and b)-f) in prompt coincidence with the observation of the 995.1-, 1796.5-, 2155.6-, 1135.2- and 339.1-keV transitions, respectively, observed following that decay.

added for comparison and an overall good agreement can be found, taking into account the errors of about 10% (20%) mentioned in that work for transitions with high (low) statistics. A complete list of all observed prompt and delayed coincidences is given in appendix C.3.

In the following a detailed discussion of the placement of the transitions in a level scheme is given, showing the most crucial  $\gamma$ - $\gamma$ -coincidence spectra, the key information which was used to create the level scheme. In several cases it was necessary to furthermore use information of the relative intensities to define the order of two or more transitions in a cascade. In those cases where a final decision of the order could not be made, this will be explicitly mentioned.

### 3.2.1 Transitions feeding the $11/2^+$ , $13/2^+$ and $17/2^-$ levels

In Ref. [29, 120] the decay of a  $17/2^-$   $\mu\text{s}$  isomeric state was discussed in detail, and the same transitions are also observed in the present experiment. Furthermore, the coinci-

dence spectra shown in Fig. 3.13a) and b) show the expected prompt coincidence of the 995.1-keV with the 358.9-keV transition and the delayed coincidence of the 334.1-keV  $\gamma$  ray and the 358.9-, 995.1- and 1354.2-keV ones. The well established decay scheme of the  $17/2^-$  isomeric state, which decays through a cascade to the  $9/2^+$  g.s., is therefore taken as a starting point to construct the level scheme. In Fig. 3.13c) the 1796.5-keV transition is observed to be in coincidence with solely the 358.9-, 995.1- and 1354.2-keV transitions. The 1796.5-keV transition is therefore placed on top of the  $13/2^+$  level. This placement and the establishment of a level at 3150 keV was previously proposed in Ref. [62], and spin and parity of ( $13/2^-$ ) were tentatively assigned. In the same publication a transition with an energy of 2156 keV was placed, connecting this level to the  $13/2^+$  level at 995 keV. The 2155.6-keV transition is also observed in the present data set in mutual prompt coincidence with solely the 995.1-keV transition (see Fig. 3.13d)) and the placement made in Ref. [62] is confirmed.

The 995.1-keV  $\gamma$  ray is furthermore observed in coincidence with two transitions having energies of 1020.1 and 1135.2 keV, which are also observed in mutual prompt coincidence with each other in Fig. 3.13e). Those observations and the fact that those three energies add up to 3150 keV suggest a placement as a cascade starting from the level at 3150 keV with the order of the 1020.1 - 1135.2 keV cascade being determined by the slightly higher relative intensity of the 1020.1-keV  $\gamma$  ray. It has to be mentioned here that the relative intensities are equal within the error bars and a reversed order of the corresponding cascade cannot be ruled out completely.

Eight weaker transitions (339.1, 391.7, 561.8, 731.0, 895.0, 1065.4, 1234.6 and 1457.0 keV) are observed in prompt coincidence with the strong 358.9-, 995.1- and 1354.2-keV transitions. The coincidence spectrum for the 339.1-keV transition is shown in Fig. 3.13f) as an example. From the obtained coincidences (see appendix C.3) it is concluded that three cascades ( $561.8 + 1234.6$ ,  $339.1 + 1457.0$  and  $731.0 + 1065.4$ ) can be placed on top of the 1354 keV level, with the 895.0- and 391.7-keV transitions connecting the intermediate states of the cascades. Those cascades are placed parallel to the 1796.5-keV transition de-exiting the level at 3150 keV, because the sum of the energies for each cascade is approximately 1796.5 keV. Adding the information of the relative intensities, the order of the cascades is fixed, and several new levels in the range between one to three MeV can be established.

The delayed coincidence spectrum shown in Fig. 3.13a) clearly shows that five other transitions (589.1, 599.2, 863.1, 873.0 and 1461.3 keV) are observed in coincidence with the 334.1-keV  $\gamma$  ray. Those transitions are observed in delayed, but not in prompt coincidence with the 334.1-, 358.9-, 995.1- and 1354.2-keV transitions. A placement on top of the  $17/2^-$   $\mu\text{s}$  isomer is therefore suggested, as it was proposed by Arndt *et al.* [62] for the 1461.3-keV one. The fact that the 589.1- and 599.2-keV  $\gamma$  rays are observed in mutual prompt coincidence with the 873.0- and 863.1-keV  $\gamma$  rays, respectively, and that both cascades have a sum energy of 1462 keV is a strong argument for placing them as parallel cascades to the 1462.3-keV transition, starting from the level at 3150

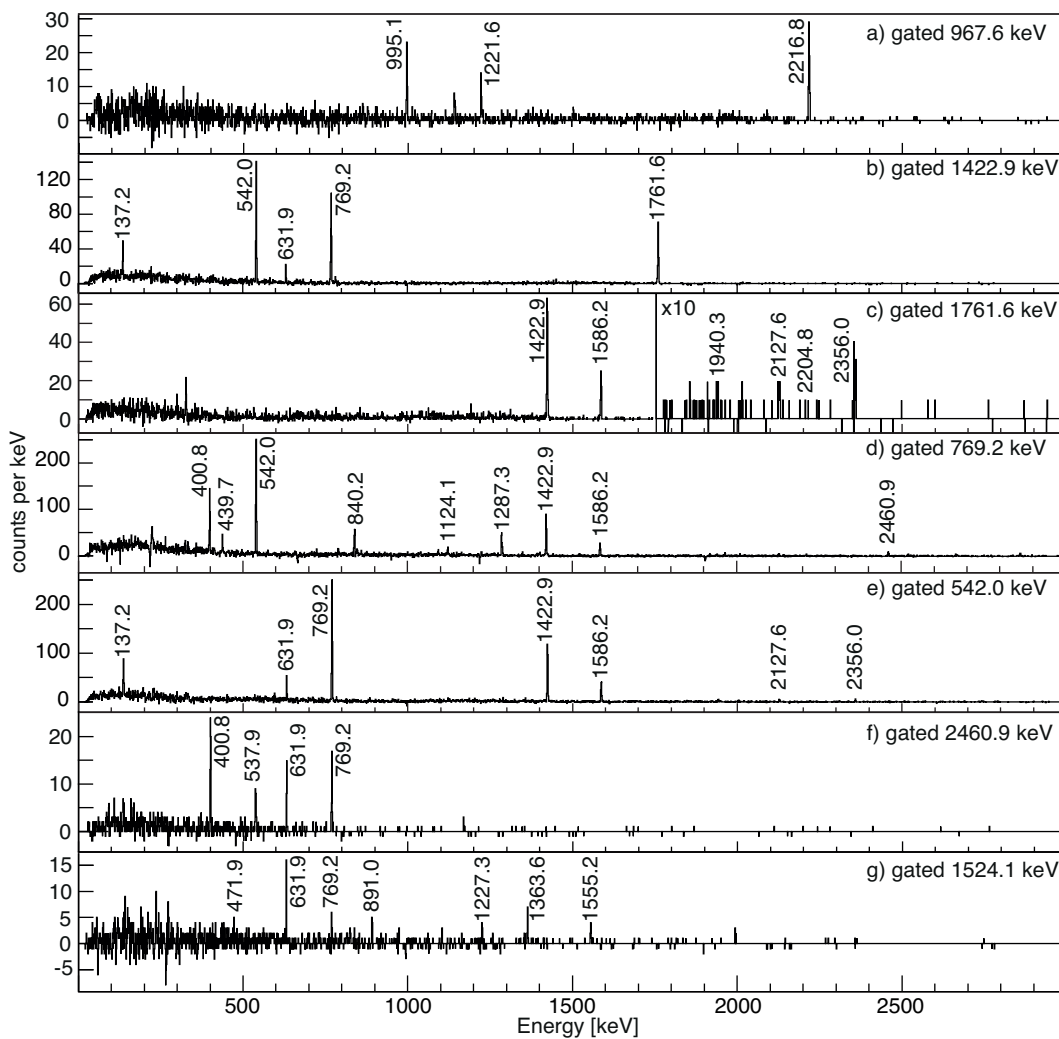


**Figure 3.14:** Germanium spectra observed in prompt coincidence with the a) 967.6-, b) 1422.9-, c) 1761.6-, d) 769.2-, e) 542.0-, f) 2460.9- or g) 1524.1-keV transition following the first  $\beta$  decay of the implanted  $^{129}\text{Cd}$  ions.

keV. Unfortunately, the order of those cascades cannot be determined based upon the experimental information.

In the prompt coincidence spectrum gated on the 995.1-keV  $\gamma$  ray three other transitions are observed, having energies of 967.6, 1130.6 and 1221.6 keV. The 1221.6-keV transition is observed in prompt coincidence with the 967.6- (see Fig. 3.14a)) and the 1130.6-keV ones, but the latter ones are not observed in coincidence with each other in the present experiment. Based upon the available experimental information the 1221.6-keV  $\gamma$  ray is placed on top of the 995-keV level establishing a new level at 2217 keV which is fed by the 967.6- and the 1130.6-keV transitions. This placement is supported by the observation of a 2216.8-keV  $\gamma$  ray, the g.s. transition of the 2217-keV level, in mutual coincidence with the 967.6- and the 1130.6-keV  $\gamma$  rays, respectively. Those cascades start from two levels at 3184 and 3348 keV, with the 3184-keV level already being proposed in Ref. [62].

### 3.2.2 The 3184-, 3348-, 3888- and 4118-keV levels

The two levels mentioned before above three MeV have a direct decay branch to the g.s. via two transitions of 3184.4 and 3348.0 keV and furthermore, several cascades could be identified via the information obtained from  $\gamma$ - $\gamma$ -coincidences having sum energies of either 3184 or 3348 keV. Transitions (752.0, 915.0, 1040.6, 1096.0, 1203.5, 1259.6 keV, 1422.9 and 1586.2 keV) from both states to levels at 1762, 2088, 2143 and 2433 keV are observed which then decay via a single transition (1761.6, 2088.0, 2143.4 and 2433.4 keV) to the g.s. The coincidence spectrum gated on the 1422.9-keV transition is shown in Fig. 3.14b). In Fig. 3.14c) one observes furthermore that the 1761.6-keV  $\gamma$  ray is in mutual coincidence with transitions having energies of 1940.3, 2127.6, 2204.8 and 2356.0 keV. Those start from levels at 3702, 3888, 3966 and 4118 keV, respectively. All these levels also have high energetic branches which go directly to the g.s. (3701.9, 3888.4, 3966.4 and 4118.3 keV) and additionally, the 3888-keV level feeds the 2143-keV level via a 1744.4-keV transition. Two additional high energy transitions with energies of 3487.7 and 3913.8 keV are tentatively proposed to be placed on top of the  $9/2^+$  g.s..

### 3.2.3 The position of the $1/2^-$ $\beta$ -decaying isomer

An important question in the level scheme of  $^{129}\text{In}$  is the position of the  $1/2^-$   $\beta$ -decaying isomer, which can be finally fixed with the experimental information presented in the following. The high relative intensities of the 137.2-, 631.9- and 769.2-keV transitions in conjunction with the obtained  $\gamma$ - $\gamma$ -coincidence information (see Fig. 3.14c)) suggest to place the 631.9- and 769.2-keV transitions directly on top of the  $\beta$ -decaying isomer. The transitions with 137.2, 631.9 and 769.2 keV have a much higher relative intensity compared to the other remaining transitions to be placed in the level scheme, and one observes a 542.0-keV transition (Fig. 3.14e)) solely in coincidence with those three and the transitions feeding the 1762-keV level. The 542.0-keV  $\gamma$  ray is therefore placed de-exciting the 1762-keV level followed by the 769.2-keV transition resulting in a level at 451 keV. With the 631.9 and the 137.2-keV transitions summing up to 769.1 keV and the fact that they are not observed in coincidence with the 769.2-keV  $\gamma$  ray, they are placed as a parallel cascade.

The order of the 137.2 - 631.9 keV cascade is determined by other transitions observed in prompt coincidence. A 400.8-keV  $\gamma$  ray is in coincidence with both of them and a 537.9-keV transition solely with the 631.9-keV transition. Several other transitions can be placed on top of the new levels at 1083 and 1220 keV starting among others also as cascades from the 3184- and the 3348-keV level. In addition to this, two new levels at around 4 MeV are established, which have no direct decay-branch to the g.s..

The  $1/2^-$   $\beta$ -decaying isomer is, according to the observations made in the present experiment, placed at 451(1) keV and with that slightly below the most recent measurement which placed it at 459(5) keV [48]. This measurement was carried out with the double

Penning trap mass spectrometer JYFLTRAP.

A 2460.9-keV transition is placed on top of the level at 1621 keV based on the coincidence spectra shown in Fig. 3.14f) and with that a new level at 4082 keV is established. An additional level at 3971 keV is found to be de-excited by several cascades to the  $1/2^-$   $\beta$ -decaying isomer, but also via a 1524.1-891.0-1555.2-keV cascade to the  $9/2^+$  g.s..

### 3.2.4 The $^{129}\text{In}$ level scheme, level feeding and log $ft$ values

The  $^{129}\text{In}$  level scheme, obtained in the present work, is presented in Fig. 3.15, showing for the first time in detail the transitions and levels populated in the  $\beta$  decay of  $^{129}\text{Cd}$  to  $^{129}\text{In}$ . Each state was assigned ( $I^\pi(\beta)$  in Table 3.5) to either the  $(3/2^+)$  or the  $(11/2^-)$  decay. The assumption that a certain state is not fed by both  $\beta$ -decays seems convincing because of the parity and large spin difference. Based on the level scheme, the observed feeding and systematics in lower-mass Cadmium isotopes [121, 122], a tentative assignment is made as presented in Table 3.5, with some of the assignments being discussed in the following. First of all, the intensity balance between the transitions populating and de-exciting certain states was used to calculate the  $\beta$ -feeding to all states. The  $\beta$ -feeding in percent per  $^{129}\text{Cd}$  decay,  $I_\beta(^{129}\text{Cd})$ , independent from which  $\beta$ -decaying state it originated, is stated in the second column in Table 3.5.

The  $9/2^+$  g.s. and the  $11/2^+$ ,  $13/2^+$  and  $17/2^-$  levels are assigned to the  $\beta$ -decay of the  $(11/2^-)$  g.s. in  $^{129}\text{Cd}$  because of their spin. On the other hand, the states at 1083 and 1220 keV are proposed to have spin and parity of  $(3/2^-)$  and  $(5/2^-)$ , respectively, mainly based on the shell-model calculations presented in section 6.3 and the systematics in odd-mass Indium isotopes below  $N=82$ . Because of the spin assignments, the observed  $\beta$ -feeding can only come from the  $(3/2^+)$   $\beta$ -decaying state in  $^{129}\text{Cd}$ . Three levels receive major feeding above three MeV, with two of them decaying to the  $9/2^+$  g.s. and the level at 1762 keV and one decaying mainly to the  $17/2^-$  and  $13/2^+$  states. All three of them are fed either by GT or fast first-forbidden non-unique decays. This leaves only  $1/2$  to  $5/2$  and  $9/2$  to  $13/2$  as possible spins for the states. The 3150-keV level can only have spin  $(13/2)$  to explain the observed branching to both mentioned states and is therefore assigned to the  $(11/2^-)$   $\beta$ -decay, while the two levels at 3184 and 3348 keV are tentatively assigned to the  $(3/2^+)$   $\beta$ -decay. This assignment is supported by the observed direct decay branch to the  $9/2^+$  g.s. and the two step cascade to the  $(5/2^-)$  level.

The assignment of the two levels at 3184 and 3348 keV to be fed solely in the decay of the  $(3/2^+)$   $\beta$ -decaying isomeric state is supported by another observation in the data. Later in this work the existence of a ms isomeric state in  $^{129}\text{Cd}$  is presented. This ms isomeric state decays only to the  $(11/2^-)$   $\beta$ -decaying level. Gating on the characteristic transitions in the decay of this long-lived state, a  $\beta$ -delayed germanium spectrum was filled (see Fig. 3.16), showing all decays following the observation of one of the four transitions observed in the de-excitation. That spectrum should show solely transitions following the  $\beta$ -decay of the  $(11/2^-)$  state. The already efficiency corrected intensity sum of the 995.1-keV and

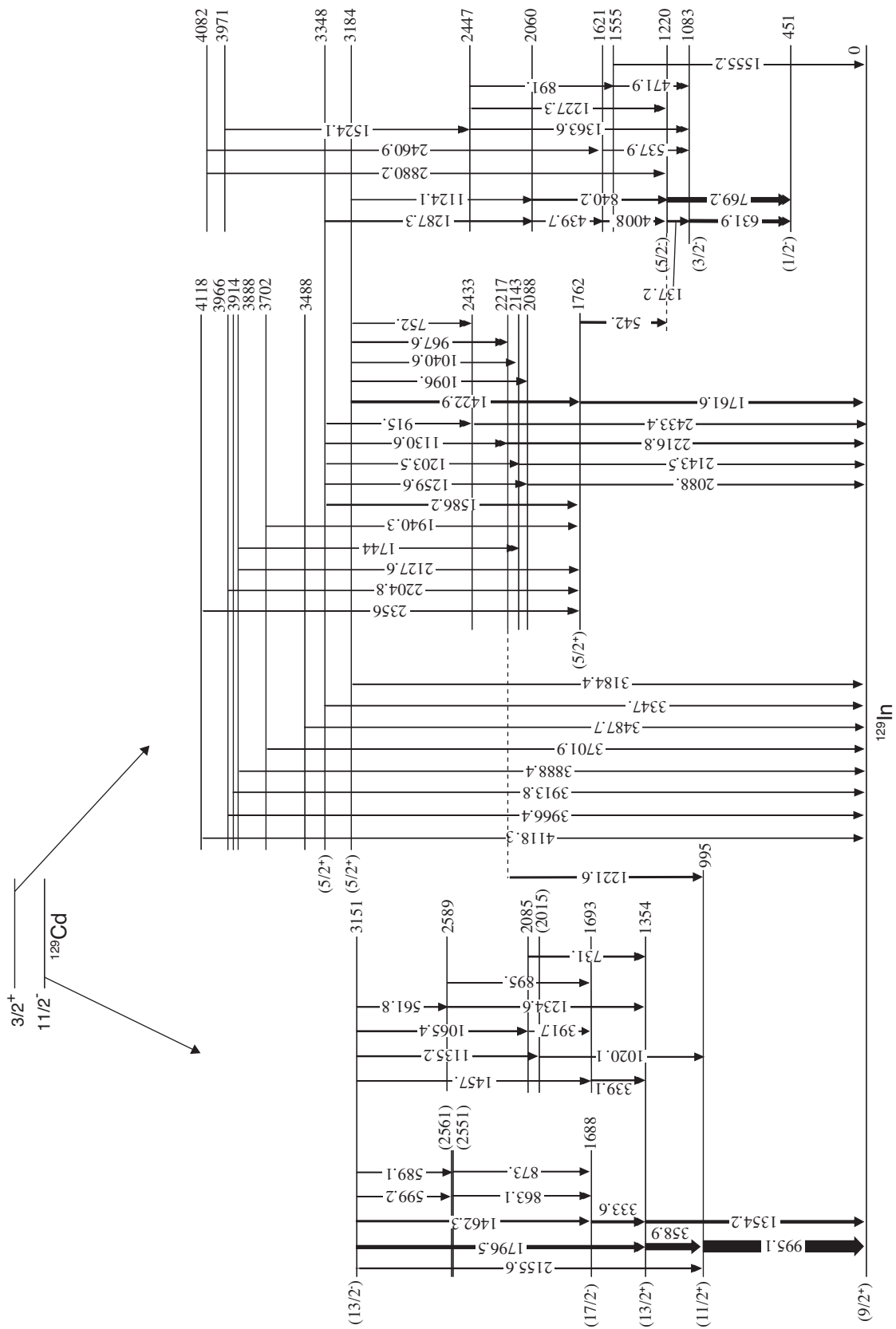


**Figure 3.15:** Level scheme of  $^{129}\text{In}$  as it was obtained in the present work through the measurement of the  $^{129}\text{Cd}$   $\beta$ -decay.

$E_{\text{Level}}$ [keV]	$I^\pi(\beta)$	$I_{\text{level}}^\pi$	$I_\beta(^{129}\text{Cd})$ [%]	$I_\beta(3/2^+)$ [%]	$I_\beta(11/2^-)$ [%]	log $ft$
0	(11/2 <sup>-</sup> )	9/2 <sup>+</sup>	11(3)	-	22(6)	5.4(1)
451	(3/2 <sup>+</sup> )	1/2 <sup>-</sup>	6(3)	12(6)	-	5.6(2)
995	(11/2 <sup>-</sup> )	11/2 <sup>+</sup>	6.5(20)	-	13(4)	5.4(1)
1083	(3/2 <sup>+</sup> )	(3/2 <sup>-</sup> )	4.0(6)	8(1)	-	5.6(1)
1220	(3/2 <sup>+</sup> )	(5/2 <sup>-</sup> )	2.7(17)	5(3)	-	5.8(3)
1354	(11/2 <sup>-</sup> )	13/2 <sup>+</sup>	3.2(12)	-	8(3)	5.5(2)
1555	(3/2 <sup>+</sup> )		< 1.0	< 2	-	> 6.1
1621	(3/2 <sup>+</sup> )		1.2(4)	2(1)	-	6.1(2)
1688	(11/2 <sup>-</sup> )	17/2 <sup>-</sup>	< 0.4	-	< 1	> 6.3
1693	(11/2 <sup>-</sup> )		0.7(6)	-	1(1)	6.3(5)
1762	(3/2 <sup>+</sup> )		0.5(10)	2(2)	-	6.0(5)
2015	(11/2 <sup>-</sup> )		1.1(3)	-	2(1)	5.9(2)
2060	(3/2 <sup>+</sup> )		1.3(6)	3(1)	-	5.8(2)
2085	(11/2 <sup>-</sup> )		< 0.1	-	< 1	> 6.2
2088	(3/2 <sup>+</sup> )		< 0.4	< 1	-	> 6.2
2143	-		-	-	-	-
2217	(11/2 <sup>-</sup> )		1.4(6)	-	3(1)	5.7(2)
2433	(3/2 <sup>+</sup> )		< 1.1	< 2	-	> 5.9
2447	(3/2 <sup>+</sup> )		1.3(11)	3(2)	-	5.7(3)
2551	(11/2 <sup>-</sup> )		< 0.5	-	< 1	> 6.1
2561	(11/2 <sup>-</sup> )		< 0.5	-	< 1	> 6.1
2589	(11/2 <sup>-</sup> )		< 1.2	-	< 2	> 5.8
3150	(11/2 <sup>-</sup> )	(13/2 <sup>-</sup> )	25.3(8)	-	52(5)	4.2(1)
3184	(3/2 <sup>+</sup> )	(5/2 <sup>+</sup> )	13.3(8)	26(3)	-	4.5(1)
3286	(3/2 <sup>+</sup> )		0.4(1)	1(1)	-	5.9(5)
3348	(3/2 <sup>+</sup> )	(5/2 <sup>+</sup> )	8.6(9)	17(2)	-	4.7(1)
3488	(3/2 <sup>+</sup> )		0.7(2)	1(1)	-	5.8(5)
3702	(3/2 <sup>+</sup> )		1.6(6)	3(1)	-	5.3(2)
3888	(3/2 <sup>+</sup> )		1.2(4)	2(1)	-	5.4(2)
3914	(3/2 <sup>+</sup> )		0.9(2)	2(1)	-	5.4(2)
3966	(3/2 <sup>+</sup> )		1.9(4)	4(1)	-	5.1(1)
3971	-		0.7(1)	-	-	-
4082	-		2.3(13)	-	-	-
4118	(3/2 <sup>+</sup> )		1.0(3)	2(1)	-	5.3(2)

**Table 3.5:** Levels in  $^{129}\text{In}$  populated by the  $\beta$ -decay of  $^{129}\text{Cd}$  and the observed  $\beta$ -feeding and corresponding log  $ft$  value.  $I_\beta(^{129}\text{Cd})$  is the  $\beta$ -feeding in percent per  $^{129}\text{Cd}$  decay independent from which  $\beta$ -decaying state it originates, while  $I_\beta(3/2^+)$  and  $I_\beta(11/2^-)$  are the  $\beta$ -feeding to that state from either the (3/2<sup>+</sup>) or the (11/2<sup>-</sup>) state in  $^{129}\text{Cd}$ .

1354.2-keV transitions in that spectrum is 447(82) counts, while a total of 558(52)  $^{129}\text{Cd}$   $\beta$  decays is observed. Including the direct feeding to the 9/2<sup>+</sup> g.s. one observes that within the error bars 100% of the  $\beta$ -feeding following the  $\beta$ -decay of (11/2<sup>-</sup>) state proceeds either via the 995.1- or the 1354.1-keV transitions or is unobserved direct feeding to the 9/2<sup>+</sup> g.s. in  $^{129}\text{In}$ . Therefore, the major  $\beta$ -decay feeding to the 3184- and 3348-keV levels has to come from the (3/2<sup>+</sup>)  $\beta$ -decaying isomeric state because only a negligible amount of the  $\beta$ -decay feeding to those states subsequently proceeds through the 995.1- or the

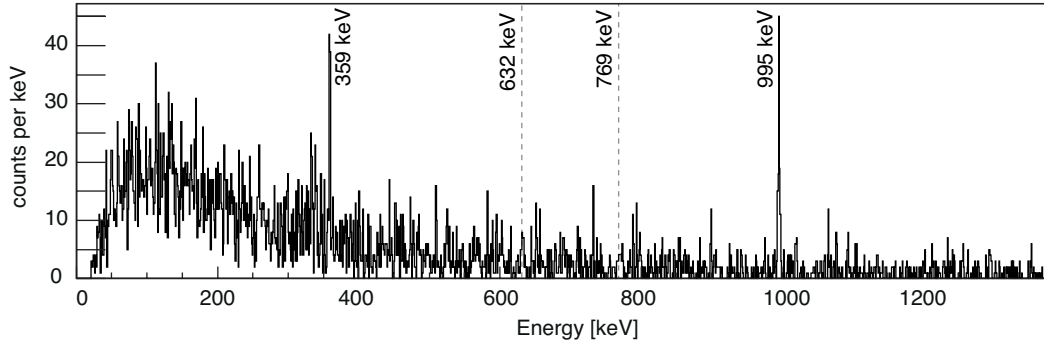


**Figure 3.16:** Ge spectrum in coincidence with the first decay of the implanted  $^{129}\text{Cd}$  ions after the observation of one of the four transitions observed in the de-excitation of the ms isomeric state in  $^{129}\text{Cd}$ . The maximum time window between the observation of one of the transitions and the decay is set to 450 ms.

1354.1-keV transitions.

Most of the remaining levels above three MeV have a similar decay pattern as the two levels at 3184 and 3348 keV and are therefore tentatively assigned to the  $(3/2^+)$   $\beta$ -decay, too. Conversely, the two levels at 3971 and 4082 keV have very different decay-branches and an assignment cannot be done in the present work. On the other hand, all remaining levels below three MeV are assigned based on the level scheme to one or the other  $\beta$ -decay as shown in Table 3.5.

The missing information for the calculation of  $\beta$ -decay feeding from either the  $(3/2^+)$  or  $(11/2^-)$  state in  $^{129}\text{Cd}$  and the corresponding  $\log ft$  values is then the number of parent decays coming from either the  $(3/2^+)$  or  $(11/2^-)$   $\beta$ -decaying states. For this, the daughter decay  $^{129}\text{In}$  to  $^{129}\text{Sn}$  was of crucial importance. The intensity of the 2118-keV transition in  $^{129}\text{Sn}$ , populated in the daughter decay of the  $9/2^+$  ground state of  $^{129}\text{In}$ , was determined. With that intensity and the known absolute intensity of that transition of 42(2) per 100 decays, measured in Ref. [119], the intensity de-exiting the  $9/2^+$  ground state of  $^{129}\text{In}$  could be estimated to 72(2)% per  $^{129}\text{Cd}$  decay. The intensity of all  $\gamma$ -transitions feeding the  $9/2^+$  state accounts to 61(2)%, and from this one obtains a direct feeding to the  $9/2^+$  state of 11(3)%. On the other hand, the remaining 28(2)% proceed via the  $1/2^-$   $\beta$ -decaying state in  $^{129}\text{In}$ . With the sum of the absolute intensities from all  $\gamma$ -transitions feeding that state being 22(1)% a direct feeding of 6(3)% is calculated.

Looking at the assignments made in Table 3.5, one observes that the full  $\beta$ -feeding coming from the  $(11/2^-)$  state proceeds either via the 995.1- and 1354.1-keV transitions or is direct feeding to the  $9/2^+$  g.s. The sum of the absolute intensities of the 995.1- and 1354.1-keV transitions is 40(2)% per  $^{129}\text{Cd}$   $\beta$  decay. With the correction for the feeding by the 1221.6-keV transition (2(1)%) and the direct feeding to the  $9/2^+$  g.s., one obtains that most likely 49(4)% of the  $\beta$ -decays originate from the  $(11/2^-)$  state in  $^{129}\text{Cd}$ . With this information the  $\beta$ -feeding can be split up, and the  $\beta$ -feeding was calculated independently for the two states as:

$$I_{\beta}(3/2^+) = \frac{I_{\beta}(^{129}\text{Cd})}{51(4)\%} \quad (3.8)$$

$$I_{\beta}(11/2^-) = \frac{I_{\beta}(^{129}\text{Cd})}{49(4)\%} \quad (3.9)$$

depending if the  $\beta$ -feeding to a state was assigned to one or the other decay. The results are again stated in Table 3.5 and with this information finally the log  $ft$  values could be deduced. For the calculations of the log  $ft$  values the half-lives as obtained in the present work were used, together with the  $Q_{\beta}$  value taken from Ref. [1].

With the log  $ft$  values being 4.2(1), 4.5(1) and 4.7(1) for the states at 3150, 3184 and 3348 keV, respectively, those states have to be fed by a transition of GT type. This fixes also the parity assignment to the levels and the level at 3150 keV is given a tentative spin and parity of  $(13/2^-)$ , while the two other states most likely are  $(5/2^+)$ .

### 3.2.5 Discussion and conclusions

The  $17/2^-$  state should not receive any measurable  $\beta$ -feeding from neither the  $(11/2^-)$  nor the  $(3/2^+)$   $\beta$ -decaying isomeric states in  $^{129}\text{Cd}$  taking into account the spin difference between the initial states ( $3/2^+$  or  $11/2^-$ ) and the final state. And indeed the experimental data shows no  $\beta$ -feeding to the  $17/2^-$  state. On the contrary, the levels at 995 and 1354 keV receive non negligible amounts of feeding. Those states were predicted to belong to the  $\pi g_{9/2}^{-1} \nu h_{11/2}^{-2}$  multiplet in Ref. [29] and therefore, very probably the first forbidden decay  $\nu h_{11/2} \rightarrow \pi g_{9/2}$  starting from the  $\nu h_{11/2}^{-1}$  g.s. in  $^{129}\text{Cd}$  can be associated. The  $\beta$ -feeding to the  $9/2^+$  g.s. is only estimated to 11(3)%, as described before, because a direct measurement of g.s. to g.s. transitions is not possible with the present set-up. The log  $ft$  values of 5.4(1) and 5.5(2) for the first forbidden decay of the type  $\nu h_{11/2} \rightarrow \pi g_{9/2}$  to the levels at 995 and 1354 keV, respectively, compare well to similar ones in the  $^{131}\text{In}$  decay with log  $ft > 5.6$  [41] and in the  $^{132}\text{In}$  decay with a log  $ft$  value of 5.6 [82].

The  $(3/2^-)$  state and the  $(5/2^-)$  state at 1083 and 1220 keV, respectively, both are clearly fed by first forbidden decays from the  $(3/2^+)$   $\beta$ -decaying isomeric state with log  $ft$  values of 5.7(3) and 5.6(1), respectively.

The 3150-keV level, having strong  $\gamma$  branches to the  $13/2^+$  and  $17/2^-$  states, receives 52(5) % of the feeding from the  $(11/2^-)$   $\beta$ -decaying state in  $^{129}\text{Cd}$ . A different assignment to that state than  $(13/2^-)$  seems unlikely based on the observed feeding and  $\gamma$  branches. Only the  $\nu g_{7/2} \rightarrow \pi g_{9/2}$  Gamow-Teller (GT) decay, the GT with the biggest energy release in the  $^{132}\text{Sn}$  region, can be related to the  $\beta$  decay from the  $(11/2^-)$  state to that level. This is also based on systematics in the region below  $^{132}\text{Sn}$  and with  $N < 82$ . In the present work a log  $ft$  of 4.2(1) was deduced from the  $\beta$ -feeding, in good agreement with the literature values for GT transitions of the similar type in several nuclei around  $^{132}\text{Sn}$ . For example in the decays of  $^{127,129}\text{In}$  log  $ft$  values in the range from 4.4 to 4.5 were measured [119] and in Ref. [82] 4.6 was found for the  $^{132}\text{In}$   $\beta$  decay.

The two levels at 3184 and 3348 keV, having a tentative assignment of  $(5/2^+)$ , receive major  $\beta$  feeding in the  $\beta$ -decay. This suggests that in all likelihood only the  $\nu g_{7/2} \rightarrow \pi g_{9/2}$  GT decay can be associated from the  $\nu d_{3/2}^{-1}$  isomeric state in  $^{129}\text{Cd}$ . The two levels then

most likely belong to the  $\pi g_{9/2}^{-1}\nu(d_{3/2}^{-1}g_{7/2}^{-1})$  multiplet and decay via an E2 transition to the  $\pi g_{9/2}^{-1}$  g.s.

As presented in the introduction, one of the questions in the region around  $^{132}\text{Sn}$  is the importance of first-forbidden decays below  $Z=50$ .  $^{129}\text{Cd}$  is the perfect probe and one observes that the  $\nu h_{11/2} \rightarrow \pi g_{9/2}$  first forbidden  $\beta$ -decay very likely is of importance. Transitions of this type are associated to the  $\beta$  feeding to the levels of the  $\pi g_{9/2}^{-1}\nu(h_{11/2}^{-2})$  multiplet and the  $(9/2^+)$  g.s. One limitation in the present experiment is unfortunately the limited possibility to determine the g.s. to g.s.  $\beta$  decay and therefore to fix the amount going to the  $(9/2^+)$  g.s.. The value stated in Table 3.5 for the g.s. to g.s.  $\beta$  decay is strictly speaking only an upper limit due to the Pandemonium effect and unobserved  $\beta$ -decay feeding. Nevertheless, it is concluded that first forbidden decays play a non negligible role in the  $^{129}\text{Cd}$  decay and have to be included when performing calculations for e.g.  $\beta$ -decay half-lives. This question was raised for example in Refs. [63, 67, 68].

### 3.3 Decay of $^{130}\text{Cd}$

The first studies of the  $N=82$  waiting point nucleus  $^{130}\text{Cd}$  using the methods of  $\beta$ - and  $\gamma$ -spectroscopy were reported in Refs. [20, 123–125]. In those works a first level scheme was proposed for  $^{130}\text{In}$  with the  $1^+$  state of the two-quasi-particle configuration  $\pi g_{9/2}^{-1}\nu g_{7/2}^{-1}$  placed at 2120 keV. Being a waiting-point nucleus in most r-process calculations, the study of this nucleus is of special interest.

#### 3.3.1 Transitions in the $^{130}\text{Cd}$ $\beta$ decay and level scheme of $^{130}\text{In}$

Fig. 3.17 shows the spectrum of the  $\gamma$  rays observed in coincidence with the  $\beta$  decays of the  $1.9 \times 10^6$  implanted  $^{130}\text{Cd}$  ions. As in the case of the results presented before, several contamination lines are still present in the spectrum even after applying all cuts for cleaning the spectrum ( $Z_{mult} = 1$  &  $\Delta z = 0$  &  $\Delta x, \Delta y < 1$ ). The spectrum contains known transitions from  $^{131}\text{Sn}$  (#) and  $^{132}\text{Sn}$  (\$), probably through random correlations of  $^{131}\text{In}$  and  $^{132}\text{In}$  decays, respectively. The peak with an energy of 511 keV (@) arises from the annihilation of positrons which have been created in pair production of high energy  $\gamma$  rays with the corresponding single escape peaks also being visible in the spectrum (SE). In addition to this, one observes known transitions from  $^{130}\text{Sn}$  (\*), populated through the  $\beta$  decay of the daughter nucleus  $^{130}\text{In}$ .

Several previously unknown transitions are observed on top of the strong transitions which were previously reported in Refs. [2, 20, 123–125] and placed in a level scheme. In the present work the transitions with energies of 1138, 2586, 4407, 4631, 5098 and 5196 keV, observed in the previously mentioned work, are not present in the decay spectrum and can therefore not be confirmed. On the contrary, several previously unknown transitions can be identified and are assigned to the decay of  $^{130}\text{Cd}$  to  $^{130}\text{In}$ . Those transitions

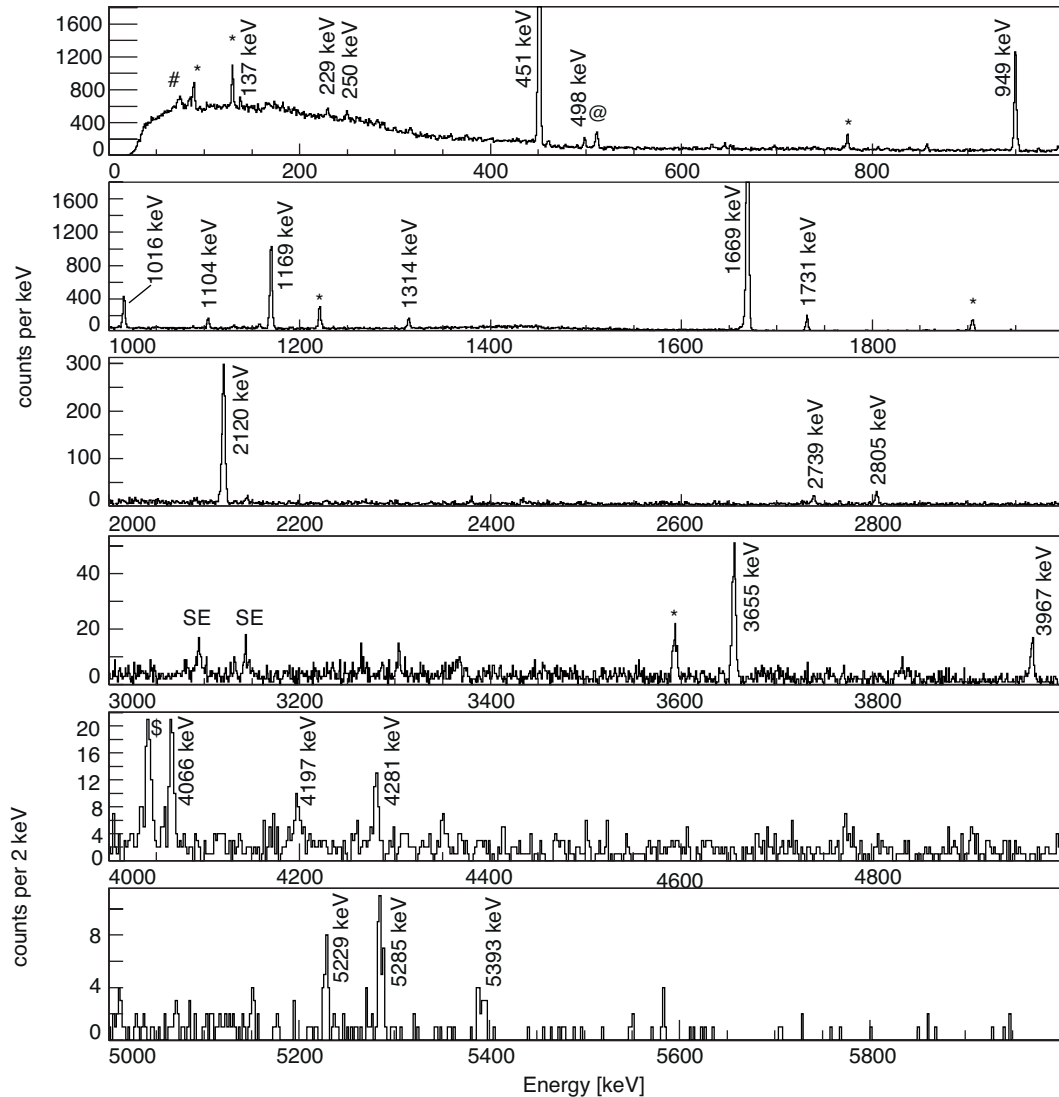


**Figure 3.17:** Ge spectrum in prompt coincidence with the first decay of the implanted  $^{130}\text{Cd}$  ions requiring a maximum time difference of 400 ms between implantation and decay and the following cuts:  $z_{mult} = 1$  &  $\Delta z = 0$  &  $\Delta x, \Delta y < 1$ . Transitions labelled with symbols correspond to known transitions in  $^{130}\text{Sn}$  (\*), populated after the  $\beta$  decay of the daughter nucleus, in  $^{131}\text{Sn}$  (#) and  $^{132}\text{Sn}$  (\$), due to false correlated  $\beta$  decays. Single escape peaks are marked with (SE) and the peak at 511 keV (@) arises from the annihilation of positrons created in pair production in the germanium detectors.

have energies of 229.1, 498.7, 1104.1, 3655.4, 3966.8, 4065.7, 4197.1, 4281.2, 5228.7, 5285.6 and 5393.3 keV.

All of the observed transitions could be placed in a level scheme and a summary of the energies, relative intensities, and the spins and parities of the initial and final levels of the transitions is given in Table 3.6. The obtained coincidence (see Table C.5 in the appendix) and relative intensity information agree with the literature values presented in Ref. [20] in all but two cases. The placements of the 2739.0- and 2804.8-keV transitions are changed in the present work. The new placement is based upon observed coincidences in the experimental data and will be explained in detail in the following, together with a discussion about the newly observed transitions.

$E_\gamma$ [keV]	$I_\gamma^{rel}$ [%]	$I_\gamma^{lit}$ [%]	$I_\gamma^{Decay}$ [%]	$E_i$ [keV]	$E_f$ [keV]	$J_i^\pi$	$J_f^\pi$
229.1	4.5(6)		2.3(3)	4197	3967		
388.4	6.8(6)	4.0(26) [2], <6.6 [20]	3.5(3)	388	0	(3 <sup>+</sup> )	1 <sup>-</sup>
450.8	103.7(53)	88.6(36) [2], 88.0 [20], 94(9) [123–125]	53.6(27)	2120	1669	1 <sup>+</sup>	(1) <sup>-</sup>
498.7	1.2(4)			1669	1170	(1) <sup>-</sup>	(0, 1) <sup>-</sup>
949.9 <sup>1</sup>	19.2(26)	22.1(33) [2], 18.9 [20], 20(7) [123–125]	9.9(13)	2120	1170	1 <sup>+</sup>	(0, 1) <sup>-</sup>
1015.8	6.8(6)	5.5(10) [2]	3.5(3)	1016	0		1 <sup>-</sup>
1104.1	1.7(4)		0.9(2)	2120	1016	1 <sup>+</sup>	
1170.0	22.0(13)	20.0(2) [2], 20.4 [20], 30(3) [123–125]	11.3(7)	1170	0	(0, 1) <sup>-</sup>	1 <sup>-</sup>
1669.2	100(5)	100 [2, 20, 123–125]	51.6(27)	1669	0	(1) <sup>-</sup>	1 <sup>-</sup>
1731.5	5.2(5)	4.4(4) [2], 4.5 [20], 4.6(5) [123, 125]	2.7(3)	2120	388	1 <sup>+</sup>	(3 <sup>+</sup> )
2120.0	13.2(14)	11.1(6) [2], 11.3 [20], 17(3) [123–125]	6.8(7)	2120	0	1 <sup>+</sup>	1 <sup>-</sup>
2739.0	0.7(3)	1.3(3) [2]	0.4(1)	3755	1016		
2804.8	1.8(3)	1.1(2) [2], 1.3(4) [123, 125]	0.9(2)	2805	0		1 <sup>-</sup>
3655.4	4.2(6)		2.1(3)	4044	388		
3966.8	1.4(2)		0.7(2)	3967	0		
4065.7	1.1(3)		0.6(1)	4066	0		
4197.1	0.6(2)		0.3(1)	4197	0		
4281.2	0.6(2)		0.3(1)	4281	0		
5228.7	0.6(2)		0.3(1)	5229	0		
5285.6	0.6(2)		0.3(1)	5286	0		
5393.3	1.2(2)	0.4(2) [2]	0.6(1)	5393	0		

**Table 3.6:** List of  $\gamma$  rays observed in the  $\beta$ -decay of  $^{130}\text{Cd}$  to  $^{130}\text{In}$  with their energy, relative  $\gamma$  intensities, absolute intensity of  $\gamma$  rays per decays of  $^{130}\text{Cd}$ , energies of the initial and final level and the spin and parity of the initial and final level proposed in the work [20].

<sup>1</sup> The 949.9-keV transition is a doublet.

First of all, the 1104.1-keV transition is observed in prompt coincidence solely with the 1015.8-keV transition (see Fig. 3.18a)), and with the sum of those two being 2119.9 keV a placement parallel to the 2120.0-keV transition is proposed. The order of the cascade is determined by the fact that the 1015.8-keV transition is in addition to this in coincidence with a 2739.0-keV  $\gamma$  ray (see Fig. 3.18b). With the 1015.8-keV transition being placed as a g.s. transition and the 2739.0-keV transition feeding the new established level at 1016 keV, it becomes obvious that the previous placement of the 2739.0-keV transition does not agree with the observations made in the present experiment.

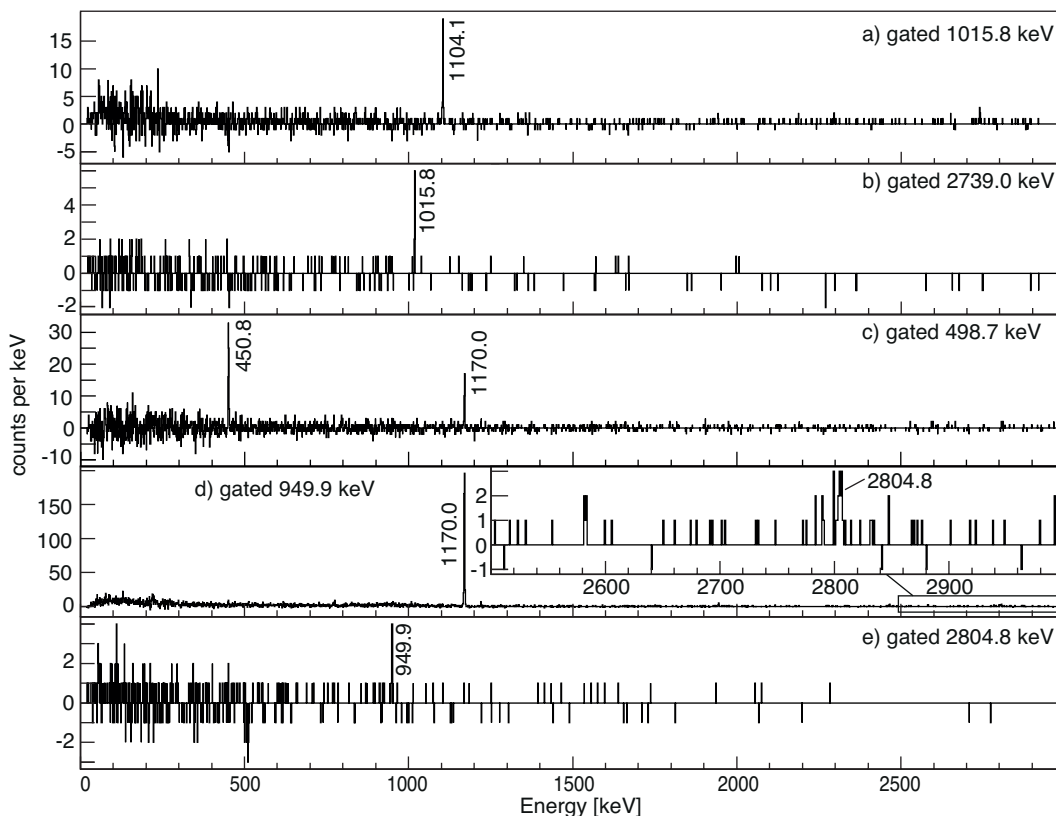


**Figure 3.18:** Germanium spectra in prompt coincidence with the observation of the a) 1015.8-, b) 2739.0-, c) 498.7-, d) 949.9- and e) 2804.8-keV transitions following the first decay of the implanted  $^{130}\text{Cd}$  ions.

The newly observed 498.7-keV transition can be placed in the already well established part of the level scheme, connecting the levels at 1170 keV and 1669 keV. This placement is made based upon the observed mutual prompt coincidence with the 450.8 and 1170.0-keV  $\gamma$  rays in Fig. 3.18c).

Most of the higher energetic transitions are not seen in coincidence with any other transition and are therefore proposed to be placed as g.s. transitions.  $^{130}\text{In}$  has two known  $\beta$ -decaying isomeric states with proposed spins and parities of  $(5^+)$  and  $(10^-)$  [126] but a placement of the higher energetic transitions on top of those is unlikely due to angular momentum selection rules. GT and ff non-unique  $\beta$ -decays from the  $0^+$  g.s. of  $^{130}\text{Cd}$  populate level in  $^{130}\text{In}$  with spins of 0 or 1. It is highly unlikely that those levels decay via a single transition to the  $(5^+)$  or  $(10^-)$   $\beta$ -decaying isomeric states. The limited statistics in the  $\gamma$ - $\gamma$  coincidence spectra of the higher energetic transitions unfortunately make it impossible to completely rule out feeding from other higher lying states. Only for two cases coincidences are observed between a transition with more than three MeV and any other transition, namely the 3655.4- and the 3966.8-keV ones. Those are seen in coincidence with the 388.4- and the 229.1-keV  $\gamma$  rays, respectively. With the sum of 3966.8 and 229.1 keV being approximately 4197 keV, it is suggested to place those two transitions as a cascade parallel to the 4197.1-keV  $\gamma$  ray. The 3655.4-keV transition on the other hand is placed on top of the isomeric state at 388 keV.

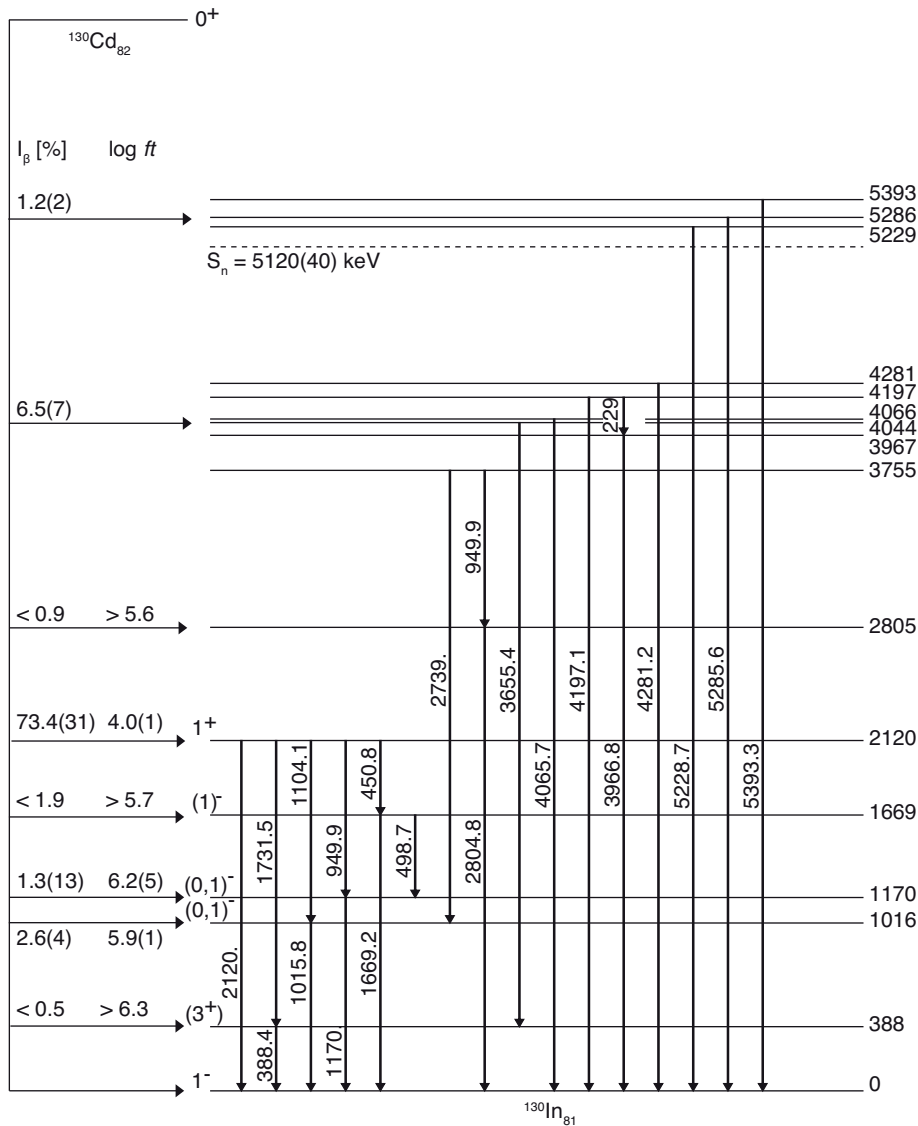


**Figure 3.19:** Level scheme of  $^{130}\text{In}$  as it was obtained in the present work through the measurement of the  $^{130}\text{Cd}$   $\beta$ -decay. The  $S_n$  is taken from Ref. [1] and spin and parities of the levels are as proposed in Ref. [20].

As it was mentioned before, the placement of the 2804.8-keV transition, as suggested in the previous work, does not agree with the observations in this work. Figures 3.18d) and e) clearly show a prompt coincidence of the 2804.8-keV transition with the 949.9-keV  $\gamma$  ray. A placement of the 2804.8-keV  $\gamma$  ray on top of the 2120-keV level (see Ref. [20]) would require to see a clear coincidence with the 450.8-keV  $\gamma$  ray because of the much higher relative intensity compared to the 949.9-keV transition. The 949.9-keV transition is a doublet, as already proposed in Ref. [20]. Only when assuming that the 949.9-keV transition is a doublet, the coincidence information can be explained. One transition connects the 2120-keV level with the level at 1170 keV and an additional transition is placed in a cascade with the 2804.8-keV transition to the g.s.

The level scheme of  $^{130}\text{In}$ , as it was deduced from the experimental information in the present experiment, is shown in Fig. 3.19. From the intensity balance of the transitions

Level [keV]	$I_\beta$ [%]	$I_{\beta,lit}$ [%]	$\log ft$	$\log ft_{lit}$
0	$\sim 6$	$\sim 5$ [2, 20, 124, 125]	$\sim 5.7$	$\sim 5.8$ [2, 20], 5.9 [124, 125]
388	$< 0.5$	$< 1.2$ [20]	$> 6.3$	$> 6.3$ [20]
1016	2.6(4)	-	5.9(1)	-
1170	1.3(13)	$< 0.7$ [2], 0.9 [20], 5.3 [124, 125]	6.2(5)	$> 6.3$ [2, 20], 5.5 [124, 125]
1669	$< 1.9$	5.8 [2], $< 6.1$ [20], 3.2 [124, 125]	$> 5.7$	5.3 [2, 20], 5.6 [124, 125]
2120	73.4(31)	70.2 [2, 20], 69.4 [124, 125]	4.0(1)	4.1 [2, 20] 4.2 [124, 125]
2805	$< 0.9$	-	$> 5.6$	-
3755	0.9(5)	-	5.3(3)	-
3967	$\sim 0$	-	-	-
4044	2.1(3)	-	4.8(1)	-
4066	0.6(1)	-	5.3(1)	-
4196	2.6(3)	-	4.6(2)	-
4281	0.3(1)	-	5.5(2)	-
5229	0.3(1)	-	5.0(2)	-
5286	0.3(1)	-	5.0(2)	-
5393	0.6(1)	0.9 [2]	4.6(2)	4.9 [2]

**Table 3.7:** Levels in  $^{130}\text{In}$  populated in the  $\beta$ -decay of  $^{130}\text{Cd}$  with the observed  $\beta$ -feeding and the  $\log ft$  value. For details see text and the corresponding literature values taken from reference [2, 20].

feeding and de-exciting the levels the  $\beta$ -feeding can be deduced assuming that no competing decay modes (e.g. internal conversion) play a significant role. The results are presented in Table 3.7 together with the  $\log ft$  values and literature values. In that table it is clearly shown that the majority of the  $\beta$  feeding proceeds to the level at 2120 keV. The feeding of 73.4(31)% measured in the present experiment agrees within the error bars with the literature value. The only level for which a difference to the literature values is observed is the 1669 keV one. This can be explained by the very similar relative intensities of the 450.8- and 1669.2-keV transitions, in contrast to observations made in Ref. [20]. The  $\log ft$  values (see Table 3.7) were calculated using the  $Q_\beta$  value of  $8344^{(+165)}_{(-157)}$  keV taken from Ref. [20] and the half-life as it was obtained in the present work.

### 3.3.2 Conclusions

The level scheme presented in this work shows several new states in the region above the  $1^+$  state at 2120 keV with all of them having rather low  $\log ft$  values, suggesting that they are fed by either a Gamow-Teller or a fast first-forbidden transition. The most stunning observation though is the presence of levels above the neutron separation energy of 5120(40) keV [1]. The population of levels above the neutron separation energy, which then decay to lower lying levels in  $^{130}\text{In}$  via  $\gamma$  transitions, was already reported in Ref.

[2] and is confirmed in our data. For those states the emission of a neutron must be hindered due to angular momentum selection rules, making it possible for the  $\gamma$ -transition to compete with the neutron emission.

The  $1^+$  state at 2120 keV is predicted to have the configuration  $\pi g_{9/2}^{-1}\nu g_{7/2}^{-1}$ , while the states above 4.4 MeV were assigned to have a  $\pi g_{9/2}\nu g_{7/2}$  four-quasi-particle (4QP) nature in Ref. [20] based on QRPA calculations. Similar to the observations in that work the measured feedings in the present experiment to levels below two MeV all have  $\log ft$  values suggesting a first forbidden non-unique transition. The assignment of spins and parities to those levels is therefore not changed in the present experiment and based on the same arguments the level at 1016 keV is tentatively given spin and parity of  $(0, 1^-)$ .

### 3.4 The $\beta$ decay of $^{131}\text{Cd}$ and $\beta$ -delayed n emission from $^{132}\text{Cd}$

One of the goals of this experiment was to obtain new information about the nuclear structure of the neutron-rich Indium isotopes, and of special interest is the nucleus  $^{131}\text{In}$  with only one proton less than the doubly-magic  $^{132}\text{Sn}$ . It has a magic neutron number ( $N=82$ ) and because of that is the perfect candidate to determine the proton single hole energies [41, 47], with the last measurement placing the  $(1/2^-)$  state at an excitation energy of 365(8) keV. The nucleus  $^{131}\text{In}$  has been subject of several studies prior to this work, and the decays of the g.s. with spin and parity  $(9/2^+)$  and the  $(1/2^-)$   $\beta$ -decaying isomer were studied in detail in Refs. [39, 40, 117]. Nevertheless, the information about excited states in  $^{131}\text{In}$  was scarce previous to this work.

Fogelberg *et al.* [39, 40] identified a  $\beta$ -decaying isomer with tentatively assigned spin and parity of  $(21/2^+)$ , and Górska *et al.* [9] showed the presence of a  $(17/2^+)$  core-excited isomer at an excitation energy of 3782 keV. The first observation of transitions populated after the  $\beta$ -decay of  $^{131}\text{Cd}$  was made in Ref. [62], where the observation of several transitions was reported and two transitions with energies of 988 and 2428 keV were tentatively placed as the transitions between the  $p_{3/2}$  and  $p_{1/2}$ , and  $f_{5/2}$  and  $p_{1/2}$  single proton hole states, respectively. In the following the results obtained in the  $\beta$  decay of  $^{131}\text{Cd}$  and after  $\beta$ -delayed neutron emission from  $^{132}\text{Cd}$  are presented, with both decays populating excited states in  $^{131}\text{In}$ .

#### 3.4.1 Transitions observed in the $\beta$ decay of $^{131}\text{Cd}$

In the present experiment  $1.8 \times 10^5$   $^{131}\text{Cd}$  ions were identified and implanted in the active stopper. More than 30 peaks are observed in the spectrum shown in Fig. 3.20, presenting the germanium spectrum recorded in prompt coincidence with the first decay correlated to the implanted  $^{131}\text{Cd}$  ions with a maximum time window of 200 ms between the implantation and the decay. To clean the spectrum, only events are taken where the decay is detected in the same DSSSD than implantation and within a maximum position difference

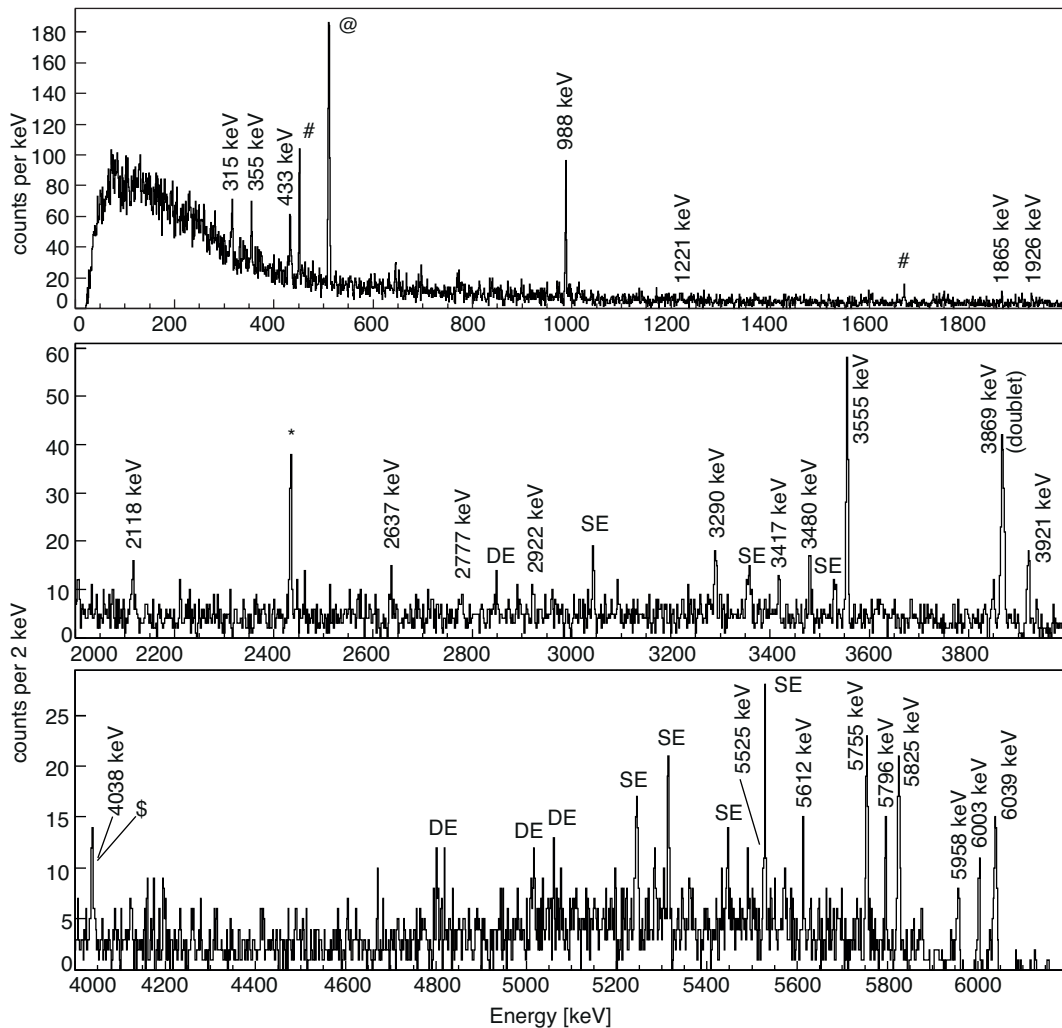


**Figure 3.20:** Ge spectrum in prompt coincidence with the first decay of the implanted  $^{131}\text{Cd}$  ions requiring  $\Delta x$  and  $\Delta y$  to be smaller than 1 mm and the implantation and decay event being detected in the same DSSSD within a maximum time difference of 200 ms. Transitions labelled with symbols correspond to known transitions in  $^{131}\text{Sn}$  (\*), populated in the  $\beta$  decay of the daughter nucleus, in  $^{130}\text{In}$  (#), populated after the  $\beta$ -delayed neutron emission, in  $^{132}\text{Sn}$  (\$) due to false correlated  $\beta$  decays. Single escape peaks are marked with (SE), double escape peaks with (DE) and the peak at 511 keV (@) arises from the annihilation of positrons created in pair production in the germanium detectors.

of 1 mm in x- and y-direction.

Transitions in the granddaughter nucleus  $^{131}\text{Sn}$  (\*), populated through the decay of the daughter  $^{131}\text{In}$ , are present in the spectrum and furthermore, transitions in  $^{130}\text{In}$  (#) can be identified. The latter ones have probably been populated through  $\beta$ -delayed neutron emission. Last but not least, transitions are observed in  $^{132}\text{Sn}$  (\$) whose origin has been discussed in detail in section 3.1.5.

As in the previous cases the 511-keV peak (@) arises from the annihilation of positrons which have been created in pair production of high energy  $\gamma$  rays leading also to single and double escape peaks in the decay spectrum especially for energies above 3 MeV. Two tests were performed to verify if specific lines are arising from the escape of one or

$E_\gamma$ [keV]	$E_{\gamma,ph}$ [keV]	$counts_\gamma$	$counts_{\gamma,AB}$	$R_{noAB,AB}$ [%]
2533 (DE)	3555	-	-	-
2847 (DE)	3869	6(3)	6(3)	100(71)
3044 (SE)	3555	12(4)	11(4)	92(45)
3358 (SE)	3869	9(3)	7(2)	78(34)
4803 (DE)	5825	16(4)	14(4)	88(33)
4982 (DE)	6003	6(2)	5(2)	83(43)
5017 (DE)	6039	7(3)	6(2)	86(47)
5244 (SE)	5755	30(6)	26(6)	87(26)
5285 (SE)	5796	-	-	-
5314 (SE)	5825	22(6)	20(5)	91(34)
5447 (SE)	5958	15(4)	11(3)	73(28)

**Table 3.8:** Energies, number of counts in the peaks with ( $counts_{\gamma,AB}$ ) and without ( $counts_\gamma$ ) add-back and the ratio between those two  $R_{noAB,AB} = \frac{counts_{\gamma,AB}}{counts_\gamma}$  for all peaks identified as single (SE) or double escape (DE) peaks in the spectrum shown in Fig. 3.20. The corresponding photo peak energy  $E_{\gamma,ph}$  is also stated.

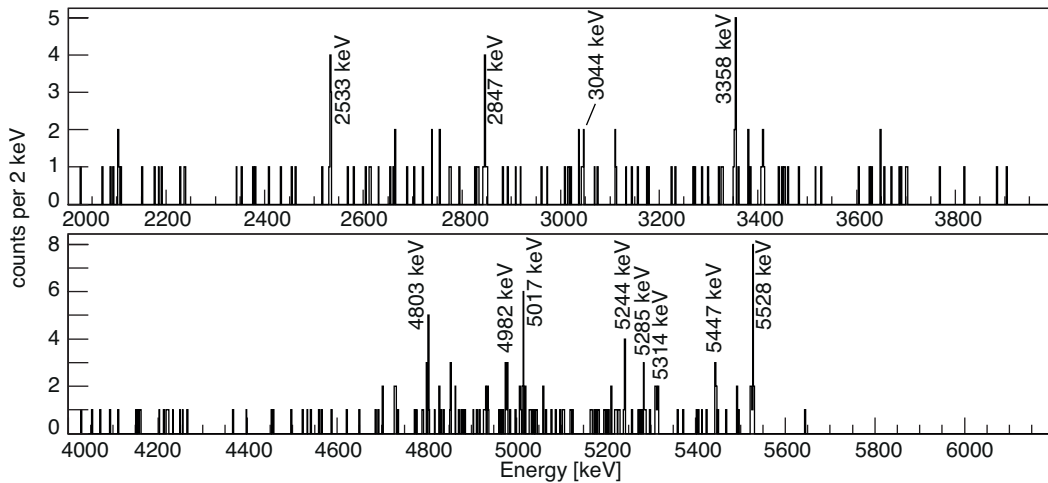


**Figure 3.21:** Germanium spectrum in prompt coincidence with the observation of a 511 keV energy deposition in the germanium detectors after the decay of  $^{131}\text{Cd}$ . The spectrum is just filled for those cases where the two energy depositions are observed in neighbouring crystals in one cluster and no cuts were applied on the position difference between implantation and decay.

two positrons. In the first test the number of counts for each peak with and without add-back were compared, because through the add-back procedure there is a certain chance to reconstruct the full photo peak energy by summing the energy deposited by positrons in one of the neighbouring crystals to the rest energy. Table 3.8 shows the number of counts in certain high energy peaks with and without add-back and the ratio between those two are stated. A general tendency can be observed that the number of counts decreases while for the case of photo-peaks an increase of counts was already presented before in section 2.3.2 where the absolute efficiency of the array was discussed.

A final conclusion about the assignment, if certain peaks are single- or double escape peaks based on the before presented results, cannot be made taking into account the

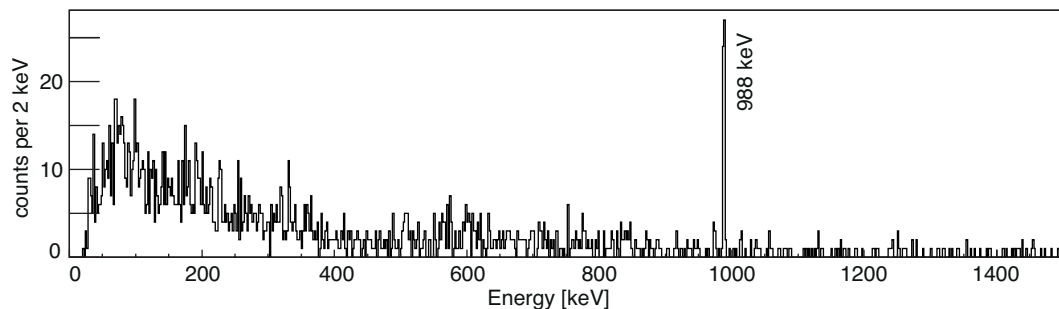


**Figure 3.22:** Ge spectrum in prompt coincidence with the first decay of the implanted  $^{132}\text{Cd}$  ions requiring  $\Delta x$  and  $\Delta y$  to be smaller than 1 mm and the implantation and decay event being detected in the same DSSSD within a maximum time difference of 200 ms.

large error bars of the fitted relative intensities. The very limited statistics, especially for the high energy  $\gamma$  rays, make it impossible to reduce this error bar. Therefore, a second test was performed for which a  $\gamma$ - $\gamma$  coincidence spectrum (see Fig. 3.21) was generated gating on the 511 keV peak in the decay spectrum and only filling the energy of crystals which are direct neighbours to the crystal where the 511 keV were detected. As expected, several peaks are visible in this spectrum at the positions of the predicted single and double escape peaks. A list of all peaks which have been assigned based on those results to be single and double escape peaks is given in Table 3.8.

Eliminating the peaks most likely related to background and single/double escape peaks, a total of 24 transitions remains and those are assigned to the  $\beta$ -decay of  $^{131}\text{Cd}$  to  $^{131}\text{In}$ . The strongest lower energetic transition observed in the present experiment has an energy of 987.9 keV, which is consistent with the observations made in Ref. [62].

Before the transitions observed in the decay of  $^{131}\text{Cd}$  to  $^{131}\text{In}$  and their placement in a level scheme are discussed in detail, a first look is now taken at the decay of  $^{132}\text{Cd}$ .

### 3.4.2 Transitions observed after $\beta$ -delayed neutron emissions of $^{132}\text{Cd}$

Hannawald *et al.* [34] measured a half-life of 97(10) ms and a neutron emission probability of 60% for the  $\beta$ -decay of  $^{132}\text{Cd}$ . Because of this high neutron emission probability it was expected to observe transitions in coincidence with the decay of  $^{132}\text{Cd}$  in both  $^{131}\text{In}$  and  $^{132}\text{In}$ . In the present experiment an even higher  $P_n$  value of  $\geq 88(3)\%$  was measured, as it will be explained in detail in section 4.3.

Approximately 16300  $^{132}\text{Cd}$  ions were identified in BigRIPS and implanted in WAS3ABi. The germanium spectrum of the  $\gamma$  rays which were observed in coincidence with the first decay of the  $^{132}\text{Cd}$  ions within a maximum time window of 200 ms after the  $\beta$ -decay is shown in Fig. 3.22. In that spectrum one observes only two transitions with the stronger of those two having an energy of 988 keV. It is suggested that this is the same transition as observed in the decay of  $^{131}\text{Cd}$ , but now being populated through  $\beta$ -delayed neutron emission of  $^{132}\text{Cd}$ . One additional line is visible at 331 keV and is assigned to the  $\beta$ -decay

of the  $\beta$ -n daughter nucleus  $^{131}\text{In}$ . The spectrum shown in Fig. 3.22 was produced using the same conditions as for the  $^{131}\text{Cd}$  decay spectra presented before.

### 3.4.3 The level scheme of $^{131}\text{In}$

In Ref. [9] it was presented that the lowest core-excited three-particle state in  $^{131}\text{In}$  are predicted to lie above 3.5 MeV and in Ref. [34] those 3QP states were predicted to be at approximately 3.5, 5 and 5.8 MeV. Below 3.5 MeV exactly three single particle states are expected, namely the proton  $p_{1/2}$ ,  $p_{3/2}$  and  $f_{5/2}$  single particle states. The position of the  $(1/2^-)$   $\beta$ -decaying isomer is well established, while information for the other single particle states is still missing. The positions of the  $3/2^-$  and  $5/2^-$  single particle states are essential ingredients for shell model calculations in this region and because of that, focus is now set first on the placement of the strongest transition with an energy of 987.9 keV. In Ref. [62] it was speculated to place this transition between the  $(3/2^-)$  and  $(1/2^-)$  single particle states.

#### 3.4.3.1 The placement of the 987.9-keV transition

The observations made in the current dataset confirm the placement of the 987.9-keV transition, mainly because the 987.9-keV transition is observed in both, the  $\beta$  decay of  $^{131}\text{Cd}$  and after  $\beta$ -delayed neutron emission of  $^{132}\text{Cd}$ . In Ref. [34] the authors have presented results showing that in the decay of  $^{132}\text{Cd}$  to the states above the neutron separation energy in  $^{132}\text{In}$  the majority of the  $\beta$  strength proceeds to levels between 5 to 5.9 MeV. With  $Q_\beta = 12.7(3)$  MeV and  $Q_{\beta,n} = 9.7(2)$  MeV [1] mainly only levels below the 3QP states in  $^{131}\text{In}$  can be populated after  $\beta$ -delayed neutron emission of  $^{132}\text{Cd}$ , namely the g.s. or the  $1/2^-$ ,  $3/2^-$  or  $5/2^-$  single particle states. Because the 987.9-keV transition is also observed after  $\beta$ -delayed neutron emission, it has to be placed in between the single particles states. The argumentation presented here in the following for the placement of the 987.9-keV transition is based upon the publications J. Taprogge *et al.* [127, 128].

From angular momentum selection rules a decay branch from the  $(3/2^-)$  or  $(5/2^-)$  state to the  $(9/2^+)$  g.s. is very unlikely and the 987.9-keV transition therefore has to be placed on top of the  $(1/2^-)$  state. This new established state at 1353 keV is now either the  $3/2^-$  or the  $5/2^-$  state. It has to be noted here that an assignment only taking into account the experimental information is not possible but there are especially two arguments which strongly support the placement of the 987.9-keV transition on top of the  $(1/2^-)$   $\beta$ -decaying state with a spin assignment of  $(3/2^-)$  to the newly established state at 1353 keV.

The first argument is that by looking at the experimentally determined energies of the  $0f_{5/2}$ ,  $0g_{7/2}$ ,  $0h_{9/2}$  orbits in comparison to the respective  $1p$ ,  $1d$  and  $1f$  spin-orbit partner orbitals in the vicinity of  $^{78}\text{Ni}$ ,  $^{132}\text{Sn}$  and  $^{208}\text{Pb}$ , one can observe that in none of the cases the  $0f_{5/2}$ ,  $0g_{7/2}$ ,  $0h_{9/2}$  orbits interloop with the spin-orbit partner orbitals, respec-

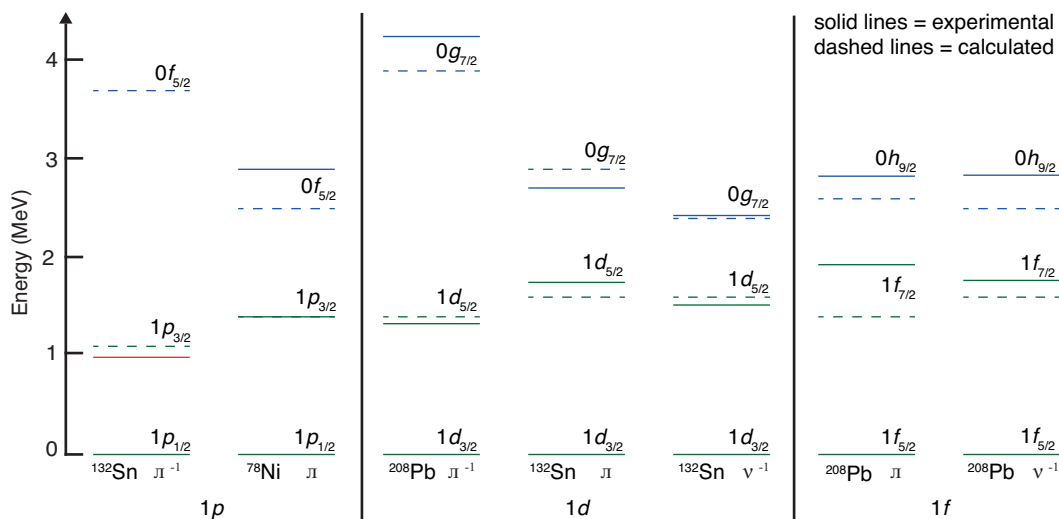


**Figure 3.23:** Systematics of experimental (solid lines) and calculated (dashed lines) energies of the  $0f_{5/2}$ ,  $0g_{7/2}$ ,  $0h_{9/2}$  orbits with respect to the corresponding  $1p$ ,  $1d$  and  $1f$  spin-orbit partner orbitals in the vicinity of  $^{78}\text{Ni}$ ,  $^{132}\text{Sn}$  and  $^{208}\text{Pb}$ . The energies are nominated to the energy of the lower lying spin-orbit partner. The position of the new state which lies at 988 keV above the  $1p_{3/2}$  is marked as a solid red line. The experimental and calculated values are taken from Ref. [129].

tively. Fig. 3.23 shows these systematics based on the experimentally determined values and additionally includes theoretical predictions for the positions [129]. The energies in the figure are nominated to the energy of the energetically lower one of the respective spin-orbit partner orbitals and it becomes clear that for the experimental values the  $0f_{5/2}$ ,  $0g_{7/2}$ ,  $0h_{9/2}$  orbits never come even closer than 900 keV to the respective  $1p$ ,  $1d$  and  $1f$  spin-orbit partner orbitals. The theoretical values are taken from Ref. [129], where a fitted nuclear Hamiltonian was employed to predict the positions of those orbitals. In all cases a very good agreement between the theoretical predictions and the experimental determined values is observed. This directly introduces the second argument to favour an assignment of spin and parity ( $3/2^-$ ) to the state at 1353 keV. In those calculations the position of the  $p_{3/2}$  orbital was predicted at 1.1 MeV above the  $p_{1/2}$  spin-orbit partner while the  $f_{5/2}$  orbital was placed 2.6 MeV higher. Taking into account that the new state is only 988 keV above the ( $1/2^-$ ) state, the 1353-keV level is preliminary given an assignment of ( $3/2^-$ ).

### 3.4.3.2 Placing the remaining transitions in a level scheme

The observed high energetic transitions above 5.9 MeV are expected to be placed as ground state transitions because the neutron separation energy is experimentally known to be 6210(40) keV (Ref. [1]). A placement of those feeding the ( $1/2^-$ ) state is unlikely because first of all, the energy would be higher than the neutron separation energy. Second of all, those high energy states are expected to have spins of  $5/2$ ,  $7/2$  or  $9/2$  when taking into account only Gamow-Teller and first forbidden non-unique  $\beta$  decays from the

$E_\gamma$ [keV]	$I_\gamma^{rel}$ [%]	$I_\gamma^{Decay}$ [%]	$E_i$ [keV]	$E_f$ [keV]
315.0	25(12)	2.2(1.0)	3869	3555
355.0*	12(4)	1.1(4)		
433.2	27(7)	2.4(6)	5958	5525
451*	11(5)	1.0(5)		
987.9	100(14)	8.8(16)	1353	365
1221.0*	29(8)	2.6(7)	(2574)	(1353)
1864.9*	16(5)	1.4(5)		
1925.9*	14(5)	1.2(5)		
2004.7*	18(5)	1.6(5)		
2117.8*	17(5)	1.5(4)		
2636.7	7(3)	0.6(2)	3990	1353
2776.8	12(3)	1.0(5)	4130	1353
2922.0*	11(4)	1.0(3)		
3290.1	26(8)	2.3(7)	4644	1353
3417.0	8(4)	0.7(4)	4770	1353
3480.0	33(7)	2.9(6)	3480	0
3555.2	98(13)	8.6(12)	3555	0
3868.8#	115(15)	10.1(13)	3869	0
3920.6	46(11)	4.1(9)	3921	0
4038.0	36(13)	3.2(11)	4038	0
5525.0	29(7)	2.5(6)	5525	0
5612.0	13(4)	1.1(3)	5612	0
5754.7	64(12)	5.6(11)	5755	0
5796.0	29(7)	2.5(6)	5796	0
5824.7	87(16)	7.7(14)	5825	0
5958.3	25(7)	2.2(6)	5958	0
6002.8	33(11)	2.9(10)	6003	0
6039.2	63(16)	5.5(14)	6039	0

**Table 3.9:** Energies, relative intensities and absolute intensities per parents decays of the transitions observed in the decay of  $^{131}\text{Cd}$  to  $^{131}\text{In}$ . The energy of the initial and final states are also stated based upon the level scheme discussed in this section. Transitions with a \* have not been placed in the level scheme and the transition marked with a # is a doublet.

$7/2^-$  ground-state of  $^{131}\text{Cd}$ . A  $\gamma$ -branch from those states to the  $(1/2^-)$   $\beta$ -decaying isomer is therefore less likely than to the g.s. Nevertheless, a placement of those transitions on top of the  $(1/2^-)$   $\beta$ -decaying isomer cannot be ruled out completely based on the experimental information.

The 3868.8-, 5612.0-, 5754.7-, 5796.0-, 5824.7-, 5958.3-, 6002.8- and 6039.2-keV transitions are all not observed in coincidence with other transitions and are placed, taking into account the previously mentioned arguments, as ground state transitions. If the 3868.8-keV transition would be feeding the  $3/2^-$  state, it should be seen in clear coincidence with the 987.9-keV transition due to the sufficient statistics, which is not the case. Also a feeding of the  $1/2^-$  state is unlikely due to the same angular momentum arguments used for the transitions around 6 MeV.

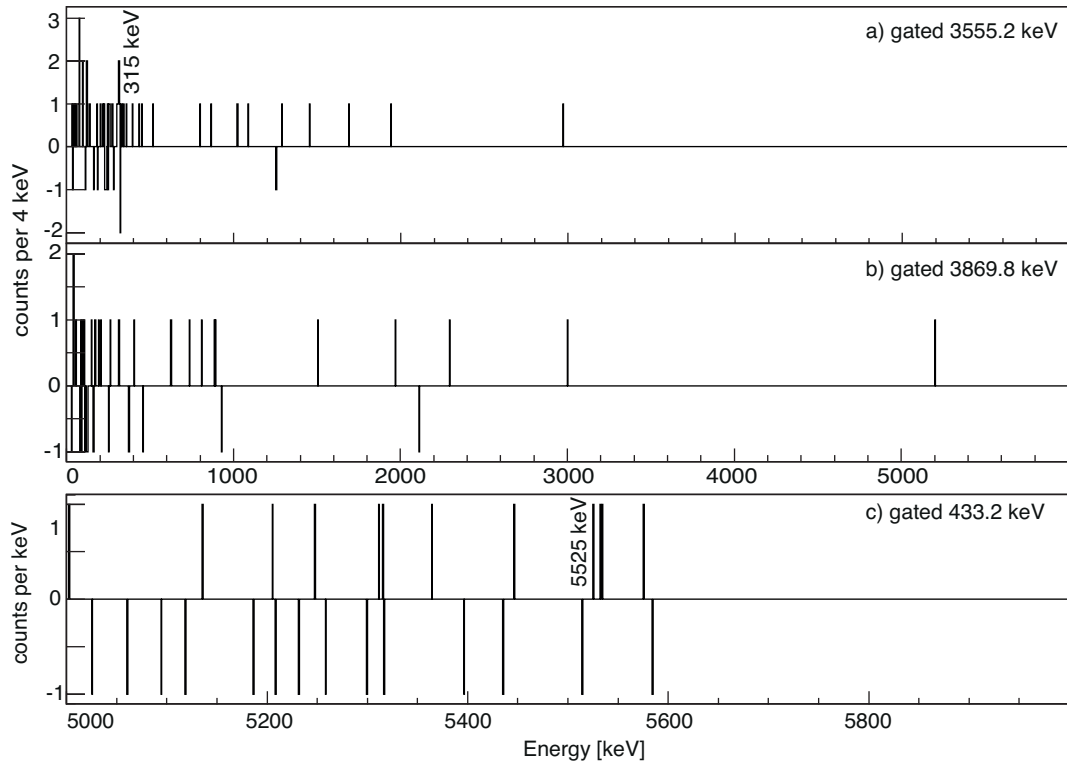


**Figure 3.24:** Germanium spectra observed in prompt coincidence with the a) 3555.2 keV, b) 3868.8 keV and c) 433.2-keV transitions observed in coincidence with the decay of the implanted  $^{131}\text{Cd}$  ions.

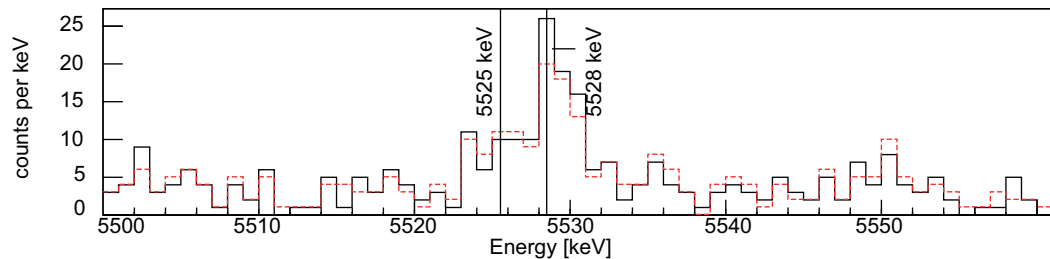


**Figure 3.25:** Comparison of the peak structure of the 5528 keV peak observed in the decay of  $^{131}\text{Cd}$  to  $^{131}\text{In}$  with no add-back (black solid) and with add-back (red dashed) applied.

The three lower energetic transitions with energies of 315.0, 355.0 and 433.2 keV are expected to be transitions within the different 3QP levels, especially because no additional levels are expected to lie close to the three SP states. Indeed the 315.0-keV  $\gamma$  ray is observed in prompt coincidence with the 3555.2-keV  $\gamma$  ray (see Fig. 3.24a)) and taking into account that their sum energy is 3869 keV, they are placed as a ground-state cascade parallel to the 3868.8-keV transition. The also very strong 3868.8-keV  $\gamma$  ray on the other hand is not observed in coincidence with any other transition as it is shown in Fig. 3.24b).

Investigating the  $\gamma - \gamma$ -coincidence spectrum of the 433.2-keV transition, shown in Fig. 3.24c), no clear coincidence can be found, so it can be noticed that there are two counts at an energy of about 5525 keV. The sum energy of these two transitions gives 6039.2 keV, which is also observed as the energy of a transition in this experiment. Before it was

mentioned that the peak at an energy of 5528 keV is associated with a single escape peak, though investigating this peak a bit more in detail (see Fig. 3.25) a large tail at the left side of this peak is observed which could arise from a second peak at 5525 keV. Comparing this double structure for the two cases with (red dashed line) and without (black solid line) add-back gives a clear hint that there is actually a photo peak at an energy of 5525 keV. While the peak at 5528 keV decreases when applying the add-back algorithm, the peak at 5525 keV increases slightly. Because of that, the latter transition is proposed to be placed, together with the 433.2-keV transition, as a ground-state cascade parallel to the 6039.2-keV one. The third low energetic transition with an energy of 355.0 keV is not observed in coincidence with any other transition in this experiment and the placement of it cannot be fixed based on the available experimental data.

The peak at 451 keV most likely is related to the strong 450.8-keV transition observed in the  $^{130}\text{Cd}$   $\beta$  decay. However, the intensity ratio between the 450.8-keV peak and the 1669.2-keV one is not in agreement with the observations made in the decay of  $^{130}\text{Cd}$ . And with the 1669.2-keV transition following the 450.8-keV one, there is no reason why the 451 keV peak has about a factor two more intensity. From this observation it is concluded that the 451 keV peak is very likely a doublet, and the observation of a transition with an energy of 451 keV in  $^{131}\text{In}$  is proposed. The intensity of this transition can be deduced from the intensity balance between the 450.8-keV and the 1669.2-keV transition, assigning the excessive intensity to the newly observed transition in  $^{131}\text{In}$ .

Of special interest is the feeding of the  $(3/2^-)$  state which is not expected to be populated directly via  $\beta$  decay in this experiment. Fig. 3.26 shows the  $\gamma$ - $\gamma$ -coincidence spectra gated on the 987.8-keV transition and for comparison also the prompt germanium spectrum. Several coincidences can be identified, although some of the coincidences are very weak and a false assignment of coincidences cannot be excluded. The transitions with energies of 1221.0, 1864.9, 1925.9, 2117.8, 2636.7, 2776.8, 3290.1 and 3417.0 keV are observed in prompt coincidence with the 987.8-keV transition and are proposed to feed the  $(3/2^-)$  state. All of those  $\gamma$  rays are not observed in coincidence with any other  $\gamma$  ray which suggests a placement directly on top of the  $3/2^-$  state. The 2636.7-, 2776.8-, 3290.1- and 3417.0-keV transitions are placed because of this coincidence argument on top of the  $3/2^-$  state depopulating 3QP states which are between 4 MeV and 4.7 MeV. Placing all of the transitions with energies between 1 to 2.5 MeV on top of the 1353-keV level would mean creating several new levels below 3.5 MeV, not in agreement with the prediction of no 3 QP states below 3.5 MeV. The placement of those is for the moment unclear and additional experimental data has to be collected to improve statistics in the  $\gamma$  -  $\gamma$  coincidence spectra to be able to place them unambiguously in the level scheme. The level scheme, as proposed in the present work, is shown in Fig. 3.27. In the figure the observation can be made that there are three well separated accumulations of levels above three MeV in the energy ranges of 3.5 to 4.2 MeV, 4.6 to 4.8 and 5.4 to 6.1 MeV.

Not taking into account the transitions, which could not be placed in the level scheme in this work, the  $\beta$ -decay feeding to the different states can be calculated from the intensity

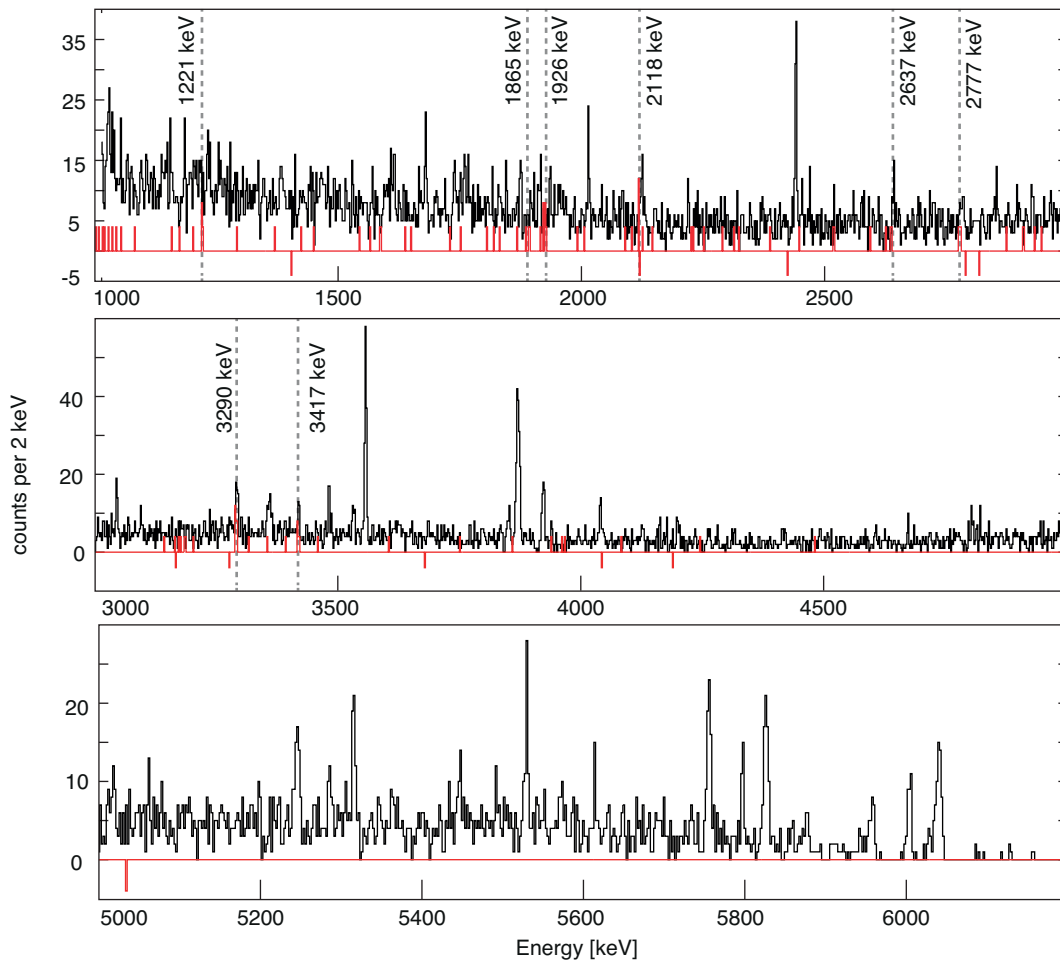


**Figure 3.26:**  $\gamma$ -spectrum (in black) in prompt coincidence with the first decay of the implanted  $^{131}\text{Cd}$  ions requiring  $\Delta x$  and  $\Delta y$  to be equal to 0 mm and the implantation and decay event being detected in the same DSSSD within a maximum time difference of 200 ms and  $\gamma$ -spectrum (in red) observed in prompt coincidence with the 987.8-keV transition in that decay.

balances. The results are summarized in Table 3.10 together with the  $\log ft$  values. While in that table the  $\beta$  feeding is shown for each transition individually, the  $\beta$  feeding which is shown in Fig. 3.27 was calculated for the states above three MeV as a sum of all feedings going to the 3QP states at approximately 5.8, 4.7 and 3.9 MeV, respectively. A feeding of 30(3) %, 3(1) % and 31(3)% was found for the states at about 5.8, 4.7 and 3.9 MeV, respectively.

The feeding to the g.s. can be calculated as the missing intensity when taking the sum of all observed  $\beta$  feedings together with the  $\beta$ -delayed neutron emission probability of  $P_n = 16(4)$  % and a value of 16(6) % is obtained. Nevertheless, this value needs to be treated with caution because of the Pandemonium effect [109] and the possibility of unobserved transitions with energies above 6.1 MeV, the upper detection limit of the Ge detectors in this experiment.

For the remaining four transitions, which are observed in prompt coincidence with the 987.8-keV transition, two possibilities are proposed. In the first scenario the transitions

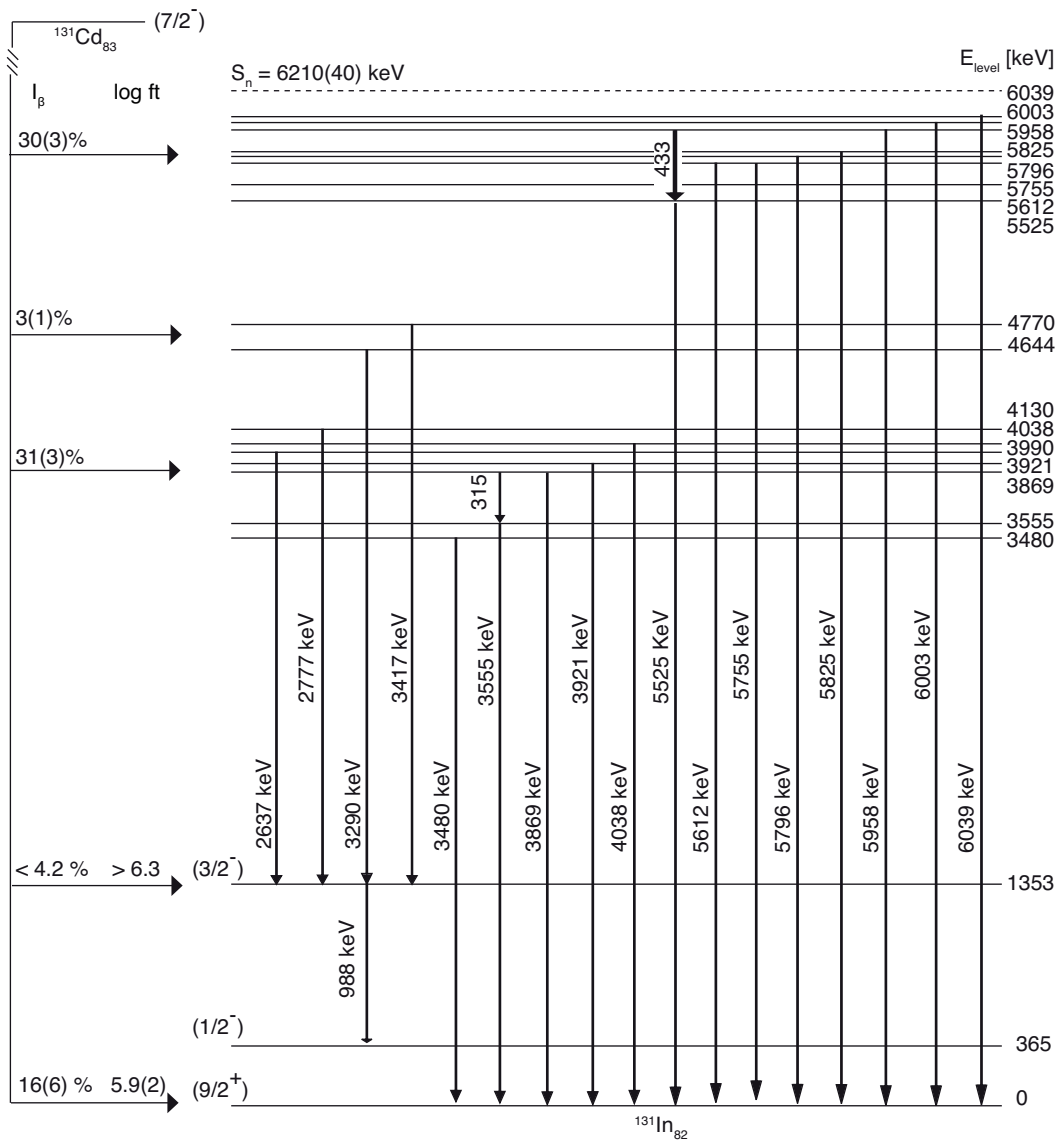


Figure 3.27: Level scheme of  $^{131}\text{In}$  as it has been obtained in the present work.

are placed directly on top of the  $(3/2^-)$  state. This scenario would result in several new states between 2.5 and 3.5 MeV and the summed relative intensity of all states feeding the  $(3/2^-)$  state would account to 129(16) %, slightly above the 100(14)% of the 987.8-keV transitions which de-excite the  $(3/2^-)$  state. An additional argument for another scenario is that the lowest core-excited three-particle states are expected to be above 3.5 MeV. Below the 3QP states only one additional SP state is expected. Therefore, in the second scenario the transitions are placed as linkers between the different 3QP states. Based on the energy difference the 1221-keV transition would start in the region around 5.8 MeV feeding one of the states around 4.7 MeV, and the remaining three transitions could be feeding the levels around 4 MeV also starting from the states around 5.8 MeV. Of course, those are just the two extreme scenarios and a mixture of both is also a valid possibility. From the available experimental data no final conclusion about the placement of these transitions can be made and it remains as an open question. Assuming the

Level [keV]	$I_\beta$ [%]	log $ft$	Level [keV]	$I_\beta$ [%]	log $ft$
0	16(6)	5.9(2)	4644	2.3(7)	5.9(2)
365	-	-	4770	0.7(4)	6.4(3)
1353	4.2(18)	6.3(2)	5525	<0.8	> 6.0
3480	2.9(6)	6.1(1)	5612	1.1(7)	6.0(3)
3555	6.5(15)	5.7(1)	5755	5.6(10)	5.2(1)
3869	12.3(16)	5.3(1)	5796	2.5(6)	5.6(1)
3921	4.1(9)	5.8(1)	5825	7.7(14)	5.1(1)
3990	0.6(2)	6.3(1)	5958	4.6(9)	5.2(1)
4038	3.2(11)	5.9(2)	6003	2.9(6)	5.4(1)
4130	1.0(5)	6.4(2)	6039	5.5(4)	5.2(1)

**Table 3.10:** Level energies and the feeding and log  $ft$  value as observed in the present dataset in the  $\beta$ -decay of  $^{131}\text{Cd}$  to  $^{131}\text{In}$ . The feeding has been calculated from the intensity balance of transitions feeding and deexciting certain states and the log  $ft$  value was calculated with a half-life value of 100(2) ms, obtained in the present work, and a Q-value of 12.7(3) MeV from Ref. [1].

unplaced transitions would be placed as described in scenario two, then the feeding of the states at 5.8 MeV would be higher while the feeding for the two other 3QP states would be relatively lower. However, it would not change the feeding in a significant way and also not alter the conclusions in the following.

### 3.4.3.3 Discussion: The structure of $^{131}\text{In}$

The decay of  $^{131,132}\text{Cd}$  was discussed in detail in this thesis and a first level scheme of  $^{131}\text{In}$  was produced, showing the position of the  $p_{3/2}$  proton-hole state and several levels in the region between three to six MeV. In a next step those results are now being discussed taking into account systematics in the  $^{132}\text{Sn}$  region and are furthermore compared to model calculations done in the work of Hannawald *et al.* [34]. They used quasi-particle random-phase approximation (QRPA) calculations with SP energies and wavefunctions from a folded Yukawa potential together with a Lipkin-Nogami microscopic pairing model [69, 130] to calculate the basic properties of the  $\beta$ -decay, namely the half-live  $T_{1/2}$  and the delayed-neutron emission probability  $P_n$ , to compare it with their experimentally deduced values. The basic input parameters are the  $Q_\beta$  and  $S_n$ , and were taken from the ETFSI-Q [131] and the FRDM model [28, 58], respectively. A modified QRPA model, with a 25%  $I^2$  reduction, was necessary in that work to reproduce the experimentally measured properties and it was furthermore concluded that the first-forbidden decays play a significant role for a good description. Fig. 3.28 shows the level scheme of  $^{131}\text{In}$  as it was obtained in the present work and includes furthermore the QRPA calculations for  $^{131}\text{In}$  of Ref. [34].

In the past the importance of the first forbidden decays in the different regions of the nuclear chart in the vicinity of  $^{132}\text{Sn}$  have been discussed in several publications. While Borzov *et al.* [67] predicted the influence to be small especially for  $N \leq 82$  and  $Z < 50$  and only for  $N > 82$  the DF3+CQRPA model showed significant smaller half-lives when

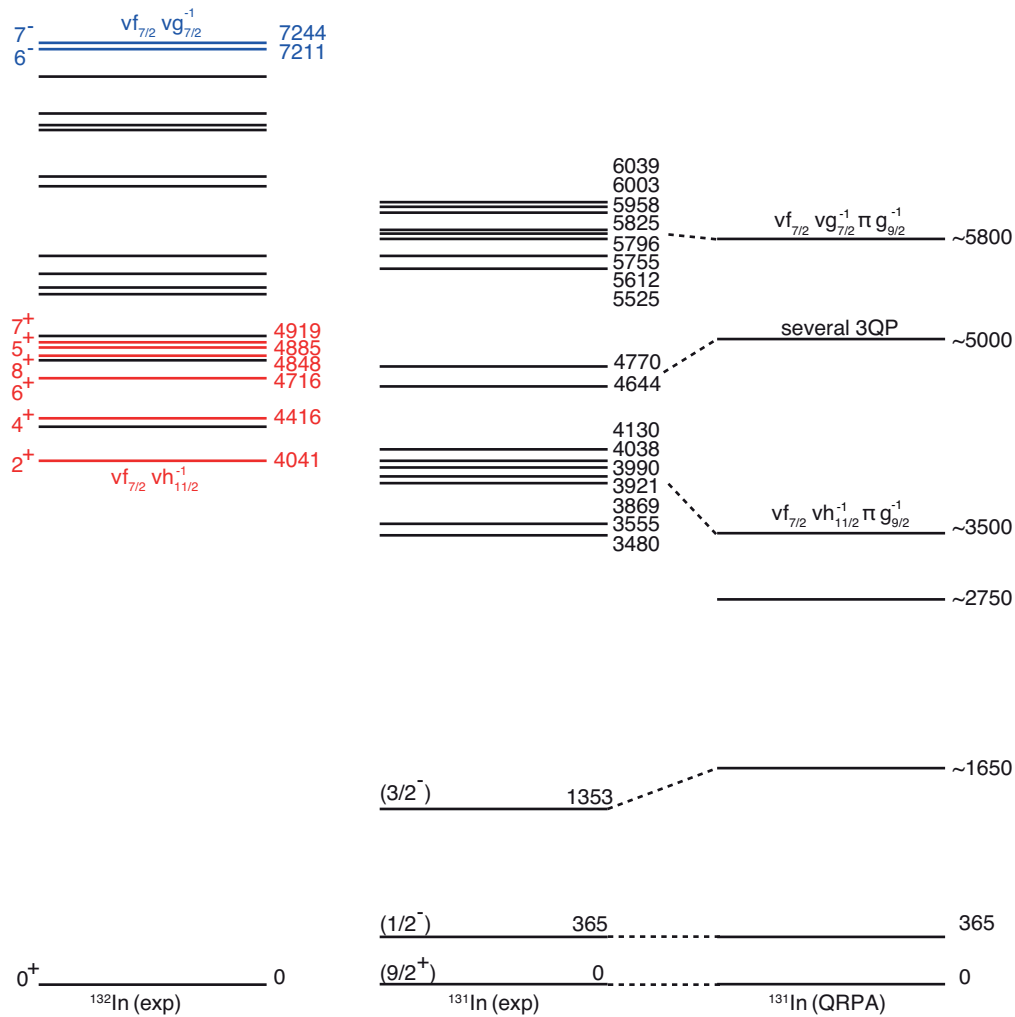


**Figure 3.28:** Experimental level schemes for  $^{131}\text{In}$  (this work) and  $^{132}\text{Sn}$  (Ref. [82]) and the QRPA calculations presented in Ref. [34] for  $^{131}\text{In}$ .

including the first forbidden decays, Möller *et al.* [63] mentions even for  $N \leq 82$  sizable influence of the ff decays. The latter of them used the Finite Range Droplet Model, one of the models commonly used for r-process calculations and therefore, the question if the models predict the contributions of first forbidden decays correctly becomes even more important. The decay from  $^{131}\text{Cd}$  to  $^{131}\text{In}$  is in any case a good test scenario to check to what extent the ff transitions affect the total half-life.

As it was introduced in section 1.4.4, the main GT branches in the  $^{132}\text{Sn}$  region are the  $\nu g_{7/2} \rightarrow \pi g_{9/2}$  and the  $\nu f_{7/2} \rightarrow \pi f_{5/2}$  ones, with the latter of them being most likely blocked due to the almost complete occupancy of the  $f_{5/2}$  shell. The  $\nu g_{7/2} \rightarrow \pi g_{9/2}$  GT decay proceeds in the  $^{132}\text{In}$  to  $^{132}\text{Sn}$  decay mainly to one level at 7211 keV which very certainly belongs to the  $\nu f_{7/2} g_{7/2}^{-1}$  multiplet [82]. The level scheme of  $^{132}\text{In}$ , as proposed in Ref. [82], is shown in Fig. 3.28 and the two states which have been assigned to the  $\nu f_{7/2} g_{7/2}^{-1}$  multiplet are shown in blue. With the experimental levels in  $^{131}\text{In}$  most likely arising from the coupling of a  $\pi g_{9/2}$  hole to the low lying excitations in the  $^{132}\text{Sn}$  core, suggestions can be made for the most probable configurations of the different level ac-

cumulations observed in  $^{131}\text{In}$ . The levels between 5.5 and 6 MeV are fed by about 30% of the  $\beta$ -decays and a different assignment than the  $\nu g_{7/2} \rightarrow \pi g_{9/2}$  transition seems unlikely. The corresponding states in the  $^{132}\text{Sn}$  core lie at around 7 MeV as mentioned before, and seem to be significantly lowered in  $^{131}\text{In}$ . Those levels are therefore preliminarily assigned to the  $\nu f_{7/2} g_{7/2}^{-1} \pi g_{9/2}^{-1}$  multiplet. Since they are fed by a GT transition the states should have spins in the range from 5/2 to 9/2 and negative parity. In the region several examples are known for  $\nu g_{7/2} \rightarrow \pi g_{9/2}$  GT decays and in most of the cases a log  $ft$  of about 4.4 was deduced [82, 119].

The lowest core states in  $^{132}\text{Sn}$  on the other hand can be found at excitation energies of about 4 MeV and those with positive parity were assigned to the  $\nu f_{7/2} h_{11/2}^{-1}$  multiplet (shown in Figure 3.28 in red). It is therefore quite likely that the lowest 3QP states in  $^{131}\text{In}$  are couplings of a  $\pi g_{9/2}$  hole to the  $2^+$  and  $4^+$  states in  $^{132}\text{Sn}$ . Those states are based on these systematic arguments proposed to have a  $\nu f_{7/2} h_{11/2}^{-1} \pi g_{9/2}^{-1}$  character, which is in good agreement with the observed feeding to those states. It is proposed that those states are fed by first forbidden transitions of the type  $\nu h_{11/2} \rightarrow \pi g_{9/2}$ .

The log  $ft$  for the ff decay of the type  $\nu f_{7/2} \rightarrow \pi g_{9/2}$ , representing the g.s. to g.s. transition, obtained in the present work is 5.9(2). Furthermore, for the states at 4644 and 4770 keV it is not possible to make suggestions for the most probable configurations, either from the experimental data or from systematics. The only conclusion to be drawn is that with the non negligible feeding everything else than a GT or ff decay is very unlikely.

Comparing the experimental results to the QRPA predictions made in Ref. [34] an overall very good agreement is found. In that work 3QP levels of configuration  $\nu f_{7/2} h_{11/2}^{-1} \pi g_{9/2}^{-1}$  are found at 3.5 MeV, having a log  $ft$  of 5.4. The levels at about 5 MeV are also not further characterized, it is only mentioned that several ff branches are responsible for the feeding resulting in a predicted log  $ft$  of 5.5. The levels with configuration  $\nu f_{7/2} g_{7/2}^{-1} \pi g_{9/2}^{-1}$  are predicted to lie at about 5.8 MeV with a log  $ft$  value of 4.6.

Concluding the results presented before, the importance of ff decays in the region  $N > 82$  and  $Z < 50$  can only be emphasized. It is suggested that 50(7)% of the  $\beta$ -feeding proceeds through first-forbidden decays, showing again that in the  $^{132}\text{Sn}$  region fast ff transitions have a non negligible influence on the  $\beta$ -decay properties, reducing the half-lives by a significant amount. The partial half-life for the first forbidden  $\beta$  decays of the  $(7/2^-)$  g.s. in  $^{131}\text{Cd}$  is calculated to be 200(7) ms with the  $\beta$  decay half-life  $T_{1/2} = 100(2)$  ms of the present work. The use of models without taking into account those branches for  $N > 82$  therefore has to be well justified.

### 3.5 Decay of $^{133}\text{Cd}$

Even though  $^{132}\text{In}$  has just one proton less and one additional neutron compared to the doubly-magic  $^{132}\text{Sn}$ , which has been experimentally studied in detail, the experimental information on  $^{132}\text{In}$  are very scarce. The ground-state spin and parity are known from

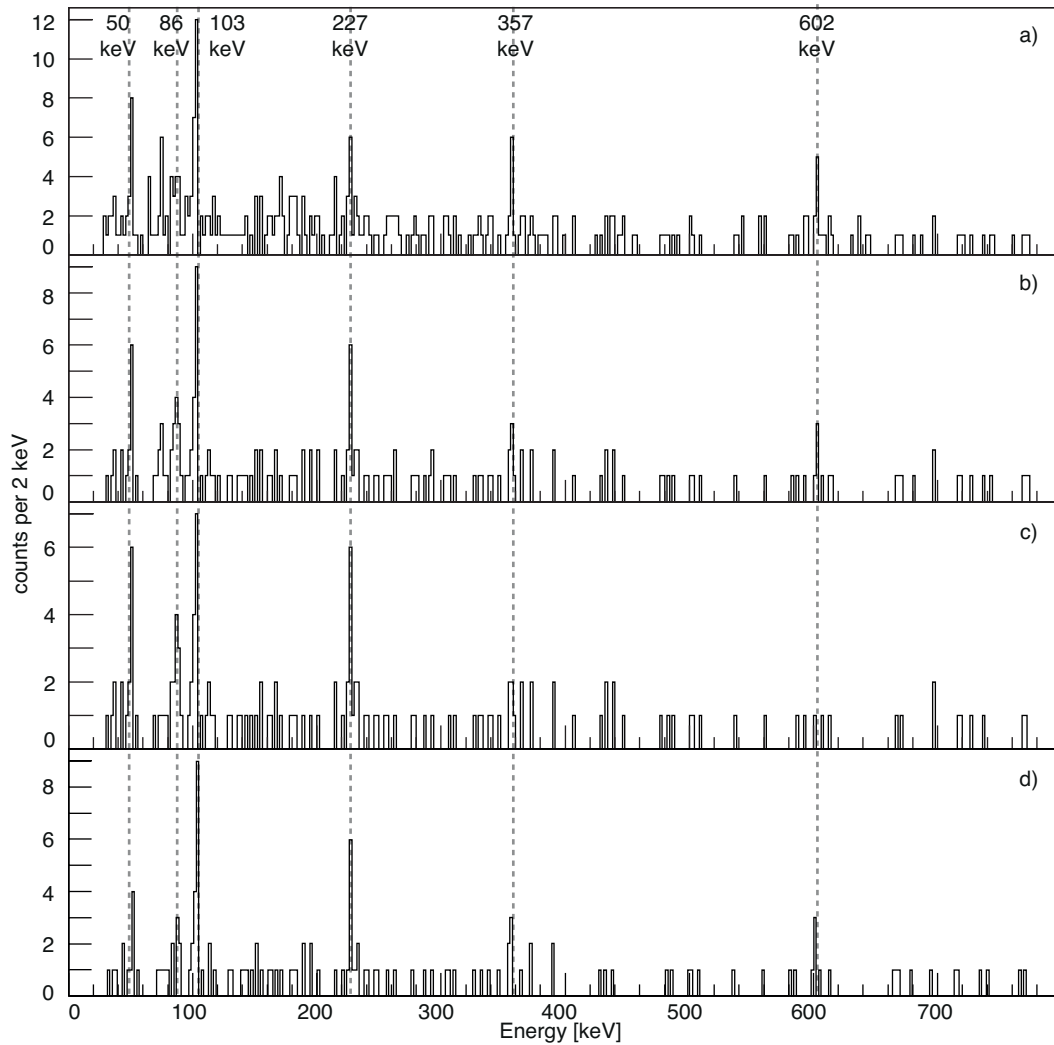


**Figure 3.29:** Ge spectrum in prompt coincidence with the first decay of the implanted  $^{133}\text{Cd}$  ions a) within a timewindow of 200 ms after the implantation, b) additional condition of only one crystal with an energy of 0-2000 keV per cluster, c) conditions of a)+b) with an additional condition that the implantation and decay events have to be in the same DSSD layer and d) conditions of a)+b) and limiting the difference between the implantation and decay pixel to be  $\leq 1$ .

experiments but no information about excited states has been available until now.

In section 4.3 results are going to be presented which show that in the present experiment the  $\beta$ -delayed neutron emission probability for the g.s. of  $^{132}\text{Cd}$  is 88(3)%, and for the g.s. of  $^{133}\text{Cd}$  a value compatible with 100%  $P_n$  was found. To obtain information about excited states in  $^{132}\text{In}$ , the choice is therefore not to investigate the  $\beta$ -decay of  $^{132}\text{Cd}$ , which was originally proposed for this experiment, but to use  $\beta$ -delayed neutron emission of  $^{133}\text{Cd}$ . As shown in section 3.4.2, the only transition observed after the  $\beta$ -decay of  $^{132}\text{Cd}$  was assigned to de-excite the  $(3/2^-)$  proton-single-hole state in  $^{131}\text{In}$ .

The spectrum presented in Fig. 3.29a) shows the germanium spectrum in prompt coincidence with the first decay after the implantation of a  $^{133}\text{Cd}$  ion within a time-window of 200 ms after the implantation. In the decay spectra several previously unknown transi-

$E_\gamma$ [keV]	counts	$I_\gamma^{rel}$ [%]	$\alpha_{th}$	$I_\gamma^{corr}$
50	14(4)	123(33)	3.75	584(157)
86	13(4)	57(16)	0.78	101(29)
102	25(5)	100(20)	0.48	148(30)
227	10(3)	44(14)	-	-
357	9(3)	48(16)	-	-
602	7(3)	49(19)	-	-

**Table 3.11:** Energies and relative intensities of the transitions observed in the decay of  $^{133}\text{Cd}$  to  $^{132}\text{In}$ . The theoretical conversion coefficients  $\alpha_{th}$  [99] are stated assuming M1 transitions and  $I_\gamma^{corr}$  are the relative intensities corrected for those conversion coefficients.

tions are observed with energies of 50, 103, 227, 357 and 602 keV, but especially the low energy part below 100 keV has a rather large background and an unambiguous identification of the transitions is not possible due to the low amount of  $^{133}\text{Cd}$  ions produced in this experiment. To reduce the background, and clean up the spectra several conditions were applied in the following spectra 3.29b) to d). In a first step the multiplicity of crystals which observe an energy between 0 to 2000 keV for each cluster was limited to one. Applying this condition, the background is clearly reduced (see Fig. 3.29b)). In that spectrum two potential transitions with energies of 75 and 86 keV are observed in addition to the previously mentioned ones. To clean up the spectrum even more, additional conditions are added to reduce the possibility of random coincidences with background events. Therefore, in Fig. 3.29c) the spectrum was generated with the additional condition that the DSSSD layer, where the implantation has been detected, has to be the same as the one in which the electron from the decay was detected ( $\Delta z = 0$ ). In this spectrum the possible transition with an energy of 75 keV disappears completely and only the 86-keV transition remains. The same behaviour can be observed when limiting the difference between the implantation and decay position obtained from the DSSSD to 1 mm ( $\Delta x, \Delta y < 1$ ) in x- and y-direction (see Fig. 3.29d)). To the five previously mentioned transitions, the 86-keV  $\gamma$  ray hence is added, so that in total six previously unknown transitions are identified in this work.

Although the statistics are very low some information can be obtained from the  $\gamma$ - $\gamma$  coincidence spectra gated on the six transitions and the spectra are shown in Fig. 3.30. There are hints for coincidences between the 86- and 357-keV transitions and also for a coincidence of the 103-keV transition with the 86-, 227- and 357-keV transitions. Unfortunately, a placement in a level-scheme is not possible based on the experimental results presented here. A summary of the energies, the counts in the peaks and the relative intensities  $I_\gamma^{rel}$  of the observed transitions is stated in Table 3.11. The low energy transitions are expected to have a M1 character if they belong to the  $\nu f_{7/2} \pi g_{9/2}^{-1}$  multiplet, as it will be discussed in the following. Table 3.11 therefore includes the theoretical conversion coefficients for a M1 transition calculated with the conversion coefficient calculator Bricc [99] and the relative intensities  $I_\gamma^{corr}$  corrected for those conversion coefficients.

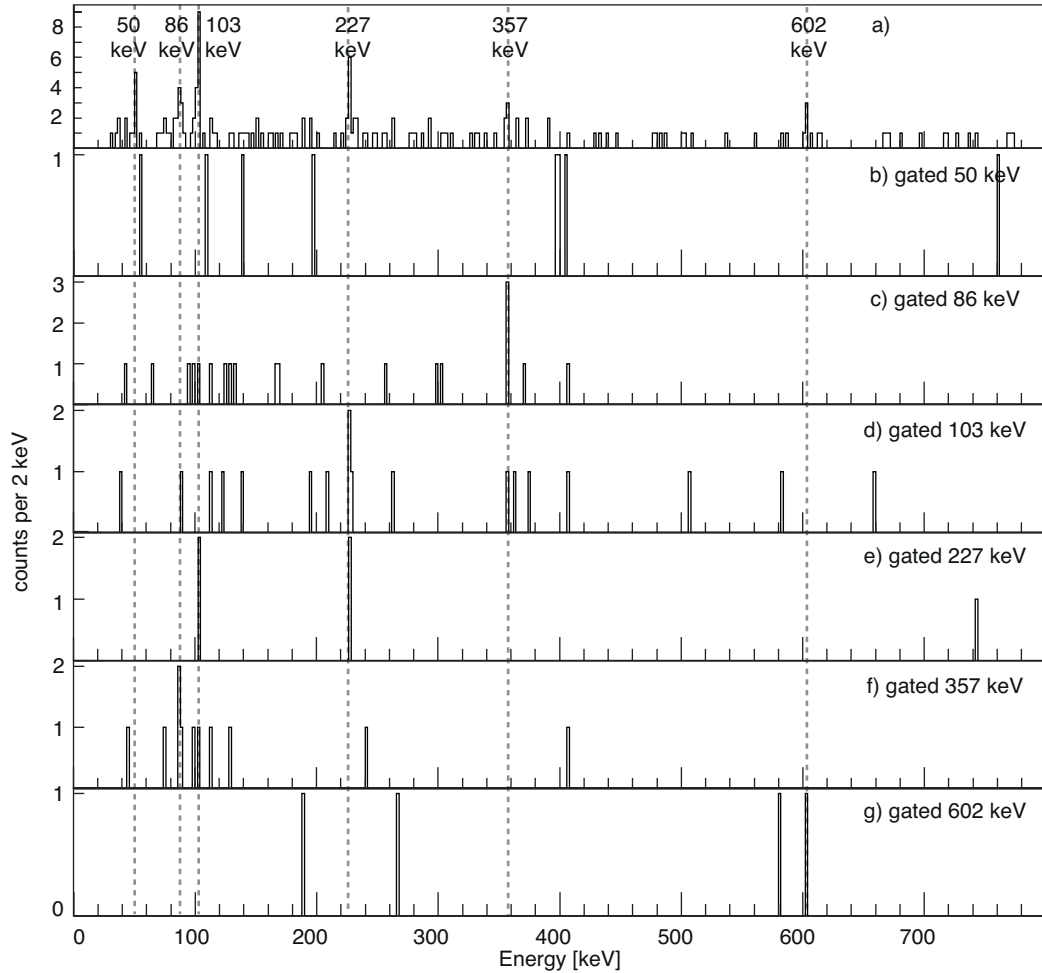


**Figure 3.30:** a) Ge spectrum in prompt coincidence with the first decay of the implanted  $^{133}\text{Cd}$  ions. b)-f)  $\gamma\gamma$  coincidence spectra gated on the 50-, 86-, 103-, 227-, 357- and 602-keV transitions with an open time condition applied.

### 3.5.1 Conclusions

The aim of measuring the decay to  $^{132}\text{In}$  was to observe for the first time the  $\nu f_{7/2}\pi g_{9/2}^{-1}$  multiplet. The  $7^-$  state was long ago proposed to be the lowest in that multiplet and would therefore most likely be the g.s. of  $^{132}\text{In}$  [81]. From the observations in Ref. [34] it was expected that in the decay of  $^{132}\text{Cd}$  about 40% of the intensity proceeds to mainly the  $1^-$  state of the  $\nu f_{7/2}\pi g_{9/2}^{-1}$  multiplet through a first forbidden  $\beta$  decay of the type  $\nu f_{7/2} \rightarrow \pi g_{9/2}$ . In that case the observation of transitions in the daughter nuclei would have very likely only come from the  $\nu f_{7/2}\pi g_{9/2}^{-1}$  multiplet, but from the results presented in the next chapter (section 4.3) it is concluded that the  $\beta$ -delayed neutron emission probability has to be higher than the suggested 60 % in the literature, and because of that no transitions in  $^{132}\text{In}$ , populated after the  $\beta$  decay of  $^{132}\text{Cd}$ , are observed. On the other hand  $^{133}\text{Cd}$  was measured to have a  $P_n$  value of 88(20)% (see section 4.3), but an assignment of transitions observed in that decay to the  $\nu f_{7/2}\pi g_{9/2}^{-1}$  multiplet is not possible based on the experimental observations. The transitions could very well be related to one of the other low lying proton-neutron particle-hole multiplets in that nuclei or transitions in between of

them. Those multiplets are e.g.  $\nu f_{7/2}\pi p_{1/2}^{-1}$ ,  $\nu p_{3/2}\pi g_{9/2}^{-1}$  and  $\nu p_{3/2}\pi p_{1/2}^{-1}$ .

The  $\nu f_{7/2}\pi g_{9/2}^{-1}$  multiplet is expected to be the energetically lowest lying one in  $^{132}\text{In}$  from systematics, and also the assignment of the  $7^-$  state to be the g.s. is very well justified by both experimental and theoretical evidences [81]. Several theoretical studies and experimental results show that in a proton-neutron particle-hole multiplet the states with angular momentum  $J = |j_p - j_h|$  and  $J = |j_p + j_h|$  are the highest ones in energies, while the states with either  $J = |j_p - j_h| + 1$  or  $J = |j_p + j_h| - 1$  are the lowest ones [132]. In the vicinity of doubly-magical nuclei several examples can be found to proof this. For example in  $^{90}\text{Nb}$  the  $(\nu g_{9/2}^{-1}\pi g_{9/2})$   $8^+$  state and in  $^{98}\text{Ag}$  the  $(\nu d_{5/2}\pi g_{9/2}^{-1})$   $6^+$  are found to be the lowest ones in their corresponding multiplets. Other examples can be found in the  $^{208}\text{Pb}$  region with the  $6^+$  state of the  $\nu f_{5/2}^{-1}\pi h_{9/2}$  multiplet having the lowest energy. The experimental results and shell-model calculations for these multiplets are summarized in Refs. [132–135].

The study of the  $\nu f_{7/2}\pi g_{9/2}^{-1}$  multiplet in  $^{132}\text{In}$  would be interesting in the sense that in the region south-east of  $^{132}\text{Sn}$  so far no experimental information is available for any proton-neutron particle-hole multiplet. The experimentally determined splitting in energy of the multiplet is a crucial test ground for the neutron-proton particle-hole interaction in that region and would allow to benchmark existing shell model calculations and their diagonal matrix elements of the effective interaction.



## Chapter 4

# Gross properties of $^{126-134}\text{Cd}$ $\beta$ decays

The data collected in the present  $\beta$ -decay experiment contains not only information from the  $\gamma$ -spectroscopy of the daughter nuclei, but it also allows to determine gross  $\beta$ -decay properties such as  $\beta$ -decay half-lives and neutron emission probabilities. These physical quantities provide important information on nuclear structure effects and changes in nuclear structure far from stability. Furthermore, they are essential  $\beta$ -decay inputs for r-process calculations.

In the following section the results obtained for the gross properties in the decay of  $^{126-134}\text{Cd}$  are presented and discussed in the context of nuclear structure changes and furthermore on the influence on r-process calculations. The first gross properties presented here are the  $\beta$ -decay half-lives, essential input for r-process calculations to determine e.g. the time-scale of the r-process to reach the heavy nuclei.

### 4.1 Analysis methods for $\beta$ -decay half-lives

In this section, the different analysis procedures employed to extract the  $\beta$ -decay half-lives of interest will be described. Since the time information is recorded on an event-by-event basis, half-lives are extracted by applying the delayed-coincidence technique. The decays observed in WAS3ABi, which have been correlated to a certain implantation, all have a time-stamp  $t_{Decay,ts}$ . Therefore, the actual decay time can be calculated as the difference of this value and the time-stamp which is associated with the implantation of the correlated ion  $t_{Imp,ts}$ .

$$t_{Decay}^i = t_{Decay,ts}^i - t_{Imp,ts} \quad (4.1)$$

The superscript  $i$  denotes here the index of the decay, where  $i = 1$  means the first decay correlated with the implanted ion after the implantation,  $i = 2$  the second one and so forth. Using these time-correlated spectra, it is then possible to determine the half-lives of interest.

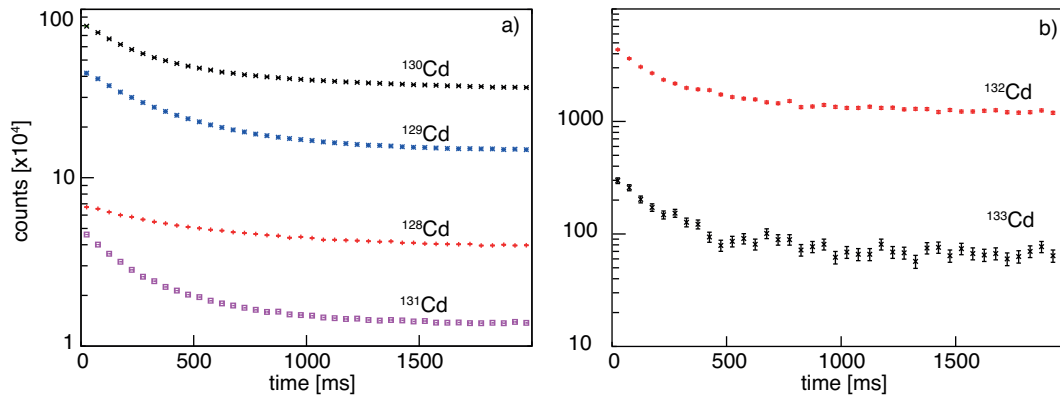


**Figure 4.1:** Time distributions of all decays correlated to the implanted a)  $^{128-131}\text{Cd}$  and b)  $^{132,133}\text{Cd}$  ions within a 2s interval after the implantation. No conditions have been applied on the position difference between the implanted ions and the correlated  $\beta$  decays.

It is worth noting that the experimental decay curves presented here include the time differences between the implantation of a given nucleus and all the beta particles registered in a close-lying pixel up to a maximum time interval of 5s. Since the selected time window for ion-beta correlations exceeds by far the expected half-lives of the nuclei under discussion, the subsequent generations of  $\beta$  decays also have to be taken into account in the fitting procedure. Figure 4.1 shows the time distributions for the Cadmium isotopes with masses  $A=128-133$ . It can be seen that the curves have different slopes due to the different half-lives of the corresponding  $\beta$  decays.

#### 4.1.1 Lifetime analysis: $\chi^2$ Fit with Bateman equations

The first method which is presented here is based upon fitting the decay-time curve containing the correlated times  $t_{Decay}^i$  from all decays which have been correlated to each implantation within a 5 seconds window via a  $\chi^2$  minimization [136]. The maximum number of decays correlated to one implantation was limited to thirty. Due to a high background rate, originating from e.g.  $\beta$  decays in surrounding pixels which are falsely correlated with the ion of interest, it was necessary to take this big amount of correlated decays per ion and it was not sufficient to limit the analysis to the first few decays.

The decay-time curve includes then the activity of the  $\beta$ -decay fission residues implanted in the WAS3ABi array and that of the  $\beta$ -decaying successors, provided that their half-lives are shorter or comparable to the maximum correlation time. The fitting function therefore has to account for the initial abundance of the mother nucleus  $N_0$ , its  $\beta$ -decay half-life, the half-lives of  $\beta$ -decaying successors and an appropriate background. Assuming that the background originates only from random correlations, a linear background function was chosen which described the data in all cases very well. Bateman [137] described the remaining amount of the n-th isotope  $N_n(t)$  with decay constant  $\lambda_n$  at a time  $t$  involved in

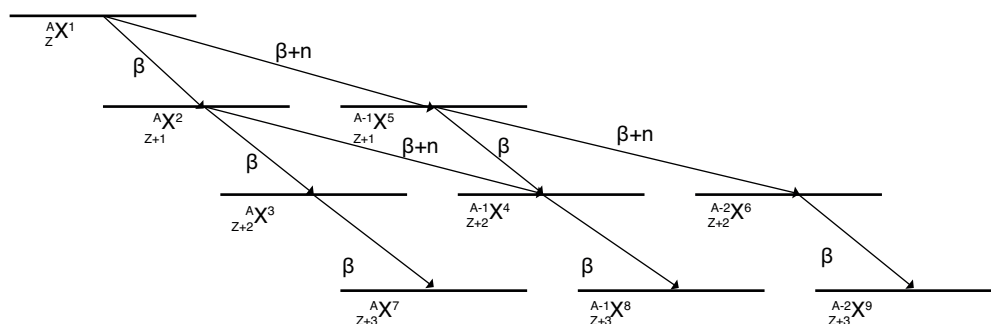


**Figure 4.2:** Illustration of the basic decay scheme of  $\beta$ -decays with the inclusion of  $\beta$ -delayed neutron emission for the parent and daughter generation nuclei.

a decay chain with the following formula:

$$N_n(t) = \prod_{j=1}^{n-1} \lambda_j \sum_{i=1}^n \sum_{j=i}^n \left( \frac{N_i(0) e^{-\lambda_j t}}{\prod_{p=i, p \neq j}^n (\lambda_p - \lambda_j)} \right) \quad (4.2)$$

with  $\lambda_j$  the decay constant of the  $j$ -th precursor. The activity of the  $n$ -th isotope  $A_n(t)$  at the time  $t$  is then given as:

$$A_n(t) = \lambda_n \cdot N_n(t) \quad (4.3)$$

For the Cadmium isotopes with masses  $A = 126-134$  it was sufficient that the fit function accounts only up to the granddaughter generation nuclei because of the much longer half-lives of the Sn successors. Still, in the  $^{132}\text{Sn}$  region and especially for the nuclei of interest the decay scheme is very complex due to a non-negligible contribution of the  $\beta$ -delayed neutron emission branch for the first two generations of nuclei. A schematic representation of the typical  $\beta$ -decay branches for the  $n$ -rich Cd isotopes of interest is illustrated in Fig. 4.2. The half-lives of the  $\beta$ -decay daughter ( $A, Z+1$ ) and the  $\beta$ -delayed neutron daughter ( $A-1, Z+1$ ) are, in most cases, significantly different and thus the result of the fit is strongly dependent on the  $\beta$ -delayed neutron emission probabilities of the decay chain members. In addition to this, some of the nuclei have  $\beta$ -decaying isomeric states which also have to be added to the fitting function resulting in the following activities for the parent  $X^1$ , the daughter  $X^2$  and the  $\beta$ -delayed neutron daughter  $X^5$ :

$$A_1 = A_1^0 e^{-\lambda_1 t} \quad (4.4)$$

$$A_2 = A_1^0 \cdot \left[ P_n^1 \cdot \bar{I}^2 \cdot \frac{\lambda_2}{\lambda_2 - \lambda_1} \cdot (e^{-\lambda_1 t} - e^{-\lambda_2 t}) + \bar{I}^2 \cdot \frac{\lambda_2^{is}}{\lambda_2^{is} - \lambda_1} (e^{-\lambda_1 t} - e^{-\lambda_2^{is} t}) \right] \quad (4.5)$$

$$A_5 = A_1^0 \cdot \left[ P_n^1 \cdot \bar{I}^5 \cdot \frac{\lambda_5}{\lambda_5 - \lambda_1} \cdot (e^{-\lambda_1 t} - e^{-\lambda_5 t}) + P_n^1 \cdot \bar{I}^5 \cdot \frac{\lambda_5^{is}}{\lambda_5^{is} - \lambda_1} (e^{-\lambda_1 t} - e^{-\lambda_5^{is} t}) \right] \quad (4.6)$$

with  $P_n^i$  the  $\beta$ -delayed neutron emission probability of the  $i$ -th nucleus,  $I^i$  the probability to populate the  $\beta$ -decaying isomeric state with an half-life of  $\lambda_i^{is}$  of the  $i$ -th nucleus and not the g.s. For the mother the production of isomeric states in the mother nucleus is ignored

since this was in first order only of importance for  $^{129}\text{Cd}$ . If no  $\beta$ -decaying isomeric state is present in the  $i$ -th nucleus then  $I^i$  is set to 0.

A short note is made here for some notation to simplify and shorten some of the equations shown in this chapter. The inverted probability of a probability  $P$  is from now on written as  $\bar{P}$  and defined as:

$$\bar{P} = 1 - P \quad (4.7)$$

Adding the activities for the granddaughter generation nuclei, stated in Appendix C.3, the total fit function is given as

$$A(t) = \sum_{i=1}^6 A_i + c \quad (4.8)$$

with  $c$  being the aforementioned constant background. The fit function  $A(t)$  was fitted in all cases via a  $\chi^2$  minimization to the experimental data trying to minimize the value:

$$\chi^2 = \sum_{i=1}^n \left[ \frac{N(t_i) - A(t_i; \lambda_1, c)}{\sigma_i} \right]^2 \quad (4.9)$$

in which  $N(t_i)$  is the number of counts in the  $i$ -th time distribution bin and  $\sigma_i$  the statistical uncertainty in the  $i$ -th bin obtained from the number of counts:

$$\sigma_i = \sqrt{N(t_i)}. \quad (4.10)$$

The three free fit parameters are the decay constant of the parent nucleus  $\lambda_1$ , the initial abundance and the constant background  $c$ .

The  $\chi^2$  minimization generally has some limitations. One of them is that the Gaussian probability hypothesis has to be justified even though the time-correlated spectra follow Poisson statistics. To fulfill this criterion, the bin size has to be chosen appropriately. In Ref. [138] the author states that for ten counts per bin the Gaussian and Poisson distributions show deviations small enough from each other to allow for the use of the  $\chi^2$  minimization method. To obey that requirement, the data has to be rebinned which subsequently leads to an information loss. In the cases with sufficient statistics the binning can be chosen small enough to maintain the shape of the decay curves to extract half-lives, but for low statistics cases as for example  $^{134}\text{Cd}$  with less than 100 implantations another method is needed to achieve reliable results.

### 4.1.2 Maximum Likelihood fit

The unbinned Maximum Likelihood method is one option to address the cases with very few statistics in the time bins and has proven to provide good results in the past [98, 139, 140]. While unbinned Maximum Likelihood for the beginning just means that each data point is used individually for the fit, it is important to choose a probability density function which best describes the experimental data. One possibility is to normalize the fit function

4.1.1 and use this one as the P.D.F. as done in the work of Z. Y. Xu [97, 141]. In the present work a different approach is used, similar to the P.D.F. used in Refs. [98, 139, 140].

The problem in the construction of an appropriate P.D.F. is that the observed decays after an implantation have no unique signature so that it is impossible to determine to which generation of the decay chain they belong or if it is even a background event. Consequently, the P.D.F. has to include the probabilities that after the implantation exactly  $n$  decays are being correlated and the probabilities for each observed decay to be a background event or a decay from a specific generation of the decay chain. Unfortunately, the formulas used are very complex and certain restrictions have to be made on the number of correlated events and on how many  $\beta$ -decay generations are taken into account. While the limit on only the parent, daughter and granddaughter generation is well justified by the argument that the grand-granddaughter in all cases has a half-life orders of magnitude higher than the parent decay, the limitation on the number of decays might be a problem. In the present case a limitation of up to three correlated decays was chosen, which implies that the correlation time has to be chosen appropriately to reduce the number of events with more than three correlated events, since those cannot be described with the P.D.F. Later in this thesis tests are presented for the choice of correlation time, and it will be shown that with up to three correlated events very good results can be achieved.

#### 4.1.2.1 The unbinned Maximum Likelihood method

The Maximum Likelihood method (MLH) [138] is used to estimate the parameters of a statistical model describing datasets which are independent and identically distributed. Crucial for this type of analysis is to define a probability density function (P.D.F.)  $f(\Theta)$  which describes the distribution of the observed data  $x_1, x_2, \dots, x_n$ .  $\Theta$  is here the parameter for which an estimator is to be found. The joint density function can then be written as:

$$f(x_1, x_2, \dots, x_n | \Theta) = f(x_1 | \Theta) \times f(x_2 | \Theta) \times \dots \times f(x_n | \Theta) \quad (4.11)$$

The likelihood function is then defined as:

$$\mathcal{L}(\Theta; x_1, x_2, \dots, x_n) = f(x_1, x_2, \dots, x_n | \Theta) = \prod_{i=1}^n f(x_i | \Theta). \quad (4.12)$$

Maximising  $\mathcal{L}$  by varying  $\Theta$  will give the most probable value of  $\Theta$  to describe the observed dataset. A problem for this method can be that the product over very small probabilities can lead to errors because of machine limitations when using computers to calculate  $\mathcal{L}$ . Therefore, it is in most cases more convenient to transform  $\mathcal{L}$  to the negative log-likelihood function (NLL):

$$NLL(\Theta; x_1, x_2, \dots, x_n) = -\ln(\mathcal{L}(\Theta; x_1, x_2, \dots, x_n)) \quad (4.13)$$

Minimising NLL will also provide the best estimator  $\Theta_0$  for the present dataset because the application of the logarithm is a monotone transformation, preserving the extrema. Before

we continue with the description of the implementation of the method in the present case, it is worthy to point out that there are two different kind of methods to treat the datasets. In the first method, the unbinned MLH, each data-point is treated individually resulting in no information loss, while in the second method, the binned MLH, the data-points are binned and  $f(\Theta)$  is defined in such a way that it describes the probability to find events in the  $i$ -th bin. The second method is often used for large datasets where the computation of the probability for each data-point becomes too CPU intensive. In the present case the unbinned MLH is used to lose as little information as possible for the very low statistic cases.

For the results presented in this thesis the RooFit package [142] was chosen, giving the user the possibility to define a P.D.F., including unit normalization, and the calculation of the negative log-likelihood function for a given dataset. Using the TMinuit package [143] the function provided by the user is then minimised using one of the predefined techniques. MIGRAD was chosen as a minimizer and the errors were calculated using MINOS, providing asymmetric errors if necessary. For a more detailed description of the used packages it is explicitly referred to the corresponding manuals [144, 145].

In the following sections the construction of the P.D.F. and the NLL function will be explained in detail.

#### 4.1.2.2 Constructing the P.D.F.

The constructed P.D.F. is based on the one used in the analysis of the  $^{100}\text{Sn}$  experiments presented in Refs. [98, 146] and has been extended to describe appropriately the expected  $\beta$ -decay chains including  $\beta$ -decaying isomeric states and the probability for  $\beta$ -delayed neutron emission.

First of all, the probability is computed that a  $\beta$  decay of the first (parent), second (daughter) or third (granddaughter) members of the decay chain undergoes a  $\beta$ -decay within a time interval between  $t_0 = 0$  and  $t$ :

$$F_1(\lambda_1, t) = 1 - e^{-\lambda_1 t} \quad (4.14)$$

$$F_2(\lambda_1, \lambda_2, t) = 1 - \frac{\lambda_1 \lambda_2}{\lambda_2 - \lambda_1} \left( \frac{e^{-\lambda_1 t}}{\lambda_1} - \frac{e^{-\lambda_2 t}}{\lambda_2} \right) \quad (4.15)$$

$$F_3(\lambda_1, \lambda_2, \lambda_3, t) = 1 - \frac{\lambda_1 \lambda_2 \lambda_3}{(\lambda_2 - \lambda_1)(\lambda_3 - \lambda_1)(\lambda_3 - \lambda_2)} \left( \frac{(\lambda_3 - \lambda_2)e^{-\lambda_1 t}}{\lambda_1} - \frac{(\lambda_3 - \lambda_1)e^{-\lambda_2 t}}{\lambda_2} - \frac{(\lambda_2 - \lambda_1)e^{-\lambda_3 t}}{\lambda_3} \right) \quad (4.16)$$

where the indices 1, 2 and 3 denote the different generations in the chain of  $\beta$ -decays.

Secondly, the probability is computed to find a parent, daughter or granddaughter decay

in a time interval from  $t$  to  $t + dt$  with  $dt \rightarrow 0$ :

$$f_1(\lambda_1, t) = \lambda_1 e^{-\lambda_1 t} \quad (4.17)$$

$$f_2(\lambda_1, \lambda_2, t) = \frac{\lambda_1 \lambda_2}{\lambda_2 - \lambda_1} \left( e^{-\lambda_1 t} - e^{-\lambda_2 t} \right) \quad (4.18)$$

$$f_3(\lambda_1, \lambda_2, \lambda_3, t) = \frac{\lambda_1 \lambda_2 \lambda_3}{(\lambda_2 - \lambda_1)(\lambda_3 - \lambda_1)(\lambda_3 - \lambda_2)} \left( (\lambda_3 - \lambda_2) e^{-\lambda_1 t} \right. \\ \left. (\lambda_3 - \lambda_1) e^{-\lambda_2 t} - (\lambda_2 - \lambda_1) e^{-\lambda_3 t} \right) \quad (4.19)$$

In addition to the probability of finding a real decay event from the  $\beta$ -decay chain of interest at a specific time  $t$ , it is also necessary to know the probability to observe a background event at this time  $t$ . Such a background probability function can be expressed by a Poisson distribution since a Poisson statistic describes the probability to observe  $n$  events within a correlation time  $t_c$ . This assumption is correct if the background events are independent from each other and have a known average rate  $b$  (background rate for the present case). The probability  $B_n$  to observe  $n$  background events in the correlation time  $t$  can then be expressed as:

$$B_n = \frac{(bt_c)^n e^{-bt_c}}{n!} \quad (4.20)$$

Other important quantities that will be used to compute the final P.D.F. are:

- $D_i$  : Probability for the  $i$ th-generation nucleus to undergo a  $\beta$  decay .
- $O_i$  : Probability for the  $\beta$  decay of the  $i$ th-generation nucleus to be detected. Consequently, this probability depends on the  $\beta$ -decay efficiency of the experimental set-up.
- $\epsilon_i$  : The efficiency of the experimental set-up to observe a decay of the  $i$ -th generation (The determination of  $\epsilon_i$  will be described in section 4.2.2.3 with the example of  $^{130}\text{Cd}$ ).

The final P.D.F. function is subdivided into four parts. Individual probability density functions are needed for events with 0, 1, 2 or 3 correlated decays/background events which have to be combined then to create the Likelihood function. The probability  $P_0$  to observe no decay within a correlation time  $t_c$  after the implantation of an ion is described as [98, 146]:

$$P_0(\lambda_1) = (\bar{D}_1 + D_1 \bar{O}_1 \bar{D}_2 + D_1 \bar{O}_1 D_2 \bar{O}_2 \bar{D}_3 + D_1 \bar{O}_1 D_2 \bar{O}_2 D_3 \bar{O}_3) \cdot B_0 \quad (4.21)$$

which can then be written using Formulas 4.14-4.19 as:

$$P_0(\lambda_1) = [\bar{F}_1(\lambda_1, t_c) + (\bar{F}_2(\lambda_1, \lambda_2, t_c) - \bar{F}_1(\lambda_1, t_c)) \cdot \bar{e}_1 + (\bar{F}_3(\lambda_1, \lambda_2, \lambda_3, t_c) - \bar{F}_2(\lambda_1, \lambda_2, t_c)) \cdot \bar{e}_1 \cdot \bar{e}_2 + \bar{F}_3(\lambda_1, \lambda_2, \lambda_3, t_c) \cdot \bar{e}_1 \cdot \bar{e}_2 \cdot \bar{e}_3] \cdot B_0. \quad (4.22)$$

This formula is only valid if no isomeric states or  $\beta$ -delayed neutron emission probabilities are considered. However, these parameters must be taken into account for the nuclei object of this work. Then,  $F_2$  and  $F_3$  have to be replaced by the probabilities  $F_2^{n,is}$  and  $F_3^{n,is}$ :

$$F_2^{n,is} = \bar{P}_n^1 \cdot \bar{I}^2 \cdot F_2(\lambda_1, \lambda_2, t) + P_n^1 \cdot \bar{I}^5 \cdot F_2(\lambda_1, \lambda_5, t) + \bar{P}_n^1 \cdot \bar{I}^2 \cdot F_2(\lambda_1, \lambda_2^{is}, t) + P_n^1 \cdot \bar{I}^5 \cdot F_2(\lambda_1, \lambda_5^{is}, t) \quad (4.23)$$

$$\begin{aligned} F_3^{n,is} = & \bar{P}_n^1 \cdot \bar{I}^2 \cdot \bar{P}_n^2 \cdot \bar{I}^3 \cdot F_3(\lambda_1, \lambda_2, \lambda_3, t) + \bar{P}_n^1 \cdot \bar{I}^2 \cdot \bar{P}_n^2 \cdot \bar{I}^3 \cdot F_3(\lambda_1, \lambda_2, \lambda_3^{is}, t) \\ & + \bar{P}_n^1 \cdot \bar{I}^2 \cdot \bar{P}_n^2 \cdot \bar{I}^3 \cdot F_3(\lambda_1, \lambda_2^{is}, \lambda_3, t) + \bar{P}_n^1 \cdot \bar{I}^2 \cdot \bar{P}_n^2 \cdot \bar{I}^3 \cdot F_3(\lambda_1, \lambda_2^{is}, \lambda_3^{is}, t) \\ & + \bar{P}_n^1 \cdot \bar{I}^2 \cdot \bar{P}_n^2 \cdot \bar{I}^4 \cdot F_3(\lambda_1, \lambda_2, \lambda_4, t) + \bar{P}_n^1 \cdot \bar{I}^2 \cdot \bar{P}_n^2 \cdot \bar{I}^4 \cdot F_3(\lambda_1, \lambda_2, \lambda_4^{is}, t) \\ & + \bar{P}_n^1 \cdot \bar{I}^2 \cdot \bar{P}_n^2 \cdot \bar{I}^4 \cdot F_3(\lambda_1, \lambda_2^{is}, \lambda_4, t) + \bar{P}_n^1 \cdot \bar{I}^2 \cdot \bar{P}_n^2 \cdot \bar{I}^4 \cdot F_3(\lambda_1, \lambda_2^{is}, \lambda_4^{is}, t) \\ & + P_n^1 \cdot \bar{I}^5 \cdot \bar{P}_n^5 \cdot \bar{I}^4 \cdot F_3(\lambda_1, \lambda_5, \lambda_4, t) + P_n^1 \cdot \bar{I}^5 \cdot \bar{P}_n^5 \cdot \bar{I}^4 \cdot F_3(\lambda_1, \lambda_5, \lambda_4^{is}, t) \\ & + P_n^1 \cdot \bar{I}^5 \cdot \bar{P}_n^5 \cdot \bar{I}^4 \cdot F_3(\lambda_1, \lambda_5^{is}, \lambda_4, t) + P_n^1 \cdot \bar{I}^5 \cdot \bar{P}_n^5 \cdot \bar{I}^4 \cdot F_3(\lambda_1, \lambda_5^{is}, \lambda_4^{is}, t) \\ & + P_n^1 \cdot \bar{I}^5 \cdot \bar{P}_n^5 \cdot \bar{I}^6 \cdot F_3(\lambda_1, \lambda_5, \lambda_6, t) + P_n^1 \cdot \bar{I}^5 \cdot \bar{P}_n^5 \cdot \bar{I}^6 \cdot F_3(\lambda_1, \lambda_5, \lambda_6^{is}, t) \\ & + P_n^1 \cdot \bar{I}^5 \cdot \bar{P}_n^5 \cdot \bar{I}^6 \cdot F_3(\lambda_1, \lambda_5^{is}, \lambda_6, t) + P_n^1 \cdot \bar{I}^5 \cdot \bar{P}_n^5 \cdot \bar{I}^6 \cdot F_3(\lambda_1, \lambda_5^{is}, \lambda_6^{is}, t) \end{aligned} \quad (4.24)$$

Due to the complexity of the formulas it is explicitly referred to the works of A. Stolz and C. Hinke [98, 146] in which the probability density functions  $p_1(\lambda_1)$ ,  $p_2(\lambda_1)$  and  $p_3(\lambda_1)$  for the first, second and third correlated decays can be found. For the present work those formulas were modified in such a way that they included the isomeric states and the  $\beta$ -delayed neutron emission probabilities, similar to the P.D.F. presented here for no correlated decay during the time window  $t_c$ .

The total likelihood function is finally given as:

$$L_{0,1,2,3}(\lambda_1) = P_0(\lambda_1)^{N_0} \prod_{1 \text{ event}} p_1(\lambda_1) \prod_{2 \text{ events}} p_2(\lambda_1) \prod_{3 \text{ events}} p_3(\lambda_1) \quad (4.25)$$

### 4.1.3 Error determination in the $\chi^2$ and MLH fits

For the MLH method only the decay constant  $\lambda_1$  was set as a free fit parameter, whereas for the  $\chi^2$  method the background rate  $c$  and the initial abundance  $N_0$  were additionally taken as free fit parameters. Therefore, the error provided after the fits in both methods only includes the statistical error, ignoring systematic uncertainties from the other input parameters such as half-lives,  $P_n$  values and probabilities to populate  $\beta$ -decaying

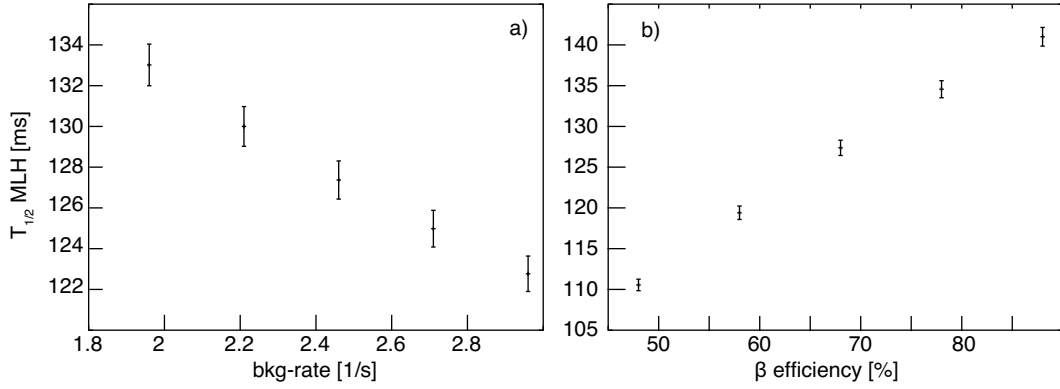


**Figure 4.3:** Half-lives determined with the MLH method for the  $\beta$  decay of the  $0^+$  g.s. in  $^{130}\text{Cd}$  for a) different background rates and b) different  $\beta$ -decay efficiencies. Only the half-life of the  $0^+$  g.s. in  $^{130}\text{Cd}$  was set as a free fit parameter, while all other input parameters were fixed. The plots should demonstrate the linear change in the fitted half-life when varying only one input parameter.

isomeric states in the nuclei. The total error  $\Delta T_{1/2}$ , which will be stated in the following chapters, is always the sum of both errors, calculated as:

$$\Delta T_{1/2} = \sqrt{(\Delta T_{1/2}^{\text{sys}})^2 + (\Delta T_{1/2}^{\text{stat}})^2} \quad (4.26)$$

with the statistical error  $T_{1/2}^{\text{stat}}$  and the systematic error  $T_{1/2}^{\text{sys}}$ .

The changes in the determined half-life were generally found to be rather linearly when changing only one of the input parameters within its error bar. This is expected for small variations of one parameter, and thus it was decided to calculate the systematic error  $\Delta_{\pm}(Y_i)$  on the  $T_{1/2}$  for the  $i$ -th input parameter  $Y_i$  as following:

$$\Delta_{\pm}(Y_i) = |T_{1/2}(Y_i \pm \Delta Y_i) - T_{1/2}(Y_i)| \quad (4.27)$$

with  $T_{1/2}(Y_i)$  the half-life obtained from the fit with the central value of the input parameter and  $T_{1/2}(Y_i \pm \Delta Y_i)$  the ones with  $Y_i$  varying  $\pm \Delta(Y_i)$ . To demonstrate that the fitted half-life changes linear when applying small changes to one input parameter, two examples are shown in Fig. 4.3. In both cases the half-lives were obtained with the MLH method and a) shows the results for different background (bkg) rates, while in b) the  $\beta$  efficiency was varied. In both plots all other input parameters were fixed and only the half-life was set as a free fit parameter. The input parameters such as half-lives and  $P_n$  values were taken from literature (Ref. [60]). In both figures we see a more or less linear dependence when only changing one input parameter within a small range.

The total systematic error can then be deduced from the individual errors with the following formula:

$$\Delta T_{1/2}^{\text{sys}} = \sqrt{\sum_i (\Delta_{\pm}(Y_i))^2}, \quad (4.28)$$

assuming that all input parameters are statistically independent. Finally, with the statistical

error taken from the fit, the total error can be calculated with Formula 4.26.

#### 4.1.4 $\gamma$ -gated half-lives for $\beta$ -decay

An important drawback of the methods presented above for the determination of  $\beta$ -decay half-lives is that they rely on the literature values or even theoretical predictions for the half-lives of the subsequent  $\beta$ -decay chain members and the  $\beta$ -delayed neutron emission probabilities of all involved nuclei. In this section a method is presented which is independent of all those values, having as the only unknown parameter the half-life of the  $\beta$ -decaying state of interest.

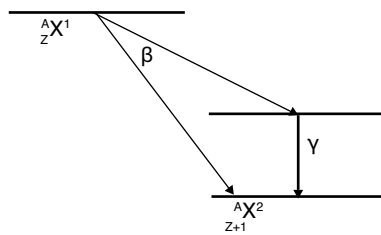


**Figure 4.4:** Illustration of the method to determine  $\beta$ -decay half-lives with a gate on a  $\gamma$  transition in the daughter nucleus to exclude background events and decays from other generations of the decay chain.

In Fig. 4.4 a simplified  $\beta$ -decay scheme is shown for a parent nucleus with mass  $A$  and nuclear charge  $Z$ . Depending on the exact properties of the  $\beta$  decay, the feeding goes to the ground state of the daughter nucleus or to excited states. If the daughter nucleus is in an excited state with a negligible half-life after the  $\beta$  decay, which then de-excites via the emission of a  $\gamma$ -ray to lower lying states in this nucleus, then this transition can be used to unambiguously identify the  $\beta$  decay. By sorting a time-correlated spectrum that only includes the  $\beta$  particles registered in prompt coincidence with the characteristic  $\gamma$  transitions of the daughter nucleus one obtains a  $\beta$  decay curve only dependent on the half-life of the nucleus of interest, thus avoiding the contributions from other generations within the decay chain. The resulting time distribution can then be fitted with a single exponential decay function. To reduce the influence of the Compton background, included in the  $\gamma$ -gate, a background subtraction is performed selecting a second gate on background in the  $\gamma$ -ray spectrum close to the peak of interest.

## 4.2 $\beta$ -decay half-life results

Thanks to the correlation between the implantation events and the decay events it is possible to extract the half-lives of the  $\beta$ -decaying states in  $^{127-134}\text{Cd}$ . The methods were described in detail in the previous sections and to verify that all three methods give proper results, they are firstly employed on well-known cases before using them for the determi-

nation of the half-lives of the cadmium isotopes.

#### 4.2.1 The test cases $^{131,132}\text{In}$ for $\gamma$ -gated half-lives

Even though the decays of  $^{131}\text{In}$  and  $^{132}\text{In}$  to  $^{131}\text{Sn}$  and  $^{132}\text{Sn}$ , respectively, are not of particular interest for this thesis, they are ideal test scenarios. The decays of these two nuclei have been studied in detail in the past and the  $\beta$ -decay half-lives and level schemes of the daughter nucleus are well-known [39, 41, 82]. In addition to this, those two nuclei had very high production yields in the present experiment resulting in sufficient statistics for the  $\gamma$ -gated method.

$^{131}\text{In}$  has three known  $\beta$ -decaying states with proposed spins and parities of  $(1/2^-)$ ,  $(9/2^+)$  and  $(21/2^+)$ . Based on the decay schemes proposed in Ref. [41], the 331-, 2434- and 4273-keV  $\gamma$ -ray transitions were selected to determine the half-lives of the  $(1/2^-)$ ,  $(9/2^+)$  and  $(21/2^+)$   $\beta$ -decaying states, respectively. In the case of the  $^{132}\text{In}$  decay the 4041 keV transition was selected for the  $\gamma$ -gated half-life determination of the  $7^-$  ground state. This is based on the level scheme published in Ref. [82]. Figures 4.5a) and b) show the time distributions gated on the 2434- and 4041-keV transitions in  $^{131}\text{In}$  and  $^{132}\text{In}$ , respectively. The corresponding least square fits to a single exponential decay function and a linear background are also shown and the measured half-lives are presented in Table 4.1. It is worth noting that the present results are in excellent agreement with the values reported in the literature [39, 82]. As can be seen in the table, the discrepancies are typically below one standard deviation. These measurements, thus, serve as a cross-check of the performance of the  $\gamma$ -gated method to determine  $\beta$ -decay half-lives.

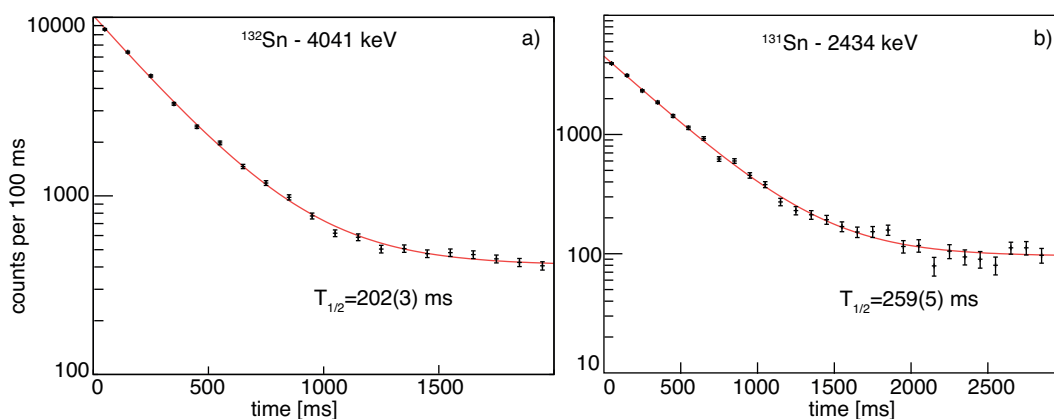


**Figure 4.5:** Time distributions (black) of the decays observed after an implantation of a)  $^{132}\text{In}$  and b)  $^{131}\text{In}$  gated on the observation of a 4041 keV and 2434 keV  $\gamma$ -ray, respectively, in prompt coincidence with the decay and the fitted single exponential decay functions (red lines).

Nuclei	initial state	$E_\gamma$ [keV]	$T_{1/2}(\gamma)$ [ms]	$T_{1/2,lit}$ [ms]
$^{131}\text{In}$	$(1/2^-)$	331	324(22)	350(50) [39]
$^{131}\text{In}$	$(9/2^+)$	2434	259(5)	280(30) [39]
$^{131}\text{In}$	$(21/2^+)$	4273	361(42)	320(60) [39]
$^{132}\text{In}$	$(7^-)$	4041	202(3)	207(6) [82]

**Table 4.1:** Summary of the half-lives from  $\beta$ -decaying isomeric states in  $^{131}\text{In}$  and  $^{132}\text{In}$  with their associated spin and parities obtained with the  $\gamma$ -gated method for several known transitions in  $^{131}\text{Sn}$  and  $^{132}\text{Sn}$  and the corresponding literature values of the half-lives for comparison.

## 4.2.2 Comparison of the three methods for $^{130}\text{Cd}$

The nucleus  $^{130}\text{Cd}$  is a perfect test case for the comparison of the three analysis procedures used in this work. Its  $\beta$  decay is well-known [147], it has a low  $\beta$ -delayed neutron emission probability of 3.6(10)% [147, 148] and just one  $\beta$ -decaying state. On top of that, a large amount of statistics was collected for this nucleus and the reported information that the  $0^+$  g.s. decays mainly to one state in  $^{130}\text{In}$  at 2120 keV [20] could be confirmed in the present analysis (see section 3.3).

### 4.2.2.1 $^{130}\text{Cd}$ : $\gamma$ -gated half-lives

First of all, the half-life of the  $0^+$  g.s. in  $^{130}\text{Cd}$  was determined applying the  $\gamma$ -gated method using the 451- and 1669-keV transitions in  $^{130}\text{In}$ . The  $\gamma$ -gated  $\beta$ -decay time distributions are shown in Fig. 4.6a) and b) with the corresponding fits. The measured half-lives are 126(1) and 128(2) ms for the 451- and 1669-keV transitions, respectively. They agree between them within the error bars, but a severe difference is observed if compared to the previously published value of 162(7) ms [20].

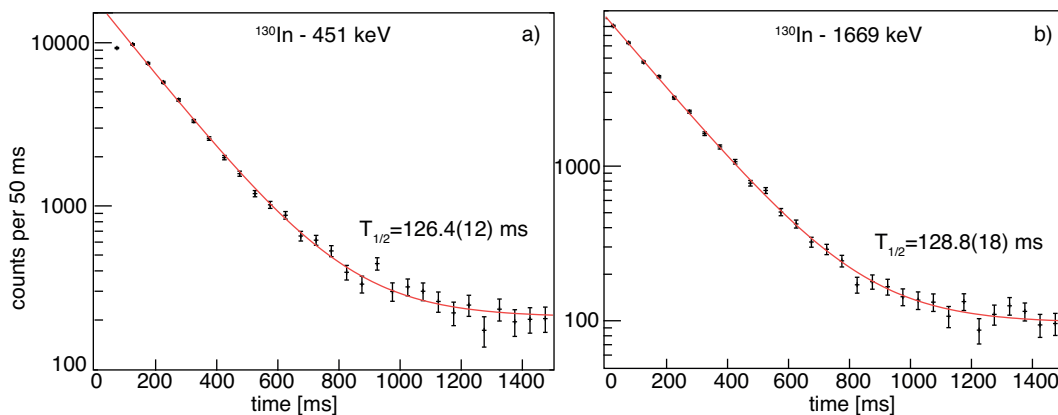


**Figure 4.6:** Time distributions (black) of the decays observed after an  $^{130}\text{Cd}$  implantation gated on the observation of a) a 451-keV and b) a 1669-keV  $\gamma$ -ray in prompt coincidence with the decay and the fitted single exponential decay functions (red lines).

4.2.2.2  $\chi^2$  fit with Bateman equations

The second fitting procedure to determine the half-life of the  $\beta$ -decaying state in  $^{130}\text{Cd}$  is the  $\chi^2$  fit with the Bateman equations. The method was already described in detail in section 4.9 and the fit function in the present case accounts for the activity of the parent, the daughter and the  $\beta$ -delayed neutron daughter. The addition of the granddaugther generation nuclei had no influence on the fit results because of the three order of magnitudes longer half-lives [2]. As input parameters the following values were used:  $P_n$  value of  $^{130}\text{Cd} = 3.6(10)\%$  [60, 147, 148], half-life of the  $1^-$  g.s. in the daughter nucleus = 290(20) ms and half-lives of the  $\beta$ -delayed neutron daughters taken from [60]. The populations of the different  $\beta$ -decaying states in the  $\beta$ -delayed neutron daughter  $^{129}\text{In}$  after the  $\beta$ -delayed neutron emission were estimated from the intensities of  $\gamma$ -rays known from  $^{129}\text{Sn}$  and corrected for the  $\beta$ -delayed neutron emission probability.

Figure 4.7 shows the time distribution of the decays correlated to the implanted  $^{130}\text{Cd}$

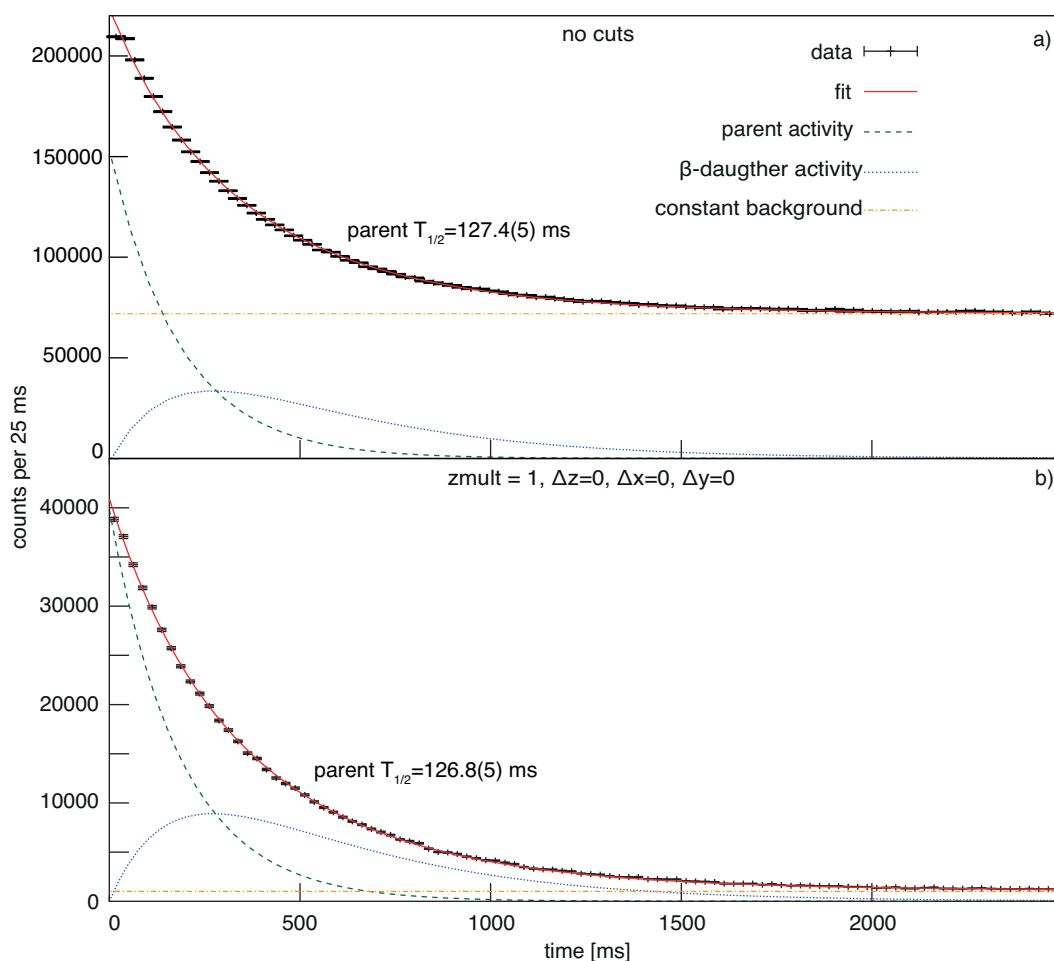


**Figure 4.7:** Time distribution of the decays correlated to the implanted  $^{130}\text{Cd}$  Cadmium ions and with a) no and b) all cuts applied on the position difference between implantation and decay ( $z_{mult} = 1$  &  $\Delta z = 0$  &  $\Delta x, \Delta y = 0$ ). The corresponding Bateman equation fit (red solid line) is shown together with the decomposition into the activity of the parent (green dashed line) and daughter (blue dotted line) nuclei, for details of the fit see text and section 4.1.1.

Nuclei	$I^\pi$	$T_{1/2,lit}$	$P_{n,lit}$ [%]
$^{130}\text{Cd}$	$0^+$	free	3.6(10)
$^{130}\text{In}$	$(1^-)$	290(20) ms	0.93(13)
$^{130}\text{In}$	$(10^-)$	538(5) ms	1.65(15)
$^{130}\text{In}$	$(5^+)$	540(10) ms	1.65(15)
$^{130}\text{Sn}$	$0^+$	3.72(7) min	0
$^{130}\text{Sn}$	$(7^-)$	1.7(1) min	0
$^{129}\text{In}$	$(9/2^+)$	611(4) ms	0.25(5)
$^{129}\text{In}$	$(1/2^-)$	1.23(3) min	0
$^{129}\text{Sn}$	$(3/2^+)$	2.23(4) min	0
$^{129}\text{Sn}$	$(11/2^-)$	6.9(1) min	0

**Table 4.2:** Summary of the input parameters e.g. half-lives and  $\beta$ -delayed neutron emission probabilities as they were used for the  $^{130}\text{Cd}$  MLH analysis. All values are taken from [60].

ions, the fitting function and the decomposition of this function into the observed activities of the parent and daughter nuclei. In that figure it is also illustrated how the cuts on the position difference ( $z_{mult} = 1$  &  $\Delta z = 0$  &  $\Delta x, \Delta y = 0$ ) between implantation and  $\beta$  decay significantly reduce the background level in the spectrum, but also the total amount of good events. Nevertheless, the half-life obtained from the fit with no cuts applied (see Fig. 4.7a) ) of  $T_{1/2}=127.4(5)$  ms is in good agreement with the value of  $T_{1/2}=126.8(3)$  ms obtained from the fit to the time distribution in Fig. 4.7b), where all cuts are applied. Both values compare within one standard deviation with the values obtained from the  $\gamma$ -gated method. The influence of the  $\beta$ -delayed neutron daughter is so small that it is not shown in the plot. The constant background which was added to the fit function to account for randomly correlated decays from other nuclei is also shown in the plot, and it can be observed that for times larger than two seconds the decay curve is dominated by the background.

### 4.2.2.3 MLH method

The third method to extract  $\beta$ -decay half-lives is the maximum likelihood analysis presented in section 4.1.2. This requires not only the information of the daughter generation nuclei but also of the granddaughter generation nuclei. The necessary input parameters are again taken from literature. They are summarized in Table 4.2 with the only free fit parameter being the half-life of the  $0^+$  g.s. in  $^{130}\text{Cd}$ . From results in this work it was deduced that the  $\beta$  decay of  $^{130}\text{Cd}$  mainly proceeds to final states that de-excite internally to the  $(1^-)$  g.s. of the daughter  $^{130}\text{In}$ . Thus, the  $(5^+)$  and  $(10^-)$   $\beta$ -decaying states can be ignored for the half-life analysis. On the contrary, the population of the different  $\beta$ -decaying states in  $^{130}\text{Sn}$  and  $^{129}\text{In}$  in the decay of the corresponding parent nucleus was deduced from the experimental data by measuring intensities of characteristic transitions. From the measured intensity of the 1221 keV transition in  $^{130}\text{Sn}$  in the actual experimental data one obtains that 100(5)% of the  $\beta$  decays from the  $(1^-)$  state in  $^{130}\text{In}$  proceed to the  $0^+$  state in  $^{130}\text{Sn}$ . For that the absolute intensity of the 1221-keV transition was taken from

Ref. [126] to be 64(4) per 100  $^{130}\text{In}$  ( $1^-$ ) decays. In Ref. [119] the absolute intensity of the 1865-keV transition in  $^{129}\text{Sn}$ , following the  $\beta$  decay of the ( $9/2^+$ ) state in  $^{129}\text{In}$ , is stated to be 32(2) per 100 decays while the 1009-keV transition in  $^{129}\text{Sn}$ , following the  $\beta$  decay of the ( $1/2^-$ ) state in  $^{129}\text{In}$ , was measured to have an absolute intensity of 2(1) per 100 decays. With those absolute intensities the population ratio of the ( $9/2^+$ ) state to the ( $1/2^-$ ) state in  $^{129}\text{In}$ , following  $\beta$ -delayed neutron emission from  $^{130}\text{Cd}$ , was deduced to be approximately 1:2.

As previously stated, the used probability density function is designed only for up to three correlated decays per implantation and the correlation time has to be chosen appropriately, as a compromise between maximizing the statistics and minimizing the number of events with more than three correlated decays. In the case of  $^{130}\text{Cd}$  the correlation time was chosen to be 500 ms, resulting in 91% of the implantations having less than 4 associated  $\beta$  decays. A more detailed investigation of the influence of the correlation time on the half-life determination will be presented in the next section.

To apply the MLH method used in this work, two additional parameters are necessary, namely the  $\beta$ -decay efficiency and the background rate. These are extracted from the fit with the Bateman equations. For no further limitation on the difference between the implantation and decay position a background rate of 1.86(1)s and an efficiency for the detection of a  $^{130}\text{Cd}$   $\beta$ -decay of 59.6(3)% are obtained. The efficiency  $\epsilon_1$  of the first generation is hereby calculated as the ratio between the observed decays  $N_{decay}$  and the total amount of implanted ions  $N_{imp}$ :

$$\epsilon_1 = \frac{N_{decay}}{N_{imp}} = \frac{A_1(0)}{\lambda_1 N_{imp}} \quad (4.29)$$

with  $N_{decay}$  calculated from the initial activity  $A_1(0)$  of the parent nucleus and its decay constant. Unfortunately, it is not possible to determine the efficiencies of the subsequent  $\beta$ -decays and therefore, the efficiency was assumed to be equal for the detection of the different decays and an error of  $\pm 5\%$  is introduced. This error was chosen after investigating the efficiency of several  $\beta$ -decays in the present dataset and including the uncertainties from the  $\chi^2$  fit. Also the background rate was varied in the range  $\pm 5\%$  for a more precise error. In the case of  $^{130}\text{Cd}$  those errors result in a much bigger error for the MLH method compared to the two other methods. It will be seen later that in the most exotic cases, for which this method was designed, the errors are dominated by the statistical error. Using the values shown in Table 4.2 we obtain a value of 125(1) ms for the half-life of the g.s. of  $^{130}\text{Cd}$  with just the statistical error included. The final uncertainty including statistical and systematic errors is calculated as presented in section 4.1.3 with the latter of them being evaluated by varying the measured  $\beta$  efficiency and background rate by 5%, as described above. Changing the population ratios of  $\beta$ -decaying isomeric states in  $^{130}\text{Sn}$  and  $^{129}\text{In}$  did not have any significant influence on the fit result. The final value obtained with the MLH analysis is then  $T_{1/2} = 125(5)$  ms.

#### 4.2.2.4 $\beta$ -decay efficiencies and numbers of observed $\beta$ decays

While the  $\beta$ -decay efficiency is a crucial input parameter for the MLH analysis, the number of observed  $\beta$  decays  $N_{decay}$  is essential for calculating the absolute  $\beta$ -decay feeding as it was done in the previous chapter.  $N_{decay}$  is obtained in all cases from the fit with the Bateman equations to the time distributions of all decays correlated to the implanted ions. The results for those fits have been shown in the case of  $^{130}\text{Cd}$  in section 4.2.2.2 and are shown later in section 4.2.3 for the remaining Cadmium isotopes. The initial activity  $A_1(0)$  is one of the free parameters in those fits, and knowing this the number of parent decays can be calculated as:

$$N_{decay} = \frac{A_1(0)}{\lambda_1} \quad (4.30)$$

with  $\lambda_1$  the decay constant of the parent nucleus.  $N_{decay}$  depends on the applied cuts ( $Z_{mult}$ ,  $\Delta z$  and/or  $\Delta x$ ,  $\Delta y$ ) and consequently the  $\beta$ -decay efficiency  $\epsilon_1$  also changes when applying different cuts (see Formula 4.29).

Nucleus	Cuts	$N_{decay}$	$\epsilon_1$	b
$^{126}\text{Cd}$	none	15489(525)	69.0(23)	0.85(1)
	$\Delta z = 0$	14962(404)	66.6(18)	0.45(1)
	$Z_{mult} = 1$	12737(365)	56.7(16)	0.55(1)
	$Z_{mult} = 1$ & $\Delta z = 0$ & $\Delta x, \Delta y = 0$	4538(203)	20.2(9)	0.01(1)
	$Z_{mult} = 1$ & $\Delta z = 0$ & $\Delta x, \Delta y < 1$	10365(351)	46.1(16)	0.17(1)
$^{127}\text{Cd}$	none	20569(473)	65.7(15)	0.94(1)
	$\Delta z = 0$	18734(612)	59.8(20)	0.48(1)
	$Z_{mult} = 1$	16501(575)	52.7(18)	0.62(1)
	$Z_{mult} = 1$ & $\Delta z = 0$ & $\Delta x, \Delta y = 0$	5454(455)	17.4(15)	0.02(1)
	$Z_{mult} = 1$ & $\Delta z = 0$ & $\Delta x, \Delta y < 1$	12484(769)	39.9(25)	0.19(1)
$^{128}\text{Cd}$	none	238619(2282)	60.4(6)	2.08(1)
	$\Delta z = 0$	194402(1787)	49.2(5)	1.01(1)
	$Z_{mult} = 1$	189054(1826)	47.8(5)	1.38(1)
	$Z_{mult} = 1$ & $\Delta z = 0$ & $\Delta x, \Delta y = 0$	49790(596)	12.6(2)	0.03(1)
	$Z_{mult} = 1$ & $\Delta z = 0$ & $\Delta x, \Delta y < 1$	124307(1568)	31.4(4)	0.40(1)
$^{129}\text{Cd}$	none	2313738(30545)	61.1(1)	1.93(1)
	$Z_{mult} = 1$ & $\Delta z = 0$ & $\Delta x, \Delta y = 0$	586086(7587)	15.5(2)	0.04(1)
	$Z_{mult} = 1$ & $\Delta z = 0$ & $\Delta x, \Delta y < 1$	1204318(13239)	31.8(3)	0.22(1)
$^{130}\text{Cd}$	none	1103633(5203)	59.6(3)	1.86(1)
	$\Delta z = 0$	1047765(4305)	56.5(2)	0.90(1)
	$Z_{mult} = 1$	877139(4445)	47.3(2)	1.22(1)
	$Z_{mult} = 1$ & $\Delta z = 0$ & $\Delta x, \Delta y = 0$	293490(1591)	15.8(1)	0.03(1)
	$Z_{mult} = 1$ & $\Delta z = 0$ & $\Delta x, \Delta y < 1$	681111(2977)	36.8(2)	0.36(1)
	none	106593(1059)	57.6(6)	1.79(1)
	$\Delta z = 0$	93951(834)	50.8(5)	0.84(1)

Table 4.3 continued on next page

**Table 4.3 – continued from previous page**

Nucleus	Cuts	$N_{decay}$	$\epsilon_1$	$b$
$^{131}\text{Cd}$	$Z_{mult} = 1$	84844(881)	45.9(5)	1.18(1)
	$Z_{mult} = 1 \ \& \ \Delta z = 0 \ \& \ \Delta x, \ \Delta y = 0$	26912(415)	14.5(2)	0.03(1)
	$Z_{mult} = 1 \ \& \ \Delta z = 0 \ \& \ \Delta x, \ \Delta y < 1$	60886(723)	32.9(4)	0.33(1)
$^{132}\text{Cd}$	none	8594(365)	52.8(22)	1.77(1)
	$\Delta z = 0$	7093(286)	43.6(18)	0.81(1)
	$Z_{mult} = 1$	6809(325)	41.9(20)	1.17(1)
	$Z_{mult} = 1 \ \& \ \Delta z = 0 \ \& \ \Delta x, \ \Delta y = 0$	1922(126)	11.8(8)	0.03(1)
	$Z_{mult} = 1 \ \& \ \Delta z = 0 \ \& \ \Delta x, \ \Delta y < 1$	4528(202)	27.8(12)	0.32(1)
$^{133}\text{Cd}$	none	641(91)	58.3(83)	1.70(1)
	$\Delta z = 0$	509(62)	46.2(57)	0.7(2)
	$Z_{mult} = 1$	427(5)	38.8(54)	1.11(2)
	$Z_{mult} = 1 \ \& \ \Delta z = 0 \ \& \ \Delta x, \ \Delta y = 0$	143(43)	13.0(39)	0.04(1)
	$Z_{mult} = 1 \ \& \ \Delta z = 0 \ \& \ \Delta x, \ \Delta y < 1$	286(86)	26.0(79)	0.12(5)

**Table 4.3:** Summary of the number of parent decays  $N_{decay}$ , the  $\beta$ -decay efficiency  $\epsilon_1$  and the background rate  $b$  for all Cadmium isotopes in the present experiment for different cuts. For details of the cuts see section 3.1.5 and the number of implanted ions was taken from Table 2.1.

The number of parent decays, the  $\beta$ -decay efficiency and the background rate  $b$  were deduced for all Cadmium isotopes and with different cuts applied. Only in the case of  $^{134}\text{Cd}$  the statistic was not sufficient to perform the Bateman equation fit. All results are summarized in Table 4.3 and Fig. 4.8 shows the two cases with no cuts and all cuts ( $Z_{mult} = 1 \ \& \ \Delta z = 0 \ \& \ \Delta x, \ \Delta y = 0$ ) applied.

The efficiencies for different nuclei seem to vary significantly.  $^{126,127}\text{Cd}$  show a higher  $\beta$ -decay efficiency, while  $^{132}\text{Cd}$  seems to have a lower one than compared to the other nuclei. One explanation is that  $^{126,127}\text{Cd}$  were mainly produced in the Pd setting and here the implantation rate was lower. On the contrary about 80% of the  $^{132}\text{Cd}$  ions belong to the Sn setting where the implantation rate in WAS3ABi was a factor two higher compared to the Pd setting. However, also other reasons such as the implantation position in z-direction, namely the layer of implantation, have to be considered. In addition to that, also the exact implantation position inside the layer can change the  $\beta$ -decay efficiency. For nuclei which are implanted on the surface or close to the surface one expects to have a different absolute efficiency than for nuclei which are implanted in the middle of the layer. This is also one reason why the changes in efficiency when applying different cuts do not seem to follow a general trend.

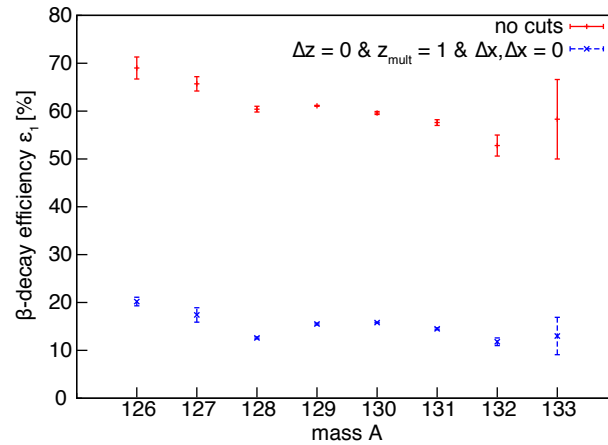


**Figure 4.8:** Shown are the  $\beta$ -decay efficiencies  $\epsilon_1$  for the two cases with no cuts and all cuts ( $Z_{mult} = 1$  &  $\Delta z = 0$  &  $\Delta x, \Delta y = 0$ ) applied.

#### 4.2.2.5 Demonstrating the goodness of the MLH Fit

In the present section a quantification will be provided for the importance of the different fit parameters, especially the correlation time.

As a first step it is important to see that the probability density function used for the MLH analysis describes the experimental data well. A Monte-Carlo simulation was therefore performed to check the used P.D.F. In that simulation the half-life of the  $0^+$  g.s. in  $^{130}\text{Cd}$  was set to the value of 127 ms, as it was obtained with the two other methods. The ToyMC package, directly accessible through RooFit [144], was used for this simulation. Both the number of events and their distribution with zero, one, two or three correlated decays to one implantation was taken from the experimental data. Figure 4.9 shows the comparison between the time distributions obtained from the experimental and simulated data. The figure is subdivided into six spectra showing in a) the time distribution of the first correlated decay after the implantation for all events where only one decay was correlated within the correlation time  $t_c$ . Spectra b) and c) show the time of the first correlated decay for events with exactly two and three correlated events within  $t_c$ , respectively. The three remaining spectra present then the time distributions for the second and third correlated decay for events with two and/or three correlated decays. In all of the six spectra 4.9a) to f) the experimental data and the data obtained in the Monte Carlo simulation fit nearly perfectly to each other. This proves that the P.D.F. constructed for this very difficult decay scenario including isomeric states and neutron emission probabilities actually describes the experimental data.

A further investigation into the distribution of the NLL was to show that a clear minimum is present at the expected value of the half-life. Also it was important to check that there are no other minima which might be a problem for the fitting routine. The NLL obtained for the case of  $^{130}\text{Cd}$  was shifted to zero and is shown in Fig. 4.10 as a function of the decay constant  $\lambda$  of the parent nucleus. The plot shows a single minimum at  $\lambda \approx 5.5 \text{ s}^{-1}$  ( $T_{1/2} \approx 126 \text{ ms}$ ) with no side minima which could result in problems with the applied

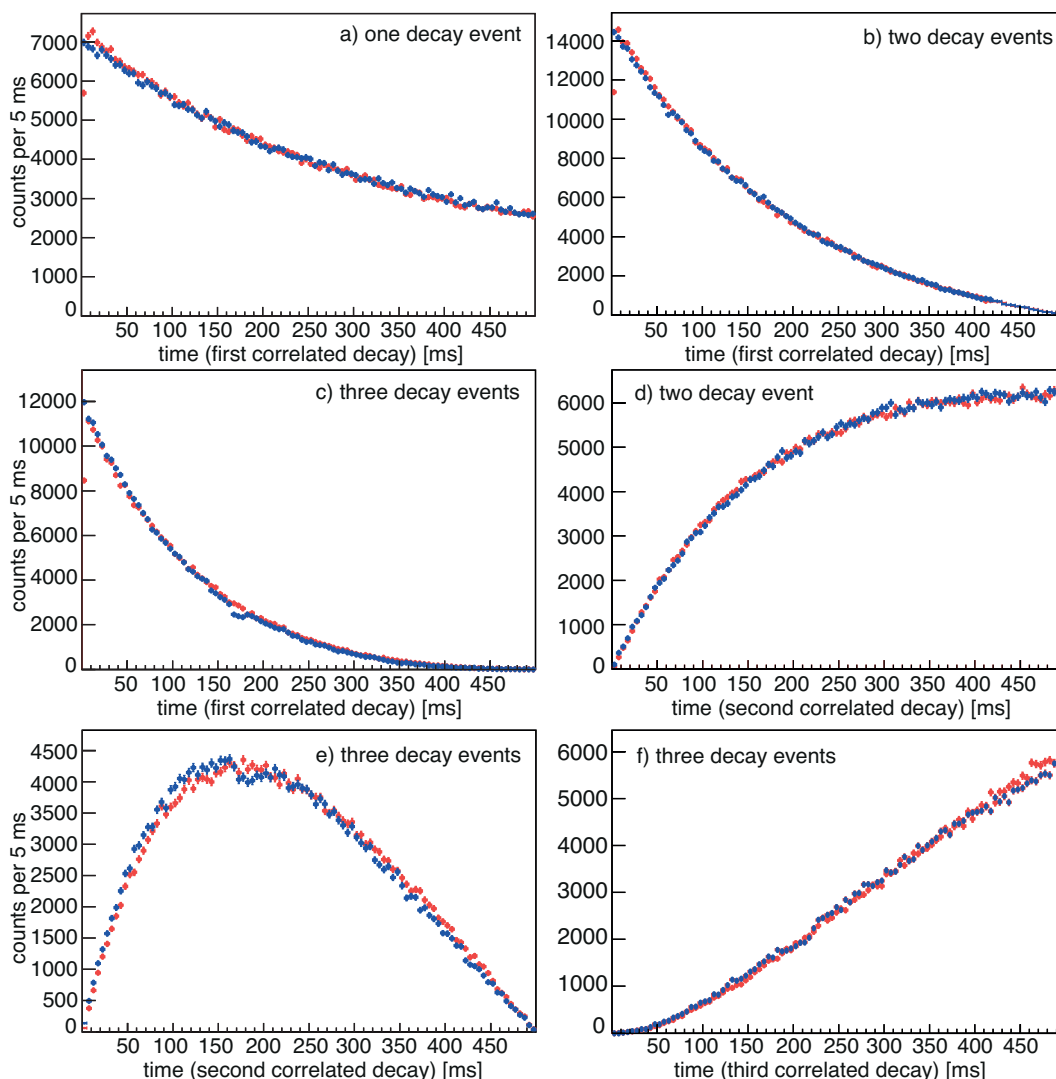


**Figure 4.9:** Comparison of the experimental data (red) with a Monte Carlo Simulation (blue) of the P.D.F. used for the MLH analysis. The individual spectra show the time distribution of a) to c) the first, d) to e) the second and f) third correlated decay after the implantation for events where exactly a) one, b) and d) two, or c), e) and f) three decays were correlated within the correlation time  $t_c$ .

fitting routine. This procedure was performed for all nuclei and there were no cases of severe problems or deviations.

While most of the fit parameters (half-lives,  $P_n$  values, background rate, efficiencies, ...) are fixed, there is one parameter which has to be chosen carefully in the MLH analysis, namely the correlation time  $T_{corr}$ . So far no explanation has been given for the choice of exactly this one in the presented scenario. To start with this topic a reminder is given that the background rate of falsely correlated events in the present experiment was high, and since the constructed P.D.F. only describes events with up to three correlated decays, it is important to limit the number of correlated events by an appropriate choice of  $T_{corr}$ . When choosing  $T_{corr}$  too long, too many events have more than three correlated decays, and due to the limitation of the P.D.F. to only describe events with up to three correlated

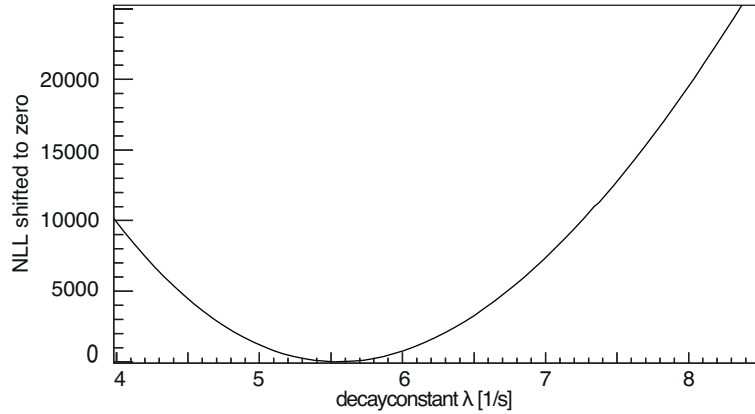


**Figure 4.10:** Distribution of the negative log-likelihood (NLL) of the used P.D.F. to describe the activity of parent, daughter and granddaughter generation nuclei for the events with zero to three correlated decay events within a correlation time window of 500 ms after the implantation of a  $^{130}\text{Cd}$  ion .

$T_{corr}$ [ms]	$T_{1/2}$ [ms]
200	126.3(6)
400	125.8(3)
600	126.1(2)
800	123.3(2)
1000	122.6(2)
2000	121.1(3)
5000	121.1(8)

**Table 4.4:** Deduced  $T_{1/2}$  values for the g.s.  $0^+$   $\beta$ -decay in  $^{130}\text{Cd}$  with the MLH method using different correlation times (maximum time window between implantation and decay) in the range from 200 to 5000 ms.

decays, those events would have to be discarded, reducing the number of good events. Therefore, in cases with very low statistics an even bigger reduction of statistics would occur and furthermore it will be shown now that the obtained half-lives with the MLH method show a deviation for a too long choice of  $T_{corr}$ . Too short choices of  $T_{corr}$  on the other hand would result in problems because experimental information on the second and third generation decays would be lost.

Table 4.4 shows the results obtained with the MLH method for correlation times in a range from 200 to 5000 ms and with the error solely being the statistical error. The aim of this test is to show the influence of changing the correlation time by fixing all other parameters, and the influence of other errors is neglected therefore for the moment being. The results demonstrate that for correlation times up to 600 ms the results are still in rather good agreement with the value obtained with the other methods, but afterwards and especially for correlation times  $\geq 1000$  ms a non-negligible deviation is observed making the use of too large correlation times an additional source of uncertainty in the MLH analysis.

### 4.2.3 $^{126-134}\text{Cd}$ half-lives

The aim of the previous section was to determine the half-life of the ( $1^-$ ) g.s. of  $^{130}\text{Cd}$  and especially compare the three methods which are now going to be used for the determination of the remaining half-lives. It has been shown that the three methods give very similar results and only the MLH method has a significantly larger error resulting from the various input parameters added for this type of analysis. Nevertheless, the MLH method has proven to work and can be applied to the most extreme cases where the two other methods cannot be applied due to the lack of statistics. In a next step the half-life of the remaining Cadmium isotopes with masses  $A = 126 - 134$  can now be deduced.

#### 4.2.3.1 The two $\beta$ -decaying states in $^{129}\text{Cd}$

The determination of the  $^{129}\text{Cd}$  half-life is the most challenging task because there are at least two initial states from which the  $\beta$ -decay can occur, and the exact population ratio of the g.s. and the  $\beta$ -decaying isomeric state in the present experiment could only

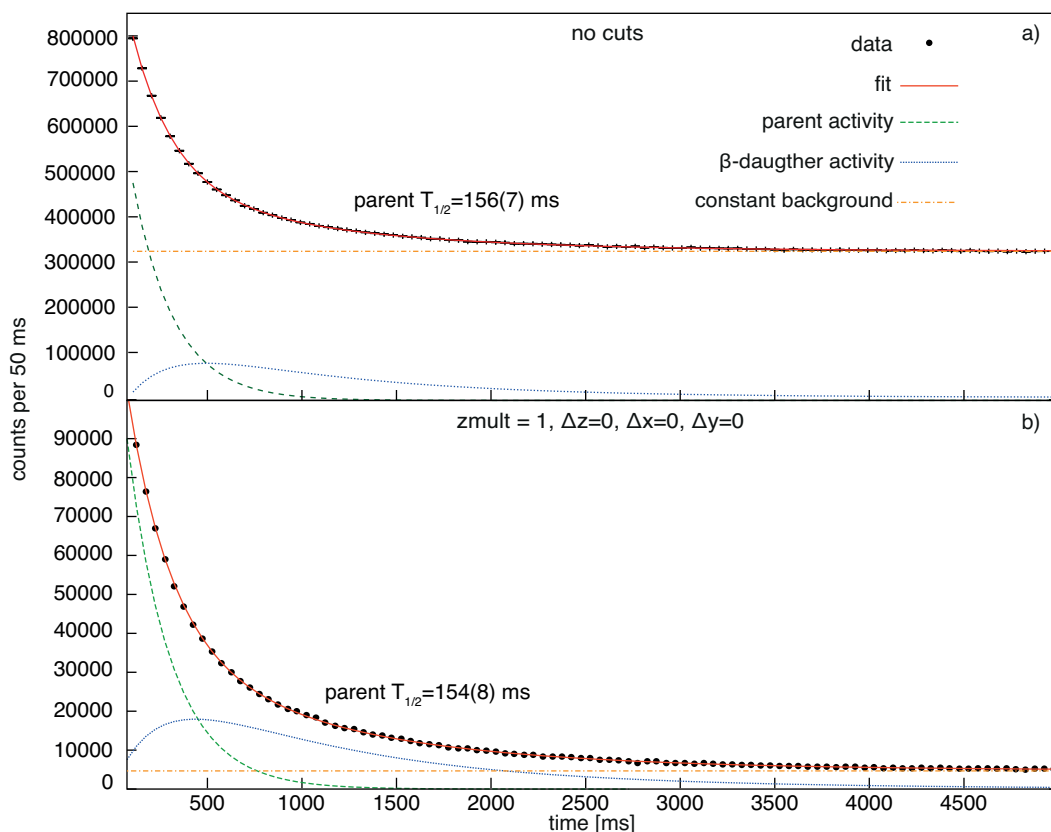


**Figure 4.11:** Time distributions of all decays correlated to the implanted  $^{129}\text{Cd}$  ions with the Bateman equation fit (solid red) via a  $\chi^2$  minimization assuming a single half-life in the  $^{129}\text{Cd}$  decay. In a) the time distribution is shown without further cuts on the implantation position while in b) all cuts ( $z_{mult} = 1$  &  $\Delta z = 0$  &  $\Delta x, \Delta y = 0$ ) are applied. The fit function accounts for the activity of the parent nucleus (dashed green), the activity of the daughter nucleus (dotted blue) and a constant background (dashed dotted orange). The activity of the 3.6 ms isomeric state in  $^{129}\text{Cd}$  is also included in the fit function.

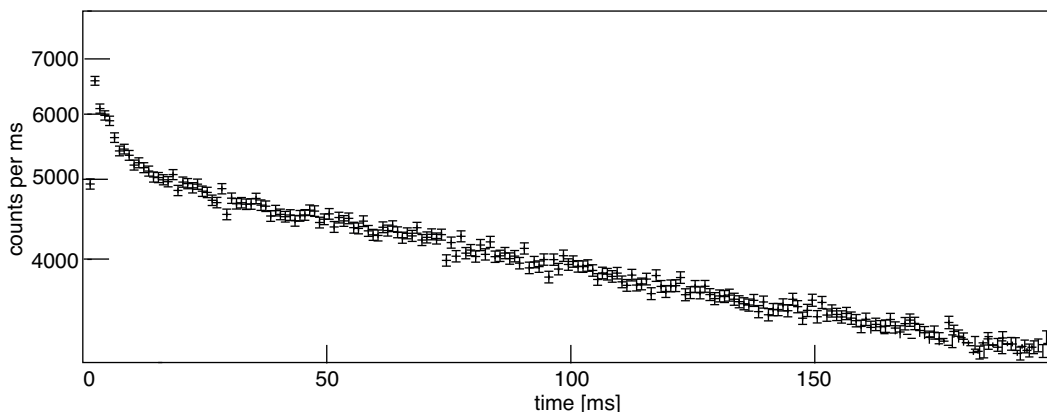


**Figure 4.12:** Time distribution of all decays correlated within the first 200 ms to the implanted  $^{129}\text{Cd}$  ions with the decay and the implantation being detected in the same DSSSD layer and the x- and y-position difference  $\Delta x, y = 0$ , clearly showing the short-lived component of a few ms half-life.

be estimated as presented in the previous chapter. The  $\beta$  decay was presented in detail in section 3.2, but the unknown spin and parity for most of the levels in the daughter nucleus, which are fed by the  $\beta$  decay, complicate the situation. Firstly, the total decay curve (see Fig. 4.11) showing the times of all decays associated with the implantation of a  $^{129}\text{Cd}$  ion up to a maximum correlation time of five seconds was inspected. The ion- $\beta$  correlations were limited with conditions as in the  $^{130}\text{Cd}$  case to minimize the background in the time-correlated spectrum (see section 4.2.2.2).

Fig. 4.12 shows the time distribution of all decays correlated to the  $^{129}\text{Cd}$  ions within the first 200 ms. One observes a drop in the first bin, related to the dead time of the data-acquisition system in the order of 1-2 ms after the implantation. The correlated decays were again required to be detected within the same DSSSD and furthermore within the same pixel as the implanted ion. Clearly the exponential decay component of the  $\beta$ -decaying states can be observed, but below 15 ms a very short-lived component seems to be added on top of the time-distribution of the  $\beta$ -decaying states in  $^{129}\text{Cd}$ . The half-life of this component is too short to be associated with either one of the  $\beta$ -decaying states. In the next chapter in section 5.2 one will see that a ms isomeric state is present in  $^{129}\text{Cd}$  which decays via a cascade to the  $(11/2^-)$   $\beta$ -decaying state in  $^{129}\text{Cd}$ . It was measured that about 3(1)% of the implanted  $^{129}\text{Cd}$  ions are found initially in that excited state, which was for the first time observed in the present experiment. In any of the following cases the fits which include activity of the  $(11/2^-)$   $\beta$ -decaying state in  $^{129}\text{Cd}$  also account for the activity of this 3.6 ms isomeric state in  $^{129}\text{Cd}$ .

The two  $\beta$ -decaying isomeric states in  $^{129}\text{Cd}$  have been previously reported to have half-lives of 104(6) and 242(8) ms by Arndt *et al.* [62, 113]. But surprisingly, the decay curve in Fig. 4.11 does not show any indication for two very different half-lives. Nevertheless, in a first step fits were performed allowing for two half-lives in  $^{129}\text{Cd}$ . From the results presented for the  $\beta$ -decay spectroscopy of  $^{129}\text{Cd}$  it was concluded that 51(4)% of the  $^{129}\text{Cd}$  ions is found in the  $(3/2^+)$   $\beta$ -decaying isomeric state, and the population ratio of

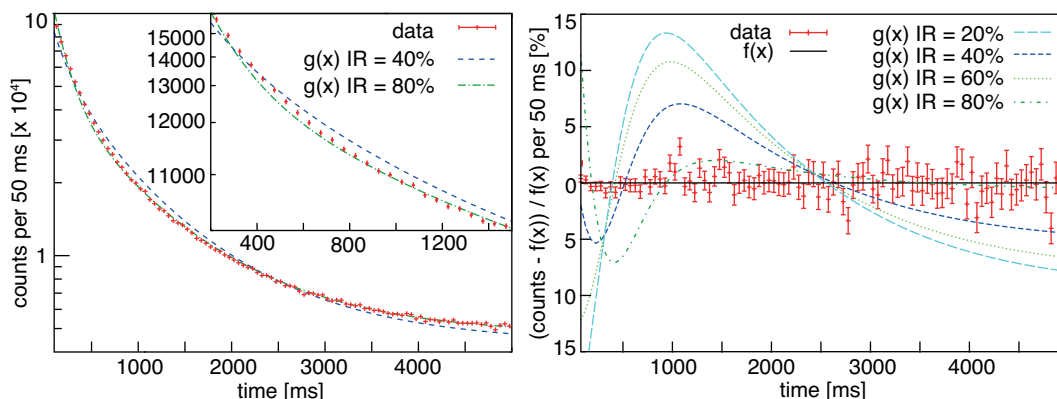


**Figure 4.13:** a) Time distribution of all decays ( $Z_{mult} = 1$  &  $\Delta z = 0$  &  $\Delta x, \Delta y = 0$ ) correlated to the implanted  $^{129}\text{Cd}$  ions with two Bateman equation fits (blue dashed = 40% population of the  $(1/2^-)$   $\beta$ -decaying isomer; green dashed dotted = 80%) via a  $\chi^2$  minimization assuming two half-lives of 104 and 242 ms ( $g(x)$ ) (see Refs. [62, 113]) in the  $^{129}\text{Cd}$  decay. And b) the fits for different IR with  $g(x)$  and the experimental data, all normalized on the fit  $f(x)$  with a single half-life of 154.0 ms.

the two  $\beta$ -decaying states in the daughter  $^{129}\text{In}$  was deduced from the intensity of characteristic transitions observed in the granddaughter nucleus (72(2)% proceeds via the  $9/2^+$  state and 28(2)% via the  $1/2^-$  state). Using those population ratios, several fits were performed using the Bateman equations with the  $\beta$ -decay half-lives of the  $9/2^+$  and  $1/2^-$  states in  $^{129}\text{In}$  taken from the literature to be  $T_{1/2} = 611(4)$  ms and  $T_{1/2} = 1.23(3)$  min, respectively [2]. In all cases the two obtained half-lives were identical or very similar and therefore, the decay curve was fitted in a second step assuming a single half-life for the parent decay ( $f(x)$ ). The fit is shown in Fig. 4.11a) to a time distribution of all decays correlated to the implanted  $^{129}\text{Cd}$  ions without further restrictions and in 4.11b) to a time distribution with all cuts applied on the position difference of implantation and  $\beta$  decay. A very good agreement is found in both cases over the full time range of five seconds. The half-life obtained from the first fit is  $T_{1/2} = 156(7)$  ms, while the second fit results in a half-life of  $T_{1/2} = 154(8)$  ms. An additional fit with two half-lives of 104 and 242 ms ( $g(x)$ ) was also performed to furthermore illustrate that two very different half-lives as proposed in Ref. [62] do not describe the experimental data. For that the isomeric ratio IR is introduced, giving the amount of  $^{129}\text{Cd}$  ions being initially in the  $\beta$ -decaying isomeric state and not the g.s. The fit result for two different IR (40% and 80%) of the  $(1/2^-)$   $\beta$ -decaying isomeric state is shown in Fig. 4.13a) with the small inlay figure showing that especially in the range from 200 to 1400 ms a significant difference between fit and data can be observed. Figure 4.13b) demonstrates this even better. In that figure the fit with a single half-life of 154.0 ms is used for the normalization, showing that the experimental data scatters as expected around the zero-line. The fit with two half-lives as measured in Ref. [62, 113] is shown for different IR and in none of the presented cases a good agreement can be found with the experimental data. Even the fit with IR = 80%, which shows a rather good agreement for times larger than 2000 ms, has a maximum deviation of about 7% in the region around 500 ms. From these observations it is concluded that the two  $\beta$ -decaying states in  $^{129}\text{Cd}$  have very similar half-lives. In the following  $\gamma$ -labeled  $\beta$ -decay

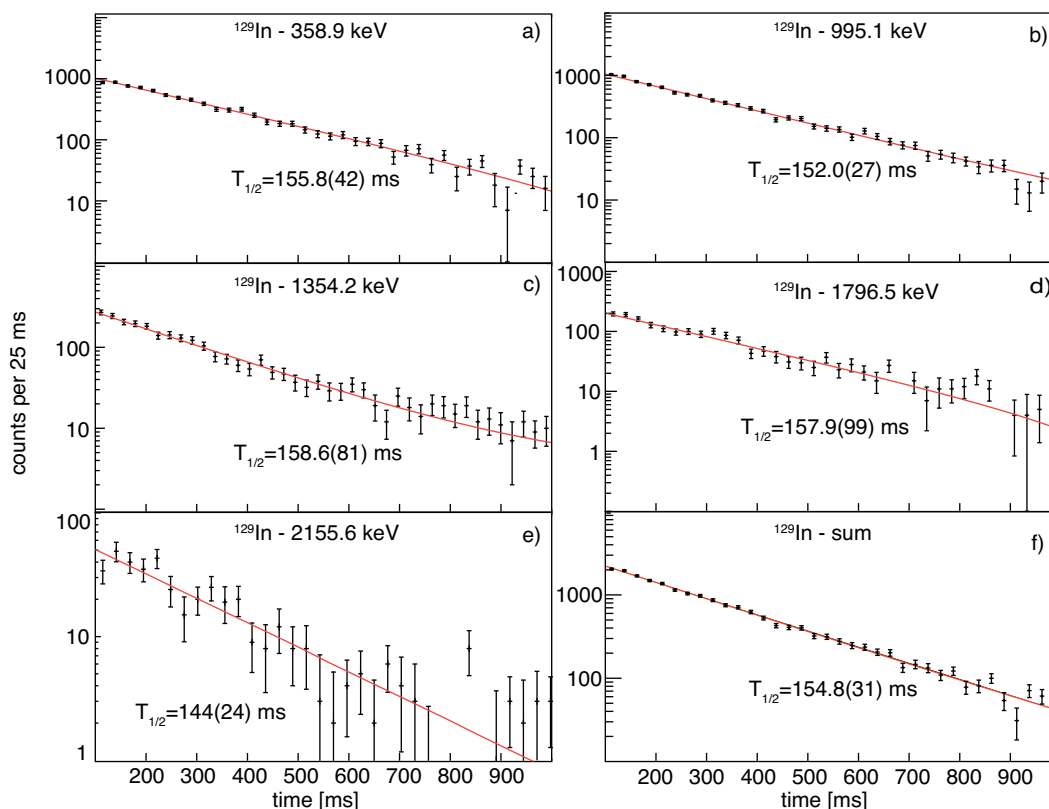


**Figure 4.14:** Time distributions (black) of the decays observed after an  $^{129}\text{Cd}$  implantation gated on the observation of a) - e) the 358.9, 995.1, 1354.2, 1796.5 or 2155.6 keV  $\gamma$ -ray, respectively, in prompt coincidence with the decay and f) the sum of all those time distributions with the fitted single exponential decay functions (red lines). The activity of the 3.6 ms isomeric state in  $^{129}\text{Cd}$  is also included in the fit function.

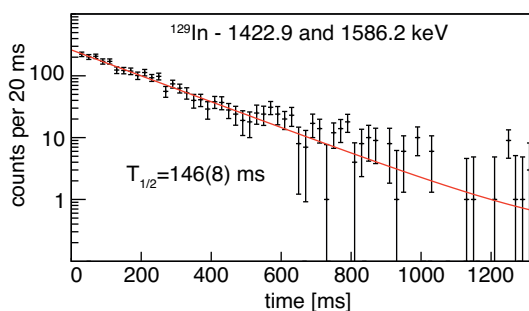


**Figure 4.15:** Time distribution of the decays observed after a  $^{129}\text{Cd}$  implantation gated on the observation of either a 1422.9 or a 1586.2 keV  $\gamma$ -ray, respectively, in prompt coincidence with the decay.

half-lives will be used to check those.

For the  $(11/2^-)$  state there are several transitions which are originating from states solely fed by this  $\beta$ -decaying state. The transitions with energies of 358.9, 995.1, 1354.2, 1796.5 and 2155.6 keV are here perfect candidates. Figures 4.14a) - e) show the  $\beta$ -decay time distributions obtained gating on those transitions and Fig. 4.14f) shows the sum time distribution of all of them with the fit resulting in a half-life of 154.8(31) ms. The fit results

Parent Nuclei	$I_{\beta}^{\pi}$	$E_{\gamma}$ [keV]	$T_{1/2}(\gamma)$ [ms]
$^{129}\text{Cd}$	$(11/2^{-})$	358.9	155.8(42)
$^{129}\text{Cd}$	$(11/2^{-})$	995.1	152.0(27)
$^{129}\text{Cd}$	$(11/2^{-})$	1354.2	158.6(81)
$^{129}\text{Cd}$	$(11/2^{-})$	1796.5	157.9(99)
$^{129}\text{Cd}$	$(11/2^{-})$	2155.6	144(24)
$^{129}\text{Cd}$	$(11/2^{-})$	sum	154.8(31)
$^{129}\text{Cd}$	$(3/2^{+})$	1422.9 + 1586.2	146(8)

**Table 4.5:** Summary of the fit results for the half-lives obtained from the  $\gamma$ -gated time distributions of several transitions in  $^{129}\text{In}$  after the  $\beta$ -decay of  $^{129}\text{Cd}$ .

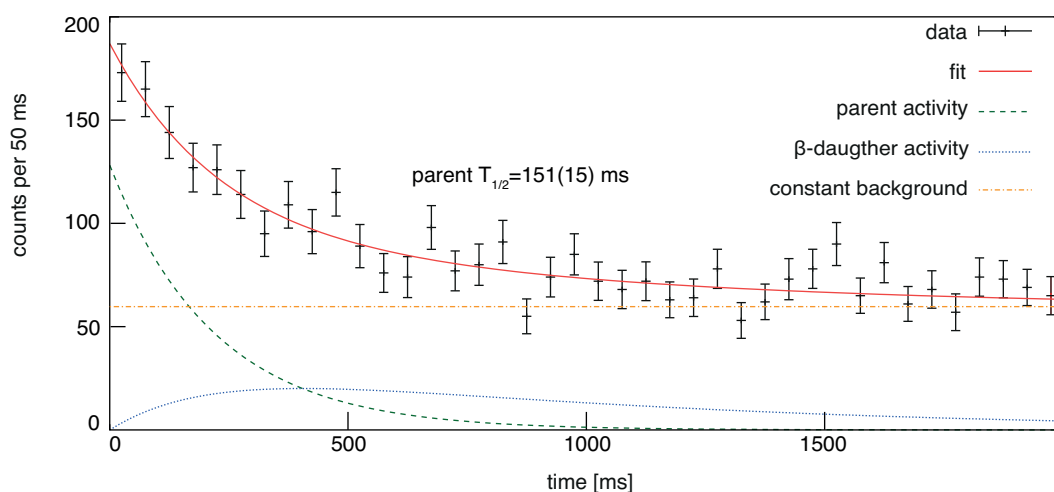


**Figure 4.16:** Time distribution of all decays correlated to the implantation of a  $^{129}\text{Cd}$  ion after the observation of one of the characteristic transitions emitted in the decay of the ms isomer in  $^{129}\text{Cd}$ . The  $\chi^2$  minimization fit with the Bateman equations (red solid) which accounts for the activity of the  $11/2^{-}$  state in the parent nucleus (green dashed), the activities of the  $9/2^{+}$  and  $1/2^{-}$  states in the daughter nucleus (blue dotted) and a constant background (orange dashed-dotted), is shown, too. The activity of the 3.6 ms isomeric state in  $^{129}\text{Cd}$  is included in the fit function as well.

of the individual time distributions for each transition are presented in Table 4.5 showing that all obtained half-lives agree within the error bars.

To obtain the time distribution of the  $(3/2^{+})$  state, the 1422.9 and the 1586.2 keV transitions were chosen, based on the level scheme presented previously in this thesis (see section 3.2.4). The corresponding time distribution is shown in Fig. 4.15 together with the fit using a single exponential decay function including a constant background. The fit results in a half-life of 146(8) ms and is therefore within the errorbars in agreement with the values obtained for the half-life of the  $(11/2^{-})$  state. This was expected from the other observations described before.

As a last check the half-life of the  $(11/2^{-})$  g.s. was deduced using a different approach. In  $^{129}\text{Cd}$  a ms isomer was found in the present work, for which the results will be presented later in this thesis in section 5.2. This isomer decays via a cascade to the  $(11/2^{-})$  g.s. Filling a time distribution of all decays following the observation of one of the characteristic

transitions emitted in the decay of the ms isomer, and with respect to the timing of that transition, results in a distribution only depending on the half-life of the  $(11/2^-)$  state. This distribution is shown in Fig. 4.16 together with the Bateman equation fit. Again, it is necessary that the fit function accounts for both, the parent and daughter activities, because of the missing signature to discriminate between them. The obtained half-life is 151(15) ms, in good agreement with the previous mentioned values obtained from the  $\gamma$ -labeled  $\beta$ -decay half-lives.

All half-lives measured for the two  $\beta$ -decaying states in  $^{129}\text{Cd}$  are found to be in good agreement with each other and it is concluded that the two states have very similar half-lives. In the following the half-lives of the  $\beta$ -decaying states in  $^{126}\text{Cd}$  to  $^{134}\text{Cd}$  are presented.

#### 4.2.3.2 The half-lives of $^{126}\text{Cd}$ to $^{134}\text{Cd}$

The ion- $\beta$  time distributions gated on some selected  $\gamma$ -ray transitions in the Cadmium isotopes  $^{126-128}\text{Cd}$  and  $^{131,132}\text{Cd}$  are shown in Fig. 4.17, together with the corresponding single-exponential decay fitting function including a constant background. As can be seen in the figure, the fits are in very good agreement with the experimental data. The results for the most intense  $\gamma$  transitions observed in this work are summarized in Table 4.6. Here, the results of the fits are listed for both, the time distributions of each individual transition and the summed time spectrum for each group of transitions arising from a given  $\beta$ -decaying state. In the case of the summed time spectra, the uncertainties in the measured values are smaller due to the increased statistics per time bin. Therefore, the value of the summed time distributions will be used in the comparison with the other two methods.

For the nuclei  $^{126-133}\text{Cd}$ , the half-life was additionally determined with a fit to the Bateman equations via a  $\chi^2$  minimization, as explained in section 4.1.1. The time distributions of all decays correlated to the implanted Cadmium ions are presented in Fig. 4.18 together with the resulting fits and their decomposition into the different activities of the  $\beta$ -decaying states in the parent and daughter generation nuclei. Note that in all cases the granddaughter generation had no significant influence because of the very long half-lives and was not included in the fits. The input parameters such as half-lives and  $\beta$ -delayed neutron emission probabilities have been taken either from Refs. [51, 60] and references therein or from the present experimental data (e.g. population of  $\beta$ -decaying states in the daughter generation nuclei). The  $\beta$  decays of the  $0^+$  ground-states of  $^{126}\text{Cd}$  and  $^{128}\text{Cd}$  were found to proceed only to the  $(3^+)$  g.s. in the daughter nucleus and no  $\beta$ -decaying isomeric states had to be taken into account in those fits. The 253-keV transition, populated in the decay from the  $1/2^-$   $\beta$ -decaying state in  $^{127}\text{In}$  to  $^{127}\text{Sn}$ , was observed in the present experiment and the intensity was obtained from fitting the peak area. With a known absolute intensity per 100 decays of 40(4) [119] the population of the  $1/2^-$   $\beta$ -decaying state in  $^{127}\text{In}$  was estimated to be 20(5)% while the remaining  $\beta$  intensity proceeds to the  $9/2^+$

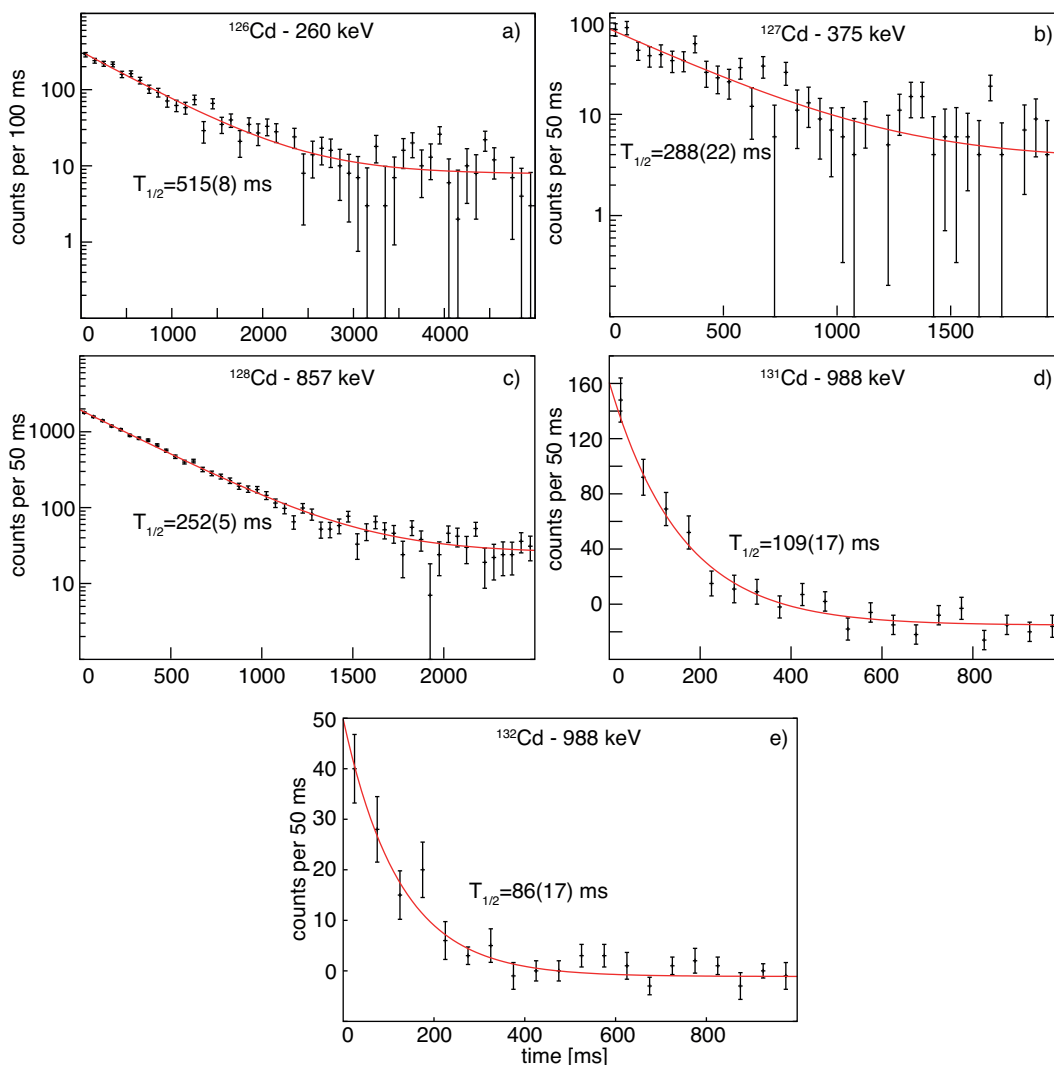


**Figure 4.17:** Time distributions (black) of the decays observed after an implantation gated on the observation of a specific  $\gamma$  transition in the daughter nucleus together with the fitted single exponential decay functions (red lines). Time distributions are shown for a) the  $^{126}\text{Cd}$  decay and the 260-keV transition in  $^{126}\text{In}$ , b) the  $^{127}\text{Cd}$  decay and the 375-keV transition in  $^{127}\text{In}$ , c) the  $^{128}\text{Cd}$  decay and the 857-keV transition in  $^{128}\text{In}$ , d) the  $^{131}\text{Cd}$  decay and the 988-keV transition in  $^{131}\text{In}$  and e) the  $^{132}\text{Cd}$  decay and the 988-keV transition in  $^{131}\text{In}$ .

g.s. in  $^{127}\text{In}$ . The population of the  $1/2^-$   $\beta$ -decaying state in  $^{131}\text{In}$  was in section 3.4.1 presented to be 8.8(16)% and no  $\beta$  feeding was observed in the present work to the  $(21/2^+)$   $\beta$ -decaying state in  $^{131}\text{In}$ . Half-lives for the  $\beta$ -decaying states in  $^{131,132}\text{In}$  were taken from the present work (see section 4.2.1). The Cadmium half-life values extracted from this analysis procedure will be presented in the following section, where the results from the three methods will be compared among them and with the literature values.

For the most exotic nucleus  $^{134}\text{Cd}$  with only 73 identified ions in BigRIPS, the only applicable method is the Maximum-Likelihood analysis (see section 4.1.2). This method was also applied to the isotopes  $^{128,131-133}\text{Cd}$  to compare the results obtained with the three methods. The background rates and efficiencies obtained from the Bateman equation fit that have been used as input parameters for the MLH analysis were already summarized

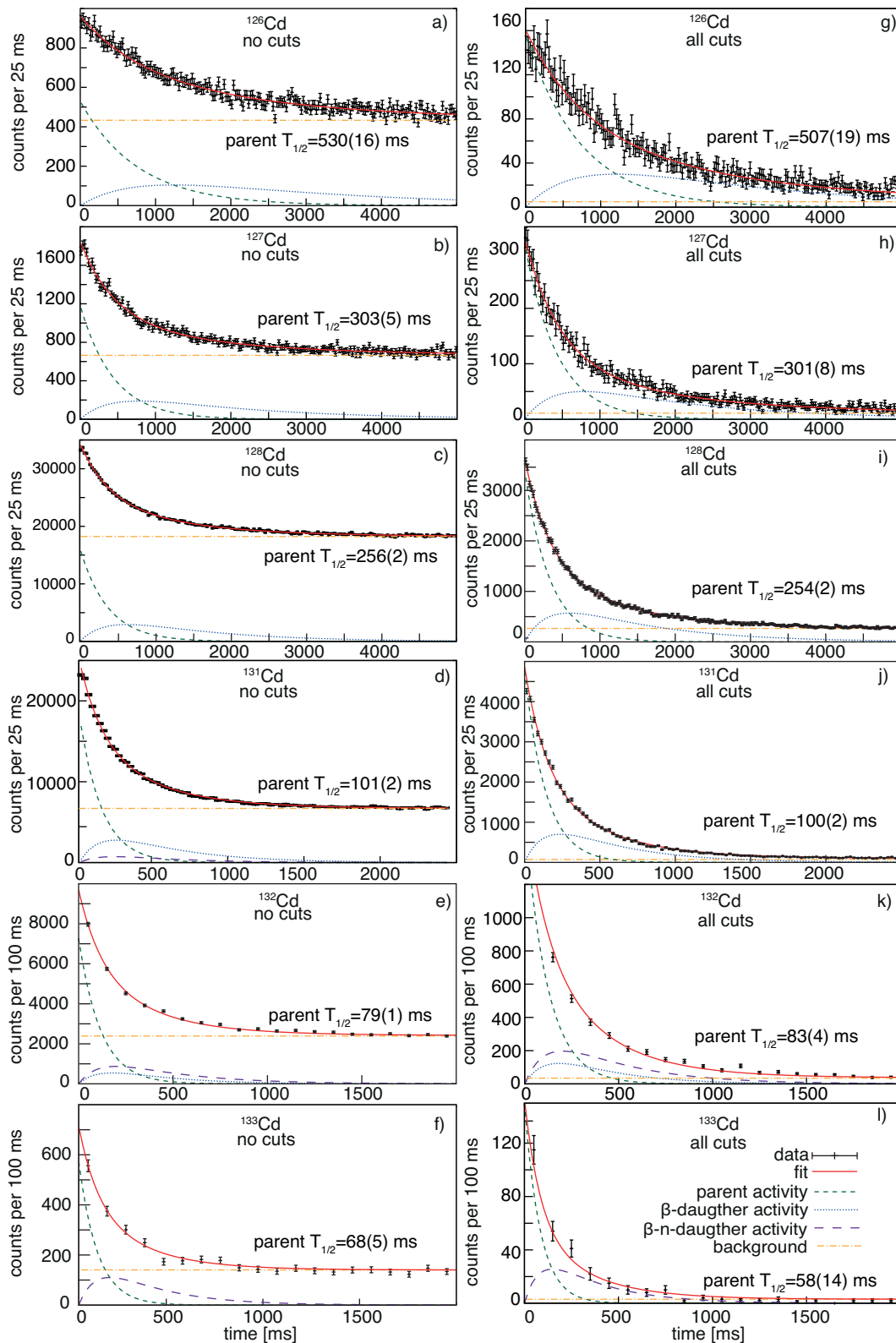


**Figure 4.18:** Time distributions of the decays correlated to the implanted  $^{126-128}\text{Cd}$  and  $^{131-133}\text{Cd}$  ions with a)-f) no and g)-k) all cuts applied on the position difference between implantation and decay. The corresponding Bateman equation fit (red solid line) is shown in each plot together with the activity of the parent (green dashed line), daughter (blue dotted line) and  $\beta$ -delayed neutron daughter (purple dashed line) nuclei. For details of the fit see text and section 4.1.1.

Parent Nuclei	$I_{\beta}^{\pi}$	$E_{\gamma}$ [keV]	$T_{1/2}(\gamma)$ ms
$^{126}\text{Cd}$	$0^+$	260.1	515(18)
$^{127}\text{Cd}$	$(3/2^+)$	376.3	288(22)
$^{128}\text{Cd}$	$0^+$	247.6	252(6)
	$0^+$	857.1	252(5)
	$0^+$	sum	254(3)
$^{129}\text{Cd}$	$(11/2^-)$	358.9	155.8(42)
	$(11/2^-)$	995.1	152.0(27)
	$(11/2^-)$	1354.2	158.6(81)
	$(11/2^-)$	1796.5	157.9(99)
	$(11/2^-)$	2155.6	144(24)
	$(11/2^-)$	sum	154.8(31)
$^{130}\text{Cd}$	$(3/2^+)$	1422.9 + 1586.2	146(8)
	$0^+$	450.8	126.4(12)
	$0^+$	1669.2	128.8(18)
	$0^+$	sum	126.8(8)
$^{131}\text{Cd}$	$(7/2^-)$	988	109(17)
	$(7/2^-)$	3555	99(15)
	$(7/2^-)$	sum	106(9)
$^{132}\text{Cd}$	$0^+$	988	86(17)

**Table 4.6:** Summary of the fit results for the half-lives obtained from the  $\gamma$ -gated time distributions for several transitions in  $^{126-132}\text{In}$  after the  $\beta$ -decay of  $^{126-132}\text{Cd}$ .

in Table 4.3. In all cases the errors of the background rate and the efficiency were taken again to be  $\pm 5\%$ . The half-lives of the daughter and granddaughter generation nuclei,  $\beta$ -delayed neutron emission probabilities and the relative population of  $\beta$ -decaying isomeric states were again taken from the literature [51, 60] or as obtained in the present work.

#### 4.2.4 Discussion and comparison to literature

While the  $\beta$ -decay half-lives close to the valley of stability show big fluctuations, the half-lives further away from stability in most cases behave very smoothly when investigating them as a function of the neutron number  $N$ . In Ref. [141] for example the half-lives of nuclei in the vicinity of  $^{78}\text{Ni}$  are presented for several isotopic chains and all of them show a rather similar behaviour without big fluctuations. This observation is made all over the nuclear chart and deviations from this behaviour are only found in the presence of changes in the nuclear structure. This can be explained by having a closer look at the total  $\beta$ -decay rate  $\lambda$  which is a summation over all decays to the energetically possible final states:

$$\lambda = \frac{1}{\ln(2)T_{1/2}} = \sum_{0 \leq E_f \leq Q_{\beta}} S_{\beta}(E_f) \times f(Z, Q_{\beta} - E_f) \quad (4.31)$$

with  $S_{\beta}(E_f)$  being the  $\beta$ -strength function and  $f(Z, Q_{\beta} - E_f)$  the phase space factor. The phase space factor is strongly dependent ( $f \sim (Q_{\beta} - E_f)^5$ ) on the energy difference between  $Q_{\beta}$  and the energy of the final state  $E_f$  in the daughter nucleus, and because of

Nuclei	$I^\pi$	$T_{1/2}(\gamma)$ [ms]	$T_{1/2}(B1)$ [ms]	$T_{1/2}(B2)$ [ms]	$T_{1/2}(M)$ [ms]	$T_{1/2}(Lit.)$
$^{126}\text{Cd}$	$0^+$	515(18)	530(16)	507(19)	-	506(15) [59]
$^{127}\text{Cd}$	$(3/2^+)$	288(22)	303(5)	301(8)	-	370(70) [60]
$^{128}\text{Cd}$	$0^+$	254(3)	256(2)	254(2)	245(10)	280(40) [61]
$^{129}\text{Cd}$	$(3/2^+)$	146(8)	156(7)	154(8)	-	104(6) [62, 112, 113, 115]
$^{129}\text{Cd}$	$(11/2^-)$	154.8(31)	156(7)	154(8)	-	242(8) [62, 112, 113, 115]
$^{130}\text{Cd}$	$0^+$	126.8(8)	127.4(5)	126.8(3)	125(5)	162(7) [20]
$^{131}\text{Cd}$	$(7/2^-)$	106(9)	101(2)	100(2)	98(4)	68(3) [34]
$^{132}\text{Cd}$	$0^+$	86(17)	79(1)	83(4)	79(4)	97(10) [34]
$^{133}\text{Cd}$	$(7/2^-)$	-	68(5)	58(14)	68(8)	57(10) [112]
$^{134}\text{Cd}$	$0^+$	-	-	-	$58^{(+24)}_{(-19)}$	-

**Table 4.7:** Summary of the results for the half-lives obtained from the three presented methods ( $\gamma$ -gated:  $T_{1/2}(\gamma)$ , Bateman equation  $\chi^2$  fit:  $T_{1/2}(B1)$  with no cuts and  $T_{1/2}(B2)$  with all cuts applied and Maximum-Likelihood analysis:  $T_{1/2}(M)$ ) and literature values  $T_{1/2}(Lit.)$  for the Cadmium isotopes with  $A = 126$  to  $134$ .

that the main contribution to the total transition rate  $\lambda$  is given by the  $\beta$ -decay branches to low-lying states in the daughter nucleus. In nuclei close to stability the  $Q_\beta$  values are typically small and therefore, the structure of excited states and the pairing interaction have big impact on  $\lambda$ , while for nuclei far from stability those effects play a less important role.

Comparing the previously reported data to the results obtained in the present work (see table 4.7 for a summary) important discrepancies are observed. Especially for the nuclei with  $A > 128$  the previous measurements showed big jumps in the half-lives with growing neutron number  $N$ , while the results of this thesis show a very smooth behaviour. In particular the half-lives obtained for  $A = 129, 130$  and  $131$  show big differences with respect to the literature values. As well, while in Ref. [62] the two half-lives for the  $\beta$ -decaying states in  $^{129}\text{Cd}$  were proposed to have significantly different half-lives, this cannot be confirmed here. In all cases the results from the three different methods agree within one standard deviation. This is of particular importance for the very exotic case of  $^{134}\text{Cd}$  in which only the MLH method can be applied.

The results, presented in Fig. 4.19, show a smooth odd-even staggering below  $N = 82$  which seems to disappear after crossing the 82-neutron shell closure. It is important to notice that there is no indication for a large  $N = 82$  shell gap in the measured half-lives in contrast to a previous measurement [34] which suggested a sudden drop in the half-life from  $N = 82$  to  $N = 83$ .

The new half-life values have been compared to two theoretical models, which are commonly used for r-process calculations.  $\beta$ -decay half-lives are crucial input parameters to the calculations because the relative abundances around the neutron shell closures are particularly sensitive to the half-lives of the r-process nuclei [14]. Such dependence is apparently independent of the astrophysical scenario considered, as indicated in a recent r-process sensitivity study [54]. The half-lives measured in this work, thus, are excellent

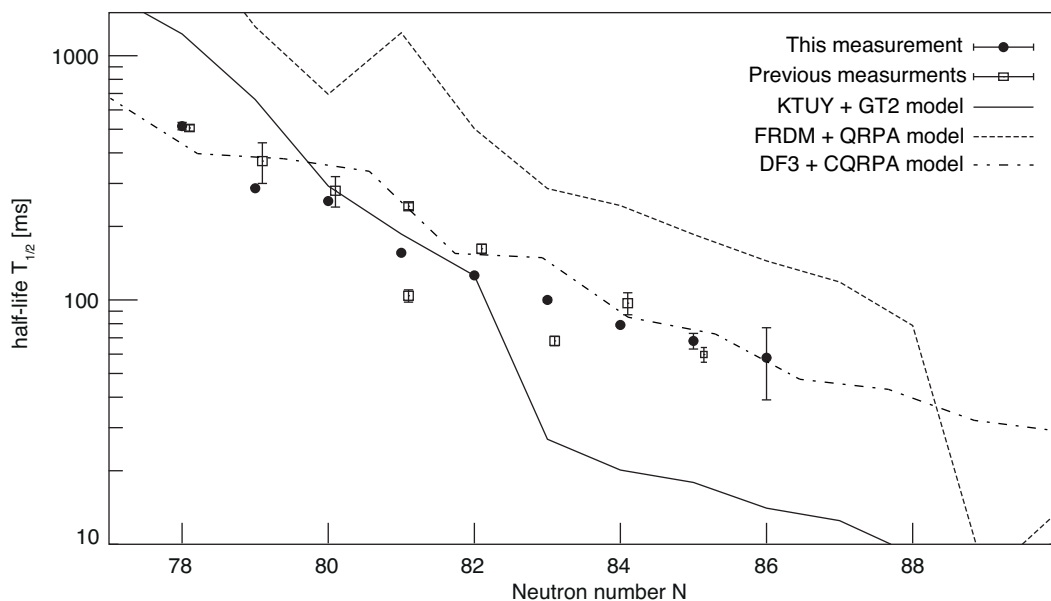


**Figure 4.19:** Experimental Cadmium half-lives for masses 126-134 obtained in this work (filled dots) and previous works (open squares) [20, 34, 59–62] and theoretical predictions by the FRDM+QRPA (dashed line) [63], KTUY+GT2 (solid lines) [64, 65] and DF3+QRPA [67, 68] models.

experimental probes to test the descriptive power of these models near the  $N=82$  neutron shell closure. Fig. 1.5 includes the predictions made by the FRDM+QRPA (dashed line) [63], KTUY+GT2 (solid lines) [64, 65] and DF3+QRPA [67, 68] models which were introduced in section 1.3 in the introduction.

The DF3+CQRPA model shows an overall very good agreement with the data, predicting the trend of the half-lives very well and lying only slightly above the experimentally obtained values for the  $N < 84$  nuclei. The other two models, presented also in Fig. 4.19, show overall a worse agreement, and especially FRDM+QRPA seems to give too long half-lives compared to the experimental data. KTUY+GT2 on the other hand provides rather good values in the region  $N \leq 82$  but seems to underestimate the half-life above the  $N=82$  gap and furthermore shows a clear jump in the half-lives at the  $N=82$  shell gap, not in agreement with the values obtained for  $^{130}\text{Cd}$  and  $^{131}\text{Cd}$ . It becomes clear that improvements have to be made for both models to describe well the experimental data and on top of that, the necessity for experimental half-lives as input parameters for r-process calculations becomes even more obvious to determine the exact flow of the r-process at the critical waiting-points.

The half-lives of all nuclei present in the experimental data was furthermore analysed in an independent approach by G. Lorusso and submitted to Physical Review Letters as Lorusso *et al.* [14]. The half-lives of the Cadmium isotopes were found to be in very good agreement when comparing the values obtained by G. Lorusso to those presented here.

### 4.3 $\beta$ delayed neutron emission probability

The  $\beta$  delayed neutron emission probabilities are of significant importance for r-process calculations, too. In the calculations they can have an influence on the shape of the final distribution as shown in Ref. [149, p. 6]. Most models are still not able to reproduce the  $P_n$  values in an adequate way in the regions far away from stability and new experimental data is needed to benchmark these models and to allow further improvements.

#### 4.3.1 Deducing the $P_n$ value in the current experiment

The  $P_n$  value is the fraction of  $\beta$ -decays proceeding to levels above the neutron separation energy which are subsequently de-excited via the emission of one or more neutrons. In the following section  $P_{1n}$  is the probability to emit one neutron, while  $P_n$  is the sum of all probabilities  $P_{xn}$  to emit  $x$  neutrons:

$$P_n = \sum_{x=1}^{\infty} P_{xn} \quad (4.32)$$

In the simplest case  $P_n$  can be calculated as the missing  $\beta$ -intensity from the daughter nucleus:

$$P_n = 100\% - I_{\beta}^{tot} \quad (4.33)$$

$I_{\beta}^{tot}$  is in all cases here the  $\beta$ -intensity proceeding to levels which decay to lower lying levels in the daughter nucleus and not via  $\beta$ -delayed neutron emission. To calculate the  $P_n$  with this formula, one must be sure that no  $\beta$ -intensity is unobserved due to efficiency problems or because of g.s. to g.s. decays. Unfortunately, with the present set-up it can not be assured that the full  $\beta$ -intensity is observed and especially there is no possibility to measure the intensity for g.s. to g.s.  $\beta$  decays. Consequently, a different approach has to be used. One possibility is to use information known from the granddaughter generation nuclei. If the  $\beta$ -decay feeding and absolute intensities of  $\gamma$  transitions are known for the granddaughter nucleus, then  $I_{\beta}^{tot}$  can be calculated from those. Fig. 4.20a) shows a basic  $\beta$ -decay scheme for the example of  $^{128}\text{Cd}$  including  $\beta$ -delayed neutron emission for the parent nucleus.  $\gamma_2$  is an electromagnetic transition observed in the granddaughter generation nucleus with known intensity  $I_{\gamma_2}$  per 100 decays of the daughter nucleus. The formula to calculate  $I_{\beta}^{tot}$  is then given as:

$$I_{\beta}^{tot} = \frac{N_{\gamma_2}}{\epsilon_{abs}^{\gamma_2} I_{\gamma_2} N_{decay}^P} \quad (4.34)$$

with  $\epsilon_{abs}^{\gamma_2}$  the absolute  $\gamma$  detection efficiency for a transition with energy  $E_{\gamma_2}$  and  $N_{decay}^P$  the number of parent decays. Combining formulas 4.33 and 4.34 the following formula is obtained:

$$P_n = 100\% - \frac{N_{\gamma_2}}{\epsilon_{abs}^{\gamma_2} I_{\gamma_2} N_{decay}^P} \quad (4.35)$$

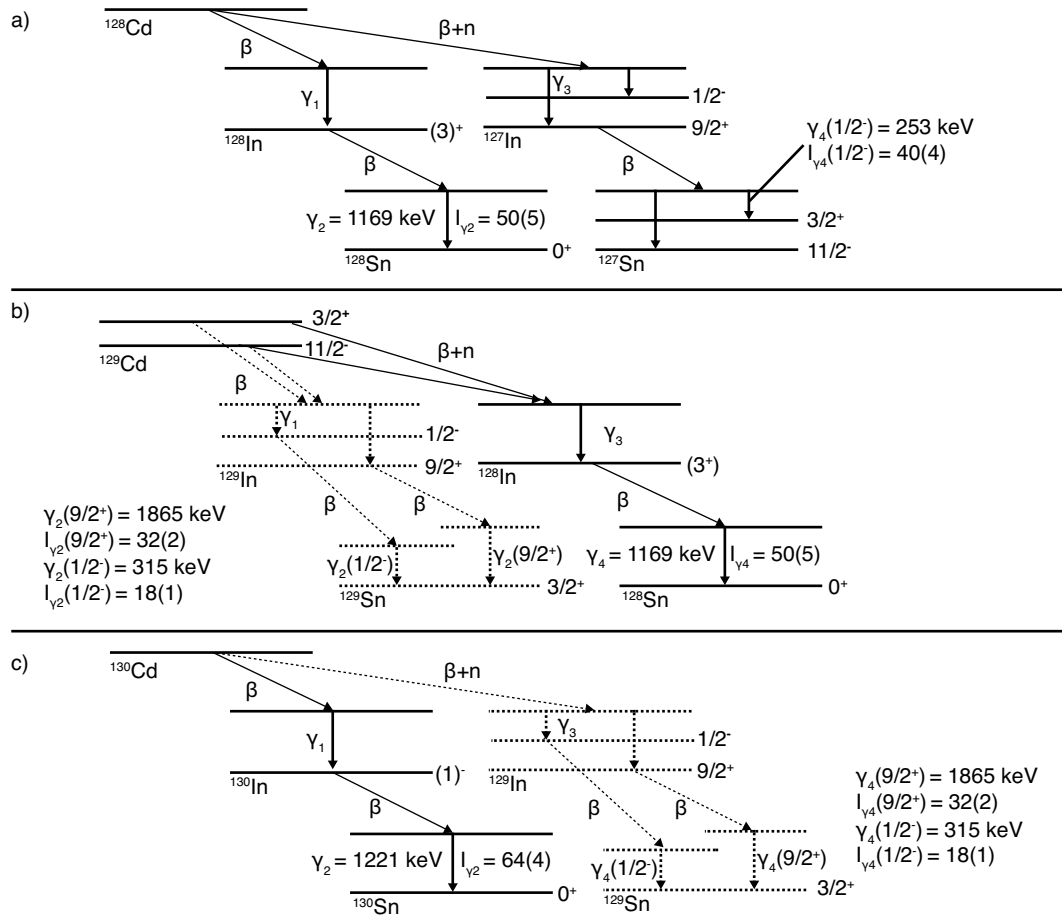


**Figure 4.20:** Basic  $\beta$ -decay schemes including  $\beta$ -delayed neutron emission for the parent nucleus to visualize the  $P_n$  determination method used in the present thesis for a)  $^{128}\text{Cd}$ , b)  $^{129}\text{Cd}$  and c)  $^{130}\text{Cd}$ . The transitions in the granddaughter generation nuclei were selected based on the level schemes and intensities  $I_{\gamma_2}$  ( $I_{\gamma_4}$ ) per 100 decays of the daughter ( $\beta$ -delayed neutron daughter) nucleus from Refs. [2, 119, 150]. Parts of the decay schemes which are dashed were not used for the analysis because the intensities in the granddaughter generation nuclei were found deficient.

To cross-check those results, one can also calculate  $P_{1n}$ , the probability to emit exactly one neutron, from the number of observed  $\gamma$ -rays in the  $\beta$ -delayed neutron granddaughter if the respective absolute intensity per 100  $\beta$ -delayed neutron daughter decays  $I_{\gamma_4}$  is known from literature. The corresponding formula would then be:

$$P_{1n} = I_{\beta,n}^{\text{tot}} = \frac{N_{\gamma_4}}{\epsilon_{\gamma_4}^{\text{abs}} I_{\gamma_4} N_{\text{decay}}^P} \quad (4.36)$$

The intention was to calculate  $\beta$  delayed neutron emission probabilities using both ways. Unfortunately, due to problems with the literature values of absolute intensities of transitions in the granddaughter or the  $\beta$ -delayed neutron granddaughter this was not possible.

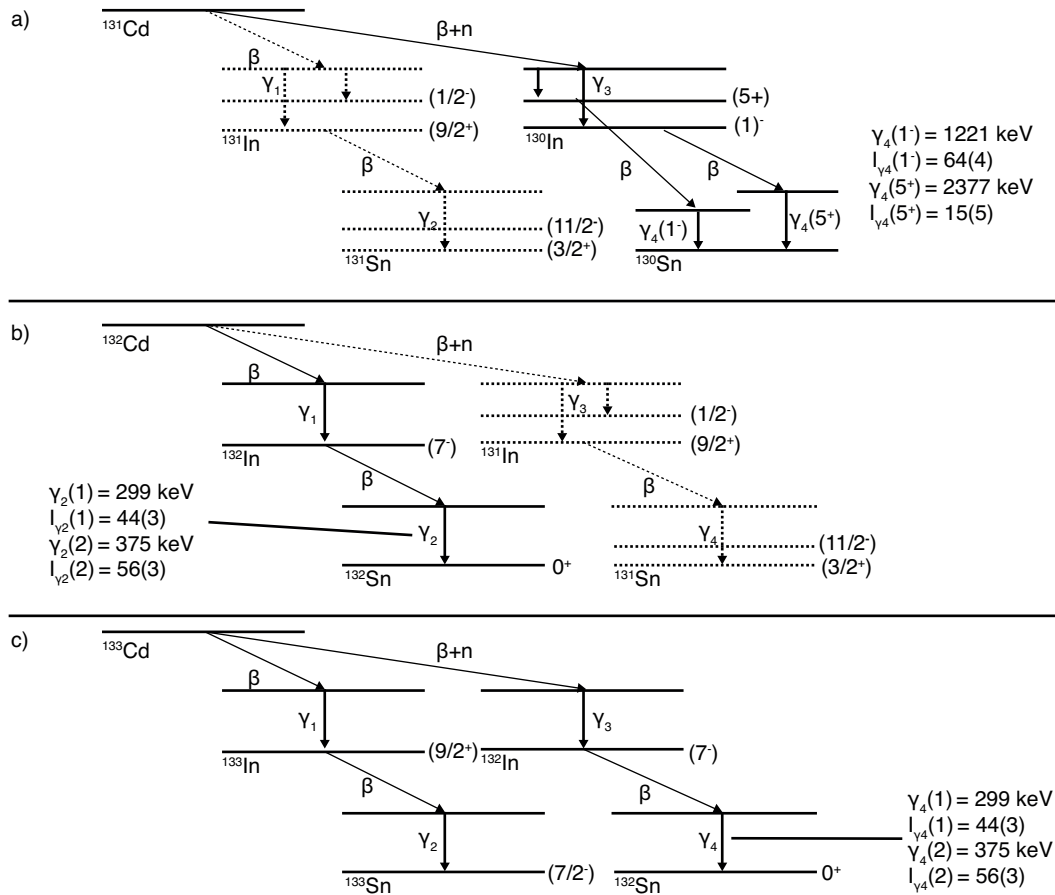


**Figure 4.21:** Basic  $\beta$ -decay schemes including  $\beta$ -delayed neutron emission for the parent nucleus to visualize the  $P_n$  determination method used in the present thesis for a)  $^{131}\text{Cd}$ , b)  $^{132}\text{Cd}$  and c)  $^{133}\text{Cd}$ . The transitions in the granddaughter generation nuclei were selected based on the level schemes and intensities  $I_{\gamma_2}$  ( $I_{\gamma_4}$ ) per 100 decays of the daughter ( $\beta$ -delayed neutron daughter) nucleus from Refs. [2, 41, 82, 126]. Parts of the decay schemes which are dashed were not used for the analysis because the intensities in the granddaughter generation nuclei were found deficient.

### 4.3.2 $P_n$ values for $^{128-133}\text{Cd}$

Fig. 4.20a) to c) and Fig. 4.21a) to c) show basic decay schemes for all Cadmium isotopes with masses  $A=128-133$ . For each case the transitions in the granddaughter generation nuclei are shown which were used for the analysis. The transitions were selected based on the level schemes presented in Refs. [2, 41, 82, 119, 126, 150], and the intensities  $I_{\gamma_2}$  ( $I_{\gamma_4}$ ) per 100 decays of the daughter ( $\beta$ -delayed neutron daughter) nucleus were taken from that reference, too.

All  $\beta$ -decay feeding in the  $\beta$  decay of  $^{128}\text{Cd}$  proceeds to the  $(3^+)$  g.s. and  $I_{\beta}^{tot}$  to  $^{128}\text{In}$  is calculated to be 93(10)% with a known intensity of 50(5) per 100  $\beta$  decays of the 1169-keV transition in  $^{128}\text{Sn}$  [150]. Neither the 253-keV transition, nor the 1597-keV transitions known from the  $\beta$ -decay of  $^{127}\text{In}$  to  $^{127}\text{Sn}$ , are observed in the present experiment in the  $\beta$ -decay of  $^{128}\text{Cd}$ . At those energies peaks with at least 100 counts would be clearly visible. The absolute intensity of the 1597-keV transition is 64(4) per 100 decays of the

9/2<sup>+</sup> g.s. of <sup>127</sup>In, while the 253-keV transition has a absolute of intensity of 40(4) per 100 decays of the (1/2<sup>-</sup>)  $\beta$ -decaying state [119]. From that an upper limit can be set on the  $P_{1n}$  value of <sup>128</sup>Cd of 1%. The value takes also the unknown relative population of the  $\beta$ -decaying states in <sup>127</sup>In into account.

The 1169-keV transition in <sup>128</sup>Sn is also observed in the  $\beta$  decay of <sup>129</sup>Cd, and with the before mentioned known intensity a  $P_{1n}$  value of 3.5(10) is obtained from the intensity of that transition in the spectrum of the <sup>129</sup>Cd  $\beta$  decay. Calculating the  $P_n$  value from the intensities of transitions in the granddaughter nucleus <sup>129</sup>Sn was not possible because the intensities per 100  $\beta$  decays of the transitions following the decay of the (1/2<sup>-</sup>)  $\beta$ -decaying state in <sup>129</sup>In were in disagreement with the observations made in the present experiment.  $I_{\beta}^{tot}$  obtained using those values was 150(10)% which clearly showed that there is a problem with the literature values (Ref. [119]) for those transitions. The nucleus <sup>129</sup>In was also not produced in the current experiment and, therefore, no correction of the wrong absolute intensities was possible. For the same reason the  $P_n$  value of <sup>130</sup>Cd could not be deduced from the intensities in the  $\beta$ -delayed neutron granddaughter. Nevertheless, a value of  $I_{\beta}^{tot} = 91(5)\%$  was obtained for <sup>130</sup>Cd using the known intensity per 100 decays of 64(4) of the 1221 keV transition [126], populated in the  $\beta$  decay of the daughter nucleus <sup>130</sup>In. With that the  $P_n$  value of <sup>130</sup>Cd is 9(5)%.

The intensities per 100 decays of transitions in <sup>131</sup>Sn [41], populated in the  $\beta$  decay of the daughter nucleus <sup>131</sup>In, were also found to be in disagreement with the observations in the present experiment. However, the nucleus <sup>131</sup>In is one of the nuclei produced in this experiment. Once the  $\beta$  decay of this nucleus has been analysed the corrected values for the absolute intensities can be used to determine the  $P_n$  value of <sup>131</sup>Cd. Nevertheless, the value could be obtained from the intensities of transitions observed in the  $\beta$ -delayed neutron granddaughter. In the present experiment the decays of two  $\beta$ -decaying states in the  $\beta$ -delayed neutron daughter <sup>130</sup>In were observed and the  $P_n$  value had to be calculated using the known intensities of 64(4) and 15(5) per 100 decays of the 1221- and 2377-keV transitions [126], following the  $\beta$  decay of the (1<sup>-</sup>) and (5<sup>+</sup>)  $\beta$ -decaying states, respectively. In that way a  $P_{1n}$  value of 16(4)% was deduced.

For <sup>132</sup>Cd a  $P_n$  value of 88(3)% was measured in the present work using the known intensities of 44(3) and 56(3) per 100 decays of the 299- and 375-keV transitions [82], populated in the  $\beta$  decay of the daughter nucleus <sup>132</sup>In. The same transitions were also used to obtain a  $P_{1n}$  value of 88(20)% for <sup>133</sup>Cd. Table 4.8 summarizes the results for the two different methods.  $P_n$  or  $P_{1n}$  values could be deduced for all Cadmium isotopes with N=80-85, and the results are going to be compared to predictions from models and discussed in the following section.

### 4.3.3 Comparison to theory and discussion

Comparing the  $P_n$  and  $P_{1n}$  values to model predictions is again of importance for r-process calculations. The models are necessary to predict the values for the very neutron-

Nuclei	$I_{\beta}^{tot}$	$P_n$	$P_{1n}$
$^{128}\text{Cd}$	93(10)	7(10)	<1
$^{129}\text{Cd}$	-	-	3.5(10)
$^{130}\text{Cd}$	91(5)	9(5)	-
$^{131}\text{Cd}$	-	-	16(4)
$^{132}\text{Cd}$	12(3)	88(3)	-
$^{133}\text{Cd}$	-	-	88(20)

**Table 4.8:** Summary of the results for the  $\beta$ -delayed neutron emission probabilities  $P_n$  obtained from the two methods in the present work.

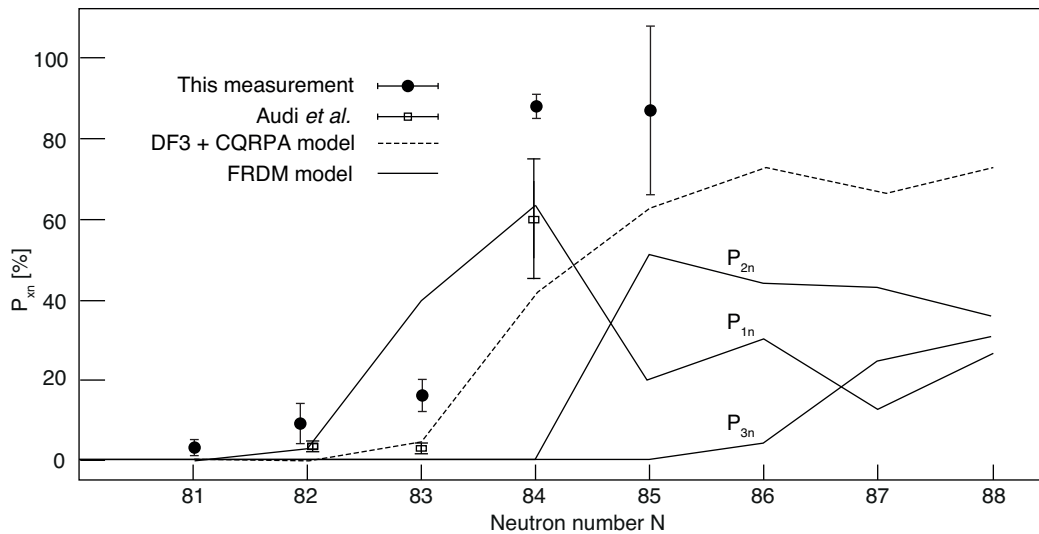


**Figure 4.22:** Comparison between the experimentally obtained  $P_n$  and  $P_{1n}$  values in the present work to the literature  $P_n$  values in Ref. [60] and predictions from two models, the DF3+CQRPA model [67, 68] and the FRDM model [63].

rich r-process nuclei not yet experimentally accessible.  $P_n$  values can have an impact on the final shape of the r-process abundance distribution because they partially define the path of the r-process. Furthermore, in the “freezing out” they are responsible for the  $\beta$ -decay path certain nuclei are taking.

Figure 4.22 shows the results obtained in the present work compared to the ones summarized in Ref. [60]. While for  $N=82$  the values agree within the error bars, for  $N>82$  the literature  $P_n$  values are lower. In the case of  $^{131}\text{Cd}$  the literature  $P_n$  value is 3.5% while in the present work a  $P_{1n}$  of 16(4)% was measured. Also for  $^{132}\text{Cd}$  the value of 88(3)% obtained in this work is not compatible with the value of 60(15)% measured in a previous work [34]. Comparing the present results to two models, the DF3+CQRPA model [67, 68] and the FRDM model [63], one observes severe differences. FRDM predicts a much higher  $P_{1n}$  at  $N=83$ , and for  $N>84$  in that model even two or three neutron emission plays a significant role. On the contrary, none of the nuclei measured here showed indications that two or more neutron emission has a significant contribution. The DF3+CQRPA model on the other hand predicts lower  $P_n$  values for  $N\geq 83$ , but is also in disagreement with the experimental data.

## Chapter 5

# Isomer spectroscopy of neutron-rich $^{128-130}\text{Cd}$

In the following chapter, results from up microseconds and milliseconds isomeric states observed in the implanted Cadmium ions will be presented and discussed. As previously discussed, isomers can be observed in the present experiment due to the possibility of producing a nucleus at the production target in an isomeric state. If the half-life of the state is long enough that a sufficient fraction of ions survive the flight through BigRIPS, then the  $\gamma$  decay of those isomeric states can be observed in delayed coincidence with the implanted ions.

### 5.1 Analysis methods and isomeric states in $^{128}\text{Cd}$

Some analysis techniques used in the following chapter have been discussed in chapter 4. Nevertheless some new methods have to be introduced before showing the results on isomeric states in the neutron-rich Cadmium isotopes. One of the main analysis differences compared to the  $\beta$ -decay data is that the implantation of an ion is followed by a prompt radiation flash [151, 152]. This leads to a high background contribution in the germanium spectra which has to be excluded. Furthermore there are some peculiarities when calculating the relative intensities and determining the half-lives of isomeric states, which needs to be explained. Again the methods are going to be explained with the example of  $^{128}\text{Cd}$ .

Prior to this work, the nucleus  $^{128}\text{Cd}$  has been investigated and several isomeric states were found. The first observation of isomeric states in  $^{128}\text{Cd}$  was made by Hoteling *et al.* [153] who found several delayed transitions with energies of 237, 440, 537, 645 and 783 keV. The 645- and 783-keV  $\gamma$  rays had been previously reported by Kautzsch *et al.* [21] and were assigned to be the  $2^+ \rightarrow 0^+$  and  $4^+ \rightarrow 2^+$  transitions, respectively. A more detailed study of the ns and  $\mu\text{s}$  isomeric states present in  $^{128}\text{Cd}$  was then performed by Cáceres *et al.* [6] who observed additional transitions with energies of 69, 450, 765

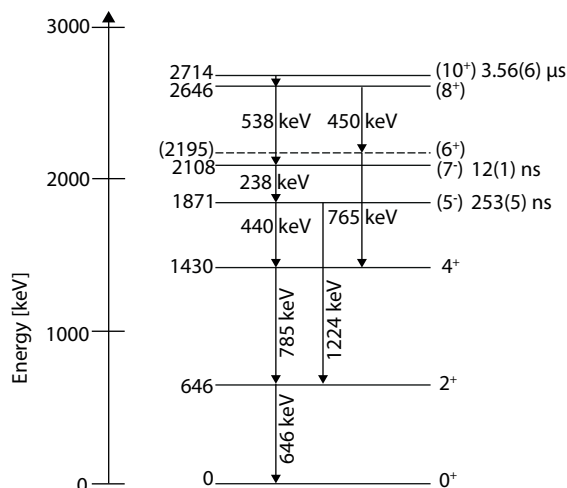


**Figure 5.1:** Level scheme of  $^{128}\text{Cd}$  as proposed in Ref. [6] and half-lives as measured in the present work.

and 1223 keV. In that work three isomeric states with half-lives of  $3.56(6) \mu\text{s}$ ,  $12(2) \text{ ns}$  and  $270(7) \text{ ns}$  were identified and a level scheme (see Fig. 5.1), using the information of the  $\gamma - \gamma$  coincidences and the lifetime analysis, was presented.

In the present work approximately  $4.0 \cdot 10^5$   $^{128}\text{Cd}$  ions were implanted in WAS3ABi which is comparable to the  $3.3 \cdot 10^5$  identified  $^{128}\text{Cd}$  ions in the experiment presented in Ref. [6]. However, the flight time through BigRIPS is approximately twice the flight time through the fragment separator FRS at GSI at the beam energies commonly used. This implies that fewer isomeric decays are observed, as a fraction of the isomers populated in the primary target have decayed in-flight.

### 5.1.1 Energy-time-matrix and delayed Ge spectra

The first spectrum, used for the analysis of the data recorded in coincidence with the implanted ions, is the Germanium energy versus time matrix. In this matrix, the measured germanium energy is plotted versus the timing with respect to the implantation trigger. Depending on the lifetime of the isomeric state and the energy of the isomeric transitions, the time information is taken either directly from the DGF or in the case of shorter lifetimes from the analogue timing branch with the TDCs and TDCI. As the timing resolution of the DGF is poorer, in comparison to the analogue timing branches, a case-by-case decision must be undertaken. However, the DGF has a much higher absolute efficiency for low energy  $\gamma$  rays.

Fig. 5.2 shows the matrix filled under the condition that a  $^{128}\text{Cd}$  ion, identified in BigRIPS, triggered the data acquisition system. The trigger opened a gate of  $110 \mu\text{s}$  for both the DGF and the analogue timing branch of the germanium detectors, allowing the observation of  $\gamma$  rays in delayed coincidence with the implantation following the decay of the isomeric state. An arbitrary offset is observed due to the electronic chain, placing the time

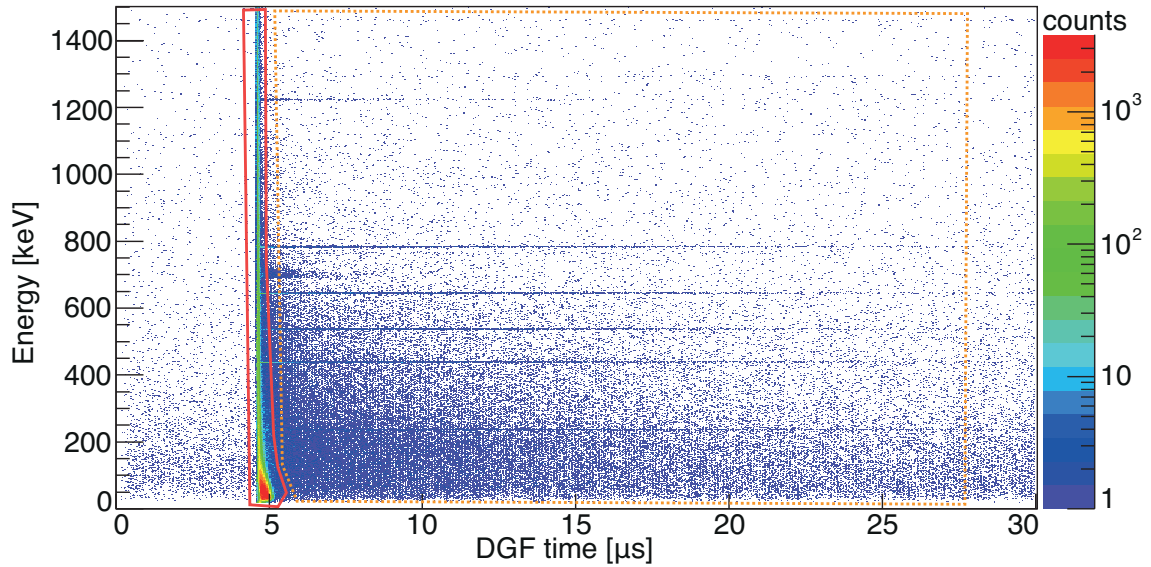


**Figure 5.2:** Germanium energy versus time matrix for  $^{128}\text{Cd}$ . The DGF timing is with respect to the implantation trigger. Highlighted in the red gate is the prompt flash and the orange dashed gate indicates the cut used in the off-line analysis for the case of  $^{128}\text{Cd}$ .

of the ion's implantation at about  $4.8 \mu\text{s}$ . The gate shown in the red color is set around the prompt flash. The prompt flash has its origin in the stopping of the heavy ions with an energy of several GeV in the active stopper. In the stopping process atomic radiation is produced which has to be excluded to obtain clean spectra and to be able to identify the isomeric transitions. Heavy ions penetrating into the active stopper knock out electrons from the stopper material, that de-accelerate under the electromagnetic field of nearby atomic nuclei via photon emission. This is called Bremsstrahlung radiation and results in a huge amount of unwanted background radiation.

The transitions arising from isomeric states are first identified in the matrix as the horizontal lines starting in the prompt radiation peak and losing intensity over time. Horizontal lines with a strong, stable intensity over time can be identified as known background transitions, for example the 1461-keV transition arising from the beta-decay of  $^{40}\text{K}$ . For a clean spectrum a two-dimensional gate is set, as illustrated by the orange dashed gate in 5.2 for the case of  $^{128}\text{Cd}$ . According to the lifetime of the isomeric state the two-dimensional gate is placed as close as necessary to the prompt flash to achieve the best possible peak-to-background ratio while not losing more statistics than necessary. The length of the two-dimensional gate and the distance to the prompt flash has to be taken into account when calculating the relative intensities from the efficiency-corrected peak-areas.

After setting the two-dimensional gate in the energy-time matrix, the inner part of the gate is projected on the energy axis. The resulting plot will from now on be referred to as the delayed germanium spectra and is used to identify and present the transitions below the isomeric state. In the delayed Ge-spectrum of  $^{128}\text{Cd}$ , shown in Fig. 5.3a), seven transitions are observed. The energies of the transitions and the information from the  $\gamma$ - $\gamma$  coincidence spectra, presented in the Figures 5.3b) to f) and Figures 5.4b) to d),

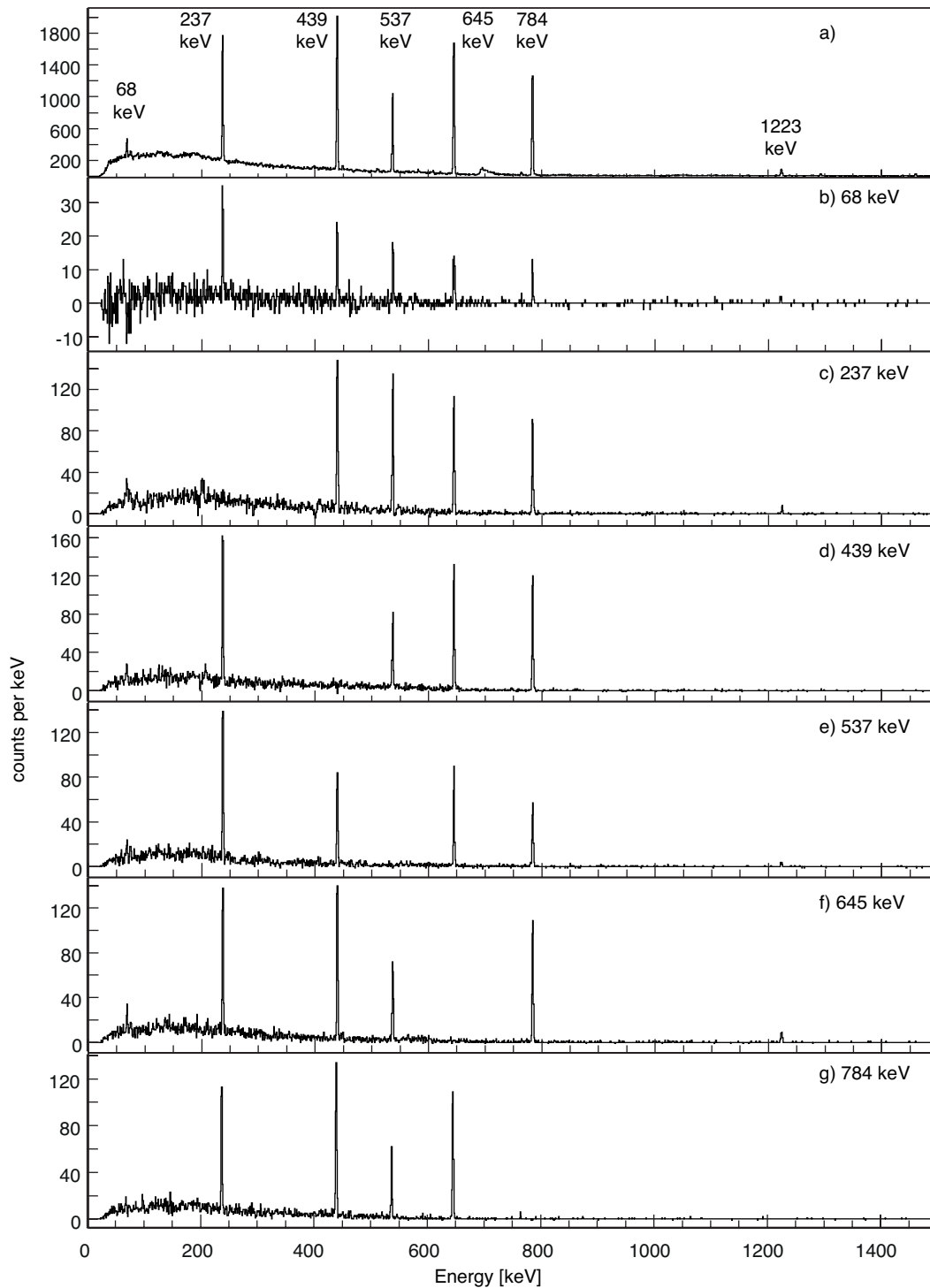


**Figure 5.3:** a) Ge spectrum in delayed coincidence with the implanted  $^{128}\text{Cd}$  ions. b)-g)  $\gamma\gamma$  coincidence spectra gated on the 68-, 237-, 439-, 537-, 645- and 784-keV transitions with no prompt time condition applied.

confirm the observations made by Cáceres *et. al.*. Again at least two isomeric states are observed in  $^{128}\text{Cd}$ , as proposed already in Ref. [6]. The two weak transitions of 449 and 764 keV were placed in [6] as a cascade from the  $(8^+)$  to the  $4^+$  state. The coincidence information, obtained here, agrees with this placement, although the 449-keV  $\gamma$  ray is

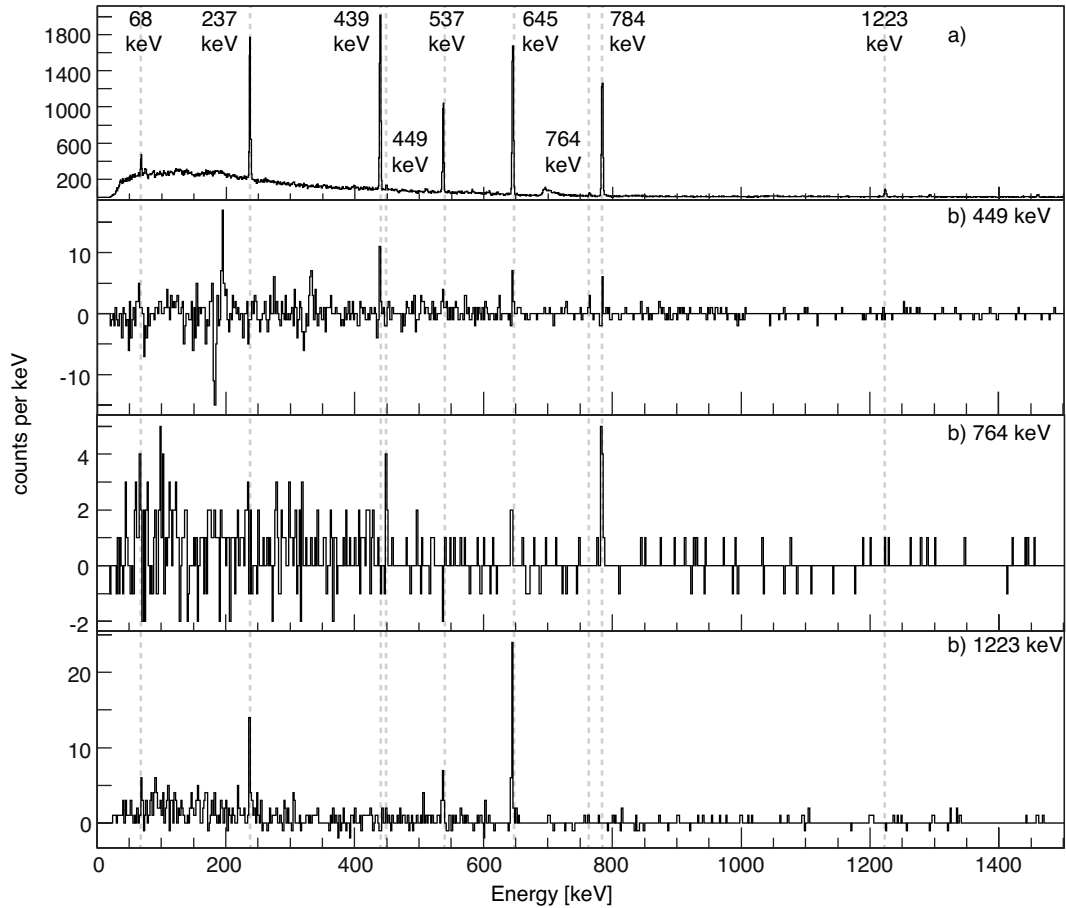


**Figure 5.4:** a) Ge spectrum in delayed coincidence with the implanted  $^{128}\text{Cd}$  ions. b)-d)  $\gamma\gamma$  coincidence spectra gated on the 449-, 764-, and 1223-keV transitions with no prompt time condition applied.

also observed in coincidence with the 439-keV  $\gamma$  ray. This makes the presence of at least one additional transition necessary, connecting the  $(6^+)$  and  $4^+$  states. This transition has not been observed yet.

### 5.1.2 Relative intensities and conversion coefficients

As previously mentioned, the peak area and therefore the relative intensity is strongly dependent on the defined gate to exclude the prompt flash. The distance and the width of the gate can change the peak area significantly. A correction must be applied especially to very short-lived cases. A small difference in the distance to the prompt flash can change the result significantly. A correction factor  $G$  is introduced to correct for the time limits set in the analysis:

$$G = \exp(-\lambda t_i) - \exp(-\lambda t_f) \quad (5.1)$$

where  $t_i$  and  $t_f$  are the lower and upper time limit set in the analysis, respectively. The relative intensity  $I_{\gamma}^{rel}$  is then calculated from the number of counts  $N_{\gamma}$  in the peak of the

$E_\gamma$ [keV]	$E_{\gamma,lit}$ [keV]	$I_\gamma$ [%]	$I_{\gamma,lit}$ [%]	$\alpha$	$\alpha_{lit}$	$\alpha_{th}$
68.1	68.7	8.1(1.1)	5.2(5)	5.68(18)	6.38(86)	5.9
237.1	237.9	53(1)	39(2)	-	-	0.07
439.2	440.0	85(1)	84(4)	-	-	-
449.3	450.4	2.1(5)	1.8(3)	-	-	-
537.1	537.6	52(1)	47(3)	-	-	-
645.1	645.8	100(2)	100(5)	-	-	-
764.3	765.0	1.8(4)	1.2(2)	-	-	-
784.0	784.6	90(2)	90(5)	-	-	-
1223.4	1224.0	10(1)	11(1)	-	-	-

**Table 5.1:** Summary of the energies, the relative intensities and conversion coefficients of the transitions observed in delayed coincidence with the  $^{128}\text{Cd}$  ions in this work and the corresponding literature values (from Ref. [6]). The theoretical conversion coefficients  $\alpha_{th}$  are calculated using Ref. [99].

transition in the delayed germanium spectrum corrected for the factor  $G$ :

$$I_\gamma^{rel} = \frac{N_\gamma}{\epsilon_{rel} I_{\gamma,norm} \cdot G} \quad (5.2)$$

where  $\epsilon_{rel}$  is the relative  $\gamma$ -ray efficiency for the given energy and  $I_{\gamma,norm}$  the intensity of the transition used for the normalisation.

The results for the relative intensities of transitions observed after the isomeric decays in  $^{128}\text{Cd}$  are summarized in Table 5.1 and compared to the values published in Ref. [6]. The relative intensities for the transitions depopulating the ( $5^-$ ) isomeric state are in good agreement with the literature values, while the values of the transitions above the ( $5^-$ ) state are all greater. The explanation for that is the different production mechanism for the nuclei in the two experiments, resulting in a different relative population of the isomeric states at the production target. However, also the different in-flight decay losses are a reason. For a more quantitative comparison of the population of the two isomeric states, the isomeric ratios at the production target will be calculated in section 5.5.

While the intensities of the individual  $\gamma$  rays were crucial to obtain the feeding of the states in the case of the  $\beta$ -decay analysis, here they can be used to calculate internal conversion coefficients. Internal conversion is a competing process to the de-excitation via  $\gamma$ -ray emission, especially in cases where the energy difference between the two states are low and for transitions with higher multiplicities. The energy of the nucleus is directly transferred to an atomic electron in the inner shells which has a certain probability of penetrating into the nucleus. Those electrons are then emitted from the atom. The ratio of de-excitations of a certain state via internal conversion ( $N_e$ ) to the de-excitations via  $\gamma$ -ray emission ( $N_\gamma$ ) is called the internal conversion coefficient:

$$\alpha = \frac{N_e}{N_\gamma} \quad (5.3)$$

The kinetic energy of the electron is then the energy between the two states reduced by

the binding energy of the electron:

$$E_{kin,e} = \Delta E - B_e \quad (5.4)$$

which varies depending on the orbital which the electron occupied. Once the electron is removed from the orbital the remaining hole will be filled by another electron placed in a higher shell, resulting in characteristic X-ray emissions.

The intensity balance of  $\gamma$  transitions feeding and de-exciting a certain state is then used to determine if internal conversion is a competing process or not. All states following the decay of the isomeric state, which have no significant half-life, should have a balanced intensity ratio between feeding and de-excitation. In the case of  $^{128}\text{Cd}$  clearly the 68-keV  $\gamma$  transition, feeding the ( $8^+$ ) state, has a smaller relative intensity than the sum of the 537-keV and the 449-keV ones, which de-excite that state. Therefore, internal conversion must be a competing process for the 68-keV transition. From the relative intensities in Table 5.1 the conversion coefficient can be calculated to 5.68(18). This value is within the error bars in agreement with the literature value of Ref. [6] and agrees fairly well with the theoretical conversion coefficient assuming an E2 transition. The 237 keV transition is expected to be converted too, however the relative intensities of the 237- and 537-keV transitions are within their errorbars identical.

### 5.1.3 Half-life analysis of isomeric states

For the determination of the half-life of isomeric states the energy-time matrix is used again. The prompt flash is this time not excluded by a two-dimensional cut, but a background subtraction will be applied. Gates are set on the energies of the transitions which are then projected on the time axis, either for each gate individually or for the sum of certain transitions depending on the statistics gathered for the individual transitions. Background gates are defined for each transition (see Figure 5.5 for an example of the defined gates) and those background gated spectra are also projected on the time axis. As a final step the background spectra are subtracted from the spectra gated on the transitions adding an appropriate normalization factor according to the gate width of the background and peak gates. The error for each bin is then calculated via error propagation using the errors from both the peak and background.

For nuclei with one isomeric state the lifetime can be extracted directly by fitting a single exponential function, taking into account that the exponential decay process can be described as:

$$N(t) = N_0 e^{-\frac{t}{\tau}} \quad (5.5)$$

where  $N_0$  is the number of initially present nuclei in an isomeric state,  $N(t)$  the remaining number at time  $t$  and  $\tau$  the lifetime of the isomeric state. Taking the first derivative we get

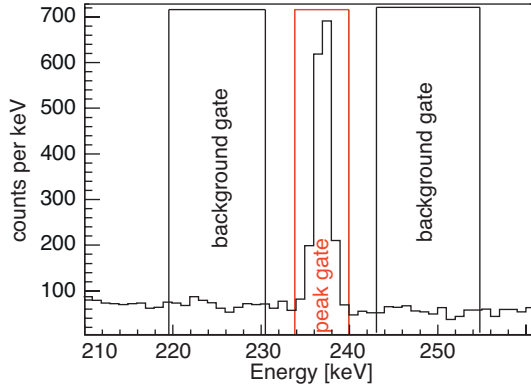


**Figure 5.5:** Delayed germanium spectrum of  $^{128}\text{Cd}$  from 210 to 260 keV to illustrate the used gates (peak and background gates) for the time distribution of the 237-keV transition shown in Fig. 5.6.

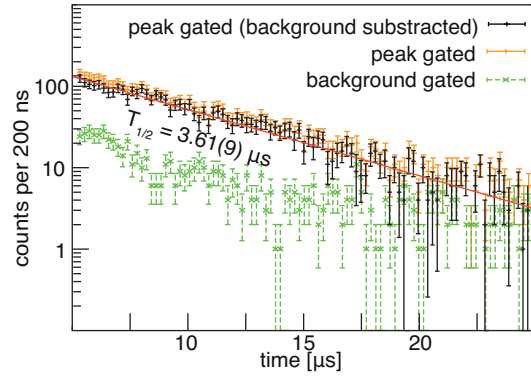


**Figure 5.6:** Example for a timing distribution obtained from the DGF timing as described in the text for the example of  $^{128}\text{Cd}$  and gated on the 237-keV transition.

the single component decay function:

$$-\frac{dN(t)}{dt} = \frac{N_0}{\tau} e^{-\frac{t}{\tau}} \quad (5.6)$$

which is then fitted to the experimental time distribution with  $N_0$  and  $\tau$  being the free fit parameters. The half-life of the isomeric state can then be calculated as:

$$T_{1/2} = \tau \cdot \ln(2) \quad (5.7)$$

In the case of  $^{128}\text{Cd}$ , the time distributions for the 237- and 537-keV transitions can be fitted with a single exponential decay function. Fig. 5.6 and Fig. 5.7a) show the time distributions gated on the 237- and 537-keV transitions, respectively, and the obtained half-lives are  $T_{1/2} = 3.61(9) \mu\text{s}$  and  $T_{1/2} = 3.53(7) \mu\text{s}$ .

The time distributions of transitions following the decay of the ( $7^-$ ) isomeric state are shown in Figure 5.7b) to d). The time distributions of the 439-, 645- and 784-keV  $\gamma$  rays all show two components, one with a short half-life and one with a longer half-life. Those time distributions were fitted with a function accounting for the activities of both the ( $10^+$ ) and the ( $7^-$ ) isomeric state:

$$-\frac{dN(t)}{dt} = -\left(\frac{dN_1(t)}{dt} + \frac{dN_2(t)}{dt}\right) \quad (5.8)$$

with  $N_1(t)$  and  $N_2(t)$  corresponding to the ( $10^+$ ) and ( $5^-$ ) isomeric states, respectively. The activity of the ( $10^+$ ) isomeric state can with formula 5.6 be written to:

$$-\frac{dN_1(t)}{dt} = \frac{N_0^1}{\tau_1} e^{-\frac{t}{\tau_1}} \quad (5.9)$$

with  $N_0^1$  the number nuclei initially being found in the ( $10^+$ ) isomeric state and  $\tau_1$  the

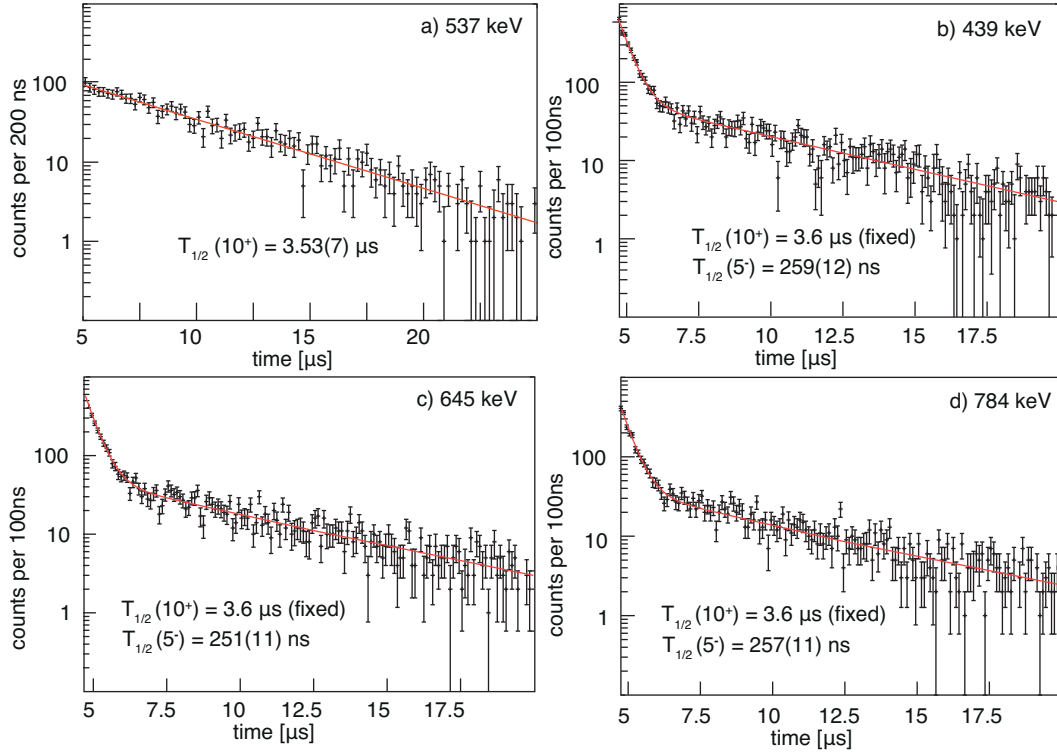


**Figure 5.7:** a) Time distribution relative to the ion implantation of the 537-keV transitions in  $^{128}\text{Cd}$  with an arbitrary offset and in red the fitted single exponential decay function (Formula 5.6). b-d) Time distributions relative to the ion implantation of the 439-, 645- and 784-keV transitions with an arbitrary offset. Those distributions were fitted to a double exponential decay function (Formula 5.8) with the half-life of the  $(10^+)$  state fixed to a value of  $T_{1/2} = 3.6 \mu\text{s}$ .

lifetime of the isomeric state. Using the Bateman equations the activity of the  $(5^-)$  state on the other hand is given as:

$$-\frac{dN_2(t)}{dt} = \frac{N_0^2}{\tau_2} e^{-\frac{t}{\tau_2}} + \frac{N_0^1}{\tau_2^2 \cdot (1/\tau_2 - 1/\tau_1)} e^{-\frac{t}{\tau_1}} - \frac{N_0^1}{\tau_1 \tau_2 \cdot (1/\tau_2 - 1/\tau_1)} e^{-\frac{t}{\tau_2}} \quad (5.10)$$

with  $N_0^2$  the number nuclei initially being found in the  $(5^-)$  isomeric state and  $\tau_2$  the lifetime of the isomeric state. The fits, shown in Figs. 5.7b) to d), were performed with the half-life of the  $(10^+)$  state fixed to a value of  $T_{1/2} = 3.6 \mu\text{s}$ . The weighted average of all three fits results in a half-life of  $T_{1/2} = 256(6) \text{ ns}$ .

The shorter half-life was also deduced with a second method. Only events where the 439-/645-/784-keV transitions are observed in coincidence with either the 237- or the 537-keV transitions were taken and the time difference  $\Delta t$  was calculated as following:

$$\Delta t = t_\gamma - t_{ref,\gamma} \quad (5.11)$$

where  $t_\gamma$  is the time of the  $\gamma$  ray of interest for extracting the short half-life component and  $t_{ref,\gamma}$  is the time of either the 237- or the 537-keV transition which is used as a reference timing. Those time distributions were then fitted with a single exponential decay function.

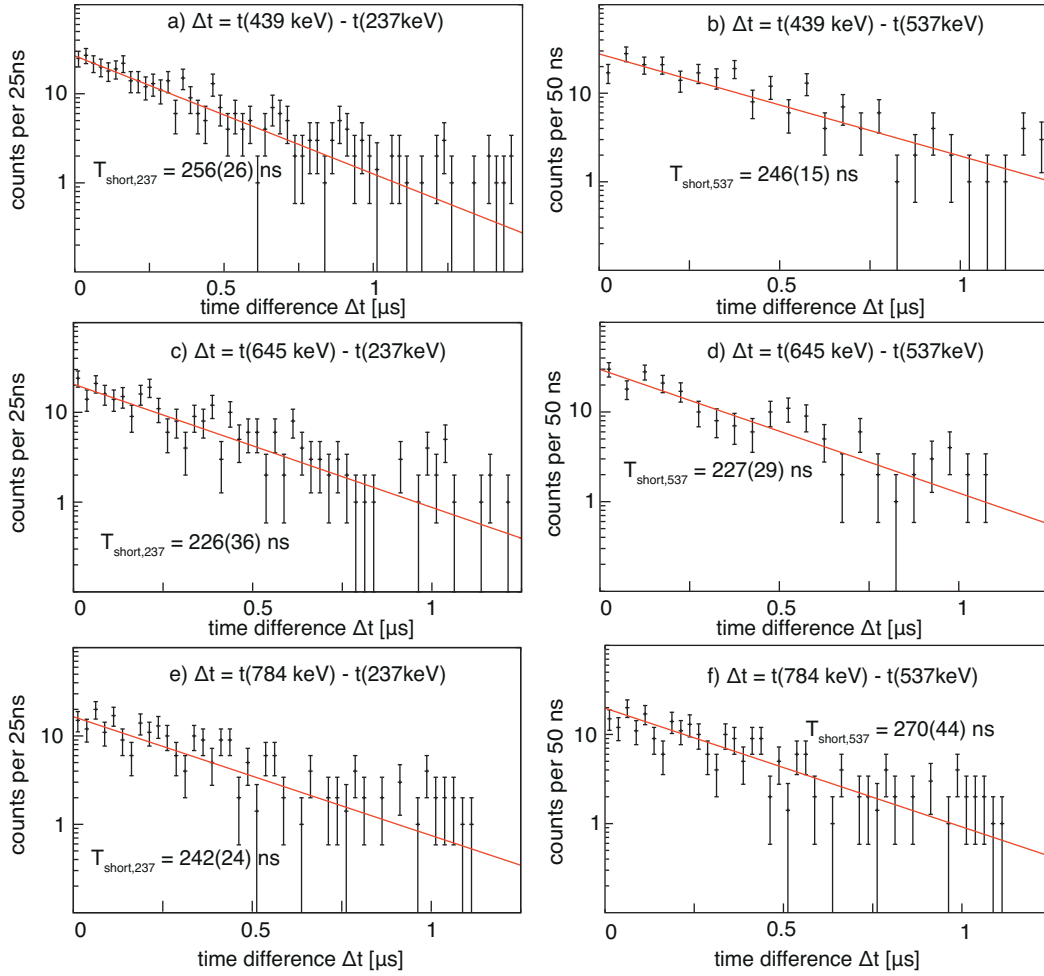


**Figure 5.8:** a)-f) Time difference  $\Delta t$  distributions of the 439-, 645- and 784-keV transitions to the 237- and 537-keV transitions and in red the fitted single exponential decay function.

$E_\gamma$ [keV]	$T_{long}$ [ $\mu\text{s}$ ]	$T_{short,doexp}$ [ns]	$T_{short,237}$ [ns]	$T_{short,537}$ [ns]
237.1	3.61(9)	-	-	-
439.2	-	259(12)	256(26)	246(15)
537.1	3.53(7)	-	-	-
645.1	-	251(11)	226(36)	227(29)
784.0	-	257(11)	242(24)	270(44)

**Table 5.2:** Half-lives of the  $(10^+)$  ( $T_{long}$ ) and the  $(5^-)$  isomeric states ( $T_{short}$ ).  $T_{short,doexp}$  is the half-life of the  $(5^-)$  state obtained from a fit with a double exponential decay function (Formula 5.8).  $T_{short,2,237}$  and  $T_{short,2,537}$  are the half-life values for the  $(5^-)$  state obtained from the fits shown in Fig. 5.8 with the 237- or the 537-keV transitions, respectively, as reference timing. For details see the text.

The time distributions and fits are shown in Fig. 5.8 and the fitted half-lives are summarized in Table 5.2. In that table  $T_{short,2,237}$  and  $T_{short,2,537}$  are the half-lives obtained from the time distributions with the 237- and the 537-keV transition, respectively, as reference timing. From those a weighted arithmetic mean was calculated and a half-life of  $T_{1/2} = 244(10)$  ns obtained for the  $(5^-)$  state. This value is in agreement with the value of  $T_{1/2} = 256(6)$  ns obtained from the double exponential fit. The half-life of the  $(10^+)$  state was

calculated to be  $T_{1/2} = 3.56(6) \mu\text{s}$  from the values stated in Table 5.2. While the half-life of the  $\mu\text{s}$  isomeric state is in good agreement with the literature value, the value obtained in this experiment for the second isomeric state is slightly lower than the value of  $T_{1/2} = 270(7) \text{ ns}$  published in Ref. [6].

#### 5.1.4 Centroid shift method

The method to determine half-lives as described in the previous section has certain limitations. In-flight decay losses and problems arising from the prompt flash prevent the observation of shorter lived isomeric states. The initial isomeric state has to survive in a sufficient amount to be observable. However, there is a possibility to identify lifetimes of intermediate states that are populated following the initial isomeric state in the order of a few ns. For this a different method is employed, the so called centroid shift method [154, 155], described in the following text.

For all combinations of  $\gamma$  rays, which follow each other in cascades, the time difference  $\Delta t$  between two  $\gamma$  rays is filled in a spectrum. For prompt coincidences the  $\Delta t$  time distribution is expected to be a symmetric peak around the zero-time, which is associated with prompt coincidences. Unfortunately, the zero-time depends on the energies of the two transitions. This behaviour is commonly known as the walk-effect, which describes the variation of the measured time for  $\gamma$  rays depending on their energy due to differences in the amplitude and/or rise-time of the signals in the detectors [156]. For two  $\gamma$  rays with nearly the same energy the effect can be neglected and the zero-time is just defined as  $t_{\gamma 2} - t_{\gamma 1} = 0$ . For the combination of a low energy  $\gamma$  ray and a  $\gamma$  ray with an energy  $E > 300 \text{ keV}$  the zero-time is extracted from the centroid of the time distribution of the prompt flash. If the intermediate level has a lifetime in the order of a few ns or more an asymmetric shift from the zero time is observed. The lower limit of this method is defined by the resolution of the short-range TDC. Two methods can be used to extract the half-life from the time difference of the two transitions. First of all the centroid position  $C$  of the time distribution can be calculated as:

$$C = \sum_{bins} \Delta t \cdot \#(\Delta t) \cdot \frac{1}{N} \quad (5.12)$$

with  $\#(\Delta t)$  the number of counts in the bin  $\Delta t$  and  $N$  the total number of counts. The error is then calculated as:

$$\Delta C = \sqrt{\sum_{bins} (\Delta t - C)^2 \cdot \#(\Delta t) \cdot \frac{1}{N^2}} \quad (5.13)$$

The calculated shift of the centroid from the zero-line corresponds then to one life-time of the intermediate state.

This method has been applied to search for shorter half-lives in the order of ns and especially to re-measure the half-life of the state between the 237- and 537-keV transitions. Fig. 5.9 shows the centroid positions of the three cases with sufficient statistics. The

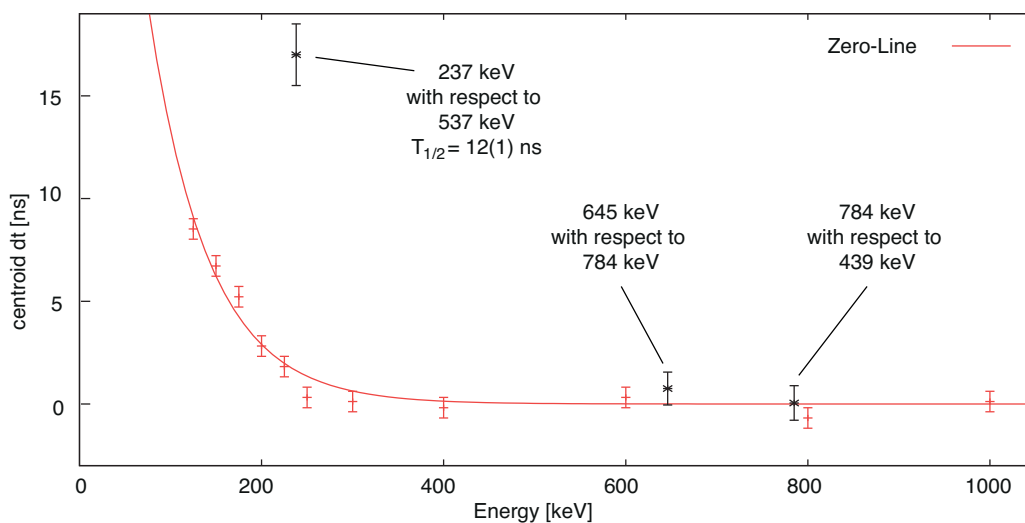


**Figure 5.9:** Shown are the centroids of the time distributions for the  $2^+$ ,  $4^+$  states and the state between the 537- and 237-keV transitions. The zero-line which has been extracted from the time distribution of the prompt flash is shown in red.

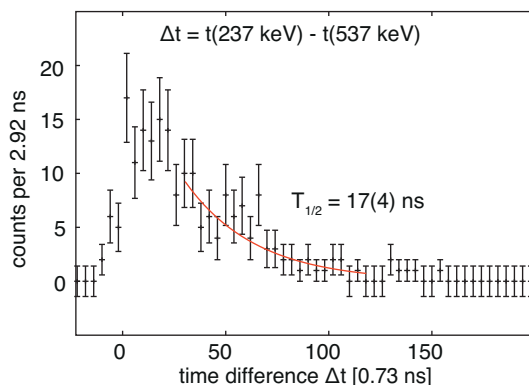


**Figure 5.10:** Time difference  $\Delta t_{\gamma\gamma}$  distributions of the 537-keV transitions to the 237-keV transition and in red the fitted single exponential decay function to the slope of the distribution.

zero-line was extracted from the time-distribution of the prompt flash. All times which are shown in this plot are taken from the long range TDC (0.73 ns/bin). For the  $2^+$  and  $4^+$  states no centroid shift can be observed. Therefore, their half-lives must be shorter than the time resolution of the TDC. For the state between the 237- and 537-keV transitions a centroid-shift is observed and a half-life of  $T_{1/2} = 12(1)$  ns is deduced from the centroid position.

A second method to determine the half-life is to fit a single exponential decay function to the exponential tail of the time-difference distribution. This is presented in Fig. 5.10. From this method a half-life of  $T_{1/2} = 17(4)$  ns is obtained, slightly higher than the value obtained by the centroid-shift method. The latter one is in good agreement with the value published in Ref. [6].

### 5.1.5 Conclusions

In summary the results obtained in the present work are in good agreement with those of Ref. [6] and no major deviations could be found. The results presented here agree with the level scheme and the interpretations presented in that work. In the following sections the results for ns,  $\mu\text{s}$  and ms isomeric states in  $^{129,130}\text{Cd}$  are presented.

## 5.2 A ms isomeric state in $^{129}\text{Cd}$

The time distribution of the  $\beta$  decays correlated to the implanted  $^{129}\text{Cd}$  ions displayed interesting behaviour in the previous chapter in section 4.2.3.1. A very short-lived component with a few ms half-life is visible in the first ms after implantation, which can not be associated to the  $\beta$ -decay half-lives as they were reported in the previous chapter. The origin of this component is now going to be investigated in detail. The results and the interpretation described in this chapter have been published in Taprogge *et al.* [157].

To reveal the origin of this component the germanium spectrum recorded in the first ten ms after the implantation was investigated and compared to the spectrum recorded for later times. Fig. 5.11a) shows the germanium spectrum recorded in the first ten ms after the implantation. In the spectrum transitions are observed which are not visible in the  $\beta$ -decay spectrum presented in the analysis of the  $^{129}\text{Cd}$  decay (see section 3.2). They have energies of 353, 406, 1181 and 1587 keV. To clarify that especially those peaks are correlated to the short lived component of a few ms half-life, Fig. 5.11b) shows the same spectrum but this time with the spectrum recorded 30 to 40 ms after the implantation subtracted. All but the four identified peaks disappear.

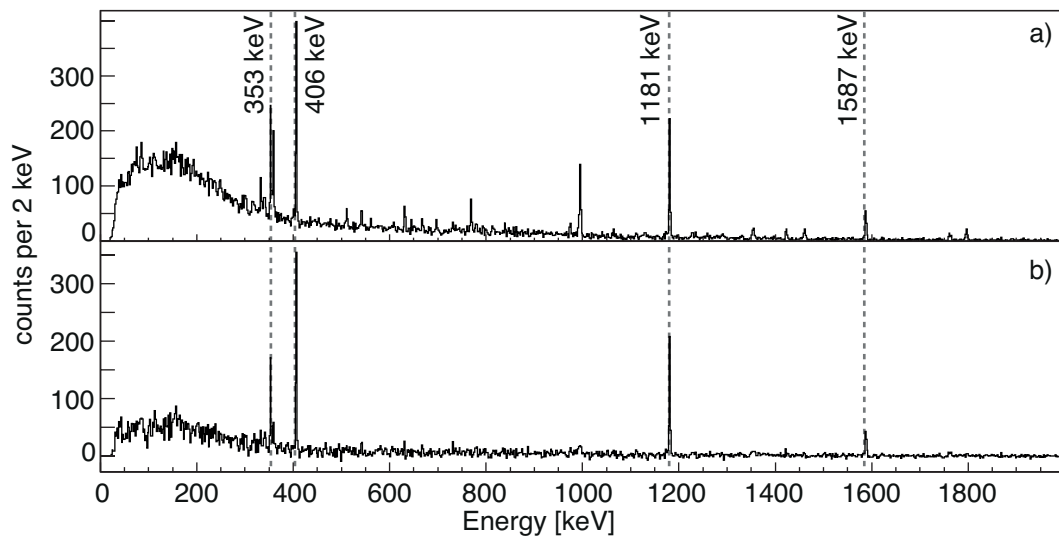


**Figure 5.11:** Germanium spectrum recorded in a) the first ten ms and b) additionally with a background subtraction of the spectrum recorded between 30 to 40 ms after the implantation of an  $^{129}\text{Cd}$  ion. The same cuts have been applied as those in spectrum 4.12.

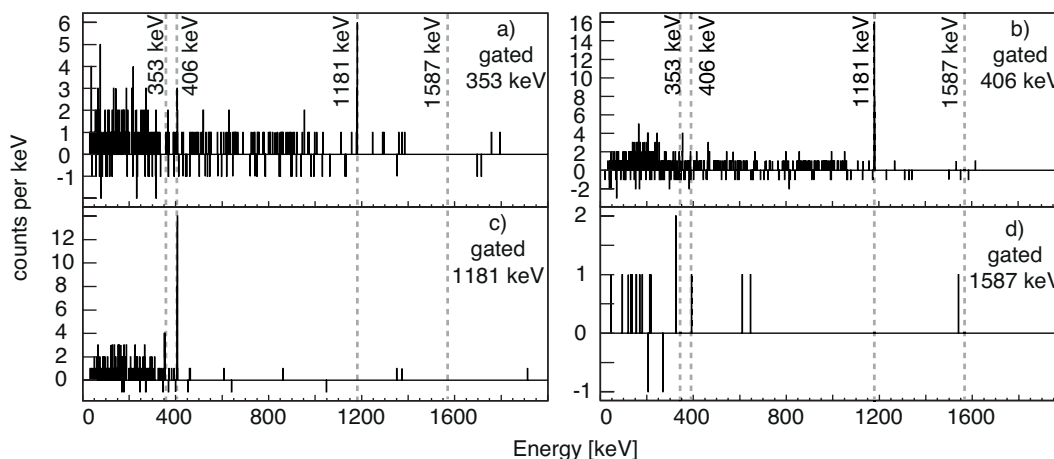


**Figure 5.12:** Germanium spectra observed in prompt coincidence with the a) 353-keV, b) 406-keV, c) 1181-keV and d) 1587-keV transitions within the first 20 ms after an  $^{129}\text{Cd}$  implantation.

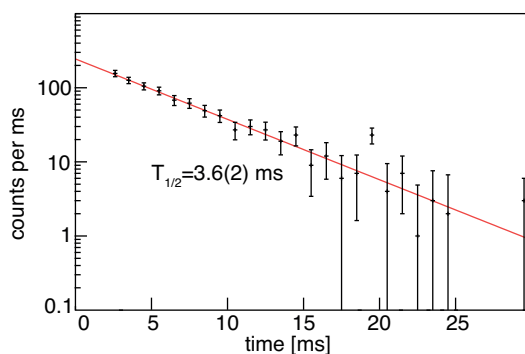


**Figure 5.13:** Sum time distribution of the 406-keV and 1181-keV transitions observed in  $^{129}\text{Cd}$  and in red the fitted single exponential decay function.

Gating on the four transitions in the  $\gamma - \gamma$  matrix (gated spectra see Fig. 5.12) reveals that the 353-, 406- and 1181-keV transitions are observed in mutual prompt coincidence suggesting that they form a cascade. A further piece of information, useful in building the decay scheme, is the lack of coincidence between 1587-keV  $\gamma$  ray with either the 406- or the 1181-keV  $\gamma$  rays. Furthermore, the sum of the energies of the latter two transitions is 1587 keV. This indicates that they form a cascade parallel to the 1587-keV transition. Unfortunately it is not possible to fix the order in this cascade. The only conclusion to be made up to here is that a previously unknown ms isomeric state in  $^{129}\text{Cd}$  is observed in the present data set. It will be shown later, that based upon state-of-the-art shell model calculations, the order in the level scheme can be fixed with the 353-keV transition placed on top of the 1587-keV one and the 406- on top of the 1181-keV  $\gamma$  ray.

The half-life of the isomeric state is obtained from the sum time distribution gated on the 406- and 1181-keV transitions; the two transitions with the highest statistics, shown in Fig. 5.13. The fit with a single exponential decay together with a constant background results in a half-life of  $T_{1/2} = 3.6(2)$  ms. Fig. 5.14 shows in addition the individual time distributions gated on all four transitions, with the corresponding single exponential decay fits. The

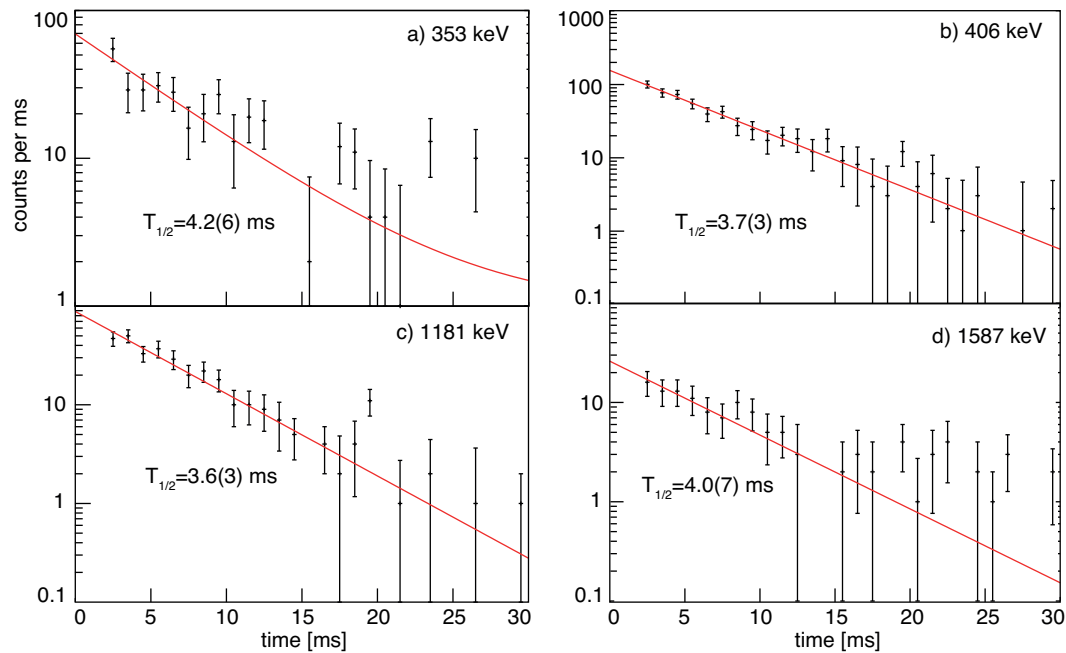


**Figure 5.14:** Time distributions gated on the a) 353-, b) 406-, c) 1181- and d) 1587-keV transition observed in delayed coincidence with the implanted  $^{129}\text{Cd}$ . The fits with a single exponential decay function are shown in red.

obtained half-lives are 4.2(6), 3.7(3), 3.6(3) and 4.0(7) ms from the time distributions gated on the 353- (Fig. 5.14a)), 406- (Fig. 5.14b)), 1181- (Fig. 5.14c)) and 1587-keV (Fig. 5.14d)) transitions, respectively. They show a very good agreement with the value obtained from the sum time distribution.

### 5.2.1 Triggering of the data acquisition to observe a ms isomeric state

The issue of how a ms  $\gamma$ -decaying isomeric state was found in  $\beta$ -decay data will now be addressed. To clarify the situation it is worth noting that the  $\beta$ -decay events are triggered by WAS3ABi, therefore an energy deposition must be observed in one of the silicon detectors, for example, due to an electron released in a  $\beta$  decay. However, as already shown during calibration, the silicon detectors can be triggered by Compton-scattered  $\gamma$  rays. The existence of the isomer in the  $\beta$ -decay data may be explained by the energy spectrum of the DSSSD.

Fig. 5.15a) shows the DSSSD spectrum recorded for all observed decays correlated in the first 10 ms (black) and from 30 ms to 40 ms (red) after an implantation of a  $^{129}\text{Cd}$  ion. While both curves show the expected continuous energy spectrum of an electron emitted in a  $\beta$ -decay, there is a noticeable difference: the black curve has a peak round 340 keV on top of the continuous energy spectrum and a second lesser peak around 400 keV. When applying further conditions, for example, in Fig. 5.15b) requiring that the energy deposition occurred in the same DSSSD as implantation, and c) that it also occurred in the same pixel, an excess of counts below 250 keV is observed in the first 10 ms compared

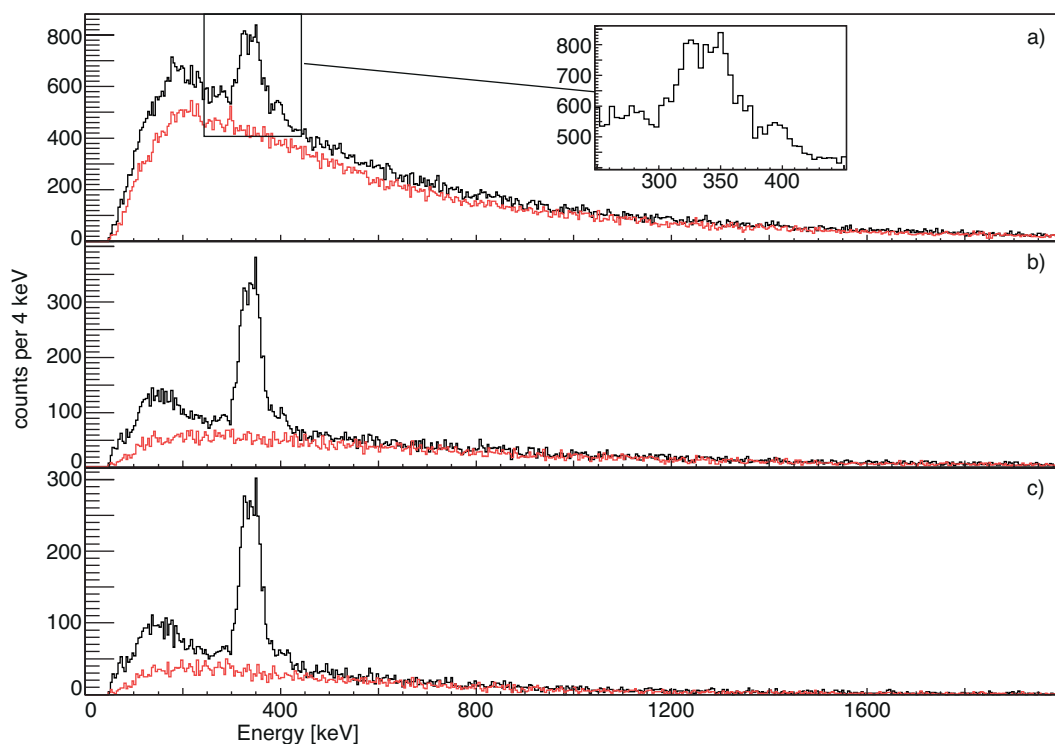


**Figure 5.15:** a) DSSSD spectra recorded in the first 10 ms (black) and from 30 to 40 ms (red) after the implantation of a  $^{129}\text{Cd}$  ion for all correlated decays, b) with the additional condition that decay and implantation were observed in the same DSSSD layer ( $dz=0$ ) and c) with the even stronger requirement that both were observed in the same pixel ( $dz=0$  and  $dxy=0$ ).

to the curve recorded for later times. In addition, one observes that the majority of energy depositions below 430 keV are related to the ms isomeric state. By looking at the peak in detail it can be seen that it has a double structure, with a maximum around 330 keV and around 350 keV.

The germanium spectra in Fig. 5.16 show the intensity difference for a) gating on an energy deposition of 295 to 430 keV in the DSSD and b) gating on the excess of energy below 250 keV. All four transitions are observed in both spectra. However, a clear difference in the relative intensities of the 353- and the 406-keV transitions is visible. In the upper spectrum it can be observed that the 353-keV peak is reduced significantly compared to the other peaks when gating on the peak structure in the DSSSD spectra. On the contrary, the 353 keV and 406 keV transitions have identical relative intensities in the lower spectrum. This suggests that there are two different mechanisms contributing to the observation of an isomeric state in the present experiment. The suggested scenarios based on the experimental information are that the excess of counts for lower energies arises from Compton scattered events triggering the data acquisition, while the peak structures belong to conversion electrons of the 353-keV transition which also result in a  $\beta$ -decay trigger.

The spectra in Fig. 5.15 show the sum of both datasets (Pd setting and Sn setting). The datasets were first investigated independently where it became clear that the y side of

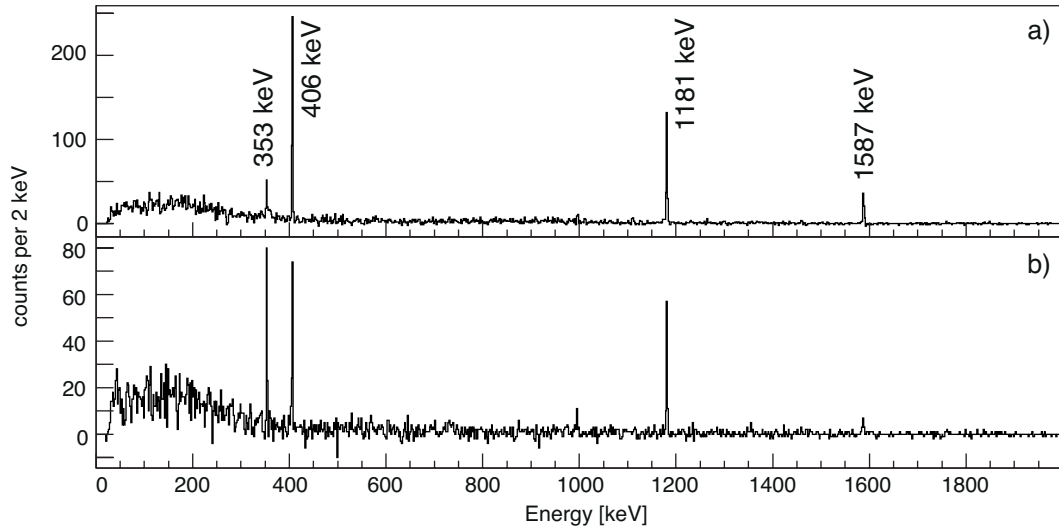


**Figure 5.16:** Germanium spectrum of decay events recorded in the first 10 ms and in the same pixel ( $dz=0$ ,  $dxy=0$ ) after a  $^{129}\text{Cd}$  implantation gated on a) the peak structure between 295 and 430 keV in the DSSSD and b) the excess of energy in the DSSSD below 250 keV.

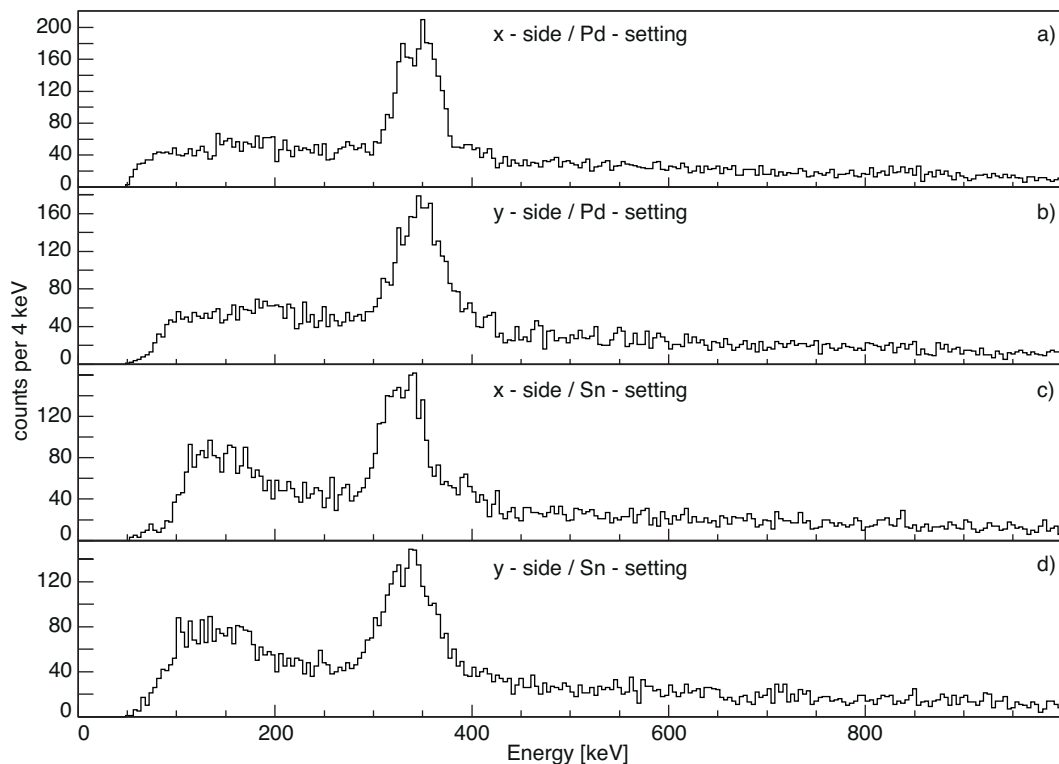


**Figure 5.17:** DSSSD energy spectra of all decay events recorded in the same pixel ( $dz=0$  and  $dxy=0$ ) as the implanted  $^{129}\text{Cd}$  ions with a) the energies taken from the DSSSD x-side and only showing the Pd-Setting of the experiment, b) y-side and Pd-Setting, c) x-side and Sn-Setting, and d) y-side and Pd-Setting.

the DSSSD has a worse energy resolution than the x-side. Fig. 5.17 shows the DSSSD spectra for both the x- and y-side and separated into the two settings. The difference in energy resolution is likely due to the detector characteristics. Therefore, only the energies obtained from the x-side were used in the analysis. Furthermore the energy calibration

is inconsistent throughout the experiment. This is observed in the energy shift of the peak's centroid between Fig. 5.15a) and c). As previously noted in section 2.2.4 an energy shift was observed in the DSSSD over the 12 days of the experiment. The energy shift differed within the individual DSSSDs. The majority of  $^{129}\text{Cd}$  ions in the Pd setting were implanted into the third DSSSD whereas in the Sn setting the fourth DSSSD was the main implantation layer for those ions. Therefore, two shift parameters had to be determined, one for each experiment, to shift the peaks to the expected positions calculated with the conversion coefficient calculator Bricc [99], assuming the conversion electrons arise mainly from the 353-keV transition. The shift parameters used for the analysis were -6 keV for DSSSD 3 and +8 keV for DSSSD 4.

### 5.2.2 Conversion coefficients and multipolarities

353 keV		406 keV	
Mult.	$\alpha_{th}$	Mult	$\alpha_{th}$
E1	0.005	E1	0.004
M1	0.016	M1	0.011
E2	0.019	E2	0.012
M2	0.062	M2	0.041
E3	0.067	E3	0.039
M3	0.224	M3	0.133

**Table 5.3:** Theoretical total conversion coefficients of the 353- and 406-keV transitions, calculated with Bricc [99] for various multipolarities.

Under the assumption that the two scenarios are correct, further information can be extracted from the spectrum shown in Fig. 5.16a). Corrected for the efficiency, 2455(146) counts are observed in the 406-keV peak and 910(360) in the 1587-keV peak. This results in a branching of approximately 3:1 for the two parallel decay branches. Furthermore, the intensity difference between the 353- and 406-keV transitions suggests that the conversion coefficient of the 353-keV transition is around a factor six higher compared to the 406-keV transition, taking into account the aforementioned branching. This is important to understand which multipolarities are the most probable ones for both transitions by comparing them to the theoretical predictions. Table 5.3 shows the calculated internal conversion coefficients for several multipolarities, from which it can be concluded that the most probable assignments are M2 or E3 for the 353-keV transition and M1 or E2 for the 406-keV one. The combinations of those multipolarities would in all cases give more or less the factor six in agreement with the experimental observations. A M1/E2 multipolarity assignment for the 406-keV transition is also reasonable taking into account the presence of a parallel decay branch (1587-keV  $\gamma$  ray).

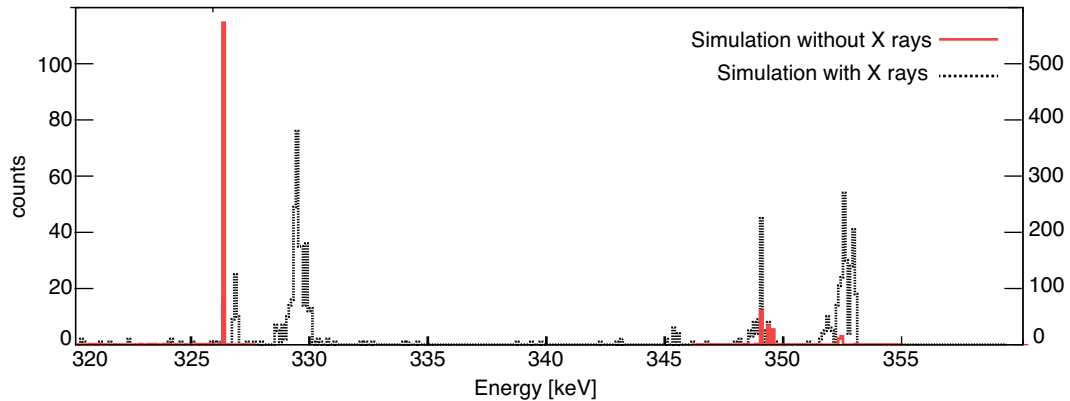


**Figure 5.18:** DSSSD energy spectra obtained from the Monte-Carlo simulation of the proposed decay scheme without taking into account the detector resolution of 20-25 keV and without (red) and with (dashed black) the consideration of the subsequent X-rays emitted after the emission of the conversion electron. The number of events simulated for both scenarios are equal but the simulation without X-rays has a different y-scale (y-scale on right side of the figure) than the simulation with X-rays (y-scale on left side of the figure) for a better legibility of the figure.

### 5.2.3 Monte Carlo simulations of the suggested scenarios

Monte Carlo simulations were performed by E. Nácher [158] in order to confirm that the suggested scenarios above are responsible for the observed structures in the DSSSDs. The Geant4 package [159] was used for the simulations, including the 8 DSSSD and the germanium detectors used during the experiment and their geometry. The energy resolution of the DSSSD was set to 20-25 keV in the region of interest, in agreement with the observed experimental DSSSD spectra. The events were generated based on the aforementioned level scheme and as it will be presented later together with the shell model calculations. The conversion coefficients used in the simulations were taken from section 5.2.2.

Before limiting the energy resolution to 20-25 keV, simulations were performed which revealed the origin of the double structure of the peak. Fig. 5.18 shows in red the expected energy spectrum in the DSSSD without considering the subsequent X-rays following the emission of a conversion electron. Clearly the expected peaks for K-, L- and higher internal conversion electrons are visible. The ratio between K- and L- (and higher) conversion electrons is around 4:1, as expected by the predictions with Bricc. In the next step the simulations included the X-rays and their summation to the observed energy in the DSSSD, based on the probability whether the X-rays are detected or escape the detector. The dashed black distribution shown in Fig. 5.18 is the expected distribution with the X-rays included. The peaks are now shifted and show a more complex distribution, with two accumulations at 330 and 350 keV. They subsequently lead to the observed double structure when including the resolution of the detector.

In the next step the simulated DSSSD spectra were compared to the experimental spectra. It was also possible to include Compton scattering of  $\gamma$  rays in the DSSSD with the

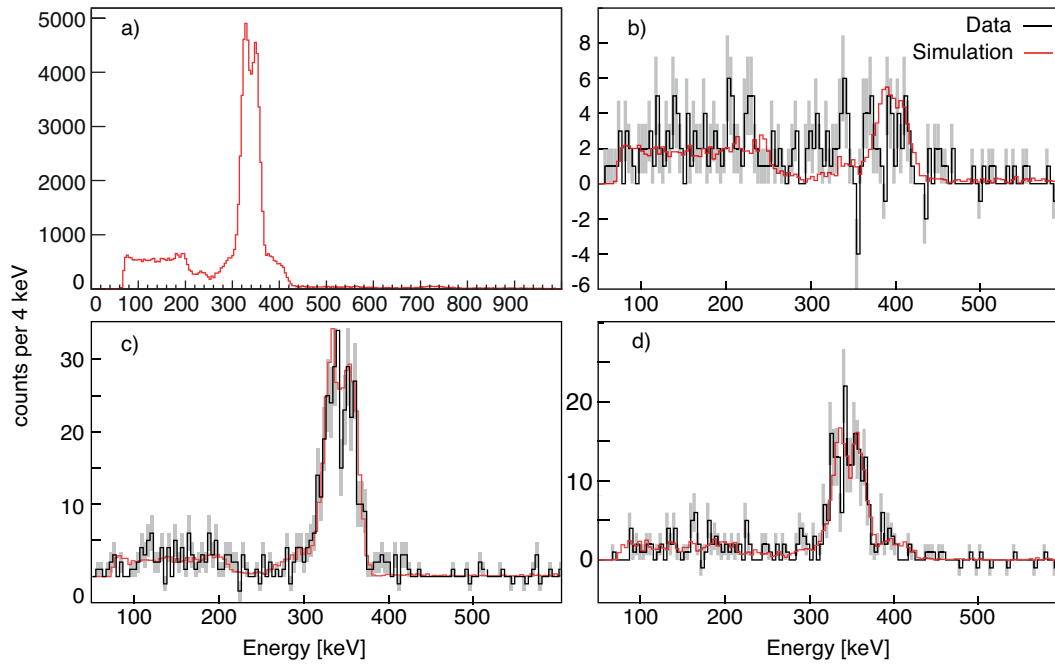


**Figure 5.19:** Measured DSSSD energy spectra (black with errors given as grey bars) and those obtained from the Monte-Carlo simulation (red), taking into account the detector resolution of 20-25 keV, with the consideration of the X-rays emitted after the emission of the conversion electron and with the Compton-scattering included in the simulations. a) shows the full DSSSD spectrum obtained with the Monte-Carlo simulation and b)-d) show the comparison of data and simulation gated on the 353-, 406- and 1181-keV  $\gamma$  rays in the germanium array.

simulations. The Monte-Carlo simulations fit very well with the experimental data when including X-rays and Compton scattering, even with limited statistics. Fig. 5.19a) shows the DSSSD spectrum obtained from the simulations and in Fig. 5.19b) to d) the measured energy spectra for all decays correlated to ion implantation within the first 10 ms, in coincidence with the 353-, 406- or 1181-keV transitions, respectively, directly compared to the simulations. In both, the simulated spectra and the spectra obtained from the experimental data, a requirement was imposed that the decay and the implantation were observed in the same pixel, including with add-back of the surrounding pixels, as described in the section regarding data treatment of WAS3ABi (see section 2.2.5). Overall, a very good agreement is found between the experimental data and the simulated data, even at low energies (below 300 keV) by including Compton scattering in the simulations. This is especially seen in Fig. 5.19c) and d).

The simulation of the DSSSD spectra with X-rays and Compton scattering included proves the suggested scenario in which Compton and conversion electrons are triggering the data acquisition, making it possible to observe the millisecond isomer in this dataset.

### 5.2.4 Conclusions

The experimental data suggests the presence of a ms isomeric state in  $^{129}\text{Cd}$  which decays via a M2 or E3 transition with an energy of 353 keV. This isomeric state has a half-life of  $T_{1/2} = 3.6(2)$  ms. In the present data set it could only be observed due to the data acquisition being triggered by Compton and conversion electrons. No similar cases could be found in the literature where a ms isomeric state was observed using this technique.

## 5.3 A $\mu$ s isomeric state in $^{129}\text{Cd}$

Prior to this thesis no excited states, except the  $\beta$ -decaying states, were known in  $^{129}\text{Cd}$ . In the following section, results are presented showing the first evidence for the presence of a  $\mu$ s isomeric state.

A total of  $3.8 \cdot 10^6$   $^{129}\text{Cd}$  ions were identified in BigRIPS and implanted in the active stopper WAS3ABi. The corresponding delayed germanium spectrum is shown in Fig. 5.20a) for a time window of 200 ns to 3.0  $\mu$ s after the implantation. Several lines below 1.5 MeV are visible with energies of 237, 439, 537, 645, 784 and 1223 keV (in the spectrum marked with a “\*”). Transitions with the same energies are known from  $^{128}\text{Cd}$  and the  $\gamma$  -  $\gamma$  coincidence spectra for these transitions show the expected coincidences for the depopulation of the isomers in  $^{128}\text{Cd}$ . Therefore, those lines are assigned to be contaminations, present in the spectra because of one neutron removal reactions in the detector materials and the degraders of BigRIPS at the last focal planes. In these cases it is  $^{128}\text{Cd}$  implanted not  $^{129}\text{Cd}$ . The AoQ ratio is deduced from the measured ToF in the first part of BigRIPS which allows for unidentified contaminations in the proceeding sections of BigRIPS, especially at the last focal planes.

An interesting observation in the spectrum shown in Fig. 5.20a) is the presence of a previously unknown transition with an energy of 3693 keV and its single escape at 3182 keV. While this spectrum was filled without using add-back in the germaniums, the spectra 5.20b) - e) show the germanium energies with the add-back algorithm applied. Strong contamination lines come also from the neutron induced reactions in the germanium detectors (in the spectra marked with a “#”). Those contamination lines can be removed by subtracting a delayed add-back spectrum from a nucleus with no observed isomeric states applying the same time window. Fig. 5.20c) shows the background subtracted add-back spectrum with  $^{127}\text{Ag}$  used for the subtraction. The contamination lines originating from neutron reactions in the germanium detectors are suppressed and nearly disappear, while the transitions associated with the decay of the  $^{128}\text{Cd}$  isomers are still present in the spectra.

Using a  $^{128}\text{Cd}$  spectrum with the same time condition for background subtraction is not possible because of different populations of the isomeric states in  $^{128}\text{Cd}$  for a one neutron

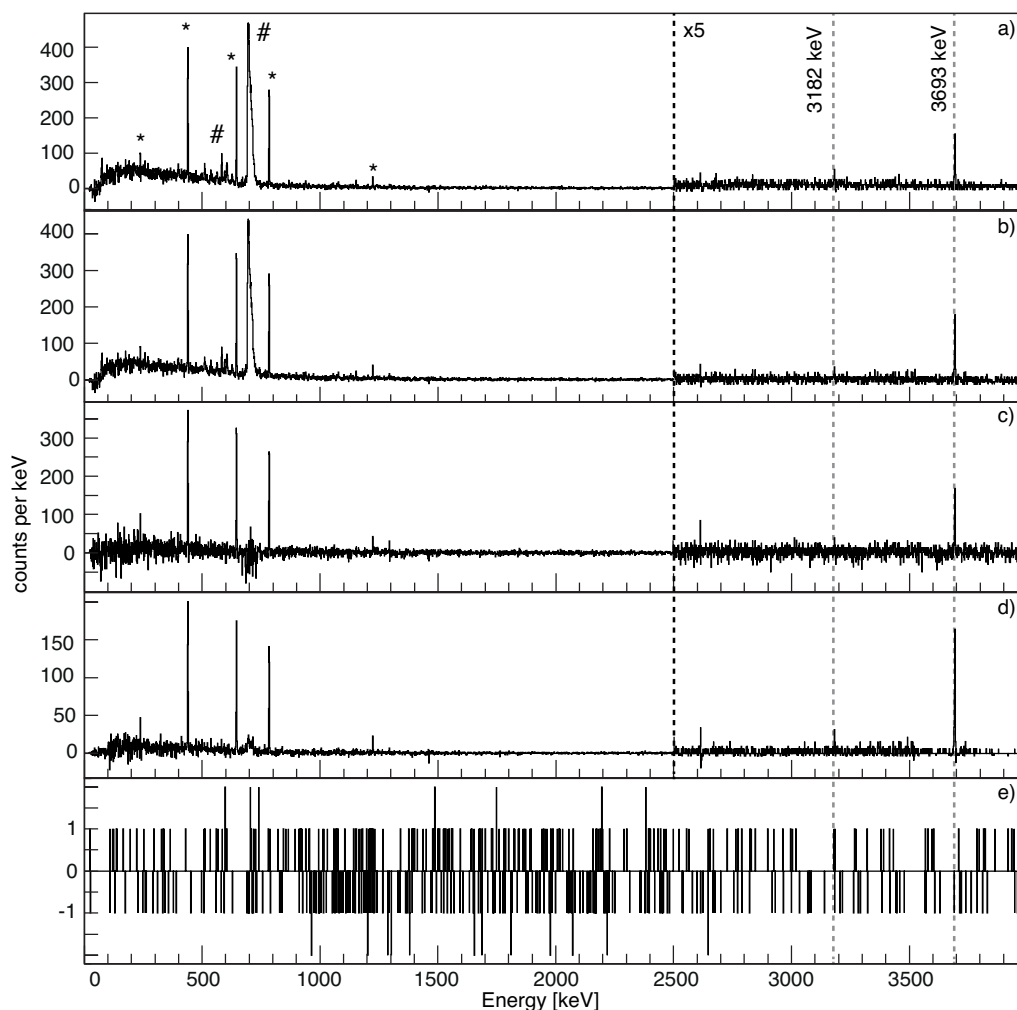


**Figure 5.20:** a) Ge spectrum in delayed coincidence with the implanted  $^{129}\text{Cd}$  ions, b) add-back spectrum in delayed coincidence with the implanted  $^{129}\text{Cd}$  ions, c) same spectrum as b) but background subtracted with  $^{127}\text{Ag}$  delayed add-back spectrum (same time condition), d) same as b) with the limitation that a maximum of two clusters and a maximum of two crystals inside each cluster has detected an energy with  $100 \text{ keV} < E < 4000 \text{ keV}$ , e)  $\gamma\gamma$  coincidence spectra gated on the 3693-keV transition with a coincidence time window of 500 ns applied. Transitions labelled with symbols correspond to known transitions in  $^{128}\text{Cd}$  (\*) and to neutron induced reactions in the germanium detectors (#).

removal reaction, compared to the isomeric production ratios in the relativistic fission in the production target. Another powerful tool to clean spectra was presented in section 3.1.2 where the use of the cluster and crystal multiplicities was introduced. As a cross check to rule out the presence of weak transitions in the lower energy part of the delayed add-back spectrum, Fig. 5.20d) shows the energy spectrum limited on cluster multiplicity two and crystal multiplicity two. Again no new lines in the low energy region can be identified, leaving only the observation of the high energy transition.

The 3693-keV transition is not observed in coincidence with any other transition in this experiment as shown in the  $\gamma - \gamma$  coincidence spectra in Fig. 5.20e). A least square fit to the time distribution of the 3693-keV transition with a single exponential decay function, shown in Fig. 5.21, results in a half-life of  $T_{1/2} = 0.9(1) \mu\text{s}$ .

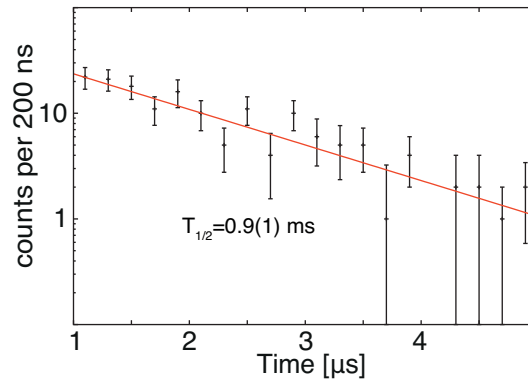


**Figure 5.21:** Time distribution of the 3693-keV transition and in red the fitted single exponential decay function.

### 5.3.1 Conclusions

Summarizing the results presented in this section, it is suggested, that a  $\mu\text{s}$  isomeric state in <sup>129</sup>Cd was observed in the present experimental data. The first suggested scenario is a core-excited isomer. It is worth mentioning that Górska *et al.* [9] identified an isomeric state at a similar excitation energy (3782(2) keV) in <sup>131</sup>In with a comparable half-life of 0.63(6)  $\mu\text{s}$ . In that work the isomeric state was identified as a high-spin, core-excited isomer with a tentative spin and parity assignment of (17/2<sup>+</sup>). However, it could also be the 27/2<sup>-</sup> state of the  $\nu h_{11/2}^{-1} \pi g_{9/2}^{-2}$  multiplet, but one will see later in chapter 6 (section 6.2) that shell-model calculations predict the 27/2<sup>-</sup> state at 1695 keV and to be a E6 spin trap and therefore to undergo  $\beta$ -decay.

## 5.4 The (8<sup>+</sup>) isomeric state in <sup>130</sup>Cd

Previous to this work one isomeric state was identified in <sup>130</sup>Cd by Jungclaus *et al.* [7] who measured a half-life of 220(30) ns and assigned a spin of 8<sup>+</sup> in analogy to <sup>98</sup>Cd. The level scheme proposed in that work is shown in Fig. 5.22. The origin of the 8<sup>+</sup> isomer in <sup>98</sup>Cd was described in Ref. [160] to be a maximum aligned pair of proton holes in the  $g_{9/2}$  orbit. The isomer in <sup>130</sup>Cd is depopulated by a cascade of four transitions with energies of 128, 138, 539 and 1325 keV. The 539- and 1325-keV transitions were assigned to the 4<sup>+</sup>  $\rightarrow$  2<sup>+</sup> and the g.s. transition in Ref. [7], respectively. One of the problems in [7] was that the order of the 128- and 138-keV transitions could not be fixed and furthermore from shell model calculations the 6<sup>+</sup> state was expected to be a ns isomer. This could not be confirmed due to limitations in the accumulated statistics in that work. A core-excited 12<sup>+</sup> isomer was observed in <sup>98</sup>Cd in addition to the 8<sup>+</sup> isomeric state [161].

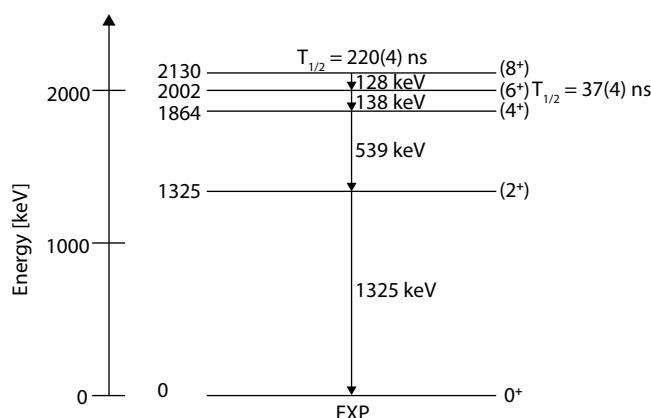


**Figure 5.22:** Level scheme of <sup>130</sup>Cd as proposed in Ref. [7] with the half-life and the order of the 128- and 138-keV transitions as observed in the present experimental data.

$E_\gamma$ [keV]	$E_{\gamma,lit}$ [keV]	$T_{1/2}$ [ns]	$I_\gamma$ [%]	$I_{\gamma,lit}$ [%]	$\alpha$	$\alpha_{lit}$
127.5	128	227(5)	48(4)	64(8)	1.08(16)	0.63(26)
137.6	138	218(10)	69(4)	67(8)	0.45(10)	0.56(25)
538.6	539	210(9)	100(3)	100(13)	-	-
1325.0	1325	200(11)	99(3)	113(17)	-	-

**Table 5.4:** Summary of the energies, the relative intensities and conversion coefficients of the transitions observed in delayed coincidence with the <sup>130</sup>Cd ions in this work and the corresponding literature values [160].

### 5.4.1 Experimental results

In this work the nature of the order of the transitions, the ns isomeric character of the (6<sup>+</sup>) state and the possible existence of a high lying 12<sup>+</sup> isomeric state are again addressed taking advantage of the much higher production yield of <sup>130</sup>Cd ions. In total  $1.9 \cdot 10^6$  <sup>130</sup>Cd ions were identified in BigRIPS and implanted in WAS3ABi. The number of implanted ions is therefore about 300 times higher than in the previous experiment. Nevertheless, the in-flight decay losses are higher with the flight time through BigRIPS being twice the flight time through the FRS. Fig. 5.23a) shows the germanium spectrum observed in delayed coincidence with the <sup>130</sup>Cd ions with the lower and upper time limits set to 200 and 900 ns. No additional transitions are observed to those in the previous experiment. Also when using add-back or changing the upper time limit to the full time range of the DGF no additional lines are present in the delayed Ge spectrum.

The four previously reported transitions are also observed in this experiment in mutual coincidence with each other (see Fig. 5.23b) to e)). The results for the relative intensities are summarized in Table 5.4 along with the calculated conversion coefficients. The conversion coefficient for the 138-keV  $\gamma$  ray agrees with the previously measured value within the uncertainties, while the conversion coefficient obtained for the 128-keV transition is slightly higher and also does not agree with the theoretical value assuming a pure E2 transition of  $\alpha_{theo} = 0.62$  [99].

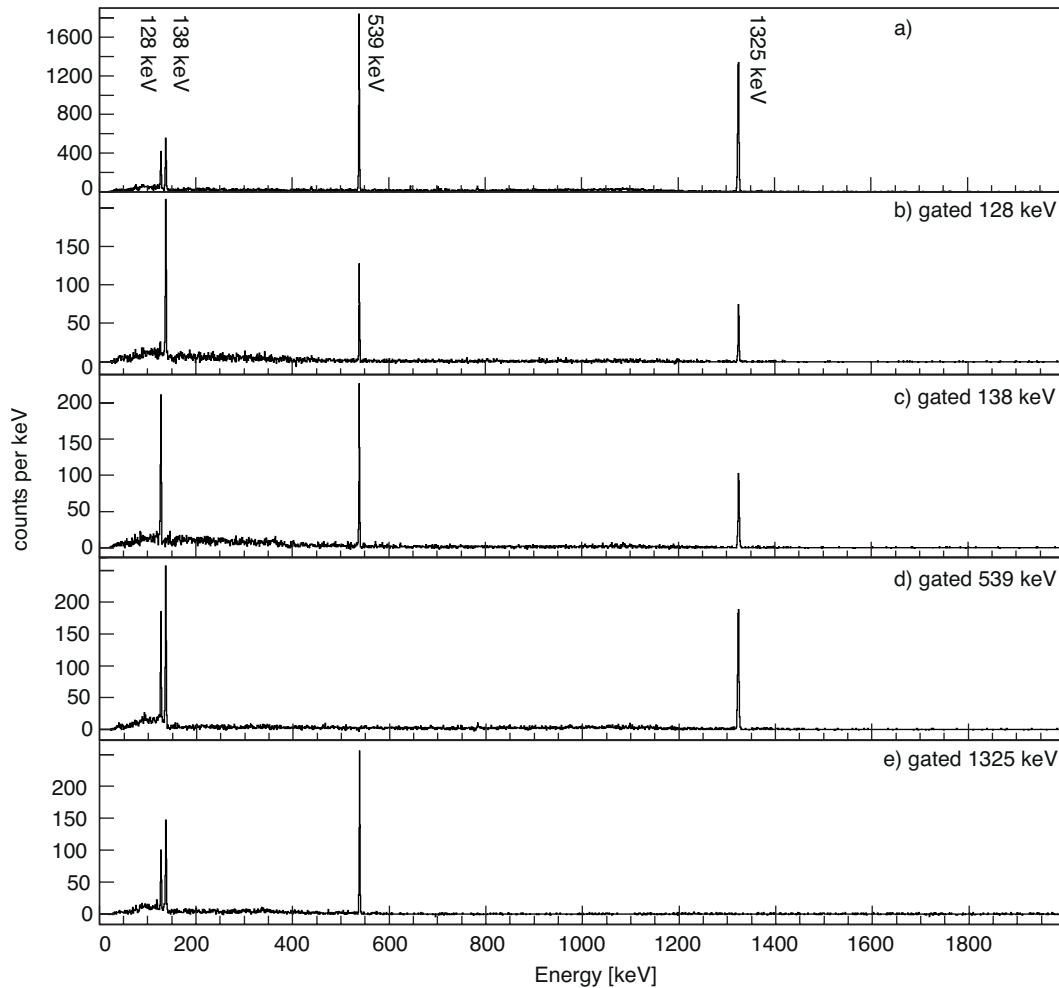


**Figure 5.23:** a) Ge spectrum in delayed coincidence with the implanted <sup>130</sup>Cd ions. b)-e)  $\gamma\gamma$  coincidence spectra gated on the 128-, 138-, 539- and 1325-keV transitions with a coincidence time window of 500 ns applied.

An open question prior to this work was the order of the 128- and 138-keV transitions. To address this question the half-life of the 6<sup>+</sup> state was investigated with the centroid-shift method. An observed centroid shift would directly fix the order of the two transitions. The timing information was taken from the long range TDC times of the analogue timing branch in the germanium electronics. One major limitation in the determination of the half-life of the 6<sup>+</sup> state is the low efficiency of the analogue timing branch for low energy transitions. As a result the time distributions shown in Fig. 5.24 have to be re-binned to observe the centroid shift and also the error bars of the calculated centroid positions are much larger than compared to the case of <sup>128</sup>Cd. Despite these limitations a centroid shift in the forward time direction is observed in Fig. 5.24a), showing that the 138-keV  $\gamma$  ray is emitted after the 128-keV  $\gamma$  ray in time.

This result is confirmed by the time difference distributions of the 128- and 138-keV transitions, respectively, and the 539-keV transition. The distributions are shown in Fig. 5.24b) and c), respectively. Fig. 5.24b) clearly shows a shifted centroid with respect to the zero time while Fig. 5.24c) shows no shift. In Fig. 5.24a) and b) the centroid positions are

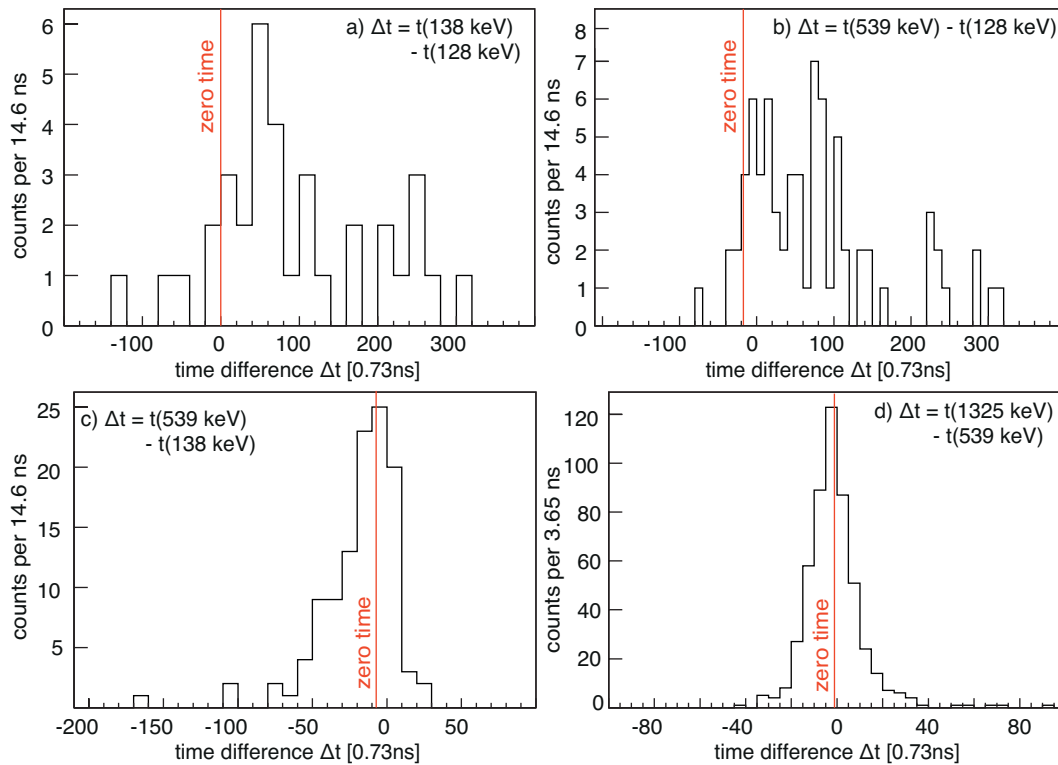


**Figure 5.24:** Time difference  $\Delta t_{\gamma\gamma}$  distributions of a) the 138-keV transition to the 128-keV transition, b) the 539-keV transition to the 128-keV transition, c) the 539-keV transition to the 138-keV transition and d) the 1325-keV transition to the 539-keV transition.

$C=71(31)$  ns and  $C=53(15)$  ns, respectively. The life-time of the 6<sup>+</sup> state is therefore  $\tau = 56(13)$  ns and with that the half-life is  $T_{1/2} = 39(9)$  ns. No shift of the centroid is observed for the time difference between the 138- and 539-keV transition which means the half-life of this state is smaller than the chosen binning. Furthermore no centroid shift can be observed in Fig. 5.24d) which leads to the conclusion that the half-life of the 2<sup>+</sup> state is also smaller than the detection limits in this experiment.

A centroid-shift for a half-life of  $T_{1/2} = 39(9)$  ns should furthermore be clearly visible when using the DGF which have a worse timing resolution but a higher efficiency for lower energetic  $\gamma$  rays. Figure 5.25 shows a matrix for the time difference between the observation of the 539-keV transition and another  $\gamma$  ray. Indeed the 539-keV transition is emitted prompt with respect to the timing of the 138-keV transition, while the centroid of the timing of the 539-keV transition is shifted with respect to the timing of the 127-keV transition and a tail is clearly visible. From the centroid shift a half-life of  $T_{1/2} = 35(5)$  ns is obtained. The small inlay graph in Figure 5.25 shows furthermore the fit of a single exponential decay function to the tail of the time distribution. The half-life obtained from the fit is  $T_{1/2} = 55(15)$  ns. From the three half-life values a weighted arithmetic mean half-life of  $37(4)$  ns can be calculated.

The next step was the re-determination of the half-life of the (8<sup>+</sup>) state. The time distributions gated on the four transitions are shown in Fig. 5.26. The distribution gated on the 128-keV transition was fitted with a single exponential decay function and a half-life

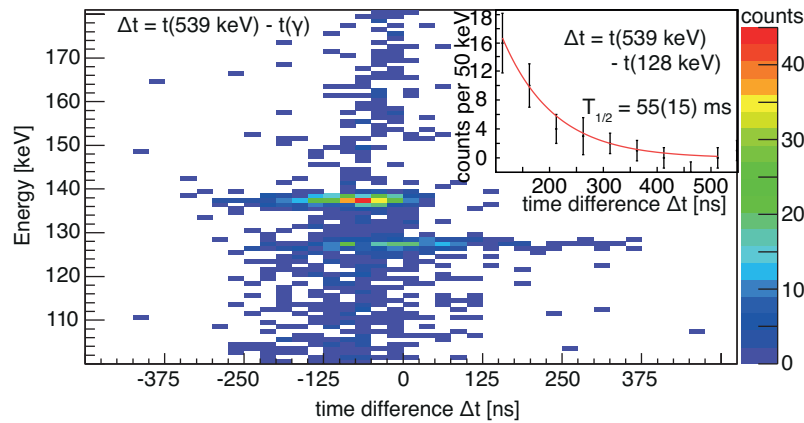


**Figure 5.25:** Time difference  $\Delta t_{\gamma\gamma}$  matrix gated on the 539-keV transition. The small inlay figure shows the projection of the matrix on the time axis gated on the 128-keV transition.

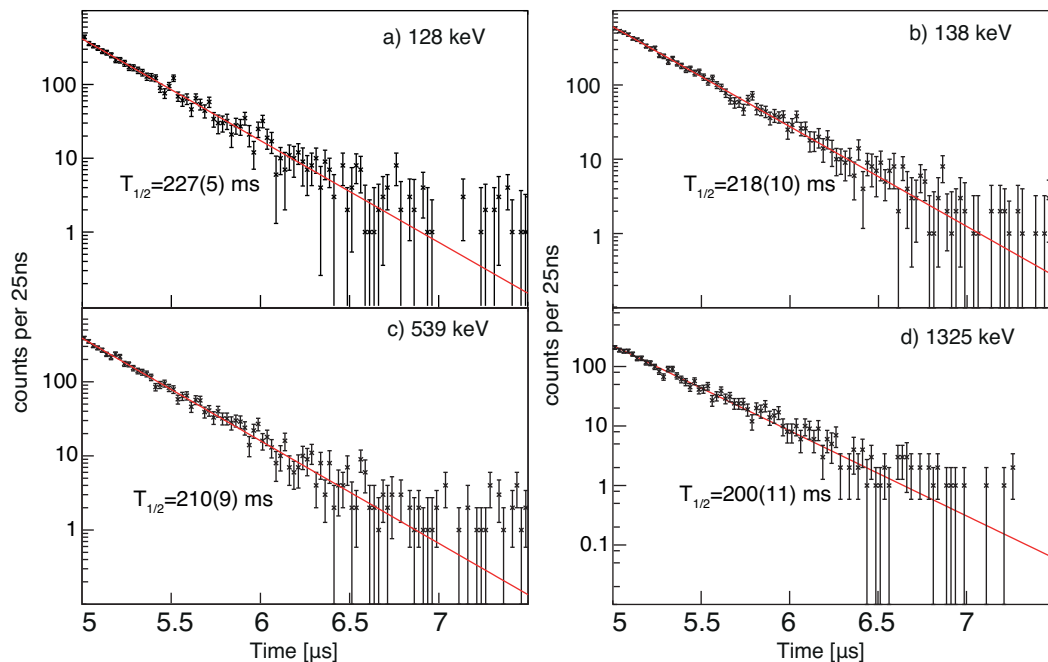


**Figure 5.26:** a)-d) Time distributions relative to the ion implantation of the 128-, 138-, 539- and 1325-keV transitions with an arbitrary offset and in red the fitted single exponential decay function.

of  $T_{1/2}=227(5)$  was obtained. With the half-life of the (6<sup>+</sup>) state being  $T_{1/2} = 37(4)$  ns, the other time distributions had to be fitted with a fit function accounting for the activity of both isomeric states (see Formula 5.8). The half-life of the (6<sup>+</sup>) state was fixed, while the half-life of the (8<sup>+</sup>) state was a free fit parameter. The fits are shown in Fig. 5.26b)-d), the obtained half-lives are stated in Table 5.4 and the weighted arithmetic mean half-life is  $T_{1/2} = 210(6)$  ns. When fitted with a single-exponential decay function the weighted arithmetic mean half-life obtained from the three time distributions in Fig. 5.26b)-d) is  $T_{1/2} = 225(2)$  ns and therefore slightly longer.

The weighted arithmetic mean half-life from the half-lives stated in Table 5.4 is  $T_{1/2} =$

220(4) ns. This result is in good agreement with the half-life of 220(30) ns given in Ref. [7].

### 5.4.2 Conclusions

With the results presented here on the decay of the  $8^+$  isomeric state the previously unknown order of the 128-keV and 138-keV  $\gamma$  rays could be fixed. The 128-keV and 138-keV transitions are now assigned to be the  $8^+ \rightarrow 6^+$  and  $6^+ \rightarrow 4^+$  transitions, respectively. In addition the isomeric character of the  $6^+$  state, suggested by the shell model calculations in Ref. [7], was confirmed and a half-life of  $T_{1/2} = 37(4)$  ns extracted. This corresponds to a reduced transition strength for the  $6^+ \rightarrow 4^+$  transition of  $B(E2) = 8(2)$  W.u.

The relative intensity of the 128-keV transition in the present work is clearly lower than that of the 138-keV transition which can not be explained with the conversion coefficients. Those should be rather similar for the 128- and the 138-keV transitions. A possible explanation is feeding of the  $6^+$  state due to an unobserved transition. Shell-model calculations in Ref. [7] suggest that there is a  $(5^-)$  state expected in close proximity to the  $6^+$  state. This state is a good candidate to explain the difference in relative intensity between the two transitions. However, no additional transitions were observed in the present experiment. The assumption that the  $6^+$  state is not solely fed by the  $8^+$  state has also consequences for the determined half-lives. If the  $6^+$  state is fed by another state then the time distributions of the 138-, 539- and 1325-keV transitions would have to be fitted to a fit function including this additional feeding. Therefore, strictly speaking only the half-life value of  $T_{1/2} = 227(5)$  ns, obtained from the fit of the 128-keV transition, should be used until this inconsistency is solved.

The presence of a core-excited isomer in  $^{130}\text{Cd}$  is still an open question since in the present work no new transitions could be identified, suggesting that, assuming it exists, the half-life is either too short or too long to be observed in the present experiment.

## 5.5 Isomeric ratios

The isomeric ratio  $R$  is the probability to produce a nucleus in a certain isomeric state at the production target. The isomeric ratio is expected to be different for different reaction mechanisms and energies and therefore it is essential to compare results from different experiments. After a short introduction on how to calculate  $R$ , the results for the isomeric ratios obtained from two experiments are presented, one of those is the EURICA experiment presented throughout this thesis. The second experiment was carried out within the RISING stopped beam campaign [101]. The isomeric ratios of the latter were also deduced as part of this thesis. This experiment is of particular interest because two production mechanisms were used: relativistic fission and relativistic fragmentation. This makes it a perfect test scenario. The half-lives and other necessary information to extract the isomeric ratios of the very neutron-rich Silver (Ag), Cadmium (Cd), Indium (In) and

Tin (Sn) isotopes in the RISING stopped beam experiment were taken from [3, 5–10].

Details on the RISING stopped beam experiments will not be presented here, but can be found in Refs. [3, 5–10]. In that experiment the exotic nuclei were produced in the fragmentation of a  $^{136}\text{Xe}$  primary beam at  $750\text{MeV}/u$  impinging on a  $4\text{g}/\text{cm}^2$  Be target and in relativistic fission of a  $^{238}\text{U}$  primary beam at  $650\text{MeV}/u$  impinging on a  $1\text{g}/\text{cm}^2$  Be target. The second production mechanism is essentially the same as the one used for the experiment presented in this thesis, but with the energy of the primary beam nearly double ( $345\text{MeV}/u$  in the experiment at the RIKEN Nishina Center).

### 5.5.1 Calculation of the isomeric ratio

The isomeric ratio  $R$  can be expressed as (all formulas have been taken from Refs. [162, 163]):

$$R = \frac{Y}{N_{imp} \cdot F \cdot G} \quad (5.14)$$

where  $N_{imp}$  the number of implanted ions of the nucleus,  $F$  and  $G$  are correction factors and  $Y$  is the observed number of decays corrected for the absolute efficiency, the branching ratio and conversion:

$$Y = \frac{N_{\gamma}(1 + \alpha_{tot})}{\epsilon_{abs} \cdot b_{\gamma}} \quad (5.15)$$

$N_{\gamma}$  is the number of observed  $\gamma$  rays for a certain transition,  $\alpha_{tot}$  the total conversion coefficient,  $\epsilon_{abs}$  the absolute efficiency for this energy and  $b_{\gamma}$  the  $\gamma$  ray branching ratio.

In-flight isomer decay losses and the finite detection time of the system have to be taken into account and therefore the correction factors  $F$  and  $G$  were introduced in formula 5.14.  $F$  is the correction factor for the losses during the flight time through the fragment-separators, which is in the order of 300 ns for the FRS and 650 ns in the case of BigRIPS.  $F$  can be written as:

$$F = \exp \left[ - \left( \lambda^q \frac{ToF}{\gamma} \right) \right]. \quad (5.16)$$

where  $ToF$  is the flight time through either the FRS or BigRIPS and  $\gamma$  the corresponding relativistic factor. The total flight time is not measured and therefore has to be taken from simulations with LISE++.  $\lambda^q$  is the decay constant of the nucleus in the isomeric state, which depends on the charge state  $q$  of the nucleus. It was here assumed that the charge state does not change inside the fragment-separators and furthermore that the ions are mainly fully stripped. The assumption that the ions are fully stripped may not be true in all cases for BigRIPS due to the lower beam energies. Nevertheless, the calculations were made assuming a fully stripped ions, as it was not possible to identify charge states. For a fully stripped ion  $\lambda^q = \lambda^0$  where  $\lambda^0$  is the decay constant of a fully stripped ion, which can be calculated with the following formula:

$$\lambda^0 = \lambda \sum_i \frac{b_{\gamma i}}{1 + \alpha_{tot}^i}. \quad (5.17)$$

The sum includes all decay branches  $i$ , directly depopulating the isomer, with  $b_{\gamma_i}$  the  $\gamma$ -ray branching ratios and  $\alpha_{tot}^i$  the total conversion coefficients for the individual branches. The conversion coefficients were either taken from literature values or calculated with the conversion coefficient calculator BRICC [99].

$G$  is the correction factor for the finite detection time of the system and is given as:

$$G = \exp(-\lambda \cdot t_l) - \exp(-\lambda \cdot t_f) \quad (5.18)$$

This correction factor has been presented in section 3.1.4 for the correction of the relative intensities.  $t_l$  and  $t_f$  are again the lower and upper time limits, respectively.

If more than one isomeric state is observed and feeding takes place from one isomeric state to another then formula 5.14 must be extended to account for the feeding:

$$R_L = \frac{Y_L}{N_{imp} \cdot F_L \cdot G_L} - b_{UL} \frac{R_U}{F_L \cdot G_L} \cdot \left[ \frac{\lambda_U (G_U - G_L)}{\lambda_L - \lambda_U} F_U + \frac{\lambda_U^0}{\lambda_L^0 - \lambda_U^0} G_L (F_U - F_L) \right] \quad (5.19)$$

with the indices “L” and “U” denoting the lower and upper lying isomeric state, respectively.

In those cases where the isomeric ratio for a given isomeric state could be calculated from not one but  $n$  decay lines, a mean isomeric ratio can be calculated:

$$R_{Mean} = \frac{\bar{H}}{F \cdot N_{imp}} \quad (5.20)$$

The introduced parameter  $\bar{H}$  is the average of all observed decay yields from the different decay lines corrected for the finite detection time:

$$\bar{H} = \frac{1}{n} \sum_{i=1}^n H_i = \frac{1}{n} \sum_{i=1}^n \frac{Y_i}{G_i} \quad (5.21)$$

The error of  $\bar{H}$  is taken to be the standard-deviation and the error of  $R_{Mean}$  is then calculated via error propagation.

### 5.5.2 Isomeric Ratios of long lived states in Ag, Cd, In, Sn populated in fragmentation and relativistic fission.

A table with all isomeric ratios for the long lived states observed in the two experiments is shown in the appendix (see Tables C.6 to C.8), comprising the results for  $^{122-126}\text{Ag}$ ,  $^{125-130}\text{Cd}$ ,  $^{125-131}\text{In}$  and  $^{128-130}\text{Sn}$ . Table 5.5 shows the summary for only the Cadmium isotopes to compare the two production mechanism: fragmentation and relativistic fission, and in the case of fission also the two experiments at different RI beam facilities.

In the following tables, the isomeric ratios are shown independently for each experiment and production mechanism. Furthermore for the RISING stopped beam experiment two different settings were analysed, with different  $B\rho$  settings of the fragment-separator FRS:

A	<i>I</i>	$T_{1/2}$ [ $\mu$ s]	$E_x$ [keV]	$R_{exp,1}$ Fragm. FRS $^{126}\text{Cd}$ [%]	$R_{exp,2}$ Fragm. FRS $^{130}\text{Cd}$ [%]	$R_{exp,3}$ Fiss. FRS $^{130}\text{Cd}$ [%]	$R_{exp,4}$ Fiss. BigRIPS $^{128}\text{Pd}$ [%]	$R_{exp,5}$ Fiss. BigRIPS $^{136}\text{Sn}$ [%]
125	35/2	3.1(1)	3896	0.9(2)	-	-	-	-
125	19/2	13.6(2)	1462	14.0(14)	-	-	-	-
126	12	1.72(7)	2977+x	0.9(1)	1.7(2)	-	-	-
127	19/2	17.5(3)	1560+x	14.7(8)	13.4(7)	8.7(19)	-	-
128	10	3.56(6)	2714	10.5(5)	9.2(4)	6.8(4)	6.2(3)	6.5(5)
128	5	0.27(1)	1871	21.6(45)	18.7(3.1)	20.2(30)	26(5)	24(5)
130	8	0.22(3)	2130	-	14.8(17)	18.0(25)	15.8(3)	16.0(4)

**Table 5.5:** Summary of the isomeric ratios in A=126-130 Cadmium isotopes for the 5 different settings/production mechanisms.  $R_{exp,1}$ ,  $R_{exp,2}$  are the isomeric ratios for the two settings with the nuclei produced in fragmentation of  $^{136}\text{Xe}$  primary beam, while for  $R_{exp,3}$ ,  $R_{exp,4}$  and  $R_{exp,5}$  the neutron-rich isotopes were produced in relativistic fission of a  $^{238}\text{U}$  beam. Information for  $I$ ,  $T_{1/2}$ , and  $E_x$  were taken from Refs. [3–7].

One focussed on  $^{126}\text{Cd}$  (Setting 1) and the second one with the FRS optimised for the transmission of  $^{130}\text{Cd}$  (Setting 2). As presented in the beginning of this thesis the EURICA experiment comprises two settings too, one with BigRIPS optimized for the transmission of  $^{128}\text{Pd}$  (Setting 4) and the other one of  $^{136}\text{Sn}$  (Setting 5). All different settings were analysed independently to observe if the settings themselves have an influence on the isomeric ratios. The nomenclature used in the following to distinguish the isomeric ratios for each setting is  $R_{exp,i}$  with  $i$  being the setting number. The relativistic fission setting of the RISING data is hereby called Setting 3.

To calculate the isomeric ratios the half-lives were taken either from the literature values or as determined in the present experiment. This is indicated in the table in the appendix. The Indium isotopes present in the RISING experiment with masses A=125-130 were also analysed as part of this thesis to obtain half-life values for the previously unknown isomeric states or to re-determine them in the case that they had been published prior to this work.

In Table 5.5 and in the summary of all isomeric states observed in the produced  $Z=47-50$  nuclei in the appendix, one observes that R for different settings but the same reaction mechanism agree all fairly well within the error bars. Even the results obtained in the two different RI beam facilities with relativistic fission at very different energies (345 and 650  $\text{MeV}/u$ ) compared to each other show a very good agreement. It is therefore concluded that the setting itself and the beam energies in the first order has no influence on the experimental isomeric ratio. In contrast the values for the two different production mechanisms show differences, but no general rule concerning the spin of the isomeric state can be deduced. Figure 5.27 shows the isomeric ratio as a function of the spin  $I$ . There one observes that for  $I \leq 4\hbar$ , the isomeric ratio ( $R \approx 5\%$ ) seems to be independent from the setting, the beam energy and the production mechanism while for  $I > 4\hbar$  no conclusions can be drawn. In the case of  $^{123}\text{Ag}$  for example we obtain almost identical R ( $R_{exp,1} =$

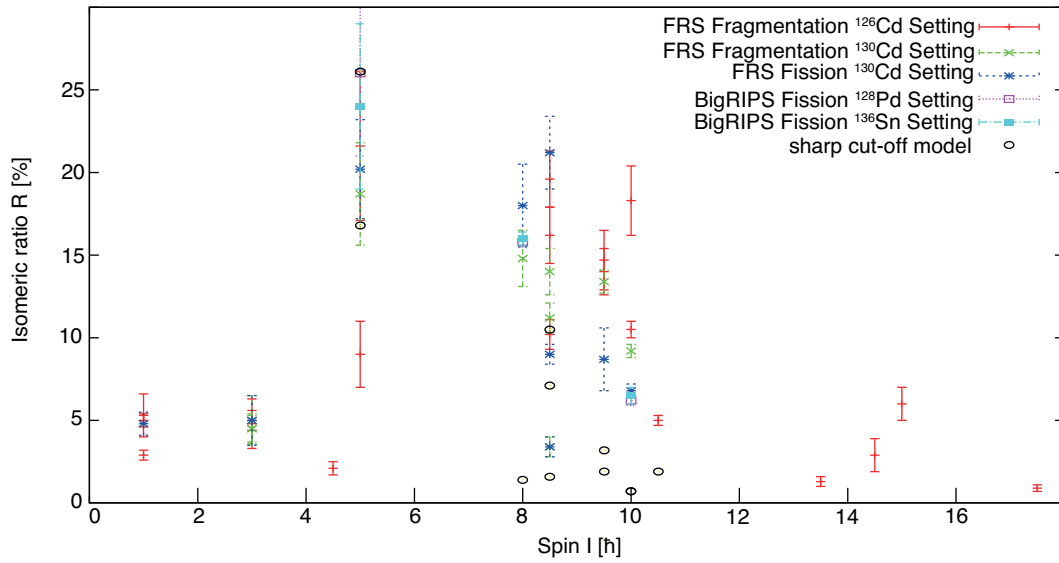


**Figure 5.27:** Isomeric ratio as a function of the spin of the isomeric state for all five settings and the theoretical predictions by the sharp cut-off model for  $^{122-126}\text{Ag}$ ,  $^{125-130}\text{Cd}$ ,  $^{125-131}\text{In}$  and  $^{128-130}\text{Sn}$

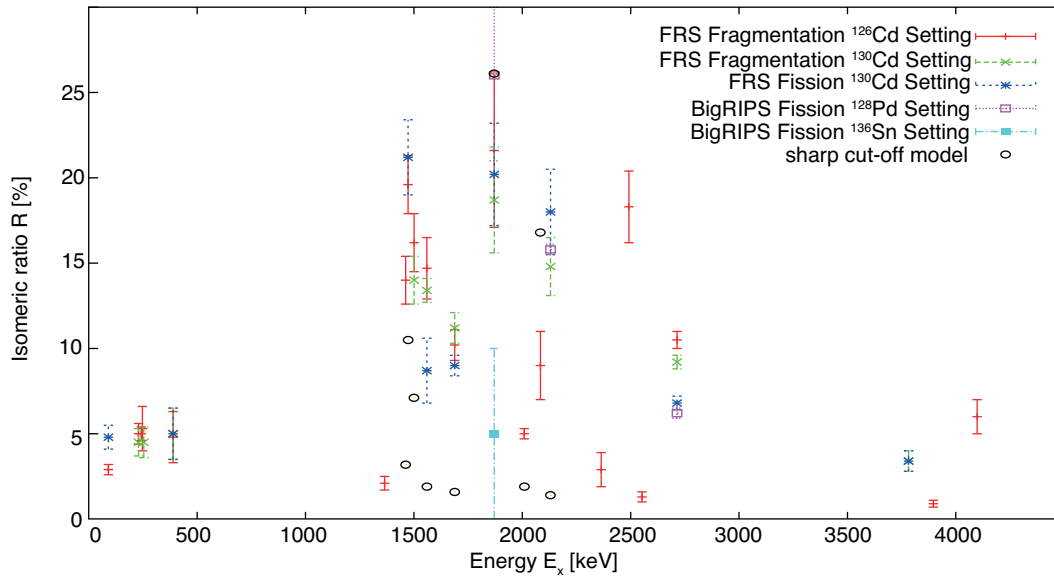


**Figure 5.28:** Isomeric ratio as a function of the excitation energy of the isomeric state for all five settings and the theoretical predictions by the sharp cut-off model for  $^{122-126}\text{Ag}$ ,  $^{125-130}\text{Cd}$ ,  $^{125-131}\text{In}$  and  $^{128-130}\text{Sn}$ .

19.6(17)% for fragmentation and  $R_{exp,3} = 21.1(22)\%$  for fission) for the  $(17/2^-)$  state, but the  $(19/2^+)$  state in  $^{127}\text{Ag}$  shows clearly a decrease when going from fragmentation to fission ( $R_{exp,1} = 14.7(8)\%$  for fragmentation and  $R_{exp,3} = 8.7(19)\%$  for fission). However, the uncertainties are large such that final conclusions are difficult. In addition, the small amount of nuclei produced with both mechanism complicates the situation further. In Figure 5.28 the isomeric ratio is shown as a function of the excitation energy  $E_x$ , where the isomeric ratio is small for  $E_x < 500$  keV, while for  $E_x > 500$  keV the data scatters and no trends can be observed.

### 5.5.3 Comparison to the sharp cut-off model and conclusions

The results presented in the previous section for the fragmentation settings can be compared to a very simplified theoretical model. To describe the population of an isomeric state in a fragmentation reaction the ABRABLA code [164] can be used. The code gives predictions for the angular momentum distribution of the fragments. The code uses the abrasion-ablation model, which is mainly divided into two steps. In the first step (“abrasion phase”), a hot pre-fragment is created by the removal of a number of nucleons of a given projectile. In the second step (“ablation phase”), this hot pre-fragment is then de-excited by the evaporation of additional nucleons. A final fragment is then created with an excitation energy below the particle emission threshold. This final fragment is de-excited by a statistical  $\gamma$ -ray cascade down to the yrast line and then along this line to the ground state. If a long-lived state is part of this cascade, the cascade may be partially hindered or stopped. The isomeric ratio is the probability, that the gamma decay from the excited final fragment proceeds via this state.

In the case that the mass difference between the projectile and the fragment is large ( $\Delta A > 10$ ), the angular momentum distribution can be approximated from an analytical formula [165]:

$$P_J = \frac{2J+1}{2\sigma_f^2} \exp \left[ -\frac{J(J+1)}{2\sigma_f^2} \right] \quad (5.22)$$

$\sigma_f^2$  is the so-called spin-cutoff parameter and is calculated from:

$$\sigma_f^2 = \langle j_z^2 \rangle \frac{(A_p - A_f)(\nu A_p + A_f)}{(\nu + 1)(A_p - 1)} \quad (5.23)$$

$A_p$  and  $A_f$  are the mass number of the projectile and the final fragment,  $\nu$  is the mean number of evaporated nucleons per abraded mass unit and  $\langle j_z^2 \rangle$  is the average square of the angular momentum projection of a nucleon in the nucleus.  $\nu$  is taken to be 2 under the assumption that the abrasion of one nucleon corresponds to an excitation energy of 27 MeV and the evaporation of one nucleon decreases the energy by 13 MeV. The factor  $\langle j_z^2 \rangle$  can be approximated on the basis of a semi-classical consideration of the angular momentum distribution in the Woods-Saxon potential:

$$\langle j_z^2 \rangle = 0,16 A_p^{2/3} \left( 1 - \frac{2}{3} \beta \right) \quad (5.24)$$

In this formula  $\beta$  is the quadrupole deformation parameter and since the nuclei of interest are close to the doubly magic  $^{132}\text{Sn}$ ,  $\beta$  is taken to be zero from here on.

The angular momentum distribution obtained in this way can now be used to make predictions for the probability that a metastable state (with given angular momentum  $J_m$ ) is populated via  $\gamma$  decay. Therefore the extremely simplifying assumption has to be made, that all states with  $J_m \geq J$ , and only those, decay to the metastable state. This approach, known in the literature as “sharp cut-off model”, was applied for studies of angular momentum distributions in projectile fragmentation [162, 163], in compound nuclei [166–168]

A	I	$R_{exp,1}$ [%] Fragm. FRS $^{126}\text{Cd}$	$R_{exp,2}$ [%] Fragm. FRS $^{130}\text{Cd}$	$R_{th}$ [%]
125	35/2	0.9(2)	-	0.0
125	19/2	14.0(14)	-	3.2
127	19/2	14.7(8)	13.4(7)	1.9
128	10	10.5(5)	9.2(4)	0.7
128	5	21.6(45)	18.7(3.1)	26.1
130	8	-	14.8(17)	1.4

**Table 5.6:** Comparison of the experimentally obtained isomeric ratios in A=126-130 Cadmium isotopes to the theoretical predictions calculated with the sharp cut-off model. For details see text.

and in fission fragments [169]. The theoretical isomeric ratio is then calculated as follows:

$$R_{th} = \int_{J_m}^{\infty} P_J dJ = \left[ -\frac{J_m(J_m + 1)}{2\sigma_f^2} \right]. \quad (5.25)$$

Substituting  $\nu = 2$ ,  $\beta = 0$ , and introducing  $\Delta A = A_p - A_f$ , Equation 5.23 and 5.24 yield:

$$\sigma_f^2 = 0,0178A_p^{2/3} \frac{\Delta A(3A_p - \Delta A)}{A_p - 1}. \quad (5.26)$$

The calculated values for the sharp cut-off model are presented in Table 5.6 as  $R_{th}$ . Unfortunately the experimental and theoretical values do not agree. One problem could be the small mass difference between the  $^{136}\text{Xe}$  primary beam and the fragmentation products in the range from A=123-131. In Refs. [162, 163] the authors state that a mass difference of  $\Delta A > 10$  is necessary to use this analytical formula. It is therefore concluded that in the present case the very simplified theoretical model are not sufficient to describe the isomeric ratio and more complex models would be necessary. The isomeric ratios determined in the present thesis are an important input parameter for future studies, to compare them to models and to estimate R at the production target for upcoming experiments of a similar type at RI beam facilities. Together with estimated half-lives they are crucial ingredients to estimate if it will be possible to observe a certain isomeric state in an experiment or not.

## Chapter 6

# Shell-model comparison

In the introduction it was mentioned that only few shell-model calculations have been performed in the region south of  $^{132}\text{Sn}$  and furthermore most of those did not show a good agreement with the experimental data. In the following sections new shell model calculations are presented which are similar to the ones in Refs. [29–31]. However, in the present work the newly established position of the  $p_{3/2}$  proton-single hole state is used together with the new energy of the  $p_{1/2}$  proton-single hole state taken from Ref. [48].

### 6.1 The NA-14 shell-model interaction

The shell-model interaction which was used for the calculations (provided by H. Grawe [170]), using the OXBASH code [36], will be referred to as “NA-14” in the following. It employs a two-body effective interaction derived from the CD Bonn nucleon-nucleon potential with a re-normalization using the  $V_{low-k}$  approach [133]. The calculations use  $^{132}\text{Sn}$  as a closed core and take into account the proton  $Z = 28-50$  and neutron  $N=50-82$  major shells, which means the  $0f_{5/2}$ ,  $1p_{3/2}$ ,  $1p_{1/2}$  and  $0g_{9/2}$  orbits for protons and the  $0g_{7/2}$ ,  $1d_{5/2}$ ,  $1d_{3/2}$ ,  $2s_{1/2}$  and  $0h_{11/2}$  orbits for neutrons. The necessary proton and neutron single particle energies are listed in Ref. [18] and were shown in Fig. 1.2 in the introduction.

For the present calculations, the energy of the  $1p_{1/2}$  orbit was set to 365 keV relative to the  $0g_{9/2}$  orbit as it was reported in Ref. [48] and furthermore, an energy difference of 988 keV was employed for the positions of the  $1p_{3/2}$  SPO with respect to the  $1p_{1/2}$  orbit. The unknown energy of the  $0f_{5/2}$  proton SPO was set to 2.6 MeV above the  $0g_{9/2}$  SPO. The effective charges were set to  $e_{\pi} = 1.5e$  and  $e_{\nu} = 0.7e$  for E2 and E3 transitions and the effective spin g-factor to  $g_s = 0.7g_s^{free}$  for M1 transitions.

The interaction was tested for several nuclei in that region for which experimental information is available, i.e.  $^{125-130}\text{Sn}$  (compilation of the results in Ref. [2]),  $^{127,128,130}\text{Cd}$  ([5–7]) and  $^{126,128}\text{Pd}$  [12]. To well describe those results, several modifications had to be made because the interaction showed too strong pairing in the proton-proton ( $\pi\pi$ ) channel and

furthermore, it was found that the neutron-neutron channel  $\nu\nu$  and the  $\pi\nu$  channels had a too weak multipole part. The  $\pi\pi$  pairing was therefore on the one hand reduced to 88% and on the other hand the  $\nu\nu$  and  $\pi\nu$  multipoles were increased by factors of 1.5 and 1.6 in the dominant  $\nu h_{11/2}^2$  and  $\nu h_{11/2}\pi g_{9/2}$  configurations, which increases the L=2 collectivity with the largest multipole part being quadrupole.

## 6.2 The ms isomeric state in $^{129}\text{Cd}$

Shell model calculations based on the interaction presented in the previous section have been performed for  $^{129}\text{Cd}$ . Those predict the existence of two isomeric states. The first one, a  $27/2^-$  level, is placed at 1695 keV and is predicted to be a E6 spin trap and therefore expected to undergo  $\beta$ -decay. The  $27/2^-$  level corresponds to two proton holes in the  $0g_{9/2}$  and one neutron hole in the  $0h_{11/2}$  orbital with maximum alignment. The second predicted isomeric state is a  $21/2^+$  level at 1806 keV and is predicted to decay to a  $15/2^-$  level via a E3 transition.

The experimental level scheme as it was obtained from the information presented in the section 5.2 is shown in Fig. 6.1 together with the shell model predictions. Shown is the proposed  $21/2^+$  isomeric level which decays to a  $15/2^-$  level and subsequently via one direct branch and additionally in a cascade via the  $13/2^-$  level to the  $11/2^-$  state. In the present shell model calculations the  $11/2^-$  state is predicted to be the g.s. with the  $3/2^+$  state being located at 287 keV. Fig. 6.1 includes furthermore the low lying neutron single hole-states and closely lying levels in the spin range from  $17/2^-$  –  $23/2^-$  with both, positive and negative parity. None of those states are predicted to be isomeric in the model calculations.

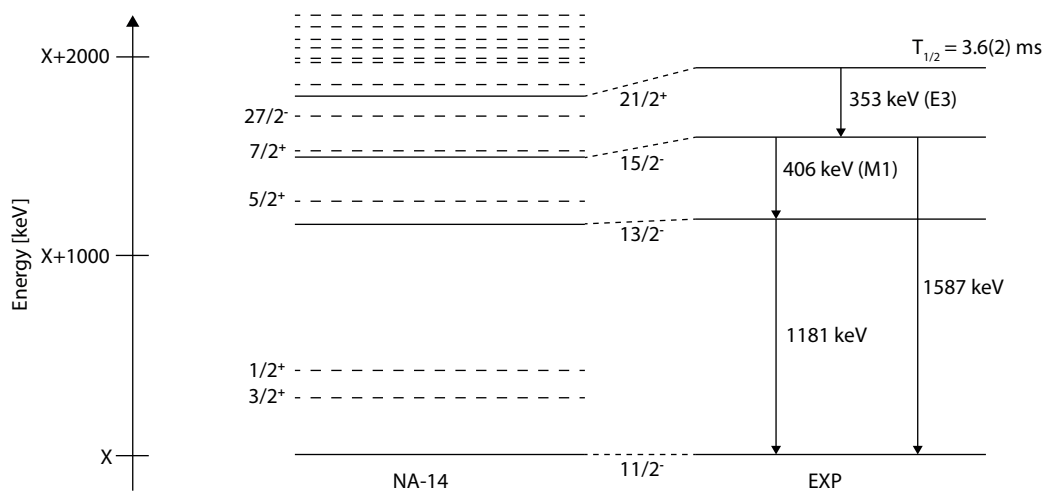


**Figure 6.1:** Level scheme for the ( $21/2^+$ ) ms isomeric state in  $^{129}\text{Cd}$  as it was obtained in the present work and comparison to shell model calculations. The shell model calculation shows furthermore the predicted positions for low-lying neutron single-hole states and levels in the spin range  $17/2^-$ - $23/2^-$  with positive and negative parity.

The  $21/2^+$  level has one proton hole in a negative parity orbital together with one proton hole in the  $0g_{9/2}$  and one neutron hole in the  $0h_{11/2}$  orbital. The proton hole in the negative parity orbital is here necessary due to the positive parity of the state. Based on the shell model calculations the main configuration of this state is  $\nu(h_{11/2}^{-1})\pi(g_{9/2}^{-1}p_{1/2}^{-1})$  which can not decay via an E3 to the  $15/2^-$  state with a configuration of  $\nu(h_{11/2}^{-1})\pi(g_{9/2}^{-2})$ , basically the  $h_{11/2}$  neutron hole coupled to the  $(2-8)^+$  states in  $^{130}\text{Cd}$ . Therefore the crucial contributions to the E3 decay are coming from the additional admixtures of  $\nu(h_{11/2}^{-1})\pi(g_{9/2}^{-1}p_{3/2}^{-1})$  and  $\nu(h_{11/2}^{-1})\pi(g_{9/2}^{-1}f_{5/2}^{-1})$  to the  $21/2^+$  state. The amount of this admixtures, partially dependent on the exact differences between the proton single-particle energies, is then crucial for the electromagnetic strength of this E3 transition. The exact position of the  $\pi 0f_{5/2}$  orbital plays here a less dominant role compared to the position of the  $\pi 1p_{3/2}$  orbital, which was determined in the decay of  $^{131,132}\text{Cd}$  in this work.

The experimentally determined reduced transition strength  $B(E3) = 0.50(3)$  W.u. for the E3 transition from the  $21/2^+$  state to the  $15/2^-$  state, calculated with the half-life of  $T_{1/2} = 3.6(2)$ ms from this work, compares very well to the value obtained from the shell model calculations which is  $B(E3) = 0.48$  W.u.. With the previous reported position of the  $\pi 1p_{3/2}$  orbital (1.65 MeV with respect to  $\pi 0g_{9/2}$  [34]), the shell model  $B(E3)$  is predicted to be 0.31 W.u., obviously not in agreement with the experimental result. The shell-model calculations in the present work with the new value for the  $\pi 1p_{3/2}$  orbital predict the branching between the 406- and 1587-keV transitions to be 2:1 which is in good agreement with the experimentally observed branching of about 3:1.

In this region unfortunately the effective charges for an E3 transition are poorly known, but with this new strong E3 transition it will be possible to determine those values accurately in the future, as soon as the still unknown position of the  $\pi 0f_{5/2}$  orbital is experimentally determined. The current uncertainties in both, the effective charges and the position of the  $\pi 0f_{5/2}$  orbital, limit the possibility to constrain on of them.

### 6.3 The decay of the $17/2^-$ isomeric state in $^{129}\text{In}$

Fig. 6.2 shows a partial level scheme of  $^{129}\text{In}$  as it was obtained in section 3.2.4 in the  $\beta$  decay of  $^{129}\text{Cd}$ . The figure furthermore includes the predictions of the shell model calculations performed for the present work (NA-14) and for comparison those taken from Ref. [29]. In the latter ones also a realistic interaction derived from the CD-Bonn nucleon-nucleon potential is employed with  $^{132}\text{Sn}$  as a closed core and taking into account the major  $N=50-82$  neutron shell. Two of the differences to NA-14 are the proton-single hole energies for the  $1p_{3/2}$  and  $1f_{5/2}$  levels as discussed in the present work and Refs. [48, 127]. One observes a much better agreement between NA-14 and the experimentally obtained level scheme as compared to the calculations by Genevey *et al.* Especially the position of the  $11/2^+$  state is about 300 keV lower in the NA-14 calculations and agrees within a few keV with the experimentally measured energy.

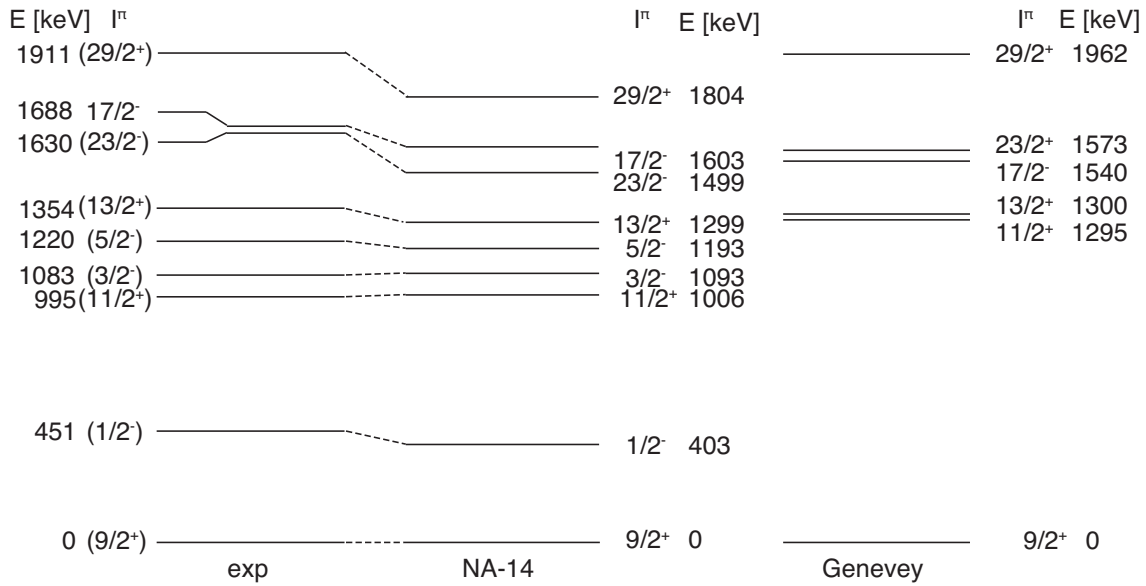


**Figure 6.2:** Partial level scheme obtained in the current work for  $^{129}\text{In}$  and comparison to the shell model calculation NA-14 (for details see section 6.1) and shell model calculations taken from Ref. [29]. In the NA-14 shell model calculations all calculated levels are shown up to a maximum spin of 19/2 and an excitation energy of 1.8 MeV. In addition to this, only the 23/2<sup>-</sup> and 29/2<sup>+</sup> isomeric states are included.

Similar to previous calculations, the NA-14 shell-model calculations predict the 17/2<sup>-</sup> state to be isomeric, which then decays via a cascade to the 9/2<sup>+</sup> g.s. The assignment of spins and parities 11/2<sup>+</sup> and 13/2<sup>+</sup> to the levels at 995 and 1354 keV [29], respectively, agrees with the present calculations and in the calculations the 17/2<sup>-</sup> state is again predicted to have a  $\pi g_{9/2}^{-1}\nu(d_{3/2}^{-1}h_{11/2}^{-1})$  configuration. Based on the calculations the levels at 995 and 1354 keV are assigned to the  $\pi g_{9/2}^{-1}\nu h_{11/2}^{-2}$  multiplet.

The NA-14 calculations predict the 1/2<sup>-</sup> level, namely the  $p_{1/2}$  single hole state at 403 keV. This value is in rather good agreement with our value of 451 keV. The closest lying low spin negative parity states in the calculations are the 3/2<sup>-</sup> and 5/2<sup>-</sup> states which are predicted to lie at 1093 and 1193 keV. With the levels at 1083 and 1220 keV both having strong  $\gamma$  branches to the (1/2<sup>-</sup>) state, they are tentatively assigned to have spins and parities of (3/2<sup>-</sup>) and (5/2<sup>-</sup>). The corresponding (3/2<sup>-</sup>) state in the lower mass odd-Indium isotopes shows a very pure  $p_{3/2}^{-1}$  configuration [121].

Summarizing it can be said that the present shell-model calculations describe very well the low-lying level structure of  $^{129}\text{In}$  and the NA-14 calculations are furthermore in better agreement compared to those from Ref. [29].

## 6.4 Shell-model calculations for the N=82 isotones

In the previous sections it was shown that the NA-14 shell-model calculations reproduce very well the experimental information obtained in the present work and those of previ-

ous works. The calculations therefore describe the relevant features in the region and are used in the following sections to calculate basic properties of the experimentally inaccessible N=82 isotones.

### 6.4.1 The evolution of the N=82 shell gap

The argumentation presented here in the following is based upon the publications J. Taprogge *et al.* [127, 128].

In a first step, the properties of the N=50 isotones below  $^{100}\text{Sn}$  [171, 172], which depend on the same proton SPO's and are therefore a perfect comparison, were investigated. Going along the chain of isotones, it was demonstrated in previous works that  $^{88}\text{Sr}$  and  $^{90}\text{Zr}$  show clear indications for proton sub shell closures. The energy of the first excited  $2^+$  state and the two proton separation energy  $\Delta_{2p}$  are significantly increased compared to the neighbouring even nuclei, as it is presented in Fig. 6.3a) and b), a behaviour typically observed for closed shell nuclei. The two proton gap  $\Delta_{2p}$  is defined here as:

$$\Delta_{2p} = M(Z + 2, N) + M(Z - 2, N) + 2 \cdot M(Z, N) \quad (6.1)$$

with  $M(Z,N)$  being the mass of a nucleus with  $Z$  protons and  $N$  neutrons. Those sub-shell closures for  $Z=38$  and  $40$  can be observed mainly because of the significant shell gaps of 1.28 and 0.65 MeV between the  $1p_{3/2}$  and the  $1p_{1/2}$ , and the  $1g_{9/2}$  and the  $1p_{1/2}$  shells, respectively. Previous shell-model calculations (presented in Fig. 6.3a) and c) as

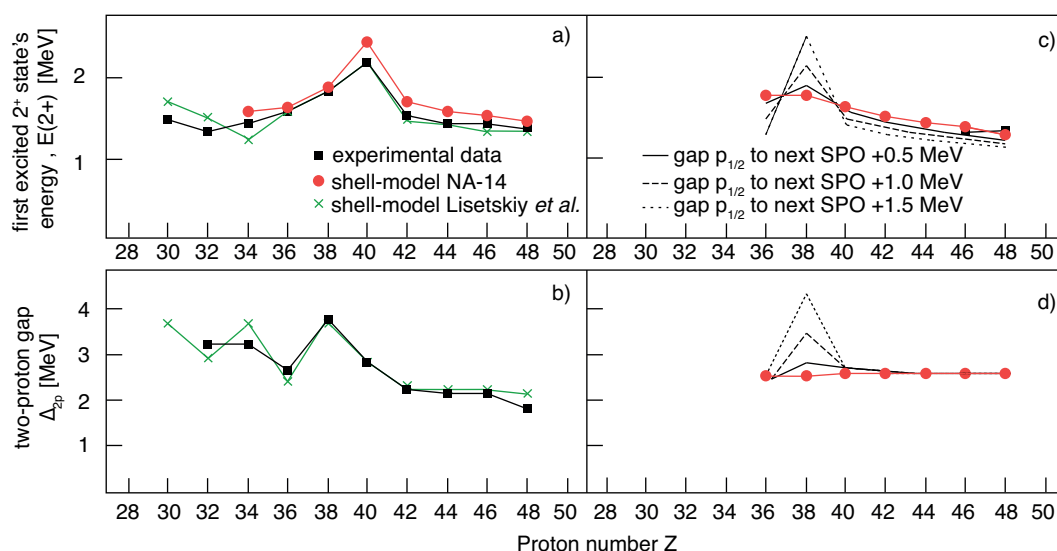


**Figure 6.3:** Comparison of the experimental and calculated a) and c)) energies of the first excited  $2^+$  state ( $E(2^+)$ ) and the (b) and d)) two proton gap  $\Delta_{2p}$  for the even N=50 a) and b)) and N=82 (c) and d)) isotones. The experimental values are shown as filled black boxes and the shell-model calculations as red dots which are presented in the case of the N=82 isotones furthermore for several increases of the 1p gap (solid black line = +0.5 MeV, dashed black line = +1.0 MeV and dotted black line = +1.5 MeV). For the N=50 isotones the shell-model calculations of Ref. [171] are presented for comparison as green stars.

blue asterisk) [139, 171, 172] have already shown good agreement with the experimental results of the N=50 isotones. The question is now if those sub-shell gaps are also present in the case of the N=82 isotones where the shell gaps are small in comparison to the N=50 isotones and have only a size of 0.37(1) and 0.99 MeV, respectively. In a first step shell-model calculations similar to the ones in this work were performed by A. Gargano for the N=50 isotones to check if the  $E(2^+)$  and the  $\Delta_{2P}$  values are well reproduced. The results are shown as red dots in Fig. 6.3a) and b) and clearly describe the experimental data very well, proving that similar calculations for the N=82 isotones have a predictive power to show if the sub-shell closures are also present here.

Using the newly measured energy of the  $p_{3/2}$  SPO, shell-model calculations (NA-14) have been performed and the energies of the first excited  $2^+$  states and the two proton separation energies were calculated. The results are presented in Fig. 6.3c) and d) as the red circles. It has to be mentioned here that for the  $\Delta_{2P}$  values a general shift of +300 keV was applied to all diagonal  $\pi\pi$  two-body matrix elements, necessary to include the Coulomb repulsion and to be consistent with the calculations performed for the N=50 isotones.

It can be observed that the energy of the first excited  $2^+$  state decreases smoothly starting from Z=36 till Z=48 and the two proton separation energy stays very constant over the whole range of even Z nuclei with N=82. Clearly no indications for sub-shell closures can be found in those two figures and it is therefore concluded that the reduction of the shell gaps by about 300 keV between the  $1p_{3/2}$  and the  $1p_{1/2}$ , and the  $1g_{9/2}$  and the  $1p_{1/2}$  shells, respectively, leads to the disappearance of the sub-shell closures when going from N=50 to N=82. It could be argued now that the unknown position of the  $f_{5/2}$  shell or the tentative assignment of  $3/2^-$  or  $5/2^+$  to the state at 1353 keV might change this behaviour and could lead to wrong predictions by the shell model. Additional shell-model calculations were therefore performed by H. Grawe to rule that possibility out by firstly interchanging the positions of the  $1p_{3/2}$  and  $1f_{5/2}$  SPOs and secondly increasing the position of the  $1f_{5/2}$  SPO from 2.6 to 4.5 MeV. Both of those changes showed no influence on the results and it can be concluded that those uncertainties do not result in a different prediction for the presence of sub-shell closures. As a last test additional shell-model calculations were performed with an increased shell gap between the  $1p_{1/2}$  and the next SPO of +0.5 (solid black line), +1.0 (dashed black line) and + 1.5 MeV (dotted black lines) to show that the shell gap between the  $1p_{1/2}$  and the next SPO is the reason for the disappearance of the sub-shell closures. Those calculations are shown in Fig. 6.3c) and d) and clearly show the reappearance of the sub-shell closures for an increased energy difference between the two SPOs.

The question is now, how the disappearance of sub-shell closures affects the N=82 shell gap below  $^{132}\text{Sn}$  and which consequences this has on the r-process calculations.

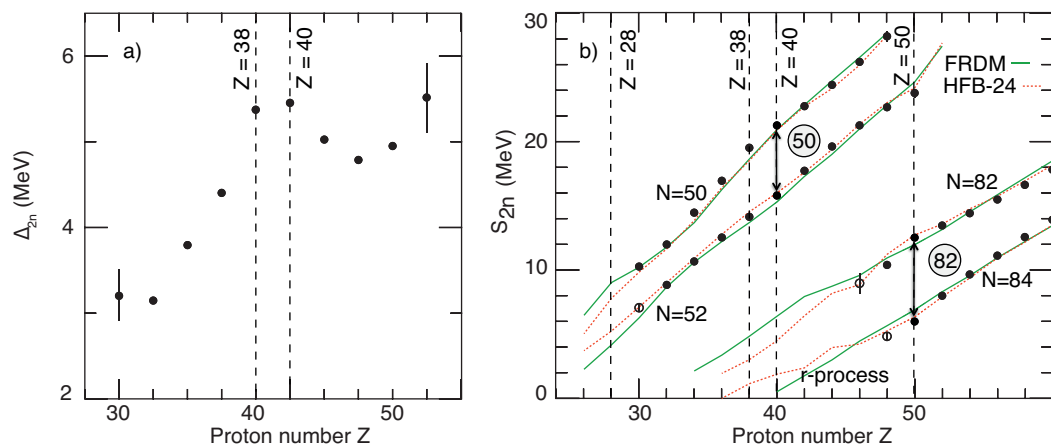


**Figure 6.4:** a) Experimentally determined two neutron gap  $\Delta_{2n}$  for the N=50 isotones in the range from Z=28 to Z=50 and b) two neutron separation energy  $S_{2n}$  for the N=50, 52, 82 and 84 isotones with the experimental values shown as black dots and calculated values from the FRDM (green line) and the HFB-24 (red dotted line) models.

#### 6.4.2 The N=82 shell gap and its impact on r-process calculations

With the results presented in the previous section and the disappearance of the sub-shell closure it can now be concluded that the N=82 shell gap is expected to shrink towards the middle of the major shell ( $Z = 28$  to  $50$ ). The maximum for a magic neutron (proton) shell gap is in all cases observed when the corresponding proton (neutron) number is magic as well and is commonly referred to as “mutual support of magicities” [173, 174]. Experimental data on masses [1] of semi-magic nuclei as well as the corresponding neutron and proton shell gaps, which have been summarized in Ref. [52], show for all known cases that the neutron (proton) shell gap reaches a minimum in the middle of the major proton (neutron) shell except for cases, e.g. the N=50 shell gap below  $^{100}\text{Sn}$ , where sub-shell closures are present. The shell gap decreases towards the mid-shell because of cross-shell excitations which on the other hand are hindered in the presence of sub-shell closures, leading to local maxima at  $Z=38$  and  $40$ , for example, in the N=50 case. Below  $^{100}\text{Sn}$  the shell gap stays nearly constant till reaching the sub-shell closures and only then starts to decrease until it reaches  $Z=32$  [175, 176]. With the new findings on the missing sub-shell closures in the N=82 isotones it is therefore expected that the shell gap already decreases between  $Z=50$  and  $Z = 40$ . This was already shown for the nuclei above  $^{132}\text{Sn}$ .

Fig. 6.4a) shows the two neutron gap for the N=50 isotones and it can be observed that the two neutron gap stays nearly constant when starting from  $^{100}\text{Sn}$  until reaching  $Z = 38$  and  $40$ . Fig. 6.4b) shows the comparison of the two neutron separation energy  $S_{2n}$  for the isotones with N= 50, 52, 82 and 84. The region of interest is here from  $Z\sim 40$  to  $Z\sim 50$  because that is the important region for the r-process below  $^{132}\text{Sn}$ . The figure shows that on the one hand the gap for the N=50 and 52 isotones stays constant until reaching the sub-shell closures and only then begins to shrink, while on the other hand it becomes clear that the models, on which has to be relied on for r-process calculations in the experimen-

tally unreachable region of the  $N=82$  isotones, show severe differences. The first model presented is the microscopic-macroscopic finite range droplet model (FRDM) [28, 58] and the second is a model based on the self-consistent Hartree-Fock-Bogoliubov theory (HFB-24) [52]. Both of them show very good agreement with the experimentally known masses but show severe differences for the unknown regions. In Fig. 6.4b) it becomes obvious that the HFB-24 model predicts the shrinking of the shell gap for the  $N=82$  isotones below  $Z=50$  while the FRDM model clearly shows a more or less constant gap size. Since it was shown in this chapter that the neutron shell gap is expected to be quenched in the region important for the  $r$ -process, it becomes obvious that the HFB-24 model seems to be the better choice at least in this region.

## Chapter 7

# Summary and outlook

In the present thesis, the  $\beta$ -decays of the neutron-rich Cadmium isotopes with masses  $A=126-134$  were studied. From the transitions observed in the daughters and  $\beta$ -delayed neutron daughters level schemes have been produced for those nuclei using information from absolute intensities and  $\gamma$ - $\gamma$  coincidences.

The level scheme of  $^{128}\text{In}$  was found to be in perfect agreement with the previously known level scheme, while the level scheme of  $^{130}\text{In}$  was extended and the placement of some transitions were changed. The main  $\beta$  feeding in both cases goes to a  $1^+$  level and this state is very probably fed by a GT transition of the type  $\nu g_{7/2} \rightarrow \pi g_{9/2}$  with a  $\log ft$  value of 4.0(1).

The half-lives of the two  $\beta$ -decaying states in  $^{129}\text{Cd}$  were found to be rather similar which is not in agreement with previous measurements. 68 transitions were furthermore placed in a level scheme of  $^{129}\text{In}$  with 29 excited states. This level scheme was compared to shell-model calculations employing a new interaction and the experimental energy of the  $p_{3/2}$  proton-hole state as it was obtained in the present thesis. An overall very good agreement was found between the calculations and the experimental level scheme. In addition to that, the importance of first forbidden  $\beta$ -decays in the region was studied. Again the  $\nu g_{7/2} \rightarrow \pi g_{9/2}$  GT transition was found to dominate the  $\beta$  decays of both the  $(11/2^-)$  and the  $(3/2^+)$  state in  $^{129}\text{Cd}$ . However a non negligible part of the decays proceeds via ff transition. In the decay of the  $(11/2^-)$  state the  $\nu h_{11/2} \rightarrow \pi g_{9/2}$  ff transition feeds the  $9/2^+$  g.s. and the  $11/2^+$  and  $13/2^+$  members of the  $\pi g_{9/2}^{-1} \nu h_{11/2}^{-2}$  multiplet. The  $(3/2^+)$  state on the other hand decays very probably via ff transitions to the  $1/2^-$ ,  $(3/2^+)$  and  $(5/2^+)$  states in  $^{129}\text{In}$ . ff transitions therefore play a non-negligible role in the  $\beta$  decay and contribute to the  $\beta$ -decay half-lives in this region.

A  $\gamma$  ray with an energy of 988 keV was observed in the decays of both  $^{131}\text{Cd}$  and  $^{132}\text{Cd}$  and was tentatively assigned to be the previously unknown  $\pi p_{3/2}$  proton single-hole state with respect to the  $^{132}\text{Sn}$  core. Using this crucial piece of information the structure of the experimentally inaccessible  $N=82$  isotones below  $^{132}\text{Sn}$  were studied using the nuclear shell model. It was found that while for the  $N = 50$  isotonic chain typical signatures of sub-shell closures are observed, they disappear for the  $N = 82$  isotones below  $^{132}\text{Sn}$ . An

absence of proton sub-shell closures along the N=82 chain of isotones implies a reduction of the N=82 shell gap below  $^{132}\text{Sn}$ . This new results suggest to give preference to mass models predicting such a reduction, as for example HFB24, for r-process calculations.

In the decay of  $^{131}\text{Cd}$  several  $\gamma$  rays were additionally observed and placed in a level scheme. The levels between 5.5 and 6 MeV were tentatively assigned to the  $\nu f_{7/2} g_{7/2}^{-1} \pi g_{9/2}^{-1}$  multiplet based on systematics and QRPA calculations. Those states are very probably fed by a GT transition of the type  $\nu g_{7/2} \rightarrow \pi g_{9/2}$ . However, the experimental results suggest that 50(7)% of the  $\beta$ -feeding proceeds through first-forbidden decays having e.g. a  $\nu h_{11/2} \rightarrow \pi g_{9/2}$  or  $\nu f_{7/2} \rightarrow \pi g_{9/2}$  character. The partial half-life for the first forbidden  $\beta$  decays of the  $(7/2^-)$  g.s. in  $^{131}\text{Cd}$  is therefore calculated to be 200(7) ms with the  $\beta$  decay half-life  $T_{1/2} = 100(2)$  ms of the present work. Based on those results it is concluded that ff decays contribute with a non-negligible amount in the region around  $^{132}\text{Sn}$  and have to be included when predicting  $\beta$ -decay half-lives with models.

First transitions in  $^{132}\text{In}$  have been observed populated after  $\beta$ -delayed neutron emission of  $^{133}\text{Cd}$ . Unfortunately it was not possible to place the transitions in a level scheme or to unambiguously assign them to the  $\nu f_{7/2} \pi g_{9/2}^{-1}$  multiplet in  $^{132}\text{In}$ . Therefore, further studies are necessary to obtain the first experimental level scheme of  $^{132}\text{In}$  and especially to determine the splitting in energy of the multiplet. Those experimental information are essential to determine the neutron-proton particle-hole interaction in that region. Furthermore it would allow to benchmark existing shell model calculations and their diagonal matrix elements of the effective interaction.

The  $\beta$ -decay half-lives of the Cadmium isotopes with masses A=126-134 have been determined in the present thesis using three different methods and especially the half-lives of  $^{133,134}\text{Cd}$  were measured for the first time in the present experiment. The results from all three methods show a very good agreement within one standard deviation, but severe differences are observed compared to previous measurements. In a second step the results were used to test different models commonly used for r-process calculations. Those models show an overall not very good agreement and only the DF3+CQRPA model comes close to the experimental values. Testing the models used to predict nuclear physics input parameters for r-process calculations is of great importance because those values can change the final abundance distribution significantly. It is therefore necessary to benchmark those models in the future for other nuclei on the r-process path which are currently experimentally not accessible.

The  $P_n$  value of  $^{133}\text{Cd}$  was measured for the first time in the present experiment and was determined to be 88(20)%. The  $P_n$  values of the Cadmium isotopes with masses A=128-132 were on top of that re-measured and again severe differences were found when compared to the literature values. The  $P_n$  values predicted by several models commonly used used to calculate nuclear physics input parameters for r-process calculations are not in good agreement with the experimentally determined values. It is concluded that the models will have to be improved in the future for a better description.

The decay of several isomeric states in the neutron-rich Cadmium isotopes has been

re-investigated in the present thesis. The previously proposed decay scheme for several isomeric states in  $^{128}\text{Cd}$  was found to be in good agreement with the observations made here. The half-lives of the three isomeric states in  $^{128}\text{Cd}$  are  $T_{1/2}=3.56(6) \mu\text{s}$ ,  $T_{1/2}=12(1) \text{ ns}$  and  $T_{1/2}=253(5) \text{ ns}$ .

In  $^{129}\text{Cd}$  an isomeric state with a half-life of  $T_{1/2}=3.6(2) \text{ ms}$  was identified for the first time via the detection of internal conversion as well as Compton electrons in WAS3ABi. The isomeric state was tentatively assigned to have spin/parity of  $21/2^+$  based on the shell-model calculations. From the relative intensities of the  $\gamma$ -rays and conversion electrons it was concluded that the isomeric state decays via an E3 transition.

In addition, a second isomeric state was identified in  $^{129}\text{Cd}$ , very probably a core-excited isomer. The isomer decays via a transition with an energy of 3693 keV and has a half-life of  $T_{1/2} = 0.9(1) \mu\text{s}$ . Further shell-model calculations are necessary to identify the origin of this isomeric state.

The decay of the  $(8^+)$  isomeric state in  $^{130}\text{Cd}$  was re-measured with higher precision and the literature half-life could be confirmed. Thanks to the high statistics accumulated in the present experiment the order of the transitions with energies of 128 and 138 keV could be fixed and the 128-keV and 138-keV transitions are now assigned to be the  $8^+ \rightarrow 6^+$  and  $6^+ \rightarrow 4^+$  transitions, respectively. The  $(6^+)$  state was measured to have a half-life of  $T_{1/2} = 37(4) \text{ ns}$  which corresponds to a reduced transition strength for the  $6^+ \rightarrow 4^+$  transition of  $B(E2) = 8(2) \text{ W.u.}$ . Nevertheless, the open question in  $^{130}\text{Cd}$  is still if a core-excited  $(12^+)$  isomeric state exists. In the present experiment no additional transitions could be identified.

Summarizing the results presented in this thesis it can be said that the knowledge of excited states in the region below the doubly-magic  $^{132}\text{Sn}$  was greatly improved and the results were in some cases used to benchmark shell-model calculations. The newly- and re-measured values for  $\beta$ -decay half-lives and  $\beta$ -delayed neutron emission probabilities are perfect probes to test models commonly used for the prediction of nuclear physics input parameters for r-process calculations. In most cases severe deficits were observed when comparing those models to the experimentally obtained values.

In the future the study of nuclei towards the neutron drip-line will be of importance. While the shell-model calculations in the present work provided the first evidence that there are no sub-shell closures at  $Z=38,40$  for the  $N=82$  nuclei this has to be confirmed experimentally. Current radioactive beam facilities unfortunately are not able to produce those nuclei with a sufficient high production rate. For example in the present experiment the primary Uranium beam provided by the RIKEN Nishina Center had a beam intensity of 6.5 to 10 pA (particle nanoampere). The goal intensity for this type of primary beam at the RIKEN Nishina Center is  $1 \text{ p}\mu\text{A}$  [177] and therefore two orders of magnitude higher than in the present experiment. Another next generation radioactive beam facility is FAIR (Facility for Antiproton and Ion Research) [178, 179], currently under construction in Darmstadt (Germany). One of the experimental set-ups to study very neutron-rich nuclei is DE-SPEC (DEcay SPECtroscopy) [180]. The nuclei of interest are going to be produced,

selected and identified with the Super-FRS (Super-Fragment Separator) [181] and then transported to the DESPEC experiment. The beam will be stopped in the highly segmented silicon-based active stopper AIDA (Advanced Implantation Detector Array) [182] which is surrounded by Ge detectors, neutron detectors, BaF<sub>2</sub> detectors for fast-timing or a total absorption  $\gamma$ -ray spectrometer. Using the improved intensities of the RIKEN Nishina Center and the new experimental set-up DESPEC at FAIR, the following questions can be addressed:

- Are there sub-shell closures for the N=82 nuclei below <sup>132</sup>Sn?
- What is the exact path of the r-process?
- Do current models which are used to predict nuclear physics input parameters describe e.g. the half-lives,  $\beta$ -delayed neutron emission probabilities and masses of nuclei on the r-process path in an adequate way?
- What is the importance of first forbidden transitions for Z<50 and N<82 and N $\geq$ 82 nuclei?

## Chapter 8

# Introducción y resumen en castellano

### 8.1 Introducción

El estudio de la estructura nuclear, en concreto de la conformación de las capas del núcleo, es de particular importancia para la comprensión de las propiedades del mismo. El núcleo es un sistema cuántico de  $N$  partículas subatómicas para las cuales la interacción básica entre los elementos constitutivos todavía no se entiende a la perfección. El como afecta y evoluciona la interacción nucleón-nucleón respecto a las propiedades del núcleo cuando nos alejamos del valle de estabilidad sigue siendo una de las cuestiones fundamentales de la física nuclear. Las regiones próximas a los núcleos doblemente mágicos, es decir aquellos con las capas protónicas y neutrónicas cerradas, son de gran importancia. Cerca de los núcleos doblemente mágicos, las energías de estados únicos de protón-hueco y las interacciones entre nucleones (protones o neutrones) pueden ser estudiados y utilizados para mejorar los modelos que describen la estructura nuclear de los núcleos lejos del valle de estabilidad.

El presente trabajo se centra en la región alrededor del núcleo doblemente mágico  $^{132}\text{Sn}$ , que tiene 50 protones ( $Z=50$ ) y 82 neutrones ( $N=82$ ). En esta región, las propiedades de los núcleos lejos del valle de estabilidad pueden ser estudiadas, dado que el  $^{132}\text{Sn}$  tiene 8 neutrones más que el último isótopo estable de estaño (ver Fig. 8.1) y es el núcleo doblemente mágico más pesado lejos de la estabilidad que es experimentalmente accesible. Una segunda motivación para estudiar esta región es que es una región crucial para astrofísica nuclear y, en particular, para el proceso de captura de neutrones rápidos, llamado  $r$ -proceso. Alrededor  $^{132}\text{Sn}$  la única información experimental disponible es para los isótopos menos exóticos, con  $Z>50$ , mientras que por debajo del  $^{132}\text{Sn}$  sólo son conocidos los estados excitados para el caso de  $N\leq 82$ . En la figura 8.1 se muestra la región alrededor del isótopo doblemente mágico  $^{132}\text{Sn}$  y la disponibilidad de los datos experimentales previos a los experimentos presentados en esta tesis. En verde se indican los núcleos para los cuales los periodos de semidesintegración  $\beta$  están ya



$E_\gamma$ [keV]	$I_\gamma^{rel}$ [%]	$I_\gamma^{lit}$ [%]	$I_\gamma^{Decay}$ [%]	$E_i$ [keV]	$E_f$ [keV]	$J_i^\pi$	$J_f^\pi$
67.9	36.5(25)	38(4)	26.5(18)	315	248	(1) <sup>-</sup>	(1) <sup>-</sup>
247.6	100(6.6)	100	72.7(49)	248	0	1(-)	3(+)
315.3	3.0(8)	-	2.2(6)	315	0	1(-)	3(+)
462.4	16.0(13)	4.8(10) + 3.9(13)	11.6(20)	-	0	-	-
857.1	98.6(55)	95(10)	71.7(42)	1173	315	1 <sup>+</sup>	(1) <sup>-</sup>
925.1	10.8(10)	12.4(12)	7.8(7)	1173	248	1 <sup>+</sup>	(1) <sup>-</sup>
1172.7	15.5(36)	10.8(11)	11.2(26)	1173	0	1 <sup>+</sup>	(3 <sup>+</sup> )

**Table 8.1:** Listado de los  $\gamma$  observados en la desintegración  $\beta$  del  $^{128}\text{Cd}$  al  $^{128}\text{In}$  indicando la energía, la intensidad relativa, la intensidad absoluta por desintegraciones del  $^{128}\text{Cd}$ , las energías del nivel inicial y final, así como el espín y la paridad del nivel inicial y final propuesto en este trabajo [61]. Los valores de la literatura son extraídos de la Referencia [61].

través del espectrómetro “Zero-Degree” al plano focal final, donde se colocó un blanco activo. El blanco activo, llamado WAS3ABi [91, 92] (Wide-range Active Silicon Strip Stopper Array for  $\beta$  and ion detection) está compuesto por ocho detectores de partículas de silicio (Double Sided Silicon Strip Detector, DSSSD), cada uno de ellos con un área activa de  $60 \times 40 \text{ mm}^2$ , un espesor de 1 mm y una segmentación de 60 bandas en la dirección x y 40 bandas en la dirección y. Los DSSSD se colocan en el centro de espectrómetro EURICA, que consta de 12 detectores de Ge del antiguo espectrómetro Euroball [100]. Cada uno de dichos detectores de Ge contiene siete cristales hiperpuros tipo n con forma hexagonal montados en un criostato. Así, utilizando correlaciones temporales y espaciales entre los iones implantados, partículas  $\beta$  y rayos  $\gamma$ , se puede investigar la estructura de niveles a baja energía de núcleos padre e hijo, por medio de espectroscopía  $\gamma$  isomérica y  $\beta$ -delayed, respectivamente.

Para mejorar la eficiencia de detección de radiación  $\gamma$  de alta energía se aplicó un procedimiento denominada *add-back*, que consiste en sumar las energías de los cristales vecinos dentro de una ventana de coincidencia. En nuestro caso particular únicamente tomaremos dos cristales vecinos que se sumarán sólo si la suma de la energía de ambos estaba por encima de 100 keV y a su vez las señales fueron registradas dentro de una ventana de coincidencia de 500 ns. La eficiencia absoluta resultante del espectrómetro de germanio para un  $\gamma$  a 1 MeV (4 MeV) se determinó que era de 8.5(4)% (2.9(2)%).

## 8.2.1 Espectroscopía de $\beta$ -delayed

### 8.2.1.1 $^{128}\text{Cd} \rightarrow ^{128}\text{In}$

En el presente trabajo se han vuelto a identificar siete transiciones pertenecientes al isótopo  $^{128}\text{In}$  [61] y están resumidas en la tabla 8.1. En ella se indican sus intensidades relativas,  $I_\gamma^{rel}$ , sus intensidades absolutas normalizadas por los decaimientos de los padres,  $I_\gamma^{Decay}$ , y la energía, el espín y la paridad de los niveles iniciales y finales. Como puede

Nivel [keV]	$I_\beta$ [%]	$I_{\beta,lit}$ [%]	$\log ft$	$\log ft_{lit}$
0		$\sim 5$		$\sim 5.8$
248	< 7	< 17	> 5.4	> 5.2
315	< 7	< 12	> 5.4	> 5.3
710	< 7	< 2	> 5.3	> 6.0
1173	96.6(44)	93(9)	4.03(11)	4.17(12)

**Table 8.2:** Los niveles en  $^{128}\text{In}$  que es poblado por las desintegraciones  $\beta$  de  $^{128}\text{Cd}$ , la alimentación procedente de la desintegración  $\beta$ , los valores  $\log ft$  y los valores correspondientes extraídos de la Referencia [61],  $\log ft_{lit}$ .

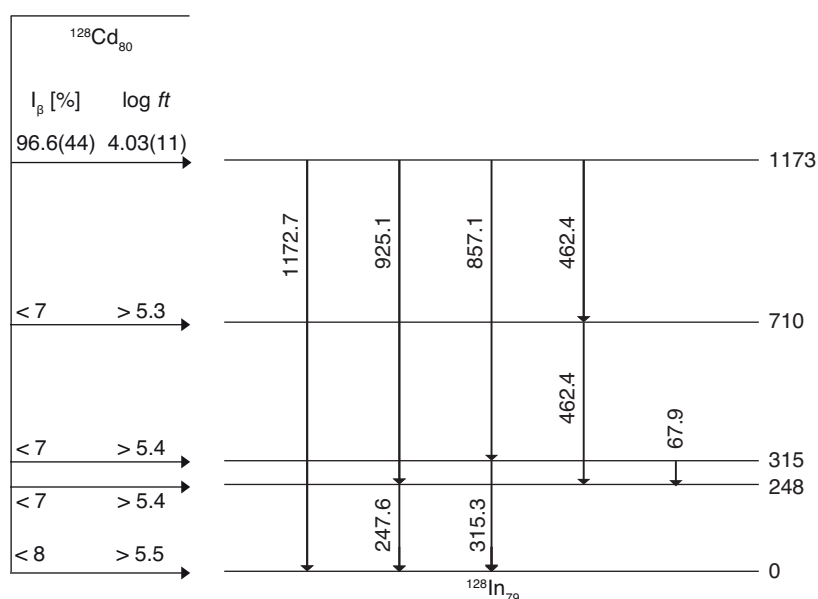


**Figure 8.2:** Esquema de niveles del  $^{128}\text{In}$ , que se obtuvo en el presente trabajo a través de la medición de la desintegración  $\beta$  del  $^{128}\text{Cd}$ .

apreciarse en dicha tabla existe una buena correspondencia entre los valores medidos en el presente trabajo y los valores de la literatura de la Referencia [61]. Por otra parte, a partir de las diferencias en las intensidades absolutas de las transiciones que pueblan y desexcitan los niveles es posible determinar la alimentación,  $I_{beta}$ , procedente de la desintegración  $\beta$  a cada uno de los niveles en el  $^{128}\text{In}$ . En la tabla 8.2 se muestran los resultados obtenidos. Además de  $I_{beta}$ , en la tabla 8.2 se incluye los valores calculados  $\log ft$ , los cuales han sido calculados considerando un  $Q$ -value de 7,070 keV, tomado de la Referencia [1], y de la vida media que se obtuvo en el presente trabajo. Esta tabla además incluye los valores de  $\log ft$  extraídos de la Referencia [61].

El esquema de niveles completo obtenido a partir de los resultados experimentales es presentado en la figura 8.2 y es esencialmente el mismo que fue sugerido por *Fogelberg et al.* [61]. Los resultados obtenidos están en total conformidad con los valores de la literatura. Con ésto se demuestra una vez más que la principal alimentación,  $I_{beta}$ , va a el estado a 1173 keV. Por lo tanto, si se considera la misma sistemática para los núcleos circundantes, con  $Z < 50$  y  $N < 82$ , y teniendo en cuenta el valor de  $\log ft$  es 4.03(11) para

esta transición, dicho estado tiene que ser poblado por una transición Gamow-Teller (GT). Por lo tanto, lo más probable es que esta transición tenga el carácter  $\nu g_{7/2} \rightarrow \pi g_{9/2}$ . Además, el log  $ft$  obtenido es del mismo orden que los valores de anteriormente medidos en transiciones análogas para los núcleos circundantes.

### 8.2.1.2 $^{129}\text{Cd} \rightarrow ^{129}\text{In}$

El decaimiento del  $^{129}\text{Cd}$  fue previamente estudiado por Arndt *et al.* [62]. En él se identifican dos estados en la desintegración  $\beta$  con vidas medias de 104(6) y 242(8) ms, respectivamente [62, 115]. Aunque para el caso del  $^{129}\text{In}$  existe más información experimental. El estado fundamental ( $9/2^+$ ) y un estado isomérico de desintegración  $\beta$  ( $1/2^-$ ) fueron expuestos hace ya mucho tiempo [117]. En una medición más reciente se sitúa el estado isomérico  $1/2^-$  a una energía de excitación de 459(5) keV [48]. Por su parte, Fogelberg *et al.* han observado la existencia de dos estados de alto espín, ( $29/2^+$ ) y ( $23/2^-$ ), con vidas medias de 110 y 700 ms, respectivamente [118]. Adicionalmente a estos estados, un estado isomérico  $17/2^-$  fue observado por Genevey *et al.* a una energía de excitación de 1688 keV y una vida media de 8,5  $\mu\text{s}$  [29]. El primer esquema de niveles completo fue propuesto por Arndt *et al.* [62]. Ellos observaron 53 transiciones en la desintegración  $\beta$  del  $^{129}\text{Cd}$  y colocaron una parte de ellos en el esquema de niveles.

$E_\gamma$ [keV]	$I_\gamma^{rel}$ [%]	$I_\gamma^{lit}$ [%]	$I_\gamma^{Decay}$ [%]	$E_i$ [keV]	$E_f$ [keV]	$J_i^\pi$	$J_f^\pi$
137.2	3.8(6)		1.3(2)	1220	1083	(5/2 <sup>-</sup> )	(3/2 <sup>-</sup> )
334.1	19.9(12)	13.0	6.6(4)	1688	1354	17/2 <sup>-</sup>	13/2 <sup>+</sup>
339.1	6.5(7)	6.0	2.1(2)	1693	1354		13/2 <sup>+</sup>
358.9	57.4(30)	50.0	19.0(10)	1354	995	13/2 <sup>+</sup>	11/2 <sup>+</sup>
391.7	1.4(7)		0.5(2)	2085	1693		
400.8	6.3(6)	7.0	2.1(2)	1621	1220		(5/2 <sup>-</sup> )
439.7	2.7(3)	4.0	0.9(1)	2060	1621		
471.9	1.5(8)		0.5(3)	1555	1083		(3/2 <sup>-</sup> )
504.5*	2.1(2)		0.7(2)				
537.9	2.8(8)	2.0	0.9(3)	1621	1083		(3/2 <sup>-</sup> )
542.0	14.5(10)	11.0	4.8(3)	1762	1220		(5/2 <sup>-</sup> )
561.8	8.5(8)	8.0	2.8(3)	3150	2589	(13/2 <sup>-</sup> )	
589.1	3.2(4)	5.2	1.1(1)	3150	2561	(13/2 <sup>-</sup> )	
599.2	2.8(4)		0.9(1)	3150	2551	(13/2 <sup>-</sup> )	
631.9	21.0(12)	30.0	7.0(4)	1083	451	(3/2 <sup>-</sup> )	1/2 <sup>-</sup>
731.0	6.2(7)	8.5	2.1(2)	2085	1354		13/2 <sup>+</sup>

Table 8.3 continua en la página siguiente

Table 8.3 – continua desde la página anterior

$E_\gamma$ [keV]	$I_\gamma^{rel}$ [%]	$I_\gamma^{lit}$ [%]	$I_\gamma^{Decay}$ [%]	$E_i$ [keV]	$E_f$ [keV]	$J_i^\pi$	$J_f^\pi$
752.0	1.4(1.2)		0.5(4)	3184	2433	(5/2 <sup>+</sup> )	
769.2	43.8(40)		14.5(13)	1220	451	(5/2 <sup>-</sup> )	1/2 <sup>-</sup>
840.2	10.8(9)	6.0	3.6(3)	2060	1220		(5/2 <sup>-</sup> )
863.1	3.8(4)	5.5	1.2(1)	2551	1688		17/2 <sup>-</sup>
873.0	3.6(5)		1.2(1)	2561	1688		17/2 <sup>-</sup>
891.0	1.4(1.2)		0.5(4)	2447	1555		
895.0	1.4(1.2)		0.5(4)	2589	1693		
915.0	1.4(1.2)		0.5(4)	3348	2433	(5/2 <sup>+</sup> )	
967.6	6.2(7)		2.0(2)	3184	2217	(5/2 <sup>+</sup> )	
995.1	100.0(51)	100.0	33.1(17)	995	0	11/2 <sup>+</sup>	9/2 <sup>+</sup>
1020.1	10.1(8)	8.5	3.3(3)	2015	995		11/2 <sup>+</sup>
1040.6	2.3(5)		0.7(2)	3184	2143	(5/2 <sup>+</sup> )	
1065.4	8.5(7)	8.0	2.8(2)	3150	2085	(13/2 <sup>-</sup> )	
1096.0	6.7(7)		3.0(2)	3184	2088	(5/2 <sup>+</sup> )	
1103.8*	2.5(13)	5.0	0.8(4)				
1124.1	2.5(13)		0.8(4)	3184	2060	(5/2 <sup>+</sup> )	
1130.6	3.4(9)		1.1(3)	3348	2217	(5/2 <sup>+</sup> )	
1135.2	6.8(7)		2.3(2)	3150	2015	(13/2 <sup>-</sup> )	
1203.5	1.4(1.2)		0.5(4)	3348	2143	(5/2 <sup>+</sup> )	
1221.6	6.3(9)		2.1(3)	2217	995		11/2 <sup>+</sup>
1227.3	3.6(27)		1.2(9)	2447	1220		(5/2 <sup>-</sup> )
1234.6	7.7(11)	5.0	2.5(3)	2589	1354		13/2 <sup>+</sup>
1259.6	1.4(5)		0.5(2)	3348	2088	(5/2 <sup>+</sup> )	
1287.3	7.0(7)		2.3(2)	3348	2060	(5/2 <sup>+</sup> )	
1354.2	20.5(12)	21.0	6.8(4)	1354	0	13/2 <sup>+</sup>	9/2 <sup>+</sup>
1363.6	1.0(5)		0.3(2)	2447	1083		
1395.9*	3.0(15)		1.0(5)				
1422.9	16.9(10)	20.0	5.6(3)	3184	1762	(5/2 <sup>+</sup> )	
1457.0	1.4(1.2)		0.5(4)	3150	1693	(13/2 <sup>-</sup> )	
1462.3	12.2(12)	11.0	4.0(4)	3150	1688	(13/2 <sup>-</sup> )	17/2 <sup>-</sup>
1500.2*	4.4(5)		1.5(2)				
1524.1	2.3(4)		0.7(1)	3971	2447		
1555.2	1.3(4)	5.0	0.4(2)	1555	0		9/2 <sup>+</sup>
1560.9*	2.7(11)	5.0	1.1(4)				
1586.2	8.3(8)	12.0	2.7(3)	3348	1762	(5/2 <sup>+</sup> )	
1689.9*	4.5(5)	6.0	1.5(2)				

Table 8.3 continua en la página siguiente

**Table 8.3 – continua desde la página anterior**

$E_\gamma$ [keV]	$I_\gamma^{rel}$ [%]	$I_\gamma^{lit}$ [%]	$I_\gamma^{Decay}$ [%]	$E_i$ [keV]	$E_f$ [keV]	$J_i^\pi$	$J_f^\pi$
1744.4	1.2(6)		0.4(2)	3888	2143		
1761.6	16.4(12)	19.0	5.4(4)	1762	0		9/2 <sup>+</sup>
1796.5	26.4(15)	32.0	8.7(5)	3150	1354	(13/2 <sup>-</sup> )	13/2 <sup>+</sup>
1890.0*	5.0(6)		1.7(2)				
1940.3	0.6(4)		0.2(1)	3702	1762		
2001.1*	5.3(12)		1.8(4)				
2088.0	8.1(9)	5.5	2.7(3)	2088	0		9/2 <sup>+</sup>
2127.6	1.4(7)		0.4(2)	3888	2143		
2143.4	1.4(7)		0.4(2)	2143	0		9/2 <sup>+</sup>
2155.6	6.4(8)		2.1(3)	3150	995	(13/2 <sup>-</sup> )	11/2 <sup>+</sup>
2204.8	0.6(4)		0.2(1)	3966	1762		
2216.8	7.5(9)	8.0	2.5(3)	2217	0		9/2 <sup>+</sup>
2295.6*	1.3(4)		0.4(1)				
2356.0	1.5(7)		0.5(2)	4118	1762		
2433.4	5.3(6)		1.7(2)	2433	0		9/2 <sup>+</sup>
2460.9	2.7(8)	6.0	0.9(2)	4082	1621		
2880.2	4.3(10)	2.5	1.4(3)	4082	1220		(5/2 <sup>-</sup> )
3184.4	4.0(7)	3.0	1.3(2)	3184	0	(5/2 <sup>+</sup> )	9/2 <sup>+</sup>
3286.1	1.3(4)		0.4(1)	3286	0		9/2 <sup>+</sup>
3348.0	3.0(10)	4.0	1.0(3)	3348	0	(5/2 <sup>+</sup> )	9/2 <sup>+</sup>
3487.7	1.4(6)	1.0	0.5(2)	3488	0		9/2 <sup>+</sup>
3701.9	4.7(17)	6.0	1.6(6)	3702	0		9/2 <sup>+</sup>
3888.4	1.1(7)	2.0	0.4(2)	3888	0		9/2 <sup>+</sup>
3913.8	2.7(5)	3.0	0.9(2)	3914	0		9/2 <sup>+</sup>
3966.4	5.0(12)	4.0	1.7(4)	3966	0		9/2 <sup>+</sup>
4118.3	1.7(5)	2.0	0.5(2)	4118	0		9/2 <sup>+</sup>

**Table 8.3:** Lista de los  $\gamma$  observados en la desintegración  $\beta$  del  $^{129}\text{Cd}$  al  $^{129}\text{In}$  con su energía, las intensidades relativas, la intensidad absoluta por desintegraciones del  $^{129}\text{Cd}$ , las energías del nivel inicial y final, así como el espín y la paridad del nivel inicial y final propuesto en este trabajo. Los valores de la literatura se tomaron de la Referencia [62].

En resumen, se puede decir que de las 85 transiciones (ver tabla 8.3) que han sido asignadas al decaimiento  $\beta$  del  $^{129}\text{Cd}$  al  $^{129}\text{In}$ , 69 están colocadas en el esquema de niveles presentado en la figura 8.3, mostrándose por primera vez un esquema muy detallado de los niveles y de las transiciones en el  $^{129}\text{In}$ . No obstante, fue imposible la colocación del resto de las transiciones en base a los datos experimentales. Todas las transiciones que no han sido colocadas en el esquema de niveles están marcadas con un (\*) en la tabla

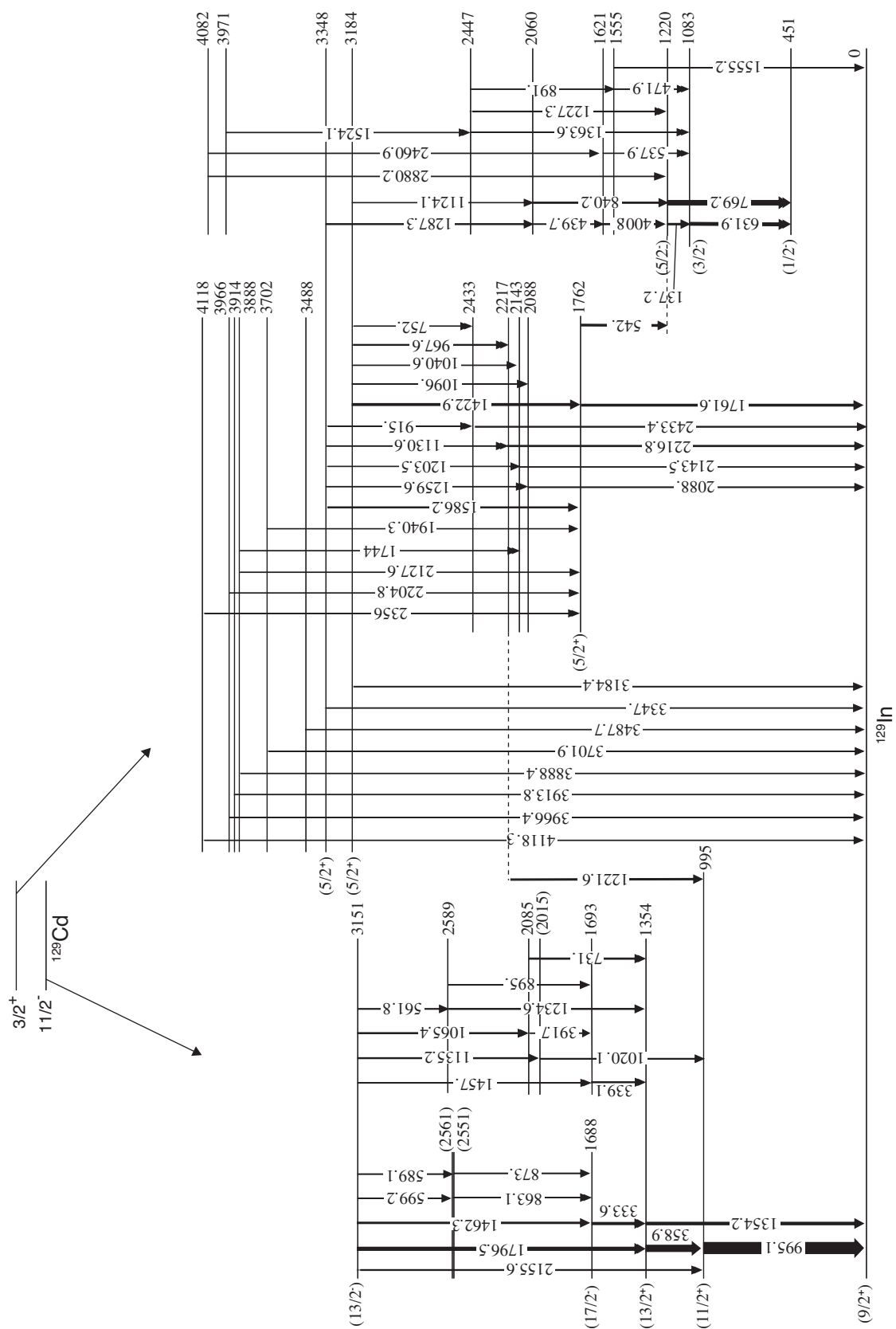


**Figure 8.3:** Esquema de niveles del  $^{129}\text{In}$ , que se obtuvo en el presente trabajo a través de la medición de la desintegración  $\beta$  del  $^{129}\text{Cd}$ .

$E_{\text{Nivel}}$ [keV]	$I^\pi(\beta)$	$I^\pi_{\text{Nivel}}$	$I_\beta(^{129}\text{Cd})$ [%]	$I_\beta(3/2^+)$ [%]	$I_\beta(11/2^-)$ [%]	log $ft$
0	(11/2 <sup>-</sup> )	9/2 <sup>+</sup>	11(3)	-	22(6)	5.4(1)
451	(3/2 <sup>+</sup> )	1/2 <sup>-</sup>	6(3)	12(6)	-	5.6(2)
995	(11/2 <sup>-</sup> )	11/2 <sup>+</sup>	6.5(20)	-	13(4)	5.4(1)
1083	(3/2 <sup>+</sup> )	(3/2 <sup>-</sup> )	4.0(6)	8(1)	-	5.6(1)
1220	(3/2 <sup>+</sup> )	(5/2 <sup>-</sup> )	2.7(17)	5(3)	-	5.8(3)
1354	(11/2 <sup>-</sup> )	13/2 <sup>+</sup>	3.2(12)	-	8(3)	5.5(2)
1555	(3/2 <sup>+</sup> )		< 1.0	< 2	-	> 6.1
1621	(3/2 <sup>+</sup> )		1.2(4)	2(1)	-	6.1(2)
1688	(11/2 <sup>-</sup> )	17/2 <sup>-</sup>	< 0.4	-	< 1	> 6.3
1693	(11/2 <sup>-</sup> )		0.7(6)	-	1(1)	6.3(5)
1762	(3/2 <sup>+</sup> )		0.5(10)	2(2)	-	6.0(5)
2015	(11/2 <sup>-</sup> )		1.1(3)	-	2(1)	5.9(2)
2060	(3/2 <sup>+</sup> )		1.3(6)	3(1)	-	5.8(2)
2085	(11/2 <sup>-</sup> )		< 0.1	-	< 1	> 6.2
2088	(3/2 <sup>+</sup> )		< 0.4	< 1	-	> 6.2
2143	-		-	-	-	-
2217	(11/2 <sup>-</sup> )		1.4(6)	-	3(1)	5.7(2)
2433	(3/2 <sup>+</sup> )		< 1.1	< 2	-	> 5.9
2447	(3/2 <sup>+</sup> )		1.3(11)	3(2)	-	5.7(3)
2551	(11/2 <sup>-</sup> )		< 0.5	-	< 1	> 6.1
2561	(11/2 <sup>-</sup> )		< 0.5	-	< 1	> 6.1
2589	(11/2 <sup>-</sup> )		< 1.2	-	< 2	> 5.8
3150	(11/2 <sup>-</sup> )	(13/2 <sup>-</sup> )	25.3(8)	-	52(5)	4.2(1)
3184	(3/2 <sup>+</sup> )	(5/2 <sup>+</sup> )	13.3(8)	26(3)	-	4.5(1)
3286	(3/2 <sup>+</sup> )		0.4(1)	1(1)	-	5.9(5)
3348	(3/2 <sup>+</sup> )	(5/2 <sup>+</sup> )	8.6(9)	17(2)	-	4.7(1)
3488	(3/2 <sup>+</sup> )		0.7(2)	1(1)	-	5.8(5)
3702	(3/2 <sup>+</sup> )		1.6(6)	3(1)	-	5.3(2)
3888	(3/2 <sup>+</sup> )		1.2(4)	2(1)	-	5.4(2)
3914	(3/2 <sup>+</sup> )		0.9(2)	2(1)	-	5.4(2)
3966	(3/2 <sup>+</sup> )		1.9(4)	4(1)	-	5.1(1)
3971	-		0.7(1)	-	-	-
4082	-		2.3(13)	-	-	-
4118	(3/2 <sup>+</sup> )		1.0(3)	2(1)	-	5.3(2)

**Table 8.4:** Los niveles en el  $^{129}\text{In}$  alimentado por las desintegraciones  $\beta$  del  $^{129}\text{Cd}$ , la población directa procedente de la desintegración  $\beta$  y los valores log  $ft$ . La población se indica por tres valores:  $I_\beta(^{129}\text{Cd})$  la población por desintegraciones del  $^{129}\text{Cd}$ ,  $I_\beta(3/2^+)$  y  $I_\beta(11/2^-)$  las poblaciones por desintegraciones del nivel (3/2<sup>+</sup>) y del (11/2<sup>-</sup>), respectivamente, en el  $^{129}\text{Cd}$ . También están indicado el espín y la paridad asignado en este trabajo.

### 8.3.

Por otro lado, es posible determinar la población directa,  $I_{\text{beta}}$ , procedente de la desintegración  $\beta$  a cada uno de los niveles en  $^{129}\text{In}$  a partir de las diferencias en las intensidades absolutas de las transiciones que pueblan y des-excitan los niveles. Los resultados se resumen en la tabla 8.4 juntos con los valores calculados log  $ft$ .

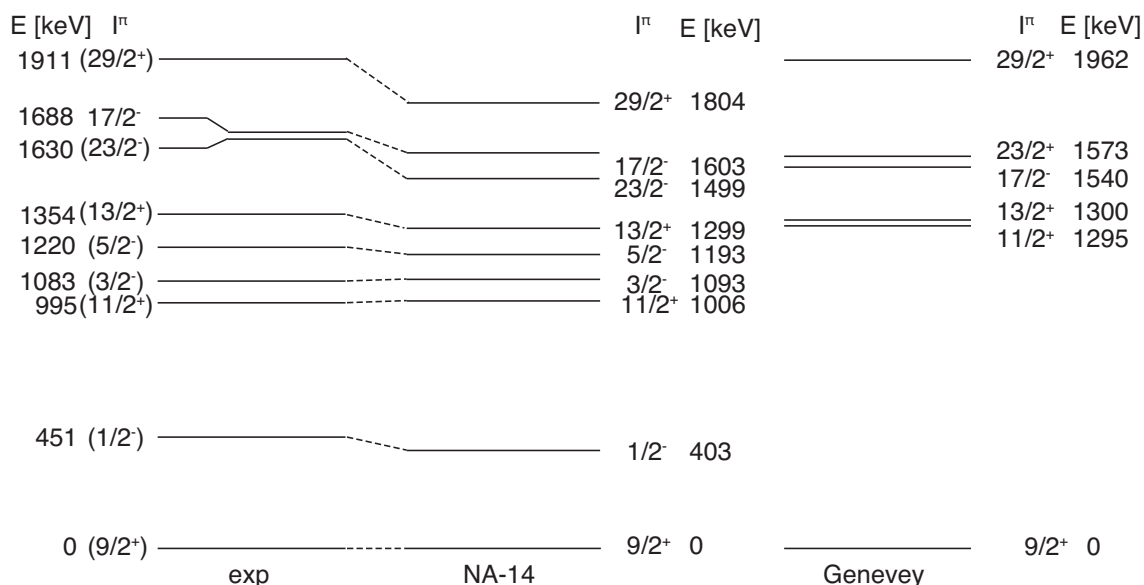


**Figure 8.4:** Esquema de niveles obtenido, así como la comparación con el cálculo teórico del modelo de capas NA-14 y los cálculos extraídos de la Referencia [29]. Sólo se muestran los niveles teóricos hasta un espín máximo de  $19/2$  y una energía de excitación de 1.8 MeV. Además de estos niveles, se han incluido los estados isoméricos con espín y paridad  $23/2^-$  y  $29/2^+$ .

La figura 8.4 muestra las predicciones del modelo de capas realizados para el presente trabajo mediante el modelo NA-14. Para su comparación se han tomado los cálculos teóricos expuestos en la Referencia [29]. En la figura anterior se observa que para el caso del modelo NA-14 el esquema de niveles está más acorde en comparación con los cálculos previos de *Genevey et al.*. En especial para la posición del estado  $11/2^+$ , en los cálculos NA-14 se encuentra unos 300 keV más abajo que en el trabajo anterior y está de acuerdo en unos pocos keV con la energía medida experimentalmente.

Al igual que en los cálculos previos, los cálculos obtenidos aplicando el modelo de capas predicen que el estado  $17/2^-$  es un isómero y su configuración es:  $\pi g_{9/2}^{-1} \nu (d_{3/2}^{-1} h_{11/2}^{-1})$ . Debido a esto y teniendo en cuenta la diferencia de espín entre los estados iniciales y el estado final, no debería existir ninguna alimentación directa procedente de la desintegración  $\beta$  de los estados  $(11/2^-)$  y  $(3/2^+)$  del  $^{129}\text{Cd}$ . De hecho, los datos experimentales no muestran una alimentación directa al estado  $17/2^-$ . Por otro lado, los niveles de energías 995 y 1354 keV, con una configuración  $\pi g_{9/2}^{-1} \nu h_{11/2}^{-2}$ , reciben una alimentación directa tal y como se esperaba debido a la desintegración  $\beta$  del tipo “*first forbidden*” (ff)  $\nu h_{11/2} \rightarrow \pi g_{9/2}$ . La población directa al estado fundamental,  $9/2^+$ , se estima en 11(3)%. Los valores de  $\log ft$ , obtenidos en este trabajo, son 5.4(1) y 5.5(2) para la desintegración  $\beta$  del tipo ff  $\nu h_{11/2} \rightarrow \pi g_{9/2}$ . Estos resultados son similares a los ya medidos previamente en dicha región, como por ejemplo en las desintegraciones  $\beta$  de  $^{131}\text{In}$  con un  $\log ft > 5.6$  [41] y del  $^{132}\text{In}$  con un  $\log ft$  de 5.6 [82].

El nivel a energía 3150 keV, que se desexcita mediante radiación  $\gamma$  a los estados  $13/2^+$  y  $17/2^-$ , es alimentado en un 52(5)% por el estado  $(11/2^-)$  en el  $^{129}\text{Cd}$ . Una asignación

diferente a este estado de  $(13/2^-)$  parece poco probable basados en la población observada y en los  $\gamma$ . Sólo la desintegración  $\beta$  del tipo *Gamow-Teller* (GT)  $\nu g_{7/2} \rightarrow \pi g_{9/2}$  puede ser relacionada con esta desintegración. Dicha asignación está basada en la sistemática de la región por debajo de  $^{132}\text{Sn}$  y con  $N < 82$ . En el presente trabajo el  $\log ft$  de 4.2(1) se deduce de la alimentación observada, en concordancia con los valores de la literatura para transiciones GT del mismo tipo y para el caso de varios núcleos en las proximidades del  $^{132}\text{Sn}$ . Por ejemplo, en las desintegraciones del  $^{127,129}\text{In}$  se midieron valores de  $\log ft$  en el rango de 4.4 a 4.5 [119] y en la Referencia [82] se obtuvo para la desintegración  $\beta$  del  $^{132}\text{In}$  un valor de 4.6.

Los dos niveles de energías 3184 y 3348 keV, que tienen una asignación provisional de  $(5/2^+)$ , reciben una mayor alimentación directa. Ésto sugiere que, sólo puede ser relacionada la desintegración  $\beta$  del tipo GT  $\nu g_{7/2} \rightarrow \pi g_{9/2}$ .

Tal como se presenta en la introducción, una de las preguntas en alrededor del  $^{132}\text{Sn}$  es la importancia de desintegraciones primeras prohibidas debajo de  $Z = 50$ . El  $^{129}\text{Cd}$  es, en este caso, la mejor sonda existente. Observándose que la desintegración  $\nu h_{11/2} \rightarrow \pi g_{9/2}$ , del tipo ff, contribuye significativamente. Esta cuestión ya fue planteada en el pasado en diversas ocasiones, ver Referencias [63,67,68]. Además se demostró que los actuales cálculos a partir del modelo de capas describen muy bien la estructura de los niveles hasta 1.8 MeV en el  $^{129}\text{In}$ , y además los cálculos tienen una mejor concordancia en comparación con los de la Referencia [29].

### 8.2.1.3 $^{130}\text{Cd} \rightarrow ^{130}\text{In}$

Los primeros estudios del  $^{130}\text{Cd}$ , utilizando el método de espectroscopía  $\beta$ - $\gamma$ , fueron reportados en la Referencia [20]. En este trabajo se propone por primera vez un esquema de niveles del  $^{130}\text{In}$  con un estado  $1^+$  de una configuración denominada "two-quasi-particle"  $\pi g_{9/2}^{-1} \nu g_{7/2}^{-1}$  a una energía de 2120 keV. Al ser considerado un "waiting-point nuclei" en la mayoría de los cálculos del proceso r, el estudio de este núcleo es de especial interés.

Todas las transiciones observadas sobre dicho núcleo han podido ser colocadas en un esquema de niveles. Un resumen de las energías, las intensidades relativas/absolutas y la información sobre los correspondientes niveles iniciales y finales de los  $\gamma$  se da en la tabla 8.5. La información obtenida sobre coincidencias y las intensidades relativas están en consonancia con los valores de la literatura [20] en todos los casos excepto en dos casos. Las colocaciones de las transiciones con energías de 2739.0 y 2804.8 keV cambian de posición. El esquema de nivel del  $^{130}\text{In}$  se muestra en la Fig. 8.5, tal y como se deduce de la información experimental obtenida. Del balance de las intensidades de las transiciones que pueblan y desexcitan los niveles se puede deducir la alimentación directa a los diversos niveles. Estos resultados son presentados en la tabla 8.6 junto con los valores de  $\log ft$  y valores de la literatura. En esa tabla se muestra claramente, que la mayoría de la alimentación procedente de la desintegración  $\beta$  procede a un nivel a 2120

$E_\gamma$ [keV]	$I_\gamma^{rel}$ [%]	$I_\gamma^{lit}$ [%]	$I_\gamma^{Decay}$ [%]	$E_i$ [keV]	$E_f$ [keV]	$J_i^\pi$	$J_f^\pi$
229.1	4.3(6)		2.3(3)	4197	3967		
388.4	6.6(6)	4.0(26)	3.5(3)	388	0	(3 <sup>+</sup> )	1 <sup>-</sup>
450.8	100(5)	88.6(36)	53.6(27)	2120	1669	1 <sup>+</sup>	(1) <sup>-</sup>
498.7	1.1(4)		0.6(2)	1669	1170	(1) <sup>-</sup>	(0, 1) <sup>-</sup>
949.9	18.5(25)	22.1(33)	9.9(13)	2120	1170	1 <sup>+</sup>	(0, 1) <sup>-</sup>
1015.8	6.6(6)	5.5(10)	3.5(3)	1016	0		1 <sup>-</sup>
1104.1	1.7(4)		0.9(2)	2120	1016	1 <sup>+</sup>	
1170.0	21.2(12)	20.0(2)	11.3(7)	1170	0	(0, 1) <sup>-</sup>	1 <sup>-</sup>
1669.2	96.4(5.0)	100	51.6(27)	1669	0	(1) <sup>-</sup>	1 <sup>-</sup>
1731.5	5.0(5)	4.4(4)	2.7(3)	2120	388	1 <sup>+</sup>	(3 <sup>+</sup> )
2120.0	12.7(14)	6.8(6)	6.8(7)	2120	0	1 <sup>+</sup>	1 <sup>-</sup>
2739.0	0.7(3)	1.3(3)	0.4(1)	3755	1016		
2804.8	1.7(3)	1.1(2)	0.9(2)	2805	0		1 <sup>-</sup>
3655.4	4.0(6)		2.1(3)	4044	388		
3966.8	1.1(2)		0.7(2)	3967	0		
4065.7	1.4(3)		0.6(1)	4066	0		
4197.1	0.6(2)		0.3(1)	4197	0		
4281.2	0.6(2)		0.3(1)	4281	0		
5228.7	0.6(2)		0.3(1)	5229	0		
5285.6	0.6(2)		0.3(1)	5286	0		
5393.3	1.1(2)		0.6(1)	5393	0		

**Table 8.5:** Lista de los  $\gamma$  observados en la desintegración  $\beta$  del  $^{130}\text{Cd}$  al  $^{130}\text{In}$  con su energía, las intensidades relativas, la intensidad absoluta por desintegraciones del  $^{130}\text{Cd}$ , las energías del nivel inicial y final, y el espín y la paridad del nivel inicial y final propuesto en este trabajo. Los valores de la literatura se toman de la Referencia [2, 20].

keV. La alimentación medida en el presente experimento a este estado de 73.4(31)% está de acuerdo dentro de las barras de error con el valor de la literatura. El único nivel en el que se observa una diferencia en los valores es el nivel a 1669 keV. Los valores de  $\log ft$  (véase la tabla 8.6) se calcularon utilizando un  $Q_\beta$  con valor de 8.344 keV tomado de la Referencia [20] y el periodo de semidesintegración que fue determinada a su vez en el presente trabajo.

El esquema de niveles presentado en este trabajo muestra varios nuevos estados en la región por encima del estado 1<sup>+</sup> a 2120 keV. Todos ellos tienen un valor  $\log ft$  que sugiere que la desintegración  $\beta$  es del tipo GT o ff. La observación más impresionante es sin embargo, la presencia de niveles por encima de la energía de separación de neutrones de 5120(40) keV, calculada a partir de la Referencia [1]. La población de niveles por encima de la energía de separación de neutrones, que luego decaen a niveles en el  $^{130}\text{Cd}$  través de una transición  $\gamma$ , ya fue reportada con anterioridad [2] y es confirmada por nuestros datos. Para dichos estados, la emisión de un neutrón debe ser obstaculizada debido a las reglas de selección momento angular, por lo que es posible que las transiciones  $\gamma$  puedan competir con la emisión de neutrones.

En el estado 1<sup>+</sup> a 2120 keV se prevé que tenga con una configuración  $\pi g_{9/2}^{-1} \nu g_{7/2}^{-1}$ , mien-

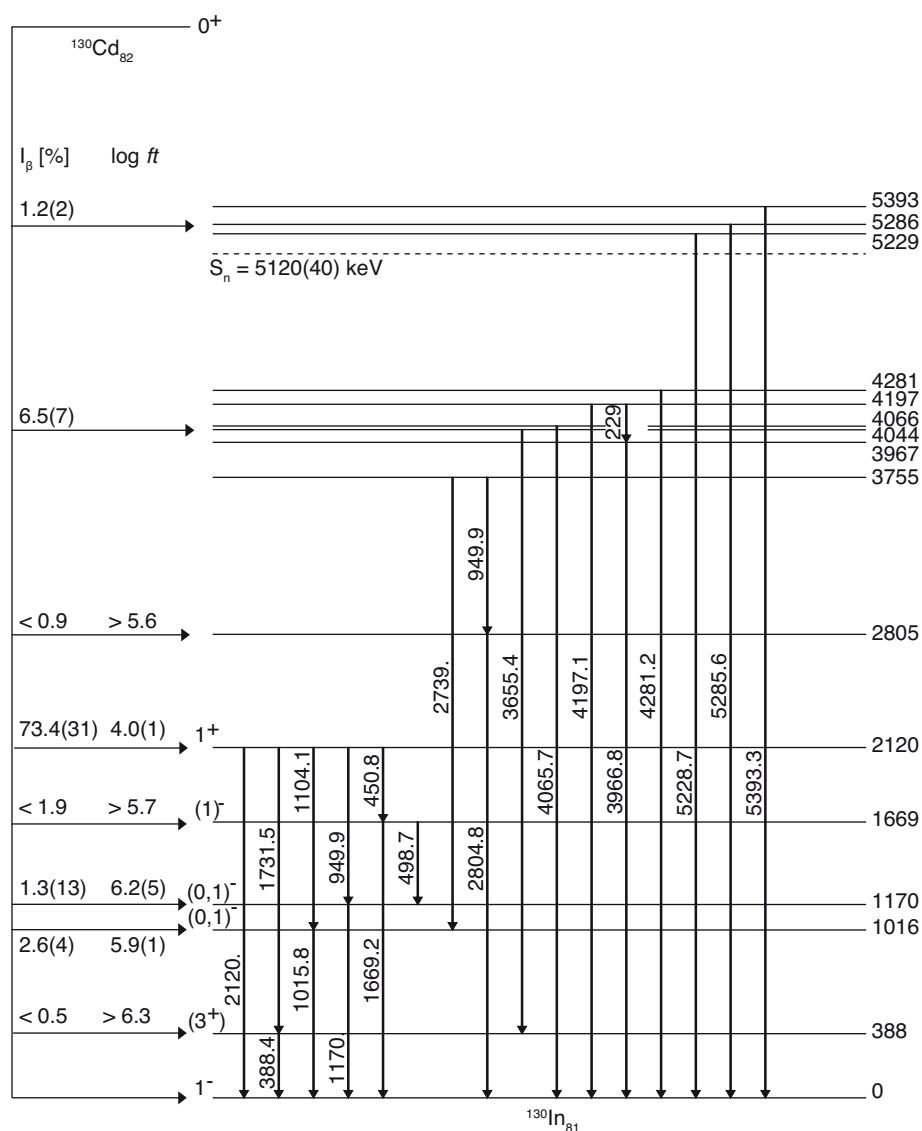


**Figure 8.5:** Esquema de niveles del  $^{130}\text{In}$ , que se obtuvo en el presente trabajo a través de la medición de la desintegración  $\beta$  de  $^{130}\text{Cd}$ .

tras que los estados por encima de 4.4 MeV fueron asignados en la Ref [20] a una configuración  $\pi g_{9/2} \nu g_{7/2}$  *Four Quasi-Particle* (4QP) en base a cálculos *Quasiparticle Random-Phase Aproximation* (QRPA). Las alimentaciones medidas en el presente experimento a niveles por debajo de 2 MeV, se observa que todas tienen valores  $\log ft$  que sugieren una transición del tipo ff. La asignación de los espines y las paridades para esos niveles no cambian en el presente trabajo. Aplicando los mismos argumentos que en el pasado, el nivel a 1016 keV se asigna provisionalmente un espín y paridad de  $(0, 1^-)$ .

Nivel [keV]	$I_{\beta}$ [%]	$I_{\beta,lit}$ [%]	log $ft$	log $ft_{lit}$
0		$\sim 5$		$\sim 5.8$
388	<0.5	< 1.2	>6.3	> 6.3
1016	2.6(4)	-	5.9(1)	-
1170	1.3(13)	< 0.7	6.2(5)	> 6.3
1669	< 1.9	5.8	>5.7	5.3
2120	73.4(31)	70.2	4.0(1)	4.1
2805	< 0.9	-	> 5.6	-
3755	0.9(5)	-	5.3(3)	-
3967	$\sim 0$	-	-	-
4044	2.1(3)	-	4.8(1)	-
4066	0.6(1)	-	5.3(1)	-
4196	2.6(3)	-	4.6(2)	-
4281	0.3(1)	-	5.5(2)	-
5229	0.3(1)	-	5.0(2)	-
5286	0.3(1)	-	5.0(2)	-
5393	0.6(1)	-	4.6(2)	-

**Table 8.6:** Los niveles en el  $^{130}\text{In}$  poblado por las desintegraciones  $\beta$  del  $^{130}\text{Cd}$ , la alimentación directa procedente de la desintegración  $\beta$ , los valores log  $ft$  y los valores correspondientes en la literatura tomados de la Referencia [2, 20].

### $^{131}\text{Cd} \rightarrow ^{131}\text{In}$

Uno de los objetivos de este experimento es obtener nueva información sobre la estructura nuclear de los isótopos del indio ricos en neutrones y en especial el  $^{131}\text{In}$  el cual posee un protón menos que el doblemente mágico  $^{132}\text{Sn}$ . El  $^{131}\text{In}$  posee un número neutrónico,  $N$ , igual a 82 que es un número de mágico y debido a eso, es el candidato perfecto para determinar las energías de estados únicos de protón-hueco [41, 47], habiéndose determinado el  $(1/2^-)$  estado como el primer estado excitado con una energía de 365(8) keV. El isótopo  $^{131}\text{In}$  ha formado parte de diversos estudios previos a este trabajo, además que las desintegraciones  $\beta$  del estado fundamental con espín y paridad  $(9/2^+)$  y de un isómero  $(1/2^-)$  fueron estudiados en detalle en las Referencias [39, 40, 117]. Sin embargo, la información sobre los estados excitados del  $^{131}\text{In}$  eran escasas previamente a este trabajo. La primera observación de transiciones después de la población en desintegraciones  $\beta$  del  $^{131}\text{Cd}$  se hizo en la Referencia [62] donde se reportó la observación de varias transiciones. Dos transiciones con energías de 988 y 2428 keV se colocaron provisionalmente como las transiciones entre los  $p_{3/2}$  y  $p_{1/2}$ , y  $f_{5/2}$  y  $p_{1/2}$  estados únicos de protón-hueco, respectivamente.

Un total de 24 transiciones se han asignadas a las desintegraciones  $\beta$  del  $^{131}\text{Cd}$  al  $^{131}\text{In}$  y están resumidas en la tabla 8.7. La transición más fuerte observada en el presente experimento tiene una energía de 987.9 keV, lo cual concuerda con las observaciones realizadas en la referencia [62]. Esta transición conecta los estados  $p_{3/2}$  y  $p_{1/2}$ . Esta asignación se sustenta en la observación en también emisión  $\beta$ -delayed de neutrones del  $^{132}\text{Cd}$  y la sistemática expuesta en la Referencia [129]. Todas las transiciones restantes

$E_\gamma$ [keV]	$I_\gamma^{rel}$ [%]	$I_\gamma^{Decay}$ [%]	$E_i$ [keV]	$E_f$ [keV]
315	24(12)	2.1(10)	3869	3555
315.0	25(12)	2.2(1.0)	3869	3555
355.0*	12(4)	1.1(4)		
433.2	27(7)	2.4(6)	5958	5525
451*	11(5)	1.0(5)		
987.9	100(14)	8.8(16)	1353	365
1221.0*	29(8)	2.6(7)	(2574)	(1353)
1864.9*	16(5)	1.4(5)		
1925.9*	14(5)	1.2(5)		
2004.7*	18(5)	1.6(5)		
2117.8*	17(5)	1.5(4)		
2636.7	7(3)	0.6(2)	3990	1353
2776.8	12(3)	1.0(5)	4130	1353
2922.0*	11(4)	1.0(3)		
3290.1	26(8)	2.3(7)	4644	1353
3417.0	8(4)	0.7(4)	4770	1353
3480.0	33(7)	2.9(6)	3480	0
3555.2	98(13)	8.6(12)	3555	0
3868.8#	115(15)	10.1(13)	3869	0
3920.6	46(11)	4.1(9)	3921	0
4038.0	36(13)	3.2(11)	4038	0
5525.0	29(7)	2.5(6)	5525	0
5612.0	13(4)	1.1(3)	5612	0
5754.7	64(12)	5.6(11)	5755	0
5796.0	29(7)	2.5(6)	5796	0
5824.7	87(16)	7.7(14)	5825	0
5958.3	25(7)	2.2(6)	5958	0
6002.8	33(11)	2.9(10)	6003	0
6039.2	63(16)	5.5(14)	6039	0

**Table 8.7:** Lista de  $\gamma$  observados en la desintegración  $\beta$  del  $^{131}\text{Cd}$  al  $^{130}\text{In}$  con su energía, las intensidades relativas, la intensidad absoluta por desintegraciones del  $^{131}\text{Cd}$  y las energías del nivel inicial y final.

se colocan en un esquema de niveles en base a las coincidencias y a la información de las intensidades relativas. Un resumen de la población observada y la colocación en el esquema de niveles se da en la tabla 8.8.

Los resultados obtenidos en el presente trabajo se utilizaron primeramente para obtener información sobre la evolución de la capa neutrónica  $N = 82$  debajo del  $Z = 50$ . Los cálculos realizados mediante el modelo de capas para  $N = 50$ , están en consonancia con los datos experimentales y así como con los previos [171, 172], tal y como se presenta en la Fig. 8.6. Claramente las capas cerradas (*sub-shell*) en  $Z = 38$  y  $40$  son visibles en tanto a la energía del primero estado  $2^+$  y en la energía de separación de dos protones  $\Delta_{2p}$ . Ahora la pregunta es si esas capas cerradas (*sub-shell*) también están presentes en el caso de los núcleos isótonos  $N = 82$ , donde las capas son más pequeñas y sólo tienen un tamaño de  $365(8)$  y  $988$  keV, respectivamente.

Nivel [keV]	$I_\beta$ [%]	log $ft$	Nivel [keV]	$I_\beta$ [%]	log $ft$
0	-	-	4644	2.3(7)	5.9(2)
365	-	-	4770	0.7(4)	6.4(3)
1353	4.2(18)	6.3(2)	5525	<0.8	> 6.0
3480	2.9(6)	6.1(1)	5612	1.1(7)	6.0(3)
3555	6.5(15)	5.7(1)	5755	5.6(10)	5.2(1)
3869	12.3(16)	5.3(1)	5796	2.5(6)	5.6(1)
3921	4.1(9)	5.8(1)	5825	7.7(14)	5.1(1)
3990	0.6(2)	6.3(1)	5958	4.6(9)	5.2(1)
4038	3.2(11)	5.9(2)	6003	2.9(6)	5.4(1)
4130	1.0(5)	6.4(2)	6039	5.5(4)	5.2(1)

**Table 8.8:** Los niveles en el  $^{131}\text{In}$  poblado por las desintegraciones  $\beta$  del  $^{131}\text{Cd}$ , la alimentación directa procedente de la desintegración  $\beta$  y los valores log  $ft$ .

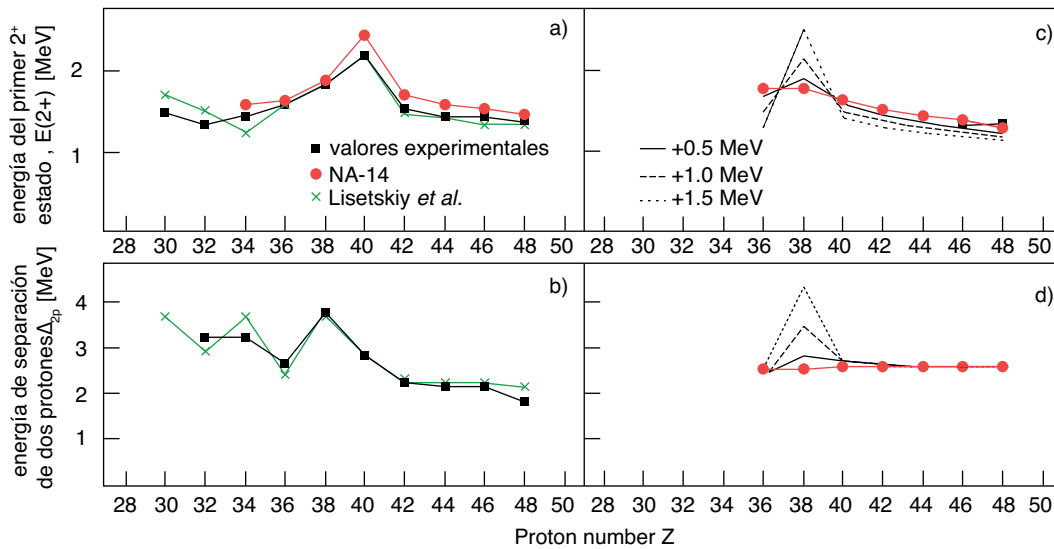


**Figure 8.6:** Comparación de los valores experimentales y calculados (a) y c)) de las energías del primer estado  $2^+$  ( $E(2^+)$ ) y (b) y d)) la energía de separación de dos protones  $\Delta_{2p}$  para los par  $N = 50$  (a) y b)) y  $N = 82$  (c) + d)) isótonos. Los valores experimentales se muestran como cuadrados negros y los cálculos del modelo de capas como puntos rojos. En el caso de los núcleos isótonos con  $N=82$  se presenta además cálculos con varios aumentos en la diferencia de energía del  $1p_{1/2}$  nivel y el siguiente SPO (línea de color negro = +0.5 MeV, La línea a trazos negra = +1.0 MeV y la línea de puntos negra = +1.5 MeV). Para los  $N = 50$  isótonos los cálculos del modelo de capas de la Referencia [171] se presentan para comparación como las estrellas verdes.

Mediante cálculos del modelo de capas (NA-14), que utilizan la nueva energía medida para la órbita de partícula única (SPO)  $p_{3/2}$ , se han obtenidos las energías de los primeros estados  $2^+$  y las energías de separación de dos protones. Los resultados se presentan en la Fig. 8.6(c+d) como los círculos rojos.

Se puede observar que la energía del primer estado  $2^+$  disminuye a partir de  $Z = 36$  hasta  $Z = 48$  y la energía de separación de dos protones se mantiene constante. Es evidente, observando estas dos figuras, que no hay indicaciones para un cierre de capas (*sub-shell*). A modo de prueba, y para demostrar que la distancia entre el nivel  $1p_{1/2}$  y el

siguiente SPO es la razón para la desaparición, se han realizado cálculos adicionales del modelo de capas con una mayor distancia entre el  $1p_{1/2}$  SPO y el siguiente SPO de +0.5 (línea de color negro), +1.0 (línea a trazos negra) y +1.5 MeV (línea negra de puntos), que también se muestran en la Fig. 8.6(c+d). Estos cálculos adicionales muestran claramente la reaparición de las capas cerradas para una mayor diferencia de energía entre los dos niveles y, por lo tanto se concluye que la reducción de la distancia de aproximadamente 300 keV entre los niveles  $1p_{1/2}$  y  $1p_{3/2}$ , y  $1g_{9/2}$  y  $1p_{1/2}$ , respectivamente, es la causa para la desaparición de las capas cerrada.

En el paso siguiente se investigó la importancia de las primeras transiciones prohibidas en la vecindad de  $^{132}\text{Sn}$ , como ya se ha sido discutido en varias publicaciones. Borzov *et al.* [67] predijo una pequeña influencia en especial para el caso  $N \leq 82$  y  $Z < 50$ , y sólo para  $N > 82$  el modelo DF3 + CQRPA mostró una significativa influencia. Möller *et al.* [63] menciona incluso para  $N \leq 82$  una influencia considerable de las transiciones tipo ff.

Las principales transiciones del tipo GT en la región del  $^{132}\text{Sn}$  son la  $\nu g_{7/2} \rightarrow \pi g_{9/2}$  y la  $\nu f_{7/2} \rightarrow \pi f_{5/2}$ , con esta última de ellas siendo bloqueada debido a la ocupación casi completa de la capa  $f_{5/2}$ . Los niveles entre 5.5 y 6 MeV se alimenten en un 30% de las transiciones  $\beta$ , y por eso una asignación diferente a  $\nu g_{7/2} \rightarrow \pi g_{9/2}$  no es muy probable. Estos niveles se asignan preliminares al  $\nu f_{7/2} g_{7/2}^{-1} \pi g_{9/2}^{-1}$  multiplete basado en las sistemáticas de la región. En esta zona varios ejemplos son conocidos por desintegraciones  $\beta$  del tipo GT  $\nu g_{7/2} \rightarrow \pi g_{9/2}$  y en la mayoría de los casos se deduce un log  $ft$  de aproximadamente 4.4.

Por otro lado, los estados más bajos en el  $^{132}\text{Sn}$  se pueden encontrar a energías de excitación de aproximadamente 4 MeV y aquellos con la paridad positiva fueron asignados al  $\nu f_{7/2} h_{11/2}^{-1}$  multiplete. Por lo tanto, es muy probable que los estados *Three Quasi-Particle* (3QP) más bajos en el  $^{131}\text{In}$  son los acoplamientos de un  $\pi g_{9/2}$  hueco a los estados  $2^+$  y  $4^+$  del  $^{132}\text{Sn}$ . Estos estados se basan en dichos argumentos sistemáticos al tener un carácter  $\nu f_{7/2} h_{11/2}^{-1} \pi g_{9/2}^{-1}$ . Son alimentados por desintegraciones  $\beta$  del tipo GT o ff, en este caso, probablemente del tipo ff  $\nu h_{11/2} \rightarrow \pi g_{9/2}$ .

Comparando los resultados experimentales a las predicciones hechas con cálculos QRPA en la Referencia [34] se encuentran todos ellos en concordancia. En estos cálculos los 3QP niveles de la configuración  $\nu f_{7/2} h_{11/2}^{-1} \pi g_{9/2}^{-1}$  se encuentran a 3.5 MeV y tienen un log  $ft$  de 5.4. La configuración de los niveles alrededor de 5 MeV no han podido determinarse. Los niveles de la configuración  $\nu f_{7/2} g_{7/2}^{-1} \pi g_{9/2}^{-1}$  se predicen a 5.8 MeV con un log  $ft$  de 4.6.

Concluyendo los resultados presentados anteriormente, se observa la gran importancia que tienen las transiciones del tipo ff en la región  $N > 82$  y  $Z < 50$ . Al menos el 50% de los desintegraciones  $\beta$  proceden de desintegraciones primeras prohibidas.

$E_\gamma$ [keV]	$I_\gamma^{rel}$ [%]	$E_\gamma$ [keV]	$I_\gamma^{rel}$ [%]
50	123(33)	227	44(14)
86	57(16)	357	48(16)
102	100(20)	602	49(19)

**Table 8.9:** Listado de los  $\gamma$  observados en la desintegración  $\beta$  del  $^{133}\text{Cd}$  con su energía y las intensidades relativas.

#### 8.2.1.4 $^{133}\text{Cd} \rightarrow ^{132}\text{In}$

En el presente trabajo, se han observado por primera vez las transiciones después de la emisión  $\beta$ -delayed de neutrones del  $^{133}\text{Cd}$ . Con una probabilidad de emisión de neutrones de 88(20)%, todas las transiciones observadas después de la desintegración  $\beta$  del  $^{133}\text{Cd}$  han sido asignado al  $^{132}\text{In}$ . El resumen de las seis transiciones observadas son expuestas en la tabla 8.9. Desafortunadamente, la información experimental recogida en el presente experimento no es suficiente como para establecer un esquema de niveles o asignar las transiciones a cada uno de los multipletes de baja energía en el  $^{132}\text{In}$  para así poder extraer más información.

### 8.2.2 Periodos de semidesintegración $\beta$

Mientras que los periodos de semidesintegración de los núcleos cercanos al valle de estabilidad muestran grandes fluctuaciones, los periodos de semidesintegración más lejos de la estabilidad cambian muy constantemente en la mayoría de los casos, estudiándolos en función del número de neutrones N. Esta observación se puede hacer en todo el diagrama Segré y las desviaciones se encuentran sólo en la presencia de cambios en la estructura nuclear. Comparando los periodos de semidesintegración de la literatura con los resultados obtenidos en el presente trabajo (véase la tabla 8.10) se observan discrepancias importantes. Especialmente para los núcleos con  $A > 128$ , las mediciones anteriores mostraron grandes saltos en las vidas medias con el número neutrónico N crecientes, mientras que los resultados de esta tesis muestran un comportamiento muy suave. En particular, los periodos de semidesintegración obtenidos para  $A = 129, 130$  y  $131$  muestran grandes diferencias con respecto a los valores de la literatura. Además, mientras que en la Referencia [62] los dos periodos de semidesintegración de los estados  $11/2^-$  y  $3/2^+$  en el  $^{129}\text{Cd}$  se propuso que tenían significativamente diferentes periodos de semidesintegración, esto no ha podido ser confirmado aquí.

Tres métodos se han utilizado para determinar los periodos de semidesintegración. Las distribuciones del tiempo de todas las desintegraciones correlacionadas con los iones implantados se ajustaron en un primer paso usando las ecuaciones Bateman y una minimización  $\chi^2$ . En un segundo paso las distribuciones se ajustaron utilizando una minimización de máxima probabilidad (*Maximum Likelihood*) utilizando una función de densidad de probabilidad que incluía las actividades de las generaciones padre, hijo, nietos y un fondo constante. El tercer método incluía un ajuste con una función de decaimiento

Isotopo	$I^\pi$	$T_{1/2}(\gamma)$ [ms]	$T_{1/2}(B1)$ [ms]	$T_{1/2}(B2)$ [ms]	$T_{1/2}(M)$ [ms]	$T_{1/2}(Lit.)$
$^{126}\text{Cd}$	$0^+$	515(18)	530(16)	507(19)	-	506(15) [59]
$^{127}\text{Cd}$	$(3/2^+)$	288(22)	303(5)	301(8)	-	370(70) [60]
$^{128}\text{Cd}$	$0^+$	254(3)	256(2)	254(2)	245(10)	280(40) [61]
$^{129}\text{Cd}$	$(3/2^+)$	146(8)	156(7)	154(8)	-	104(6) [62, 112, 113, 115]
$^{129}\text{Cd}$	$(11/2^-)$	154.8(31)	156(7)	154(8)	-	242(8) [62, 112, 113, 115]
$^{130}\text{Cd}$	$0^+$	126.8(8)	127.4(5)	126.8(3)	125(5)	162(7) [20]
$^{131}\text{Cd}$	$(7/2^-)$	106(9)	101(2)	100(2)	98(4)	68(3) [34]
$^{132}\text{Cd}$	$0^+$	86(17)	79(1)	83(4)	79(4)	97(10) [34]
$^{133}\text{Cd}$	$(7/2^-)$	-	68(5)	58(14)	68(8)	57(10) [112]
$^{134}\text{Cd}$	$0^+$	-	-	-	$58^{(+24}_{-19})$	-

**Table 8.10:** Resumen de los resultados para el periodo de semidesintegración, obtenidos mediante los tres métodos presentados ( $\gamma$ -gated:  $T_{1/2}(\gamma)$ , ecuaciones Bateman:  $T_{1/2}(B)$  y el análisis de la máxima probabilidad (MLH):  $T_{1/2}(M)$ ) y los valores de la literatura  $T_{1/2}(Lit)$  para los isotopos cadmio con  $A = 126-134$ .

exponencial sólo para las distribuciones del tiempo, lo que requiere la observación de una transición específica en los núcleos hijos. En todos los casos los resultados de los tres métodos diferentes están de acuerdo dentro de una desviación estándar.

Los resultados, presentados en la Fig. 8.7, muestran un buen escalonamiento par-impar debajo de  $N = 82$ , que parece desaparecer después de atravesar el cierre de capas. Es importante tener en cuenta que en este trabajo no se ha observado ningún cambio abrupto para el cierre de capas  $N = 82$  en los periodos de semidesintegración medidos, al contrario que la anterior medición [34] que sugería una caída repentina en el periodo de semidesintegración del  $N = 82$  hasta el  $N = 83$ .

Los nuevos valores de los periodos de semidesintegración se han comparado con tres modelos teóricos, dos de ellos son los utilizados comúnmente para los cálculos del proceso  $r$ . El periodo de semidesintegración  $\beta$  es un parámetro de entrada crucial para estos cálculos, dado que la abundancia relativa del proceso  $r$  es particularmente sensible para los núcleos próximos al cierre de capas [14]. Esta dependencia es aparentemente independiente del escenario astrofísico considerado, como se indica en un reciente estudio del proceso  $r$  [54]. Los periodos de semidesintegración en este trabajo, por lo tanto, son excelentes sondas experimentales para poner a prueba el poder descriptivo de estos modelos cerca del cierre de capas  $N=82$ . El primer modelo que se presenta aquí se llama FRDM + QRPA [28, 58, 63, 69, 72, 73] y el segundo modelo es el KTUY+GT2 [64, 65]. El modelo DF3+CQRPA [67, 68] se muestra en la Fig. 8.7 como una línea de puntos discontinua.

El modelo DF3 + CQRPA muestra una muy buena concordancia con los datos. La predicción de la tendencia de los periodos de semidesintegración es correcta y se encuentra sólo ligeramente por encima de los valores obtenidos experimentalmente para los núcleos  $N < 84$ . Los otros dos modelos, presentados también en Fig. 8.7, no muestran generalmente de acuerdo, especialmente FRDM + QRPA, que parece predecir periodos

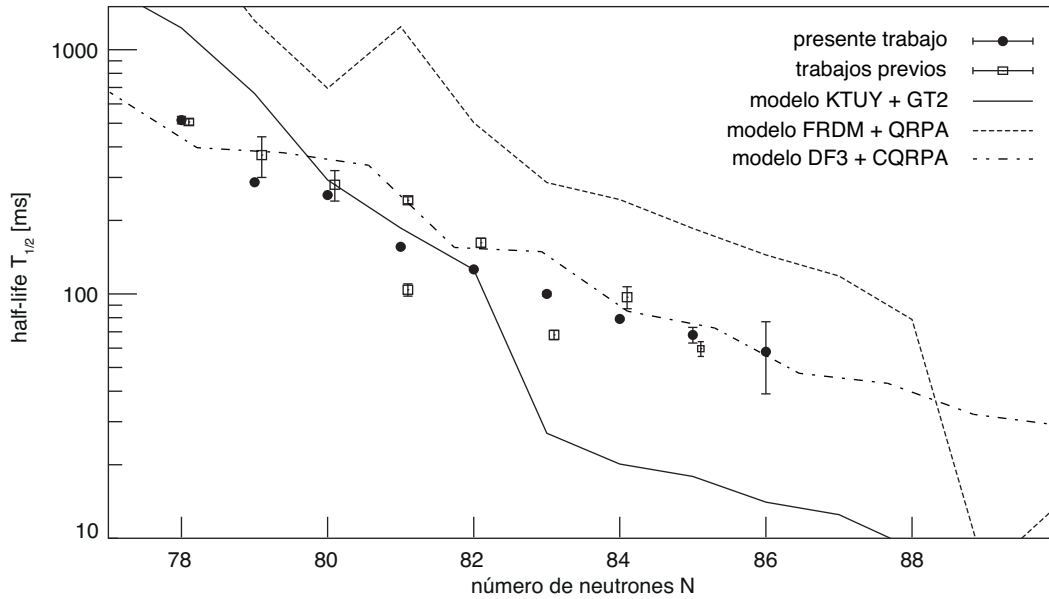


**Figure 8.7:** Vidas medias de los cadmios ( $A=126-134$ ) obtenidas en este trabajo (puntos negros) y los trabajos previos (cuadrados blancos) [20, 34, 59–62] y las predicciones teóricas del modelos FRDM + QRPA (línea discontinua) [63] y KTUY+GT2 (línea continua) [64, 65].

de semidesintegración mas largos en comparación con los datos experimentales. Por otro lado KTUY + GT2 proporciona buenos valores en el lugar de la región  $N < 82$  pero parece subestimar el periodo de semidesintegración por encima del cierre de capas  $N = 82$  y, además, muestra un salto en los periodos de semidesintegración del  $N=82$  al  $N=83$ , en desacuerdo con los valores obtenidos para el  $^{130}\text{Cd}$  y el  $^{131}\text{Cd}$ . Se hace evidente que algunas mejoras tienen que ser hechas para los dos modelos para describir bien los datos experimentales. Además, la necesidad de disponer de los periodos de semidesintegración experimentales como parámetros de entrada para el cálculo del proceso  $r$  se hace aún más evidentes a la hora de determinar el flujo exacto del proceso  $r$  a los puntos de espera.

### 8.2.3 Probabilidades de emisión de neutrones $P_n$

Las probabilidades de emisión de neutrones  $P_n$  se dedujo utilizando las poblaciones procedentes de las desintegraciones  $\beta$  para los niveles e intensidades absolutas de las transiciones  $\gamma$  conocidas de los núcleos nietos.  $\gamma_2$  es una transición electromagnética observada en el núcleo nieto con intensidad  $I_{\gamma_2}^{Decay}$  conocida, para desintegraciones  $\beta$  de los núcleos hijos. La fórmula para calcular la intensidad total observada,  $I_{\beta}^{tot}$ , viene dada como:

$$I_{\beta}^{tot} = \frac{N_{\gamma_2}}{\epsilon_{abs}^{\gamma_2} I_{\gamma_2}^{Decay} P_{Decay}} \quad (8.1)$$

Isotopo	$I_{\beta}^{tot}$	$P_n^{\gamma 2}$	$P_{1n}^{\gamma 4}$
$^{128}\text{Cd}$	93(10)	7(10)	<1
$^{129}\text{Cd}$	-	-	3.5(10)
$^{130}\text{Cd}$	91(5)	9(5)	-
$^{131}\text{Cd}$	-	-	16(4)
$^{132}\text{Cd}$	12(3)	88(3)	-
$^{133}\text{Cd}$	-	-	88(20)

**Table 8.11:** Resumen de los resultados para los  $P_n$  obtenidos mediante los dos métodos en el presente trabajo.

con  $\epsilon_{abs}^{\gamma 2}$ , como la eficiencia absoluta por la detección de una transición de energía  $E_{\gamma 2}$  y  $N_{Decay}^P$  el número de desintegraciones  $\beta$ .  $P_n$  se calcula entonces como:

$$P_n^{\gamma 2} = 1 - \frac{N_{\gamma 2}}{\epsilon_{abs}^{\gamma 2} I_{\gamma 2} N_{Decay}^P} \quad (8.2)$$

Para comprobar estos resultados, el  $P_{1n}$  ha sido calculado según la cantidad de los  $\gamma$  observados en el núcleo nieto después de la emisión  $\beta$ -delayed de neutrones con la intensidad absoluta  $I_{\gamma 4}^{Decay}$  de la literatura. La fórmula correspondiente sería entonces:

$$P_{1n}^{\gamma 4} = I_{\beta, n}^{tot} = \frac{N_{\gamma 4}}{\epsilon_{abs}^{\gamma 4} I_{\gamma 4} N_{Decay}^P} \quad (8.3)$$

Los resultados se resumen en la tabla 8.11.

Comparando los valores  $P_n$  con las predicciones de los modelos es nuevamente de importancia para los cálculos del proceso r. La figura 8.8 muestra los resultados obtenidos en el presente trabajo en comparación con los que se resumen en la Referencia [60]. Mientras que para  $N = 82$  los valores están de acuerdo dentro de las barras de error, para  $N > 82$  el  $P_n$  de la literatura no está en concordancia. En el caso del  $^{131}\text{Cd}$  la literatura menciona un  $P_n$  de 3.5%, mientras que en el presente trabajo se midió un  $P_{1n}$  de 16(4)%. También para el  $^{132}\text{Cd}$  el valor obtenido es de 88(3)% y no es compatible con el valor de 60(15)% medido en un trabajo previo [34]. Al comparar los resultados actuales con dos modelos, el modelo DF3 + CQRPA [67, 68] y el modelo FRDM [63], se observan diferencias importantes. FRDM por ejemplo predice un mucho mayor  $P_{2n}$  en  $N = 83$  y  $N > 83$ . El contrario, en ninguno de los núcleos medidos en el presente trabajo se hallaron indicios de que la emisión de dos neutrones tiene una contribución significativa. Por otro lado el modelo DF3 + CQRPA predice valores de  $P_{1n}$  más bajos para  $N \geq 83$ , además de estar en desacuerdo con los datos experimentales.

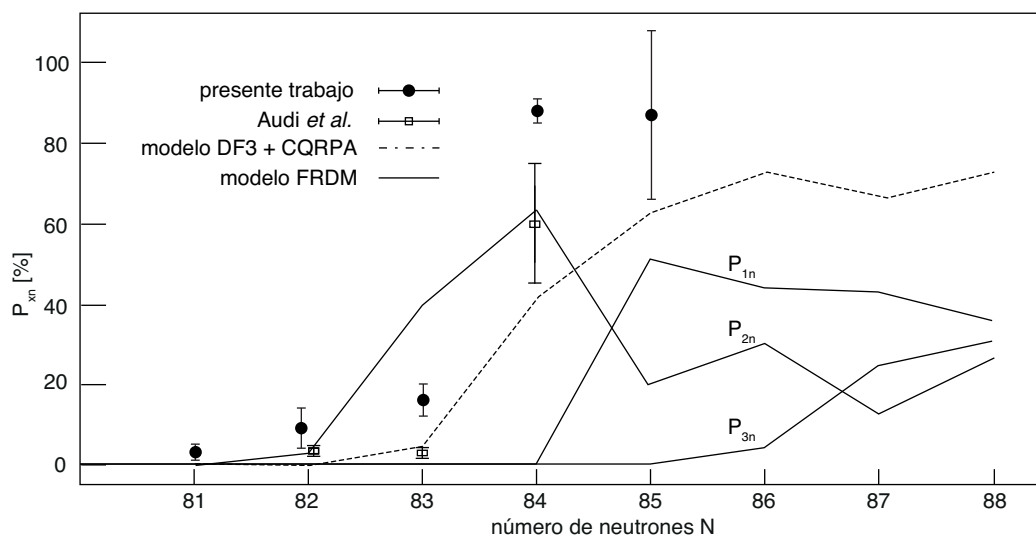


**Figure 8.8:** La comparación entre los valores de  $P_n$  experimentalmente obtenidos en el presente trabajo con los valores de la literatura en Referencia [60] y predicciones de dos modelos, el modelo DF3+CQRPA [67, 68] y el modelo FRDM [63].

## 8.2.4 Estados isoméricos

### 8.2.4.1 $^{128}\text{Cd}$

Las desintegraciones de varios estados isoméricos del  $^{128}\text{Cd}$  fueron observados en el presente trabajo así como todos ellos fueron ya observados anteriormente por Cáceres *et al.* [6]. Los resultados para las intensidades relativas de las transiciones que suceden la desintegración de los estados isoméricos se resumen en la tabla 8.12 junto con los valores publicados en la Referencia [6] para su comparación. Resumiendo, se puede decir que los resultados obtenidos en el presente trabajo están en concordancia con los de la Referencia [6] y no han se ha podido encontrar desviaciones. Por ello, se mostró de acuerdo con el esquema de niveles y las interpretaciones hechas en [6].

$E_\gamma$ [keV]	$E_{\gamma,lit}$ [keV]	$I_\gamma$ [%]	$I_{\gamma,lit}$ [%]	$\alpha$	$\alpha_{lit}$
68.1	68.7	8.1(1.1)	5.2(5)	5.68(18)	6.38(86)
237.1	237.9	53(1)	39(2)	-	-
439.2	440.0	85(1)	84(4)	-	-
449.3	450.4	2.1(5)	1.8(3)	-	-
537.1	537.6	52(1)	47(3)	-	-
645.1	645.8	100(2)	100(5)	-	-
764.3	765.0	1.8(4)	1.2(2)	-	-
784.0	784,6	90(2)	90(5)	-	-
1223.4	1224.0	10(1)	11(1)	-	-

**Table 8.12:** Resumen de las energías, las intensidades relativas y los coeficientes de conversión de las transiciones observadas en coincidencia retardada con los iones del  $^{128}\text{Cd}$  en este trabajo y los valores de la literatura correspondiente ([6]).

### 8.2.4.2 $^{129}\text{Cd}$ - ms

La desintegración de un estado isomérico en el núcleo rico en neutrones  $^{129}\text{Cd}$  se ha observado a través de la detección de la conversión interna y electrones Compton, proporcionando primera información experimental en estados excitados en este núcleo. Cuatro transiciones con energías de 353, 406, 1181 y 1586 keV han podido ser identificadas y se les asignan a la desintegración de este estado. A partir de las intensidades medidas de los  $\gamma$  y electrones de conversión interna, una multipolaridad de E3 fue asignada provisionalmente a la transición isomérica. Un periodo de semidesintegración de  $T_{1/2} = 3.6(2)$  ms se determinó para el nuevo estado a partir del ajuste de una función de decaimiento exponencial sólo a las distribuciones de tiempo de las transiciones. Al estado se le asignó un espín y paridad de  $(21/2^+)$ , sobre la base de una comparación con cálculos del modelo de capas. El esquema de niveles obtenido experimentalmente y los correspondientes cálculos del modelo de capas se muestran en la Fig. 8.9 están en buen acuerdo.

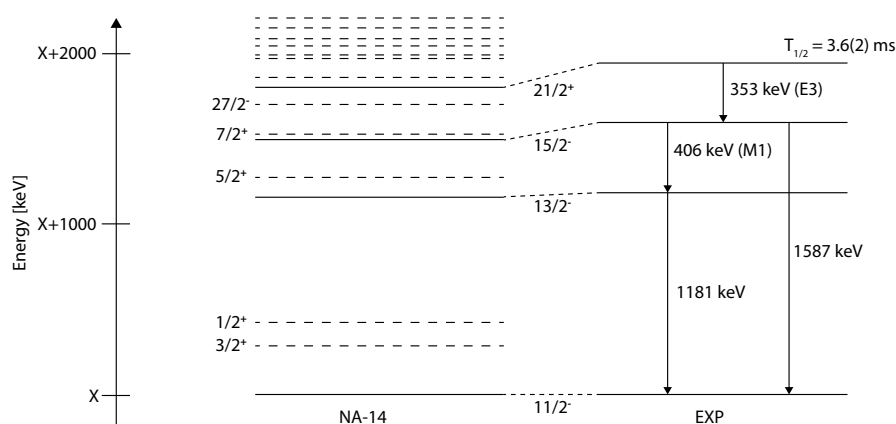


**Figure 8.9:** Esquema de niveles para el  $(21/2^+)$  ms estado isomérico en el  $^{129}\text{Cd}$ , que se obtuvo en el presente trabajo y la comparación con el cálculo del modelo de capas. El modelo de capas demuestra, además, las posiciones previstas para (neutron single hole states) neutrones de estados de baja energía para huecos únicos y otros niveles en el rango de espín  $17/2$ - $23/2$  con paridad positiva y negativa.

### 8.2.4.3 $^{129}\text{Cd}$ - $\mu\text{s}$

En el  $^{129}\text{Cd}$ , además, se identificó una transición retardada con una energía de 3693 keV. La transición 3693 keV no se observa en coincidencia con cualquier otra transición en este experimento. Y con un ajuste de mínimos cuadrados con una función de decaimiento exponencial únicamente a la distribución del tiempo de la transición dio como resultado un periodo de semidesintegración de  $T_{1/2} = 0.9(1) \mu\text{s}$ . Resumiendo los resultados, se sugiere que un estado isomérico de un  $\mu\text{s}$  está presente en el  $^{129}\text{Cd}$ . Con los cálculos del modelo de capas aún en curso, la naturaleza de este estado isomérico es por el momento desconocida. Sin embargo, vale la pena mencionar que Górska *et al.* [9] identificó un estado isomérico con una energía de excitación similar (3.782(2) keV) en el  $^{131}\text{In}$  y con un periodo de semidesintegración comparable de 0.63(6)  $\mu\text{s}$ . En ese trabajo se identificó el estado isomérico como un estado excitado de alto espín con una asignación provisional del espín y la paridad de  $(17/2^+)$ .

### 8.2.4.4 $^{130}\text{Cd}$

Por último, pero no menos importante, la desintegración del estado isomérico ( $8^+$ ) en el  $^{130}\text{Cd}$  se volvió a medir. Cuatro transiciones con energías de 127.5, 137.6, 538.6 y 1325.0 keV pudieron ser identificadas y se les asignaron a la desintegración de este estado. El periodo de semidesintegración del ( $8^+$ ) fue medido, siendo  $T_{1/2} = 225(2)$  ns. Los resultados para las intensidades relativas de las transiciones que suceden a la desintegración de los estados isoméricos se resumen en la tabla 8.13 junto con los valores publicados en la Referencia [7] para su comparación. Adicionalmente, el orden previamente desconocido de los  $\gamma$  con energías de 128 keV y 138 keV han podido ser fijados. Las transiciones de 128 keV y 138 keV se asignan ahora a las transiciones  $8^+ \rightarrow 6^+$  y  $6^+ \rightarrow 4^+$ , respectivamente. Además el carácter ns del estado  $6^+$ , sugerido por los cálculos del modelo de capas en [7], fue confirmado. El centroide de la distribución de la diferencia en el tiempo entre transiciones que pueblan y desexcitan el nivel ( $6^+$ ) esta dislocado y una periodo de semidesintegración de  $T_{1/2} = 37(4)$  ns ha podido deducirse a partir de la posición del centroide.

$E_\gamma$ [keV]	$E_{\gamma,lit}$ [keV]	$T_{1/2}$ [ns]	$I_\gamma$ [%]	$I_{\gamma,lit}$ [%]	$\alpha$	$\alpha_{lit}$
127.5	128	227(5)	48(4)	2.06(26)	1.08(16)	0.63(26)
137.6	138	233(4)	69(4)	2.16(27)	0.45(10)	0.56(25)
538.6	539	226(2)	100(3)	3.21(43)	-	-
1325.0	1325	219(3)	99(3)	3.62(56)	-	-

**Table 8.13:** Resumen de las energías, las intensidades relativas y los coeficientes de conversión de las transiciones observadas en coincidencia retardada con los iones de  $^{130}\text{Cd}$  en este trabajo y los valores de la literatura correspondiente [160].

# Appendices



# Appendix A

## Sorting manual

The sorting of the EURICA data consists of several steps and a short manual is now given here for future references. We start with three different types of data-files after the experiment:

- A BigRIPS ROOT file (in the following: “BigRIPS.root”), containing information on AoQ and Z on an event-by-event basis
- Several WAS3ABi \*.ridf files (in the following: “dataXXXX.root”, with XXXX replaced by the 4 digit run number), one for each run of the experiment
- Several EURICA \*.root files (in the following: “go4\_XXXX.root”, with XXXX replaced by the 4 digit run number), one for each run of the experiment

Each of the files contains the timestamp information for each event, to be able to correlate the events off-line.

### A.0.5 Installation of the sorting software

This manual assumes that the RIKEN software Anaroot is installed as explained in the manual [183]. The sorting software has two folders, named “include” and “script\_136sn” (or “script\_128pd” for the Palladium data set). The “include” folder contains the C++ class CDecay, used for the decay events. To compile the C++ files contained in both folder we run the following commands:

```
> cd YOURPATH/include
> make clean
> make
```

Before we can use the CDecay class, we have to add the following line to our “/bashrc” file:

```
export LD_LIBRARY_PATH=$LD_LIBRARY_PATH:$/YOURPATH/include
```

And after that we can also compile the files in the “script\_136sn” folder:

```
> cd YOURPATH/script_136sn
> make clean
> make
```

## A.0.6 The important files + setting up the working directories

There are several lookup-table and calibration files in the “script\_136sn” folder:

- DSSD\_E\_calib.input : energy calibration file, containing calibration factor and offset for each WAS3ABi x- and y-strip
- DSSD\_T\_offset.input: time calibration file, to time-align all WAS3ABi TDC channels
- ADC\_table.input: lookup-table for the WAS3ABi ADC channel
- ADC\_thr.input: thresholds for the WAS3ABi ADC channel, to eliminate the under-flow
- TDC\_table.input : lookup-table for the WAS3ABi TDC channel

And to run the individual sorting steps individually, it is necessary to change in each of the steps the INPUT/OUTPUT files directories and file names. The codelines in the files to change are:

- “WASABI2Tr.cpp”:

```
printf(filename, "../rawdata/sistopper/uranium2012/exp/data%04d.ridf", runN);
printf(rootname, "../root/sistopper/sn136test/WASABI%04d.root", runN);
```

- “DSSDGeMerge.cpp”:

```
printf(dssdfile, "../root/sistopper/sn136test/WASABI%04d.root", runD);
printf(gammafile, "../root/euroball/go4_%04d.root", runG);
printf(outfile, "../root/sistopper/sn136test/WASABI_EURICA%04d.root", runD);
```

- “separate.cpp”:

```
printf(dssdfile, "../root/sistopper/sn136test/WASABI_EURICA%04d.root", runN);
printf(bigripsfile, "../root/bigrips/v2/BigRIPS.root");
printf(outfile, "../root/final/sn136test/beta_ion_%04d.root", runN);
```

- “BuildDecay.cpp”:

```
printf(dssdfile, "../root/final/sn136test/beta_ion_%04d.root", runD);
printf(outfile, "../root/final/sn136test/decay_%04d.root", runD);
```

This file furthermore contains the important variable to define the length of the correlation time:

```
Long64_t time_window = 5e8;
```

where  $1e8$  is equal to 1 second.

- “MakeGGMatrixDecayOnIsotope.cpp”:

```
sprintf(decayfile, "../root/final/sn136test/decay_%04d.root", runD);  
sprintf(outfile, "../root/final/sn136test/DECAYGGMatrix_%04d.root", runD);
```

After changing all the filenames and directories it's necessary to compile again the “script\_136sn” folder:

```
> cd YOURPATH/script_136sn  
> make clean  
> make
```

### A.0.7 The sorting process

Now we are ready to run the sorting process for each run individually by running the following commands in this exact order:

```
> ./WASABI2Tr RUNNUMBER RUNNUMBER  
> ./DSSDGeMerge RUNNUMBER RUNNUMBER  
> ./separate RUNNUMBER RUNNUMBER  
> ./BuildDecay RUNNUMBER RUNNUMBER  
> ./MakeGGMatrixDecayOneIsotope RUNNUMBER RUNNUMBER
```

where we replace RUNNUMBER with the 4 digit number assigned to each run.

## A.1 Latest Germanium calibration file

Cluster	Crystal	gain	offset
0	0	0.10412240	0.06365909
0	1	0.10408037	-0.14345665
0	2	0.10417903	-0.26500545
0	3	0.10337872	-0.21654931
0	4	0.10362086	0.18102195
0	5	0.10370917	-0.23104998
0	6	0.10387536	-0.02399329
1	0	0.10415689	0.15700082
1	1	0.10422559	0.14211469
1	2	0.10415676	0.21689859
1	3	0.10457421	0.39321337
1	4	0.10464589	0.07640114
1	5	0.10977858	0.26601406
1	6	0.00000000	0.00000000
2	0	0.10384130	0.04822838
2	1	0.10368668	0.35256218
2	2	0.10321463	0.28829814
2	3	0.10317423	0.28716545
2	4	0.10289391	-0.10085037
2	5	0.10289160	0.24159921
2	6	0.10287190	0.24837613
3	0	0.0	0.0
3	1	0.10382205	0.15356682
3	2	0.10335474	0.73946150
3	3	0.10355125	-0.09465847
3	4	0.10641613	0.11569086
3	5	0.10222683	15.24297507
3	6	0.10260690	0.26879165
4	0	0.10444889	0.01557740
4	1	0.10406073	0.20967684
4	2	0.10398509	-0.08017359
4	3	0.10404469	-0.03329095
4	4	0.10374749	0.12151728
4	5	0.10382306	0.16983148
4	6	0.10390485	0.23369277
5	0	0.10381161	0.28488731
5	1	0.10401055	0.17431950
5	2	0.10360866	0.37638464
5	3	0.10359581	0.09906557
5	4	0.10402654	0.22783494
5	5	0.10383899	0.04385693

**Table A.1:** Latest Germanium calibration.

Cluster	Crystal	gain	offset
5	6	0.10380930	-0.28834536
6	0	0.10404299	0.07667495
6	1	0.10386257	0.21660659
6	2	0.10402918	0.15582311
6	3	0.10391670	0.22401595
6	4	0.10361632	-0.06148804
6	5	0.10331073	-0.12617416
6	6	0.10313430	-0.01268929
7	0	0.00000000	0.00000000
7	1	0.00000000	0.00000000
7	2	0.00000000	0.00000000
7	3	0.00000000	0.00000000
7	4	0.00000000	0.00000000
7	5	0.00000000	0.00000000
7	6	0.00000000	0.00000000
8	0	0.10377655	0.07496108
8	1	0.10395288	-0.08398664
8	2	0.10423716	-0.11939608
8	3	0.10357635	0.08423299
8	4	0.10382484	0.31107846
8	5	0.10395358	0.30379053
8	6	0.09332704	0.23402800
9	0	0.10398172	-0.11637612
9	1	0.10383086	-0.02211838
9	2	0.00000000	0.00000000
9	3	0.10406208	-0.05740683
9	4	0.10411094	0.22541174
9	5	0.10382954	0.04890944
9	6	0.10392070	-0.18147286
10	0	0.10433940	0.04325240
10	1	0.10413133	0.23308433
10	2	0.10399521	0.01384240
10	3	0.10396134	-0.03340972
10	4	0.10414422	0.09723009
10	5	0.10383193	0.16624009
10	6	0.10378884	0.35516079
11	0	0.10431537	0.23650266
11	1	0.10404564	0.27835635
11	2	0.10348024	0.08439080
11	3	0.10334771	-0.16410358
11	4	0.10287190	0.09235437
11	5	0.10310893	0.13452084
11	6	0.10291265	-0.04621966

**Table A.2:** Latest Germanium calibration.



## Appendix B

### EURICA angles

Cluster	distance $r$ [mm]	$\Theta$	$\Phi$	$\Psi$
0	-	-	-	-
1	188.0	55.7	339.5	151.8
2	191.9	56.3	272.2	158.0
3	190.4	125.0	50.9	335.7
4	188.6	124.2	339.6	328.3
5	190.0	123.7	272.0	277.4
6	182.2	88.1	164.7	151.0
7	-	-	-	-
8	207.9	51.2	129.8	9.5
9	205.4	54.4	195.3	282.1
10	196.7	126.1	130.0	187.9
11	195.7	122.9	194.4	160.7

**Table B.1:** Position of the central crystal of each germanium detector in the spherical coordinate system with the radial distance  $r$ , the polar angle  $\Theta$  and the azimuthal angle  $\Phi$ .  $\Psi$  is the rotation angle of the crystal A with respect to the projection of the y-axis on the cluster, for details see text. [184]

The measurement of the position of the central crystal of each cluster and the rotation angle was performed by J. Wu in the framework of his Phd thesis and the results are stated in table B.1. Starting from that in the following the positions for each crystal are calculated.

To measure and calculate the position of the individual crystals two coordinate systems were used. First of all the Cartesian coordinate system is used, where the center of the coordinate system is defined in the center of WAS3ABI which is also the center of the germanium array. The z-axis is defined as the central beam trajectory in beam direction, the x-axis is defined parallel to the floor and rectangular pointing to the left side of the beam direction and the y-axis is consequently pointing upwards.

The position of each crystal is calculated in the spherical coordinate system with  $r$  the radial distance of the crystal to the center of the coordinate system, the polar angle  $\Theta$  which is the angle between the vector connecting the origin with the position of the detector and

the z-axis. The third coordinate, the azimuthal angle  $\Phi$ , is defined as the angle between the x-axis and the projection of the vector connecting the origin with the position of the detector on the x-y-plane. The transformation between the two used coordinate systems can be done by using some simple geometrical formulas. To transform from the Cartesian coordinate system  $(x,y,z)$  to the spherical coordinate system  $(r,\Theta,\Phi)$  the following formulas are used:

$$r = \sqrt{x^2 + y^2 + z^2} \quad (\text{B.1})$$

$$\Theta = \arccos\left(\frac{z}{\sqrt{x^2 + y^2 + z^2}}\right) \quad (\text{B.2})$$

$$\Phi = \arctan\left(\frac{y}{x}\right) \quad (\text{B.3})$$

The definition of the inverse tangent in formula B.3 depends on in which quadrant of the x-y-plane the individual position is which has consequently to be taken into account when doing the transformation. To perform the transformation from coordinates stated in the spherical coordinate system to the Cartesian ones, the following transformation formulas are used:

$$x = r \sin(\Theta) \cos(\Phi) \quad (\text{B.4})$$

$$y = r \sin(\Theta) \sin(\Phi) \quad (\text{B.5})$$

$$z = r \cos(\Theta) \quad (\text{B.6})$$

Using the information from table B.1 and the known distance  $d$  between the center of the crystals A-F to the center of the central crystal G of 6.2 cm, the position of each crystal can be calculated. Therefore, the position shift  $(\Delta x, \Delta y, \Delta z)$  in each of the three directions x, y and z was determined assuming that the surface of each cluster is plane and that each cluster is perfectly pointing to the center of the cluster array, which in first order are valid assumptions. Those calculations were performed in the Cartesian coordinate system and then later transformed to the spherical coordinate system.

To calculate the y-position the rotation angle  $\Psi$  of the cluster has to be taken into account and the angle  $\alpha$  of the vector connecting the position of the central crystal to the origin with the y-axis, see figures B.1 and B.2. The position shift in the y-direction due to the rotation angle  $\Psi$  is then defined as:

$$\Delta y_1 = \cos(\Psi) \cdot d \quad (\text{B.7})$$

which has to be corrected for the inclination of the detector with respect to the y-axis to the total shift in y-direction (see fig. B.2):

$$\Delta y = \sin(\alpha) \cdot \Delta y_1 \quad (\text{B.8})$$

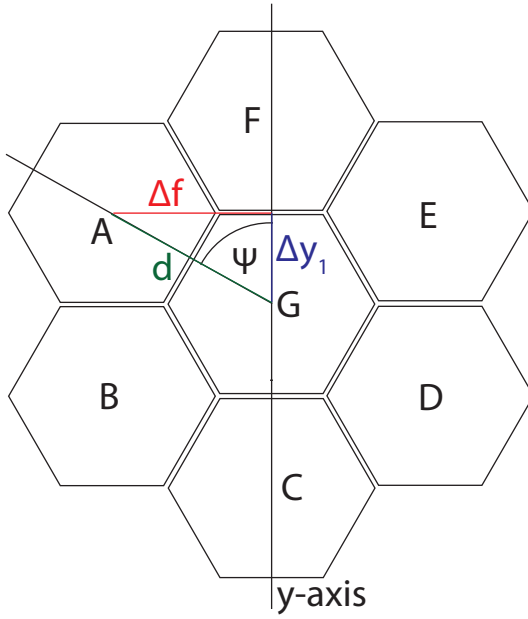


**Figure B.1:** Schematic for the calculation of the angles of the detectors in the EURICA array.

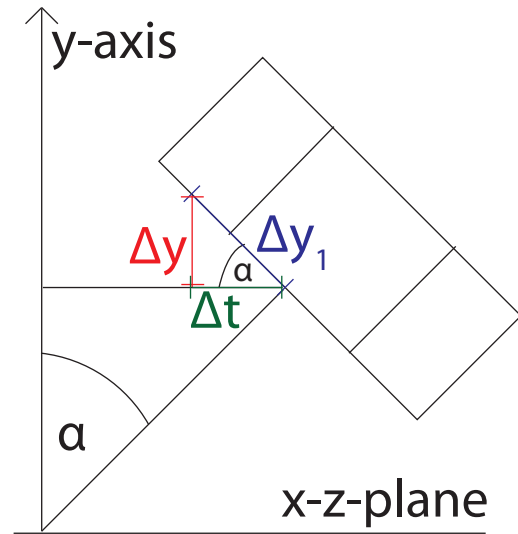


**Figure B.2:** Schematic for the calculation of the angles of the detectors in the EURICA array.

From the rotation angle  $\Psi$  the shift in the x-z plane can be calculated as:

$$\Delta f = \sin(\Psi) \cdot d \quad (\text{B.9})$$

which is then used to calculate the shift  $\Delta x_1$  and  $\Delta z_1$  (see fig. B.3):

$$\Delta x_1 = \sin(\beta) \cdot \Delta f \quad (\text{B.10})$$

$$\Delta z_1 = -\cos(\beta) \cdot \Delta f \quad (\text{B.11})$$

where  $\beta$  is the angle of the vector connecting the origin with the position of the detector projected on the x-z plane to the x-axis. An additional shift in x- and z-direction is introduced due to the inclination of the detector with respect to the y-axis. Those additional shifts ( $\Delta x_2$ ,  $\Delta z_2$ ) are calculated as following:

$$\Delta x_2 = -\cos(\beta) \cdot \Delta t \quad (\text{B.12})$$

$$\Delta z_2 = -\sin(\beta) \cdot \Delta t \quad (\text{B.13})$$

with  $\Delta t$  defined as shown in fig. B.2. Using the shifts in each direction the final position of each crystal can be calculated and the results are summarized in Tables B.2 and B.3.

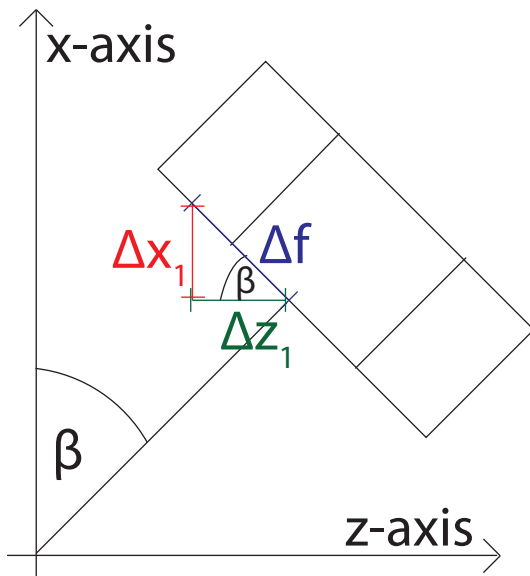


**Figure B.3:** Schematic for the calculation of the angles of the detectors in the EURICA array.

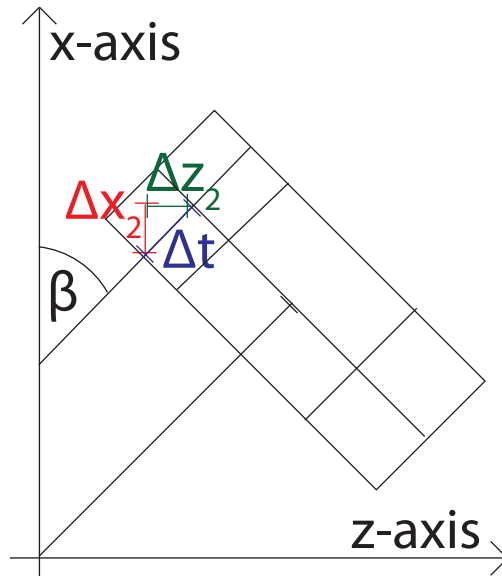


**Figure B.4:** Schematic for the calculation of the angles of the detectors in the EURICA array.

Cluster	Crystal	Letter	r	theta	phi
0	0	A	0	0	0
0	1	B	0	0	0
0	2	C	0	0	0
0	3	D	0	0	0
0	4	E	0	0	0
0	5	F	0	0	0
0	6	G	0	0	0
1	0	A	198	45.4	-0.7
1	1	B	198	63.4	-1.2
1	2	C	198	73.7	-17.2
1	3	D	198	68.3	-35.4
1	4	E	198	51.4	-42.5
1	5	F	198	37.7	-25.5
1	6	G	188	55.7	-20.3
2	0	A	201.7	39.6	83.6
2	1	B	201.7	44.1	-70.5
2	2	C	201.7	61.7	-67.8
2	3	D	201.7	73.5	-82.1
2	4	E	201.7	70.3	79.5
2	5	F	201.7	54.5	70.5
2	6	G	191.9	56.3	-87.8
3	0	A	200.3	139.8	36.9
3	1	B	200.3	122.9	29.3
3	2	C	200.3	109	41.6
3	3	D	200.3	109.1	60.5
3	4	E	200.3	123.2	72.5
3	5	F	200.3	140	64.7
3	6	G	190.4	125	50.9
4	0	A	198.5	128.4	-42.4
4	1	B	198.5	111.5	-35.2
4	2	C	198.5	106.2	-17.1
4	3	D	198.5	116.4	-1.2
4	4	E	198.5	134.4	-0.8
4	5	F	198.5	142	-25.4
4	6	G	188.6	124.2	-20.3
5	0	A	199.9	120.7	70.9
5	1	B	199.9	107.2	83.8
5	2	C	199.9	108.3	-77.5
5	3	D	199.9	123	-66.4
5	4	E	199.9	139.4	-75.9
5	5	F	199.9	137.9	77.0
5	6	G	190	123.7	-88

**Table B.2:** Angles of the detectors in the EURICA array.

Cluster	Crystal	Letter	r	theta	phi
6	0	A	192.5	97.3	-31.7
6	1	B	192.5	81.7	-33
6	2	C	192.5	70.4	-21.8
6	3	D	192.5	72	-5.4
6	4	E	192.5	85.1	3.3
6	5	F	192.5	100.2	-0.8
6	6	G	182.2	88.1	-15.3
7	0	A	0	0	0
7	1	B	0	0	0
7	2	C	0	0	0
7	3	D	0	0	0
7	4	E	0	0	0
7	5	F	0	0	0
7	6	G	0	0	0
8	0	A	217	45.4	-29.3
8	1	B	217	61.3	-34.2
8	2	C	217	67.8	-51
8	3	D	217	60.2	-67.2
8	4	E	217	43.9	-70.5
8	5	F	217	34.7	-48.8
8	6	G	207.9	51.2	-50.2
9	0	A	214.6	39	24.9
9	1	B	214.6	53.6	36.1
9	2	C	214.6	68	26.6
9	3	D	214.6	70.2	8.9
9	4	E	214.6	58.6	-4.2
9	5	F	214.6	42.2	-0.3
9	6	G	205.4	54.4	15.3
10	0	A	206.4	113.4	-63.9
10	1	B	206.4	109	-45.9
10	2	C	206.4	119.4	-30.8
10	3	D	206.4	136.6	-31.4
10	4	E	206.4	143	-56.5
10	5	F	206.4	129.3	-71.8
10	6	G	196.9	126.1	-50
11	0	A	205.3	129.4	-5.9
11	1	B	205.3	112.4	-1.5
11	2	C	205.3	105.4	15.3
11	3	D	205.3	113.7	31.5
11	4	E	205.3	131	34.1
11	5	F	205.3	140.5	13.1
11	6	G	195.7	122.9	14.4

**Table B.3:** Angles of the detectors in the EURICA array.

## Appendix C

# Complementary experimental information

### C.1 Efficiency calibration coefficients

	Sources no Qbeta no addback	Sources w Qbeta no addback	Sources w Qbeta w addback	Sources+ <sup>132</sup> Sn w Qbeta no addback	Sources+ <sup>132</sup> Sn w Qbeta w addback
A	12.871	11.4925	10.5578	9.85194	9.79743
B	4.11787	3.12	2.10007	1.20019	1.20009
D	7.68014	8.81991	9.05312	8.81516	9.04626
E	-0.79994	-0.606144	-0.463273	-0.646293	-0.589841
F	0.171989	-0.0230241	-0.035691	-0.0920761	-0.138474
G	2.08366	7.52746	12.9147	45.0243	123.039

**Table C.1:** Coefficients of the fits of the absolute efficiency calibration. Sources = <sup>152</sup>Eu+<sup>133</sup>Ba.

### C.2 $\gamma$ - $\gamma$ -coincidence information $\beta$ -decay

$E_\gamma$ [keV]	observ. coincidences [keV]
67.9 857, 248*	
247.6	(68, 462, 857, 925) *
315.3	857
462.4	248*, 462
857.1	68, 248*, 315
925.1	248*, 857
1172.7	-

**Table C.2:** Coincidences (\* = delayed coincidence) observed for the transitions in <sup>128</sup>In, populated after the  $\beta$  decay of <sup>128</sup>Cd.

$E_\gamma$ [keV]	observed coincidences [keV]
137.2	401,440,542,632
314.7	
333.6	359,589*,599*,863*,873*,995,1354,1462
339.1	359,392,562,895,995,1065,1354,1457
358.9	334,339,562,731,995,1065,1235,1797
391.7	339,359,995,1065,1354
400.8	137,440,632,769,1124,1287
439.7	401,538,632,769,1124,1287
471.9	631
537.9	440,632,1287
542.0	137,632,769,1423,1586,2127,2356
561.8	339,359,995,1235,1354
589.1	334*,359*,873,995*,1354*
599.2	334*,359*,863,995*,1354*
631.9	137,401,440,472,537,542,840,1287,1364,1423,1524,1586
696.9	
731.0	281,359,995,1065,1354
738.0	
752.0	2433
769.2	401,440,542,840,1124, 1287,1423,1586
840.2	137,632,769,1124,1287
863.1	334*,359*,599,995*
873.0	334*,359*,589,995*
895.0	339,359,562,995
967.6	995,1222,2217
995.1	339,359,562,731,1020,1065,1135,1222,1227,1235,1796,2155
915.0	
1020.1	995,1135
1040.6	359,995,2143,
1065.4	339,359,392,731,995,1354
1096.0	2088
1103.8	
1124.1	401,440,632,769,840
1130.6	995,1222,2217
1135.2	995,1020
1221.6	968,995,1131
1227.3	995,1525

**Table C.3:** Coincidences (\* = delayed coincidence) observed for the transitions in  $^{129}\text{In}$ , populated after the  $\beta$  decay of  $^{129}\text{Cd}$ .

$E_\gamma$ [keV]	observed coincidences [keV]
1234.6	359,562,995,1354
1259.6	542,769,995,2087
1287.3	137,401,440,537,632,769,840
1354.2	339,562,731,1065,1235,1796
1363.6	632,1525
1395.9	1890
1422.9	137,542,632,769,1762
1461.3	334*
1500.2	
1524.1	632,769,891,1227,1364,1555
1555.2	
1560.9	
1586.2	137,542,632,769,1762
1689.9	995
1761.6	1423,1586,2128,2356
1796.5	359,995,1354
1890.0	
2001.1	995
2088.0	1096,1260
2127.6	1762, 769, 542
2143.5	1041
2155.6	995
2216.8	968,1131
2295.6	1222
2433.4	915
2460.9	401,537,632,769
2880.2	
3184.4	
3286.1	
3347.0	
3487.7	
3701.9	
3888.4	
3913.8	
3966.4	
4118.3	

**Table C.4:** Coincidences (\* = delayed coincidence) observed for the transitions in  $^{129}\text{In}$ , populated after the  $\beta$  decay of  $^{129}\text{Cd}$ .

$E_\gamma$ [keV]	observ. coincidences [keV]
229.1	3966.8
388.4	1731.5, 3655.4
450.8	498.7, 1170.0, 1669.2
498.7	450.8, 1170.0
949.9	1170.0, 2804.8
1015.8	1104.1, 2739.0
1104.1	1015.8
1170.0	450.8, 498.7, 949.9
1669.2	450.8
1731.5	388.4*
2120.0	-
2739.0	1015.8
2804.8	949.9
3655.4	388.4
3966.8	229.1
4065.7	
4197.1	
4281.2	
5228.7	
5285.6	
5393.3	

**Table C.5:** Coincidences (\* = delayed coincidence) observed for the transitions in  $^{130}\text{In}$ , populated after the  $\beta$  decay of  $^{130}\text{Cd}$ .

### C.3 Formulas for the half-life analysis

$$\begin{aligned}
 A_3 = A_1^0 \cdot [ & \overline{P}_n^1 \cdot \overline{P}_n^2 \cdot \overline{P}_n^3 \cdot \lambda_2 \cdot \lambda_3 \cdot \left( \frac{e^{-\lambda_1 t}}{(\lambda_2 - \lambda_1) \cdot (\lambda_3 - \lambda_1)} + \frac{e^{-\lambda_2 t}}{(\lambda_1 - \lambda_2) \cdot (\lambda_3 - \lambda_2)} + \frac{e^{-\lambda_3 t}}{(\lambda_1 - \lambda_3) \cdot (\lambda_2 - \lambda_3)} \right) \\
 & + \overline{P}_n^1 \cdot \overline{P}_n^2 \cdot \overline{P}_n^3 \cdot \lambda_2^{\text{is}} \cdot \lambda_3 \cdot \left( \frac{e^{-\lambda_1 t}}{(\lambda_2^{\text{is}} - \lambda_1) \cdot (\lambda_3 - \lambda_1)} + \frac{e^{-\lambda_2^{\text{is}} t}}{(\lambda_1 - \lambda_2^{\text{is}}) \cdot (\lambda_3 - \lambda_2^{\text{is}})} + \frac{e^{-\lambda_3 t}}{(\lambda_1 - \lambda_3) \cdot (\lambda_2^{\text{is}} - \lambda_3)} \right) \\
 & + \overline{P}_n^1 \cdot \overline{P}_n^2 \cdot \overline{P}_n^3 \cdot \lambda_2^{\text{is}} \cdot \lambda_3^{\text{is}} \cdot \left( \frac{e^{-\lambda_1 t}}{(\lambda_2 - \lambda_1) \cdot (\lambda_3^{\text{is}} - \lambda_1)} + \frac{e^{-\lambda_2 t}}{(\lambda_1 - \lambda_2) \cdot (\lambda_3^{\text{is}} - \lambda_2)} + \frac{e^{-\lambda_3^{\text{is}} t}}{(\lambda_1 - \lambda_3^{\text{is}}) \cdot (\lambda_2 - \lambda_3^{\text{is}})} \right) \\
 & \left. + \overline{P}_n^1 \cdot \overline{P}_n^2 \cdot \overline{P}_n^3 \cdot \lambda_2^{\text{is}} \cdot \lambda_3^{\text{is}} \cdot \left( \frac{e^{-\lambda_1 t}}{(\lambda_2^{\text{is}} - \lambda_1) \cdot (\lambda_3^{\text{is}} - \lambda_1)} + \frac{e^{-\lambda_2^{\text{is}} t}}{(\lambda_1 - \lambda_2^{\text{is}}) \cdot (\lambda_3^{\text{is}} - \lambda_2^{\text{is}})} + \frac{e^{-\lambda_3^{\text{is}} t}}{(\lambda_1 - \lambda_3^{\text{is}}) \cdot (\lambda_2^{\text{is}} - \lambda_3^{\text{is}})} \right) \right] \quad (\text{C.1})
 \end{aligned}$$

$$\begin{aligned}
 A_6 = A_1^0 \cdot [ & P_n^1 \cdot P_n^5 \cdot \overline{P}_n^6 \cdot \lambda_5 \cdot \lambda_6 \cdot \left( \frac{e^{-\lambda_1 t}}{(\lambda_5 - \lambda_1) \cdot (\lambda_6 - \lambda_1)} + \frac{e^{-\lambda_5 t}}{(\lambda_1 - \lambda_5) \cdot (\lambda_6 - \lambda_5)} + \frac{e^{-\lambda_6 t}}{(\lambda_1 - \lambda_6) \cdot (\lambda_5 - \lambda_6)} \right) \\
 & + P_n^1 \cdot P_n^5 \cdot \overline{P}_n^6 \cdot \lambda_5^{\text{is}} \cdot \lambda_6 \cdot \left( \frac{e^{-\lambda_1 t}}{(\lambda_5^{\text{is}} - \lambda_1) \cdot (\lambda_6 - \lambda_1)} + \frac{e^{-\lambda_5^{\text{is}} t}}{(\lambda_1 - \lambda_5^{\text{is}}) \cdot (\lambda_6 - \lambda_5^{\text{is}})} + \frac{e^{-\lambda_6 t}}{(\lambda_1 - \lambda_6) \cdot (\lambda_5^{\text{is}} - \lambda_6)} \right) \\
 & + P_n^1 \cdot P_n^5 \cdot \overline{P}_n^6 \cdot \lambda_5^{\text{is}} \cdot \lambda_6^{\text{is}} \cdot \left( \frac{e^{-\lambda_1 t}}{(\lambda_5 - \lambda_1) \cdot (\lambda_6^{\text{is}} - \lambda_1)} + \frac{e^{-\lambda_5 t}}{(\lambda_1 - \lambda_5) \cdot (\lambda_6^{\text{is}} - \lambda_2)} + \frac{e^{-\lambda_6^{\text{is}} t}}{(\lambda_1 - \lambda_6^{\text{is}}) \cdot (\lambda_5 - \lambda_6^{\text{is}})} \right) \\
 & \left. + P_n^1 \cdot P_n^5 \cdot \overline{P}_n^6 \cdot \lambda_5^{\text{is}} \cdot \lambda_6^{\text{is}} \cdot \left( \frac{e^{-\lambda_1 t}}{(\lambda_5^{\text{is}} - \lambda_1) \cdot (\lambda_6^{\text{is}} - \lambda_1)} + \frac{e^{-\lambda_5^{\text{is}} t}}{(\lambda_1 - \lambda_5^{\text{is}}) \cdot (\lambda_6^{\text{is}} - \lambda_5^{\text{is}})} + \frac{e^{-\lambda_6^{\text{is}} t}}{(\lambda_1 - \lambda_6^{\text{is}}) \cdot (\lambda_5^{\text{is}} - \lambda_6^{\text{is}})} \right) \right] \quad (\text{C.2})
 \end{aligned}$$

$$\begin{aligned}
A_4 = A_1^0 \cdot & \left[ \overline{P}_n^1 \cdot P_n^2 \cdot \overline{P}_n \cdot \overline{P}_n \cdot \overline{P}_n \cdot \overline{P}_n \cdot \lambda_2 \cdot \lambda_4 \cdot \left( \frac{e^{-\lambda_1 t}}{(\lambda_2 - \lambda_1) \cdot (\lambda_4 - \lambda_1)} + \frac{e^{-\lambda_2 t}}{(\lambda_1 - \lambda_2) \cdot (\lambda_4 - \lambda_2)} + \frac{e^{-\lambda_4 t}}{(\lambda_1 - \lambda_4) \cdot (\lambda_2 - \lambda_4)} \right) \right. \\
& + \overline{P}_n^1 \cdot P_n^2 \cdot \overline{P}_n \cdot \overline{P}_n \cdot \overline{P}_n \cdot \lambda_2 \cdot \lambda_4 \cdot \left( \frac{e^{-\lambda_1 t}}{(\lambda_2^s - \lambda_1) \cdot (\lambda_4 - \lambda_1)} + \frac{e^{-\lambda_2^s t}}{(\lambda_1 - \lambda_2^s) \cdot (\lambda_4 - \lambda_2^s)} + \frac{e^{-\lambda_4 t}}{(\lambda_1 - \lambda_4) \cdot (\lambda_2^s - \lambda_4)} \right) \\
& + \overline{P}_n^1 \cdot P_n^2 \cdot \overline{P}_n \cdot \overline{P}_n \cdot \overline{P}_n \cdot \lambda_2 \cdot \lambda_4 \cdot \left( \frac{e^{-\lambda_1 t}}{(\lambda_2 - \lambda_1) \cdot (\lambda_4^s - \lambda_1)} + \frac{e^{-\lambda_2 t}}{(\lambda_1 - \lambda_2) \cdot (\lambda_4^s - \lambda_2)} + \frac{e^{-\lambda_4 t}}{(\lambda_1 - \lambda_4) \cdot (\lambda_2 - \lambda_4^s)} \right) \\
& + \overline{P}_n^1 \cdot P_n^2 \cdot \overline{P}_n \cdot \overline{P}_n \cdot \overline{P}_n \cdot \lambda_2 \cdot \lambda_4 \cdot \left( \frac{e^{-\lambda_1 t}}{(\lambda_2^s - \lambda_1) \cdot (\lambda_4^s - \lambda_1)} + \frac{e^{-\lambda_2^s t}}{(\lambda_1 - \lambda_2^s) \cdot (\lambda_4^s - \lambda_2^s)} + \frac{e^{-\lambda_4 t}}{(\lambda_1 - \lambda_4) \cdot (\lambda_2^s - \lambda_4^s)} \right) \\
& + P_n^1 \cdot \overline{P}_n^5 \cdot \overline{P}_n \cdot \overline{P}_n \cdot \overline{P}_n \cdot \lambda_5 \cdot \lambda_4 \cdot \left( \frac{e^{-\lambda_1 t}}{(\lambda_5 - \lambda_1) \cdot (\lambda_4 - \lambda_1)} + \frac{e^{-\lambda_5 t}}{(\lambda_1 - \lambda_5) \cdot (\lambda_4 - \lambda_5)} + \frac{e^{-\lambda_4 t}}{(\lambda_1 - \lambda_4) \cdot (\lambda_5 - \lambda_4)} \right) \\
& + P_n^1 \cdot \overline{P}_n^5 \cdot \overline{P}_n \cdot \overline{P}_n \cdot \overline{P}_n \cdot \lambda_5 \cdot \lambda_4 \cdot \left( \frac{e^{-\lambda_1 t}}{(\lambda_5^s - \lambda_1) \cdot (\lambda_4 - \lambda_1)} + \frac{e^{-\lambda_5^s t}}{(\lambda_1 - \lambda_5^s) \cdot (\lambda_4 - \lambda_5^s)} + \frac{e^{-\lambda_4 t}}{(\lambda_1 - \lambda_4) \cdot (\lambda_5^s - \lambda_4)} \right) \\
& + P_n^1 \cdot \overline{P}_n^5 \cdot \overline{P}_n \cdot \overline{P}_n \cdot \overline{P}_n \cdot \lambda_5 \cdot \lambda_4 \cdot \left( \frac{e^{-\lambda_1 t}}{(\lambda_5 - \lambda_1) \cdot (\lambda_4^s - \lambda_1)} + \frac{e^{-\lambda_5 t}}{(\lambda_1 - \lambda_5) \cdot (\lambda_4^s - \lambda_5)} + \frac{e^{-\lambda_4 t}}{(\lambda_1 - \lambda_4) \cdot (\lambda_5 - \lambda_4^s)} \right) \\
& \left. + P_n^1 \cdot \overline{P}_n^5 \cdot \overline{P}_n \cdot \overline{P}_n \cdot \overline{P}_n \cdot \lambda_5 \cdot \lambda_4 \cdot \left( \frac{e^{-\lambda_1 t}}{(\lambda_5^s - \lambda_1) \cdot (\lambda_4^s - \lambda_1)} + \frac{e^{-\lambda_5^s t}}{(\lambda_1 - \lambda_5^s) \cdot (\lambda_4^s - \lambda_5^s)} + \frac{e^{-\lambda_4 t}}{(\lambda_1 - \lambda_4) \cdot (\lambda_5^s - \lambda_4^s)} \right) \right] \quad (C.3)
\end{aligned}$$

## C.4 Isomeric ratios

Isotope	$I^\pi$	$E_{\text{level}}$ [keV]	$\tau_{\text{lit}}$	$E_\gamma$ [keV]	$R_{\text{exp},1}$ [%]	$R_{\text{exp},2}$ [%]	$R_{\text{exp},3}$ [%]	$R_{\text{exp},4}$ [%]	$R_{\text{exp},5}$ [%]	$R^{\text{th}}$ [%]
$^{122}\text{Ag}$ $^{123}\text{Ag}$	1 <sup>+</sup> 17/2 <sup>-</sup>	91 1473	9.1(1) $\mu\text{s}$ [8] 567(23) ns [8]	91	2.9(3)		4.8(7)			94.9
				Mean	19.6(17)		21.1(22)			10.5
$^{124}\text{Ag}$ $^{125}\text{Ag}$	3 <sup>+</sup> 17/2 <sup>-</sup>	230 1501	2.1(3) $\mu\text{s}$ [8] 684(50) ns [8]	349	21.9(33)		20.5(48)			
				685	19.0(29)		21.3(41)			
				769	17.9(29)		21.6(56)			
				Mean	2.1(4)				50.1	
				382	2.6(9)					
$^{126}\text{Ag}$ $^{125}\text{Cd}$	3 <sup>+</sup> (35/2 <sup>+</sup> )	254 3896	39(9) $\mu\text{s}$ [8] 4.5(1) $\mu\text{s}$ [3]	155	5.0(6)	4.5(8)				69.6
				Mean	16.2(17)	14.0(14)			7.1	
				683	16.7(29)	14.1(21)				
				728	15.9(26)	14.0(21)				
				254	0.9(2)	4.5(9)			64.9	
$^{126}\text{Cd}$	12 (19/2 <sup>+</sup> )	1462	19.6(3) $\mu\text{s}$ [3]	Mean	0.9(2)					0.0
				99	0.7(1)					
				786	1.0(1)					
				Mean	14.0(14)				3.2	
				487	14.0(17)					
$^{126}\text{Cd}$	12	2977+x	2480(100) ns [4]	720	14.0(13)					
				797	14.0(25)					
				Mean	0.9(1)	1.7(2)				
				652	0.9(4)	1.8(9)				
				815	0.9(4)	1.5(7)				

Table C.6: Isomeric Ratios for Ag, Cd, In and Sn isotopes.

Isotope	$J^\pi$	$E_{level}$ [keV]	$T_{1/2}$	$E_\gamma$ [keV]	$R_{exp,1}$ [%]	$R_{exp,2}$ [%]	$R_{exp,3}$ [%]	$R_{exp,4}$ [%]	$R_{exp,5}$ [%]	$R_{th}$ [%]
$^{127}\text{Cd}$	(19/2 <sup>+</sup> )	1560 + x	25.2(4) $\mu\text{s}$ [5]	Mean	14.7(8)	13.4(7)	8.7(19)			1.9
				711	14.7(15)	13.4(12)	5.7(23)			
				739	14.4(11)	13.7(10)	9.7(9)			
				821	15.1(12)	13.7(11)	10.8(11)			
				849	14.4(17)	12.9(14)	8.7(19)			
$^{128}\text{Cd}$	(10 <sup>+</sup> )	2714	5.14(9) $\mu\text{s}$ [6]	Mean	10.5(5)	9.2(4)	6.8(4)	6.2(3)	6.5(5)	0.7
				238	10.5(7)	9.3(5)	6.8(6)	6.0(4)	6.3(5)	
				537	10.6(9)	9.1(6)	6.7(6)	6.4(5)	6.8(6)	
				Mean	21.6(45)	18.7(31)	20.2(30)	26(5)	24(5)	26.1
				440	20.4(61)	20.6(40)	21.1(45)			
$^{130}\text{Cd}$	(8 <sup>+</sup> )	2130	317(43) ns [7]	646	22.3(59)	18.7(39)	19.8(42)			
				785	22.2(57)	17.1(36)	20.1(41)			
				Mean	14.8(17)	14.8(17)	18.0(25)	15.8(3)	16.0(4)	1.4
				539	16.7(42)	16.7(42)	20.4(52)			
				1325	13.1(33)	13.1(33)	15.5(39)			
$^{125}\text{In}$	21/2 <sup>-</sup>	2009.4 [30]	11(2) $\mu\text{s}$ [185]	Mean	5.0(3)					1.9
				737	5.0(7)					
				1173	5.1(7)					
				243	5.0(4)					
				Mean	4.9(3)					
$^{126}\text{In}$	1 <sup>-</sup> ???	243 [30] ??	29(2) $\mu\text{s}$ [185] 106(44) ns [185]	614	4.8(18)					93.0
				865	5.0(18)					
				Mean	5.0(19)					
				1067	5.0(19)					
				Mean	5.0(19)					

Table C.7: Same as table C.6

Isotope	$I^\pi$	$E_{\text{level}}$ [keV]	$\tau_{\text{fit}}$	$E_\gamma$ [keV]	$R_{\text{exp},1}$ [%]	$R_{\text{exp},2}$ [%]	$R_{\text{exp},3}$ [%]	$R_{\text{th}}$ [%]
$^{127}\text{In}$	(29/2 <sup>+</sup> )	(2364) [30]	18.0(7) $\mu\text{s}$ [185]	Mean	2.9(1)			0.0
				221	3.0(4)			
				233	2.8(4)			
		??	340(50) ns [185]	Mean	1.7(2)			
$^{128}\text{In}$	1 <sup>-</sup>	248 [30]	78(20) $\mu\text{s}$ [185]	248	5.3(13)			91.4
		??	226(187) $\mu\text{s}$ [185]	323	8.3(66)			
		1688 [30]	16.0(4) $\mu\text{s}$ [185]	Mean	10.2(9)	11.2(9)	9.0(6)	1.6
$^{129}\text{In}$	17/2 <sup>-</sup>			332	9.7(7)	10.3(9)	8.6(7)	
				359	10.8(9)	11.1(11)	9.3(9)	
				995	11.1(11)	12.1(14)	9.5(10)	
				1354	9.2(12)	11.3(17)	8.5(13)	
$^{130}\text{In}$	3 <sup>+</sup>	389 [30]	6.3(2) $\mu\text{s}$ [185]	389	4.8(15)	5.0(15)	5.0(15)	49.0
			910(90) ns [9]	3782		3.4(6)	3.4(6)	0.3
			317(43) ns [10]	Mean	6.0(1.0)			0.0
$^{131}\text{In}$	(17/2 <sup>+</sup> )			426	6.9(10)			
				1061	5.0(7)			
				321	18.3(21)			0.7
$^{128}\text{Sn}$	(10 <sup>+</sup> )	2492	4.3(2) $\mu\text{s}$ [10]	605	1.3(3)			0.0
			313(14) ns [10]	Mean	9.0(20)			16.8
			91(6) ns [10]	774	9.2(56)			
$^{130}\text{Sn}$	5 <sup>-</sup>	2552 [186]	2.165(25) $\mu\text{s}$ [10]	1221	8.8(54)			
				2084 [126]				
				2434 [126]	393	10.9(12)		0.1

Table C.8: Same as table C.6

# List of Figures

1.1	The region around the doubly magic $^{132}\text{Sn}$ and an overview what experimental information was available previous to this work as presented in Refs. [1,2]. . . . .	1
1.2	Comparison of the SPE (particles and holes) for protons ( $\pi$ ) and neutrons ( $\nu$ ) and the two doubly-magic nuclei $^{132}\text{Sn}$ and $^{208}\text{Pb}$ . . . . .	7
1.3	R Process Path. . . . .	8
1.4	Mass predictions for different models. . . . .	9
1.5	Experimental Cadmium half-lives for masses 126-134 obtained in previous works and comparison to different models. . . . .	11
1.6	Overview on known $\log ft$ values for superallowed, allowed, first and second forbidden transitions in $\beta$ -decay. . . . .	16
1.7	Schematic presentation of the proton and neutron orbitals near the $Z=50$ and $N=82$ shell gaps. The arrows indicate the most important Gamow-Teller (solid) and first forbidden (dashed) decays. . . . .	17
2.1	Schematic of abrasion fission, a method to produce radioactive ion beams. . . . .	20
2.2	Schematic of the RI Beam factory at RIKEN with the last step of the acceleration procedure, the super-conducting ring cyclotron (SRC), the two-stage fragment separator BigRIPS and the Zero-Degree Spectrometer. . . . .	21
2.3	Schematics of a parallel plate avalanche counter. . . . .	22
2.4	Schematic figure of one MUSIC, an ionisation chamber. . . . .	23
2.5	Identification plot of all implanted ions in a) the Pd Setting (RIBF 60&62 experiment) and in b) the Sn Setting (RIBF-85 experiment) at the RIKEN RIBF facility. . . . .	25
2.6	Identification plot showing the sum of both settings. The mass-to-charge ratio (AoQ) was measured in BigRIPS using the F3-F5 ToF measurement and nuclear charge was determined using the F11 ionization chamber. . . . .	25
2.7	Time interval distribution of two successive $^{129}\text{Cd}$ implantations, fitted by an exponential function. . . . .	26
2.8	Picture showing the active stopper WAS3ABi. . . . .	29
2.9	Schematic of WAS3ABi with its eight DSSSD and the additional Q-beta plastic and Q-veto detectors. . . . .	29

2.10	WAS3ABi electronics scheme. . . . .	29
2.11	Illustration of the method used to determine the implantation position in WAS3ABi. . . . .	30
2.12	Time distributions of all x strips in DSSSD 4 where the ion was implanted in DSSSD 4 x-strip 30. . . . .	31
2.13	Time distributions of all y strips in DSSSD 4 where the ion was implanted in DSSSD 4 y-strip 30. . . . .	31
2.14	Implantation pattern in a) x- and b) y-direction for the Pd and the Sn setting. . . . .	32
2.15	Projection of Fig. 2.14b) on a) the x- and b) the y-axis for the case of $^{130}\text{Cd}$ and the fitted Gaussian distribution. . . . .	33
2.16	$z_{imp}$ distribution for the Pd and the Sn setting. . . . .	34
2.17	Matrix for calibrating a single DSSSD strip showing the example of DSSSD 3 x-strip 20. . . . .	35
2.18	Illustration of the method to determine the interaction position of $\beta$ -like particles in WAS3ABi. . . . .	37
2.19	$\Delta z$ distribution of all $\beta$ decays correlated to the implanted Cadmium ions in a) the Pd setting and b) the Sn setting. . . . .	38
2.20	Zoom on the $\Delta x$ - $\Delta y$ pattern of all $\beta$ decays correlated to the implanted $^{130}\text{Cd}$ ions in the Pd setting. . . . .	39
2.21	$\Delta x$ - $\Delta y$ pattern of all $\beta$ decays correlated to the implanted Cadmium ions in a) the Pd setting and b) the Sn setting. . . . .	40
2.22	Picture of one half of the EURICA Array including the former Euroball cluster detectors and NaI detectors. . . . .	41
2.23	Picture of the other half of the EURICA Array including the former Euroball cluster detectors and the chamber with the active stopper WAS3ABi. . . . .	41
2.24	Schematic of the germanium detector and definition of the coordinate system. . . . .	42
2.25	Scheme of the electronics used for the read-out of the germanium detectors. . . . .	43
2.26	Time difference between two $\gamma$ -rays in the same cluster on the x-axis and the energy $E_{\Delta t}$ . . . . .	44
2.27	Absolute Efficiency of the EURICA Ge-Array without and with the Q-beta detector installed. . . . .	46
2.28	Absolute Efficiency of the EURICA Ge-Array without and with the add-back procedure applied. . . . .	47
2.29	Absolute Efficiency of the EURICA Ge-Array without and with the add-back procedure applied for up to 4.5 MeV. . . . .	48
2.30	Schematic of the merging process for the three data acquisition systems based on the timestamp of each system. . . . .	50

3.1	$\beta$ -delayed germanium spectra for the Cadmium isotopes with masses A=128-131. . . . .	54
3.2	Proposed level scheme for $^{128}\text{In}$ taken from Ref. [61]. . . . .	55
3.3	$\beta$ -Ge-energy-time matrix for the example of $^{128}\text{Cd}$ . . . . .	55
3.4	Basic $\beta$ -decay scheme of $^{128}\text{Cd}$ . . . . .	56
3.5	$\beta$ -delayed germanium spectra for first, second, third and fourth decay after a $^{128}\text{Cd}$ implantation. . . . .	57
3.6	Delayed Ge spectra recorded in coincidence with the implantation of a $^{130}\text{Cd}$ ion for different cluster and crystal multiplicities. . . . .	58
3.7	$\gamma$ - $\gamma$ matrix for the first $\beta$ decay correlated to an implanted $^{128}\text{Cd}$ ion. . . . .	59
3.8	Germanium spectra observed in prompt coincidence with the 67.9-keV, 247.6-keV and 857.1-keV transitions recorded in coincidence with the decay of the implanted $^{128}\text{Cd}$ ions . . . . .	60
3.9	Basic $\beta$ -decay scheme of $^{132}\text{In}$ . . . . .	63
3.10	Germanium spectra of all decays correlated to the implanted $^{132}\text{In}$ ions for different cuts. . . . .	64
3.11	Ge spectrum in coincidence with the first observed decay of the implanted $^{128}\text{Cd}$ ions. . . . .	66
3.12	Ge spectrum in prompt coincidence with the first decay of the implanted $^{129}\text{Cd}$ ions. . . . .	69
3.13	Germanium spectra observed in coincidence with the 334.1-, 995.1-, 1796.5-, 2155.6-, 1135.2- and 339.1-keV transitions in $^{129}\text{In}$ . . . . .	73
3.14	Germanium spectra observed in prompt coincidence with the 967.6-, 1422.9-, 1761.6-, 769.2-, 542.0-, 2460.9- or 1524.1-keV transition in $^{129}\text{In}$ . . . . .	75
3.15	Level scheme of $^{129}\text{In}$ as it was obtained in the present work through the measurement of the $^{129}\text{Cd}$ $\beta$ -decay. . . . .	78
3.16	Ge spectrum in coincidence with the first decay of the implanted $^{129}\text{Cd}$ ions after the observation of one of the four transitions observed in the de-excitation of the ms isomeric state in $^{129}\text{Cd}$ . . . . .	80
3.17	Ge spectrum in prompt coincidence with the first decay of the implanted $^{130}\text{Cd}$ ions. . . . .	83
3.18	Germanium spectra in prompt coincidence with the observation of the 1015.8-, 2739.0-, 498.7-, 949.9- and 2804.8-keV transitions in $^{130}\text{In}$ . . . . .	85
3.19	Level scheme of $^{130}\text{In}$ as it was obtained in the present work. . . . .	86
3.20	Ge spectrum in prompt coincidence with the first decay of the implanted $^{131}\text{Cd}$ ions. . . . .	89
3.21	Germanium spectrum in prompt coincidence with the observation of a 511-keV $\gamma$ ray after the decay of $^{131}\text{Cd}$ . . . . .	90
3.22	Ge spectrum in prompt coincidence with the first decay of the implanted $^{132}\text{Cd}$ ions. . . . .	91

3.23	Systematics of experimental and calculated energies of the $0f_{5/2}$ , $0g_{7/2}$ , $0h_{9/2}$ orbits with respect to the corresponding $1p$ , $1d$ and $1f$ spin-orbit partner orbitals in the vicinity of $^{78}\text{Ni}$ , $^{132}\text{Sn}$ and $^{208}\text{Pb}$ . . . . .	93
3.24	Germanium spectra observed in prompt coincidence with the 3555.2 keV, 3868.8 keV and 433.2-keV transitions in $^{131}\text{In}$ . . . . .	95
3.25	Comparison of the peak structure of the 5528 keV peak observed in the decay of $^{131}\text{Cd}$ with and without add-back. . . . .	95
3.26	$\gamma$ -spectrum in prompt coincidence with the first decay of the implanted $^{131}\text{Cd}$ ions and the coincidence spectrum with the 987.8-keV transition. . . . .	97
3.27	Level scheme of $^{131}\text{In}$ as it has been obtained in the present work. . . . .	98
3.28	Experimental and calculated level schemes for $^{131}\text{In}$ and $^{132}\text{Sn}$ . . . . .	100
3.29	Ge spectrum in prompt coincidence with the first decay of the implanted $^{133}\text{Cd}$ ions. . . . .	102
3.30	$\gamma\gamma$ coincidence spectra gated on the 50-, 86-, 103-, 227-, 357- and 602-keV transitions in $^{132}\text{In}$ . . . . .	104
4.1	Time distributions of all decays correlated to the implanted $^{128-131}\text{Cd}$ and $^{132,133}\text{Cd}$ ions within a 2s interval after the implantation. . . . .	108
4.2	Illustration of the basic decay scheme of $\beta$ -decays. . . . .	109
4.3	Half-lives determined with the MLH method for the $\beta$ decay of the $0^+$ g.s. in $^{130}\text{Cd}$ for different background rates and $\beta$ -decay efficiencies. . . . .	115
4.4	Illustration of the method to determine $\beta$ -decay half-lives with a gate on a $\gamma$ transition in the daughter nucleus. . . . .	116
4.5	Time distributions of the decays observed after an implantation of $^{132}\text{In}$ and $^{131}\text{In}$ gated on the observation of a 4041 keV and 2434 keV $\gamma$ -ray. . . . .	117
4.6	Time distributions of the decays observed after an $^{130}\text{Cd}$ implantation gated on the observation of a 451- or 1669-keV $\gamma$ -ray. . . . .	118
4.7	Time distribution of the decays correlated to the implanted $^{130}\text{Cd}$ Cadmium ions. . . . .	119
4.8	$\beta$ -decay efficiencies for different cuts. . . . .	124
4.9	Comparison of the experimental data with a Monte Carlo Simulation of the P.D.F. used for the MLH analysis. . . . .	125
4.10	Distribution of the negative log-likelihood for the decay of $^{130}\text{Cd}$ . . . . .	126
4.11	Time distributions of all decays correlated to the implanted $^{129}\text{Cd}$ ions with the Bateman equation fit. . . . .	127
4.12	Time distribution of all decays correlated within the first 200 ms to the implanted $^{129}\text{Cd}$ ions. . . . .	128
4.13	Time distributions of all decays correlated to the implanted $^{129}\text{Cd}$ ions with the Bateman equation fit 2. . . . .	129
4.14	Time distributions of the decays observed after an $^{129}\text{Cd}$ implantation gated on the observation of the 358.9, 995.1, 1354.2, 1796.5 or 2155.6 keV $\gamma$ -ray. . . . .	130

4.15	Time distribution of the decays observed after a $^{129}\text{Cd}$ implantation gated on the observation of either a 1422.9 or a 1586.2 keV $\gamma$ -ray. . . . .	130
4.16	Time distribution of all decays correlated to the implantation of a $^{129}\text{Cd}$ ion after the observation of one of the characteristic transitions emitted in the decay of the ms isomer in $^{129}\text{Cd}$ . . . . .	131
4.17	Time distributions of the decays of different Cadmium isotopes observed after an implantation gated on the observation of a specific $\gamma$ transition in the daughter nucleus. . . . .	133
4.18	Time distributions of the decays correlated to the implanted $^{126-128}\text{Cd}$ and $^{131-133}\text{Cd}$ ions. . . . .	134
4.19	Experimental Cadmium half-lives for masses 126-134 obtained in this work and previous works and comparison to different models. . . . .	137
4.20	Basic $\beta$ -decay schemes including $\beta$ -delayed neutron emission for the parent nucleus to visualize the $P_n$ determination method 1. . . . .	139
4.21	Basic $\beta$ -decay schemes including $\beta$ -delayed neutron emission for the parent nucleus to visualize the $P_n$ determination method 2. . . . .	140
4.22	Comparison between the experimentally obtained $P_n$ values in the present work to the literature values and different models. . . . .	142
5.1	Level scheme of $^{128}\text{Cd}$ as proposed in Ref. [6] and half-lives as measured in the present work. . . . .	144
5.2	Germanium energy versus time matrix for the example of $^{128}\text{Cd}$ . . . . .	145
5.3	$\gamma\gamma$ coincidence spectra gated on the 68-, 237-, 439-, 537-, 645- and 784-keV transitions in $^{128}\text{Cd}$ . . . . .	146
5.4	$\gamma\gamma$ coincidence spectra gated on the 449-, 764-, and 1223-keV transitions in $^{128}\text{Cd}$ . . . . .	147
5.5	Delayed germanium spectrum of $^{128}\text{Cd}$ from 210 to 260 keV to illustrate the used gates (peak and background gates) for the time distribution of the 237-keV transition shown in Fig. 5.6. . . . .	150
5.6	Example for a timing distribution obtained from the DGF timing as described in the text for the example of $^{128}\text{Cd}$ and gated on the 237-keV transition. . . . .	150
5.7	Time distribution relative to the ion implantation of the 537-keV, 439-, 645- and 784-keV transitions in $^{128}\text{Cd}$ . . . . .	151
5.8	Time difference $\Delta t$ distributions of the 439-, 645- and 784-keV transitions to the 237- and 537-keV transitions. . . . .	152
5.9	Centroids of the time distributions for the $2^+$ , $4^+$ states and the state between the 537- and 237-keV transitions in $^{128}\text{Cd}$ and the zero-line. . . . .	154
5.10	Time difference $\Delta t_{\gamma\gamma}$ distributions of the 537-keV transitions to the 237-keV transition in $^{128}\text{Cd}$ . . . . .	154
5.11	Germanium spectrum recorded in coincidence with the decays correlated to the $^{129}\text{Cd}$ ions. . . . .	155

5.12	Germanium spectra observed in prompt coincidence with the 353-keV, 406-keV, 1181-keV and 1587-keV transitions within the first 20 ms after an $^{129}\text{Cd}$ implantation. . . . .	156
5.13	Sum time distribution of the 406-keV and 1181-keV transitions observed in $^{129}\text{Cd}$ and in red the fitted single exponential decay function. . . . .	156
5.14	Time distributions gated on the 353-, 406-, 1181- and 1587-keV transition observed in delayed coincidence with the implanted $^{129}\text{Cd}$ . . . . .	157
5.15	DSSSD spectra recorded in the first 10 ms and from 30 to 40 ms after the implantation of a $^{129}\text{Cd}$ ion. . . . .	158
5.16	Germanium spectrum of decay events recorded in the first 10 ms after a $^{129}\text{Cd}$ implantation gated on the DSSSD energy. . . . .	159
5.17	DSSSD energy spectra for all decays correlated to the $^{129}\text{Cd}$ ions with the energies taken from the DSSSD x- or y- side and the Pd-Setting or the Sn-Setting. . . . .	159
5.18	DSSSD energy spectra obtained from the Monte-Carlo simulation without taking into account the detector resolution. . . . .	161
5.19	DSSSD energy spectra obtained from the Monte-Carlo simulation and comparison to experimental spectra. . . . .	162
5.20	Ge spectrum in delayed coincidence with the implanted $^{129}\text{Cd}$ ions. . . . .	164
5.21	Time distribution of the 3693-keV transition and in red the fitted single exponential decay function. . . . .	165
5.22	Level scheme of $^{130}\text{Cd}$ as proposed in Ref. [7]. . . . .	166
5.23	Ge spectrum in delayed coincidence with the implanted $^{130}\text{Cd}$ ions and $\gamma\gamma$ coincidence spectra. . . . .	167
5.24	Time difference $\Delta t_{\gamma\gamma}$ distributions for different transitions in $^{130}\text{Cd}$ . . . . .	168
5.25	Time difference $\Delta t_{\gamma\gamma}$ matrix gated on the 539-keV transition. . . . .	169
5.26	Time distributions relative to the ion implantation of the 128-, 138-, 539- and 1325-keV transitions in $^{130}\text{Cd}$ . . . . .	169
5.27	Isomeric ratio as a function of the spin of the isomeric state for all five settings and the theoretical predictions by the sharp cut-off model for $^{122-126}\text{Ag}$ , $^{125-130}\text{Cd}$ , $^{125-131}\text{In}$ and $^{128-130}\text{Sn}$ . . . . .	174
5.28	Isomeric ratio as a function of the excitation energy of the isomeric state for all five settings and the theoretical predictions by the sharp cut-off model for $^{122-126}\text{Ag}$ , $^{125-130}\text{Cd}$ , $^{125-131}\text{In}$ and $^{128-130}\text{Sn}$ . . . . .	174
6.1	Experimental decay scheme for the $(21/2^+)$ ms isomeric state in $^{129}\text{Cd}$ and comparison to shell model calculations. . . . .	178
6.2	Partial level scheme of $^{129}\text{In}$ and comparison to the shell model calculation NA-14 and shell model calculations taken from Ref. [29]. . . . .	180
6.3	Comparison of the experimental and calculated energies of the first excited $2^+$ state and the two proton gap $\Delta_{2P}$ for the even $N=50$ and $N=82$ isotones. . . . .	181

6.4	Experimentally determined two neutron gap $\Delta_{2n}$ for the N=50 isotones in the range from Z=28 to Z=50 and two neutron separation energy $S_{2n}$ for the N=50,52,82 and 84 isotones. . . . .	183
8.1	La región alrededor del doblemente mágico núcleo $^{132}\text{Sn}$ y la información experimental disponible antes del experimento presentado en esta tesis [1, 2]. . . . .	190
8.2	Esquema de niveles del $^{128}\text{In}$ , que se obtuvo en el presente trabajo a través de la medición de la desintegración $\beta$ del $^{128}\text{Cd}$ . . . . .	192
8.3	Esquema de niveles de $^{129}\text{In}$ , que se obtuvo en el presente trabajo a través de la medición de la desintegración $\beta$ del $^{129}\text{Cd}$ . . . . .	196
8.4	Esquema de niveles de $^{129}\text{In}$ obtenido, así como la comparación con el cálculo teórico del modelo de capas NA-14. . . . .	198
8.5	Esquema de niveles del $^{130}\text{In}$ , que se obtuvo en el presente trabajo a través de la medición de la desintegración $\beta$ de $^{130}\text{Cd}$ . . . . .	201
8.6	Comparación de los valores experimentales y calculados de las energías del primer $2^+$ estado ( $E(2^+)$ ) y la energía de separación de dos protones $\Delta_{2p}$ para los par N = 50 y N = 82 isótonos. . . . .	204
8.7	Vidas medias de los cadmios (A=126-134) obtenidas en este trabajo y los trabajos previos y las predicciones teóricas del modelos FRDM + QRPA y KTUY+GT2. . . . .	208
8.8	La comparación entre los valores de $P_n$ experimentalmente obtenidos en el presente trabajo con los valores de la literatura y predicciones de dos modelos, el modelo DF3+CQRPA y el modelo FRDM. . . . .	210
8.9	Esquema de niveles para el (21/2 <sup>+</sup> ) ms estado isomérico en el $^{129}\text{Cd}$ . . . . .	211
B.2	Schematic for the calculation of the angles of the detectors in the EURICA array. . . . .	223
B.3	Schematic for the calculation of the angles of the detectors in the EURICA array. . . . .	224
B.4	Schematic for the calculation of the angles of the detectors in the EURICA array. . . . .	224

## List of Tables

1.1	Classification of $\beta$ -decays and selection rules. . . . .	15
-----	----------------------------------------------------------------	----

2.1	Number of identified Cadmium ( $A=126-133$ ) ions in BigRIPS (Id Bigrips) in both settings, number of implanted Cadmium ions in WAS3ABi (Implantations) and the sum of implanted ions. . . . .	26
2.2	Number of identified Cadmium ( $A=126-133$ ) ions in both settings with at least one correlated $\beta$ decay (Id Beta) and sum of implanted Cadmium ions in WAS3ABi (Implantations). . . . .	27
2.3	List of calibration sources. . . . .	45
2.4	Average Efficiency of one crystal for each cluster with and without the Q-beta detector at 500 keV . . . . .	46
3.1	Intensities of selected transitions in $^{132}\text{Sn}$ populated after the $\beta$ -decay of $^{132}\text{In}$ . . . . .	62
3.2	List of $\gamma$ rays observed in the $\beta$ -decay of $^{128}\text{Cd}$ to $^{128}\text{In}$ . . . . .	66
3.3	Levels in $^{128}\text{In}$ populated by the $\beta$ -decay of $^{128}\text{Cd}$ . . . . .	67
3.4	List of $\gamma$ rays observed in the $\beta$ -decay of $^{129}\text{Cd}$ to $^{129}\text{In}$ . . . . .	72
3.5	Levels in $^{129}\text{In}$ populated by the $\beta$ -decay of $^{129}\text{Cd}$ . . . . .	79
3.6	List of $\gamma$ rays observed in the $\beta$ -decay of $^{130}\text{Cd}$ to $^{130}\text{In}$ . . . . .	84
3.7	Levels in $^{130}\text{In}$ populated in the $\beta$ -decay of $^{130}\text{Cd}$ . . . . .	87
3.8	List of peaks identified as single (SE) or double escape (DE) peaks in the spectrum shown in Fig. 3.20. . . . .	90
3.9	List of transitions in the decay of $^{131}\text{Cd}$ to $^{131}\text{In}$ . . . . .	94
3.10	List of levels observed in the decay of $^{131}\text{Cd}$ to $^{131}\text{In}$ . . . . .	99
3.11	Energies and relative intensities of the transitions observed in the decay of $^{133}\text{Cd}$ to $^{132}\text{In}$ . The theoretical conversion coefficients $\alpha_{th}$ [99] are stated assuming M1 transitions and $I_{\gamma}^{corr}$ are the relative intensities corrected for those conversion coefficients. . . . .	103
4.1	Summary of the half-lives from $\beta$ -decaying isomeric states in $^{131}\text{In}$ and $^{132}\text{In}$ . . . . .	118
4.2	Summary of the input parameters e.g. half-lives and $\beta$ -delayed neutron emission probabilities as they were used for the $^{130}\text{Cd}$ MLH analysis. . . . .	120
4.3	Summary of the number of parent decays $N_{decay}$ , the $\beta$ -decay efficiency $\epsilon_1$ and the background rate $b$ for all Cadmium isotopes. . . . .	123
4.4	Deduced $T_{1/2}$ values for the g.s. $0^+$ $\beta$ -decay in $^{130}\text{Cd}$ with the MLH method. . . . .	126
4.5	Summary of the fit results for the half-lives of $^{129}\text{Cd}$ obtained from the $\gamma$ -gated time distributions. . . . .	131
4.6	Summary of the half-lives obtained from the $\gamma$ -gated time distributions for several transitions in $^{126-132}\text{In}$ . . . . .	135
4.7	Summary of the results for the half-lives obtained from the three presented methods. . . . .	136
4.8	Summary of the results for the $P_n$ obtained from the two methods in the present work. . . . .	142

5.1	Summary of transitions observed after the decay of the isomers in $^{128}\text{Cd}$ .	148
5.2	Half-lives of the ( $10^+$ ) ( $T_{long}$ ) and the ( $5^-$ ) isomeric states ( $T_{short}$ ).	152
5.3	Theoretical total conversion coefficients of the 353- and 406-keV transitions, calculated with Bricc [99] for various multipolarities.	160
5.4	Summary of transitions observed in delayed coincidence with the $^{130}\text{Cd}$ ions.	166
5.5	Summary of the isomeric ratios in A=126-130 Cadmium isotopes for the 5 different settings/production mechanisms.	173
5.6	Comparison of the experimentally obtained isomeric ratios in A=126-130 Cadmium isotopes to the theoretical predictions.	176
8.1	Listado de los $\gamma$ observados en la desintegración $\beta$ del $^{128}\text{Cd}$ al $^{128}\text{In}$ .	191
8.2	Los niveles en $^{128}\text{In}$ que es poblado por las desintegraciones $\beta$ de $^{128}\text{Cd}$ .	192
8.3	Lista de los $\gamma$ observados en la desintegración $\beta$ del $^{129}\text{Cd}$ al $^{129}\text{In}$ .	195
8.4	Los niveles en el $^{129}\text{In}$ alimentado por las desintegraciones $\beta$ del $^{129}\text{Cd}$ .	197
8.5	Lista de los $\gamma$ observados en la desintegración $\beta$ del $^{130}\text{Cd}$ al $^{130}\text{In}$ .	200
8.6	Los niveles en el $^{130}\text{In}$ poblado por las desintegraciones $\beta$ del $^{130}\text{Cd}$ .	202
8.7	Listado de los $\gamma$ observados en la desintegración $\beta$ del $^{131}\text{Cd}$ al $^{131}\text{In}$ .	203
8.8	Los niveles en el $^{131}\text{In}$ poblado por las desintegraciones $\beta$ del $^{131}\text{Cd}$ .	204
8.9	Listado de los $\gamma$ observados en la desintegración $\beta$ del $^{133}\text{Cd}$ con su energía y las intensidades relativas.	206
8.10	Resumen de los resultados para el periodo de semidesintegración, obtenidas de los tres métodos presentados.	207
8.11	Resumen de los resultados para los $P_n$ obtenidos mediante los dos métodos en el presente trabajo.	209
8.12	Resumen de las energías, las intensidades relativas y los coeficientes de conversión de las transiciones observadas en coincidencia retardada con los iones de $^{128}\text{Cd}$ .	211
8.13	Resumen de las energías, las intensidades relativas y los coeficientes de conversión de las transiciones observadas en coincidencia retardada con los iones de $^{130}\text{Cd}$ .	212
A.1	Latest Germanium calibration.	218
A.2	Latest Germanium calibration.	219
B.1	Position of the central crystal of each germanium detector in the spherical coordinate system.	221
B.2	Angles of the detectors in the EURICA array.	225
B.3	Angles of the detectors in the EURICA array.	226
C.1	Coefficients of the fits of the absolute efficiency calibration. Sources = $^{152}\text{Eu} + ^{133}\text{Ba}$ .	227
C.2	Coincidences (* = delayed coincidence) observed for the transitions in $^{128}\text{In}$ , populated after the $\beta$ decay of $^{128}\text{Cd}$ .	227

---

C.3	Coincidences (* = delayed coincidence) observed for the transitions in $^{129}\text{In}$ , populated after the $\beta$ decay of $^{129}\text{Cd}$ . . . . .	228
C.4	Coincidences (* = delayed coincidence) observed for the transitions in $^{129}\text{In}$ , populated after the $\beta$ decay of $^{129}\text{Cd}$ . . . . .	229
C.5	Coincidences (* = delayed coincidence) observed for the transitions in $^{130}\text{In}$ , populated after the $\beta$ decay of $^{130}\text{Cd}$ . . . . .	230
C.6	Isomeric Ratios for Ag, Cd, In and Sn isotopes. . . . .	233
C.7	Same as table C.6 . . . . .	234
C.8	Same as table C.6 . . . . .	235



# Bibliography

- [1] M. Wang *et al.*, Chinese Physics C **36**, 1603 (2012).
- [2] NNDC ENSDF, <http://www.nndc.bnl.gov/ensdf/>, Accessed: 2015-01-20.
- [3] F. Naqvi, *Probing the collectivity in neutron-rich Cd isotopes via  $\gamma$ -ray spectroscopy*, PhD thesis, University of Cologne, 2011.
- [4] L. Cáceres, *Nuclear structure studies in the vicinity of the double-magic  $^{132}\text{Sn}$  nucleus*, PhD thesis, Universidad Autónoma de Madrid, 2008.
- [5] F. Naqvi *et al.*, Phys. Rev. C **82**, 034323 (2010).
- [6] L. Cáceres *et al.*, Phys. Rev. C **79**, 011301 (2009).
- [7] A. Jungclaus *et al.*, Phys. Rev. Lett. **99**, 132501 (2007).
- [8] S. Lalkovski *et al.*, Phys. Rev. C **87**, 034308 (2013).
- [9] M. Górska *et al.*, Physics Letters B **672**, 313 (2009).
- [10] S. Pietri *et al.*, Phys. Rev. C **83**, 044328 (2011).
- [11] G. S. Simpson *et al.*, Phys. Rev. Lett. **113**, 132502 (2014).
- [12] H. Watanabe *et al.*, Phys. Rev. Lett. **111**, 152501 (2013).
- [13] H. Watanabe *et al.*, Phys. Rev. Lett. **113**, 042502 (2014).
- [14] G. Lorusso, submitted to Phys. Rev. Lett. (2014).
- [15] J. Dobaczewski, I. Hamamoto, W. Nazarewicz, and J. A. Sheikh, Phys. Rev. Lett. **72**, 981 (1994).
- [16] B. Pfeiffer, K. Kratz, and F. Thielemann, Zeitschrift für Physik A Hadrons and Nuclei **357**, 235 (1997).
- [17] B. Chen *et al.*, Physics Letters B **355**, 37 (1995).
- [18] H. Grawe, K. Langanke, and G. Martínez-Pinedo, Reports on Progress in Physics **70**, 1525 (2007).

- [19] Y.-Z. Qian, Nuclear Physics A **752**, 550 (2005), Proceedings of the 22nd International Nuclear Physics Conference (Part 2).
- [20] I. Dillmann *et al.*, Phys. Rev. Lett. **91**, 162503 (2003).
- [21] T. Kautzsch, Eur. Phys. J. A **9**, 201 (2000).
- [22] H. Grawe, Shell Model from a Practitioner's Point of View, in *The Euroschool Lectures on Physics with Exotic Beams, Vol. I*, edited by J. Al-Khalili and E. Roeckl, , Lecture Notes in Physics Vol. 651, pp. 33–75, Springer Berlin Heidelberg, 2004.
- [23] T. Otsuka, Shell structure of exotic nuclei, in *The Euroschool Lectures on Physics with Exotic Beams, Vol. III*, edited by J. Al-Khalili and E. Roeckl, , Lecture Notes in Physics Vol. 764, pp. 1–25, Springer Berlin Heidelberg, 2009.
- [24] O. Haxel, J. H. D. Jensen, and H. E. Suess, Phys. Rev. **75**, 1766 (1949).
- [25] M. G. Mayer, Phys. Rev. **75**, 1969 (1949).
- [26] M. G. Mayer, Phys. Rev. **74**, 235 (1948).
- [27] P. Brussaard and P. W. M. Glaudemans, *Shell model applications in nuclear spectroscopy* (North-Holland, Amsterdam, 1977).
- [28] P. Möller, J. R. Nix, and K.-L. Kratz, At. Data Nucl. Data Tab. **66**, 131 (1997).
- [29] J. Genevey *et al.*, Phys. Rev. C **67**, 054312 (2003).
- [30] A. Scherillo *et al.*, Phys. Rev. C **70**, 054318 (2004).
- [31] G. S. Simpson *et al.*, Journal of Physics: Conference Series **267**, 012031 (2011).
- [32] R. Machleidt, Phys. Rev. C **63**, 024001 (2001).
- [33] L. Coraggio, A. Covello, A. Gargano, N. Itaco, and T. T. S. Kuo, Phys. Rev. C **66**, 064311 (2002).
- [34] M. Hannawald *et al.*, Phys. Rev. C **62**, 054301 (2000).
- [35] M. Hjorth-Jensen, T. T. Kuo, and E. Osnes, Physics Reports **261**, 125 (1995).
- [36] B. A. Brown *et al.*, MSU-NSCL report 1289 (2009).
- [37] E. Caurier, G. Martínez-Pinedo, F. Nowacki, A. Poves, and A. P. Zuker, Rev. Mod. Phys. **77**, 427 (2005).
- [38] H. Huck *et al.*, Phys. Rev. C **24**, 2227 (1981).
- [39] B. Fogelberg and J. Blomqvist, Nuclear Physics A **429**, 205 (1984).
- [40] B. Fogelberg and J. Blomqvist, Physics Letters B **137**, 20 (1984).
- [41] B. Fogelberg *et al.*, Phys. Rev. C **70**, 034312 (2004).

- [42] P. Hoff *et al.*, *Hyperfine Interactions* **129**, 141 (2000).
- [43] P. Hoff *et al.*, *Phys. Rev. Lett.* **77**, 1020 (1996).
- [44] K. L. Jones *et al.*, *Nature* **465**, 454 (2010).
- [45] J. Blomqvist, A. Kerek, and B. Fogelberg, *Zeitschrift für Physik A Atoms and Nuclei* **314** (1983).
- [46] M. Sanchez-Vega *et al.*, *Phys. Rev. C* **60**, 024303 (1999).
- [47] B. Fogelberg *et al.*, *Physics Letters B* **209**, 173 (1988).
- [48] A. Kankainen *et al.*, *Phys. Rev. C* **87**, 024307 (2013).
- [49] O. Sorlin and M.-G. Porquet, *Progress in Particle and Nuclear Physics* **61**, 602 (2008).
- [50] Board on Physics and Astronomy, *Connecting quarks with the cosmos: 11 science questions for the new century* (US. National Academy Press, Washington, DC, 2003).
- [51] NNDC NUDAT 2, <http://www.nndc.bnl.gov/nudat2/>, Accessed: 2015-02-23.
- [52] S. Goriely, N. Chamel, and J. M. Pearson, *Phys. Rev. C* **88**, 024308 (2013).
- [53] A. Arcones and G. Martínez-Pinedo, *Phys. Rev. C* **83**, 045809 (2011).
- [54] Surman, R. *et al.*, *EPJ Web of Conferences* **66**, 07024 (2014).
- [55] R. Surman, M. R. Mumpower, J. Cass, and A. Aprahamian, The Sensitivity of r-PROCESS Nucleosynthesis to the Properties of Neutron-Rich Nuclei, in *Fission and Properties of Neutron-Rich Nuclei - Proceedings of the Fifth International Conference on ICFN5.*, edited by J. H. Hamilton and V. Ramayya Akunuri, pp. 538–545, World Scientific Publishing Co. Pte. Ltd., 2014, 1309.0058.
- [56] M. Mumpower, R. Surman, M. Beard, D. L. Fang, and A. Aprahamian, (2014), arXiv:1411.3978.
- [57] P. Möller, J. R. Nix, W. D. Myers, and W. J. Swiatecki, *At. Data Nucl. Data Tab.* **59**, 185 (1995).
- [58] P. Möller, W. D. Myers, H. Sagawa, and S. Yoshida, *Phys. Rev. Lett.* **108**, 052501 (2012).
- [59] M. L. Gartner and J. C. Hill, *Phys. Rev. C* **18**, 1463 (1978).
- [60] G. Audi, O. Bersillon, J. Blachot, and A. Wapstra, *Nuclear Physics A* **729**, 3 (2003), The 2003 {NUBASE} and Atomic Mass Evaluations.
- [61] B. Fogelberg, in *Proc. Intern. Conf. Nuclear Data for Science and Technology*, p. 873, Mito, Japan, 1988.

- [62] O. Arndt *et al.*, *Acta Phys.Pol.* **B40**, 437 (2009).
- [63] P. Möller, B. Pfeiffer, and K.-L. Kratz, *Phys. Rev. C* **67**, 055802 (2003).
- [64] H. Koura, T. Tachibana, M. Uno, and M. Yamada, *Progress of Theoretical Physics* **113**, 305 (2005).
- [65] T. Tachibana, International Conference on Exotic Nuclei and Atomic Masses, Arles, France, in *Proceedings of ENAM 95*, p. 763, 1995.
- [66] T. Tachibana, M. Yamada, and Y. Yoshida, *Progress of Theoretical Physics* **84**, 641 (1990), <http://ptp.oxfordjournals.org/content/84/4/641.full.pdf+html>.
- [67] I. N. Borzov, *Phys. Rev. C* **67**, 025802 (2003).
- [68] I. Borzov, J. Cuenca-García, K. Langanke, G. Martínez-Pinedo, and F. Montes, *Nuclear Physics A* **814**, 159 (2008).
- [69] P. Möller and J. Randrup, *Nuclear Physics A* **514**, 1 (1990).
- [70] R. Casten, *Nuclear structure from a simple perspective*. Oxford studies in nuclear physics 23, 2. ed. (Oxford University Press, (New York), 2005).
- [71] J. Krumlinde and P. Möller, *Nuclear Physics A* **417**, 419 (1984).
- [72] K. Takahashi, *Progress of Theoretical Physics* **47**, 1500 (1972).
- [73] K. Takahashi, M. Yamada, and T. Kondoh, *Atomic Data and Nuclear Data Tables* **12**, 101 (1973).
- [74] S. Fayans, S. Tolokonnikov, E. Trykov, and D. Zawischa, *Nuclear Physics A* **676**, 49 (2000).
- [75] A. B. Migdal and S. A. Moszkowski, *American Journal of Physics* **36**, 855 (1968).
- [76] W. Pauli, *Rapports du Septieme Conseil de Physique Solvay*, Brussels, 1933.
- [77] F. Reines and C. L. Cowan, *Nature* **178**, 446 (1956).
- [78] E. Fermi, *Zeitschrift für Physik* **88**, 161 (1934).
- [79] K. S. Krane, *Introductory Nuclear Physics*, 3. ed. (Wiley and Sons, New York, 1988).
- [80] B. Singh, J. Rodriguez, S. Wong, and J. Tuli, *Nuclear Data Sheets* **84**, 487 (1998).
- [81] T. Bjornstad *et al.*, *Nuclear Physics A* **453**, 463 (1986).
- [82] B. Fogelberg *et al.*, *Phys. Rev. Lett.* **73**, 2413 (1994).
- [83] P. Van Duppen, Isotope separation on line and post acceleration, in *The Euroschool Lectures on Physics with Exotic Beams, Vol. II*, edited by J. Al-Khalili and E. Roeckl, , Lecture Notes in Physics Vol. 700, pp. 37–77, Springer Berlin Heidelberg, 2006.

- [84] A. S. Nettleton, *A study of the fragmentation-fission of  $^{238}\text{U}$  on a  $^9\text{Be}$  target at 81 MeV/u*, PhD thesis, Michigan State University, 2011.
- [85] M. Bernas *et al.*, *Physics Letters B* **331**, 19 (1994).
- [86] Y. Yano, *Nuclear Instruments and Methods in Physics Research Section B: Beam Interactions with Materials and Atoms* **261**, 1009 (2007), *The Application of Accelerators in Research and Industry Proceedings of the Nineteenth International Conference on The Application of Accelerators in Research and Industry Nineteenth International Conference on The Application of Accelerators in Research and Industry*.
- [87] T. Kubo, *Nuclear Instruments and Methods in Physics Research Section B: Beam Interactions with Materials and Atoms* **204**, 97 (2003), *14th International Conference on Electromagnetic Isotope Separators and Techniques Related to their Applications*.
- [88] T. Ohnishi *et al.*, *Journal of the Physical Society of Japan* **79**, 073201 (2010).
- [89] H. Kumagai *et al.*, *Nuclear Instruments and Methods in Physics Research Section A: Accelerators, Spectrometers, Detectors and Associated Equipment* **470**, 562 (2001).
- [90] R. Schneider and A. Stolz, *Technical Manual Ionisation Chamber MUSIC80*, 2000.
- [91] S. Nishimura *et al.*, *RIKEN Accel. Progr. Rep.* **46**, 182 (2013).
- [92] P.-A. Söderström *et al.*, *Nuclear Instruments and Methods in Physics Research Section B: Beam Interactions with Materials and Atoms* **317**, **Part B**, 649 (2013), *XVth International Conference on ElectroMagnetic Isotope Separators and Techniques Related to their Applications*, December 2–7, 2012 at Matsue, Japan.
- [93] J. Wu *et al.*,  *$\beta$ -decay of neutron-rich  $Z=60$  nuclei and the origin of rare earth elements*, *AIP Conference Proceedings Vol. 1594*, pp. 388–393, 2014.
- [94] G. Lorusso *et al.*,  *$\beta$ -decay spectroscopy at RIBF- The EURICA project*, *AIP Conference Proceedings Vol. 1594*, pp. 370–379, 2014.
- [95] S. Nishimura, *Progress of Theoretical and Experimental Physics* **03C006** (2012).
- [96] EURICA Page, <http://ribf.riken.jp/EURICA/index.php?Ancillary%20Detectors>, Accessed: 2015-02-20.
- [97] Z. Xu, *Beta-decay spectroscopy on neutron-rich nuclei in a range of  $Z = 26 - 32$* , PhD thesis, The University of Tokyo, 2014.
- [98] C. Hinke, *Spectroscopy of the doubly magic nucleus  $^{100}\text{Sn}$  and its decay*, PhD thesis, Technischen Universität München, 2010.

- [99] T. Kibédi *et al.*, Nuclear Instruments and Methods in Physics Research Section A: Accelerators, Spectrometers, Detectors and Associated Equipment **589**, 202 (2008).
- [100] J. Eberth *et al.*, Progress in Particle and Nuclear Physics **28**, 495 (1992).
- [101] S. Pietri, Acta Physica Polonica, B **38**, 1255 (2007).
- [102] RADWARE, <http://radware.phy.ornl.gov/main.html>, Accessed: 2014-10-01.
- [103] H. Baba *et al.*, RIKEN Accel. Progr. Rep. **43**, 222 (2009).
- [104] H. Baba *et al.*, Nuclear Instruments and Methods in Physics Research Section A: Accelerators, Spectrometers, Detectors and Associated Equipment **616**, 65 (2010).
- [105] H. G. Essel, in *IEEE Trans. NS NS-43*, 143, 1996.
- [106] H. G. Essel and N. Kurz, in *IEEE Trans. NS NS-47*, 337, 2000.
- [107] J. Adamczewski-Musch *et al.*, Go4 Introduction v.4.5, 16.08.2011.
- [108] H. Göktürk, B. Ekström, E. Lund, and B. Fogelberg, Zeitschrift für Physik A Atomic Nuclei **324**, 117 (1986).
- [109] J. Hardy, L. Carraz, B. Jonson, and P. Hansen, Physics Letters B **71**, 307 (1977).
- [110] H. Mach *et al.*, Nuclear Physics A **588**, c179 (1995), Proceedings of the Fifth International Symposium on Physics of Unstable Nuclei.
- [111] LOGFT, <http://www.nndc.bnl.gov/logft/>, Accessed: 2014-12-05.
- [112] O. Arndt, Kernspektroskopische Untersuchungen in der  $^{132}\text{Sn}$ -Region, Diploma thesis, Universität Mainz, 2003.
- [113] O. Arndt *et al.*, Annual Reports of the Institute for Nuclear Chemistry, University of Mainz, Germany, A15, 2003.
- [114] I. Dillmann *et al.*, Annual Reports of the Institute for Nuclear Chemistry, University of Mainz, Germany, A14, 2003.
- [115] K.-L. Kratz *et al.*, The European Physical Journal A - Hadrons and Nuclei **25**, 633 (2005).
- [116] D. T. Yordanov *et al.*, Phys. Rev. Lett. **110**, 192501 (2013).
- [117] L. E. De Geer and G. B. Holm, Phys. Rev. C **22**, 2163 (1980).
- [118] B. Fogelberg, H. Mach, H. Gausemel, J. P. Omtved, and K. A. Mezilev, Nuclear Fission and Fission-Product Spectroscopy, AIP Conf. Proc. No. 447, p. 191, AIP, Melville, NY, 1998.
- [119] H. Gausemel *et al.*, Phys. Rev. C **69**, 054307 (2004).

- [120] J. Genevey *et al.*, Phys. Rev. C **65**, 034322 (2002).
- [121] H. Huck *et al.*, Phys. Rev. C **39**, 997 (1989).
- [122] P. Hoff, B. Ekström, H. Göktürk, and B. Fogelberg, Nuclear Physics A **459**, 35 (1986).
- [123] I. Dillmann *et al.*, Annual Reports of the Institute for Nuclear Chemistry, University of Mainz, Germany, A16, 2002.
- [124] I. Dillmann *et al.*, Annual Reports of the Institute for Nuclear Chemistry, University of Mainz, Germany, A18, 2002.
- [125] I. Dillmann, Kernspektroskopische Untersuchungen am N=82 r-Prozess "Waiting-Point"-Nuklid  $^{130}\text{Cd}$ , Diploma thesis, Johannes-Gutenberg-Universität, 2002.
- [126] B. Fogelberg, K. Heyde, and J. Sau, Nuclear Physics A **352**, 157 (1981).
- [127] J. Taprogge *et al.*, Phys. Rev. Lett. **112**, 132501 (2014).
- [128] J. Taprogge *et al.*, Phys. Rev. Lett. **113**, 049902 (2014).
- [129] J. Duflo and A. P. Zuker, Phys. Rev. C **59**, R2347 (1999).
- [130] G. Rudstam, K. Aleklett, and L. Sihver, Atomic Data and Nuclear Data Tables **53**, 1 (1993).
- [131] J. Pearson, R. Nayak, and S. Goriely, Physics Letters B **387**, 455 (1996).
- [132] A. Covello, L. Coraggio, A. Gargano, and N. Itaco, Physics of Atomic Nuclei **67**, 1611 (2004).
- [133] L. Coraggio, A. Covello, A. Gargano, N. Itaco, and T. Kuo, Progress in Particle and Nuclear Physics **62**, 135 (2009).
- [134] L. Coraggio, A. Covello, A. Gargano, and N. Itaco, Phys. Rev. C **85**, 034335 (2012).
- [135] L. Coraggio, A. Covello, A. Gargano, and N. Itaco, Phys. Rev. C **70**, 034310 (2004).
- [136] J. Berkson, Ann. Statist. **8**, 457 (1980).
- [137] H. Bateman, Cambr. Phil Soc. Proc. **5**, 423 (1910).
- [138] P. Bevington and D. K. Robinson, *Data Reduction and Error Analysis for the Physical Sciences*, 3rd edition ed. (McGraw-Hill Science/Engineering/Math, 2012).
- [139] C. B. Hinke *et al.*, Nature **486**, 341 (2012).
- [140] P. T. Hosmer, *Beta-decay studies of  $^{78}\text{Ni}$  and other neutron-rich nuclei in the astrophysical r-process*, PhD thesis, Michigan State University, 2005.
- [141] Z. Y. Xu *et al.*, Phys. Rev. Lett. **113**, 032505 (2014).

- [142] RooFit, <http://roofit.sourceforge.net>, Accessed: 2014-02-14.
- [143] TMinuit-function minimization and error analysis reference manual 94.1, [hep.fi.infn.it/minuit.pdf](http://hep.fi.infn.it/minuit.pdf), Accessed: 2014-02-11.
- [144] D. K. W. Verkerke, Roofit users manual v2.07, [http://roofit.sourceforge.net/docs/RooFit\\_Users\\_Manual\\_2.07-29.pdf](http://roofit.sourceforge.net/docs/RooFit_Users_Manual_2.07-29.pdf), 2006.
- [145] F. James, Minuit - function minimization and error analysis reference manual version 94.1, <http://hep.fi.infn.it/minuit.pdf>, 1994.
- [146] A. Stolz, PhD thesis, Technischen Universitat Munchen, 2001.
- [147] M. Hannawald *et al.*, Nuclear Physics A **688**, 578 (2001), Nuclei in the Cosmos.
- [148] B. Pfeiffer, K.-L. Kratz, and P. Möller, Progress in Nuclear Energy **41**, 39 (2002).
- [149] D. Testov, *Effect of shell closure  $N = 50$  and  $N = 82$  on the structure of very neutron-rich nuclei produced at ALTO. Measurements of neutron emission probabilities and half lives of nuclei at astrophysical  $r$ -processes path*, PhD thesis, Université Paris Sud, 2014.
- [150] B. Fogelberg and P. Carlé, Nuclear Physics A **323**, 205 (1979).
- [151] R. Anholt *et al.*, Phys. Rev. A **33**, 2270 (1986).
- [152] R. Anholt *et al.*, Phys. Rev. Lett. **53**, 234 (1984).
- [153] N. Hoteling *et al.*, Phys. Rev. C **76**, 044324 (2007).
- [154] Z. Bay, Phys. Rev. **77**, 419 (1950).
- [155] W. Andrejtscheff, M. Senba, N. Tsoupas, and Z. Ding, Nuclear Instruments and Methods in Physics Research **204**, 123 (1982).
- [156] W. R. Leo, *Techniques for Nuclear and Particle Physics Experiments*, 2nd rev. ed. ed. (Springer-Verlag Berlin Heidelberg, 1994).
- [157] J. Taprogge *et al.*, Physics Letters B **738**, 223 (2014).
- [158] E. Nacher, Private Communication, 2013.
- [159] S. Agostinelli *et al.*, Nuclear Instruments and Methods in Physics Research Section A: Accelerators, Spectrometers, Detectors and Associated Equipment **506**, 250 (2003).
- [160] M. Górska *et al.*, Phys. Rev. Lett. **79**, 2415 (1997).
- [161] A. Blazhev *et al.*, Phys. Rev. C **69**, 064304 (2004).
- [162] M. Pfützner *et al.*, Phys. Rev. C **65**, 064604 (2002).
- [163] K. A. Gladnishki *et al.*, Phys. Rev. C **69**, 024617 (2004).

- [164] M. de Jong *et al.*, Nuclear Physics A **628**, 479 (1998).
- [165] M. de Jong, A. Ignatyuk, and K.-H. Schmidt, Nuclear Physics A **613**, 435 (1997).
- [166] J. R. Huizenga and R. Vandenbosch, Phys. Rev. **120**, 1305 (1960).
- [167] R. Vandenbosch and J. R. Huizenga, Phys. Rev. **120**, 1313 (1960).
- [168] I. S. Grant and M. Rathle, Journal of Physics G: Nuclear Physics **5**, 1741 (1979).
- [169] H. Naik, S. Dange, R. Singh, S. Das, and R. Guin, Nuclear Physics A **648**, 45 (1999).
- [170] H. Grawe, Private Communication, 2014.
- [171] A. F. Lisetskiy, B. A. Brown, M. Horoi, and H. Grawe, Phys. Rev. C **70**, 044314 (2004).
- [172] T. Faestermann *et al.*, Progress in Particle and Nuclear Physics **69**, 85 (2013).
- [173] K.-H. Schmidt and D. Vermeulen, in *Atomic Masses and Fundamental Constants 6*, edited by J. A. Nolen and W. Benenson, pp. 119–128, Springer US, 1980.
- [174] N. Zeldes *et al.*, Nuclear Physics A **399**, 11 (1983).
- [175] J. Hakala *et al.*, Phys. Rev. Lett. **101**, 052502 (2008).
- [176] R. N. Wolf *et al.*, Phys. Rev. Lett. **110**, 041101 (2013).
- [177] T. Suda, Journal of Physics: Conference Series **267**, 012008 (2011).
- [178] FAIR, <http://www.fair-center.eu>, Accessed: 2015-02-11.
- [179] C. Sturm and H. Stöcker, Physics of Particles and Nuclei Letters **8**, 865 (2011).
- [180] B. Rubio *et al.*, International Journal of Modern Physics E **15**, 1979 (2006).
- [181] H. Geissel *et al.*, Nuclear Instruments and Methods in Physics Research Section B: Beam Interactions with Materials and Atoms **204**, 71 (2003).
- [182] AIDA Collaboration, Technical Report For the Design, Construction and Commissioning of the Advanced Implantation Detector Array (AIDA), [http://www2.ph.ed.ac.uk/%7Etd/AIDA/Design/tdr\\_aida.pdf](http://www2.ph.ed.ac.uk/%7Etd/AIDA/Design/tdr_aida.pdf), 2008, Accessed: 2015-02-11.
- [183] AnaRoot Manual, <https://ribf.riken.jp/RIBFDAQ>, Accessed: 2014-10-06.
- [184] J. Wu, Cluster position measurement report, Private Communication, 2013.
- [185] J. Taprogge *et al.*, to be published.
- [186] R. L. Lozeva *et al.*, Phys. Rev. C **77**, 064313 (2008).